



UiT The Arctic University of Norway

Faculty of Science and Technology

Department of Chemistry

**Structural characterisation and drug-lipid interaction
by NMR spectroscopy**

Fredrik Garnås Rylandsholm

A dissertation for the degree of Philosophiae Doctor

June 2024

*That's the trouble with science. It's never done. Always upending itself.
Ruining perfect systems for the little inconvenience of them being wrong.*

- Zahel to Kaladin, Rhythm of War chapter 15 by Brandon Sanderson

Acknowledgments

Research and writing can sometimes feel like a solitary experience, but this work would never have been here without all the incredible people supporting me and my work.

First and foremost, my supervisor Johan deserves a great deal of thanks for the incredible trust he has put in me by hiring me to this position and giving me the freedom to pursue all my different projects, while also giving me vital guidance and help, and making sure I am included in different collaborations.

A special thanks goes to John Sigurd for keeping an eye on my progress, fighting my case when needed, and for funding my projects and ideas.

Thank you, Lotte and Katja, for welcoming me in your group for a short while. It was good to work on new ideas in a fresh environment.

To Phil and Martin, thank you for including me in your projects and showing faith in my work. Thank you for all the scientific, and not so scientific, discussions throughout the years.

Thank you to all the people I've met throughout my years in Tromsø, and a special thanks goes to all the incredible people I've met through Dungeons and Dragons Adventurer's League Tromsø. Thank you for keeping me busy, for something other to think about than just my work, and for all the good memories.

A special thanks also goes out to the people who picked at the seams of this thesis: Jonina, Phil, and Miriam. Thank you all for your expedited feedback, without you this thesis would have been much messier.

Mom, Dad, Edvin, and Helene, I'm sorry I've not visited more, I've just been a little bit busy putting together this work.

And finally, to Hans. Thank you for keeping me afloat all this time, thank you for listening to me rant about something or tell you excitedly about an experiment that finally worked after the n^{th} attempt. I love you.



Lillehammer, May 2024

Table of Contents

Acknowledgments	III
Abstract	VIII
Sammendrag	X
Scientific environment	XII
List of papers	XIII
Summary of papers and author contributions	XIV
Abbreviations	XX
1. Introduction.....	1
1.1 From wonder drug to antimicrobial resistance crisis.....	1
1.2 Antimicrobial peptides	4
1.2.1 Structural properties of peptides	4
1.3 Bacterial membranes	8
1.4 Membrane interaction models	11
1.4.1 Pore model.....	12
1.4.2 Carpet model	13
1.4.3 Detergent model	14
1.4.4 Other activity models	14
1.5 Other AMP activities	15
1.6 Understanding the structure of natural products.....	17
1.7 NMR spectroscopy	20
1.7.1 <i>J</i> -coupling constants	21
1.7.2 Secondary chemical shifts	23
1.7.3 Nuclear Overhauser Effect	25
1.7.4 Anisotropy	30
1.8 Binding	39
1.8.1 Fluorescence.....	40

1.8.2	Microscale Thermophoresis	41
2.	Methodology	45
2.1	Synthesis of SMA-QA	45
2.2	Preparation of large multilamellar vesicles	45
2.3	Preparation of nanodiscs	46
2.4	Preparation of stretching gel	46
2.5	Evaluating against computational data	48
3.	Aims of the current thesis	49
4.	Results and discussion	51
4.1	Structure elucidation and antiproliferative activity of a new natural product, Commafric A (Paper I)	51
4.2	LPS as an initial target and barrier for cationic AMPs (Paper II)	55
4.2.1	Nuclear magnetic resonance	56
4.2.2	Antimicrobial activity	58
4.2.3	Surface plasmon resonance	58
4.2.4	Live-cell NMR	61
4.3	Peptide-lipid interactions (Paper III)	63
4.3.1	Synthesis of SMA-QA	63
4.3.2	Preparation of nanodiscs	66
4.3.3	Microscale Thermophoresis	66
4.3.4	K_D comparison	67
4.3.5	K_P and fluorescence intensity	69
4.3.6	Comparison between vesicles and nanodiscs	70
4.4	Cyclic Tetrapeptides containing a $\beta^{2,2}$ -amino acid (Paper IV)	73
4.4.1	Backbone conformation	73
4.5	Conformational studies of cyclic hexapeptides using VCD and NMR (Paper V)	76
4.5.1	Anisotropy	78

4.5.2	<i>J</i> -coupling.....	80
4.6	Peptide conformations by NMR (Paper VI).....	82
4.7	Alignment of SMA-QA nanodiscs (Paper VI).....	84
4.8	Future prospects.....	87
5.	Concluding remarks.....	89
	References.....	93

Abstract

Since the discovery of antimicrobial agents and the extensive use in infection treatment and prevention, antimicrobial resistance (AMR) has become a rapidly increasing problem. The World health organisation (WHO) surveys a wide range of human pathogens, including several multi-resistant pathogens causing infections with high morbidity and mortality. Emphasising the urgency of new treatment strategies, is the fact that WHO estimates that by 2050, antibiotic resistance will surpass deaths due to cancer, with up to 10 million people dying each year. There is a sore need for new alternatives and strategies. One prominent alternative is antimicrobial peptides (AMPs). AMPs are an integral part of life, as host-defence peptides, and are found in all domains of life. Bacteria have lower chance of developing resistance against AMPs, partially because of their diverse modes-of-action. This is therefore a promising strategy to prolong the potential usage of AMPs in future therapy. Since the discovery of AMPs, there has been extensive work revealing their modes-of-action and connections between structure and effect. As they are a diverse group of molecules, and their targets are even more complicated, there are still many things that are not yet fully understood. Expanding our knowledge regarding AMP-target interactions, future research can potentially resolve the emerging challenges in infection control and treatment, broadening the currently available treatment options.

In this dissertation for the degree of philosophiae doctor, this work focuses on both refining methodological approaches and generating a new understanding about selected AMPs. Efforts towards developing a robust platform for further investigation of AMPs looking for complementary agents to antibiotics or adjuvating strategies to aid for more effective antibiotic treatment strategies have been initiated. For that purpose, finetuned instrumental approaches are crucial for driving our research further in this field and uncovering new knowledge.

NMR spectroscopy is an information-rich and versatile tool, that is already widely used to investigate intricate peptide-membrane interactions. However, observations were made about possible improvements to study and develop methods to investigate the interaction between peptides and membranes, including their binding to and conformational changes in contact with lipid membranes. Self-aligning SMA-QA nanodiscs showed signs of bound peptide at even natural abundance, though isotope labelling will be necessary to properly study the peptides. As part of this effort, microscale thermophoresis was used in tandem as a low-

threshold method to investigate peptide interactions with different membrane models. Results showed that positively charged SMA-QA nanodiscs are good membrane models for cationic AMPs, that yield results comparable to more labour-intensive methods such as surface plasmon resonance.

Finally, both standard NMR techniques and anisotropic NMR procedures were used to elucidate the structure of a new natural product, Commafric A, and investigate the conformational changes of five cyclic tetrapeptides with an unusual α,α -disubstituted $\beta^{2,2}$ -amino acid depending on their primary structure, and five cyclic hexapeptides in gradually more lipophilic environments. Even with widely different antimicrobial effects, the backbone conformations did not change significantly between the peptides, indicating that antimicrobial effect is affected primarily by amino acid composition, rather than peptide conformation.

Sammendrag

Siden antimikrobielle agenter først ble oppdaget og etter lang tids overforbruk i behandling og forebygging av infeksjoner har antibiotikaresistens blitt et økende problem. Verdens helseorganisasjon (WHO) holder allerede øye med en rekke menneskelige patogener, inkludert flere multiresistente bakterier som fører til høy sykdomsfremkomst og dødelighet. Noe som understreker alvorligheten i situasjonen er det faktum at WHO estimerer at innen 2050 vil antibiotikaresistens forårsake flere årlige dødsfall enn kreft, med opptil 10 millioner mennesker som dør hvert år. Det er et sårt behov for nye alternativer og strategier. Et fremtredende alternativ er antimikrobielle peptider (AMP). AMP er allerede en viktig basis for liv, som vert-beskyttelsespeptider, og finnes i alle livets domener. Bakterier har en generelt lavere sjanse for å utvikle resistens mot AMP, delvis på grunn av hvordan peptider interagerer med bakterier. Dette er derfor en lovende strategi for å forlenge bruk av AMP i fremtidig terapi. Siden AMP først ble oppdaget har det vært gjort mye arbeid for å forstå virkemåten deres og sammensetningen mellom struktur og effekt. Da de er en sammensatt gruppe molekyler, med enda mer kompliserte biologiske mål, er det fremdeles mye som ikke er fullstendig forstått. Ved å utvide forståelsen vår rundt interaksjoner mellom AMP og biologiske mål kan fremtidig forskning løse den kommende utfordringen rundt infeksjonskontroll og behandling, og utvide de behandlingsmåtene vi har tilgjengelig i dag.

I denne avhandlingen for graden philosophiae doctor har arbeidet fokusert på å videreutvikle metodiske tilnærminger og frembringe en ny forståelse rundt utvalgte AMP. Dette er en del av en pågående innsats for å utvikle en plattform som kan bli brukt i videre arbeid mot å finne komplementære agenter til antibiotika eller subsidierende strategier som kan brukes til mer effektive antimikrobielle behandlingsstrategier. For det formålet er fininnstilte instrumentelle tilnærmelser uhyre viktig for å drive forskning videre i dette feltet og avdekke ny viten.

NMR spektroskopi er et mangfoldig verktøy som gir mye informasjon og som allerede er brukt til mange formål for å utforske intrikate interaksjoner mellom peptider og membraner. Observasjoner ble gjort om mulige forbedringer for å studere og videreutvikle metoder til å etterforske disse interaksjonene mellom peptider og membraner, inkludert binding og konformasjonelle endringer i kontakt med lipidmembraner. SMA-QA nanodisker som retter seg inn av seg selv i magnetiske felt viste spor av bundet peptid selv ved naturlig isotopmengde, men isotopmerking er nødvendig for å kunne studere peptidene fullstendig. Som en del av dette arbeidet ble mikroskala termodiffusjon brukt i tandem som en lavterskel-

teknikk til å undersøke interaksjonen mellom peptider og ulike membranmodeller. Resultatene viste at de positivt ladede SMA-QA nanodiskene er gode membranmodeller for kationiske AMP, og viser sammenliknbare resultater til mer arbeidsintensive metoder som overflateplasmonresonans.

Både standard NMR teknikker og anisotropiske NMR prosedyrer ble brukt for å kartlegge strukturen av et nytt naturprodukt, Commafric A, og utforske konformasjonelle endringer i fem sykliske tetrapeptider med en uvanlig α,α -disubstituert $\beta^{2,2}$ -aminosyre på bakgrunn av primærstrukturen deres, og fem sykliske heksapeptider i gradvis mer lipofile miljøer. Selv med sterkt varierende antimikrobielle effekter, viste det seg at konformasjonen av ryggraden ikke endret seg mye mellom de ulike peptidene, noe som indikerer at antimikrobiell effekt primært er avhengig av komposisjonen av aminosyrer, heller enn peptidenes konformasjon.

Scientific environment

The work in this project (NanoAMP, NFR-project: 275186) has been performed as a part of DigiBiotics (NFR-project: 269414) at the chemistry department at UiT the Arctic University of Norway.¹ DigiBiotics is a scientific consortium consisting of researchers with different backgrounds, founded as a response to the increasing antimicrobial resistance problem. The goal of the consortium is to look for new antimicrobial agents from arctic marine sources, refine structures through digital methods, and test on patient-like biological models. Focusing on cyclic antimicrobial hexapeptides, and their potential for reduced resistance development.

The Digibiotics project is divided into six work packages (WPs): WP1 Biodiscovery; WP2 Organic Synthesis; WP3 Optical spectroscopy and *ab initio* calculations; WP4 NMR spectroscopy (where I have performed my work); WP5 Molecular Dynamics simulation; WP6 Activity and resistance studies.

Especially WP2, which has provided the cyclic hexapeptides, has been vital for the completion of this project. Some work has also been performed together with WPs 3 and 5, which has provided energetically optimised conformers for the cyclic hexapeptides.

Additionally, a research stay at the Technical University of Denmark was conducted, under the guidance of Associate Professor Charlotte Held Gotfredsen. Their expertise on alignment in the magnetic field by graphene oxide seemed like a good fit for this project, while also strengthening Nordic collaborations between NMR labs.

The engineering and administrative staff at both UiT and DTU deserves a great deal of thanks, as this work could not have been completed without you.

List of papers

- I. Dinku, W. , Isaksson, J., Rylandsholm F. G., Bouř , P., Brichtová, E., Choi, S. U., Lee, S. H., Jung, Y. S., No, Z. S., Svendsen, J. S. M., Aasen, A. J., & Dekebo, A. Anti-proliferative activity of a novel tricyclic triterpenoid acid from *Commiphora africana* resin against four human cancer cell lines. *Appl Biol Chem* **2020**, *63* <https://doi.org/10.1186/s13765-020-00499-w>
- II. Jakubec, M., Rylandsholm, F. G., Rainsford, P., Silk, M., Bril'kov, M., Kristoffersen, T., Juskewitz, E., Ericson, J. U., & Svendsen, J. S. M. Goldilocks Dilemma: LPS Works Both as the Initial Target and a Barrier for the Antimicrobial Action of Cationic AMPs on *E. coli*. *Biomolecules* **2023**, *13*(7) <https://doi.org/10.3390/biom13071155>
- III. Rainsford, P., Rylandsholm, F. G., Jakubec, M., Silk, M., Juskewitz, E., Ericson, J. U., Svendsen, J. S. M., Engh, R. A. & Isaksson, J. Label-free measurement of antimicrobial peptide interactions with lipid vesicles and nanodiscs using microscale thermophoresis. *Sci Rep* **2023**, *13*(12619) <https://doi.org/10.1038/s41598-023-39785-0>
- IV. Simonovic, D., Rylandsholm, F. G., Jakubec, M., Isaksson, J. M., Devold, H., Dey, H., Anderssen, T., Haug, T., & Strøm, M. B. The role of amphipathicity and *L*- to *D*-amino acid substitution in a small antimicrobial cyclic tetrapeptide scaffold containing a halogenated α,α -disubstituted $\beta^{2,2}$ -amino acid residue. *Manuscript*.
- V. Eikås, K. D. R., Rylandsholm, F. G., Kristoffersen, T., Jakubec, M., Silk, M. R., Svendsen, J. S. M., Isaksson, J., Ruud, K., & Krupová, M. Conformational Studies of Cyclic Hexapeptides with Vibrational Circular Dichroism and Nuclear Magnetic Resonance. *Manuscript*.
- VI. Rylandsholm, F. G., Rainsford, P. B., Krupová, M., Kristoffersen, T., Haugen, T., Brandsdal, B. O., Svendsen, J. S. & Isaksson, J. Structural analysis of four cyclic antimicrobial hexapeptides in aqueous solution and in micelles, towards membrane-mimicking nanodiscs. *Manuscript*.

Summary of papers and author contributions

Paper I. Anti-proliferative activity of a novel tricyclic triterpenoid acid from *Commiphora africana* resin against four human cancer cell lines.

Applied Biological Chemistry, 2020

Worku Dinku, Johan Isaksson, **Fredrik Garnås Rylandsholm**, Petr Bouř, Eva Brichtová, Sang Un Choi, Sang-Ho Lee, Young-Sik Jung, Zae Sung No, John Sigurd Mjøen Svendsen, Arne Jørgen Aasen, and Aman Dekebo.

A new natural product, commafric A, was extracted from the plant *Commiphora Africana*. The structure of commafric A was characterised by NMR, IR, and VCD. One stereocentre could not be accurately described by VCD or NMR, so anisotropic NMR techniques were utilised for the final characterisation.

The anti-proliferative activity of commafric A was evaluated against four human cancer cell lines. Significant effects were registered against non-small cell lung cancer (A549) with IC50 values of 4.52 µg/ml, suggesting that Commafric A has the potential to be further optimised as a lead compound in the search for new anticancer drugs.

Author contributions

Extraction, isolation, and characterisation: WD. First draft: WD. VCD analysis: PB and EB. NMR spectroscopy: JI and FGR Interpretation of NMR data: JI, FGR, and JSMS. Revisions: JSMS. Supervision: AJAa. Bioassays and HRMS analysis: SU and SL. Supervision of bioassay tests: YJ and ZS. Conceptualisation, design, and direction: AD.

Paper II. Goldilocks Dilemma: LPS Works Both as the Initial Target and a Barrier for the Antimicrobial Action of Cationic AMPs on *E. coli*

Biomolecules, 2023

Martin Jakubec, **Fredrik Garnås Rylandsholm**, Philip Rainsford, Mitchell Silk, Maxim Bril'kov, Tone Kristoffersen, Eric Juskewitz, Johanna U. Ericson, and John Sigurd M. Svendsen.

Five cationic antimicrobial peptides (AMPs) were fully characterised by NMR spectroscopy. Their minimal inhibition concentration (MIC) values were collected against a selection of *E. coli* bacteria with different mutations to the lipopolysaccharide (LPS) functionality. The interaction between the AMPs and the bacterial membranes were explored by a combination of SPR and NMR spectroscopy by using three membrane models imitating eukaryotic cells, prokaryotic cells, and Gram-negative cells.

The results indicated that LPS are the drivers for the initial interaction with the Gram-negative membrane, acting as a kinetic barrier. If the binding to LPS is too strong (indicated by a low dissociation rate), the cationic AMP is effectively restricted from moving from LPS to the membrane, diminishing the antimicrobial activity. The results also showed that the ability of the studied AMPs to bind to LPS and translocate into the lipid membrane is related to the cationic charge (arginine vs. lysine) and the distribution of hydrophobicity along the molecule (alternating vs. clumped tryptophan).

Author contributions

Conceptualisation and design: MJ. Peptide synthesis: MS, TK, and JSMS. SPR data collection and analysis: MJ and MB. NMR spectroscopy and data analysis: MJ, FGR, and PR. Obtaining bacterial strains and collection of MIC values: EJ and JUE. Figures: MJ, FGR, and PR. Grant proposal and funding application: JUE and JSMS.

Paper III. Label-free measurement of antimicrobial peptide interactions with lipid vesicles and nanodiscs using microscale thermophoresis.

Scientific Reports, 2023

Philip Rainsford, **Fredrik Garnås Rylandsholm**, Martin Jakubec, Mitchell Silk, Eric Juskewitz, Johanna U. Ericson, John-Sigurd Svendsen, Richard A. Engh, and Johan Isaksson

Microscale thermophoresis (MST) was established as a low-threshold, label-free method to investigate the interaction between peptides and lipid membranes, utilising the intrinsic fluorescence of tryptophan. The method was used to extract the constants for membrane binding (K_D) and partitioning coefficient (K_P) from a set of five AMPs (The same as in Paper II) in different membrane model systems: vesicles and nanodiscs assembled by either anionic styrene maleic acid (SMA) polymer or cationic quaternary ammonium SMA (SMA-QA) polymer.

The measured K_D values correlate well with the corresponding measurements obtained by surface plasmon resonance (SPR) and reflects the minimal inhibition concentrations (MIC) towards *S. aureus* and *E. coli*. MST is therefore a promising method for cost-efficient detection of peptide-lipid interactions or mapping of sample conditions in preparation for more in-depth studies that require expensive sample preparation, large sample volumes, labelling, and/or instrument time.

Author contributions

Conceptualisation: PR. Peptide synthesis and purification: MS. MIC assay: EJ. Nanodisc and vesicle preparation, and MST: PR and FGR. Vesicle preparation and SPR: MJ. Data analysis: PR, MJ, and JI. Original draft: PR. Visualisation: PR. Writing and editing: PR, MJ, FGR, MS, JI, and RE. Supervision: JI, RE, JSS, and JE.

Paper IV. The role of amphipathicity and *L*- to *D*-amino acid substitution in a small antimicrobial cyclic tetrapeptide scaffold containing a halogenated α,α -disubstituted $\beta^{2,2}$ -amino acid residue.

Manuscript

Danijela Simonovic, **Fredrik Garnås Rylandsholm**, Martin Jakubec, Johan Mattias Isaksson, Hege Devold, Hymonti Dey, Trude Anderssen, Tor Haug, and Morten B. Strøm

A small library of nine cyclic tetrapeptides containing an unusual fluorinated lipophilic $\beta^{2,2}$ -amino acid was synthesised, and their antimicrobial activity and haemolytic toxicity were investigated. The tetrapeptide library was designed from the starting sequence c(Lys- $\beta^{2,2}$ -Leu-Lys) by changing the order of amino acids, introducing *D*-amino acids, or substituting Leu with bulky Phe.

The backbone conformation of a selection of the peptides were examined by NMR spectroscopy, collecting *J*-coupling constants, NOE distances, and secondary chemical shifts. The backbone conformations were found to not change considerably depending on primary structure or stereochemistry of the amino acids.

Many of the modifications had minimal effect on antimicrobial activity while having a substantial impact on, especially *D*-amino acids caused a decrease in haemolytic toxicity. These findings were supported by surface plasmon resonance (SPR). In summation, this study supports the notion that antimicrobial activity is mostly dependent on primary peptide structure rather than conformation.

Author contributions

Conceptualisation: MBS. Peptide synthesis: DS. Bioactivity screening: DS and HD. SPR: MJ. NMR: FGR. Data analysis and writing: DJ, FGR, MJ, TH, JMI, and MBM.

Paper V. Conformational Studies of Cyclic Hexapeptides with Vibrational Circular Dichroism and Nuclear Magnetic Resonance.

Manuscript

Karolina Di Remigio Eikås, **Fredrik Garnås Rylandsholm**, Tone Kristoffersen, Martin Jakubec, Mitchell Ramesh Silk, John Sigurd Mjøen Svendsen, Johan Mattias Isaksson, Kenneth Ruud, and Monika Krupová

Two different methods for *ab initio* calculation of molecular conformations were validated by vibrational circular dichroism (VCD) and NMR spectroscopy. The structure and conformation of four cyclic AMPs (the active AMPs from paper II) were simulated by a classical molecular dynamics (MD) sampling approach, which was compared with an alternative CREST based computational protocol.

It was found that calculations based on an MD conformational ensemble provide very good agreement with experimental spectra, while the CREST based calculations in most cases fail to reproduce the experimental spectral patterns in VCD or the molecular information obtained by NMR spectroscopy. This is in part due to a strong preference of the CREST approach for conformations with internal sidechain-backbone hydrogen bonding, which is caused by a combination of several factors, such as use of an implicit solvent model during the simulation, the length and nature of amino acid side chains, and/or use of dispersion-corrected energies.

Author contributions

Conceptualisation: MK and KDRE. VCD experiment: MK. Peptide synthesis: TK and MR. NMR spectroscopy: FGR, MJ, and JMI. Computations: MK and KDRE. First draft: KDRE and MK. Writing and editing: KDRE, FGR, JMI, and MK. Supervision: JSMS, JMI, KR and MK.

Paper VI. Structural analysis of four cyclic antimicrobial hexapeptides in aqueous solution and in micelles, towards membrane-mimicking nanodiscs

Manuscript

Fredrik Garnås Rylandsholm, Philip Rainsford, Monika Krupova, Tone Kristoffersen, Tonje Haugen, Bjørn Olav Brandsdal, John Sigurd Mjøen Svendsen, and Johan Isaksson

Nuclear Overhauser effect (NOE) derived distances were extracted for two cyclic hexapeptides, c(WWWRRR) and c(WWWKKK) (the two most active AMPs from Paper II), in water, DMSO, and SDS micelles. They were then used as constraints for molecular modelling of the molecular conformations. The resulting optimised conformers showed that the backbone remained mostly rigid, forming two β -turns, while the sidechains remain flexible in all environments. Analysis of chemical shifts, scalar couplings, and theoretical structures simulated in an explicit bilayer agreed on the results.

Pilot experiments on SMA-QA nanodiscs indicated that they are viable as membrane model for investigating the interaction between AMPs and lipid membranes. The discs are able to self-align in a magnetic field, and the strength of the alignment was explored in relation to sample temperature, lipid concentration, and nanodisc size. It was also shown that signal can be obtained from bound peptide, but further investigations with isotopically labelled peptides are needed to extract relevant structural data under conditions where the nanodisc is not over-saturated by peptides.

Author contributions

Conceptualisation: FGR and JI. Peptide synthesis: TK. Nanodisc preparation and NMR: FGR. Computations: PR, TH, and MK. Data analysis: FGR, PR, and JI. Original draft: FGR and JI. Writing and editing: FGR, PR, and JI. Supervision: JI.

Abbreviations

AMR	AntiMicrobial Resistance
AMP	AntiMicrobial Peptide
Arg / R	Arginine
cAMP	cyclic AntiMicrobial Peptide
CL	CardioLipin
COSY	COrrrelation SpectroscopY
CREST	Conformer-Rotamer Ensemble Sampling Tool
DLS	Dynamic Light Scattering
DMPC	1,2-Dimyristoyl-sn-glycero-3-phosphocholine
DMPG	1,2-Dimyristoyl-sn-glycero-3-phosphoglycerol
DMSO	DiMethylSulfOxide
FTIR	Fourier-Transformed InfraRed spectroscopy
GL	GlycoLipids
HDP	Host-Defence Peptide
HMBC	Heteronuclear Multiple Bond Correlation
HSQC	Heteronuclear Single Quantum Coherence
IPAP	In-Phase/Anti-Phase
IR	InfraRed
LC	Liquid Crystal
LMV	Large Multilamellar Vesicles
LUV	Large Unilamellar Vesicles
LYS / K	Lysine
MAE	Mean Absolute Error
MD	Molecular Dynamics
MIC	Minimum Inhibitory Concentration
MST	MicroScale Thermometry
NMR	Nuclear Magnetic Resonance
NOE	Nuclear Overhauser Effect
NOESY	Nuclear Overhauser Effect SpectroscopY
PAA	PolyAcrylAmide
PBLG	Poly(γ -Benzyl-L-Glutamate)
PC	PhosphatidylCholine

PE	PhosphatidylEthanolamine
PG	PhosphatidylGlycerol
Phe / F	Phenylalanine
PI	Phosphatidylinositol
PMMA	Poly(-MethylMethAcrylate)
PS	PhosphatidylSerine
RCSA	Residual Chemical Shift Anisotropy
RDC	Residual Dipolar Coupling
RF	Radio frequency
ROESY	Rotating-frame Overhauser Effect Spectroscopy
SAG	Strain-induced Alignment in a Gel
SEC	Size-Exclusion Chromatography
SM	SphingoMyelin
SMA	Styrene Maleic Acid
SMA-QA	Styrene Maleic Acid Quaternary Amine
SPR	Surface Plasmon Resonance
ssNMR	solid-state Nuclear Magnetic Resonance
TEMED	N,N,N',N'-Tetramethylethylenediamine
T-Jump	Temperature-Jump
TRIC	Temperature-Related Intensity Change
TMP	TriMethyl Phosphate
TMS	TetraMethylSilane
TMSP-d4	3-(Trimethylsilyl)propionic-2,2,3,3-d4 acid sodium salt
TOCSY	Total Correlation Spectroscopy
Trp / W	Tryptophan
Tyr / Y	Tyrosine
USD	U. S. dollar (\$)
VCD	Vibrational Circular Dichroism
WHO	World Health Organisation

1. Introduction

1.1 From wonder drug to antimicrobial resistance crisis

The serendipitous discovery of penicillin by Alexander Flemming in 1928 was one of the great breakthroughs in modern medicine.^{2, 3} A drug that killed bacteria with this level of efficacy, without being toxic to the host, revolutionised infection treatment, and expanded the treatment range considerably. The overall morbidity and mortality of infections were greatly reduced to those who could be treated with penicillin. However, only small quantities of penicillin were available at any time, as production was slow and did not yield any large amounts. Consequently, extended or even limited clinical use was not yet possible. During the second world war, governments funded great investments into medical research: Oxford scientists led by Howard Florey and Ernst Chain together with the US army found out that Penicillin could be mass produced in big vats with agitation and air bubbling through.^{4, 5} This upscaling of penicillin production, coupled with the discovery of streptomycin, was the beginning of an optimistic period for antimicrobial discovery, that would later be labelled as “the Golden Era”, lasting from 1945 to 1963.^{6, 7} In fact, about half of the antibiotics that were used well into the 2000s were discovered between 1950 and 1960.⁸

This great advancement was not to last. Fleming stated already in his Nobel prize acceptance lecture in 1945 that he had observed antimicrobial resistance (AMR) in samples in his lab.² He observed that Penicillin is not toxic to the host in any way, meaning that it is not possible to administer a harmful or lethal dose. On the contrary, the danger comes in making the dose too low: Then the Penicillin does not kill off all the bacteria, and the surviving bacteria instead develop modes of resistance against the antibiotics. While there were growing concerns of AMR in the years leading up to 1981, no real action was taken to prevent it.⁶ Antibiotics were both widely used in agriculture as a growth promotor, and overused in human healthcare.

There are estimates that suggests that microorganisms have been producing antibiotics for as long as 2 billion years.⁹ The two main hypotheses as to their original function are secondary metabolites as biological weapons when fighting for space and nutrition, and signalling molecules.¹⁰⁻¹² The concentrations of antibiotics found in nature are often too low to have any

antibacterial effect,¹³ but have been shown to affect the global transcription patterns,^{14, 15} regulate the expression of genes associated with virulence,¹⁶⁻¹⁸ induce the SOS response in bacteria,^{19, 20} and play a role in quorum sensing and host-parasite interactions.^{18, 21, 22} Additionally, it is a major driver for horizontal gene transfer, sharing resistance mechanisms in bacteria to increase survival.²³⁻²⁵

Antimicrobial resistance is an outcome of evolution, and does not require pre-exposure of microorganisms to antimicrobials to emerge.¹¹ In fact, multiple genes for antimicrobial resistance have been isolated from 30,000 year old permafrost samples.²⁶ The rapid emergence of resistance in clinical settings is consistent with the hypothesis that the microbes already has pathways for resistance that they are able to select from. In accordance with this, antimicrobial resistance would sometimes be observed as soon as a new antimicrobial was discovered, or within only 2-3 years.^{7-9, 27-30} Resistance to penicillin was observed years before it became commercially available,²⁸ and treatment failure in clinical settings due to resistance to penicillin treatment was reported only a year after introduction into the market.²⁹ Especially beta-lactams were hindered by rapid evolution of beta lactamases only a short time after the broad introduction of penicillin. Resistance against methicillin predates clinical use of penicillin.³⁰ In summation, antimicrobial resistance is a naturally occurring phenomenon, but human overconsumption is increasing the rate at which it is expressed.

The world started to realise AMR as an emerging challenge, and from around 1992 AMR has gained increased awareness, being seen as a global issue on the level with global warming.⁶ Unfortunately, no new breakthroughs have happened in antimicrobial discovery since 1987.⁷ This is due to a number of factors: antibiotic research is costly, takes time, and antibiotics have a high risk of resistance developing shortly after new drugs become available. New antibiotics are kept off the market, to be used only on more extreme cases, leading to pharmaceutical companies focusing their time and money on developing and producing other drugs that yield a higher profit. As a response to this hesitation from the pharmaceutical industry, several public-private and even pharmaceutical initiatives are funding research institutions and pharmaceutical companies to continue searching, or even reusing old drugs in new ways.³¹⁻³⁷

Drug development is both time consuming and exceedingly expensive. The development of a new antibiotic is estimated to take somewhere between 10 and 20 years, costing more than 1.5

billion USD.³⁸ There are currently 26 antimicrobial drugs in phase-I development, 25 in phase-II, and 11 in phase-III.³¹ 62% of the compounds in phase-I and 56% in phase-II are new pharmacophores, some of them with new modes-of-action, hopefully meaning that they are less likely to encounter cross-species AMR. Only two new small molecule antimicrobial drugs were approved between 2020 and 2022: the fluorquinolone levonadifloxacin and its prodrug in India in 2020, and the oxazolidinone contezolid in China in 2021. External funding is essential to make sure that new antimicrobials reach and stay in the market.³⁹

Introducing a drug to the market is not a guarantee for the company's success: The biopharmaceutical company Achaogen was forced to file for bankruptcy in 2019, less than a year after the FDA approved their antibiotic plazomicin.^{40, 41} Another company, Melinta, that has successfully developed four antibiotics and released them to the market filed for bankruptcy later the same year.^{42, 43} Both because their income was not enough to pay for the large expenses they had used to develop and test the drugs.

In 2019, infections caused by AMR bacteria was the third biggest cause of death worldwide.⁴⁴ Especially six pathogens, designated as the ESKAPE pathogens by the World Health Organisation (WHO), are being closely monitored: *Enterococcus faecium*, *Staphylococcus aureus*, *Klebsiella pneumoniae*, *Acinetobacter baumannii*, *Pseudomonas aeruginosa*, and *Escherichia coli*.^{45, 46} They are all multi-drug resistant and should be considered high priority when working on development of new antibiotics.⁴⁶ The ESKAPE bacteria was the cause of approximately 73% of the AMR-caused deaths in 2019.⁴⁴ WHO estimates that by 2050, antimicrobial resistance will surpass even cancer in yearly causes of death, with up to 10 million people dying every year.⁴⁷ Something that, in turn, is estimated to cost the world up to 100 trillion USD in lost work force. If researchers do not find a way to tackle AMR, the world will soon be a very different place. Medical procedures that are considered routine today, such as organ transplants, chemotherapy, or treatment of preterm infants, will be impossible to perform without antibiotics.⁶

1.2 Antimicrobial peptides

The field of antimicrobial peptide (AMP) research began in earnest with the discovery of cecropin A and B as part of the humoral immune system of moths (*Hyalophora cecropia*) in the early 1980s.⁴⁸ It was discovered that the two new AMPs had a broad spectrum activity (works against a wide variety of microorganisms⁴⁹) against Gram-positive and Gram-negative bacteria, and fungi. Following that discovery, several new groups of AMPs were discovered: sarcotoxins from fly larvae (*Sarcophaga peregrina*),⁵⁰ defensins from mammalian macrophages,^{51, 52} and magainins from frog skin (*Xenopus laevis*).⁵²

While these AMPs were shown to have a good response against microorganisms and low host toxicity, other AMPs did not show the same trend. Melittin from venom of the honey bee (*Apis mellifera*)^{53, 54} and alamethicin from fungus (*Trichoderma viride*) showed a strong cytotoxic or cytolytic activity against host cells.⁵⁵ While cecropins and melittin are structurally similar, with large hydrophobic- and hydrophilic regions, they show very different activity: Both groups are active against the bacteria *Escherichia coli*, but melittin also shows lytic properties towards human liver cells, meaning that there had to be some kind of recognition by the cecropins to prevent them from harming the cells of the insect itself.

Looking at these examples from nature, it is clear that AMPs are abundantly found as host-defence-peptides (HDPs), and they form the backbone of the natural defence of many organisms. Including, but not limited to, viruses,⁵⁶ bacteria,⁵⁷ plants,^{58, 59} humans and other mammals,^{60, 61} reptiles,^{52, 62} horseshoe crabs,⁶³⁻⁶⁵ and marine invertebrates. The online antimicrobial peptide database, ADP3,⁶⁶ lists over 2600 examples of cationic AMPs from all kingdoms of life.⁶⁷

1.2.1 Structural properties of peptides

Peptides are characterised by the peptide bond; the bond between the carboxylic acid and an amine group, where the π -bond resonance delocalises the double bonds across the peptide bond, giving the amide bond a preference of being planar. The primary structure of a peptide is described by the amino acid sequence, with the number of amino acids typically being below 50, with some ranging up into the mid 100's.^{67, 68} The distinction between peptide and

protein is somewhat vague, and when the number of amino acids climb above 100, they are usually described as proteins.

The secondary structure of peptides consist of folded sections (alpha helices, beta sheets, and turns) connected by loops and unfolded flexible regions (random coil).⁶⁹ The secondary structure is largely dependent on hydrogen bonds and the phi (Φ) and psi (Ψ) angles around the alpha position on the backbone (See Figure 1). AMPs usually have a net charge between +2 and +9, from a mix of cationic (commonly Arg or Lys) and amphipathic (50% or more hydrophobic) amino acids.⁶⁸ The sum of these causes an amphipathic secondary structure in the presence of a biological membrane, with the hydrophobic residues on one side and the hydrophilic residues on the other.

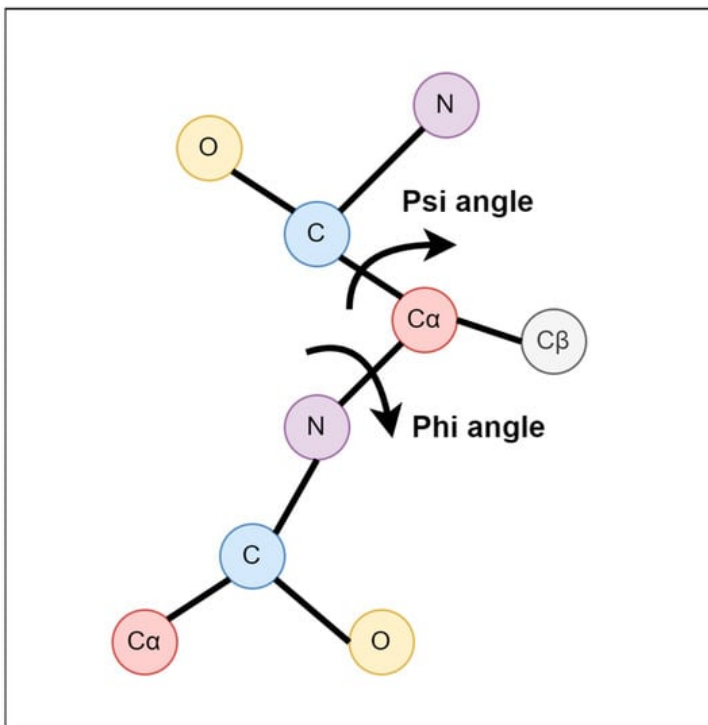


Figure 1. Torsion angles phi (ϕ) and psi (ψ). The phi angle is the angle around the -N-C α - bond, and the psi angle is the angle around the -C α -C- bond. Reprinted with permission by the Multidisciplinary Digital Publishing Institute (MDPI), Kabir et al.^{70, 71}

Nature produces AMPs in two different ways. the first is a ribosomal translation on an mRNA template, through a cleavage of the active sequence from a larger pre-protein.^{67, 72, 73} These peptides have the limitation that they only contain the natural amino acids, though sometimes they include post-translational modifications. An example is the human cathelicidin LL-37, which is synthesised from human cationic antimicrobial protein-18 kDa (hCAP18) by proteinase 3.⁶⁷ The second method is non-ribosomally, where multiple enzymes work in succession to catalyse the reaction needed to end up with the correct AMP. Which then allows for a very different assembly of AMPs, so that they concise of a mixture of normal amino acids together with non-canonical amino acids not found in any proteins. Lipopeptides such as colistin (polymyxin E)⁷⁴ and daptomycin⁷⁵ are produced as metabolites in bacteria or fungi. Gramicidin S contains ornithine amino acid, which is almost never seen in nature, from its non-ribosomal synthesis through peptide synthetase such as g-S synthetase I and II.⁷⁶ Glycopeptides,^{77, 78} such as vancomycin⁷⁹ and chloramphenicol,⁸⁰ are produced with the help of a series of enzymes.⁸¹ Just like LEGO bricks, which can be combined in various ways to build different structures, AMPs are typically composed of a limited set of different building blocks that can be put together in a virtually limitless variation of ways.

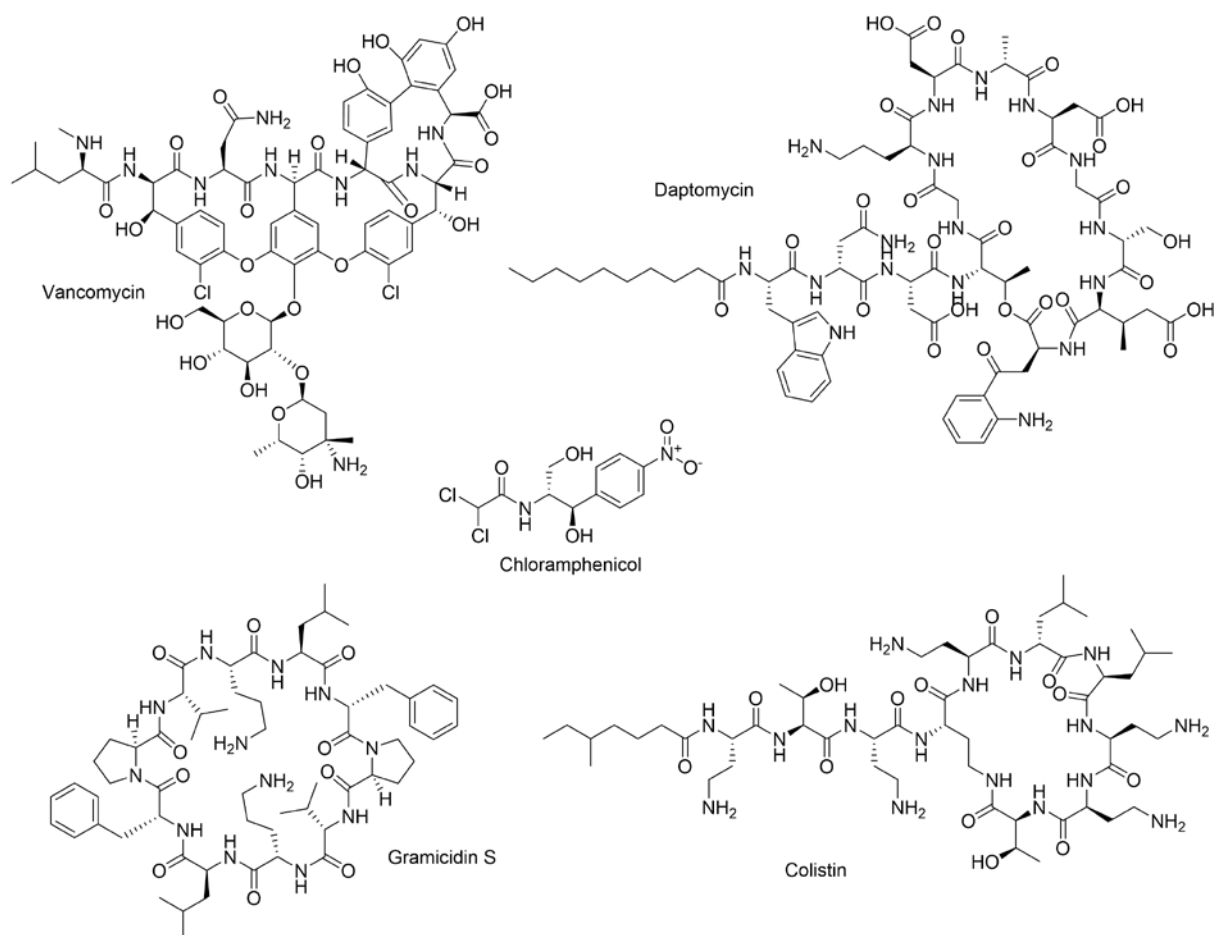


Figure 2. A selection of non-ribosomally produced AMPs mentioned above. IUPAC names were collected from PubChem⁸² and drawn in ChemDraw.

AMPs are great antimicrobial agents because there is a relatively low expectation of resistance development.⁸³ Part of the reason is that they work well in very low dosages, giving little opportunity for resistance development, and they show a broad-range protection against diverse microorganisms. Some bacteria can develop resistance against AMPs.⁸³ Resistance mechanisms can include molecules neutralising the peptide,⁸⁴ enzymatic decay by bacterial proteases,⁸⁵ or modification of the charge of the bacterial membrane itself to hinder AMP binding or uptake.^{67, 86, 87} Fortunately, there is a high fitness cost to adapt the bacterial membrane, so the frequency of AMP resistance is low, and even when it happens, it is only at a low level of resistance.⁸³ The bactericidal effect increases sharply within a narrow dose range, so very few bacteria survive long enough to develop resistance. To that extent, increased hydrophobicity and fewer charges on the peptides seem to decrease resistance development even further, as peptides with less charges are less affected by the change in

membrane charge. Finally, while classical antibiotics usually have only one target, as a direct consequence of how they have developed alongside their producers, AMPs have less of a direct site of interaction and can affect various targets within the cell at once.

Molecular dynamics calculations suggest that antimicrobial peptides can self-aggregate in solution to form miniature versions of the water-membrane interface, to form the right conformation for direct insertion into the membrane in a fully functional state to effectively exert antimicrobial action.⁸⁸ Aggregation has been observed in several different peptides, among others melittin, which forms tetramers, and dermaseptin S4.⁸⁹ Hydrophobicity has a positive correlation on aggregation, especially Trp.⁹⁰ Aggregation leads to a better antimicrobial activity, up to a point: the very best aggregates are not the best antimicrobials.⁸⁹

1.3 Bacterial membranes

The bacterial membrane consists of the cytoplasmic, or inner, membrane and a cell wall (see Figure 3).⁹¹ The cytoplasmic membrane is a lipid bilayer, consisting of almost equal parts lipids and proteins. The lipids are amphipathic phospholipids with a hydrophilic head and a hydrophobic tail. The bilayer is perturbed by different proteins, serving different roles, such as molecule transport, enzymatic activities, signal transduction, intercellular joining, cell-cell recognition, and attachment to the cytoskeleton and extracellular matrix. Primarily, the structure of the bacterial cell wall is used to classify into Gram- positive and Gram-negative bacteria.

In Gram-positive bacteria, the cell wall consists of a thick peptidoglycan layer of tens of nanometres (20-80 nm⁹²), with large pores (up to 60 nm in diameter and 23 nm depth).⁹³ Additionally, teichoic acids in the form of wall teichoic acids covalently bonded to phosphatidylglycerol (PG), and lipoteichoic acid bound to the membrane, provide stability for the PG and keep a negative charge over the membrane surface.⁷⁴

Gram-negative bacteria only have a thin peptidoglycan layer (1.5-10 nm⁹²), but the big difference is the outer lipid bilayer.⁹¹ It is less porous than the cell wall of the Gram-positive cell-wall and contains lipopolysaccharides (LPS) anchored in the membrane by lipid A. The LPS are covered by a high number of negatively charged phosphate groups that are engaged

in salt-bridges with divalent cations (Ca^{2+} and Mg^{2+}).⁷⁴ This highly polar environment serves as a barrier against most hydrophobic AMPs, explaining the difference in how AMPs can be active against Gram-positive bacteria, while having no effect against Gram-negative bacteria.

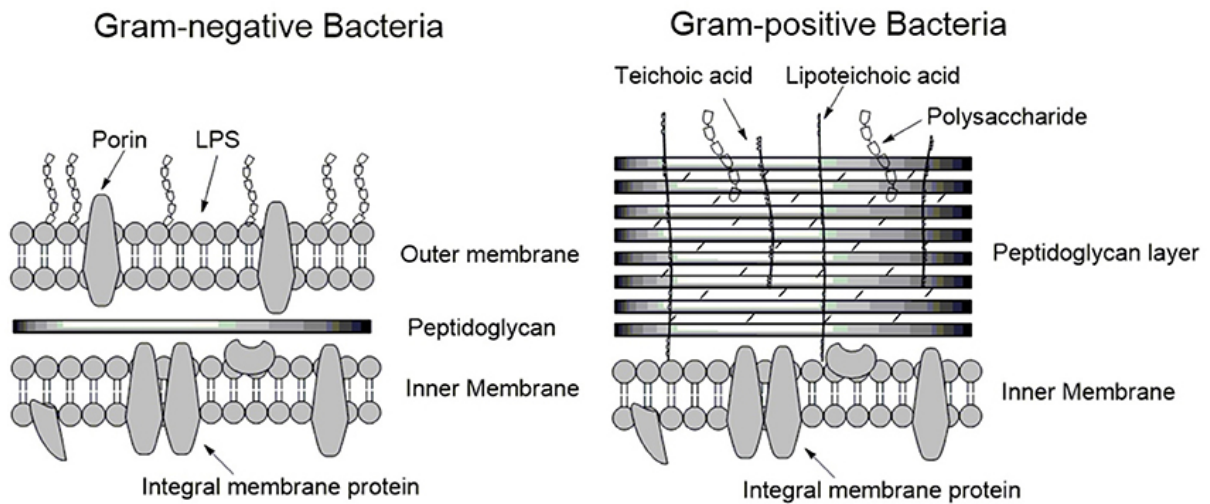


Figure 3. Schematic membrane structures of Gram-positive and Gram-negative bacteria. The cytoplasmic membranes of both types of bacteria are similar. Gram-positive bacteria have a thick layer of peptidoglycan surrounding the cytoplasmic membrane, protecting the bacterium. In contrast, the layer of peptidoglycan in Gram-negative bacteria is thin and an additional outer membrane is present. LPS forms a major part of the outer leaflet of the outer membrane/cell wall, the inner leaflet is comprised of phospholipids. Reprinted with permission by *Frontiers in Neuroscience*, Li et al.⁴⁴

The phospholipid composition varies between Gram-negative and Gram-positive bacteria, including between different species and strains, but commonly they include zwitterionic phosphatidylethanolamine (PE) and more rarely phosphatidylcholine (PC) species, where PE is the most abundant, making up 75% of the phospholipid membrane of *E. coli*.^{94, 95} The negative membrane charge is usually provided by anionic phospholipids like PG and cardiolipin (CL).

The negatively charged phospholipids is one of the differences between bacterial and mammalian cells. While they are both present in both types of cells, the mammalian cells (where they make up about 17%), typically contain phosphatidylserine (PS) or phosphatidylinositol (PI).⁹⁶ The biggest difference is arguably that the negative phospholipids in the mammalian cells remain in the inner leaflet, making the outer leaflet neutral, consisting

mostly of zwitterionic PC, glycolipids (GL), and sphingomyelin (SM). This big difference in the two leaflets create an asymmetry specific for the mammalian cells.⁹⁷ Negative charge on the membrane has shown to have a positive influence on AMP-lipid interaction.^{98, 99} Mammalian cells also contain cholesterol in the membrane, which causes a tighter packing and the general structure of the membrane to be less accessible for AMPs.¹⁰⁰ Cholesterol regulates the fluidity of the membrane and increase the membrane stability.

PE and CL are more common in bacterial membranes than mammalian membranes, and they have a cone-like geometry. The cones misshape the bacterial membrane, into what is referred to as a saddle-splay structure.¹⁰¹ The resulting curvature stress causes a weakness in the membranes.¹⁰² AMPs can use the increased curvature to disrupt the membrane through a range of processes, including creating pores, or protrusions called blebs, buds, or rod-like projections.

Many AMPs are shown to target the cytoplasmic membranes.^{52, 55, 74, 103-106} They target lipid membranes in mainly two ways: membrane disruption and membrane lysis. The former describes the reduction of integrity in the bacterial membrane, which might cause membrane lysis. The latter is a complete loss of membrane integrity.

There are indications that AMPs can cause cell lysis by disrupting the membrane wall and hindering cell wall synthesis.^{107, 108} A reduction of membrane fluidity is followed by a process where the lipid phase separates. Then, lipid synthesis protein functionality is impaired by conformational changes induced by the change in lipid packing.

The way AMPs access the membrane of Gram-negative bacteria can be divided into several steps that include electrostatic and lipophilic bindings (Figure 4).⁷⁴ First, electrostatic interactions between AMPs and LPS adsorbs the AMPs to the bacterial surface. Then AMPs permeate the outer membrane by a combination of electrostatic interactions, hydrogen bonds with the phospholipid heads, hydrophobic interactions with the lipid tails, and disrupting salt bridges. The AMPs adsorb on the cytoplasmic membrane by electrostatic interactions with anionic lipids, hydrogen bonds with head groups, and hydrophobic interactions with lipid tails. At this point, the AMPs manage to cause cytoplasmic membrane disruption.

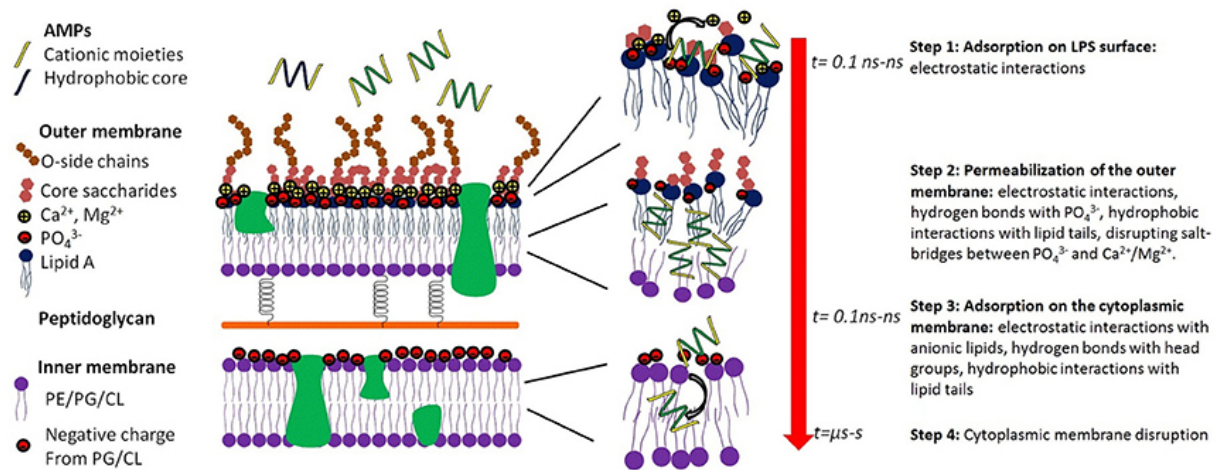


Figure 4. Key molecular events of the interaction of AMP which results in killing Gram-negative bacteria. Reprinted with permission by *Frontiers in Neuroscience*, Li et al.⁴⁴

As the cell lysis takes place, the bacterial membrane is completely dissolved as the lipids are removed from the membrane. The result of the cell lysis is therefore a significant increase in permeability of the membrane, and the cell loses its contents and metabolites.¹⁰⁹

1.4 Membrane interaction models

As previously mentioned, the bacterial membrane is the first point of interaction for AMPs and the description of peptide-lipid interaction is an evolving field where there is still more to learn. The specific way the AMPs destroy the bacterial membrane can be described by several different models, but unfortunately, the different interaction models used have been shown to give conflicting results.¹¹⁰ This section aims to describe some common membrane interaction models shown in Figure 5. It should be noted that this is not intended to be an exhaustive list and that while the mechanism of membrane lysis by AMPs are usually accounted to the pore-, carpet-, or detergent models of AMP activity discussed in this chapter, those are not the only methods discussed in literature.

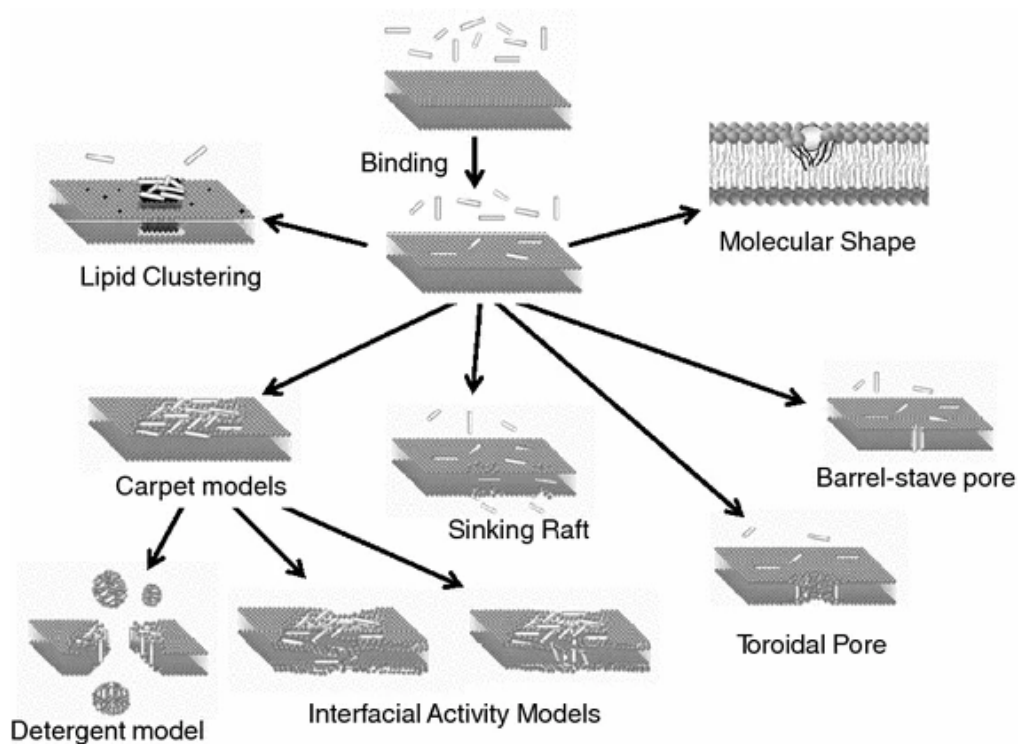


Figure 5. Overview of some popular models of AMP activity. While many experimental observations are well described by one or more of these models, none of the models describes all experimental observations. Reprinted with permission by Springer, Wimley and Hristova.¹¹¹

1.4.1 Pore model

There are two different pore models: the barrel-stave pore model and the toroidal pore model. In the barrel-stave pore model, AMPs interact laterally with each other to form a water filled channel reminiscent of a membrane protein ion channel.^{55, 111} In the toroidal pore model, AMPs affect the local curvature of the bilayer to form a high curvature toroid, disrupting the normal segregation of the polar and non-polar environments. One clear difference between the two is that in the barrel-stave model, the peptides interact with the hydrocarbon core surrounding the pore, while in the toroidal pore model, the peptides interact with the lipid head groups.¹¹²

Different investigation methods draw different conclusions on the barrel stave versus toroidal model,¹¹³ with suggestions that the barrel-stave model is even exclusive to alamethicin.¹¹⁴ Alamethicin can be parallel or perpendicular to the bilayer normal, depending on the lipid composition and peptide concentration,¹¹⁵ it can form a barrel-stave pore with eight units.¹¹⁶ Melittin works in the same way. These two peptides seem to be the exception rather than the

rule. They are not really AMPs, but rather nonspecific membrane-permeabilising peptide toxins.

Magainin 2 forms larger pores than alamethicin, but they are toroidal, and needs large quantities of peptide perpendicular to the membrane.¹⁰³ While magainin 2 seems to follow the toroidal pore model in bacterial cells, it seems to follow the carpet model in mammalian cells.¹¹⁷ To make matters more complicated, it has been documented that Magainin 2 and PGLa, both found in the skin of the frog *Xenopus laevis*, interact synergistically:^{118, 119} Together in a 1:1 ratio, they form transmembrane pores of heteromolecular dimers. They even work significantly better together than either AMP does alone.

The primary method of differentiating between the different pore types is to measure the conductivity across a membrane.¹²⁰ The method was first suggested by looking at flip-flop mechanism of Magainin 2 and how it caused pore formation.¹²¹

1.4.2 Carpet model

While secropin isolated from insects has a broad antimicrobial effect on Gram-negative and Gram-positive bacteria, secropin derived from pig intestines, secropin P1, only affect Gram-positive bacteria.¹²² It was discovered through fluorescence measurement that the AMPs did not insert fully into the hydrophobic core of the membrane. Contemporary models and methods to describe them often came out with conflicting results.¹²³

The carpet model describes an initial binding of the AMP to the membrane surface, followed by adjusting the conformation so that the hydrophilic part of the peptide face away from the membrane surface and the hydrophilic part onto the membrane surface, meaning the peptide does not fully insert into the membrane.¹²² The AMP concentration continues to build up, “carpeting” the surface. At a critical point, the concentration is sufficient to disrupt the curvature of the membrane.¹⁰² The membrane disruption induce transient holes to form, causing content to leak from inside the barrier. AMP activity relies more on positively charged amphipathic features for the initial binding, rather than exact amino acid sequence or secondary structure.^{55, 102} These general properties allow the peptide to form strong non-specific interactions with the cell membrane.

One of the requirements for the carpet model to work is a high local concentration of peptides.⁸⁹ Observations were done which indicated that small openings in the membrane were sufficient for ion release and hindering cell respiration.¹²⁴ Part of the selection towards bacterial cells over host cells can be contributed to the fact that the osmosis of red blood cells requires larger pores and higher peptide-to-lipid ratios than the ones observed in the carpet model.⁸⁹ Additionally, the presence of cholesterol in the mammalian cell membrane inhibit both channel formation and the following membrane destabilisation.¹²⁵

1.4.3 Detergent model

Permeabilisation is an important early step in antimicrobial activity.^{126, 127} The detergent model is used to describe the catastrophic collapse of the membrane integrity.¹¹¹ Bechinger and Lohner⁸⁹ observed that peptides interacted with bacterial membranes similarly to how detergents interact with fatty acids. The carpet model needed a critical concentration to work, but antimicrobial activity was observed at a significantly lower peptide-to-lipid ratio than the carpet model demanded.⁸⁹

Similarities have been drawn with detergents and how they dissolve membranes.^{55, 89} AMPs have also shown that they can self-aggregate into oligomers of different sizes, before they insert into the membrane. The suggestion is that they also solubilise parts of the membrane, carrying away lipids in micelles or bicelles.⁸⁹ This results in large holes in the membrane surface and thereby membrane lysis. Bechinger and Lohner suggested that the peptides were able to form oligomers that could incorporate lipids by inserting into the bacterial membrane. This process could be a better description of the special cases of pore-forming peptides. Recently, cryo-electron tomography at nanometre scale has been used to capture images supporting this model.¹¹²

1.4.4 Other activity models

Wimley⁵⁵ pointed out that the contents of vesicles are released too slow to account for true pores. The interfacial model was suggested as an attempt to explain it. Interfacial activity is defined as the ability of a molecule to bind to a membrane, partition into a membrane-water

interface, and to alter the packing of the lipids.⁵⁵ The hydrocarbon membrane core is one of the most hydrophobic microenvironments found in nature. AMPs cause a mixing of the hydrophobic and hydrophilic groups of the membrane, which leads to membrane permeabilisation.¹¹¹

Epanand and colleagues suggested a lipid clustering model, in which cationic peptides cause anionic lipids to cluster in the membrane.^{128, 129} Multi-cationic compounds induce lipid phase separation, affecting the lateral lipid packing, which creates phase boundary effects that lower the permeability barrier between the cell and the surroundings.¹²⁹ The mechanism is expected to be mostly important to molecules with sequential positive charges within a flexible moiety, that can adapt to the rearrangement of charged groups on the membrane surface. Importantly, the lipid clustering model does not exclude other models as contributing factors. Instead, it is suggested to be a contributing factor to pore formation in the toroidal pore model, or the interaction between peptides and membrane in the carpet model.¹²⁸

Almeida and colleagues introduced the sinking raft model to describe AMP activity in terms of binding, insertion, and perturbation.¹³⁰⁻¹³⁴ They observed that dimers or trimers of α -helical peptides would aggregate together on the membrane surface and then sink into the outer leaflet of the bilayer. As the peptides sink deeper into the bilayer, the hydrophobic residues remain in contact with the lipid acyl chains, while the hydrophilic residues line a hole in the centre of the multimer.

While there are many different models attempting to describe the peptide-membrane interactions, none of them describe the interactions perfectly, and the results vary with the observational method that has been utilised.^{55, 111} This once again highlights how complicated nature is.

1.5 Other AMP activities

While the focus of this thesis is on antibacterial effects, peptides are known to have extensive effects against other microorganisms and human cells. The antimicrobial peptide database APD3 currently (as of April 2024) lists 1399 antifungal, 290 anticancer, 244 antiviral, 136 anti-HIV, and 14 spermicidal peptides, among their 3940 AMPs.⁶⁶ Some peptides have

multiple medicinal effects: magainin 2 and PGLa from the skin of the frog *X. laevis* are shown to be antibacterial, antifungal, antiviral, and have anticancer activity.¹¹⁸

AMPs are exciting anticancer drugs due to a variety of reasons.¹³⁵ As already discussed, peptides show a low propensity for resistance due their short interaction time-frame⁴⁵ and how they express anticancer effects through a series of mechanisms.¹³⁶⁻¹³⁸ AMPs interact with varied membrane- and intracellular targets, which makes them more resilient than single target drugs.¹³⁷⁻¹³⁹ Additionally, the dual antibacterial and anticancer nature is a great built-in advantage, as cancer treatment often leaves the immune system weakened.¹⁴⁰⁻¹⁴³ Maybe most important for cancer treatment, AMPs show a good solubility and tumour penetration, which allows them to reach both primary and metastatic tumour sites.^{137, 139, 144} This is again reflected in a high selectivity towards cancer cells,^{137, 138, 145} leading to a general low toxicity to host cells and reduced side- effects.¹³⁹

Increased electronegative charge is one of the main reasons why cationic AMPs can discover cancer cells.¹⁴⁵ Normally, the electronegative phospholipids PE and PS are found mostly on the inner leaflet of mammalian cells. Elevated reactive oxygen species and hypoxia in the tumour microenvironment give rise to dysregulation of phospholipid transporters, which transport PE and PS to the outer leaflet.¹⁴⁵ Additionally, various anionic glycoproteins are overexpressed in cancers, increasing the negative charge on the membrane surface. Some promising anticancer AMPs are cathelicidins from lysosomes of macrophages and polymorphonuclear leukocytes, LL-37 (the only human cathelicidin), and its bovine homologs BMAP-27 and -28. LL-37 and mimics work as anticancer AMPs,¹⁴⁶ and have contraceptive purposes.¹⁴⁷

LL-37 is especially interesting as a contraceptive, as it is naturally produced and transformed into ALL-38 in the vagina after intercourse to protect the vaginal epithelium against microbes introduced during intercourse, and to kill off feeble sperm.¹⁴⁷ ALL-38 has equal antimicrobial effects to LL-37.^{146, 147} Additionally, magainin and nisin, especially magainin 2 and nisin A, have been shown to have contraceptive properties.^{147, 148} AMPs can also have a contraceptive effect as spermicidal drugs.¹⁴⁹ The fact that several AMPs also work against sexually transmitted infections (STIs)¹⁴⁸ and HIV¹⁵⁰ at the same time solves a lot of problems with modern contraceptives. Defensins, protegrins, cathelicidins, cecropins, polyphemusins, magainins, and melittins have shown to work against various STI-causing pathogens and

HIV/herpes simplex virus.¹⁴⁹ Cecropin even inhibit HIV production by infected T cells and fibroblasts.¹⁵⁰

1.6 Understanding the structure of natural products

Plants have been used as medical sources for thousands of years.¹⁵¹ Tablets from Mesopotamia dated to 2600 BCE mention, among others, myrrh (*Commiphora* species), poppy juice (*Papaver somniferum*), and cypress (*Cupressus sempervirens*) as medicinal plants. Morphine, from the seeds of the opium poppy, was the first commercially pure natural product to enter the market, in 1826.¹⁵¹ Aspirin (acetylsalicylic acid) was the first semi-synthetic drug, based on the natural product salicylic acid found in the bark of the Willow tree (*Salix alba*) and in Meadowsweet (*Filipendula ulmaria*, previously called *Spiraea ulmaria*).¹⁵² When looking at all the drugs that were commercially approved between 1981 and 2019, only 24.6% were purely synthetic drugs. The rest were either unaltered natural products, or some sort of modification on natural products (pharmacophores, derivatives, mimics, ...).^{153, 154} The big advantage of natural products is that they are molecules that have naturally developed with a host organism over millennia, being tailored to a specific need.¹⁵⁵ As such, natural products are typically divided into primary and secondary metabolites.¹⁵⁶ Primary metabolites are key components in maintaining normal, physiological processes such as growth, development, and reproduction. Secondary metabolites are often specialised molecules, found only in a small selection of species or cells.

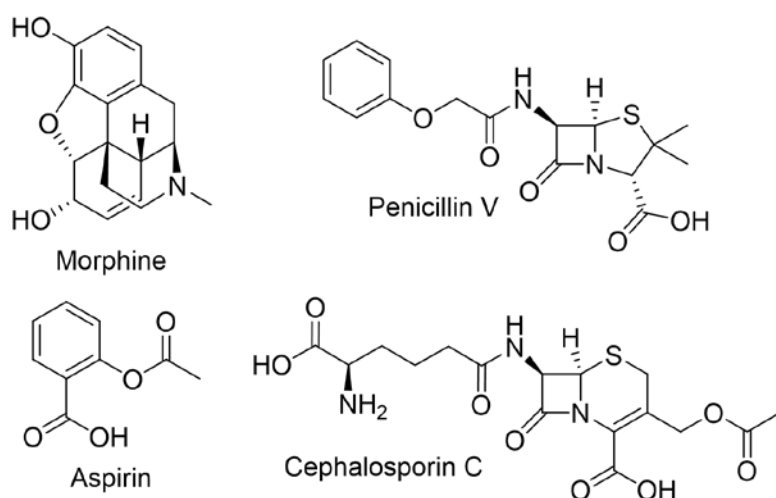


Figure 6. The structure of four natural products-inspired pharmaceuticals.^{152, 157-159}

The already mentioned penicillins and the aminoglycoside streptomycin, tetracyclines, and macrolides, are all examples of natural products produced by microorganisms.¹⁵¹ The β -lactam structure found in penicillin is also found in other classes of antibiotics, including cephalosporins,¹⁵⁸ cephamycins,¹⁶⁰ monobactams,¹⁶¹ and carbapenems.¹⁶² Cephalosporin C from *Cephalosporium acremonium* (now *Sarocladium strictum*) fungus (see Figure 6) is one example.¹⁵¹ The four-membered β -lactam ring is the pharmacophore disrupting cell-wall synthesis in bacteria, and therefore the target of any antimicrobial resistance.¹⁵¹ Therefore, part of the work going into modification of the Penicillins is aiming to make the β -lactam ring less available for antimicrobial resistance mechanisms.

Natural products as a class of drugs are high in steric complexity and contain many more chiral centres than synthetic products.¹⁵⁵ Partly as a consequence of being made by enzymes, partly from their highly specialised nature where they are meant to interact with biological sites that are three dimensional and chiral themselves.¹⁶³⁻¹⁶⁵ A simple change in the stereochemistry of the commercialised drug might, at best, have no effect whatsoever, but might also end up having catastrophically harmful effects. Consequently, when new natural products are discovered, a lot of work goes into ascertain how they are structured.

One famous example of how important the absolute structure of a natural product can be is the Thalidomide scandal in the late 1950s to early 1960s:^{166, 167} The racemic mixture of Thalidomide was sold under a series of brand names as a cure for morning sickness. It was later shown that (*R*)-Thalidomide induced a sedative effect, while (*S*)-Thalidomide was seen causing severe birth defects.¹⁶⁸⁻¹⁷⁰ It is estimated that over 10,000 babies were born with these defects by the time the drug was taken off the market. It has since been proven that (*S*)-Thalidomide promotes degradation of SALL4, a transcription protein that is vital for limb development.¹⁶⁶ The drug is not useless, though: Thalidomide is currently given as a drug against leprosy, multiple myeloma, and advanced wasting sickness related to HIV infection.^{167, 171, 172}

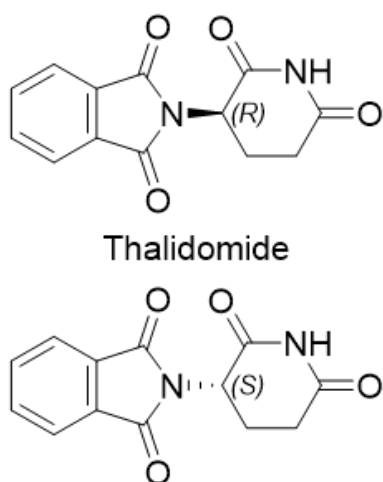


Figure 7. Structure of the two enantiomers of Thalidomide. While one enantiomer relieves morning sickness, the mirror image causes severe birth defects.¹⁶⁶

Nature provides a potent scaffold that synthetic chemists can improve upon. A wide range of penicillins and opiates are some prominent examples of this. A large part of the efficacy of natural products come from their 3D structure and their interaction with the drug target.¹⁶³⁻¹⁶⁵ To gain a better understanding of the drug mechanisms, it is therefore imperative to know the absolute configuration of the molecule. Chirality makes the elucidation of the 3D structure difficult. The gold standard regarding 3D structure is often given to X-ray crystallography.¹⁶⁵ However, not all compounds are amenable to crystallisation, and the identification of suitable crystallisation conditions can be both time-consuming and in some cases a lottery. The most common techniques to start investigating the structure of new natural products are usually mass spectrometry, UV, and nuclear magnetic resonance (NMR) spectrometry. By using specialised equipment and techniques, mass spectrometry and NMR spectroscopy is also able to reliably differentiate between diastereomers and even enantiomers.¹⁷³⁻¹⁷⁸

1.7 NMR spectroscopy

NMR spectroscopy is maybe one of the most information-rich methods regarding the structure of molecules. NMR spectroscopy is routinely used to elucidate unknown structures from isotropic information such as chemical shifts (chemical environment), spin-spin J -coupling constants (connectivity), secondary chemical shifts (secondary structure of peptides/proteins), and nuclear Overhauser effect (NOE) derived distances (intramolecular through-space distances).¹⁷⁹ Standard NMR techniques are not able to distinguish between enantiomers.

If an alignment media is introduced into the NMR sample, partial alignment can be obtained. This partial alignment creates an anisotropic environment that yield new information absent in the isotropic sample. The new information can be used to obtain the relative configuration of the molecule, or even the absolute configuration, if at least one stereocentre is known or if it is combined with an optically active spectroscopy technique, such as vibrational circular dichroism (VCD) or Raman optical activity (ROA).¹⁸⁰ Anisotropy has been used to assign or correct errant structure elucidations.¹⁸¹⁻¹⁸⁷ Chiral alignment media can also be applied, which can distinguish between enantiomers, where the alignment effect is opposite between them.^{174,}

177

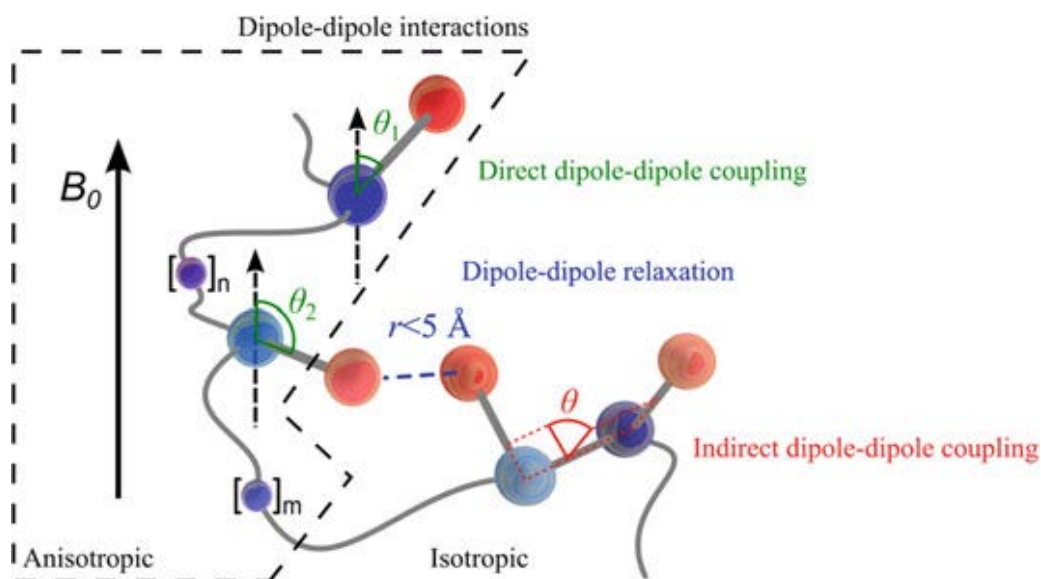


Figure 8. Concepts of magnetic dipole-dipole interactions and the obtainable 3D structural information. In green are the direct dipole-dipole couplings, which may be used to gain information of angles and distances of internuclear vectors independent on their situation in the molecular structure. In blue is the dipole-dipole relaxation, which may give access to local internuclear distances through space. Indirect dipole-dipole couplings are highlighted in red which, among multiple uses, hold local information of the relative position of nuclei, mediated through the bonds in the structure. It is indicated whether the information may be extracted from spectra of molecules under isotropic conditions or if anisotropic conditions are also needed. Reprinted with permission by Springer Nature, Hoek.¹⁸⁸

1.7.1 J -coupling constants

J -coupling constants derives from indirect dipole-dipole couplings, and are also called scalar couplings.^{189, 190} They originate from magnetic interactions relayed by bonding electrons where the spins are indirectly connected.¹⁸⁸ The magnetic moment of the nuclei slightly polarises the electrons involved in the chemical bond, which is then transmitted by overlapping orbitals to other nuclei. The spin state of one nucleus then influences the effective external magnetic field around a neighbouring nucleus, which is seen through line splitting. The interaction is independent on the applied magnetic field, which is why J -coupling constants have the same values between different NMR instruments with different field strengths. The scalar coupling is also the basis of most through-bond NMR experiments.¹⁷⁹

$^3J_{HH}$ -coupling constants are typically recorded for proteins and peptides, as they give information about the backbone. Obtaining $^3J_{HH}$ -coupling constants is relatively easy, as they can be read directly from the 1D 1H spectrum and can be easily extracted as long as the peaks

are not overlapping, and the separation is decent.¹⁸⁸ Alternatively, several 2D experiments are designed to extract the coupling constants, even if some peaks are overlapped, such as the E.COSY experiment.¹⁹¹⁻¹⁹³ There are even some 3D HNHA experiments that are designed to extract the $^3J_{HH}$ -coupling constants in proteins.¹⁹⁴

The size of the $^3J_{HH}$ -coupling constants are dependent on the orbital overlap of the hydrogen atoms.¹⁸⁸ This relationship is described by the semi-empirical Karplus equations, given as the sinusoidal graph in Figure 9, and can be used to extract dihedral angles.¹⁹⁵ The relative size of the J -coupling constants are also dependent on the atoms involved, meaning that HN-CH will have different coupling constants for the same angles compared to HC-CH, due to a difference in magnetic moment, including an effect from the surrounding nuclei.¹⁹⁵⁻¹⁹⁷ The differences in bond lengths, also depending on the atoms in question, are also important to the constants.

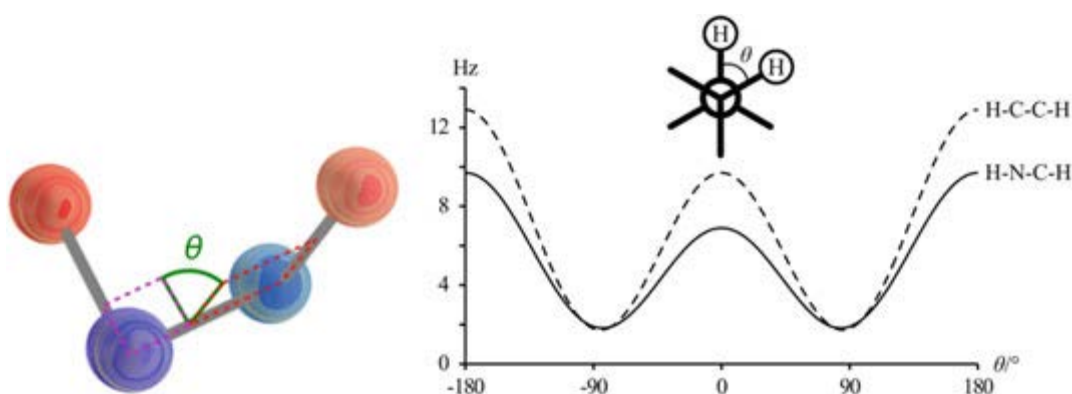


Figure 9. Left: Dihedral angle between protons (red) three bonds apart, blue may be carbons or heteroatoms. Right: Dependence of 3J -coupling constant on dihedral angle for peptide data as given by Karplus equations.¹⁹⁵ Reprinted with permission by Springer Nature, Hoeck.¹⁸⁸

The general shape of the Karplus equation is given in equation (1).¹⁹⁵

$$^3J_{HH}(\theta) = A \cos^2 \theta + B \cos \theta + C \quad (1)$$

where θ is the dihedral angle, and the constants A, B, and C depend on the type of the coupling. The equation was derived from peptide moieties, where they used the NH-CH bond with A = 6.4, B = -1.4, and C = 1.9.

When looking at several computationally obtained conformers for comparison to experimental values, the weighted J -coupling constants are weighted as the constants, not weighted as the corresponding dihedral angles.

1.7.2 Secondary chemical shifts

The backbone of a polypeptide makes for an especially good probe for the peptide's overall structure. Secondary chemical shifts ($\Delta\delta$) of H_α , C_α , H_N , and C_β are used to measure the secondary chemical shifts by looking at the difference between the experimentally obtained chemical shifts and random coil reference shifts (equation (2)).¹⁹⁸⁻²⁰²

$$\Delta\delta = \delta^{exp} - \delta^{ref} \quad (2)$$

The reference value can be obtained in several different ways, with slight variations. One of the areas that the field of secondary chemical shifts are continuously evolved, is the improvement of the reference values. Following are four different methods of obtaining secondary chemical shift reference values.

Schwarzinger *et al.*²⁰³ utilised a sequence-dependent correction. An Ac-GGXGG-NH₂ peptide was synthesised with X being one of the 20 naturally occurring amino acids, and the effect of X on the two amino acids in each direction was recorded as the difference from X=G. This method is a considerably quicker way of exploring how neighbouring amino acids are affected by all natural amino acids compared to synthesising all the different polypeptide variations. Doing that would require synthesising 400 unique peptides for the dipeptide combinations, and all the combinations for the tripeptide would require a prodigious 8000 unique peptides.

Kjaergaard *et al.*^{204, 205} built on the study by Schwarzinger *et al.*²⁰³ They found Glutamine to be a better representation of the random coil based on the likeness of the sidechain to the other amino acids.^{205, 206} With only a single heavy γ -atom, glutamine is the best general representation of the natural amino acids. Contrary to this, glycine is conformationally abnormal with an unusual conformational freedom, which shows up as the random coil chemical shifts being affected on a different magnitude compared to all the other amino acids.

Glycine was therefore not expected to be a representative amino acid for secondary chemical shift correction. Additionally, Kjaergaard *et al.* pointed out that the peptide structure is highly temperature dependant, and therefore included a temperature gradient from 5 to 45°C making sure the results are comparable to any relevantly recorded NMR data.^{204, 205}

De Simone *et al.*²⁰⁷ developed the CamCoil approach, where random coil chemical shift values were collected from the flexible loop regions of proteins in a database of 1772 proteins. This approach allows discrimination of dependence of the chemical shifts on the primary structure of proteins from the effects that are associated with the secondary and tertiary structures.²⁰⁷ In other words, the random coil values that are extracted are only dependent on the amino acid order.

Tamiola *et al.*^{208, 209} utilised ncIDP (neighbour corrected Intrinsically Disordered Protein), a library of 6903 chemical shifts from 14 polypeptides, yielding random coil chemical shift values for 20 amino acids with 40 sequence-dependent correction factors that discriminates between the left and right amino acid.

A common procedure to report secondary chemical shifts include the difference between C_{α} , and C_{β} chemical shifts,¹⁹⁸ with the advantage that it cancels out chemical shift referencing errors.²¹⁰ The H_N secondary chemical shift can give information about hydrogen bonding,¹⁹⁸ as intramolecular hydrogen bonding causes deshielding of the proton, resulting in a downfield shift.

Generally speaking, positive values (+2 ppm) indicate an alpha helix structure, negative values (-2ppm) indicate beta strand or extended structure, and values close to zero (within ± 2 ppm) indicate a random coil.²¹⁰ Consecutive values of ± 2 ppm is usually interpreted as having fully formed a secondary structure. Additionally, it is known that aromatic residues have a long-range effect on chemical shifts, especially on protons.²⁰³

1.7.3 Nuclear Overhauser Effect

A very useful technique in NMR spectroscopy is to be able to collect correlations through space via the nuclear Overhauser effect (NOE). NOE correlations originate from cross-relaxation.^{179, 188}

Relaxation in NMR is the mechanisms of which the system returns back to equilibrium after perturbation by radio frequency (RF) pulses.¹⁸⁸ T_1 relaxation is the recovery of the original longitudinal magnetisation, while T_2 relaxation is the loss of transverse magnetisation. For small molecules T_1 and T_2 relaxation are in the same order of magnitude, while macromolecules or solids operate with considerably shorter T_2 relaxation times. The longitudinal relaxation (T_1) is the focus to understand NOE relaxation, and is facilitated by the translations, rotation, and internal motion of the molecule. The mechanism of the NOE relaxation is dominated by the relative spin dipole reorientation of neighbouring nuclei under rapid isotropic tumbling. The population of one spin changes as the population of another nuclear spin is perturbed. This is the reason why NOEs are dependent on the rotational correlation time (τ_c).

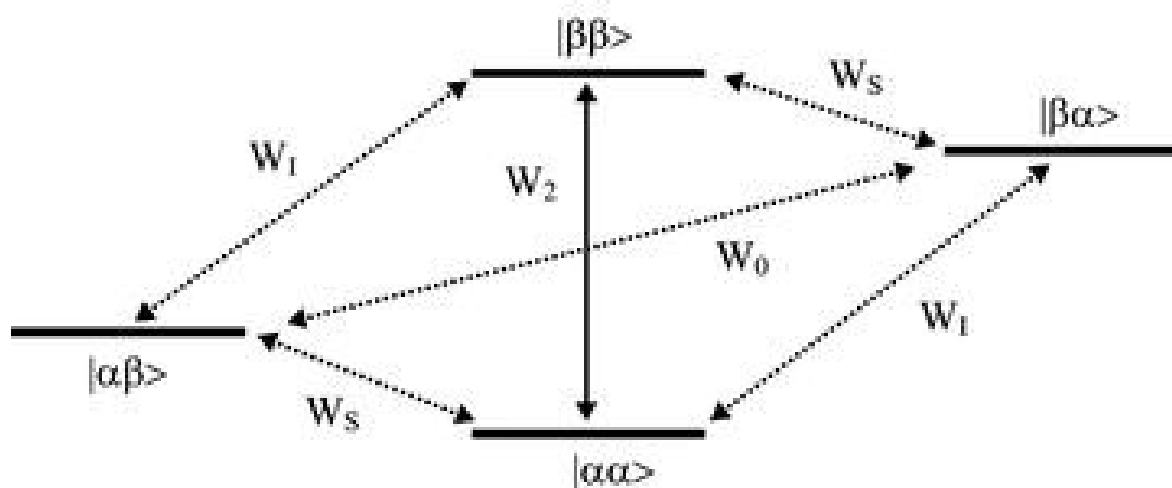


Figure 10. Energy level diagram for the two-spin system IS with all possible transition rates indicated. Reprinted with permission by Springer Nature, Lundström.²¹¹

The NOE itself is given by the W_0 (zero quantum) and W_2 (double quantum) cross-relaxations (Figure 10), where both spins switch spin state simultaneously.^{179, 188} The cross-relaxation rate determines the intensity of the cross-peaks. In the most common NOE experiments, the NOE evolves without RF irradiation for a fixed period, the mixing time (τ_m).

In the nuclear Overhauser effect spectroscopy (NOESY) experiment, the NOE enhancements build up linearly to begin with, reaching a maximum where linearity is lost, then decays back to zero (Figure 13). This observed effect is a combination of the buildup, spin diffusion, and relaxation. Spin-diffusion is negligible to begin with, but as the cross-relaxation builds up, the spin diffusion increases and becomes significant. As the longitudinal relaxation also add to the spin diffusion, the intensity of the crosspeak decays.

NOESY crosspeaks have a sign dependence on the size of the molecule (See Figure 11).¹⁷⁹ For small molecules, NOESY crosspeaks are the same phase as rotating-frame Overhauser effect spectroscopy (ROESY) crosspeaks, with the dipole-dipole peaks being of opposite sign to the diagonal. Meanwhile, exchange peaks in both NOESY and ROESY spectra are always the same sign as the diagonal. The difference is that in a NOESY experiment, the NOE passes through zero for larger molecules and both dipole-dipole crosspeaks and exchange crosspeaks have the same sign as the diagonal (see Figure 11). For ROESY this never happens because small molecules stimulate W_2 while large molecules stimulate W_0 .

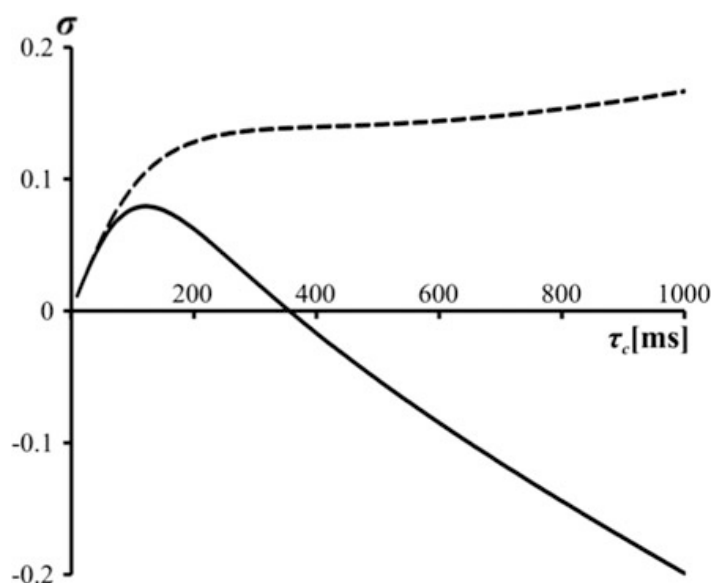


Figure 11. The theoretical cross-relaxation rate (r) of NOE (—) and T-ROE (- -) experiments at 500 MHz, for a distance of 2.5 Å. Note that the crossover point is dependent on the field strength. The cross-relaxation rate is shown in contrast to the often-depicted maximum homonuclear enhancement, as the cross-relaxation rate is the actual observable parameter in NOE experiments. Reprinted with permission by Springer Nature, Hoeck.¹⁸⁸

ROESY spectra suffers from transfers from total correlation spectroscopy (TOCSY), because it is set up with a low-power spin lock pulse, which is similar to the TOCSY spin-lock pulse.¹⁷⁹ For the same reason, ROESY can also show correlation spectroscopy (COSY) peaks between J -coupled spins. These extra peaks make NOESY spectra easier to analyse, making them preferred where applicable.

NOE correlations can be used to qualitatively determine stereochemistry or confirm assignment of novel or known compounds.¹⁸⁸ The information gained is highly local, as there is a $1/r^6$ dependence between intensity of the signal and distance (See equations (3) and (4)). This allows distances of up to 4-5 Å to be observed, depending on the rotational correlation time and nuclei pair. The rotational correlation time of a molecule is dependent on the size of the molecule, the temperature, the shape and flexibility of the molecule, and the viscosity of the solvent.¹⁷⁹ As with most NMR experiments, having adequate delays between scans is very important. If the T_1 relaxation is not completed, the intensity of following scans will be

altered accordingly, leading to wrong relative intensities and distances will be estimated from wrong data.¹⁸⁸

Spin diffusion happens when the magnetisation between two nuclei, A and B, can develop long enough for the magnetisation to be transferred further to another nucleus, from B to C (Figure 12). Now the intensity of the signal a-c indicate that nuclei a and c are closer than they really are, meaning false peaks can be observed that indicate that there is a connection that there should not be.

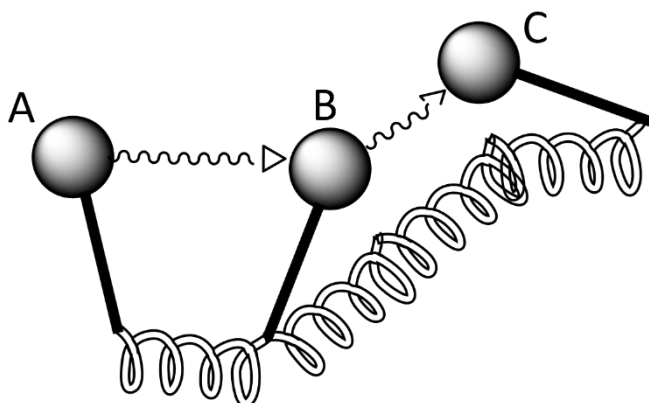


Figure 12. Simplified figure showing how a signal from nucleus A can be transferred to B and further to C if the mixing time becomes too long. The result is a crosspeak showing a false connection between nuclei A and C.

The intensity of a cross-peak is given by equation (3).^{179, 188}

$$\sigma_{AB} = \left(\frac{\mu_0}{4\pi}\right) \frac{2\hbar^2 \gamma_A^2 \gamma_B^2}{10} r^{-6} \left(\frac{6\tau_c}{1+4\omega^2\tau_c^2} - \tau_c\right) \quad (3)$$

where σ is the cross-relaxation; μ_0 is the vacuum permeability constant; \hbar is the reduced Planck constant; γ is the gyromagnetic ratios of the nuclei; r is the distance between the involved nuclei; τ_c is the rotational correlation time of the molecule.

Equation (3) can be simplified into equation (4) if some assumptions are made: if the equation is considered for only identical nuclei (HH); all constants are covered by a new constant, k , that is similar for all observed NOEs; all rotational correlation times are equal; the acquired

mixing time is short, so NOEs are observed before spin-diffusion kicks in; the cross-relaxations of multiple involved spins behave as isolated spins.

$$\sigma_{AB} = kr^{-6} \quad (4)$$

This shows that the relationship between intensity and distance is to the power of -6, and that signal is quickly lost. The cross-relaxation rate is further correlated to the observed intensity (η) through equation (5).

$$\eta_{AB} = \sigma_{AB}\tau_m \quad (5)$$

where τ_m is the mixing time used in the experiment. If the mixing time is the same, the intensities and distances from two different cross-peaks can be related by equation (5). Then, if a distance between two protons X and Y, r_{XY} , is known, the distance between two protons A and B, r_{AB} , can be calculated by equation (6).

$$\frac{\eta_A}{\eta_X} = \frac{r_{AB}^{-6}}{r_{XY}^{-6}} \rightarrow r_{AB} = r_{XY} \left(\frac{\eta_A}{\eta_X} \right)^{\frac{1}{6}} \quad (6)$$

The fact that one distance can be approximated when another distance is known is called the isolated spin-pair approximation (ISPA) or initial rate approximation (IRA).^{212, 213} For quantitative NOE experiments, one reference method is to use intramolecular reference distances. The most common are either ortho aromatic protons (2.46 Å) or diastereotopic geminal protons (1.75 Å).¹⁷⁹

NOE build-up curves (Figure 13) can be constructed from steadily increasing NOESY/ROESY mixing times to avoid including spin-diffusion peaks.¹⁸⁸ The latter will show up with a delayed onset of intensity (as it does not appear until spin-diffusion has started).

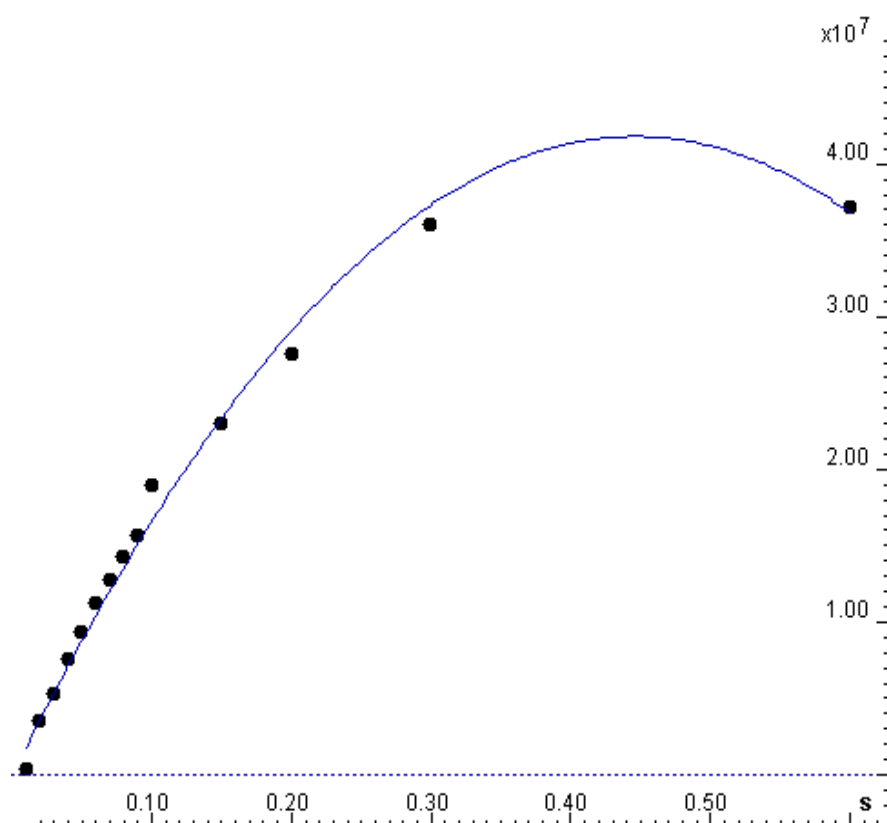


Figure 13. NOE intensity buildup curve of the cyclic hexapeptide *c*(WRWRWR) in water. Note how the initial buildup is approximately linear, and then curves off towards the top (Figure not previously published).

1.7.4 Anisotropy

The downside with classical NMR experiments is that they cannot distinguish between enantiomers. Different to *J*-coupling constants and NOE derived distances, which give extremely localised information, anisotropy-based methods yield global structural information, as they are relative to the external magnetic field.^{188, 214}

Liquid state NMR operate in a state of isotropy, meaning the molecules tumble freely in solution, so observable dipole-dipole couplings cancel each other out. Solid-state NMR does not undergo unrestricted isotropic molecular motion, often from being a solid powder, containing molecules oriented in all different directions (See Figure 14).²¹⁵ This means the material is anisotropic, inducing the different nuclei to experience the magnetic field differently from their distinct orientations. High-speed rotation at 54.74° relative to the magnetic field, or magic angle spinning (MAS), can be used to average the different peaks into an isotropic-like environment. Without magic angle spinning, the dipole-dipole couplings

do not cancel, and broad peaks containing information of all the different orientations are observed. By changing the angle of an NMR sample incrementally, it is possible to obtain anisotropic information about the molecule.²¹⁶

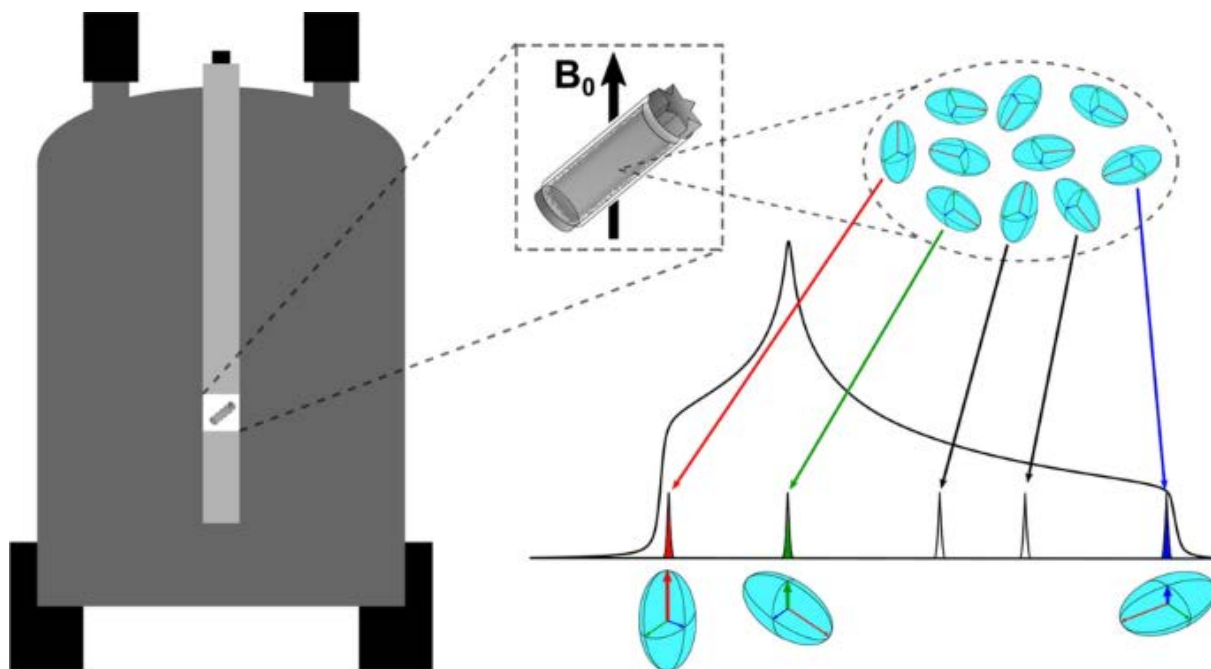


Figure 14. Representation of a solid-state NMR experiment, showing how molecules aligned in different directions give rise to different parts of the powder pattern of the solid-state NMR signals. Reprinted with permission from Springer Nature, Nardelli et al.^{71, 217}

Cortieu and coworkers¹⁷⁵ first reported enantiodiscriminating properties of poly(γ -benzyl-L-glutamate) (PBLG). Thiele and coworkers showed that the methylene groups in strychnine could be distinguished.^{218, 219} Following this, the groups of Thiele and Reggelin, among others, started investigating the enantiodiscriminating properties of PBLG and other novel liquid crystal (LC) systems.²²⁰⁻²²³ At the same time, work was done by the groups of Kessler and Luy on swollen polymers as alignment media for small molecules, showing an easier scalability of residual dipolar couplings (RDCs), in addition to a weaker degree of alignment.^{174, 224-227}

There are three different anisotropic measurements that are observed: residual quadrupolar coupling (RQC) of deuterium in the solvent, which is most often used to measure the degree of alignment;²²⁸ residual dipolar coupling (RDC), which was the main point of interest for a long time; residual chemical shift anisotropy (RCSA), which in the last two decades have gotten a lot of traction as an excellent complimentary method to RDCs.¹⁸⁴

1.7.4.1 Residual dipolar couplings

Nematic liquid crystal solutions were observed by Saupe in the 1960's;^{229, 230} LC solutions where molecules are more or less oriented with the long axis roughly parallel in a magnetic field. The issue was that the observed dipolar coupling that originated from the alignment was in the kHz range, far above the range of scalar J -coupling constants, rendering them unfit for NMR analysis of anything other than small or highly symmetrical molecules.²³¹ The introduction of alignment media that induced only a very low degree of order (an order parameter $S < 10^{-3}$), so that the dipolar coupling is smaller than the $^1J_{CH}$ scalar coupling, made RDCs viable as a means of structure determination.

RDCs originates from a direct dipole-dipole coupling between two nuclei in an external magnetic field.²¹⁴ The direct dipolar coupling constant D comes from the magnetic fields generated from the spins, relative to the external magnetic field. The dependence on the magnetic field means that the 3D structure of molecules can be determined, as angular knowledge of internuclear vectors is established, even if they are far apart in the structure (Figure 8).¹⁸⁸ RDCs and computer-generated structures can be used synergistically to investigate stereochemistry and conformation of complex structures.^{232, 233}

The direct dipole-dipole interaction can be defined between two isolated heteronuclear spins I and S by equation (7):²³¹

$$D_{IS} = -\frac{\mu_0\gamma_I\gamma_S\hbar}{8\pi^2} \left\langle \frac{3\cos^2\theta_{IS}-1}{2} \frac{1}{r_{IS}^3} \right\rangle \quad (7)$$

where μ_0 is the vacuum permeability and γ_I and γ_S are the gyromagnetic ratios of the two spins I and S. The angle θ_{IS} is the angle between the vector connecting I and S and the direction of the magnetic field; the symbols $\langle \rangle$ indicate a time average over all orientations

sampled by the interspin vector and r_{IS} is the distance between the spins (= length of the vector r_{IS}). If I and S are directly bonded heteronuclear spins (^1H and ^{13}C or ^1H and ^{15}N) this distance is the bond length. For flexible compounds, r_{IS} and Θ_{IS} are additionally averaged by the internal motion of the compound.

The dipolar coupling D can be observed as an additional contribution (positive or negative) to the line splitting under anisotropic conditions (Equation (8)).

$$T = J + D \quad (8)$$

where T is the total coupling observed and J is the scalar coupling.^{231, 234} The anisotropic contribution to the scalar coupling is very small, and is usually overlooked.¹⁸⁸

The alignment of the molecule can be described by an alignment tensor A , a symmetric and traceless 3x3 matrix that describes the preferred orientation of the molecule.^{231, 235} The matrix contains five independent elements, meaning that more than five non-parallel (linearly independent) RDC values are needed to be able to utilise them for structural analysis.^{231, 236} RDC is mostly used for one bond ^1H - ^{13}C correlations, but other experiments like ^1H - ^{15}N are also available.

The issue has been raised on whether a single alignment tensor is enough to describe a flexible molecule with subsequently many different conformations.¹⁸⁵ A program that is able to sample a selection of alignment tensors dependent on different conformational clusters might yield a better description of the system. Unfortunately, the development of methods to make RDCs applicable to flexible compounds is still in its early stages.²³¹ The main issue is that two averaging processes are observed at the same time: averaging of the tumbling motion of the molecule and averaging of the conformational flexibility. To properly observe the flexible moiety, five independent RDCs would be needed for every single conformer.^{185, 231} As for now, the total number of possible conformers are reduced by other methods, such as NOE distances and J coupling constants, before the RDCs are applied on the limited sampling. The field is still evolving, but one solution is the molecular dynamics with orientational constraints (MDOC) simulation, where the tensor is handled as an orientational constraint pseudo-forcefield, generating a large ensemble of compatible conformers.²³⁷⁻²⁴⁰ To

obtain the best results, the method is still combined with NOE distances and $^3J_{\text{HH}}$ coupling constants.

It was also discovered that most small, monomeric proteins can be accurately described by a single structure, yielding decent Quality factors (Q-factors) (further explained in chapter 1.7.4.6).²¹⁴ Residues having large amplitudes or anisotropic motion will need a few more, and adding only one extra structure might reduce the Q-factor by a significant amount. RDCs can in fact be used to investigate structures as big as over 100 kDa,²⁴¹ and are being used to investigate the structure of unfolded proteins.^{214, 242-244}

1.7.4.2 Residual chemical shift anisotropy

Partial alignment causes an incomplete averaging of the chemical shielding tensor, which provides structural information in the form of relative orientations between different chemical shift anisotropy (CSA) tensors.^{183, 184, 245} This change can be measured as residual chemical shift anisotropy (RCSA) and is observed as a downfield or upfield change of the chemical shift for the different nuclei (See Figure 15). RCSA is applied for ^{13}C by acquiring standard 1D ^{13}C NMR spectra. This allows even quaternary carbons to be observed, which is one of the reasons why RCSA is an excellent supplement to RDCs.²⁴⁶ Though, as all the peaks will shift in different directions, a chemical shift standard such as tetramethyl silane (TMS) is needed.¹⁸⁴

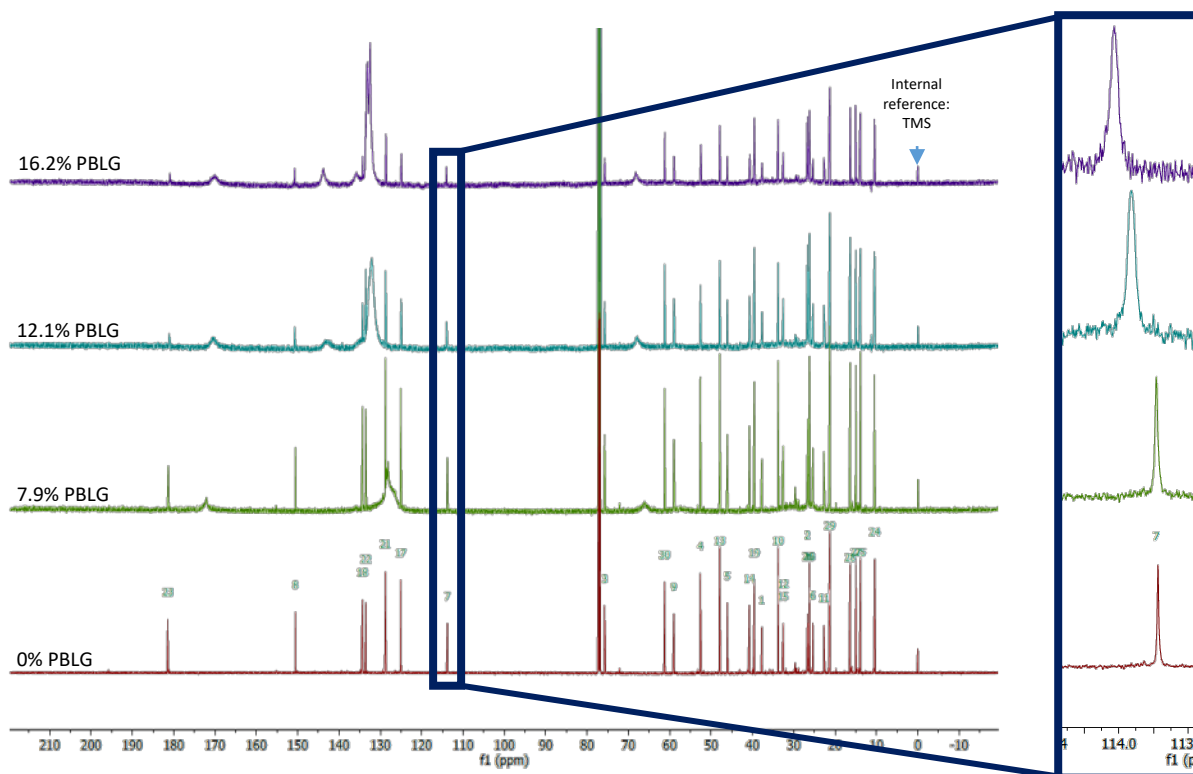


Figure 15. ^{13}C spectra for commafric A in CDCl_3 with 0.03% (v/v) TMS at different PBLG concentrations. Zoomed-in outclip of C7, showing the change in ppm values, not to mention a decrease of signal-to-noise ratio. Figure from supporting information of paper I, reprinted with permission by Springer Nature, Dinku et al.^{71, 181}

Hybridisation is important for the carbon CSA. Historically, RCSAs obtained from polymeric gels have been very small, especially from sp^3 hybridised carbons.¹⁸³ Sp^2 hybridisation leads to larger values than sp^3 hybridisation, which leads to larger RCSAs.¹⁸⁴ Meaning that RCSAs even more useful for molecules with many sp^2 hybridised carbons.

1.7.4.3 Alignment media

To obtain the partial alignment, the sample needs to be introduced to an alignment media. There are two kinds of alignment media introduced for small organic compounds: liquid crystal (LC) solutions and stretched polymers (SPs), the latter is also sometimes called strain-induced alignment in a gel (SAG).^{184, 216, 231} The interaction with the alignment media is thought to be solely steric, unless a charged alignment media is used.^{233, 247}

There are several systems that can be used for macromolecules in water. Some prominent examples are bicelles,²⁴⁸ lamellar LC,²⁴⁹ bacteriophages,²⁵⁰ and graphene oxide.²⁵¹ Small molecules are often analysed in organic solvents, and need different alignment media. There is a range of different polymers for LCs and SPs,^{184, 188, 232, 252, 253} but the most prominent one for LCs is arguably poly(γ -benzyl-*L*-glutamate) (PBLG).

1.7.4.4 Liquid Crystal

The anisotropy is introduced to the sample by simply dissolving the LC polymer into the sample tube.^{183, 221, 228, 254} The solution is then homogenised by forcing the LC back and forth inside the NMR tube. A hand-driven centrifuge is very practical for this part (also quicker than a proper centrifuge, and less likely to break the NMR tubes). The homogeneity is verified by measuring the quadrupolar splitting (RQC) of the deuterium signal through a 1D ²H experiment.

LCs are able to distinguish between enantiomers, as was shown with the chiral PBLG LC and its enantiomer PBDG (poly(γ -benzyl-*D*-glutamate)) enantiodiscriminating between the two enantiomers of isopinocampheol (IPC).²²¹ The selectivity of LCs is thought to come from chiral helices.¹⁷⁶

1.7.4.5 Stretched polymers

Stretched polymers are crosslinked polymers that swell in the solvents used. They are selected based on the solvent, such as the poly(-methylmethacrylate) (PMMA)^{225, 253} gel in chloroform and polyacrylamide (PAA) gel in water.^{252, 255}

The gels can either be stretched or compressed.¹⁸⁴ For the latter, SAG is the most fitting acronym. The drawback of compressing the gel is that the long axis of the molecule aligns orthogonally to the magnetic field, causing small RDCs. Denser gels were used to increase RDCs, which led to hindering rotational diffusion. This increase line broadening and reduce sensitivity.²⁵⁶ Stretched gels, on the contrary, lead the molecule to align parallel to the

magnetic field, doubling the RDCs, meaning a more dilute gel can be used, which is favoured.¹⁸⁴

Originally, SPs were based on self-stretching gels in NMR tubes.¹⁸⁴ Kuchel *et al.*²⁵⁷ introduced a stretching apparatus in 2006 where they could extract RDCs and ²³Na RQCs in gelatine SP mechanically, which was further developed by Kummerlöve *et al.*²⁵⁸ to cover all gels. Consisting of a rubber tube and clamps, the stretching apparatus uniformly stretches the gels mechanically inside the NMR tube to gradually increase anisotropy.^{253, 259}

In the self-stretching method, the gel can be cast in a size that will be sterically hindered from swelling normally either radially or vertically inside the NMR tube.^{176, 184, 188, 225, 260} Either the stick can be cast with a wider diameter than the tube, or a rod can be inserted into the tube to hinder vertical swelling (“confinement method”¹⁷⁶). The anisotropy is then introduced with steric interaction surfaces either vertically or horizontally, as the gel swells. The strength of the alignment can normally not be changed once the gel is cast, but rather tuned by changing the amount of cross-linker during the synthesis.^{225, 260} The vertical swelling was the first type to be introduced, but the main setback is that it takes up to several weeks to fully swell inside the NMR tube.^{188, 225} Because many proteins are not stable for that long time, they cannot be analysed by the vertically swelling gels. The radial swelling with vertical restriction was introduced as a solution to this, as it only takes up to a couple of days.^{188, 225}

SPs can also differentiate between enantiomers,^{174, 261, 262} but the number of systems that work for this purpose are fewer than for LCs. One prominent SP example that can distinguish between enantiomers is gelatine, and recently an SP able to discriminate between enantiomers in water, DMSO, and methanol has also been reported.¹⁷⁶ The field is continuously evolving with new systems that can be used to extract structural information.

1.7.4.6 Practical aspects

RCSA from a sample in chloroform with PBLG as the LC is calculated by equation (9) (adapted from Liu *et al.*¹⁸³)

$$RCSA_i = (\delta_{A1}^i - \delta_{I0}^i) - \left(\frac{[PBLG]_{A1}}{[PBLG]_{I1}} \times (\delta_{I1}^i - \delta_{I0}^i) \right) \quad (9)$$

where I0 is an isotropic measurement without PBLG; I1 is a second isotropic measurement, just below the critical PBLG concentration differentiating the isotropic and anisotropic states (c_{crit}); A1 is an anisotropic measurement above c_{crit} .

RDC is measured as the increase or decrease in the splitting in 2D ^1H - ^{13}C spectra. For f2 splitting, a common experiment is the HSQC-CLIP,^{263, 264} and for f1 splitting, the HSQC-IPAP.^{184, 265} For molecules with few protons, f2 splitting is fine, but for molecules with many protons, the proton-proton dipolar couplings can severely broaden the observed signals, making the measurements inaccurate at higher PBLG concentrations.¹⁸⁴ Therefore, HSQC-IPAP can be a better alternative. The splitting is measured in Hz. The advantage of the f2 dimension is that it gives higher resolution.

To validate the fitness of the theoretical structures, they are put through a fitting procedure.¹⁸⁴ The quality of fit is evaluated by a quality factor (Q factor), which reflects the average percentage disagreement between experimental and calculated RDC and RCSA values, as defined by equation 10. A lower Q factor corresponds to a better fit, while a higher Q factor could indicate problems with the conformations or configurations, and alternative structural proposals should be considered. A Q factor of 40% roughly corresponds to an R value of 0.9, commonly found in structures with 2-3 Å resolution, while a Q value of 20% or less indicates a structure of high resolution and accuracy, within 1.5 Å.²¹⁴

$$Q = \sqrt{\frac{\sum_{i=1}^N (V_i^{exp} - V_i^{calc})^2}{\sum_{i=1}^N (V_i^{exp})^2}} \quad (10)$$

where N represents the total number of data points measured, and V_i^{exp} and V_i^{calc} represent the experimental and calculated values of the i^{th} data point, respectively.

The preferred method of computing back-calculations of RDCs from 3D structures for small molecules is singular value decomposition (SVD).^{236, 247, 266} The method has proven reliable and applicable for the structures frequently used in literature,¹⁸⁸ especially when only a few (at least six) RDCs are known.²⁴⁷

One point that might cause issues, is that there are a whole new set of issues that arises if the molecule is close to planar.²⁶⁷⁻²⁶⁹ A flat molecular structure limits the sampling of anisotropic

data, potentially leading to an incorrectly determined alignment tensor and the experimental and back-calculated data to lead to the preference for an incorrect isomer. For a perfectly planar molecule, there are only three independent in-plane RDCs and the plane norm orientation from RCSA becomes redundant, which makes the SVD analysis with five independent RDCs difficult.^{268, 269}

Finally, it is important to keep in mind the reliability of the results from anisotropy is dependent on theoretical structures.¹⁸⁴ When comparing different diastereomers or enantiomers, changes in the computationally obtained structures can yield a different Q factor if the structures are not properly sampled.

1.8 Binding

Binding to a substrate is often described with the dissociation constant K_D , which describes the relationship between the rate constants k_{on} and k_{off} (equation (11)). A lower K_D describes a stronger binding.²⁷⁰

$$K_D = \frac{k_{off}}{k_{on}} \quad (11)$$

where k_{off} and k_{on} are the off- and on-rate constants, respectively. Another important constant is the partition coefficient K_P , which describes the preference of the substrate towards a lipid environment over an aqueous environment (equation (12)).²⁷¹

$$K_P = \frac{[substrate\ in\ lipid]}{[substrate\ in\ water]} \quad (12)$$

K_P is usually used to describe the concentration of a drug in the target tissue as opposed to the surrounding blood vessels,²⁷² which can be expanded to describe the preference of the substrate towards a lipid environment over an aqueous environment.²⁷¹

K_D and K_P can be considered to complement each other: K_D describes the interaction between the substrate and the lipids, while K_P describes the preference for the hydrophobic over the hydrophilic environment. The relationship between them is negatively correlating, though moderately linear for any given AMP in different lipid compositions.²⁷³

1.8.1 Fluorescence

The interface between lipids and water is a favourable environment for Trp. The amphiphilic properties of the amino acid give it very important roles for the hydrophobic-hydrophilic interface, such as functioning as an anchor along the lipid surface for stabilising membrane-spanning proteins.^{274, 275} Trp is the most energy-taxing amino acid to synthesise, partially explaining why animals do not make it themselves and instead obtain it from plants. Following, Trp is a scarce and precious amino acid in the cell and is only used parsimoniously: only 1.1% the amino acids in cytoplasmic proteins are Trp, while the same amino acid makes up 2.9% of the amino acids in membrane-bound proteins. The cation- π interaction that comes from the aromatic rings of Trp being close to Lys or Arg can provide energy stabilisation of several kilocalories, which is often more than ionic bridges.²⁷⁵

Additional to be more abundant in membrane-bound proteins, Trp is also found in many AMPs.²⁷⁶ The amino acid has shown to be advantageous in stabilising folding into lipid bilayers.²⁷⁵ Interestingly, the amino acid has an intrinsic fluorescence; a fluorophore can absorb a photon of the correct wavelength to reach an excited state.²⁷⁷ The fluorescence happens when the fluorophore subsequently emits a photon of a longer wavelength. This shift in wavelength of the photon from the absorbed to the emitted is known as Stokes law.

The fluorescence quantum yield is the fraction of the absorbed photons that are emitted as fluorescence.²⁷⁸ The quantum yield is dependent on many factors: temperature, fluorophore concentration, and level of quenching being some of them.

Quenching is a description of how the fluorophore is hindered from emitting a photon when a photon source is present.²⁷⁹ The fluorophore can generally be quenched by either static or dynamic quenching. The former describes processes where the fluorophore is being prevented from reaching the excited state, while the latter describes any non-radiative (without releasing a photon) way of going from the excited state to the ground state. The most used example of dynamic quenching is to force the fluorophore to collide with a quencher, which is often a solvent.

Trp is very sensitive to the polarity of the local environment:²⁸⁰ the quantum yield increases in intensity when it is exposed to a hydrophobic environment, and is reduced when it is exposed to an aqueous environment. The water works as a dynamic quencher of the fluorophore signal, so with increased lipid concentration, an increase in the quantum yield is expected. Therefore, to determine K_P in peptide-membrane interactions, the fluorescent intensity is monitored in the presence of an increasing amount of lipid.²⁸¹

1.8.2 Microscale Thermophoresis

Microscale thermophoresis (MST) is a relatively new technique pioneered by Nanotemper, used to investigate the binding of a substrate to a target, usually an enzyme to a ligand.²⁸²

Thermophoresis describes the movement of molecules along a temperature gradient (normally hot to cold), determined by the concentration of a substrate in the cold environment relative to the concentration in the hot environment. This relationship is described by the Soret coefficient, S_T .

$$S_T = \frac{[Hot]}{[Cold]} \quad (13)$$

The mixture of the substrate and target is held in a series of capillaries inside the MST instrument, and the capillaries are heated with an IR laser (Figure 15). A volume with a 50 μm volume is heated by 4-6°C, creating a small temperature gradient for the substrate and target to move along.

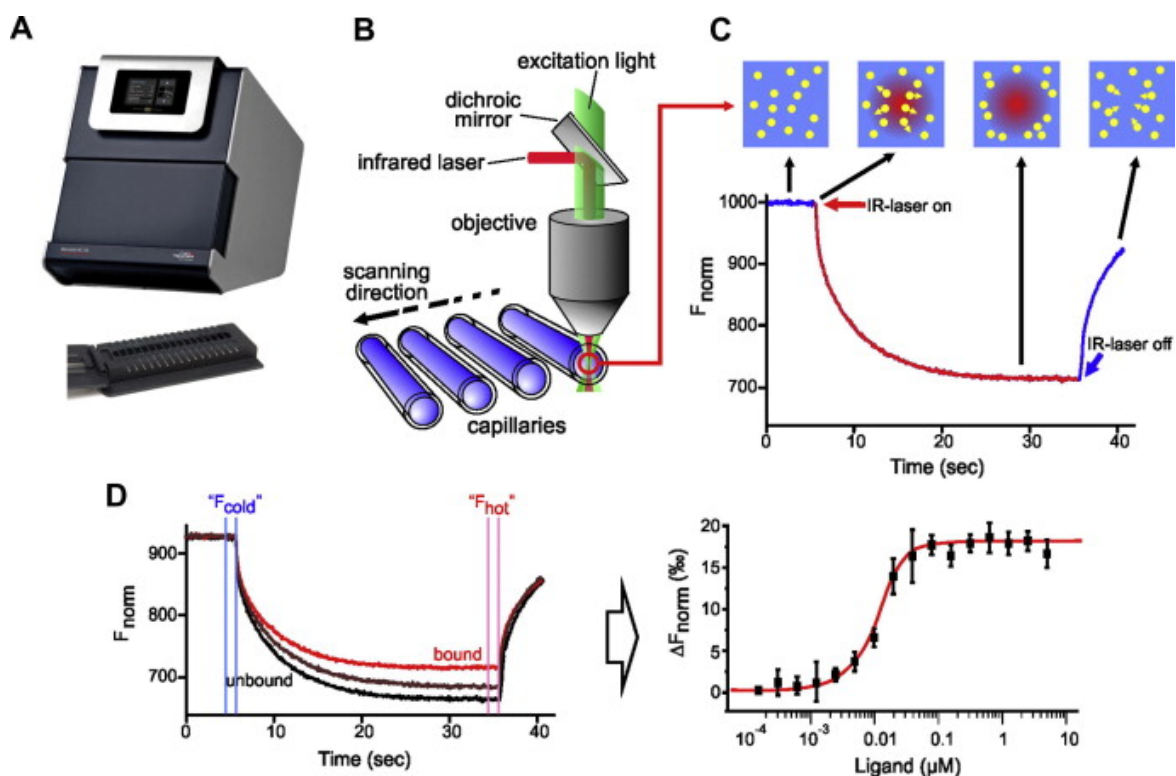


Figure 16. MST setup and experiments. (A) The NanoTemper MST instrument with a capillary tray which can accommodate up to 16 capillaries with increasing ligand concentration. (B) Schematic representation of MST optics. (C) Typical signal of an MST experiment, showing the initial fluorescence in blue, the effect of the IR laser in red, and the inverse T-jump in blue again. (D) Typical binding experiment. The thermophoretic movement of a fluorescent molecule (black trace; “unbound”) changes upon binding to a non-fluorescent ligand (red trace; “bound”), resulting in different traces. Reprinted with permission by Elsevier, Jerabeck-Willemsen et al.²⁸²

S_T is obtained by observing the fluorescence of a target, either as the intrinsic fluorescence or from an attached fluorophore tag.¹⁰⁰ The intrinsic fluorescence can be obtained with residues such as Trp or Tyr. In the NanoTemper instrument, the initial fluorescence is monitored 1-3 seconds before the IR laser is activated. When the laser is activated, a temperature-related intensity change (TRIC) occurs due to the dependence on a quantum yield of a fluorophore on temperature; the TRIC is observed within the first second and is referred to as the T-Jump (Temperature-Jump).

After the initial 1-1.5 seconds, the TRIC has taken place and the thermophoresis of the target occurs until a steady state is reached, normally within 15-30 seconds. Then, the IR laser is deactivated, and a reversed T-Jump is observed as the capillary cools down and the temperature gradient dissipates, and the target returns to a stable condition.

S_T can be determined from the relative intensity of the fluorophore during the application of the laser right after the T-Jump section (F_{Hot}) compared to before the laser is applied (F_{Cold}), where the intensity correlates to the relative concentrations in either environment (F_{norm}).

$$S_T = F_{norm} = \frac{F_{Hot}}{F_{Cold}} \quad (14)$$

S_T can also be described more thoroughly through equation (15).

$$S_T = \frac{A}{kT} \left(-S_{hyd} + \frac{\beta\sigma^2_{eff}}{4\epsilon\epsilon_0 T} \chi\lambda_{DH} \right) \quad (15)$$

where S_{hyd} is the entropy of solvation of the complex, A is the size of the complex, T is temperature, k is Planck's constant, and $\frac{\beta\sigma^2_{eff}}{4\epsilon\epsilon_0 T}$ describes the overall properties of the complex. This means that the MST response is very sensitive to small changes to the complex when binding takes place.

One of the advantages of MST is that by sampling F_{Hot} at different stages, different information can be extracted: By selecting the T-Jump region at about 1.5 seconds, changes in the environment of the fluorophore can be observed, or by waiting for the steady state, the thermophoretic properties of the whole fluorophore-containing complex can be observed. The steady-state region of the MST trace was previously considered the best practice region to use. As the prolonged heat exposure from the IR laser may influence the stability of complexes, the best practise analysis has been reevaluated, and is now considered to be the T-Jump section.²⁸³ The steady-state region is now considered to be best to look at the stability of complexes.²⁸⁴

For the experimental setup, the source of fluorescence must be at a fixed concentration. As the protein or enzyme usually is the fluorophore, the substrate concentration is varied over a series of dilutions. Each point is a separate sample in a capillary tube in the NanoTemper instrument, along with one sample each of only substrate and only target. The result from the MST run should be a sigmoidal dose-response curve that can fit into the hill model (equation (16)), where y_0 is the response of the target on its own and B_{max} is the difference between y_0 and the maximum response. MST can detect bindings all the way down to nM and pM ranges.

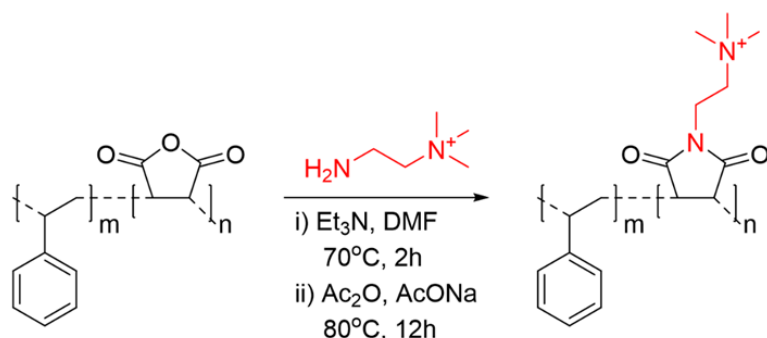
$$y = y_0 + \frac{B_{max}K_D[Ligand]}{K_D[Ligand]} \quad (16)$$

So far, not many studies use MST to investigate peptide-lipid interactions. One early study found the K_D of a 13 residue AMP, L-RW, to DMPC and DMPG lipids in a series of different buffer conditions.¹⁰⁰ The observed K_D s were in the low μ M range, which is typical for many peptides. The disadvantage of the study is that L-RW was covalently bonded to a bulky label, fluorescein isothiocyanate (FITC), to observe the binding. The label itself comes with its own physiochemical properties, which will likely influence the properties of the bonding, along with the properties of the complex itself. Therefore, a label-free method would be more practical.

2. Methodology

The materials and methods used in this work have been thoroughly described in the papers and manuscripts. The following chapter aims not to repeat what is already available there, but to make some of the discussed topics more easily available and to add information that did not fit the publications.

2.1 Synthesis of SMA-QA



Following the procedure of Ravula *et. al.*,^{285, 286} (2-aminoethyl)trimethylammonium chloride hydrochloride (9.38 mmol, 1.3 g) was added to a solution of styrene maleic acid anhydride (SMA, 1g) in anhydrous DMF (5 mL), followed by trimethylamine (56.7 mmol, 5 mL) upon which the mixture took a dark yellow colour. The reaction mixture was stirred at 70°C for 2 hours, then cooled to room temperature, and precipitated with diethyl ether. The precipitate was washed 3 times with diethyl ether and dried *in vacuo*. The dried intermediate was dissolved in acetic anhydride (317 mmol, 30 mL), to which sodium acetate (8.05 mmol, 660 mg) and triethyl amine (1.98 mmol, 200 mg) were added. The reaction mixture was stirred at 80°C for 12 hours, cooled down, and precipitated in ether. The precipitate was washed 3 times in ether and dried *in vacuo*. The product was then dissolved in water and passed through a Sephadex LH-20 column. The product was collected and then lyophilized to give a crystalline brown powder and confirmed by IR stretching frequency shift from 1774 cm^{-1} to 1693 cm^{-1} .

2.2 Preparation of large multilamellar vesicles

To a pear flask was added lipid (100 mg DMPC / 5.1 mg DMPG + 94.9 mg DMPC). Chloroform was added until all was dissolved. The solution was slowly evaporated on a rotavapor at an angle for 1 hour to make a thin film. The film was then lyophilized overnight to get rid of trace amounts of chloroform. The film was diluted to a 20 mM solution by adding

distilled water (7.15 mL). The solution was agitated with a Pasteur pipette to make sure everything was dissolved and homogenous, then transferred to 7 1 mL Eppendorf tubes. The tubes were freeze thawed three times by alternating between liquid nitrogen and hot water. The tubes were then stored in a freezer (-20°C) until needed.

2.3 Preparation of nanodiscs

SMA nanodiscs were prepared by adding an 8% SMA stock solution to the thawed lipid stock to a final concentration of 1% SMA.²⁸⁷ SMA-QA nanodiscs were prepared by adding a 100 mg/mL SMA-QA stock to a final concentration depending on size goal (lipid:SMA-QA ratio of 1:1.5 for 10 nm discs; 1:1 for 20 nm discs; 1:0.25 for 30 nm discs). The combined SMA/SMA-QA and lipid mixture were incubated over night at room temperature and purified by SEC. Fractions containing nanodiscs were combined and concentrated using centrifugation filters. Total lipid concentration was determined by ³¹P NMR with 2 μL 5% Trimethyl Phosphate (TMP) as internal reference. Nanodisc size was confirmed using a Malvern Zetasizer Nano ZS (Malvern Panalytical Ltd, Malvern, United Kingdom).

2.4 Preparation of stretching gel

The method for preparation of stretching gels is based on the ratios from the published method of Tycko, Blanco, and Ishii,²⁵² a list of tips from NewEra,²⁸⁸ in conjunction with own adjustments.²⁸⁹

Gels were cast in room temperature in a Gel Chamber with an internal diameter of 5.4 mm, under a blanket of argon gas. 1% (w/V) ammonium persulphate solution was freshly prepared. One side of the gel chamber was covered with parafilm, and then acrylamide solution (acrylamide/bisacrylamide 19:1), 1% ammonium persulphate solution, N,N,N',N'-Tetramethylethylenediamine (TEMED), and H₂O, were quickly added in that order under a blanket of argon gas. The polyacrylamide (PAA) gel was left overnight to set before it was carefully removed from the Gel Chamber with a Gel Press. Unreacted acrylamide was removed by adding the wet gel to a tube filled with H₂O and left for a minimum of two hours, for a total of three times. The gel was then left to dry overnight at room temperature on top of

a piece of parafilm. The dried gel was dropped into a 2 mM solution of each cyclic hexapeptide in H₂O/ D₂O 90%/10% and 0.5% TMSP-d₄ as internal standard. After about two weeks, the gels were fully stretched laterally, and NMR spectra were collected.



Figure 17. (Left) The New Era gel transfer set used to transfer the PAA gel from the casting/swelling chamber, in the middle, to the open-ended NMR tube. (Middle) Two sticks of cast PAA gels after washing, ready for drying on parafilm. (Right) Dried PAA gel and stretched PAA gel in an open-ended NMR tube with a bottom plug and top rod, Eppendorf tube for scale.

Some observations made on gel preparation:

- 1% (w/V) ammonium persulphate solution needs to be prepared freshly. Even just a week-old solution can cause the finished gel to be malformed or large parts of the gel to not set properly.
- The water was added last as it is the biggest volume, so it will mix the ingredients thoroughly. Mixing in another order and shaking with parafilm on both sides also work, but the gel sets quick, and adding the water last to mix everything yielded more homogenous gels.
- 1050 μ L gel solution in the 5.4 mm Gel Chamber yields a gel that is approximately 4 cm long.
- NEVER touch the wet gel with gloves: It is sticky and will leave parts on the glove so that it becomes malformed if not destroyed.
- The gel can dry malformed in a petri dish, but parafilm is slippery enough so that the gel dries into a more or less straight stick.

- The open-ended NMR tube from NewEra has a tendency to crack when inserting the end plug, no matter how careful you are.
- It might help running some water through the open-ended NMR tube before transferring the swelled gel from the gel chamber. That way there is less chance of the gel sticking to the walls.
- You can insert the gel in the “bottom” part of the open-ended NMR tube, you do not need to push it through the whole open-ended NMR tube.
- It is better to swell the gel in a normal NMR tube in a solution of your analyte. The open-ended NMR tubes are expensive and take long to arrive.
- Liu *et al.* have produced two papers that are excellent step-by-step guidelines for how to prepare and obtain anisotropic NMR spectra in both LCs and SPs.^{183, 184}

2.5 Evaluating against computational data

When evaluating computationally simulated conformers for chemical shifts or J -coupling constants, mean absolute error (MAE) is used.^{188, 290}

$$MAE = \frac{1}{n} \sum |x_i^{exp} - x_i^{calc}| \quad (17)$$

3. Aims of the current thesis

The project was focused on how to use NMR spectroscopy to extract configurational and conformational information of molecules in different environments.

The main research aim:

1. Investigate structural properties of peptides in different environments, including membrane model systems, using NMR spectroscopy.

Secondary research aims:

2. Investigate membrane mimicking models, such as nanodiscs and micelles, with varied lipid compositions as membrane models.
3. Explore methods to extract key structural and dynamic parameters from membrane-active, antimicrobial peptides (AMPs).
4. Utilise data obtained by NMR in conjunction with computational methods.

4. Results and discussion

4.1 Structure elucidation and antiproliferative activity of a new natural product, Commafric A (Paper I)

Commifora africana is a plant that is used in a variety of natural medicine in broad parts of the African continent.¹⁸¹ Several natural products with medicinal use have been extracted from the plant already, with effects such as antitumor-, anti HIV-1, and analgesic activity.

The resin of *C. Africana* was extracted, and two natural products were purified, Commafric A and α -amyrin. The latter was already known in literature and is thoroughly studied. The structure of Commafric A was mapped through a combination of MS, UV, and NMR. The relative configuration of most stereocentra were found by using NOESY/ROESY spectra and anchored by looking at the biological precursor.

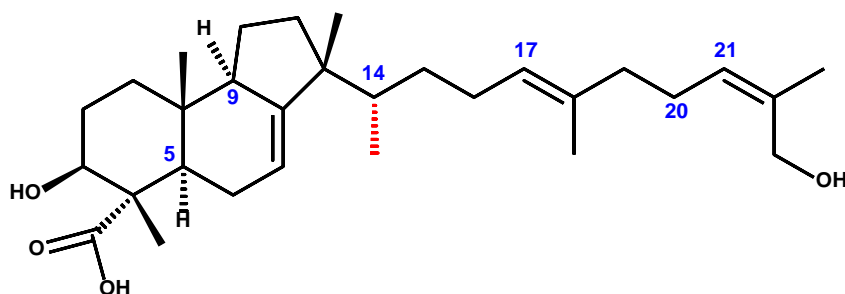


Figure 18. The full structure of the new natural compound (3*S*,4*S*,14*S*,7*E*,17*E*,21*Z*)-3,30-dihydroxypodioda-7,17,21-trien-4-carboxylic acid (Commafric A).

Unfortunately, it was not possible to crystallise for X-ray crystallography. The only part that could not be solved from NOE/ROE distances was the chirality of carbon number 14. Theoretical VCD spectra were simulated computationally by making 27 conformers for both the *S*- and *R*-configuration, focusing on the tricyclic system, while the tail (C14-C30) was not considered. Comparison of the theoretical and experimental VCD spectra seemed to prefer the *S* configuration of C14, but arguments could be made that parts of the different spectra

favoured either configuration (See Figure 19). $^3J_{\text{CH}}$ coupling constants were also inconclusive, while NOE distances slightly favoured the *S* configuration.

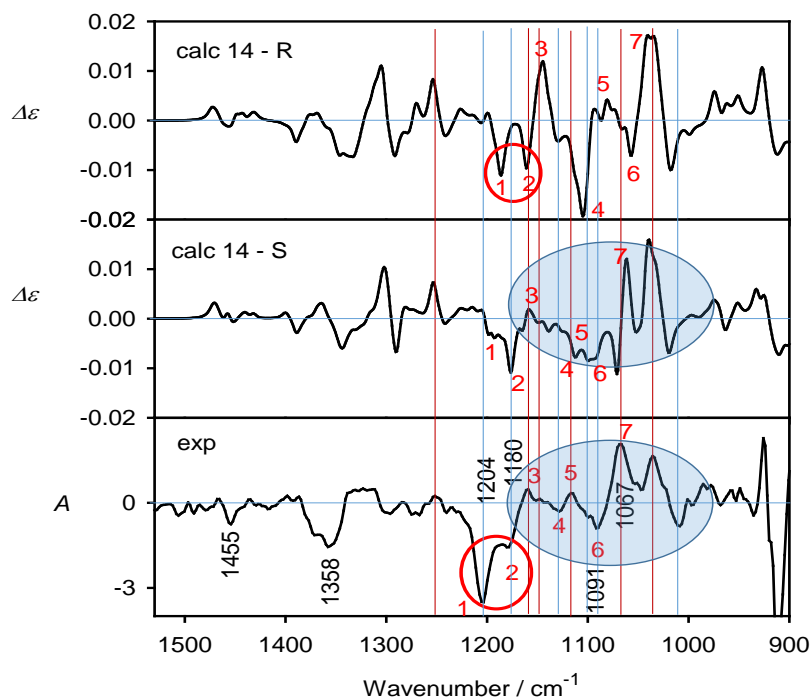


Figure 19. VCD spectra calculated for the *R* and *S* C14 isomers (upper and middle panels, frequency scaled by 0.967) and the experiment (lower panel). Experimental wavenumbers are denoted in black, and selected bands are assigned identifiers denoted in red. Positive experimental bands are traced with red lines and negative experimental bands are traced with blue lines. Figure from paper I, reprinted with permission by Springer Nature, Dinku et al.^{71, 181}

From previous experience working with PBLG to extract RDCs and RCSAs in chloroform, it was decided that this technique was the best solution to extract the absolute configuration of C14. NMR spectra were acquired in chloroform to keep track of any changes in chemical shifts from the originally utilised dichloromethane. Subsequently, IPAP-HSQC spectra for RDCs and ^{13}C spectra with TMS as an internal reference for the RCSAs were extracted, at increasing concentrations of PBLG (See Figure 15). By using the conformers made for VCD and NOE, the *S* configuration of carbon-14 was deemed a significantly better fit than the *R* configuration (Figure 20).

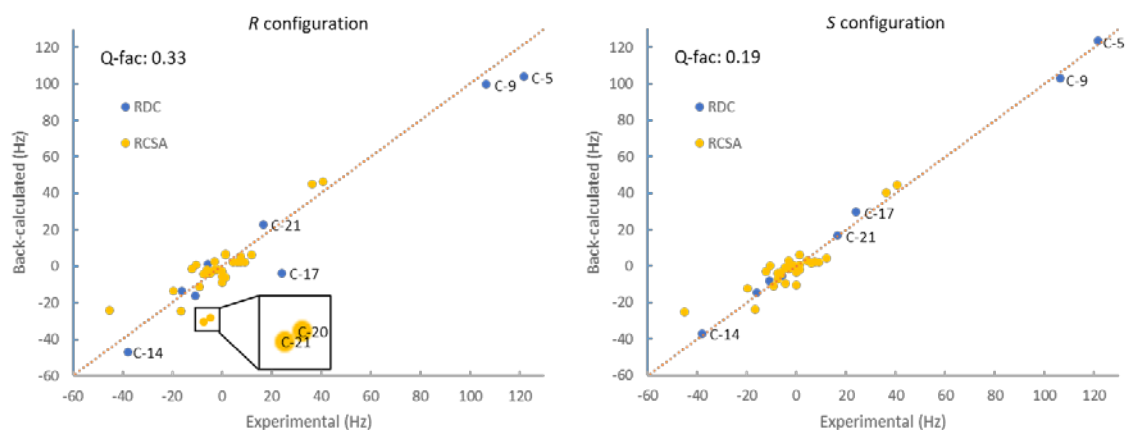


Figure 20. Comparison of RDC and RCSA data collected in PBLG of Commafric A, showing the S conformer as the preferred conformation. Figure from paper I, reprinted with permission by Springer Nature, Dinku et al.^{71, 181}

Note that as the PBLG concentration increased, the viscosity of the sample increases significantly, and a centrifuge is needed to be able to mix the sample back and forth in the NMR tube. The LC is too viscous to simply shake by hand. A hand centrifuge is very practical for this purpose, as it takes considerably shorter time to wind up and down than a traditional centrifuge, saving time during the mixing stage of preparing the LC. Another challenge encountered was that increased concentration of PBLG caused the lock to be troublesome to obtain, and it would sometimes be lost during a run. Additionally, there were trouble shimming properly. The problem with the lock stems from the anisotropic peak becoming prominent in the ^2H spectrum and then the lock program not being able to properly select what signal to lock onto. Two ways to fix this is either to lock on a sample with only pure chloroform, and then changing back to the Commafric A sample without locking or shimming, or to use a special lock program where the initial ^2H splitting was checked and a selective pulse for locking only one of the components of the quadrupolar doublet was used.

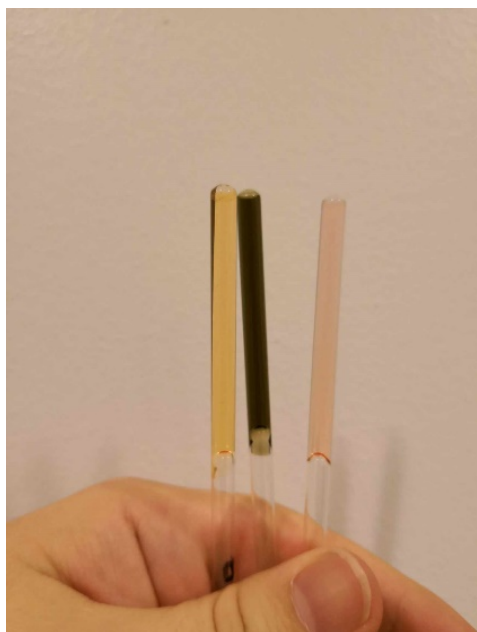


Figure 21. Three NMR samples with high concentrations of PBLG. After being held upside-down for five minutes, the solution slowly started to move (see the surface).

When comparing the experimental RDCs and RCSAs to the conformers in MSpin, different selections of conformers were tested. From just the three most advantageous (energy-wise) to the full selection. Though the Q-factors changed slightly between selections, the result was always in the favour of the *S*-stereoisomer.

Regarding TMS as an internal reference, work on PMMA stretching gel indicate that CCl_4 is a slightly better reference, as there is no change in the shift for the reference.²⁵³ TMS has a very slight drift, but is often seen in a standard lab, is cheaper than CCl_4 , and is also much safer to handle. The slight drift in chemical shift does not make up for the challenges of the alternative reference material CCl_4 .

Antiproliferative activity was checked against four human cell lines and showed moderate activity against non-small cell lung cancer (A549), suggesting that Commafric A has the potential to be further optimised as a lead compound in the search for new anticancer drugs.

Commafric A also was a good system to start working on with anisotropy, as a structured system to establish the techniques on.

4.2 LPS as an initial target and barrier for cationic AMPs (Paper II)

As described in the introduction, AMPs are growing in interest as an alternative to classical antibiotic drugs.²⁹¹ The largest class of currently investigated AMPs contain a significant fraction of cationic residues, especially arginine and lysine. Additionally, the antimicrobial peptide database APD3 shows that 80% of all AMPs contain at least one hydrophobic phenylalanine or tryptophan.⁶⁶

As the main mode of action of AMPs seem to be membrane disruption, the hydrophobic bulk is important for the interfacial interaction with the membrane. The interaction with lipopolysaccharides (LPS) from the Gram-negative bacteria is less investigated. LPS is a major component of the outer membrane of Gram-negative bacteria, and work as a barrier that any molecule needs to pass to interact with the membrane.

Like Goldilocks in the fairytale wanted a chair, bowl of porridge, and bed that was “just right”, the peptide needs to have a hydrophobic:hydrophilic ratio that is “just right” so that the interaction with the LPS is strong enough for initial electrostatic interaction to be drawn to the bacteria, but not so strong that it binds too well to the LPS.

A toolbox was presented, using SPR and live-cell NMR with a series of cyclic cationic AMPs (cAMPs) (Figure 22) and three *E. coli* strains, including LPS-deficient (NR 698) and LPS colistin-resistant (CCUG 70662) strains (Table 1). *E. coli* strain CCUG 70662 was cultivated in the absence and presence of colistin. In the presence of colistin, phosphoethanolamine added to the lipid A moiety of LPS, reducing the overall negative charge of LPS.^{292, 293} In *E. coli* strain NR 698, translocation of LPS from the periplasmic space to the outer leaflet is hindered, making the outer membrane structurally deficient.²⁹⁴ By having a series of strains with different modifications to LPS, the role of LPS to antimicrobial activity can be better defined. Additionally, different lipid models were used with increasing negative charge, from pure DMPC to DMPC/DMPG (95:5) and DMPC containing 10% LPS. Both the inclusion of DMPG and LPS allows for investigations towards the effect of charge, while also looking at the character of those charges.

4.2.1 Nuclear magnetic resonance

Four cyclic hexapeptides were already chosen and utilised by DigiBiotics, due to already established knowledge on alternating versus clustered distribution of hydrophobic and charged residues,²⁹⁵⁻²⁹⁹ where the clustering of Trp and charged residues is shown to have a direct positive correlation to antimicrobial activity.⁹⁰

The structure of the five hexapeptides were elucidated using standard methods: The chemical shifts of the amino acids were found using a combination of COSY, HSQC, and TOCSY for the sidechains, and the quaternary carbons were found through HMBC, while the nitrogen signals were found through ¹⁵N-HSQC. The amino acid order was found by using NOESY signals between ¹⁵N-H and H_α. (Tables of all chemical shifts can be found in the supporting information of the paper).

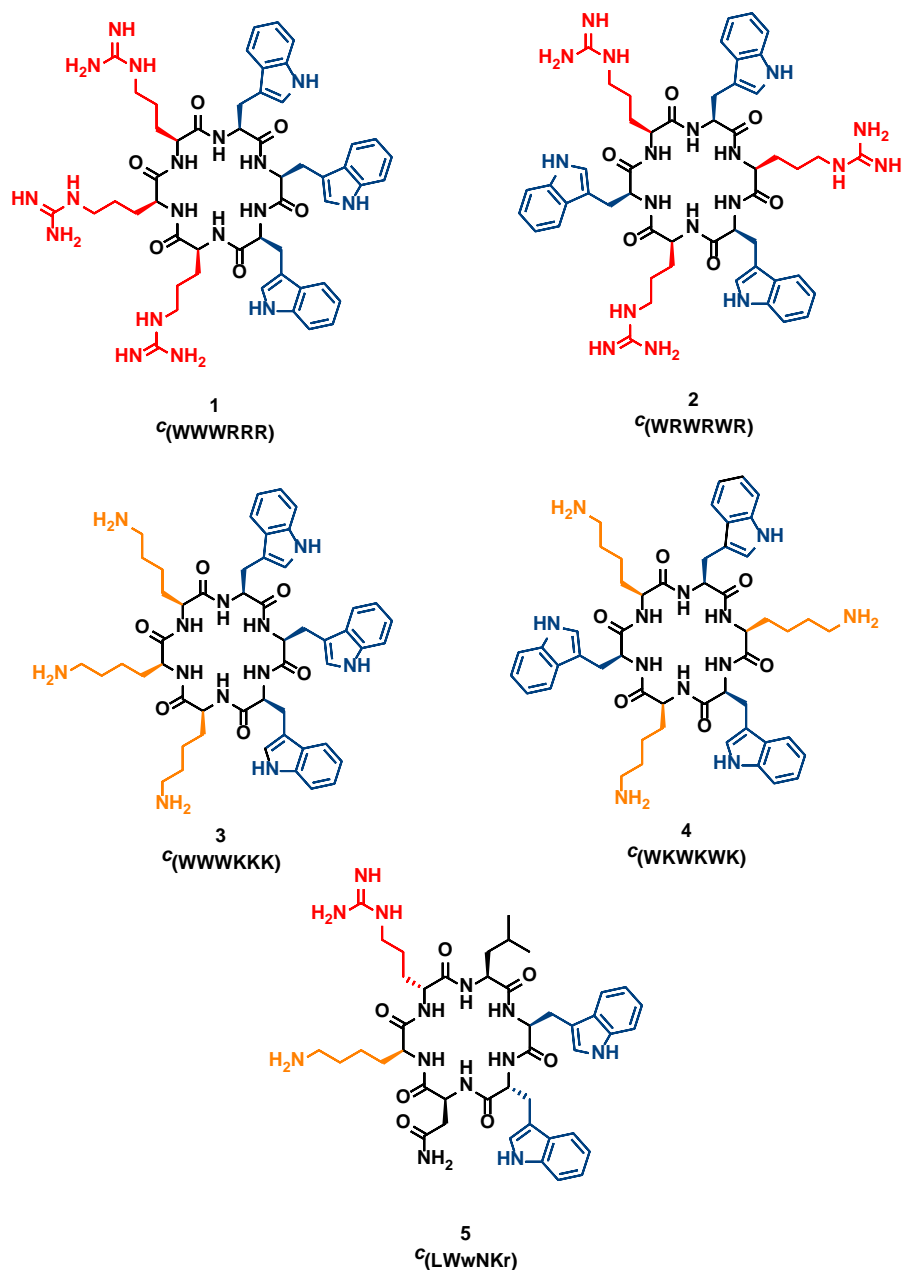


Figure 22. The four cyclic hexapeptides (1-4) that were chosen by DigiBiotics as the main focus, together with a fifth, inactive peptide (5). Coloured red/orange—R/K, blue—W. Uppercase letters indicate *l*-amino acids, lowercase letters indicate *d*-amino acids. Figure from paper III, reprinted with permission by Springer Nature, Rainsford et al.^{71, 285}

A fifth peptide with a similar structure was chosen, which had proven to be a poor antimicrobial and lipid binder.

4.2.2 Antimicrobial activity

The antimicrobial activity was tested against *S. aureus*, *P. aeruginosa*, and three strains of *E. coli* (Table 1). Clumped residues were found to be more effective than alternating, and Arg is more effective than Lys. Cultivating in the presence of colistin leads to an overall reduction in the negative charge of LPS, due to the addition of phosphoethanolamine to the lipid A moiety of LPS.^{292, 293}

The colistin-resistant strain CCUG 70662 is still susceptible to the hexapeptides after colistin cultivation has induced modification of lipid A. Colistin binds to LPS, displacing divalent cations from LPS, increasing the fluidity of LPS and causing major disruption of the lipid membrane. No change in activity against CCUG 70662+ with modified lipid A suggests the mode of action of the peptides is not directly related to lipid A binding.

Table 1. MIC and ζ potentials for the tested peptides against *P. aeruginosa*, *S. aureus*, and the three *E. coli* strains: ATCC 25922, LPS deficient—NR 698, and colistin-resistant CCUG 70662, which was tested after cultivation with (+) and without (–) 4 $\mu\text{g}/\text{mL}$ of colistin, which caused a decrease of negative charge of the cell wall. MIC values for *P. aeruginosa*, *S. aureus*, and *E. coli* ATCC 25922 are reproduced from Rainsford et al.²⁸⁵ Table from paper II, reprinted with permission by the Multidisciplinary Digital Publishing Institute (MDPI), Jakubec et al.^{71, 291}

AMP	MIC ($\mu\text{g}/\text{mL}$)					
	<i>P. aeruginosa</i> ATCC 27853	<i>S. aureus</i> ATCC 9144	<i>E. coli</i> ATCC 25922	<i>E. coli</i> CCUG 70662–	<i>E. coli</i> CCUG 70662+	<i>E. coli</i> NR 698
Zeta potential	-	-	$-21.3 \pm 0.6 \text{ mV}$	$-21.8 \pm 0.8 \text{ mV}$	$-14.3 \pm 0.5 \text{ mV}$	$-21.2 \pm 0.6 \text{ mV}$
c(LWwNKr)	>250	>250	>250	>250	>250	32
c(WKWKWK)	>250	128	64	64	64	4
c(WRWRWR)	64	32	32	16	32	2
c(WWWKWK)	32	32	8	4	4	2
c(WWWRRR)	16	4	8	8	8	4

4.2.3 Surface plasmon resonance

Surface plasmon resonance (SPR) can be used to measure partitioning of small molecules into lipid bilayers. Liposomes are immobilised on the surface of the SPR chip, and AMPs are injected over the lipid bilayer at increasing concentrations. The measured response in the plasmon wave allows for determination of the partitioning constant K_P and the dissociation

rate k_{off} , along with making an estimate of the dissociation constant K_D from the steady state data using a generalised binding model. k_{on} can then be estimated from the relation between K_D and k_{off} (equation (11)).

Lipid models were chosen as pure DMPC, DMPC:DMPG (95:5), and DMPC liposomes containing 10% LPS (isolates from *E. coli* O111:B4). DMPC liposomes represent neutral membranes such as those found in eucaryotic cells, making it a useful probe for lipophilicity of the peptides. Inclusion of 5% DMPG makes the net charge of the membrane surface negative, akin to a procaryotic membrane. Inclusion of the LPS in the membrane makes it the closest to the outer membrane of Gram-negative bacteria, as LPS is unique to those membranes. LPS also introduce an anionic charge through ketodeoxyoctanic acid components.³⁰⁰ Using these different lipid models allows for investigating into how AMPs interact with different membranes and how different charge interactions affect the binding.

The measured K_P for the different peptide-membrane combinations spans a wide range of values over three orders of magnitude (Figure 23). The peptide c(WWWRRR) interacts strongest with the DMPC lipid bilayer, while the negative control peptide c(LWwNKr) has the weakest interaction, as expected. The active peptides have K_P values up to one order magnitude higher than the inactive peptide. Introducing the 5% DMPG into the bilayer doubles K_P for all peptides, except for c(WKWKWK), where the increase less significant.

The K_P in DMPC liposomes follows the trend of the MIC against the Gram-positive bacteria *S. aureus*. The negative charge of DMPG and LPS both increase the affinity for the membrane, but all peptides except c(WWWKKK) saw a greater increase with LPS than with DMPG. c(LWwNKr) showed a four-fold increase in K_P when LPS was introduced.

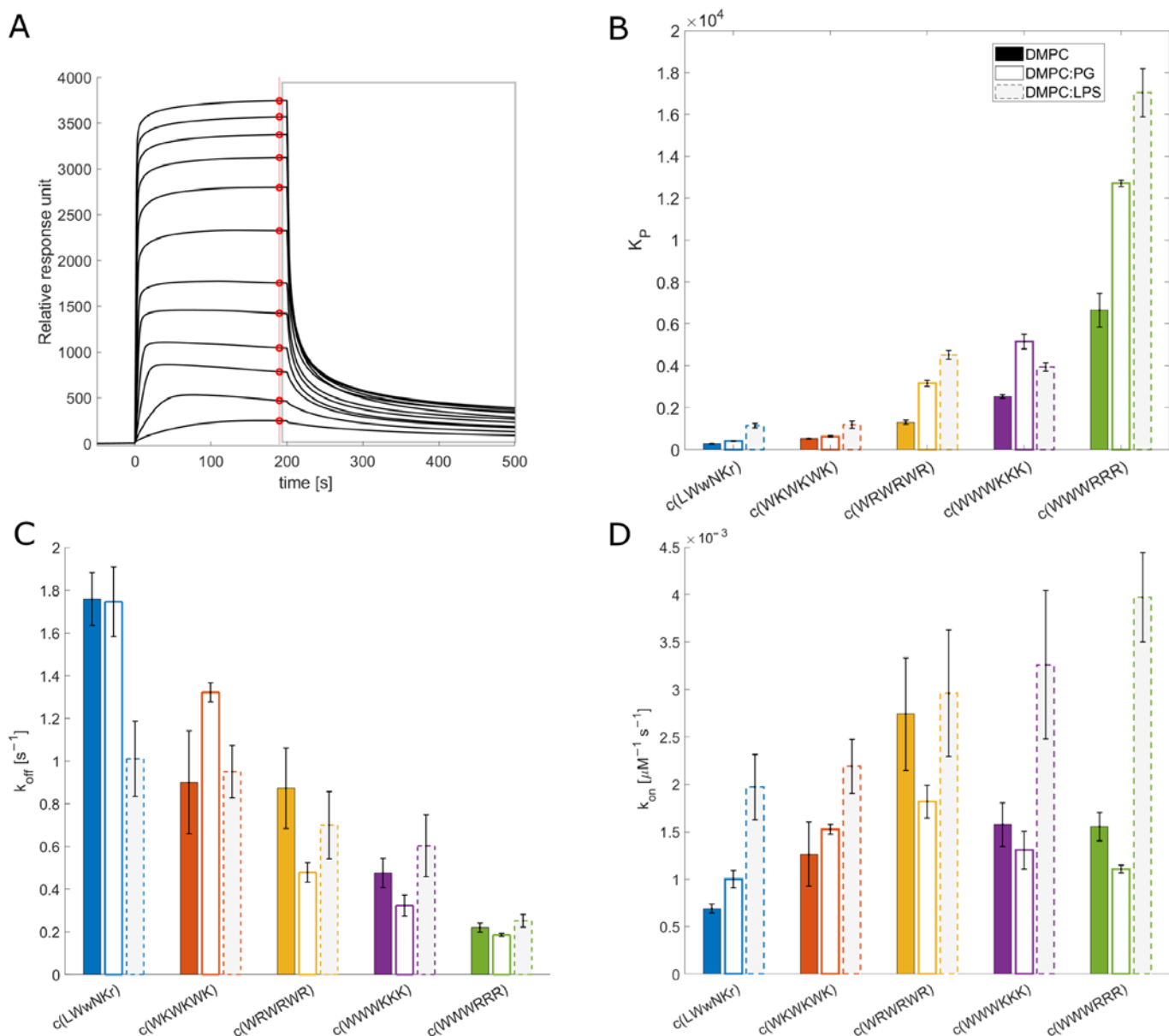


Figure 23. SPR results (A): Example SPR traces from $c(WWWRRR)$ interaction (from 4 to 128 μM) with DMPC:PG liposomes. Red points indicate values used for steady-state fitting (to obtain K_D and K_P). The grey rectangle indicates the dissociation process, which is used to obtain k_{off} according to Figuera et al.³⁰¹ (B): Partitioning constants K_P . Full, empty, and grey bars correspond to DMPC, DMPC:PG (95:5), and DMPC:LPS (90:10) liposomes, respectively. (C): Dissociation rate k_{off} . (D): Association rate k_{on} , which is obtained by calculation using measured K_D (Paper II, Figure S1). Values for DMPC and DMPC:PG interaction are reproduced from Rainsford et al.²⁸⁵ Figure from paper II, reprinted with permission by the Multidisciplinary Digital Publishing Institute (MDPI), Jakubec et al.^{71, 291}

LPS did also not affect k_{off} rate for any of the active peptides but increased the k_{on} rate across the board. Meaning that LPS is a driver for initial interaction, but not the final destination, which remains the lipid membrane. $c(\text{WWWRRR})$ is observed to have the same MIC values as $c(\text{WWWKKK})$ towards all strains, even when the k_{on} values for the former is higher and Lys is shown to be less destructive towards bacterial membranes than Arg. This result shows what is meant by the Goldilocks dilemma: $c(\text{WWWRRR})$ has a higher k_{on} but lower k_{off} than $c(\text{WWWKKK})$, which is mirrored in a similar MIC value. What this means is that $c(\text{WWWRRR})$ is more easily attracted to LPS but is hindered from passing on to the membrane surface as quickly. $c(\text{WWWKKK})$ has the best combination of k_{on} and k_{off} between the tested peptides, placing it in the Goldilocks zone; not too strong, and not too weak, but just right.

Some care needs to be taken, though, as k_{on} is based on the measured K_{D} and k_{off} . With a more complex membrane model, including more possible binding sites, the measured K_{D} can be a composite K_{D} from several different bindings, and therefore the estimated k_{on} might be affected.

4.2.4 Live-cell NMR

Looking at the line shape in 1D ^1H NMR can be used to investigate the same interactions, keeping the peptide concentration constant and adding in liposomes. The size of the AMP-vesicle complex results in line broadening and signal loss. The signal loss can be quantified to estimate K_{D} ,³⁰² as long as the exchange rate between the bound and unbound states are sufficiently slow. The results are in line with the SPR results, though with slightly different absolute values.

The same method was used with *E. coli* strains for the lipids. There were significant differences between the different strains, showing the AMP:strain specificity. Both clumped peptides showed a decrease in K_{D} when the lipid A part of LPS was modified, strengthening the idea that the interaction of the clumped arginine is mostly driven by hydrophobic interactions, while the alternating peptides are driven by charge interactions. $c(\text{WRWRWR})$ also seemed to show an affinity towards lipid A.

One thing to keep in mind is that this method assumes that the signal loss is solely dependent on binding. It can also be affected by relaxation as an effect of exchange within the NMR time scale (k_{ex}) (equation 18), where faster exchange will make more of an impact. SPR showed that all five tested peptides have relatively slow off-rates ($k_{off} < 10 \text{ s}^{-1}$). Therefore, the contributions from the on/off-exchange process are not expected to significantly affect the signal loss. Chenal and colleagues have extracted K_{DS} in peptides bound to membranes using similar parameters, showing that they are decent assumptions to make.³⁰³

$$k_{ex} = [PL]k_{off} + k_{on}*[P][L] \quad (18)$$

where [P], [L] and [PL] are concentrations of free peptide, free vesicle and peptide-vesicle complex, respectively.³⁰⁴

This work shows that simple models show simple, straightforward answers. Unfortunately, real bacteria are complicated, which results in a more complex result when LPS is introduced, or when bacteria are used. This is a field that still needs a lot of work and investigations into all aspects of it.

4.3 Peptide-lipid interactions (Paper III)

A low-threshold method that does not require labelling to explore peptide-lipid interactions is a very useful tool. Nanodiscs and peptides are produced in small quantities, while also being necessary for different experiments, favouring experiments that use small quantities. Additionally, the newly established, positively charged SMA-QA nanodiscs, makes for a good system to investigate to what degree a positive or negative charge of the polymer that keeps the nanodiscs together effects binding.

4.3.1 Synthesis of SMA-QA

Ravula *et al.* describe three methods of synthesising SMA-QA, with small variations mostly to temperature and time. The most successful synthesis came when replicating the conditions from the figure within their first article focusing on SMA-QA nanodiscs.²⁸⁶

The biggest challenge in synthesising SMA-QA was the purification: The procedure documented by Ravula and colleagues²⁸⁶ utilises a column with Sephadex-LH20 packing material, a crosslinked dextran-based resin. At the time of synthesis, the production of this material was discontinued, and only expensive rest-stocks were available. An attempt was therefore made on using the non-purified product, to control if the purification was necessary. When mixing lipids and the impure SMA-QA stock, the lipid solution became clear, indicating that nanodiscs had formed. The resulting batches were attempted purified by size-exclusion chromatography (SEC), but the instrument showed no signals corresponding to nanodiscs or polymer, most probably because the amount of polymer used made the solution too diluted so that the polymer was not registered by the UV or charge measurements in the SEC instrument. The challenge with using the non-purified SMA-QA polymer is that the size of the SMA-QA nanodiscs are closely related to the ratio between polymer and lipid, and working with an impure product will influence the ratio to an unknown amount.

One of the reasons why the assembled discs could not be collected could be because they were too diluted. As it was a new system, only small amounts were used at any time, so not to waste valuable material. During more concentrated runs later on, it was observed that the SMA-QA polymer has such an intense dark brown colour, even in solution, that when purifying SMA-QA nanodiscs on the SEC column, a brown band can be followed visually on

the column, which elutes considerably later than the discs and any unused lipids (Figure 24). In the end, the Sephadex-LH20 packing material was acquired and used in the same way as silica in a standard column chromatography utilised in synthetic chemistry. SMA-QA dissolved in water is simply passed through the column, with water as the solvent. As SMA-QA has a dark, brown colour, it is easy to follow as it moves through the column, and only the resulting brown fractions were collected and lyophilized to make large, reflective, dark brown crystals.

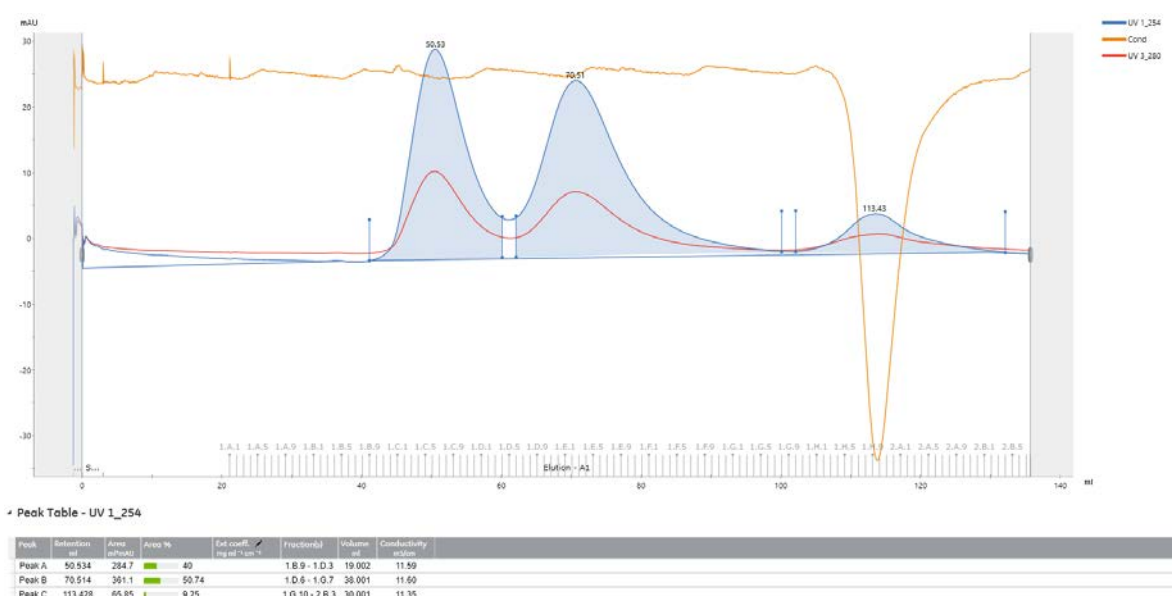


Figure 24. SEC chromatogram showing the UV signal (blue: 254 nm, red: 280 nm) and conductivity (yellow line) from the purification of SMA-QA nanodiscs of approximately 30 nm diameter. The first peak is SMA-QA nanodiscs, the second is unused lipid vesicles, and the last peak is unreacted SMA-QA polymer. Note the large dip in conductivity when the SMA-QA polymer passes through.

The original articles only show the FTIR and ssNMR spectra. Due to no access to ssNMR, SMA-QA was ordered to be used as reference material through BioNordica AS (produced by anatrance). By comparing the FTIR spectra of the starting material, SMA anhydride, to the locally synthesised, and the purchased SMA-QA, it was concluded that the polymer has successfully been synthesised and purified (Figure 25).

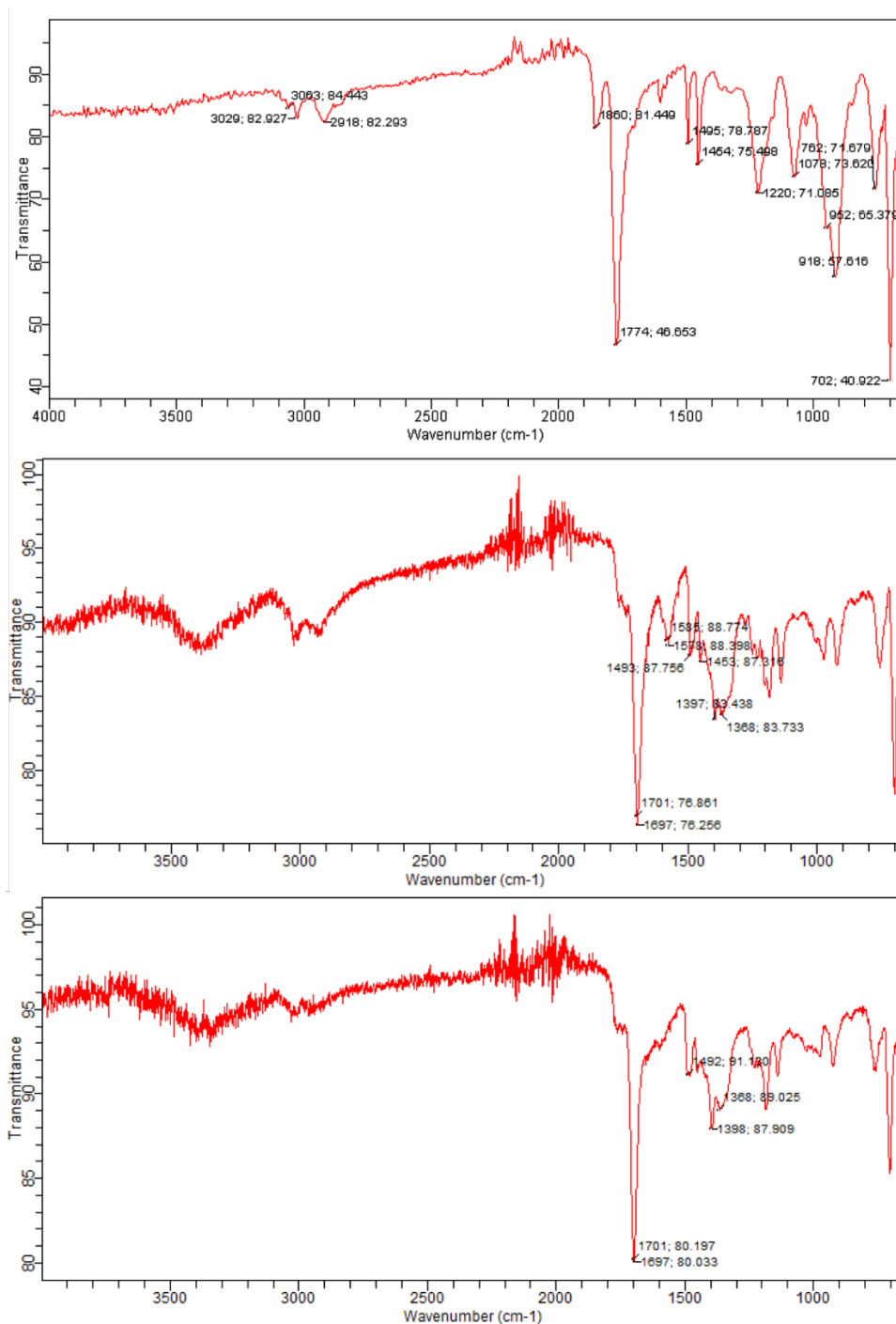


Figure 25. TOP: FT-IR spectrum of SMA anhydride, the starting material for the synthesis of SMA-QA. MIDDLE: FT-IR spectrum of SMA-QA, synthesized from SMA anhydride. BOTTOM: FT-IR spectrum of SMA-QA, bought from BioNordika AS, and produced by anatrice. Figure originally printed as Figure S8 in supporting information in Paper III,^{71, 285} but was remade here for better resolution.

4.3.2 Preparation of nanodiscs

The synthesis of SMA nanodiscs with either purely DMPC or DMPC:5% DMPG followed already established procedures.²⁸⁷

Originally, the LUVs were passed 15 times through an extruder, though there were some problems with the equipment leaking too much material (between 20 and 100%), so a decision was made to stop using the extruder. This did not result in any major changes in the finished nanodiscs. Additionally, it was investigated whether adding the SMA-QA polymer before or after freeze-thawing the LUV solution displayed any differences to yields or sizes of the nanodiscs, but no major changes were observed.

The size of the nanodiscs were checked at both 25°C and 30°C. The former for reference to the NMR spectra, and the latter to find the amount of lipids per disc, as the reference size of PC lipid heads are at 30°C.³⁰⁵⁻³⁰⁷ The thickness of the SMA polymer is estimated to be 0.9 nm.³⁰⁸ To our knowledge, the thickness of the SMA-QA polymer has not been instrumentally measured, so we used the same value as the SMA polymer as an estimate.

4.3.3 Microscale Thermophoresis

As an initial investigation into the interaction between AMPs and lipids, microscale thermophoresis (MST) was chosen as a quick and material-efficient tool. The question of how the difference in charge between nanodiscs made with SMA and SMA-QA polymers would affect the binding was also raised.

The AMPs utilised by DigiBiotics are all Trp rich (Figure 22). The intrinsic fluorescence of Trp therefore make MST a well-suited method for investigating these peptides, as they do not require any external labelling that might otherwise affect the peptides or membranes. A fifth peptide was chosen as a negative control, as it was previously shown to not have any observed activity against *E. coli* or *S. Aureus* (Table 1).^{285, 291} Surface plasmon resonance (SPR) was also used as an established method to evaluate the validity of the results gained by MST.

For the vesicles and discs, pure DMPC and DMPC with 5% DMPG were chosen as the model systems to investigate what effect a small negative charge has on the binding of peptides. The

SMA nanodiscs were explored in some preliminary tests, and the results indicated that the negative charge of the polymer affected the binding through electrostatic interactions. Positively charged SMA-QA based nanodiscs were chosen as a counterpoint to examine the effects of charge on the binding.

4.3.4 K_D comparison

The MST instrument was designed for obtaining K_D , which makes the dissociation constant fairly easy to obtain from the instrument. Yu *et al.*¹⁰⁰ proved that the method can be used to obtain K_D for labelled AMPs. K_D s for vesicles and the two different nanodisc systems were acquired by following the best-practise protocol, using the T-jump section (1.5 seconds) of the MST trace (summary in Table 2).

Table 2. Summary of K_D determined using SPR and MST. Errors represent the standard deviation of the triplicates. Where K_D is preceded by '>', the value represents a minimum value due to insufficient curve sampling and no error is reported. Table from article III, reprinted with permission by Springer Nature, Rainsford et al.^{71, 285}

Peptide	SPR (K_D mM)		Vesicle (K_D mM)		SMA-QA (K_D mM)		SMA (K_D mM)	
	DMPC	DMPC/PG	DMPC	DMPC/PG	DMPC	DMPC/PG	DMPC	DMPC/PG
<i>c(LWwNKr)</i>	2548 ± 493	1033 ± 58	> 670	>650	-	>1000	-	-
<i>c(WKWKWK)</i>	712 ± 27	474 ± 45	282 ± 58	112 ± 29	>713	-	8.6 ± 0.5	9.8 ± 0.3
<i>c(WRWRWR)</i>	318 ± 62	105 ± 7	73 ± 53	24 ± 7	>541	>615	2.7 ± 0.5	5.6 ± 1.1
<i>c(WWWKKK)</i>	302 ± 32	112 ± 15	28 ± 3	17 ± 13	267 ± 47	145 ± 55	1.1 ± 0.3	1.1 ± 0.5
<i>c(WWWRRR)</i>	142 ± 35	70 ± 1	21 ± 3	10 ± 5	142 ± 17	40 ± 5	1.2 ± 0.5	2.2 ± 0.4

The results from MST agree with the results from SPR and literature,^{276, 309} showing that K_D is reduced with anionic lipids (DMPG), indicating better binding. The lipid vesicles show sigmoidal-like response curves, as expected. The nanodiscs are largely likewise, with some

major differences, though; The curve of SMA nanodiscs is shifted to the left, to lower peptide concentrations, while the curve of SMA-QA is shifted so far to the right, to higher lipid concentrations, that it becomes impractical to check the full sigmoidal curve due to increased possibility for turbidity and light scattering effects. This means that the AMPs bind best to SMA-nanodiscs, then vesicles, and worst to SMA-QA nanodiscs. Though the bindings are still below the mM range.

The reason why the SMA nanodiscs bind AMPs so well can partially be explained by looking closer at the response curve itself: There is a second dip after the initial binding, which is common with higher order bindings. The most plausible explanation is that the peptides bind directly to the SMA polymer itself before they are released and bind to the disc proper. The experiments with only free polymer and peptide and demonstrate that the binding of the AMPs to the SMA polymer is comparable to the initial binding to the SMA nanodisc. The SMA-QA polymer, on the contrary, binds weaker to the AMPs than the SMA-QA disc itself. The clear difference between the two polymers can be contributed to the charges of the polymers themselves, where SMA has anionic charges (at pH 7.4) that causes electrostatic attraction while SMA-QA has positive charges that causes static repulsion.

The K_{DS} observed through MST show the same relative results as SPR and MIC: c(LWwNKr) has a significantly higher K_D than the other four peptides; the clustered Trp peptides show a significantly lower K_D than the alternating peptides; Arg show lower K_D than Lys. In short, $c(WWWRRR) > c(WWWKKK) > c(WRWRWR) > c(WKWKWK) > c(LWwNKr)$. The K_{DS} from the SMA-QA nanodiscs also correspond well to the results from SPR, but when the concentrations approach the mM region, the data sets are not sufficient to give reliable results, which resolves as large errors. This is because the interaction with the SMA-QA nanodiscs are too weak to be properly sampled under the mM range, where the turbidity starts causing errors through light scattering.

Looking at lipid composition, the presence of DMPG lipids decreases the K_D for all peptides by a factor of two when the full sigmoidal curve can be sampled. The results are in line with results from literature, showing that AMPs can bind in the low μM range to both vesicles and nanodiscs in the presence of anionic lipids, while the binding is weaker in zwitterionic membranes.

4.3.5 K_P and fluorescence intensity

K_P (Partition coefficient) is a measure of how a molecule favours a lipophilic environment over an aqueous one, with a high K_P indicating that it has a high lipophilicity. It is measured through the change in fluorescence intensity of a fluorophore as it moves into a lipid environment. Single wavelength fluorescence intensities are measured at the beginning of the MST trace as “initial fluorescence”, and no extra acquisition time is needed. As K_P and K_D are complimentary, an instrument that can acquire both simultaneously is a great strength. To our knowledge, this is the first attempt at using MST to acquire K_P .

K_P was extracted by fitting the acquired data to the hyperbolic curve, after removal of non-hyperbolic points:

$$\frac{I}{I_{aq}} = 1 + \frac{\left(K_P V_m [Lipid] \frac{I_L}{I_{aq}}\right)}{1 + (K_P V_m [Lipid])} \quad (19)$$

where (I) is normalised to the fluorescence intensity of the AMP in an aqueous environment (I_{aq}), V_m is the molar volume of the lipids (the volume of one mole lipids) and I_L is the fluorescence intensity of the AMP in the lipid environment. For V_m , the average molar volume of the lipid composition is used. In the case of the DMPC only environments, V_m is taken as the V_m of DMPC (1.023 nm³), and in the DMPC-DMPG mixture V_m is the weighted average relative to the composition used ($V_{m\text{DMPG}}=0.997$ nm³).³⁰⁷

The collected data for the lipid-only blanks showed a linear increase in signal in the mM concentration range, showing that turbidity has the same effect on K_P as with K_D . The nanodiscs show the same linearity, but with more intense signals. SPR derived K_P follows the same trend as K_D , that clustered Trp is better than alternating, and Arg is better than Lys. MST derived K_P is inconsistent with SPR and MST derived K_D .

There are several possible reasons for the inconsistency. Deviant points are excluded from the fit, which increases uncertainty and error of extracting K_P . The hyperbolic shape is best described by the initial points, but those points are also the most affected from the high peptide-lipid ratios. For SMA-QA nanodiscs and LUVs, only 4-5 points were left in the end, after most points had to be removed due to a bad fit with the hyperbolic curve.

Label-free MST relies on intrinsic fluorescence of Trp, which is affected by static and dynamic quenching at different levels and may experience blue-shift, modes of binding, and tendency to self-aggregate. A significant blue-shift will displace the signal maximum away from the static detection frequency of the instrument, resulting in the detected signal being lower than expected.

To conclude, MST is currently unreliable to acquire K_P , but newer NanoTemper instruments employ a spectral shift technology that could alleviate the observed issues, encouraging further exploration in the field. As K_P can be extracted from the same raw data as K_D , without using any extra material or time, this is very promising.

4.3.6 Comparison between vesicles and nanodiscs

Major differences between the different lipid systems needs to be addressed to avoid any biased conclusions that arise from using multiple systems. The vesicles have a diameter of 140 nm, being packed with 200,000 lipids. Meanwhile, the 22 nm DMPG SMA-QA nanodiscs have approximately 1300 lipids, in addition to the polymer itself. The AMPs have weights between 884 and 1027 Da, meaning that the binding of AMP to the lipid system yields very different relative contributions to the total weights of the AMP-lipid complexes. Additionally, the discs have all lipids available for binding while only the outer layer of the vesicles are available. The opposite charges of the two different polymers might influence the availability of the outermost lipids, though.

Peptides have shown a preference to bind to curved objects as the curvature itself causes the lipid packing to have defects. The vesicles are curved and in the liquid-ordered phase at 25°C, close to the phase transition temperature (T_m) of DMPC at 24°C.³⁰⁷ Contrary to this, the bacterial membrane is planar on the local level, which is the same as nanodiscs. The SMA nanodiscs are also less tightly packed than the vesicles, and have a reduced melting point.³¹⁰ The middle lipids are in a more ordered phase,³¹¹ while the outer lipids are perturbed by the styrene groups of SMA, making them more disordered.³¹⁰ The SMA-QA nanodiscs are expected to behave similarly here. As the AMPs favour lipids in the disordered phase, a heterogeneous distribution of AMPs across the nanodiscs is expected.

There is an expectation that the charge is a large contribution to AMP packing. The positive charge of the SMA-QA polymer might actually repel the positively charged AMPs away from the most disordered part of the nanodiscs into the less favoured ordered lipids. ³¹P NMR showed that the DMPG percentage for the SMA and SMA-QA discs were 2.7 and 4.5, respectively, from the initial 5% before nanodisc formation, indicating that the charge of the polymer affects the amount of negatively charged lipids in the nanodisc. In addition, the different amount of DMPG between the two different nanodiscs will affect the net charge of the membrane surface, affecting the peptide binding. The charge might also affect the placement of the negatively charged lipids, causing another form of heterogeneity within the discs. In other words, the negatively charged SMA nanodiscs induce the negatively charged DMPG lipids to make up more of the middle part of the nanodisc. Meanwhile, the positively charged SMA-QA polymer induce the negatively charged DMPG lipids to make up more of the outer part of the nanodisc. The result is more of the SMA nanodisc to be favourable for the AMPs, and less of the SMA-QA nanodisc to be favourable for the AMPs.

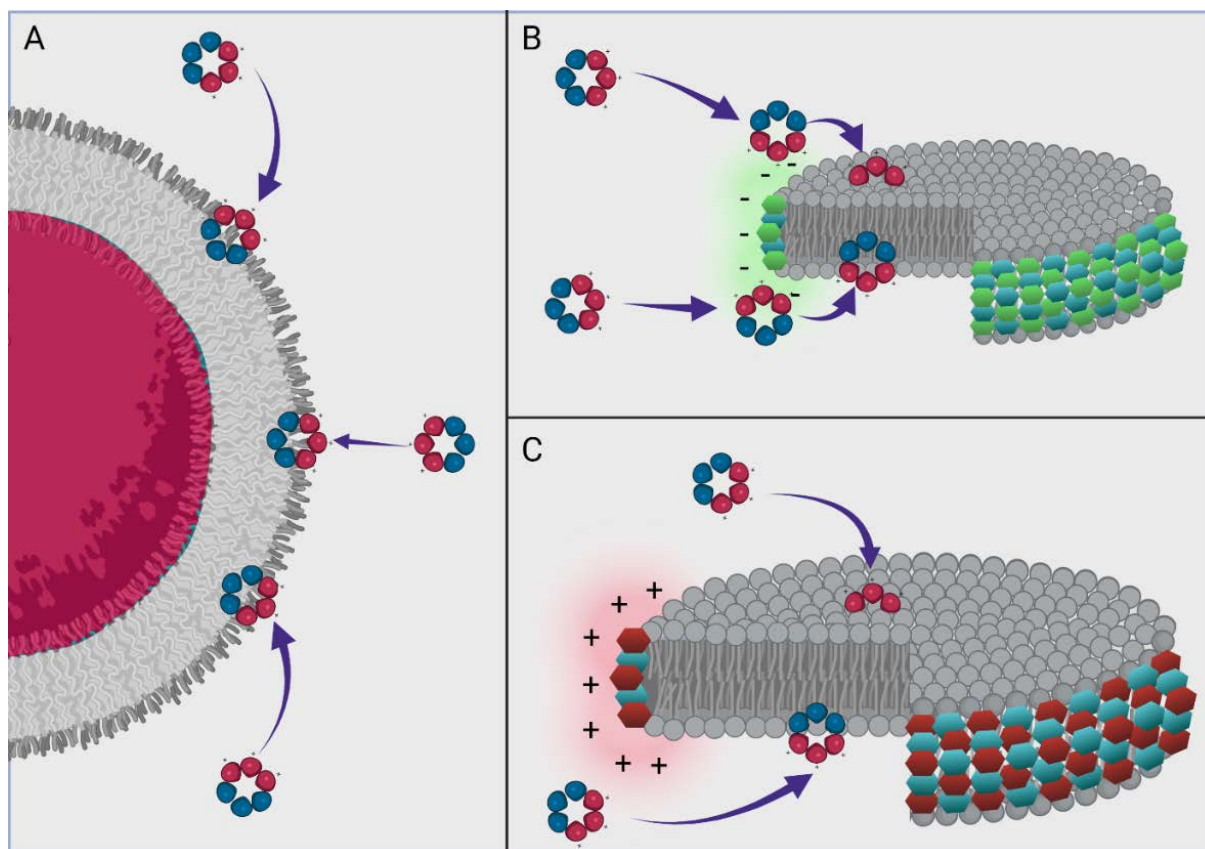


Figure 26. Visualisation of the difference in shape and characteristics of the lipid models and how this impacts the interactions of antimicrobial peptides. Note how the AMPs move to different sections of the nanodiscs. Figure from article III, reprinted with permission by Springer Nature, Rainsford et al.⁷¹.
285

The interaction between AMP and SMA-QA is 4-10 times weaker than the same for the vesicles. The curvature of the vesicles, the repulsion from SMA-QA polymer, the lessened availability of the disordered, and possibly negatively charged, lipids in the nanodiscs could explain that difference.

In the end, SMA-QA nanodiscs are able to reproduce the bindings observed in SPR for the stronger binding AMPs reasonably well. Conclusively, SMA-QA nanodiscs are good representative model systems for AMP-lipid interactions, keeping the drawbacks in mind. Considering MST as an easy-to-use method with low cost in terms of materials, this is a very useful method to investigate peptide-lipid interactions. One drawback of the MST method is that as the peptide concentration is kept constant, concentration-dependent interactions, such as self-aggregation, cannot be observed.

4.4 Cyclic Tetrapeptides containing a $\beta^{2,2}$ -amino acid (Paper IV)

Nine cyclic tetrapeptides were synthesised with Lys, Leu, Arg, and Phe in different positions, including variations between *L*- and *D*-enantiomers (See Figure 2 in paper IV).³¹² Common between them all was the α,α -disubstituted $\beta^{2,2}$ -amino acid containing two 4-(trifluoromethyl)benzyl sidechains, termed $\beta^{2,2}$.

All peptides were tested against Gram-positive and -negative bacteria, in addition to haemolytic toxicity against human red blood cells. Changing amino acid enantiomer did not change the antimicrobial activity, but *D*-Arg and -Lys analogues were considerably less haemolytic than their all-*L* counterparts, suggesting that the mode-of-action is driven by physical properties rather than a specific interaction. Changing the stereochemistry of one cationic residue, in addition to the amphipathicity, can serve to reduce haemolytic toxicity. Substituting Leu with the bulkier Phe residue could improve antimicrobial activity, though the effect on toxicity may vary.

For SPR, DMPC with and without 10% (w/w) *E. coli* O111:B4 LPS was utilised. Again, *D* variants of Arg and Lys show a higher K_P , or preference towards the DMPC lipid environment. Inclusion of LPS resulted in an overall decrease in K_P of most of the cyclic tetrapeptides. This can indicate a more efficient translocation of the cyclic tetrapeptides through the outer membrane, but also reduced activity against Gram-negative bacteria.

k_{off} was unaffected by inclusion of LPS, indicating that the dissociation was significantly faster from LPS than the membrane, making the membrane the major site for retention. This is consistent with the results discussed in Paper II (chapter 4.2.3 Surface plasmon resonance), where LPS was shown as an initiator for AMP interaction to lipid membranes. A connection between retention of the peptides in the bilayer and haemolytic toxicity was also observed.

4.4.1 Backbone conformation

Cyclic tetrapeptides are known to be very hard to synthesise, partly due to having a rigid backbone conformation.³¹³ Both resulting from only 12 atoms in the ring, on top of the restrictions from the semi-locked amide bonds. Introducing a 13th atom in the ring in the form of exchanging one of the natural amino acids with a $\beta^{2,2}$ -amino acid makes the synthesis

easier, which brings the question of whether it also opened for more flexibility in the backbone conformation.

The backbone conformation controls the overall structure of the peptide. Following, as part of the investigation into antimicrobial peptides, it is interesting to investigate what role the amino acids themselves have, and to what extent the order makes a difference. A selection of cyclic tetrapeptides with varying amino acid sequence and configuration were chosen.

Secondary chemical shifts comparison is a well-documented method for predicting the secondary structure of peptides and proteins. The method is normally applied to larger, linear peptides or proteins, and the reference values only include natural amino acids. It is known that aromatic residues have a long-range effect on chemical shifts, especially on protons. Therefore, peptides were analysed as linear peptides with two phenylalanines on each side, to mimic the effect the non-natural $\beta^{2,2}$ -amino acid would have on the rest of the system. With these accommodations, it is not possible to predict a secondary structure of alpha helix or beta sheet, which also would not make sense for a cyclic peptide with four amino acids. Using secondary chemical shifts instead produce more manageable numbers to work with compared to direct comparison of the chemical shifts: Instead of having big differences between the carboxyl carbons and alpha protons, they can all be compared with only small differences in ppm. The secondary chemical shifts allow for comparing the chemical shifts to a predicted mean.

Three different methods by Kjaergaard *et al.*,²⁰⁴ De Simone *et al.*,²⁰⁷ and Tamiola *et al.*²⁰⁸ were compared. The resulting secondary chemical shifts did not differ significantly, so only one set was included in the publication for simplicity. Kjaergaard *et al.* include correction factors for the two preceding and two following amino acids, which in this case would best fit with the long-range aromatic residue effect from the $\beta^{2,2}$ -amino acid.

Cross-relaxation rates were collected through NOESY experiments for the Arg containing peptides, and ROESY for the Lys containing spectra. $^3J_{\text{HH}}$ -couplings were collected from 1D ^1H NMR coupling patterns and E.COSY spectra.

Secondary coupling constants, J -couplings, and NOE distances did not show any major changes in backbone conformation for the four peptides, regardless of the order of amino acids or even the configuration of said amino acids (D vs L). Concluding, even though the synthesis of the cyclic tetrapeptides becomes significantly easier with the more flexible $\beta^{2,2}$ -amino acid, it is not flexible enough to allow for variation in the backbone conformation.

These observation builds up on the notion that it is not the 3D structure, but the composition of the AMPs that direct their abilities.

4.5 Conformational studies of cyclic hexapeptides using VCD and NMR (Paper V)

VCD has been proven to be highly sensitive to backbone conformation of peptides and proteins and has been used to investigate the absolute configuration of chiral molecules.²⁸⁹

Even with cyclisation, hexapeptides still possess significant conformational flexibility. VCD shows that the backbone conformation of the four hexapeptides does not change considerably between them, so the backbone is not influenced significantly by the amino acid sidechains.

An extensive conformational search needs to be done before calculating IR or VCD spectra or NMR data. CREST (Conformer-Rotamer Ensemble Sampling Tool) has been developed for that purpose. One initial issue is that the four cyclic hexapeptides have longer and charged sidechains, compared to what CREST was made for. To validate the method, CREST is compared with a classical molecular dynamics (MD) method, using VCD spectra and various data obtained by NMR: *J*-coupling constants, anisotropic parameters, and chemical shifts.

There are two major differences between MD and CREST: CREST uses an implicit solvent model during the simulation, while MD place explicit solvent molecules which allows for specific solvent-solute interactions to be explicitly accounted for. MD also provides statistical averaging of conformations observed during the simulation run, while CREST uses energies and Boltzmann averages to identify important conformations.

For VCD in D₂O, CREST and MD result in different spectral patterns. The backbone conformations are generated mostly through hydrogen bonding between carbonyl oxygens and amide hydrogens. The absence of explicit water molecules in CREST causes a strong preference for hydrogen bonding between the carbonyl oxygen in the backbone and the Lys amino group hydrogens, which again has a considerable influence on the backbone conformation.

Structures were additionally simulated in DMSO, to see if CREST fared better in organic solvents. DMSO is a strong hydrogen bond acceptor interacting strongly with amide and amine hydrogens of the peptide backbone and polar side chains. In contrast to water, it lacks hydrogens which can participate as hydrogen bond donors with carbonyls on the peptide backbone. Again, CREST and MD produce quite different spectra: Lys and carbonyl oxygen on the backbone form hydrogen bond interaction. MD, in the meantime, has the sidechains

going out from the backbone. These differences cause big differences in the backbone conformation.

NMR support the findings, that MD produce significantly better conformers that reproduce experimental results (Table 3-Table 5). The NMR data is more thoroughly discussed below, and tables with raw data can be found in the manuscript supporting information.

Table 3. Mean absolute error for chemical shift comparison of c(WKWKWK). Table from supporting information of paper V, printed with permission.²⁸⁹

Mean absolute error for chemical shift comparison of c(WKWKWK)					
Solvent	Spectrum	Full peptide		Backbone only	
		CREST	MD	CREST	MD
water	¹ H	2.468	0.862	2.539	0.53
	¹³ C	14.875	8.108	15.812	7.758
DMSO	¹ H	0.756	0.536	0.605	0.478
	¹³ C	7.026	6.291	7.972	6.293

Table 4. Summary of Q-factors obtained from comparing RDCs and RCSAs to computational conformations of the four cyclohexapeptides. Table from supporting information of paper V, printed with permission.²⁸⁹

Q-factors from RDC and RCSA in water		
Peptide	MD	CREST
c(WWWKKK)	0.971	0.965
c(WKWKWK)	0.990	0.996
c(WWWRRR)	0.991	0.992
c(WRWRWR)	0.964	0.985

Table 5. Mean absolute errors from comparing theoretical and experimental $^3J_{H(N)-C\alpha-H}$ Coupling constants for the four cyclic hexapeptides in water and DMSO. The spectral quality for c(WWWRRR) in DMSO was not good enough to extract any values. Table from supporting information of paper V, printed with permission.²⁸⁹

Peptide	Water		DMSO	
	CREST	MD	CREST	MD
c(WWWKKK)	1.33	1.78	0.92	1.55
c(WKWKKK)	1.65	1.27	1.54	0.56
c(WWWRRR)	2.05	1.25	1.60	0.69
c(WRWRWR)	1.44	2.01	1.20	0.73

4.5.1 Anisotropy

The first step in transferring the accumulated experience with anisotropic NMR measurements to the cyclic hexapeptides in water was to find a fitting anisotropic medium.

Pf1 bacteriophages were the first alignment media candidate, but a cloudy precipitate would form once the peptides were added. One plausible explanation is that Pf1 bacteriophages are very electronegative,²⁴⁷ which make for powerful electrostatic interactions when combined with the highly positively charged peptides. The resulting complex then precipitates out of the solution.

The next idea was to use the functionalised graphene oxide system for anisotropy measurement in water, explored by the group of Gotfredsen.²⁵¹ The graphene oxide was tested with a range of cyclic peptides, including peptides **1-4**. No alignment measurements could be obtained in the system. At the minimum graphene oxide concentration needed for alignment, there would be precipitation the moment peptide was added. Likewise, when starting with a high enough peptide concentration to run NMR spectra, precipitation would occur the moment graphene oxide was added.

Testing was continued to search for any trends. Exploratory titration revealed that Trp rich peptides precipitate at lower concentrations than peptides with less Trp. This led to the suspicion that there were some π - π interactions. To our knowledge, there is no work on exactly how the graphene oxide is oxidated. The working theory in Gotfredsen's group is that there is a combination of different oxidation levels. The oxygens are included as a variation of

hydroxide-, carboxyl-, carboxylic acid-, and ether-functionalisation, including some possibility of trapped oxygen. This again leaves large areas of the graphene oxide in its original state as graphite, with large, conjugated π -systems. When the Trp rich peptides get into contact with these areas, they form strong π - π interactions, and precipitate out of the solution. That meant that the graphene oxide unfortunately was not a fitting system for the DigiBiotics peptides.

Instead of continuing to look for fitting LCs, a decision was made to utilise a polyacrylamide (PAA) stretching gel. The casting of the gel itself was based on the content proportions from the work by Tycko, Blanco, and Ishii,²⁵² aided by a list of tips from NewEra.²⁸⁸ The main problem with the method is that there seems to be little documentation on the practical how-to steps. Some of the lessons learned are listed in chapter 2.4 Preparation of stretching gel (page 46).

There are several ways of stretching the gel (swelling): it can be swelled in the New Era swelling chamber, which is a relatively quick process of only one to two days; it can be swelled vertically within the NMR tube, a slow process that can take several weeks; it can be swelled radially, which is considerably quicker than vertically.¹⁸⁸ Swelling in the New Era swelling chamber was attempted first, but several issues were initially encountered with the procedure: the gel might break upon transfer into the open-ended NMR tube; the open-ended NMR tube might break when inserting the end-plug; the wear and tear on the equipment, especially the o-ring on the piston, is considerable, and ordering replacement parts from New Era (France) is costly and time-consuming. As an alternative, radial and vertical swelling inside the NMR tube was tested in parallel.

For the radial swelling, the PAA stretching gel was cast in a 3 mm NMR tube. To obtain the gel, the NMR tube was smashed. At this point, the gel should be left to dry before removing from the glass remains, as the gels are more fragile in their swelled state. By carefully removing glass parts away from the gels, two out of four gels were successfully obtained. The last two cracked and broke upon removal from the tube remains, as they were extracted before fully drying. The thin tubes were coerced to swell radially in a 5 mm NMR tube by inserting a silicone plunger all the way down to the top of the gel stick. The stick had unfortunately swelled vertically by forming a spiral within the confines of the tube within the next day.

Fortunately, there was enough time for vertical swelling, and previous experiments had proved that the peptides were stable in water for long periods of time (no discernible changes over three years in NMR tubes). This worked without problems. The signals from the PAA gel have strong ^{13}C - and ^{15}N signals. Therefore, no ^{15}N -HCQC IPAP signals of the backbone or sidechains of the four peptides could be obtained at natural isotope abundance. The ^{13}C NMR signals of the PAA gel also eclipsed the carbonyl signals, but fortunately, not many other 1D ^{13}C signals. Most of the RCSAs and some ^1H - ^{13}C RDCs could then be obtained.

Unfortunately, there are few signals on the backbone itself, meaning the anisotropic data is not widely useful for backbone conformational analysis. RCSAs were extracted from the carbonyls, alpha-, and beta carbons, in addition to the RDCs for the alpha- and beta C-H bonds.

Another potential issue is that the computational simulations are operating with a single alignment tensor. The conformers were mainly created with VCD spectra in mind, and the NMR parameters were simply calculated from the structurally optimised conformers. The fact that the NMR parameters were not utilised as constraints when optimising the conformations could explain some of the poorer fits. There is also the question if the molecule being relatively flat would affect this sampling in any way, as a planar molecule will have redundant RCSAs and the handling of RDCs becomes problematic.

4.5.2 *J*-coupling

Several different 2D methods were applied to attempt to extract the *J*-couplings from the AMPs, especially the 3J H-N- C_α -H coupling constant would be useful for finding the backbone angles. Unfortunately, none of the methods attempted gave any spectra with sufficient spectral resolution or signal-to-noise ratio to find the couplings. The same methods were tested on strychnine as a sample molecule, and the *J*-couplings could be extracted here. The conclusion was that a series of reasons partly explain why: the water suppression might have interfered with the signals from the peptides; the concentration in the strychnine sample was several times higher during tests; some intrinsic properties of the sample may have made the methods unfit, such as the flexibility of the backbone. The issue was not pursued further, as obtaining the *J*-coupling constants from the peptide was not within the scope of the thesis.

The end goal was to be able to compare structural information in solution and inside of the SMA-QA nanodiscs, and J -coupling constants were not expected to be measurable in the lipid environment.

The backbone J -couplings were extracted from 1D ^1H NMR spectra. For a few less resolved signals, the coupling constants were found by lineshape fitting from a high resolution and zero filled ^{15}N -HSQC F2 slice.

4.6 Peptide conformations by NMR (Paper VI)

NOE cross-relaxation data was extracted from NOESY spectra in water, while DMSO and SDS required ROESY spectra due to intermediate tumbling rates. Distances were extracted through Dynamics Center where distances were referenced by the ortho aromatic protons on the Trp sidechains furthest from the diagonal, and referenced to the other ortho aromatic protons at 2.46 Å,¹⁷⁹ in addition to the diastereotopic geminal protons at 1.75 Å where possible. Peptide c(WWWRRR) in DMSO had many overlapping peaks, so all the ortho aromatic proton peaks were sampled and the average intensity of those were used to set the reference distance. The same peptide in SDS had even more overlaps, so only qualitative data (weak, medium, or strong) were collected.

All cross peaks were referenced to their corresponding connections through chemical shifts. Overlapping peaks caused several intramolecular interactions to be possible, and they were noted down before they were used to make an input file for molecular modelling.

Structures calculations of c(WWWRRR) and c(WWWKKK) in water, DMSO, and SDS micelles were performed using X-PLOR. Initially, only NOE derived distances were used as constraints. Scalar couplings were subsequently added as constraints. The ten lowest energy conformations were averaged and are presented in Figure 27.

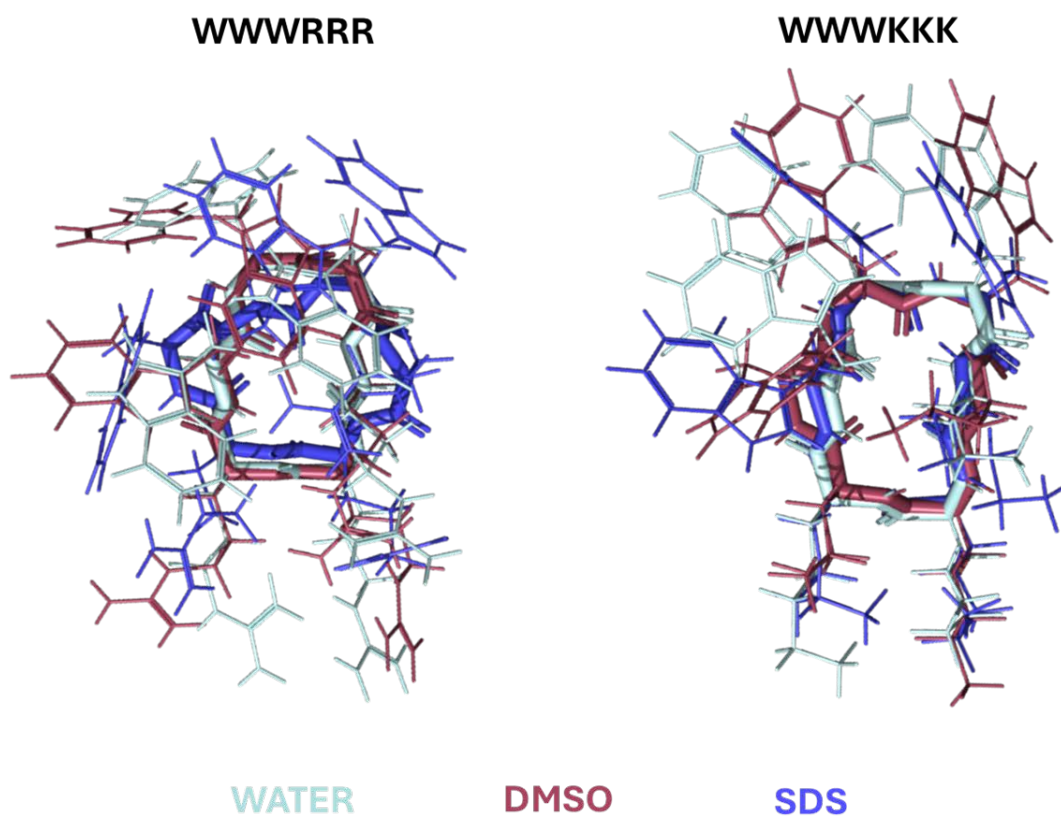


Figure 27. Averaged top ten conformers of peptides c(WWWRRR) and c(WWWKKK) in water, DMSO, and SDS micelles. Figure reprinted from Supporting Information of Paper VI.

Both peptides adopt conformations consisting of two β -turns, occurring between two Trp and between two Arg/Lys. The backbone conformation remains mostly rigid between the different environments, while the sidechains are more flexible. The MIC values are different between the two AMPs (Table 1), once again pointing to amino acid composition as a stronger driver for antimicrobial resistance than backbone conformation.

4.7 Alignment of SMA-QA nanodiscs (Paper VI)

Ravula *et al.* present self-aligning discs based on the SMA-EA or SMA-QA polymers.^{286, 314-316} They report that the alignment of nanodiscs can be tuned by changing either the temperature or the concentration of nanodiscs.³¹⁶ In their article on SMA-EA nanodiscs the concentration effect is collected at a slightly elevated temperature (32°C) and the temperature effect is collected at a fairly high concentration (40 mg lipid/mL). While working on the nanodiscs, no RQC of D₂O were observed under that temperature, and most of the stable work is done at a slightly higher temperature of 40°C.

There was an intent to describe the relation to concentration more thoroughly. While Ravula *et al.*^{286, 317} estimate the lipid concentrations from the starting lipid concentration before nanodisc formation, our experience is that the end concentration can vary significantly and suggest that it should always be checked by ³¹P NMR. Unfortunately, this makes the use of phosphorous buffer unviable. Normally, 1 mL 20 mM lipid would end up as ~0.5 mL 3 mM lipid concentration nanodiscs. One attempt at a higher concentration and larger volume yielded ~3 mL 129 mM lipid concentration nanodiscs from 4 mL 147.51 mM DMPC (100 mg/mL). The higher yield in the latter nanodisc assembly is primarily contributed to the larger volume of starting material.

SMA-QA nanodiscs have been reported to self-align at higher temperatures,³¹⁶ and it could be confirmed that a deuterium splitting was observable above 305 K, reaching a maximum around 310 K (Figure 28). To be consistent, and be sure to operate within the full alignment, further experiments were performed at 313 K (40°C). The size of the splitting is also dependent on nanodisc size and -concentration.

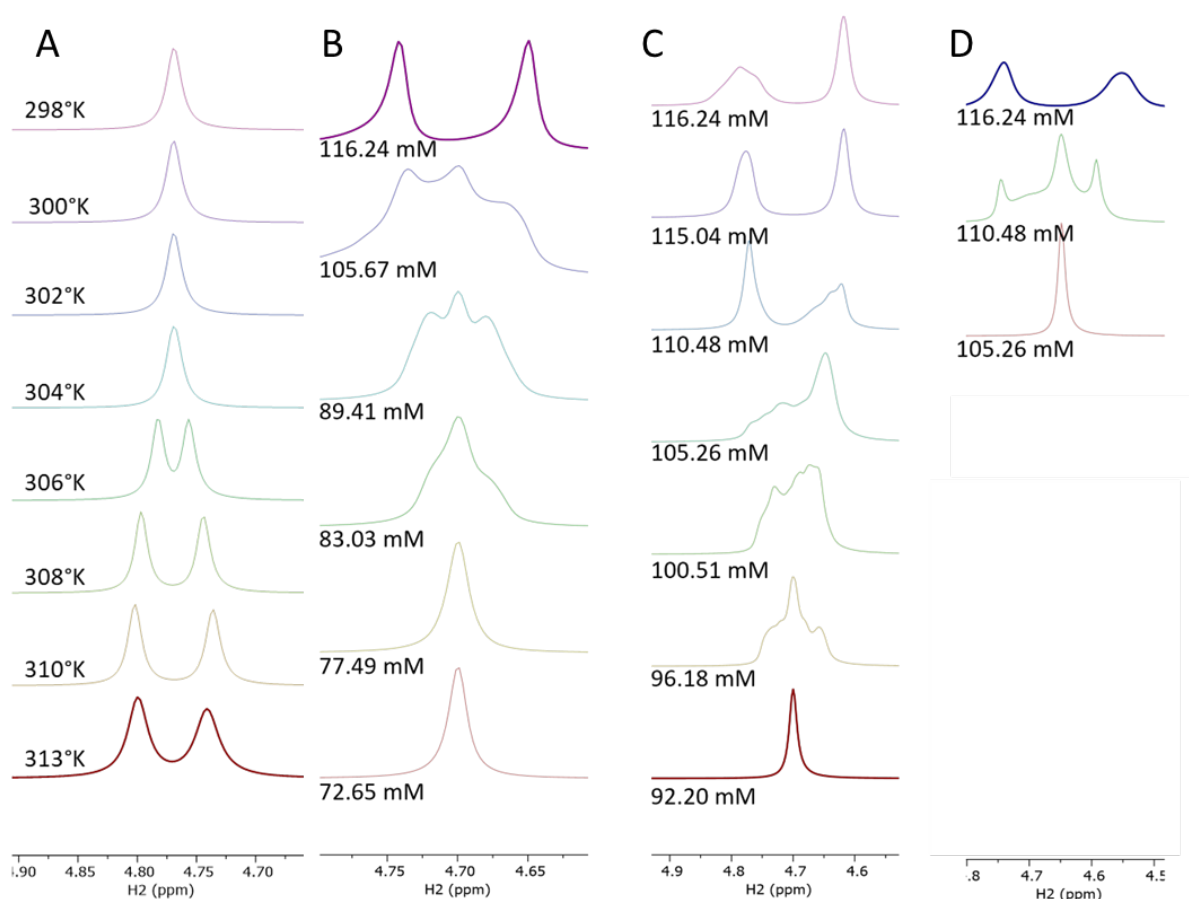


Figure 28. Effects on SMA-QA nanodisc alignment on concentration and temperature, measured as RQC of deuterium. A) Increase of deuterium signal splitting in a 5 mm NMR tube with increased temperature. The concentration is 6.88 mM lipid in 30.57 ± 12.72 nm SMA-QA DMPC nanodiscs. B) Dilution in a 5 mm NMR tube. C) dilution in a 3 mm NMR tube. D) dilution by adding the cyclic tetrapeptide c(WKWKWK) in a 3 mm NMR tube. All NMR spectra were collected at 313 K. For A, B, and C, the concentrations are given as lipid concentration, and the size of the SMA-QA DMPC nanodiscs are 20.79 ± 11.14 nm. The dilution in both 3 mm tubes were done by the same volumes, to compare the loss of signal splitting with and without peptide. The dilutions were done with a 90/10 H_2O/D_2O mixture. Figure is a combination of two figures from paper VI, reprinted with permission.³¹⁸

Interestingly, by performing experiments in both 3 mm and 5 mm NMR tubes, it was discovered that the splitting collapses at higher concentrations in 5 mm tubes (Figure 28), suggesting that the phase of the nanodisc alignment is directly affected by the physical boundaries imposed by the glass walls. It was also noted that as the viscosity of the solution is increased due to the nanodisc concentration, it is harder to transfer to the 3 mm NMR tubes.

A titration was performed to investigate the viability of obtaining NMR data from within the SMA-QA nanodisc in its aligned state. AMP was added gradually to the nanodisc solution and the 1H NMR spectra were recorded (Figure 29). There were virtually no signal from the

peptides in ratios of 100 peptides per disc, while broad peaks started appearing at 500:1 ratio. This is interpreted as the discs being saturated somewhere between 100 and 500 peptides per disc, or between 20 and 4 lipids per peptide. The broad peaks of the peptide signal stem from a myriad of interactions, among them the viscosity of the solution, the intermediate-to-fast exchange between the bound and unbound state with the nanodisc, the lipid environment.

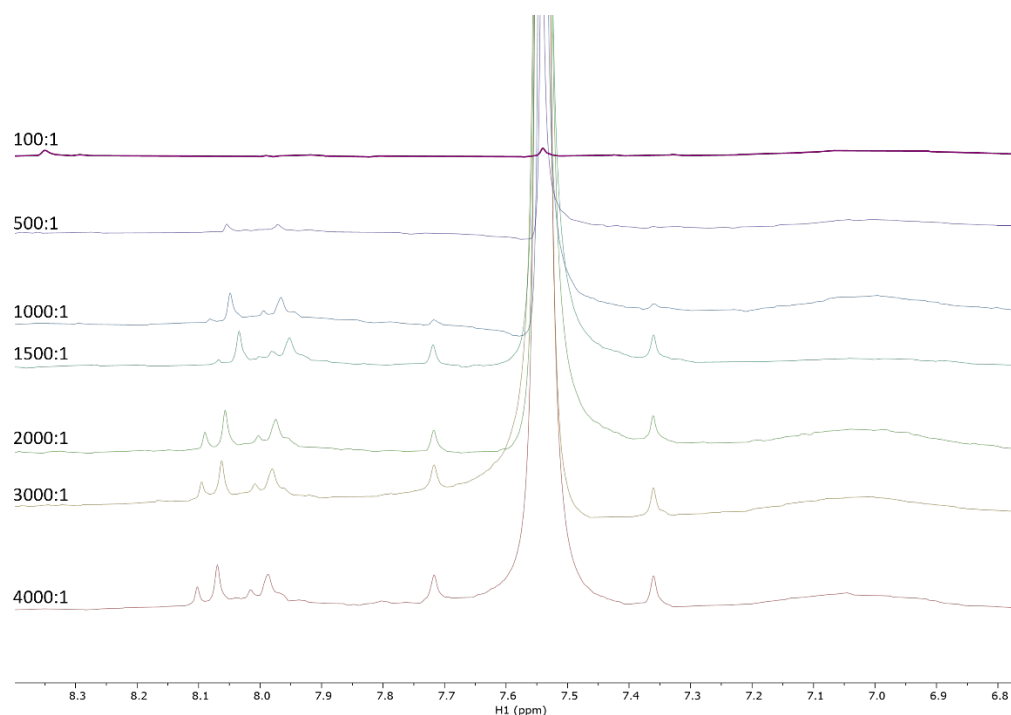


Figure 29. Zoomed in part of the 1D ^1H spectra of 30.57 ± 12.72 nm SMA-QA DMPC nanodisc with increasing amounts of cyclic hexapeptide *c*(WWWKKK). Ratios given are peptides per disc, and the disc is estimated to contain ~ 2000 lipid molecules. The figure is only part of a figure from Paper VI, reprinted with permission.³¹⁸

The SMA-QA nanodiscs have been found to bind peptides in ratios that can be used for ^{15}N labelled peptides to possibly acquire chemical shifts and anisotropic RDCs and RCSAs. This can then be used to further investigate binding properties of peptides. The control of the alignment should be further studied before properly beginning with labelled peptides, but it has now been shown that SMA-QA nanodiscs can be very useful to investigate the interaction between cationic AMPs and lipid membranes.

4.8 Future prospects

With the SMA-QA nanodiscs better understood, the next step would be to use isotopically labelled AMPs, to study what information could easily be gained from the AMP-lipid binding.

A first step could be to begin with the smaller 10 nm SMA-QA nanodiscs, as the slow tumbling of the larger nanodiscs reduce the signal they produce. It would also be interesting to use peptides that form α -helices on the surface on the lipid surface, such as Magainin 2^{52, 319} or CM15,³²⁰ as a larger conformational change between the different environments can better help developing the methods.

A second step would be to investigate the perturbation of the AMPs themselves. Paramagnetic relaxation enhancement (PRE) is a method that works for this purpose.³²¹⁻³²³ Using paramagnetic salts change the relaxation times for the part of the peptide exposed to the aqueous solution, giving an idea of how deep into the lipid membrane the peptides bind.

With the bindings and perturbation properly studied, the very reason why the SMA-QA self-aligning nanodiscs were chosen could be addressed: anisotropy. It would be possible to extract RDCs and RCSAs from the peptide in aligned discs and use them to further study how the conformers change in the nanodiscs. Paper III demonstrated that the interaction with LUVs and nanodiscs are different for a series of reasons. By comparing the results from the SDS micelles and magnetically aligned nanodiscs, it would be possible to further look into the differences between micelles and nanodiscs, and how the models used to investigate interactions affect the results.

While the peptides provided by the DigiBiotics project filled the purpose for method development and screening of conditions, they are not structurally varied enough to invest in isotopes to study further. Especially the alternating peptides are too symmetrical to properly study by NMR spectroscopy. By focusing on other, relevant, peptides, it would be possible to investigate other interesting scientific questions like carpeting or insertion by MST and PRE, followed by anisotropic NMR. Conformational switches in lipid environment could be explored by anisotropic NMR. The nature of ordered versus disordered aggregation on lipid surfaces and in lipid environments through NMR spectroscopy would be very interesting to look at. There are claims of cyclic peptides with alternating D and L amino acids that self-

assemble into nanotubes in lipid environments.^{324, 325} It would be very interesting to investigate whether they form these nanotubes, or if there is some other form of unordered aggregation forming.

5. Concluding remarks

Natural products are still the main source of new therapeutics. In paper I, a new natural product, Commafric A, with antiproliferative activity against human lung cancer has been fully elucidated by standard and anisotropic NMR techniques. This work is essential in understanding the 3D structure of new potential drugs, showcasing how NMR plays a vital role in pharmaceutical development.

Antimicrobial peptides are emerging as a supplementary strategy to the antibiotics used in clinical treatment options today. In paper IV, the backbone structure of five cyclic tetrapeptides with an α,α -disubstituted $\beta^{2,2}$ -amino acid were studied by NMR spectroscopy, showing that the antimicrobial effect is not impacted by the backbone conformation but rather the amino acid composition.

Structural information, including chemical shifts, J -coupling constants, and anisotropically obtained Q-factors acquired by NMR spectroscopy in papers II and V were used to compare two different methods to computationally simulate conformational structures of four cyclic Trp-rich hexapeptides with either clumped or alternating Lys or Arg. NMR spectroscopy supported the findings by VCD, and found MD to be a better computational methodology than CREST due to a significantly better fit to the models. This shows that NMR spectroscopy is a versatile, information-rich technique with varied applications and that explicit solvent molecules make for better computations.

In paper III, microscale thermophoresis has been further established as a cost-effective method to investigate peptide-lipid interactions, without a label for Trp-rich peptides. Labels have previously been used to measure interactions, but as a label comes with its own physiochemical properties, the results may be misleading. The intrinsic fluorescence of Trp alleviates this problem, as it is a common constituent in many AMPs. As a part of this, SMA-QA based nanodiscs showed interactions on par with more established labour-heavy methods, establishing them as a better biological representation for cationic AMPs than the more well-used SMA nanodiscs. Additionally, MST as a technique to describe peptide-lipid interactions is still in its infancy, giving ample opportunity to further develop the method to include other biologically relevant systems. Allowing us the opportunity to examine the interactions between antimicrobial agents and their targets.

In paper VI, the preparation of SMA-QA nanodisc were thoroughly described, both the synthesis of the polymer, and the preparation of the discs. The self-alignment of the discs in a magnetic field has been studied, and further connections between size and temperature to degree of alignment has been documented. It was proven that peptides bound to the discs can be observed by NMR in aligned conditions, allowing for anisotropic measurements in biologically relevant systems that are smaller than bicelles.

Additionally, NOE distances and *J*-coupling constants obtained in water, DMSO, and SDS micelles were used as conformational constraints to simulate conformations of the two cyclic hexapeptides c(WWWKKK) and c(WWWRRR). The simulations did not show any significant backbone changes between the environments, once again showing that conformation is not as important to antimicrobial effect as amino acid composition. It is already known that Arg is more effective for antimicrobial effect than Lys when coupled with Trp.

To further develop the work with SMA-QA based nanodiscs in the future, peptides that change conformation to an α -helix in lipid environments would be a good idea: With larger conformational changes between environments, there are more information that can be used to develop the methodologies further.

In conclusion, NMR spectroscopy has been used to fully elucidate Commafric A, a new natural product, describe the conformation of cyclic peptides, and study properties of a nanodisc that self-aligns in the magnetic field. NMR spectroscopy is a continuously expanding field of study and will be very helpful in understanding new antimicrobial agents and help find solutions to the antimicrobial crisis.

References

- (1) Svendsen, J. S. *DigiBiotics*. UiT The Arctic University of Norway, 2018. <https://site.uit.no/antibiotics/> (accessed 26.02.2024).
- (2) Fleming, S. A. *Nobel Lecture: Penicillin*. Nobel Prize Outreach AB, 1945. (accessed 26.02.2024).
- (3) Fleming, A. On the Antibacterial Action of Cultures of a Penicillium, with Special Reference to their Use in the Isolation of *B. influenzae*. *The British Journal of Experimental Pathology* **1929**, *10* (3), 226-236.
- (4) Maurois, A. *The Life of Sir Alexander Fleming, Discoverer of Penicillin*; E. P. Dutton & Co., 1959.
- (5) Chain, E.; Florey, H. W.; Gardner, A. D.; Heatley, N. G.; Jennings, M. A.; Orr-Ewing, J.; Sanders, A. G. Penicillin as a Chemotherapeutic Agent. *The Lancet* **1940**, *236* (6104), 226-228. DOI: 10.1016/s0140-6736(01)08728-1.
- (6) Podolsky, S. H. The evolving response to antibiotic resistance (1945–2018). *Palgrave Communications* **2018**, *4* (1). DOI: 10.1057/s41599-018-0181-x.
- (7) Lewis, K. The Science of Antibiotic Discovery. *Cell* **2020**, *181* (1), 29-45. DOI: 10.1016/j.cell.2020.02.056 From NLM Medline.
- (8) Davies, J. Where have All the Antibiotics Gone? *Can J Infect Dis Med Microbiol* **2006**, *17* (5), 287-290. DOI: 10.1155/2006/707296 From NLM PubMed-not-MEDLINE.
- (9) Hall, B. G.; Barlow, M. Evolution of the serine beta-lactamases: past, present and future. *Drug Resist Updat* **2004**, *7* (2), 111-123. DOI: 10.1016/j.drup.2004.02.003 From NLM Medline.
- (10) Davies, J. What are antibiotics? Archaic functions for modern activities. *Mol. Microbiol.* **1990**, *4* (8), 1227-1232. DOI: 10.1111/j.1365-2958.1990.tb00701.x From NLM Medline.
- (11) Sengupta, S.; Chattopadhyay, M. K.; Grossart, H. P. The multifaceted roles of antibiotics and antibiotic resistance in nature. *Front Microbiol* **2013**, *4*, 47. DOI: 10.3389/fmicb.2013.00047 From NLM PubMed-not-MEDLINE.
- (12) Raaijmakers, J. M.; Mazzola, M. Diversity and natural functions of antibiotics produced by beneficial and plant pathogenic bacteria. *Annu Rev Phytopathol* **2012**, *50*, 403-424. DOI: 10.1146/annurev-phyto-081211-172908 From NLM Medline.
- (13) Andersson, D. I.; Hughes, D. Microbiological effects of sublethal levels of antibiotics. *Nat Rev Microbiol* **2014**, *12* (7), 465-478. DOI: 10.1038/nrmicro3270 From NLM Medline.
- (14) Goh, E. B.; Yim, G.; Tsui, W.; McClure, J.; Surette, M. G.; Davies, J. Transcriptional modulation of bacterial gene expression by subinhibitory concentrations of antibiotics. *Proc Natl Acad Sci U S A* **2002**, *99* (26), 17025-17030. DOI: 10.1073/pnas.252607699 From NLM Medline.
- (15) Shaw, K. J.; Miller, N.; Liu, X.; Lerner, D.; Wan, J.; Bittner, A.; Morrow, B. J. Comparison of the changes in global gene expression of *Escherichia coli* induced by four bactericidal agents. *J. Mol. Microbiol. Biotechnol.* **2003**, *5* (2), 105-122. DOI: 10.1159/000069981 From NLM Medline.
- (16) Otto, M. P.; Martin, E.; Badiou, C.; Lebrun, S.; Bes, M.; Vandenesch, F.; Etienne, J.; Lina, G.; Dumitrescu, O. Effects of subinhibitory concentrations of antibiotics on virulence factor expression by community-acquired methicillin-resistant *Staphylococcus aureus*. *J. Antimicrob. Chemother.* **2013**, *68* (7), 1524-1532. DOI: 10.1093/jac/dkt073 From NLM Medline.

- (17) Goerke, C.; Koller, J.; Wolz, C. Ciprofloxacin and trimethoprim cause phage induction and virulence modulation in *Staphylococcus aureus*. *Antimicrob. Agents Chemother.* **2006**, *50* (1), 171-177. DOI: 10.1128/AAC.50.1.171-177.2006 From NLM Medline.
- (18) Nalca, Y.; Jansch, L.; Bredenbruch, F.; Geffers, R.; Buer, J.; Haussler, S. Quorum-sensing antagonistic activities of azithromycin in *Pseudomonas aeruginosa* PAO1: a global approach. *Antimicrob. Agents Chemother.* **2006**, *50* (5), 1680-1688. DOI: 10.1128/AAC.50.5.1680-1688.2006 From NLM Medline.
- (19) Kimmitt, P. T.; Harwood, C. R.; Barer, M. R. Toxin gene expression by shiga toxin-producing *Escherichia coli*: the role of antibiotics and the bacterial SOS response. *Emerg Infect Dis* **2000**, *6* (5), 458-465. DOI: 10.3201/eid0605.000503 From NLM Medline.
- (20) Lopez, E.; Elez, M.; Matic, I.; Blazquez, J. Antibiotic-mediated recombination: ciprofloxacin stimulates SOS-independent recombination of divergent sequences in *Escherichia coli*. *Mol. Microbiol.* **2007**, *64* (1), 83-93. DOI: 10.1111/j.1365-2958.2007.05642.x From NLM Medline.
- (21) Kai, T.; Tateda, K.; Kimura, S.; Ishii, Y.; Ito, H.; Yoshida, H.; Kimura, T.; Yamaguchi, K. A low concentration of azithromycin inhibits the mRNA expression of N-acyl homoserine lactone synthesis enzymes, upstream of *lasI* or *rhlII*, in *Pseudomonas aeruginosa*. *Pulm Pharmacol Ther* **2009**, *22* (6), 483-486. DOI: 10.1016/j.pupt.2009.04.004 From NLM Medline.
- (22) Melhus, A. Effects of amoxicillin on the expression of cytokines during experimental acute otitis media caused by non-typeable *Haemophilus influenzae*. *J. Antimicrob. Chemother.* **2001**, *48* (3), 397-402. DOI: 10.1093/jac/48.3.397 From NLM Medline.
- (23) Soucy, S. M.; Huang, J.; Gogarten, J. P. Horizontal gene transfer: building the web of life. *Nat Rev Genet* **2015**, *16* (8), 472-482. DOI: 10.1038/nrg3962 From NLM Medline.
- (24) Ding, M.; Ye, Z.; Liu, L.; Wang, W.; Chen, Q.; Zhang, F.; Wang, Y.; Sjoling, A.; Martin-Rodriguez, A. J.; Hu, R.; et al. Subinhibitory antibiotic concentrations promote the horizontal transfer of plasmid-borne resistance genes from *Klebsiella pneumoniae* to *Escherichia coli*. *Front Microbiol* **2022**, *13*, 1017092. DOI: 10.3389/fmicb.2022.1017092 From NLM PubMed-not-MEDLINE.
- (25) Yashi, L.; Mingyao, D.; Zhiqing, H.; Qi, L.; Meiling, P.; Xiaoyao, F.; Yunfei, L.; Changhua, S.; Zujun, L. Antimicrobial resistance genes horizontal transfer in soil under sub-inhibitory concentrations of antimicrobics. *Acta Ecologica Sinica* **2022**, *42* (5), 529-541. DOI: 10.1016/j.chnaes.2021.12.006.
- (26) D'Costa, V. M.; King, C. E.; Kalan, L.; Morar, M.; Sung, W. W.; Schwarz, C.; Froese, D.; Zazula, G.; Calmels, F.; Debruyne, R.; et al. Antibiotic resistance is ancient. *Nature* **2011**, *477* (7365), 457-461. DOI: 10.1038/nature10388 From NLM Medline.
- (27) Silver, L. L. Challenges of antibacterial discovery. *Clin Microbiol Rev* **2011**, *24* (1), 71-109. DOI: 10.1128/CMR.00030-10.
- (28) Abraham, E. P.; Chain, E. An Enzyme from Bacteria able to Destroy Penicillin. *Nature* **1940**, *146* (3713), 837-837. DOI: 10.1038/146837a0.
- (29) Rammelkamp, C. H.; Maxon, T. Resistance of *Staphylococcus aureus* to the Action of Penicillin. *Experimental Biology and Medicine* **1942**, *51* (3), 386-389. DOI: 10.3181/00379727-51-13986.
- (30) Larsen, J.; Raisen, C. L.; Ba, X.; Sadgrove, N. J.; Padilla-Gonzalez, G. F.; Simmonds, M. S. J.; Loncaric, I.; Kerschner, H.; Apfalter, P.; Hartl, R.; et al. Emergence of methicillin resistance predates the clinical use of antibiotics. *Nature* **2022**, *602* (7895), 135-141. DOI: 10.1038/s41586-021-04265-w From NLM Medline.

- (31) Butler, M. S.; Henderson, I. R.; Capon, R. J.; Blaskovich, M. A. T. Antibiotics in the clinical pipeline as of December 2022. *J Antibiot (Tokyo)* **2023**, *76* (8), 431-473. DOI: 10.1038/s41429-023-00629-8 From NLM Medline.
- (32) Theuretzbacher, U.; Outtersson, K.; Engel, A.; Karlen, A. The global preclinical antibacterial pipeline. *Nat Rev Microbiol* **2020**, *18* (5), 275-285. DOI: 10.1038/s41579-019-0288-0 From NLM Medline.
- (33) Alm, R. A.; Gallant, K. Innovation in Antimicrobial Resistance: The CARB-X Perspective. *ACS Infect Dis* **2020**, *6* (6), 1317-1322. DOI: 10.1021/acsinfecdis.0c00026 From NLM Medline.
- (34) Alt, S.; Haggstrom, D.; Kessmann, H.; Kloss, F.; Schneider, C. E.; Jager, T.; Schwede, T.; Brakhage, A.; Dehio, C. INCATE: a partnership to boost the antibiotic pipeline. *Nat Rev Drug Discov* **2022**, *21* (9), 621-622. DOI: 10.1038/d41573-022-00138-7 From NLM Medline.
- (35) Engel, A. Fostering Antibiotic Development through Impact Funding. *ACS Infect Dis* **2020**, *6* (6), 1311-1312. DOI: 10.1021/acsinfecdis.0c00069 From NLM Medline.
- (36) McCall, B. New fund stimulates the ailing antibiotic pipeline. *Lancet Infect Dis* **2020**, *20* (9), 1017. DOI: 10.1016/S1473-3099(20)30629-0 From NLM Medline.
- (37) Miethke, M.; Pieroni, M.; Weber, T.; Brönstrup, M.; Hammann, P.; Halby, L.; Arimondo, P. B.; Glaser, P.; Aigle, B.; Bode, H. B.; et al. Towards the sustainable discovery and development of new antibiotics. *Nature Reviews Chemistry* **2021**, *5* (10), 726-749. DOI: 10.1038/s41570-021-00313-1.
- (38) Towse, A.; Hoyle, C. K.; Goodall, J.; Hirsch, M.; Mestre-Ferrandiz, J.; Rex, J. H. Time for a change in how new antibiotics are reimbursed: Development of an insurance framework for funding new antibiotics based on a policy of risk mitigation. *Health Policy* **2017**, *121* (10), 1025-1030. DOI: 10.1016/j.healthpol.2017.07.011 From NLM Medline.
- (39) Cama, J.; Leszczynski, R.; Tang, P. K.; Khalid, A.; Lok, V.; Dowson, C. G.; Ebata, A. To Push or To Pull? In a Post-COVID World, Supporting and Incentivizing Antimicrobial Drug Development Must Become a Governmental Priority. *ACS Infect Dis* **2021**, *7* (8), 2029-2042. DOI: 10.1021/acsinfecdis.0c00681 From NLM Medline.
- (40) Mullard, A. Achaogen bankruptcy highlights antibacterial development woes. *Nat Rev Drug Discov* **2019**, *18* (6), 411. DOI: 10.1038/d41573-019-00085-w From NLM PubMed-not-MEDLINE.
- (41) Dall, C. Achaogen bankruptcy raises worry over antibiotic pipeline. CIDRAP, <https://www.cidrap.umn.edu/antimicrobial-stewardship/achaogen-bankruptcy-raises-worry-over-antibiotic-pipeline>.
- (42) Dall, C. Antibiotic developer Melinta files for bankruptcy. CIDRAP, <https://www.cidrap.umn.edu/antimicrobial-stewardship/antibiotic-developer-melinta-files-bankruptcy>.
- (43) Cross, R. Antibiotics maker Melinta declares bankruptcy. In *Chemical & Engineering News*, American Chemical Society: 2020; Vol. 98.
- (44) Antimicrobial Resistance, C. Global burden of bacterial antimicrobial resistance in 2019: a systematic analysis. *Lancet* **2022**, *399* (10325), 629-655. DOI: 10.1016/S0140-6736(21)02724-0 From NLM Medline.
- (45) Felicio, M. R.; Silva, O. N.; Goncalves, S.; Santos, N. C.; Franco, O. L. Peptides with Dual Antimicrobial and Anticancer Activities. *Front Chem* **2017**, *5*, 5. DOI: 10.3389/fchem.2017.00005 From NLM PubMed-not-MEDLINE.

- (46) De Oliveira, D. M. P.; Forde, B. M.; Kidd, T. J.; Harris, P. N. A.; Schembri, M. A.; Beatson, S. A.; Paterson, D. L.; Walker, M. J. Antimicrobial Resistance in ESKAPE Pathogens. *Clin Microbiol Rev* **2020**, *33* (3). DOI: 10.1128/CMR.00181-19 From NLM Medline.
- (47) O'Neill, J. The Review on Antimicrobial Resistance: Tackling a crisis for the health and wealth of nations. **2014**.
- (48) Steiner, H.; Hultmark, D.; Engstrom, A.; Bennich, H.; Boman, H. G. Sequence and specificity of two antibacterial proteins involved in insect immunity. *Nature* **1981**, *292* (5820), 246-248. DOI: 10.1038/292246a0 From NLM Medline.
- (49) Melander, R. J.; Zurawski, D. V.; Melander, C. Narrow-Spectrum Antibacterial Agents. *Medchemcomm* **2018**, *9* (1), 12-21. DOI: 10.1039/C7MD00528H From NLM PubMed-not-MEDLINE.
- (50) Okada, M.; Natori, S. Purification and characterization of an antibacterial protein from haemolymph of *Sarcophaga peregrina* (flesh-fly) larvae. *Biochem. J* **1983**, *211* (3), 727-734. DOI: 10.1042/bj2110727 From NLM Medline.
- (51) Ganz, T.; Selsted, M. E.; Szklarek, D.; Harwig, S. S.; Daher, K.; Bainton, D. F.; Lehrer, R. I. Defensins. Natural peptide antibiotics of human neutrophils. *J Clin Invest* **1985**, *76* (4), 1427-1435. DOI: 10.1172/JCI112120 From NLM Medline.
- (52) Zasloff, M. Magainins, a class of antimicrobial peptides from *Xenopus* skin: isolation, characterization of two active forms, and partial cDNA sequence of a precursor. *Proc Natl Acad Sci U S A* **1987**, *84* (15), 5449-5453. DOI: 10.1073/pnas.84.15.5449 From NLM Medline.
- (53) Mackler, B. F.; Kreil, G. Honey bee venom melittin: correlation of nonspecific inflammatory activities with amino acid sequences. *Inflammation* **1977**, *2* (1), 55-65. DOI: 10.1007/BF00920875 From NLM Medline.
- (54) Habermann, E. Bee and wasp venoms. *Science* **1972**, *177* (4046), 314-322. DOI: 10.1126/science.177.4046.314 From NLM Medline.
- (55) Wimley, W. C. Describing the mechanism of antimicrobial peptide action with the interfacial activity model. *ACS Chem Biol* **2010**, *5* (10), 905-917. DOI: 10.1021/cb1001558 From NLM Medline.
- (56) Tencza, S. B.; Douglass, J. P.; Creighton, D. J., Jr.; Montelaro, R. C.; Mietzner, T. A. Novel antimicrobial peptides derived from human immunodeficiency virus type 1 and other lentivirus transmembrane proteins. *Antimicrob. Agents Chemother.* **1997**, *41* (11), 2394-2398. DOI: 10.1128/AAC.41.11.2394 From NLM Medline.
- (57) Hassan, M.; Kjos, M.; Nes, I. F.; Diep, D. B.; Lotfipour, F. Natural antimicrobial peptides from bacteria: characteristics and potential applications to fight against antibiotic resistance. *J Appl Microbiol* **2012**, *113* (4), 723-736. DOI: 10.1111/j.1365-2672.2012.05338.x From NLM Medline.
- (58) Datta, S.; Roy, A. Antimicrobial Peptides as Potential Therapeutic Agents: A Review. *International Journal of Peptide Research and Therapeutics* **2020**, *27* (1), 555-577. DOI: 10.1007/s10989-020-10110-x.
- (59) Li, J.; Hu, S.; Jian, W.; Xie, C.; Yang, X. Plant antimicrobial peptides: structures, functions, and applications. *Bot Stud* **2021**, *62* (1), 5. DOI: 10.1186/s40529-021-00312-x From NLM PubMed-not-MEDLINE.
- (60) Wiesner, J.; Vilcinskas, A. Antimicrobial peptides: the ancient arm of the human immune system. *Virulence* **2010**, *1* (5), 440-464. DOI: 10.4161/viru.1.5.12983 From NLM Medline.

- (61) Wang, X.; Sun, Y.; Wang, F.; You, L.; Cao, Y.; Tang, R.; Wen, J.; Cui, X. A novel endogenous antimicrobial peptide CAMP(211-225) derived from casein in human milk. *Food Funct* **2020**, *11* (3), 2291-2298. DOI: 10.1039/c9fo02813g From NLM Medline.
- (62) van Hoek, M. L.; Prickett, M. D.; Settlege, R. E.; Kang, L.; Michalak, P.; Vliet, K. A.; Bishop, B. M. The Komodo dragon (*Varanus komodoensis*) genome and identification of innate immunity genes and clusters. *BMC Genomics* **2019**, *20* (1), 684. DOI: 10.1186/s12864-019-6029-y From NLM Medline.
- (63) Miyata, T.; Tokunaga, F.; Yoneya, T.; Yoshikawa, K.; Iwanaga, S.; Niwa, M.; Takao, T.; Shimonishi, Y. Antimicrobial peptides, isolated from horseshoe crab hemocytes, tachyplesin II, and polyphemusins I and II: chemical structures and biological activity. *J. Biochem.* **1989**, *106* (4), 663-668. DOI: 10.1093/oxfordjournals.jbchem.a122913 From NLM Medline.
- (64) Amiss, A. S.; von Pein, J. B.; Webb, J. R.; Condon, N. D.; Harvey, P. J.; Phan, M. D.; Schembri, M. A.; Currie, B. J.; Sweet, M. J.; Craik, D. J.; et al. Modified horseshoe crab peptides target and kill bacteria inside host cells. *Cell Mol Life Sci* **2021**, *79* (1), 38. DOI: 10.1007/s00018-021-04041-z From NLM Medline.
- (65) Wang, W. F.; Xie, X. Y.; Huang, Y.; Li, Y. K.; Liu, H.; Chen, X. L.; Wang, H. L. Identification of a Novel Antimicrobial Peptide From the Ancient Marine Arthropod Chinese Horseshoe Crab, *Tachyplesus tridentatus*. *Front Immunol* **2022**, *13*, 794779. DOI: 10.3389/fimmu.2022.794779 From NLM Medline.
- (66) Wang, G.; Li, X.; Wang, Z. APD3: the antimicrobial peptide database as a tool for research and education. *Nucleic Acids Res.* **2016**, *44* (D1), D1087-1093. DOI: 10.1093/nar/gkv1278 From NLM Medline.
- (67) Andersson, D. I.; Hughes, D.; Kubicek-Sutherland, J. Z. Mechanisms and consequences of bacterial resistance to antimicrobial peptides. *Drug Resist Updat* **2016**, *26*, 43-57. DOI: 10.1016/j.drup.2016.04.002 From NLM Medline.
- (68) Haney, E. F.; Mansour, S. C.; Hancock, R. E. Antimicrobial Peptides: An Introduction. *Methods Mol Biol* **2017**, *1548*, 3-22. DOI: 10.1007/978-1-4939-6737-7_1 From NLM Medline.
- (69) Sun, P. D.; Foster, C. E.; Boyington, J. C. Overview of protein structural and functional folds. *Curr Protoc Protein Sci* **2004**, *Chapter 17* (1), Unit 17 11. DOI: 10.1002/0471140864.ps1701s35 From NLM Medline.
- (70) Kabir, M. W. U.; Alawad, D. M.; Mishra, A.; Hoque, M. T. TAFPred: Torsion Angle Fluctuations Prediction from Protein Sequences. *Biology (Basel)* **2023**, *12* (7). DOI: 10.3390/biology12071020 From NLM PubMed-not-MEDLINE.
- (71) Creative Commons Attribution (CC BY) 4.0 International License <https://creativecommons.org/licenses/by/4.0/>.
- (72) Hancock, R. E. Peptide antibiotics. *Lancet* **1997**, *349* (9049), 418-422. DOI: 10.1016/S0140-6736(97)80051-7 From NLM Medline.
- (73) Arnison, P. G.; Bibb, M. J.; Bierbaum, G.; Bowers, A. A.; Bugni, T. S.; Bulaj, G.; Camarero, J. A.; Campopiano, D. J.; Challis, G. L.; Clardy, J.; et al. Ribosomally synthesized and post-translationally modified peptide natural products: overview and recommendations for a universal nomenclature. *Nat. Prod. Rep.* **2013**, *30* (1), 108-160. DOI: 10.1039/c2np20085f From NLM Medline.
- (74) Li, J.; Koh, J. J.; Liu, S.; Lakshminarayanan, R.; Verma, C. S.; Beuerman, R. W. Membrane Active Antimicrobial Peptides: Translating Mechanistic Insights to Design. *Front Neurosci* **2017**, *11*, 73. DOI: 10.3389/fnins.2017.00073 From NLM PubMed-not-MEDLINE.

- (75) Robbel, L.; Marahiel, M. A. Daptomycin, a bacterial lipopeptide synthesized by a nonribosomal machinery. *J. Biol. Chem.* **2010**, *285* (36), 27501-27508. DOI: 10.1074/jbc.R110.128181 From NLM Medline.
- (76) Pavithra, G.; Rajasekaran, R. Gramicidin Peptide to Combat Antibiotic Resistance: A Review. *International Journal of Peptide Research and Therapeutics* **2019**, *26* (1), 191-199. DOI: 10.1007/s10989-019-09828-0.
- (77) Simons, A.; Alhanout, K.; Duval, R. E. Bacteriocins, Antimicrobial Peptides from Bacterial Origin: Overview of Their Biology and Their Impact against Multidrug-Resistant Bacteria. *Microorganisms* **2020**, *8* (5). DOI: 10.3390/microorganisms8050639 From NLM PubMed-not-MEDLINE.
- (78) Butler, M. S.; Hansford, K. A.; Blaskovich, M. A.; Halai, R.; Cooper, M. A. Glycopeptide antibiotics: back to the future. *J Antibiot (Tokyo)* **2014**, *67* (9), 631-644. DOI: 10.1038/ja.2014.111 From NLM Medline.
- (79) Breukink, E.; de Kruijff, B. Lipid II as a target for antibiotics. *Nat Rev Drug Discov* **2006**, *5* (4), 321-332. DOI: 10.1038/nrd2004 From NLM Medline.
- (80) Allen, M. M.; Yuen, C.; Medeiros, L.; Zizlsperger, N.; Farooq, M.; Kolodny, N. H. Effects of light and chloramphenicol stress on incorporation of nitrogen into cyanophycin in *Synechocystis* sp. strain PCC 6308. *Biochim. Biophys. Acta* **2005**, *1725* (2), 241-246. DOI: 10.1016/j.bbagen.2005.04.011 From NLM Medline.
- (81) Yim, G.; Thaker, M. N.; Koteva, K.; Wright, G. Glycopeptide antibiotic biosynthesis. *J Antibiot (Tokyo)* **2014**, *67* (1), 31-41. DOI: 10.1038/ja.2013.117 From NLM Medline.
- (82) Kim, S.; Chen, J.; Cheng, T.; Gindulyte, A.; He, J.; He, S.; Li, Q.; Shoemaker, B. A.; Thiessen, P. A.; Yu, B.; et al. PubChem 2023 update. *Nucleic Acids Res.* **2023**, *51* (D1), D1373-D1380. DOI: 10.1093/nar/gkac956 From NLM Medline.
- (83) Spohn, R.; Daruka, L.; Lazar, V.; Martins, A.; Vidovics, F.; Grezal, G.; Mehi, O.; Kintszes, B.; Szamel, M.; Jangir, P. K.; et al. Integrated evolutionary analysis reveals antimicrobial peptides with limited resistance. *Nat Commun* **2019**, *10* (1), 4538. DOI: 10.1038/s41467-019-12364-6 From NLM Medline.
- (84) Gunn, J. S.; Ryan, S. S.; Van Velkinburgh, J. C.; Ernst, R. K.; Miller, S. I. Genetic and functional analysis of a PmrA-PmrB-regulated locus necessary for lipopolysaccharide modification, antimicrobial peptide resistance, and oral virulence of *Salmonella enterica* serovar typhimurium. *Infect Immun* **2000**, *68* (11), 6139-6146. DOI: 10.1128/IAI.68.11.6139-6146.2000 From NLM Medline.
- (85) Stumpe, S.; Schmid, R.; Stephens, D. L.; Georgiou, G.; Bakker, E. P. Identification of OmpT as the protease that hydrolyzes the antimicrobial peptide protamine before it enters growing cells of *Escherichia coli*. *J. Bacteriol.* **1998**, *180* (15), 4002-4006. DOI: 10.1128/JB.180.15.4002-4006.1998 From NLM Medline.
- (86) Kupferwasser, L. I.; Skurray, R. A.; Brown, M. H.; Firth, N.; Yeaman, M. R.; Bayer, A. S. Plasmid-mediated resistance to thrombin-induced platelet microbicidal protein in staphylococci: role of the qacA locus. *Antimicrob. Agents Chemother.* **1999**, *43* (10), 2395-2399. DOI: 10.1128/AAC.43.10.2395 From NLM Medline.
- (87) Nizet, V. Antimicrobial peptide resistance mechanisms of human bacterial pathogens. *Curr Issues Mol Biol* **2006**, *8* (1), 11-26. DOI: 10.21775/cimb.008.011 From NLM Medline.
- (88) Petkov, P.; Lilikova, E.; Ilieva, N.; Litov, L. Self-Association of Antimicrobial Peptides: A Molecular Dynamics Simulation Study on Bombinin. *Int J Mol Sci* **2019**, *20* (21). DOI: 10.3390/ijms20215450 From NLM Medline.

- (89) Bechinger, B.; Lohner, K. Detergent-like actions of linear amphipathic cationic antimicrobial peptides. *Biochim. Biophys. Acta* **2006**, *1758* (9), 1529-1539. DOI: 10.1016/j.bbamem.2006.07.001 From NLM Medline.
- (90) Clark, S.; Jowitt, T. A.; Harris, L. K.; Knight, C. G.; Dobson, C. B. The lexicon of antimicrobial peptides: a complete set of arginine and tryptophan sequences. *Commun Biol* **2021**, *4* (1), 605. DOI: 10.1038/s42003-021-02137-7 From NLM Medline.
- (91) Strahl, H.; Errington, J. Bacterial Membranes: Structure, Domains, and Function. *Annu Rev Microbiol* **2017**, *71*, 519-538. DOI: 10.1146/annurev-micro-102215-095630 From NLM Medline.
- (92) Alegun, O.; Pandeya, A.; Cui, J.; Ojo, I.; Wei, Y. Donnan Potential across the Outer Membrane of Gram-Negative Bacteria and Its Effect on the Permeability of Antibiotics. *Antibiotics (Basel)* **2021**, *10* (6). DOI: 10.3390/antibiotics10060701 From NLM PubMed-not-MEDLINE.
- (93) Pasquina-Lemonche, L.; Burns, J.; Turner, R. D.; Kumar, S.; Tank, R.; Mullin, N.; Wilson, J. S.; Chakrabarti, B.; Bullough, P. A.; Foster, S. J.; et al. The architecture of the Gram-positive bacterial cell wall. *Nature* **2020**, *582* (7811), 294-297. DOI: 10.1038/s41586-020-2236-6 From NLM Medline.
- (94) Sohlenkamp, C.; Geiger, O. Bacterial membrane lipids: diversity in structures and pathways. *FEMS Microbiol. Rev.* **2016**, *40* (1), 133-159. DOI: 10.1093/femsre/fuv008 From NLM Medline.
- (95) Bogdanov, M.; Pyrshev, K.; Yesylevskyy, S.; Ryabichko, S.; Boiko, V.; Ivanchenko, P.; Kiyamova, R.; Guan, Z.; Ramseyer, C.; Dowhan, W. Phospholipid distribution in the cytoplasmic membrane of Gram-negative bacteria is highly asymmetric, dynamic, and cell shape-dependent. *Sci Adv* **2020**, *6* (23), eaaz6333. DOI: 10.1126/sciadv.aaz6333 From NLM Medline.
- (96) Kobayashi, T.; Menon, A. K. Transbilayer lipid asymmetry. *Curr Biol* **2018**, *28* (8), R386-R391. DOI: 10.1016/j.cub.2018.01.007 From NLM Medline.
- (97) Bevers, E. M.; Comfurius, P.; Zwaal, R. F. Regulatory mechanisms in maintenance and modulation of transmembrane lipid asymmetry: pathophysiological implications. *Lupus* **1996**, *5* (5), 480-487. DOI: 10.1177/096120339600500531 From NLM Medline.
- (98) Lad, M. D.; Birembaut, F.; Clifton, L. A.; Frazier, R. A.; Webster, J. R.; Green, R. J. Antimicrobial peptide-lipid binding interactions and binding selectivity. *Biophys. J.* **2007**, *92* (10), 3575-3586. DOI: 10.1529/biophysj.106.097774 From NLM Medline.
- (99) Vorobyov, I.; Allen, T. W. On the role of anionic lipids in charged protein interactions with membranes. *Biochim. Biophys. Acta* **2011**, *1808* (6), 1673-1683. DOI: 10.1016/j.bbamem.2010.11.009 From NLM Medline.
- (100) Yu, L.; Fan, Q.; Yue, X.; Mao, Y.; Qu, L. Activity of a novel-designed antimicrobial peptide and its interaction with lipids. *J. Pept. Sci.* **2015**, *21* (4), 274-282. DOI: 10.1002/psc.2728 From NLM Medline.
- (101) Schmidt, N. W.; Mishra, A.; Lai, G. H.; Davis, M.; Sanders, L. K.; Tran, D.; Garcia, A.; Tai, K. P.; McCray, P. B.; Ouellette, A. J.; et al. Criterion for amino acid composition of defensins and antimicrobial peptides based on geometry of membrane destabilization. *J. Am. Chem. Soc.* **2011**, *133* (17), 6720-6727. DOI: 10.1021/ja200079a From NLM Medline.
- (102) Schmidt, N. W.; Wong, G. C. Antimicrobial peptides and induced membrane curvature: geometry, coordination chemistry, and molecular engineering. *Curr. Opin. Solid State Mater. Sci.* **2013**, *17* (4), 151-163. DOI: 10.1016/j.cossms.2013.09.004 From NLM PubMed-not-MEDLINE.

- (103) Ludtke, S. J.; He, K.; Heller, W. T.; Harroun, T. A.; Yang, L.; Huang, H. W. Membrane pores induced by magainin. *Biochemistry* **1996**, *35* (43), 13723-13728. DOI: 10.1021/bi9620621 From NLM Medline.
- (104) Li, Q.; Cebrian, R.; Montalban-Lopez, M.; Ren, H.; Wu, W.; Kuipers, O. P. Outer-membrane-acting peptides and lipid II-targeting antibiotics cooperatively kill Gram-negative pathogens. *Commun Biol* **2021**, *4* (1), 31. DOI: 10.1038/s42003-020-01511-1 From NLM Medline.
- (105) Stephani, J. C.; Gerhards, L.; Khairalla, B.; Solov'yov, I. A.; Brand, I. How do Antimicrobial Peptides Interact with the Outer Membrane of Gram-Negative Bacteria? Role of Lipopolysaccharides in Peptide Binding, Anchoring, and Penetration. *ACS Infect Dis* **2024**, *10* (2), 763-778. DOI: 10.1021/acsinfecdis.3c00673 From NLM Medline.
- (106) Hadjicharalambous, A.; Bournakas, N.; Newman, H.; Skynner, M. J.; Beswick, P. Antimicrobial and Cell-Penetrating Peptides: Understanding Penetration for the Design of Novel Conjugate Antibiotics. *Antibiotics (Basel)* **2022**, *11* (11). DOI: 10.3390/antibiotics11111636 From NLM PubMed-not-MEDLINE.
- (107) Wadhvani, P.; Epand, R. F.; Heidenreich, N.; Burck, J.; Ulrich, A. S.; Epand, R. M. Membrane-active peptides and the clustering of anionic lipids. *Biophys. J.* **2012**, *103* (2), 265-274. DOI: 10.1016/j.bpj.2012.06.004 From NLM Medline.
- (108) Schneider, T.; Sahl, H. G. An oldie but a goodie - cell wall biosynthesis as antibiotic target pathway. *Int J Med Microbiol* **2010**, *300* (2-3), 161-169. DOI: 10.1016/j.ijmm.2009.10.005 From NLM Medline.
- (109) Zhang, Q. Y.; Yan, Z. B.; Meng, Y. M.; Hong, X. Y.; Shao, G.; Ma, J. J.; Cheng, X. R.; Liu, J.; Kang, J.; Fu, C. Y. Antimicrobial peptides: mechanism of action, activity and clinical potential. *Mil Med Res* **2021**, *8* (1), 48. DOI: 10.1186/s40779-021-00343-2 From NLM Medline.
- (110) Wang, X.; van Beekveld, R. A. M.; Xu, Y.; Parmar, A.; Das, S.; Singh, I.; Breukink, E. Analyzing mechanisms of action of antimicrobial peptides on bacterial membranes requires multiple complimentary assays and different bacterial strains. *Biochim Biophys Acta Biomembr* **2023**, *1865* (6), 184160. DOI: 10.1016/j.bbmem.2023.184160 From NLM Medline.
- (111) Wimley, W. C.; Hristova, K. Antimicrobial peptides: successes, challenges and unanswered questions. *J. Membr. Biol.* **2011**, *239* (1-2), 27-34. DOI: 10.1007/s00232-011-9343-0 From NLM Medline.
- (112) Chen, E. H.; Wang, C. H.; Liao, Y. T.; Chan, F. Y.; Kanaoka, Y.; Uchihashi, T.; Kato, K.; Lai, L.; Chang, Y. W.; Ho, M. C.; et al. Visualizing the membrane disruption action of antimicrobial peptides by cryo-electron tomography. *Nat Commun* **2023**, *14* (1), 5464. DOI: 10.1038/s41467-023-41156-2 From NLM Medline.
- (113) Wimley, W. C.; White, S. H. Determining the membrane topology of peptides by fluorescence quenching. *Biochemistry* **2000**, *39* (1), 161-170. DOI: 10.1021/bi991836l From NLM Medline.
- (114) Yang, L.; Harroun, T. A.; Weiss, T. M.; Ding, L.; Huang, H. W. Barrel-stave model or toroidal model? A case study on melittin pores. *Biophys. J.* **2001**, *81* (3), 1475-1485. DOI: 10.1016/S0006-3495(01)75802-X From NLM Medline.
- (115) He, K.; Ludtke, S. J.; Heller, W. T.; Huang, H. W. Mechanism of alamethicin insertion into lipid bilayers. *Biophys. J.* **1996**, *71* (5), 2669-2679. DOI: 10.1016/S0006-3495(96)79458-4 From NLM Medline.
- (116) Qian, S.; Wang, W.; Yang, L.; Huang, H. W. Structure of the alamethicin pore reconstructed by x-ray diffraction analysis. *Biophys. J.* **2008**, *94* (9), 3512-3522. DOI: 10.1529/biophysj.107.126474 From NLM Medline.

- (117) Imura, Y.; Choda, N.; Matsuzaki, K. Magainin 2 in action: distinct modes of membrane permeabilization in living bacterial and mammalian cells. *Biophys. J.* **2008**, *95* (12), 5757-5765. DOI: 10.1529/biophysj.108.133488 From NLM Medline.
- (118) Strandberg, E.; Tremouilhac, P.; Wadhvani, P.; Ulrich, A. S. Synergistic transmembrane insertion of the heterodimeric PGLa/magainin 2 complex studied by solid-state NMR. *Biochim. Biophys. Acta* **2009**, *1788* (8), 1667-1679. DOI: 10.1016/j.bbamem.2008.12.018 From NLM Medline.
- (119) Roy, A.; Sarangi, N. K.; Ghosh, S.; Prabhakaran, A.; Keyes, T. E. Leaflet by Leaflet Synergistic Effects of Antimicrobial Peptides on Bacterial and Mammalian Membrane Models. *J Phys Chem Lett* **2023**, *14* (16), 3920-3928. DOI: 10.1021/acs.jpcclett.3c00119 From NLM Medline.
- (120) Jean-Francois, F.; Elezgaray, J.; Berson, P.; Vacher, P.; Dufourc, E. J. Pore formation induced by an antimicrobial peptide: electrostatic effects. *Biophys. J.* **2008**, *95* (12), 5748-5756. DOI: 10.1529/biophysj.108.136655 From NLM Medline.
- (121) Matsuzaki, K.; Murase, O.; Fujii, N.; Miyajima, K. An antimicrobial peptide, magainin 2, induced rapid flip-flop of phospholipids coupled with pore formation and peptide translocation. *Biochemistry* **1996**, *35* (35), 11361-11368. DOI: 10.1021/bi960016v From NLM Medline.
- (122) Gazit, E.; Boman, A.; Boman, H. G.; Shai, Y. Interaction of the mammalian antibacterial peptide cecropin P1 with phospholipid vesicles. *Biochemistry* **1995**, *34* (36), 11479-11488. DOI: 10.1021/bi00036a021 From NLM Medline.
- (123) Pouny, Y.; Rapaport, D.; Mor, A.; Nicolas, P.; Shai, Y. Interaction of antimicrobial dermaseptin and its fluorescently labeled analogues with phospholipid membranes. *Biochemistry* **1992**, *31* (49), 12416-12423. DOI: 10.1021/bi00164a017 From NLM Medline.
- (124) Silvestro, L.; Gupta, K.; Weiser, J. N.; Axelsen, P. H. The concentration-dependent membrane activity of cecropin A. *Biochemistry* **1997**, *36* (38), 11452-11460. DOI: 10.1021/bi9630826 From NLM Medline.
- (125) Christensen, B.; Fink, J.; Merrifield, R. B.; Mauzerall, D. Channel-forming properties of cecropins and related model compounds incorporated into planar lipid membranes. *Proc Natl Acad Sci U S A* **1988**, *85* (14), 5072-5076. DOI: 10.1073/pnas.85.14.5072 From NLM Medline.
- (126) Lehrer, R. I.; Barton, A.; Daher, K. A.; Harwig, S. S.; Ganz, T.; Selsted, M. E. Interaction of human defensins with *Escherichia coli*. Mechanism of bactericidal activity. *J Clin Invest* **1989**, *84* (2), 553-561. DOI: 10.1172/JCI114198 From NLM Medline.
- (127) Westerhoff, H. V.; Juretic, D.; Hender, R. W.; Zasloff, M. Magainins and the disruption of membrane-linked free-energy transduction. *Proc Natl Acad Sci U S A* **1989**, *86* (17), 6597-6601. DOI: 10.1073/pnas.86.17.6597 From NLM Medline.
- (128) Epanand, R. F.; Maloy, W. L.; Ramamoorthy, A.; Epanand, R. M. Probing the "charge cluster mechanism" in amphipathic helical cationic antimicrobial peptides. *Biochemistry* **2010**, *49* (19), 4076-4084. DOI: 10.1021/bi100378m From NLM Medline.
- (129) Epanand, R. M.; Epanand, R. F. Lipid domains in bacterial membranes and the action of antimicrobial agents. *Biochim. Biophys. Acta* **2009**, *1788* (1), 289-294. DOI: 10.1016/j.bbamem.2008.08.023 From NLM Medline.

- (130) Pokorny, A.; Almeida, P. F. Kinetics of dye efflux and lipid flip-flop induced by delta-lysin in phosphatidylcholine vesicles and the mechanism of graded release by amphipathic, alpha-helical peptides. *Biochemistry* **2004**, *43* (27), 8846-8857. DOI: 10.1021/bi0497087 From NLM Medline.
- (131) Pokorny, A.; Kilelee, E. M.; Wu, D.; Almeida, P. F. The activity of the amphipathic peptide delta-lysin correlates with phospholipid acyl chain structure and bilayer elastic properties. *Biophys. J.* **2008**, *95* (10), 4748-4755. DOI: 10.1529/biophysj.108.138701 From NLM Medline.
- (132) Gregory, S. M.; Cavanaugh, A.; Journigan, V.; Pokorny, A.; Almeida, P. F. A quantitative model for the all-or-none permeabilization of phospholipid vesicles by the antimicrobial peptide cecropin A. *Biophys. J.* **2008**, *94* (5), 1667-1680. DOI: 10.1529/biophysj.107.118760 From NLM Medline.
- (133) Gregory, S. M.; Pokorny, A.; Almeida, P. F. Magainin 2 revisited: a test of the quantitative model for the all-or-none permeabilization of phospholipid vesicles. *Biophys. J.* **2009**, *96* (1), 116-131. DOI: 10.1016/j.bpj.2008.09.017 From NLM Medline.
- (134) Almeida, P. F.; Pokorny, A. Mechanisms of antimicrobial, cytolytic, and cell-penetrating peptides: from kinetics to thermodynamics. *Biochemistry* **2009**, *48* (34), 8083-8093. DOI: 10.1021/bi900914g From NLM Medline.
- (135) Dennison, S. R.; Whittaker, M.; Harris, F.; Phoenix, D. A. Anticancer alpha-helical peptides and structure/function relationships underpinning their interactions with tumour cell membranes. *Curr Protein Pept Sci* **2006**, *7* (6), 487-499. DOI: 10.2174/138920306779025611 From NLM Medline.
- (136) Domalaon, R.; Findlay, B.; Ogunsina, M.; Arthur, G.; Schweizer, F. Ultrashort cationic lipopeptides and lipopeptoids: Evaluation and mechanistic insights against epithelial cancer cells. *Peptides* **2016**, *84*, 58-67. DOI: 10.1016/j.peptides.2016.07.007 From NLM Medline.
- (137) Riedl, S.; Zweytick, D.; Lohner, K. Membrane-active host defense peptides--challenges and perspectives for the development of novel anticancer drugs. *Chem. Phys. Lipids* **2011**, *164* (8), 766-781. DOI: 10.1016/j.chemphyslip.2011.09.004 From NLM Medline.
- (138) Gaspar, D.; Veiga, A. S.; Sinthuvanich, C.; Schneider, J. P.; Castanho, M. A. Anticancer peptide SVS-1: efficacy precedes membrane neutralization. *Biochemistry* **2012**, *51* (32), 6263-6265. DOI: 10.1021/bi300836r From NLM Medline.
- (139) Wu, D.; Gao, Y.; Qi, Y.; Chen, L.; Ma, Y.; Li, Y. Peptide-based cancer therapy: opportunity and challenge. *Cancer Lett* **2014**, *351* (1), 13-22. DOI: 10.1016/j.canlet.2014.05.002 From NLM Medline.
- (140) Moon, S.; Williams, S.; Cullen, M. Role of prophylactic antibiotics in the prevention of infections after chemotherapy: a literature review. *Support Cancer Ther* **2006**, *3* (4), 207-216. DOI: 10.3816/SCT.2006.n.018 From NLM PubMed-not-MEDLINE.
- (141) Ramadori, G.; Cameron, S. Effects of systemic chemotherapy on the liver. *Annals of Hepatology* **2010**, *9* (2), 133-143. DOI: 10.1016/s1665-2681(19)31651-5.
- (142) Lin, X. B.; Dieleman, L. A.; Ketabi, A.; Bibova, I.; Sawyer, M. B.; Xue, H.; Field, C. J.; Baracos, V. E.; Ganzle, M. G. Irinotecan (CPT-11) chemotherapy alters intestinal microbiota in tumour bearing rats. *PLoS ONE* **2012**, *7* (7), e39764. DOI: 10.1371/journal.pone.0039764 From NLM Medline.
- (143) Hobson, C. A.; Vigue, L.; Magnan, M.; Chassaing, B.; Naimi, S.; Gachet, B.; Claraz, P.; Storme, T.; Bonacorsi, S.; Tenaillon, O.; et al. A Microbiota-Dependent Response to Anticancer Treatment in an In

- Vitro Human Microbiota Model: A Pilot Study With Hydroxycarbamide and Daunorubicin. *Front Cell Infect Microbiol* **2022**, *12*, 886447. DOI: 10.3389/fcimb.2022.886447 From NLM Medline.
- (144) Figueiredo, C. R.; Matsuo, A. L.; Massaoka, M. H.; Polonelli, L.; Travassos, L. R. Anti-tumor activities of peptides corresponding to conserved complementary determining regions from different immunoglobulins. *Peptides* **2014**, *59*, 14-19. DOI: 10.1016/j.peptides.2014.06.007 From NLM Medline.
- (145) Baxter, A. A.; Lay, F. T.; Poon, I. K. H.; Kvensakul, M.; Hulett, M. D. Tumor cell membrane-targeting cationic antimicrobial peptides: novel insights into mechanisms of action and therapeutic prospects. *Cell Mol Life Sci* **2017**, *74* (20), 3809-3825. DOI: 10.1007/s00018-017-2604-z From NLM Medline.
- (146) Kuroda, K.; Okumura, K.; Isogai, H.; Isogai, E. The Human Cathelicidin Antimicrobial Peptide LL-37 and Mimics are Potential Anticancer Drugs. *Front Oncol* **2015**, *5*, 144. DOI: 10.3389/fonc.2015.00144 From NLM PubMed-not-MEDLINE.
- (147) Tanphaichitr, N.; Srakaew, N.; Alonzi, R.; Kiattiburut, W.; Kongmanas, K.; Zhi, R.; Li, W.; Baker, M.; Wang, G.; Hickling, D. Potential Use of Antimicrobial Peptides as Vaginal Spermicides/Microbicides. *Pharmaceuticals (Basel)* **2016**, *9* (1). DOI: 10.3390/ph9010013 From NLM PubMed-not-MEDLINE.
- (148) Reddy, K. V.; Yedery, R. D.; Aranha, C. Antimicrobial peptides: premises and promises. *Int J Antimicrob Agents* **2004**, *24* (6), 536-547. DOI: 10.1016/j.ijantimicag.2004.09.005 From NLM Medline.
- (149) Yedery, R. D.; Reddy, K. V. Antimicrobial peptides as microbicidal contraceptives: prophecies for prophylactics--a mini review. *Eur J Contracept Reprod Health Care* **2005**, *10* (1), 32-42. DOI: 10.1080/13625180500035124 From NLM Medline.
- (150) Wachinger, M.; Kleinschmidt, A.; Winder, D.; von Pechmann, N.; Ludvigsen, A.; Neumann, M.; Holle, R.; Salmons, B.; Erfle, V.; Brack-Werner, R. Antimicrobial peptides melittin and cecropin inhibit replication of human immunodeficiency virus 1 by suppressing viral gene expression. *J Gen Virol* **1998**, *79* (Pt 4), 731-740. DOI: 10.1099/0022-1317-79-4-731 From NLM Medline.
- (151) Newman, D. J.; Cragg, G. M.; Snader, K. M. The influence of natural products upon drug discovery. *Nat. Prod. Rep.* **2000**, *17* (3), 215-234. DOI: 10.1039/a902202c From NLM Medline.
- (152) Miner, J.; Hoffhines, A. The discovery of aspirin's antithrombotic effects. *Tex Heart Inst J* **2007**, *34* (2), 179-186. From NLM Medline.
- (153) Newman, D. J.; Cragg, G. M. Natural Products as Sources of New Drugs over the Nearly Four Decades from 01/1981 to 09/2019. *J. Nat. Prod.* **2020**, *83* (3), 770-803. DOI: 10.1021/acs.jnatprod.9b01285 From NLM Medline.
- (154) Atanasov, A. G.; Zotchev, S. B.; Dirsch, V. M.; International Natural Product Sciences, T.; Supuran, C. T. Natural products in drug discovery: advances and opportunities. *Nat Rev Drug Discov* **2021**, *20* (3), 200-216. DOI: 10.1038/s41573-020-00114-z From NLM Medline.
- (155) Ortholand, J. Y.; Ganesan, A. Natural products and combinatorial chemistry: back to the future. *Curr. Opin. Chem. Biol.* **2004**, *8* (3), 271-280. DOI: 10.1016/j.cbpa.2004.04.011 From NLM Medline.
- (156) Dewick, P. M. *Medicinal Natural Products*; John Wiley & Sons, Ltd, 2009. DOI: 10.1002/9780470742761.
- (157) Sheehan, J. C.; Henery-Logan, K. R. The Total Synthesis of Penicillin V. *Journal of the American Chemical Society* **2002**, *81* (12), 3089-3094. DOI: 10.1021/ja01521a044.

- (158) Abraham, E. P.; Newton, G. G. The structure of cephalosporin C. *Biochem. J* **1961**, *79* (2), 377-393. DOI: 10.1042/bj0790377 From NLM Medline.
- (159) Mackay, M.; Hodgkin, D. C. A crystallographic examination of the structure of morphine. *Journal of the Chemical Society (Resumed)* **1955**. DOI: 10.1039/jr9550003261.
- (160) Clarke, A. M.; Zemcov, S. J. Antibacterial activity of the cephamycin cefotetan: an in-vitro comparison with other beta-lactam antibiotics. *J. Antimicrob. Chemother.* **1983**, *11 Suppl*, 67-72. DOI: 10.1093/jac/11.suppl_a.67 From NLM Medline.
- (161) Lindner, K. R.; Bonner, D. P.; Koster, W. H. Monobactams. In *Kirk-Othmer Encyclopedia of Chemical Technology*, 2000.
- (162) Birnbaum, J.; Kahan, F. M.; Kropp, H.; MacDonald, J. S. Carbapenems, a new class of beta-lactam antibiotics. Discovery and development of imipenem/cilastatin. *Am J Med* **1985**, *78* (6A), 3-21. DOI: 10.1016/0002-9343(85)90097-x From NLM Medline.
- (163) Zask, A.; Murphy, J.; Ellestad, G. A. Biological stereoselectivity of atropisomeric natural products and drugs. *Chirality* **2013**, *25* (5), 265-274. DOI: 10.1002/chir.22145 From NLM Medline.
- (164) Orlando, B. J.; Lucido, M. J.; Malkowski, M. G. The structure of ibuprofen bound to cyclooxygenase-2. *J Struct Biol* **2015**, *189* (1), 62-66. DOI: 10.1016/j.jsb.2014.11.005 From NLM Medline.
- (165) Carlomagno, T. NMR in natural products: understanding conformation, configuration and receptor interactions. *Nat. Prod. Rep.* **2012**, *29* (5), 536-554. DOI: 10.1039/c2np00098a From NLM Medline.
- (166) Donovan, K. A.; An, J.; Nowak, R. P.; Yuan, J. C.; Fink, E. C.; Berry, B. C.; Ebert, B. L.; Fischer, E. S. Thalidomide promotes degradation of SALL4, a transcription factor implicated in Duane Radial Ray syndrome. *Elife* **2018**, *7*. DOI: 10.7554/eLife.38430 From NLM Medline.
- (167) Kim, J. H.; Scialli, A. R. Thalidomide: the tragedy of birth defects and the effective treatment of disease. *Toxicol. Sci.* **2011**, *122* (1), 1-6. DOI: 10.1093/toxsci/kfr088 From NLM Medline.
- (168) Smith, S. W. Chiral toxicology: it's the same thing...only different. *Toxicol. Sci.* **2009**, *110* (1), 4-30. DOI: 10.1093/toxsci/kfp097 From NLM Medline.
- (169) Hoglund, P.; Eriksson, T.; Bjorkman, S. A double-blind study of the sedative effects of the thalidomide enantiomers in humans. *J Pharmacokinet Biopharm* **1998**, *26* (4), 363-383. DOI: 10.1023/a:1021008016719 From NLM Medline.
- (170) Eriksson, T.; Bjorkman, S.; Roth, B.; Hoglund, P. Intravenous formulations of the enantiomers of thalidomide: pharmacokinetic and initial pharmacodynamic characterization in man. *J. Pharm. Pharmacol.* **2000**, *52* (7), 807-817. DOI: 10.1211/0022357001774660 From NLM Medline.
- (171) Palumbo, A.; Facon, T.; Sonneveld, P.; Blade, J.; Offidani, M.; Gay, F.; Moreau, P.; Waage, A.; Spencer, A.; Ludwig, H.; et al. Thalidomide for treatment of multiple myeloma: 10 years later. *Blood* **2008**, *111* (8), 3968-3977. DOI: 10.1182/blood-2007-10-117457 From NLM Medline.
- (172) Calabrese, L.; Fleischer, A. B. Thalidomide: current and potential clinical applications. *Am J Med* **2000**, *108* (6), 487-495. DOI: 10.1016/s0002-9343(99)00408-8 From NLM Medline.
- (173) Jeziorowski, S.; Thiele, C. M. Poly-gamma-p-Biphenylmethyl-Glutamate as Enantiodifferentiating Alignment Medium for NMR Spectroscopy with Temperature-Tunable Properties. *Chemistry* **2018**, *24* (58), 15631-15637. DOI: 10.1002/chem.201802921 From NLM PubMed-not-MEDLINE.

- (174) Kobzar, K.; Kessler, H.; Luy, B. Stretched gelatin gels as chiral alignment media for the discrimination of enantiomers by NMR spectroscopy. *Angew. Chem. Int. Ed. Engl.* **2005**, *44* (20), 3145-3147. DOI: 10.1002/anie.200462736 From NLM PubMed-not-MEDLINE.
- (175) Sarfati, M.; Courtieu, J.; Lesot, P. First successful enantiomeric discrimination of chiral alkanes using NMR spectroscopy. *Chem. Commun.* **2000**, (13), 1113-1114. DOI: 10.1039/b002806l.
- (176) Schmidt, M.; Sun, H.; Leonov, A.; Griesinger, C.; Reinscheid, U. M. Chiral discrimination of amines by anisotropic NMR parameters using chiral polyacrylamide-based gels. *Magn. Reson. Chem.* **2012**, *50 Suppl 1*, S38-44. DOI: 10.1002/mrc.3886 From NLM Medline.
- (177) Tichotova, M.; Landovsky, T.; Lang, J.; Jeziorowski, S.; Schmidts, V.; Kohout, M.; Babor, M.; Lhotak, P.; Thiele, C. M.; Dvorakova, H. Enantiodiscrimination of Inherently Chiral Thiocalixarenes by Residual Dipolar Couplings. *J. Org. Chem.* **2023**. DOI: 10.1021/acs.joc.2c02594 From NLM Publisher.
- (178) Domalain, V.; Tognetti, V.; Hubert-Roux, M.; Lange, C. M.; Joubert, L.; Baudoux, J.; Rouden, J.; Afonso, C. Role of cationization and multimers formation for diastereomers differentiation by ion mobility-mass spectrometry. *J. Am. Soc. Mass. Spectrom.* **2013**, *24* (9), 1437-1445. DOI: 10.1007/s13361-013-0690-1 From NLM Medline.
- (179) Claridge, T. D. W. *High-Resolution NMR Techniques*; Elsevier, 2016.
- (180) Haesler, J.; Schindelholz, I.; Riguet, E.; Bochet, C. G.; Hug, W. Absolute configuration of chirally deuterated neopentane. *Nature* **2007**, *446* (7135), 526-529. DOI: 10.1038/nature05653 From NLM PubMed-not-MEDLINE.
- (181) Dinku, W.; Isaksson, J.; Rylandsholm, F. G.; Bour, P.; Brichtová, E.; Choi, S. U.; Lee, S. H.; Jung, Y. S.; No, Z. S.; Svendsen, J. S. M.; et al. Anti-proliferative activity of a novel tricyclic triterpenoid acid from resin against four human cancer cell lines. *Applied Biological Chemistry* **2020**, *63* (1). DOI: 10.1186/s13765-020-00499-w.
- (182) García, M. E.; Pagola, S.; Navarro-Vázquez, A.; Phillips, D. D.; Gayathri, C.; Krakauer, H.; Stephens, P. W.; Nicotra, V. E.; Gil, R. R. Stereochemistry Determination by Powder X-Ray Diffraction Analysis and NMR Spectroscopy Residual Dipolar Couplings. *Angew. Chem.* **2009**, *121* (31), 5780-5784. DOI: 10.1002/ange.200900760.
- (183) Liu, Y.; Cohen, R. D.; Gustafson, K. R.; Martin, G. E.; Williamson, R. T. Enhanced measurement of residual chemical shift anisotropy for small molecule structure elucidation. *Chem Commun (Camb)* **2018**, *54* (34), 4254-4257. DOI: 10.1039/c8cc00552d.
- (184) Liu, Y.; Navarro-Vazquez, A.; Gil, R. R.; Griesinger, C.; Martin, G. E.; Williamson, R. T. Application of anisotropic NMR parameters to the confirmation of molecular structure. *Nat Protoc* **2019**, *14* (1), 217-247. DOI: 10.1038/s41596-018-0091-9.
- (185) Böttcher, B. a. T., C.M. . Determining the Stereochemistry of Molecules from Residual Dipolar Couplings (RDCs). *eMagRes* **2012**, *1* (1). DOI: 10.1002/9780470034590.emrstm1194.
- (186) Hansmann, S.; Larem, T.; Thiele, C. M. Enantiodifferentiating Properties of the Alignment Media PELG and PBLG – A Comparison. *Eur. J. Org. Chem.* **2016**, *2016* (7), 1324-1329. DOI: 10.1002/ejoc.201501410.

- (187) Kolmer, A.; Edwards, L. J.; Kuprov, I.; Thiele, C. M. Conformational analysis of small organic molecules using NOE and RDC data: A discussion of strychnine and alpha-methylene-gamma-butyrolactone. *J Magn Reson* **2015**, *261*, 101-109. DOI: 10.1016/j.jmr.2015.10.007 From NLM PubMed-not-MEDLINE.
- (188) Hoeck, C. R. *Solving a 3D Structural Puzzle*; Springer Cham, 2018. DOI: 10.1007/978-3-319-96172-9.
- (189) Ramsey, N. F.; Purcell, E. M. Interactions between Nuclear Spins in Molecules. *Physical Review* **1952**, *85* (1), 143-144. DOI: 10.1103/PhysRev.85.143.
- (190) Ramsey, N. F. Electron Coupled Interactions between Nuclear Spins in Molecules. *Physical Review* **1953**, *91* (2), 303-307. DOI: 10.1103/PhysRev.91.303.
- (191) Griesinger, C.; Sørensen, O. W.; Ernst, R. R. Practical aspects of the E.COSY technique. Measurement of scalar spin-spin coupling constants in peptides. *Journal of Magnetic Resonance (1969)* **1987**, *75* (3), 474-492. DOI: 10.1016/0022-2364(87)90102-8.
- (192) Gil, S.; Espinosa, J. F.; Parella, T. IPAP-HSQMBC: measurement of long-range heteronuclear coupling constants from spin-state selective multiplets. *J Magn Reson* **2010**, *207* (2), 312-321. DOI: 10.1016/j.jmr.2010.09.017 From NLM Medline.
- (193) Luy, B.; Hauser, G.; Kirschning, A.; Glaser, S. J. Optimized NMR spectroscopic method for the configurational analysis of chemically equivalent vicinal protons. *Angew. Chem. Int. Ed. Engl.* **2003**, *42* (11), 1300-1302. DOI: 10.1002/anie.200390335 From NLM PubMed-not-MEDLINE.
- (194) Otten, R.; Wood, K.; Mulder, F. A. Comprehensive determination of (3)J (HNHalpha) for unfolded proteins using (13)C'-resolved spin-echo difference spectroscopy. *J. Biomol. NMR* **2009**, *45* (4), 343-349. DOI: 10.1007/s10858-009-9382-3 From NLM Medline.
- (195) Karplus, S.; Karplus, M. Nuclear magnetic resonance determination of the angle psi in peptides. *Proc Natl Acad Sci U S A* **1972**, *69* (11), 3204-3206. DOI: 10.1073/pnas.69.11.3204 From NLM Medline.
- (196) Altona, C.; Haasnoot, C. A. G. Prediction of anti and gauche vicinal proton-proton coupling constants in carbohydrates: A simple additivity rule for pyranose rings. *Organic Magnetic Resonance* **1980**, *13* (6), 417-429. DOI: 10.1002/mrc.1270130606.
- (197) Haasnoot, C. A. G.; DeLeeuw, F. A. A. M.; Altona, C. The relationship between proton-proton NMR coupling constants and substituent electronegativities--I: An empirical generalization of the Karplus Equation. *Tetrahedron* **1980**, *36*, 2783-2792.
- (198) Farina, B.; Del Gatto, A.; Comegna, D.; Di Gaetano, S.; Capasso, D.; Isernia, C.; Saviano, M.; Fattorusso, R.; Zaccaro, L.; Russo, L. Conformational studies of RGDechi peptide by natural-abundance NMR spectroscopy. *J. Pept. Sci.* **2019**, *25* (5), e3166. DOI: 10.1002/psc.3166 From NLM Medline.
- (199) Wishart, D. S.; Case, D. A. Use of chemical shifts in macromolecular structure determination. *Methods Enzymol.* **2001**, *338*, 3-34. DOI: 10.1016/s0076-6879(02)38214-4 From NLM Medline.
- (200) Wishart, D. S.; Nip, A. M. Protein chemical shift analysis: a practical guide. *Biochem. Cell Biol.* **1998**, *76* (2-3), 153-163. DOI: 10.1139/bcb-76-2-3-153 From NLM Medline.
- (201) Wishart, D. S.; Sykes, B. D. Chemical shifts as a tool for structure determination. *Methods Enzymol.* **1994**, *239*, 363-392. DOI: 10.1016/s0076-6879(94)39014-2 From NLM Medline.
- (202) Wishart, D. S.; Sykes, B. D.; Richards, F. M. The chemical shift index: a fast and simple method for the assignment of protein secondary structure through NMR spectroscopy. *Biochemistry* **1992**, *31* (6), 1647-1651. DOI: 10.1021/bi00121a010 From NLM Medline.

- (203) Schwarzinger, S.; Kroon, G. J.; Foss, T. R.; Chung, J.; Wright, P. E.; Dyson, H. J. Sequence-dependent correction of random coil NMR chemical shifts. *J. Am. Chem. Soc.* **2001**, *123* (13), 2970-2978. DOI: 10.1021/ja003760i From NLM Medline.
- (204) Kjaergaard, M.; Brander, S.; Poulsen, F. M. Random coil chemical shift for intrinsically disordered proteins: effects of temperature and pH. *J. Biomol. NMR* **2011**, *49* (2), 139-149. DOI: 10.1007/s10858-011-9472-x From NLM Medline.
- (205) Kjaergaard, M.; Poulsen, F. M. Sequence correction of random coil chemical shifts: correlation between neighbor correction factors and changes in the Ramachandran distribution. *J. Biomol. NMR* **2011**, *50* (2), 157-165. DOI: 10.1007/s10858-011-9508-2 From NLM Medline.
- (206) Ting, D.; Wang, G.; Shapovalov, M.; Mitra, R.; Jordan, M. I.; Dunbrack, R. L., Jr. Neighbor-dependent Ramachandran probability distributions of amino acids developed from a hierarchical Dirichlet process model. *PLoS Comput Biol* **2010**, *6* (4), e1000763. DOI: 10.1371/journal.pcbi.1000763 From NLM Medline.
- (207) De Simone, A.; Cavalli, A.; Hsu, S. T.; Vranken, W.; Vendruscolo, M. Accurate random coil chemical shifts from an analysis of loop regions in native states of proteins. *J. Am. Chem. Soc.* **2009**, *131* (45), 16332-16333. DOI: 10.1021/ja904937a From NLM Medline.
- (208) Tamiola, K.; Acar, B.; Mulder, F. A. Sequence-specific random coil chemical shifts of intrinsically disordered proteins. *J. Am. Chem. Soc.* **2010**, *132* (51), 18000-18003. DOI: 10.1021/ja105656t From NLM Medline.
- (209) Tamiola, K.; Mulder, F. A. Using NMR chemical shifts to calculate the propensity for structural order and disorder in proteins. *Biochem. Soc. Trans.* **2012**, *40* (5), 1014-1020. DOI: 10.1042/BST20120171 From NLM Medline.
- (210) Marsh, J. A.; Singh, V. K.; Jia, Z.; Forman-Kay, J. D. Sensitivity of secondary structure propensities to sequence differences between alpha- and gamma-synuclein: implications for fibrillation. *Protein Sci.* **2006**, *15* (12), 2795-2804. DOI: 10.1110/ps.062465306 From NLM Medline.
- (211) Lundström, P. *Nuclear Overhauser Effect*; Springer, 2013. DOI: 10.1007/978-3-642-16712-6_308.
- (212) Borgias, B. A.; Gochin, M.; Kerwood, D. J.; James, T. L. Relaxation matrix analysis of 2D NMR data. *Prog. Nucl. Magn. Reson. Spectrosc.* **1990**, *22* (1), 83-100. DOI: 10.1016/0079-6565(90)80015-a.
- (213) Hu, H.; Krishnamurthy, K. Revisiting the initial rate approximation in kinetic NOE measurements. *J Magn Reson* **2006**, *182* (1), 173-177. DOI: 10.1016/j.jmr.2006.06.009 From NLM PubMed-not-MEDLINE.
- (214) Chen, K.; Tjandra, N. The use of residual dipolar coupling in studying proteins by NMR. *Top. Curr. Chem.* **2012**, *326*, 47-67. DOI: 10.1007/128_2011_215 From NLM Medline.
- (215) Polenova, T.; Gupta, R.; Goldbourt, A. Magic angle spinning NMR spectroscopy: a versatile technique for structural and dynamic analysis of solid-phase systems. *Anal. Chem.* **2015**, *87* (11), 5458-5469. DOI: 10.1021/ac504288u From NLM Medline.
- (216) Kummerlöwe, G.; Grage, S. L.; Thiele, C. M.; Kuprov, I.; Ulrich, A. S.; Luy, B. Variable angle NMR spectroscopy and its application to the measurement of residual chemical shift anisotropy. *J Magn Reson* **2011**, *209* (1), 19-30. DOI: 10.1016/j.jmr.2010.11.019 From NLM Medline.

- (217) Nardelli, F.; Borsacchi, S.; Calucci, L.; Carignani, E.; Martini, F.; Geppi, M. Anisotropy and NMR spectroscopy. *Rendiconti Lincei. Scienze Fisiche e Naturali* **2020**, *31* (4), 999-1010. DOI: 10.1007/s12210-020-00945-3.
- (218) Thiele, C. M. Simultaneous assignment of all diastereotopic protons in strychnine using RDCs: PELG as alignment medium for organic molecules. *J. Org. Chem.* **2004**, *69* (22), 7403-7413. DOI: 10.1021/jo049867w From NLM Medline.
- (219) Thiele, C. M.; Berger, S. Probing the diastereotopicity of methylene protons in strychnine using residual dipolar couplings. *Org. Lett.* **2003**, *5* (5), 705-708. DOI: 10.1021/ol0275163 From NLM PubMed-not-MEDLINE.
- (220) Meyer, N. C.; Krupp, A.; Schmidts, V.; Thiele, C. M.; Reggelin, M. Polyacetylenes as enantiodifferentiating alignment media. *Angew. Chem. Int. Ed. Engl.* **2012**, *51* (33), 8334-8338. DOI: 10.1002/anie.201201891 From NLM Medline.
- (221) Marx, A.; Schmidts, V.; Thiele, C. M. How different are diastereomorphous orientations of enantiomers in the liquid crystalline phases of PBLG and PBDG: a case study. *Magn. Reson. Chem.* **2009**, *47* (9), 734-740. DOI: 10.1002/mrc.2454 From NLM Medline.
- (222) Montag, T.; Thiele, C. M. Cross-linked helically chiral poly-(gamma-benzyl-L-glutamate) as enantiodiscriminating alignment medium. *Chemistry* **2013**, *19* (7), 2271-2274. DOI: 10.1002/chem.201202554 From NLM Medline.
- (223) Krupp, A.; Reggelin, M. Phenylalanine-based polyarylacetylenes as enantiomer-differentiating alignment media. *Magn. Reson. Chem.* **2012**, *50 Suppl 1*, S45-52. DOI: 10.1002/mrc.3894 From NLM Medline.
- (224) Luy, B.; Kobzar, K.; Kessler, H. An easy and scalable method for the partial alignment of organic molecules for measuring residual dipolar couplings. *Angew. Chem. Int. Ed. Engl.* **2004**, *43* (9), 1092-1094. DOI: 10.1002/anie.200352860 From NLM PubMed-not-MEDLINE.
- (225) Gayathri, C.; Tsarevsky, N. V.; Gil, R. R. Residual dipolar couplings (RDCs) analysis of small molecules made easy: fast and tuneable alignment by reversible compression/relaxation of reusable PMMA Gels. *Chemistry* **2010**, *16* (12), 3622-3626. DOI: 10.1002/chem.200903378 From NLM PubMed-not-MEDLINE.
- (226) Luy, B.; Kobzar, K.; Knor, S.; Furrer, J.; Heckmann, D.; Kessler, H. Orientational properties of stretched polystyrene gels in organic solvents and the suppression of their residual ¹H NMR signals. *J. Am. Chem. Soc.* **2005**, *127* (17), 6459-6465. DOI: 10.1021/ja043344o From NLM PubMed-not-MEDLINE.
- (227) Freudenberger, J. C.; Spittler, P.; Bauer, R.; Kessler, H.; Luy, B. Stretched poly(dimethylsiloxane) gels as NMR alignment media for apolar and weakly polar organic solvents: an ideal tool for measuring RDCs at low molecular concentrations. *J. Am. Chem. Soc.* **2004**, *126* (45), 14690-14691. DOI: 10.1021/ja046155e From NLM Medline.
- (228) Marx, A.; Thiele, C. Orientational properties of poly-gamma-benzyl-L-glutamate: influence of molecular weight and solvent on order parameters of the solute. *Chemistry* **2009**, *15* (1), 254-260. DOI: 10.1002/chem.200801147 From NLM PubMed-not-MEDLINE.
- (229) Saupe, A. Recent Results in the Field of Liquid Crystals. *Angewandte Chemie International Edition in English* **1968**, *7* (2), 97-112. DOI: 10.1002/anie.196800971.

- (230) Saupe, A.; Englert, G. High-Resolution Nuclear Magnetic Resonance Spectra of Orientated Molecules. *Phys. Rev. Lett.* **1963**, *11* (10), 462-464. DOI: 10.1103/PhysRevLett.11.462.
- (231) Thiele, C. M. Residual Dipolar Couplings (RDCs) in Organic Structure Determination. *Eur. J. Org. Chem.* **2008**, *2008* (34), 5673-5685. DOI: 10.1002/ejoc.200800686.
- (232) Li, G. W.; Liu, H.; Qiu, F.; Wang, X. J.; Lei, X. X. Residual Dipolar Couplings in Structure Determination of Natural Products. *Nat Prod Bioprospect* **2018**, *8* (4), 279-295. DOI: 10.1007/s13659-018-0174-x From NLM PubMed-not-MEDLINE.
- (233) Schmidts, V. Perspectives in the application of residual dipolar couplings in the structure elucidation of weakly aligned small molecules. *Magn. Reson. Chem.* **2017**, *55* (1), 54-60. DOI: 10.1002/mrc.4543 From NLM PubMed-not-MEDLINE.
- (234) Kummerlöwe, G.; Luy, B. Residual dipolar couplings as a tool in determining the structure of organic molecules. *TrAC, Trends Anal. Chem.* **2009**, *28* (4), 483-493. DOI: 10.1016/j.trac.2008.11.016.
- (235) Kramer, F.; Deshmukh, M. V.; Kessler, H.; Glaser, S. J. Residual dipolar coupling constants: An elementary derivation of key equations. *Concepts in Magnetic Resonance Part A* **2004**, *21A* (1), 10-21. DOI: 10.1002/cmr.a.20003.
- (236) Navarro-Vazquez, A. MSpin-RDC. A program for the use of residual dipolar couplings for structure elucidation of small molecules. *Magn. Reson. Chem.* **2012**, *50 Suppl 1*, S73-79. DOI: 10.1002/mrc.3905 From NLM PubMed-not-MEDLINE.
- (237) Fares, C.; Lingnau, J. B.; Wirtz, C.; Sternberg, U. Conformational Investigations in Flexible Molecules Using Orientational NMR Constraints in Combination with (3)J-Couplings and NOE Distances. *Molecules* **2019**, *24* (23). DOI: 10.3390/molecules24234417 From NLM Medline.
- (238) Sternberg, U.; Tzvetkova, P.; Muhle-Goll, C. The simulation of NMR data of flexible molecules: sagittamide A as an example for MD simulations with orientational constraints. *Phys. Chem. Chem. Phys.* **2020**, *22* (30), 17375-17384. DOI: 10.1039/d0cp01905d From NLM PubMed-not-MEDLINE.
- (239) Sternberg, U.; Witter, R.; Ulrich, A. S. All-atom molecular dynamics simulations using orientational constraints from anisotropic NMR samples. *J. Biomol. NMR* **2007**, *38* (1), 23-39. DOI: 10.1007/s10858-007-9142-1 From NLM Medline.
- (240) Sternberg, U.; Witter, R. Molecular dynamics simulations on PGLa using NMR orientational constraints. *J. Biomol. NMR* **2015**, *63* (3), 265-274. DOI: 10.1007/s10858-015-9983-y From NLM Medline.
- (241) Schwieters, C. D.; Suh, J. Y.; Grishaev, A.; Ghirlando, R.; Takayama, Y.; Clore, G. M. Solution structure of the 128 kDa enzyme I dimer from Escherichia coli and its 146 kDa complex with HPr using residual dipolar couplings and small- and wide-angle X-ray scattering. *J. Am. Chem. Soc.* **2010**, *132* (37), 13026-13045. DOI: 10.1021/ja105485b From NLM Medline.
- (242) Meier, S.; Grzesiek, S.; Blackledge, M. Mapping the conformational landscape of urea-denatured ubiquitin using residual dipolar couplings. *J. Am. Chem. Soc.* **2007**, *129* (31), 9799-9807. DOI: 10.1021/ja0724339 From NLM Medline.
- (243) Nodet, G.; Salmon, L.; Ozenne, V.; Meier, S.; Jensen, M. R.; Blackledge, M. Quantitative description of backbone conformational sampling of unfolded proteins at amino acid resolution from NMR residual dipolar couplings. *J. Am. Chem. Soc.* **2009**, *131* (49), 17908-17918. DOI: 10.1021/ja9069024 From NLM Medline.

- (244) Esteban-Martin, S.; Fenwick, R. B.; Salvatella, X. Refinement of ensembles describing unstructured proteins using NMR residual dipolar couplings. *J. Am. Chem. Soc.* **2010**, *132* (13), 4626-4632. DOI: 10.1021/ja906995x From NLM Medline.
- (245) Hallwass, F.; Schmidt, M.; Sun, H.; Mazur, A.; Kummerlowe, G.; Luy, B.; Navarro-Vazquez, A.; Griesinger, C.; Reinscheid, U. M. Residual chemical shift anisotropy (RCSA): a tool for the analysis of the configuration of small molecules. *Angew. Chem. Int. Ed. Engl.* **2011**, *50* (40), 9487-9490. DOI: 10.1002/anie.201101784 From NLM Medline.
- (246) Nath, N.; Schmidt, M.; Gil, R. R.; Williamson, R. T.; Martin, G. E.; Navarro-Vazquez, A.; Griesinger, C.; Liu, Y. Determination of Relative Configuration from Residual Chemical Shift Anisotropy. *J. Am. Chem. Soc.* **2016**, *138* (30), 9548-9556. DOI: 10.1021/jacs.6b04082 From NLM PubMed-not-MEDLINE.
- (247) Zweckstetter, M. NMR: prediction of molecular alignment from structure using the PALES software. *Nat Protoc* **2008**, *3* (4), 679-690. DOI: 10.1038/nprot.2008.36 From NLM Medline.
- (248) Tjandra, N.; Bax, A. Direct measurement of distances and angles in biomolecules by NMR in a dilute liquid crystalline medium. *Science* **1997**, *278* (5340), 1111-1114. DOI: 10.1126/science.278.5340.1111 From NLM Medline.
- (249) Rückert, M.; Otting, G. Alignment of Biological Macromolecules in Novel Nonionic Liquid Crystalline Media for NMR Experiments. *Journal of the American Chemical Society* **2000**, *122* (32), 7793-7797. DOI: 10.1021/ja001068h.
- (250) Hansen, M. R.; Mueller, L.; Pardi, A. Tunable alignment of macromolecules by filamentous phage yields dipolar coupling interactions. *Nat. Struct. Biol.* **1998**, *5* (12), 1065-1074. DOI: 10.1038/4176 From NLM Medline.
- (251) Pedersen, K. D.; Zhang, J.; Gotfredsen, C. H. Practical considerations for working with graphene oxide as alignment media for RDC measurements. *Magn. Reson. Chem.* **2021**, *59* (7), 738-745. DOI: 10.1002/mrc.5143 From NLM PubMed-not-MEDLINE.
- (252) Tycko, R.; Blanco, F. J.; Ishii, Y. Alignment of Biopolymers in Strained Gels: A New Way To Create Detectable Dipole-Dipole Couplings in High-Resolution Biomolecular NMR. *Journal of the American Chemical Society* **2000**, *122* (38), 9340-9341. DOI: 10.1021/ja002133q.
- (253) Hellemann, E.; Gil, R. R. New Stretching Method for Aligning Gels: Its Application to the Measurement Residual Chemical Shift Anisotropies (RCSAs) without the Need for Isotropic Shift Correction. *Chemistry* **2018**, *24* (15), 3689-3693. DOI: 10.1002/chem.201704541 From NLM PubMed-not-MEDLINE.
- (254) Marx, A.; Bottcher, B.; Thiele, C. M. Enhancing the orienting properties of poly(γ -benzyl-L-glutamate) by means of additives. *Chemistry* **2010**, *16* (5), 1656-1663. DOI: 10.1002/chem.200902287 From NLM PubMed-not-MEDLINE.
- (255) Sass, H. J.; Musco, G.; Stahl, S. J.; Wingfield, P. T.; Grzesiek, S. Solution NMR of proteins within polyacrylamide gels: diffusional properties and residual alignment by mechanical stress or embedding of oriented purple membranes. *J. Biomol. NMR* **2000**, *18* (4), 303-309. DOI: 10.1023/a:1026703605147 From NLM Medline.
- (256) Bax, A.; Grishaev, A. Weak alignment NMR: a hawk-eyed view of biomolecular structure. *Curr Opin Struct Biol* **2005**, *15* (5), 563-570. DOI: 10.1016/j.sbi.2005.08.006 From NLM Medline.

- (257) Kuchel, P. W.; Chapman, B. E.; Muller, N.; Bubb, W. A.; Philp, D. J.; Torres, A. M. Apparatus for rapid adjustment of the degree of alignment of NMR samples in aqueous media: verification with residual quadrupolar splittings in (^{23}Na) and (^{133}Cs) spectra. *J Magn Reson* **2006**, *180* (2), 256-265. DOI: 10.1016/j.jmr.2006.03.002 From NLM Medline.
- (258) Kummerlöwe, G.; McCord, E. F.; Cheatham, S. F.; Niss, S.; Schnell, R. W.; Luy, B. Tunable alignment for all polymer gel/solvent combinations for the measurement of anisotropic NMR parameters. *Chemistry* **2010**, *16* (24), 7087-7089. DOI: 10.1002/chem.201000108 From NLM Medline.
- (259) Kummerlöwe, G.; Halbach, F.; Laufer, B.; Luy, B. Precise Measurement of RDCs in Water and DMSO Based Gels Using a Silicone Rubber Tube for Tunable Stretching. *The Open Spectroscopy Journal* **2008**, *2* (1), 29-33. DOI: 10.2174/1874383800802010029.
- (260) Freudenberger, J. C.; Knor, S.; Kobzar, K.; Heckmann, D.; Paululat, T.; Kessler, H.; Luy, B. Stretched poly(vinyl acetate) gels as NMR alignment media for the measurement of residual dipolar couplings in polar organic solvents. *Angew. Chem. Int. Ed. Engl.* **2005**, *44* (3), 423-426. DOI: 10.1002/anie.200461241 From NLM Medline.
- (261) Kummerlöwe, G.; Kiran, M. U.; Luy, B. Covalently cross-linked gelatin allows chiral distinction at elevated temperatures and in DMSO. *Chemistry* **2009**, *15* (45), 12192-12195. DOI: 10.1002/chem.200902193 From NLM Medline.
- (262) Buchler, S. S.; Kummerlöwe, G.; Luy, B. Naturally occurring biodegradable polymers as the basis of chiral gels for the distinction of enantiomers by partially oriented NMR spectroscopy. *Int J Artif Organs* **2011**, *34* (2), 134-138. DOI: 10.5301/ijao.2011.6419 From NLM Medline.
- (263) Enthart, A.; Freudenberger, J. C.; Furrer, J.; Kessler, H.; Luy, B. The CLIP/CLAP-HSQC: pure absorptive spectra for the measurement of one-bond couplings. *J Magn Reson* **2008**, *192* (2), 314-322. DOI: 10.1016/j.jmr.2008.03.009 From NLM Medline.
- (264) Timari, I.; Kaltschnee, L.; Kolmer, A.; Adams, R. W.; Nilsson, M.; Thiele, C. M.; Morris, G. A.; Kover, K. E. Accurate determination of one-bond heteronuclear coupling constants with "pure shift" broadband proton-decoupled CLIP/CLAP-HSQC experiments. *J Magn Reson* **2014**, *239*, 130-138. DOI: 10.1016/j.jmr.2013.10.023 From NLM PubMed-not-MEDLINE.
- (265) Ottiger, M.; Delaglio, F.; Bax, A. Measurement of J and dipolar couplings from simplified two-dimensional NMR spectra. *J Magn Reson* **1998**, *131* (2), 373-378. DOI: 10.1006/jmre.1998.1361 From NLM Medline.
- (266) Losonczi, J. A.; Andrec, M.; Fischer, M. W.; Prestegard, J. H. Order matrix analysis of residual dipolar couplings using singular value decomposition. *J Magn Reson* **1999**, *138* (2), 334-342. DOI: 10.1006/jmre.1999.1754 From NLM Medline.
- (267) Ndukwe, I. E.; Lam, Y. H.; Pandey, S. K.; Haug, B. E.; Bayer, A.; Sherer, E. C.; Blinov, K. A.; Williamson, R. T.; Isaksson, J.; Reibarkh, M.; et al. Unequivocal structure confirmation of a breitfussin analog by anisotropic NMR measurements. *Chem Sci* **2020**, *11* (44), 12081-12088. DOI: 10.1039/d0sc03664a From NLM PubMed-not-MEDLINE.
- (268) Bryce, D. L.; Bax, A. Application of correlated residual dipolar couplings to the determination of the molecular alignment tensor magnitude of oriented proteins and nucleic acids. *J. Biomol. NMR* **2004**, *28* (3), 273-287. DOI: 10.1023/B:JNMR.0000013701.16162.0c From NLM Medline.

- (269) Boisbouvier, J.; Bryce, D. L.; O'Neil-Cabello, E.; Nikonowicz, E. P.; Bax, A. Resolution-optimized NMR measurement of (1)D(CH), (1)D(CC) and (2)D(CH) residual dipolar couplings in nucleic acid bases. *J. Biomol. NMR* **2004**, *30* (3), 287-301. DOI: 10.1007/s10858-005-1846-5 From NLM Medline.
- (270) Jarmoskaite, I.; AlSadhan, I.; Vaidyanathan, P. P.; Herschlag, D. How to measure and evaluate binding affinities. *Elife* **2020**, *9*. DOI: 10.7554/eLife.57264 From NLM Medline.
- (271) Florindo, C.; Araujo, J. M.; Alves, F.; Matos, C.; Ferraz, R.; Prudencio, C.; Noronha, J. P.; Petrovski, Z.; Branco, L.; Rebelo, L. P.; et al. Evaluation of solubility and partition properties of ampicillin-based ionic liquids. *Int. J. Pharm.* **2013**, *456* (2), 553-559. DOI: 10.1016/j.ijpharm.2013.08.010 From NLM Medline.
- (272) Lin, J. H.; Sugiyama, Y.; Awazu, S.; Hanano, M. In vitro and in vivo evaluation of the tissue-to-blood partition coefficient for physiological pharmacokinetic models. *J Pharmacokinet Biopharm* **1982**, *10* (6), 637-647. DOI: 10.1007/BF01062545 From NLM Medline.
- (273) Hollmann, A.; Martinez, M.; Noguera, M. E.; Augusto, M. T.; Disalvo, A.; Santos, N. C.; Semorile, L.; Maffia, P. C. Role of amphipathicity and hydrophobicity in the balance between hemolysis and peptide-membrane interactions of three related antimicrobial peptides. *Colloids Surf B Biointerfaces* **2016**, *141*, 528-536. DOI: 10.1016/j.colsurfb.2016.02.003 From NLM Medline.
- (274) Hait, S.; Mallik, S.; Basu, S.; Kundu, S. Finding the generalized molecular principles of protein thermal stability. *Proteins* **2020**, *88* (6), 788-808. DOI: 10.1002/prot.25866 From NLM Medline.
- (275) Barik, S. The Uniqueness of Tryptophan in Biology: Properties, Metabolism, Interactions and Localization in Proteins. *Int J Mol Sci* **2020**, *21* (22). DOI: 10.3390/ijms21228776 From NLM Medline.
- (276) Christiaens, B.; Symoens, S.; Verheyden, S.; Engelborghs, Y.; Joliot, A.; Prochiantz, A.; Vandekerckhove, J.; Rosseneu, M.; Vanloo, B. Tryptophan fluorescence study of the interaction of penetratin peptides with model membranes. *Eur. J. Biochem.* **2002**, *269* (12), 2918-2926. DOI: 10.1046/j.1432-1033.2002.02963.x From NLM Medline.
- (277) Valeur, B.; Berberan-Santos, M. N. A Brief History of Fluorescence and Phosphorescence before the Emergence of Quantum Theory. *J. Chem. Educ.* **2011**, *88* (6), 731-738. DOI: 10.1021/ed100182h.
- (278) Levitus, M. Tutorial: measurement of fluorescence spectra and determination of relative fluorescence quantum yields of transparent samples. *Methods Appl Fluoresc* **2020**, *8* (3), 033001. DOI: 10.1088/2050-6120/ab7e10 From NLM PubMed-not-MEDLINE.
- (279) van de Weert, M.; Stella, L. Fluorescence quenching and ligand binding: A critical discussion of a popular methodology. *J. Mol. Struct.* **2011**, *998* (1-3), 144-150. DOI: 10.1016/j.molstruc.2011.05.023.
- (280) Kraft, C. A.; Garrido, J. L.; Leiva-Vega, L.; Romero, G. Quantitative analysis of protein-lipid interactions using tryptophan fluorescence. *Sci Signal* **2009**, *2* (99), p14. DOI: 10.1126/scisignal.299p14 From NLM Medline.
- (281) Matos, P. M.; Franquelim, H. G.; Castanho, M. A.; Santos, N. C. Quantitative assessment of peptide-lipid interactions. Ubiquitous fluorescence methodologies. *Biochim. Biophys. Acta* **2010**, *1798* (11), 1999-2012. DOI: 10.1016/j.bbamem.2010.07.012 From NLM Medline.
- (282) Jerabek-Willemsen, M.; André, T.; Wanner, R.; Roth, H. M.; Duhr, S.; Baaske, P.; Breitsprecher, D. MicroScale Thermophoresis: Interaction analysis and beyond. *J. Mol. Struct.* **2014**, *1077*, 101-113. DOI: 10.1016/j.molstruc.2014.03.009.

- (283) Lopez-Mendez, B.; Baron, B.; Brautigam, C. A.; Jowitt, T. A.; Knauer, S. H.; Uebel, S.; Williams, M. A.; Sedivy, A.; Abian, O.; Abreu, C.; et al. Reproducibility and accuracy of microscale thermophoresis in the NanoTemper Monolith: a multi laboratory benchmark study. *Eur Biophys J* **2021**, *50* (3-4), 411-427. DOI: 10.1007/s00249-021-01532-6 From NLM Medline.
- (284) Lopez-Mendez, B.; Uebel, S.; Lundgren, L. P.; Sedivy, A. Microscale Thermophoresis and additional effects measured in NanoTemper Monolith instruments. *Eur Biophys J* **2021**, *50* (3-4), 653-660. DOI: 10.1007/s00249-021-01529-1 From NLM Medline.
- (285) Rainsford, P.; Rylandsholm, F. G.; Jakubec, M.; Silk, M.; Juskewitz, E.; Ericson, J. U.; Svendsen, J. S.; Engh, R. A.; Isaksson, J. Label-free measurement of antimicrobial peptide interactions with lipid vesicles and nanodiscs using microscale thermophoresis. *Sci Rep* **2023**, *13* (1), 12619. DOI: 10.1038/s41598-023-39785-0 From NLM Medline.
- (286) Ravula, T.; Hardin, N. Z.; Ramadugu, S. K.; Cox, S. J.; Ramamoorthy, A. Formation of pH-Resistant Monodispersed Polymer-Lipid Nanodiscs. *Angew. Chem. Int. Ed. Engl.* **2018**, *57* (5), 1342-1345. DOI: 10.1002/anie.201712017.
- (287) Jakubec, M.; Barias, E.; Furse, S.; Govasli, M. L.; George, V.; Turcu, D.; Iashchishyn, I. A.; Morozova-Roche, L. A.; Halskau, O. Cholesterol-containing lipid nanodiscs promote an alpha-synuclein binding mode that accelerates oligomerization. *FEBS J* **2021**, *288* (6), 1887-1905. DOI: 10.1111/febs.15551 From NLM Medline.
- (288) NewEra. *Some Reflections on Gel NMR Sample Preparation*. <https://newera-spectro.com/some-reflection-on-gel-nmr-sample-preparation> (accessed 2023 03.08).
- (289) Eikås, K. D. R.; Rylandsholm, F. G.; Kristoffersen, T.; Jakubec, M.; Silk, M. R.; Svendsen, J. S. M.; Isaksson, J.; Ruud, K.; Krupová, M. Conformational Studies of Cyclic Hexapeptides with Vibrational Circular Dichroism and Nuclear Magnetic Resonance. .
- (290) Willmott, C. J.; Matsuura, K. Advantages of the mean absolute error (MAE) over the root mean square error (RMSE) in assessing average model performance. *Climate Research* **2005**, *30*, 79-82. DOI: 10.3354/cr030079.
- (291) Jakubec, M.; Rylandsholm, F. G.; Rainsford, P.; Silk, M.; Bril'kov, M.; Kristoffersen, T.; Juskewitz, E.; Ericson, J. U.; Svendsen, J. S. M. Goldilocks Dilemma: LPS Works Both as the Initial Target and a Barrier for the Antimicrobial Action of Cationic AMPs on *E. coli*. *Biomolecules* **2023**, *13* (7). DOI: 10.3390/biom13071155.
- (292) Li, B.; Yin, F.; Zhao, X.; Guo, Y.; Wang, W.; Wang, P.; Zhu, H.; Yin, Y.; Wang, X. Colistin Resistance Gene *mcr-1* Mediates Cell Permeability and Resistance to Hydrophobic Antibiotics. *Front Microbiol* **2019**, *10*, 3015. DOI: 10.3389/fmicb.2019.03015 From NLM PubMed-not-MEDLINE.
- (293) Feng, S.; Liang, W.; Li, J.; Chen, Y.; Zhou, D.; Liang, L.; Lin, D.; Li, Y.; Zhao, H.; Du, H.; et al. MCR-1-dependent lipid remodelling compromises the viability of Gram-negative bacteria. *Emerg Microbes Infect* **2022**, *11* (1), 1236-1249. DOI: 10.1080/22221751.2022.2065934 From NLM Medline.
- (294) Kruger, M.; Richter, P.; Strauch, S. M.; Nasir, A.; Burkovski, A.; Antunes, C. A.; Meissgeier, T.; Schlucker, E.; Schwab, S.; Lebert, M. What an *Escherichia coli* Mutant Can Teach Us About the Antibacterial Effect of Chlorophyllin. *Microorganisms* **2019**, *7* (2). DOI: 10.3390/microorganisms7020059 From NLM PubMed-not-MEDLINE.

- (295) Speck, S.; Courtiol, A.; Junkes, C.; Dathe, M.; Muller, K.; Schulze, M. Cationic synthetic peptides: assessment of their antimicrobial potency in liquid preserved boar semen. *PLoS ONE* **2014**, *9* (8), e105949. DOI: 10.1371/journal.pone.0105949 From NLM Medline.
- (296) Lau, Q. Y.; Ng, F. M.; Cheong, J. W.; Yap, Y. Y.; Tan, Y. Y.; Jureen, R.; Hill, J.; Chia, C. S. Discovery of an ultra-short linear antibacterial tetrapeptide with anti-MRSA activity from a structure-activity relationship study. *Eur. J. Med. Chem.* **2015**, *105*, 138-144. DOI: 10.1016/j.ejmech.2015.10.015 From NLM Medline.
- (297) Gopal, R.; Kim, Y. J.; Seo, C. H.; Hahm, K. S.; Park, Y. Reversed sequence enhances antimicrobial activity of a synthetic peptide. *J. Pept. Sci.* **2011**, *17* (5), 329-334. DOI: 10.1002/psc.1369 From NLM Medline.
- (298) Gopal, R.; Na, H.; Seo, C. H.; Park, Y. Antifungal activity of (KW)_n or (RW)_n peptide against *Fusarium solani* and *Fusarium oxysporum*. *Int J Mol Sci* **2012**, *13* (11), 15042-15053. DOI: 10.3390/ijms131115042 From NLM Medline.
- (299) Finger, S.; Kerth, A.; Dathe, M.; Blume, A. The efficacy of trivalent cyclic hexapeptides to induce lipid clustering in PG/PE membranes correlates with their antimicrobial activity. *Biochim. Biophys. Acta* **2015**, *1848* (11 Pt A), 2998-3006. DOI: 10.1016/j.bbamem.2015.09.012 From NLM Medline.
- (300) Rietschel, E. T.; Kirikae, T.; Schade, F. U.; Mamat, U.; Schmidt, G.; Loppnow, H.; Ulmer, A. J.; Zahringer, U.; Seydel, U.; Di Padova, F.; et al. Bacterial endotoxin: molecular relationships of structure to activity and function. *FASEB J.* **1994**, *8* (2), 217-225. DOI: 10.1096/fasebj.8.2.8119492 From NLM Medline.
- (301) Figueira, T. N.; Freire, J. M.; Cunha-Santos, C.; Heras, M.; Goncalves, J.; Moscona, A.; Porotto, M.; Salome Veiga, A.; Castanho, M. A. Quantitative analysis of molecular partition towards lipid membranes using surface plasmon resonance. *Sci Rep* **2017**, *7*, 45647. DOI: 10.1038/srep45647 From NLM Medline.
- (302) Shortridge, M. D.; Hage, D. S.; Harbison, G. S.; Powers, R. Estimating protein-ligand binding affinity using high-throughput screening by NMR. *J. Comb. Chem.* **2008**, *10* (6), 948-958. DOI: 10.1021/cc800122m From NLM Medline.
- (303) Sadi, M.; Carvalho, N.; Leger, C.; Vitorge, B.; Ladant, D.; Guijarro, J. I.; Chenal, A. B2LiVe, a label-free 1D-NMR method to quantify the binding of amphitropic peptides or proteins to membrane vesicles. *Cell Rep Methods* **2023**, *3* (11), 100624. DOI: 10.1016/j.crmeth.2023.100624 From NLM Medline.
- (304) Kleckner, I. R.; Foster, M. P. An introduction to NMR-based approaches for measuring protein dynamics. *Biochim. Biophys. Acta* **2011**, *1814* (8), 942-968. DOI: 10.1016/j.bbapap.2010.10.012 From NLM Medline.
- (305) Kučerka, N.; Liu, Y.; Chu, N.; Petrache, H. I.; Tristram-Nagle, S.; Nagle, J. F. Structure of Fully Hydrated Fluid Phase DMPC and DLPC Lipid Bilayers Using X-Ray Scattering from Oriented Multilamellar Arrays and from Unilamellar Vesicles. *Biophys. J.* **2005**, *88* (4), 2626-2637. DOI: 10.1529/biophysj.104.056606.
- (306) Hu, M.; de Jong, D. H.; Marrink, S. J.; Deserno, M. Gaussian curvature elasticity determined from global shape transformations and local stress distributions: a comparative study using the MARTINI model. *Faraday Discuss.* **2013**, *161*, 365-382; discussion 419-359. DOI: 10.1039/c2fd20087b From NLM Medline.
- (307) Marsh, D. *Handbook of lipid bilayers*; CRC Press, 2013.

- (308) Dorr, J. M.; Scheidelaar, S.; Koorengel, M. C.; Dominguez, J. J.; Schafer, M.; van Walree, C. A.; Killian, J. A. The styrene-maleic acid copolymer: a versatile tool in membrane research. *Eur Biophys J* **2016**, *45* (1), 3-21. DOI: 10.1007/s00249-015-1093-y From NLM Medline.
- (309) Zhang, A. H.; Edwards, I. A.; Mishra, B. P.; Sharma, G.; Healy, M. D.; Elliott, A. G.; Blaskovich, M. A. T.; Cooper, M. A.; Collins, B. M.; Jia, X.; et al. Elucidating the Lipid Binding Properties of Membrane-Active Peptides Using Cyclised Nanodiscs. *Front Chem* **2019**, *7*, 238. DOI: 10.3389/fchem.2019.00238 From NLM PubMed-not-MEDLINE.
- (310) Grethen, A.; Oluwole, A. O.; Danielczak, B.; Vargas, C.; Keller, S. Thermodynamics of nanodisc formation mediated by styrene/maleic acid (2:1) copolymer. *Sci Rep* **2017**, *7* (1), 11517. DOI: 10.1038/s41598-017-11616-z From NLM PubMed-not-MEDLINE.
- (311) Stepien, P.; Augustyn, B.; Poojari, C.; Galan, W.; Polit, A.; Vattulainen, I.; Wisnieska-Becker, A.; Rog, T. Complexity of seemingly simple lipid nanodiscs. *Biochim Biophys Acta Biomembr* **2020**, *1862* (11), 183420. DOI: 10.1016/j.bbamem.2020.183420 From NLM Medline.
- (312) Simonovic, D.; Rylandsholm, F. G.; Jakubec, M.; Isaksson, J. M.; Devold, H.; Dey, H.; Anderssen, T.; Haug, T.; Strøm, M. B. The role of amphipathicity and L- to D-amino acid substitution in a small antimicrobial cyclic tetrapeptide scaffold containing a halogenated α,α -disubstituted $\beta^{2,2}$ -amino acid residue. .
- (313) Sarojini, V.; Cameron, A. J.; Varnava, K. G.; Denny, W. A.; Sanjayan, G. Cyclic Tetrapeptides from Nature and Design: A Review of Synthetic Methodologies, Structure, and Function. *Chem Rev* **2019**, *119* (17), 10318-10359. DOI: 10.1021/acs.chemrev.8b00737 From NLM Medline.
- (314) Ravula, T.; Hardin, N. Z.; Ramamoorthy, A. Polymer nanodiscs: Advantages and limitations. *Chem. Phys. Lipids* **2019**, *219*, 45-49. DOI: 10.1016/j.chemphyslip.2019.01.010.
- (315) Ravula, T.; Ramadugu, S. K.; Di Mauro, G.; Ramamoorthy, A. Bioinspired, Size-Tunable Self-Assembly of Polymer-Lipid Bilayer Nanodiscs. *Angew. Chem. Int. Ed. Engl.* **2017**, *56* (38), 11466-11470. DOI: 10.1002/anie.201705569.
- (316) Ravula, T.; Ramamoorthy, A. Magnetic Alignment of Polymer Macro-Nanodiscs Enables Residual-Dipolar-Coupling-Based High-Resolution Structural Studies by NMR Spectroscopy. *Angew. Chem. Int. Ed. Engl.* **2019**, *58* (42), 14925-14928. DOI: 10.1002/anie.201907655.
- (317) Ravula, T.; Kim, J.; Lee, D. K.; Ramamoorthy, A. Magnetic Alignment of Polymer Nanodiscs Probed by Solid-State NMR Spectroscopy. *Langmuir* **2020**, *36* (5), 1258-1265. DOI: 10.1021/acs.langmuir.9b03538 From NLM Medline.
- (318) Rylandsholm, F. G.; Rainsford, P. B.; Krupova, M.; Kristoffersen, T.; Haugen, T.; Brandsdal, B. O.; Svendsen, J. S.; Isaksson, J. Structural analysis of four cyclic antimicrobial hexapeptides in aqueous solution and in micelles, towards membrane-mimicking nanodiscs.
- (319) Bechinger, B. Pore-forming Polypeptides in Lipid Membranes. *J. Membrane Biol.* **1997**, *156*, 197-211.
- (320) Pistolesi, S.; Pogni, R.; Feix, J. B. Membrane insertion and bilayer perturbation by antimicrobial peptide CM15. *Biophys. J.* **2007**, *93* (5), 1651-1660. DOI: 10.1529/biophysj.107.104034 From NLM Medline.
- (321) Pu, M.; Orr, A.; Redfield, A. G.; Roberts, M. F. Defining specific lipid binding sites for a peripheral membrane protein in situ using subtesla field-cycling NMR. *J. Biol. Chem.* **2010**, *285* (35), 26916-26922. DOI: 10.1074/jbc.M110.123083 From NLM Medline.

- (322) Clore, G. M.; Iwahara, J. Theory, practice, and applications of paramagnetic relaxation enhancement for the characterization of transient low-population states of biological macromolecules and their complexes. *Chem Rev* **2009**, *109* (9), 4108-4139. DOI: 10.1021/cr900033p From NLM Medline.
- (323) Dittmer, J.; Thogersen, L.; Underhaug, J.; Bertelsen, K.; Vosegaard, T.; Pedersen, J. M.; Schiott, B.; Tajkhorshid, E.; Skrydstrup, T.; Nielsen, N. C. Incorporation of antimicrobial peptides into membranes: a combined liquid-state NMR and molecular dynamics study of alamethicin in DMPC/DHPC bicelles. *J Phys Chem B* **2009**, *113* (19), 6928-6937. DOI: 10.1021/jp811494p From NLM Medline.
- (324) Ghadiri, M. R.; Granja, J. R.; Milligan, R. A.; McRee, D. E.; Khazanovich, N. Self-assembling organic nanotubes based on a cyclic peptide architecture. *Nature* **1993**, *366* (6453), 324-327. DOI: 10.1038/366324a0.
- (325) Horne, W. S.; Stout, C. D.; Ghadiri, M. R. A heterocyclic peptide nanotube. *J. Am. Chem. Soc.* **2003**, *125* (31), 9372-9376. DOI: 10.1021/ja034358h.

You can never know everything, and part of what you know is always wrong. Perhaps even the most important part. A portion of wisdom lies in knowing that. A portion of courage lies in going on anyways.

- Lan Mandragoran to Rand al'Thor in Winter's Heart chapter 32, A Wheel of Time novel by
Robert Jordan

Paper I

ARTICLE

Open Access



Anti-proliferative activity of a novel tricyclic triterpenoid acid from *Commiphora africana* resin against four human cancer cell lines

Worku Dinku¹, Johan Isaksson², Fredrik Garnås Rylandsholm², Petr Bouř³, Eva Brichtová^{3,4}, Sang Un Choi⁵, Sang-Ho Lee⁵, Young-Sik Jung⁵, Zae Sung No⁶, John Sigurd Mjøen Svendsen², Arne Jørgen Aasen² and Aman Dekebo^{1*}

Abstract

Myrrh, a resin derived from the damaged bark of *Commiphora* genus, has traditionally been used for treatment of various human diseases, such as amenorrhea, ache, tumors, fever, and stomach pains. In spite of this widespread use of the myrrh in Ethiopia, the pharmacological activity and chemical composition have not been studied in detail. A new tricyclic triterpene acid (3S,4S,14S,7E,17E,21Z)-3,30-dihydroxydiododa-7,17,21-trien-4-carboxylic acid (commafric A) has been isolated from a crude methanolic extract of *Commiphora africana* (A. Rich.) Engl. resin along with the known pentacyclic triterpene α -amyrin. The structure of commafric A was characterized using different spectroscopic techniques such as 1D and 2D NMR, IR, and VCD combined with computations. The anti-proliferative activity of both isolated compounds was evaluated using SRB based colorimetric cellular assay against four human cancer cell lines. Etoposide was used as a positive control. Commafric A showed significant anti-proliferative effects against non-small cell lung cancer (A549) with IC₅₀ values of 4.52 μ g/ml. The pentacyclic triterpene α -amyrin showed a weak anti-proliferative activity against A2780 (ovarian cancer), MIA-PaCa-2 (pancreatic cancer), and SNU638 (stomach cancer) cell lines tested with IC₅₀ values ranging 9.28 to 28.22 μ g/ml. Commafric A possessed anti-proliferative activity against non-small cell lung cancer (A549), which suggests that commafric A has potential to be further optimized being a lead compound in the search for new drugs against cancer diseases.

Keywords: *Commiphora africana*, Commafric A, Anti-proliferative, SRB, A549 cell line

Introduction

Natural products are very inspiring in the drug discovery process. Aziz et al. [1] reviewed several drugs that have been obtained from different plant sources. Some of them can be obtained from *Commiphora africana* (A. Rich.) Engl. (Burseraceae), which is a bush about 1.5 m tall and is wide-spread in African countries, such as Sudan, Ethiopia, Eritrea, Somalia, Kenya, Uganda, and Mozambique [2]. Roots, bark and leaves are traditionally used to treat

measles, hyperlipidemia, and cardiovascular disorders [3, 4]. The leaves are also used as a sedative and soporific [3], and the resin is used for antiseptic washes and baths to treat skin infections, sores, and leprosy [5]. Ethnobotanical information has indicated that bark, resin, and leaves of *C. africana* are used to treat snakebite, skin wounds, tumor, stomachache, and as anti-ticks [6]. A fraction obtained after partitioning the crude ethanolic extract roots of *C. africana* exhibited a promising in vitro antimicrobial activity [4].

The resin of *C. africana* contains betulin [7], which has been shown to have antitumor activity, especially in combination with cholesterol [8]. Betulinic acid derivatives can inhibit HIV-1 [9]. Other *Commiphora* species

*Correspondence: amandekab@gmail.com

¹ Department of Applied Chemistry, Adama Science and Technology University, Adama, Ethiopia

Full list of author information is available at the end of the article

have also provided pharmaceutically interesting compounds. Furanouedesma-1,3-diene, the major compound of myrrh [10, 11], has been reported to exhibit analgesic activity in mice [12].

Previously, we have described oxygenated furanosesquiterpenes, curzerenone, and furanodienone from the resins of *C. sphaerocarpa* (Chiov.), *C. holtziana* (Engl.), and *C. kataf* [11, 13, 14]. Messina et al. [15] has shown that furanodienone has anti-inflammatory, antimicrobial, and anticancer activities. Additionally, the cytotoxicity of nordammarane triterpenes, such as vibusambucin A, 12 β -hydroxy-3,15-dioxo-20,21,22-23,24,25,26,27-octanordammarane, and hupehenol A against KB, HepG-2, LU-1, and MCF-7 cell lines has been reported [16]. The resins of *C. confusa* contain triterpenes of the dammarane type [17] with moderate cytotoxic activity against HepG2 [18]. From the resin of *C. erlangeriana* we have previously isolated polygamain-type lignans named erlangerin A, and erlangerin B, and two lignans related to podophyllotoxin, erlangerin C, and erlangerin D [19]. The effects of the erlangerins C and D are closely related to those of podophyllotoxin. They induce concentration-dependent cytotoxicity in the murine macrophage cells (RAW 264.7) and a cytostatic effect in HeLa, EAhy926, and L929 cell lines [20].

In spite of the use of *Commiphora africana* in traditional medicine, to the best of our knowledge, there has been no study aimed at isolation and characterization of anti-proliferative constituents of this plant. As part of the exploration of the pharmacological potential of the resins from *Commiphora* genus, we herein report the isolation, structural elucidation, and anti-proliferative activity screening of a new oxygenated podioda-7,17,21-triene [21, 22] and α -amyryn obtained from *C. africana*.

Materials and methods

Plant material

Resins and botanical specimens of *C. africana* were collected from district of Yabello, Borena zone, Ethiopia in December 2016 and identified by a botanist Shambel Alemu at the Biology Department, Addis Ababa University. A voucher specimen has been deposited at the National Herbarium (number: 072801) of Addis Ababa University, Addis Ababa, Ethiopia. This tree is known by its vernacular name HAMMESA DIHRO (Afaan Oromo). There is no permission required to collect samples from wild to investigate their chemical composition and evaluate their anti-proliferative effects.

Extraction and isolation

The resin (322.5 g) of *C. africana* was air dried and extracted with methanol (1 L \times 3) for 3 days at 25 °C. The solvent was removed *in vacuo* to yield a yellow

extract (151.2 g, 46.82%). The extract (80.0 g) was suspended in water (800 ml) and successively partitioned with *n*-hexane (800 ml \times 3), chloroform (800 ml \times 3), EtOAc (800 ml \times 3), and *n*-BuOH (800 ml \times 3) yielding an *n*-hexane (33.39 g, 40.22%), a chloroform (41.26 g, 49.7%), an EtOAc (0.11 g, 0.132%), and an *n*-butanol fraction (0.074 g, 0.093%). Part of the *n*-hexane fraction (7 g) was flash chromatographed on a silica gel column using *n*-hexane/EtOAc (7:3) as an eluent furnishing commafric A (1) (430 mg), and α -amyryn (2) (22 mg) (Fig. 1).

General experimental procedure

Melting points are uncorrected. TLC was performed on precoated plates (Silica gel 60 F₂₅₄, Merck) using *n*-hexane/EtOAc/MeOH (10:10:0.1) as a developing solvent and with vanillin-H₂SO₄ as the detecting reagent. CC was performed on silica gel. IR spectra were measured on a Perkin Elmer 1600 instrument using KBr tablets. Optical rotation was measured on a Perkin-Elmer 241 polarimeter. UV spectra were recorded on a Shimadzu UV-VIS spectrophotometer. LC-Mass was acquired on Waters ACQUITY H-CLASS Liquid Chromatograph/SQD2 Mass Spectrometer; Injection mode: FIA, Eluent: Methanol/Water (10 mM ammonium acetate)=70/30 flow rate: 0.3 ml/min, Ionization mode: ESI (positive), Capillary voltage: 3 kV, Cone voltage: 30 V. HRESIMS data were obtained on Waters ACQUITY UPLC I - Class Liquid Chromatograph/TQ-S micro Tandem Mass-Spectrometer, Ionization mode: electrospray ionization (ESI), Mass Analyzer, JMS-700 Mass High Resolution Mass Spectrometer (Jeol LTD, Tokyo, Japan): Tandem (triple) quadrupole at mass range of 5–2000 m/z and scan speed 15,000 Da/sec.

Nuclear magnetic resonance spectroscopy

¹H and ¹³C NMR data for commafric A (1) was acquired on an Avance III HD spectrometer (Bruker-BioSpin GmbH, Germany) equipped with an inverse detected TCI cryoprobe with a cryogenic enhancement for ¹H, ²H, and ¹³C, operating at 600 MHz for ¹H. All spectra were recorded using TopSpin 3.5pl7 at 298 K in dichloromethane-*d*₂ and chloroform-*d*₁, using gradient selected and adiabatic inversion versions of pulse sequences where applicable. Analysis of NOE buildup for compound 1 was performed by complete relaxation matrix analysis using Mspin 2.3.2-694 (Mestrelab Research S. L., Spain). The results are presented as Boltzmann averaged NOE enhancement across the conformational ensemble generated for analysis of IR and VCD section. The sample for anisotropic NMR measurements (10 mg) was dissolved in CDCl₃ with 0.03% TMS to which increasing amounts

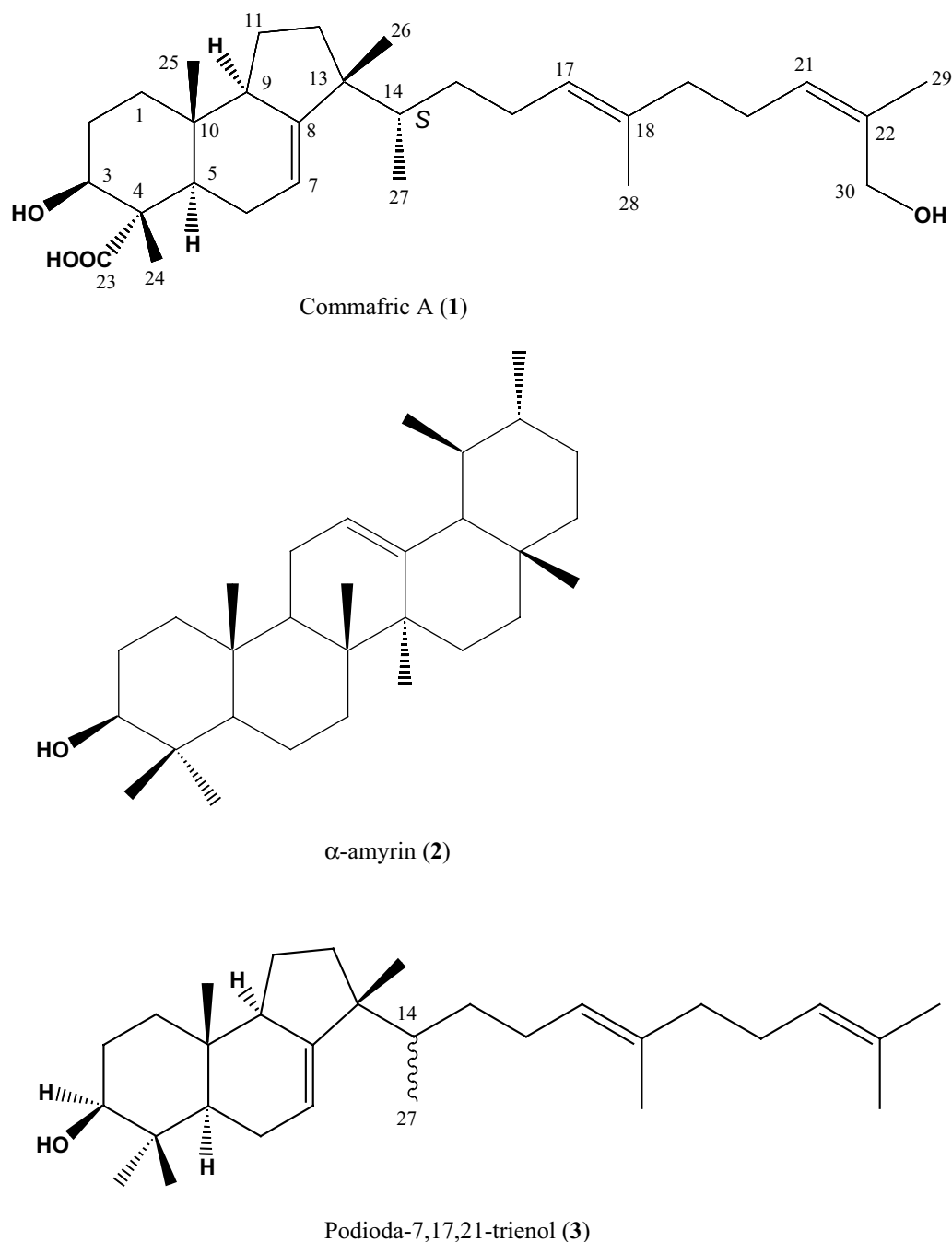


Fig. 1 Chemical structures of compounds isolated from *C. africana* and a reference compound podioda -7,17,21-trienol (3)

of poly- γ -benzyl-L-glutamate (PBLG, 150,000–300,000 Da, Sigma-Aldrich CAS 25014-27-1) was added to yield weight-to-volume ratios of 7.9%, 12.1%, and 16.2%. For compound **1** 1D carbon, CLIP-HSQC, IPAP-HSQC, and J-res carbon was acquired to extract the $^1J_{CH}$ coupling constants and anisotropic carbon

shifts. The data treatment is thoroughly described in additional file.

Experimental vibrational circular dichroism (VCD) spectra

VCD and absorption spectra of **1** were measured in $CDCl_3$ solutions (~ 1 mg/100 μ l) using a BaF_2 cell of an optical path of 50 μ m and a BioTools ChiralIR-2X

instrument. Spectra of pure CDCl_3 solvent were subtracted as a baseline; the accumulation time was ~ 12 h using blocks of 1200 scans and 4 cm^{-1} resolution.

Computations

Using the Gaussian suite of programs [23] a systematic conformer search of compound **1** was performed considering the three torsional angles in the vicinity of the tricyclic system. Other C–C–C–C dihedral angles were all-*trans* and all-extended (180°) at the beginning of the optimizations and left to optimize without constraints. The B3LYP [24] PCM [25] (chloroform)/6–31++G** level was used for all quantum chemistry. For stable conformers thus obtained the magnetic field perturbation theory [26, 27] was used to simulate IR and VCD intensities; final spectra were obtained as a Boltzmann average, using a convolution with Lorentzian lines ($\text{FWHM} = 10 \text{ cm}^{-1}$). Since the consideration of the full molecular flexibility was not possible with our computational means, atomic axial tensors of the linear side chain (from carbon number 16) were deleted for VCD generation. The chain itself is not chiral and thus supposedly the error introduced by this approximation is small, whereas the dominant signal from the chiral more rigid molecular part may help to assign the absolute configuration. Alternated simulations of the spectra based on molecular dynamics were attempted as well, but did not provide results significantly different from the limited conformer model. Boltzmann-averaged isotropic shielding and spin–spin coupling constants were computed at the same level as for VCD.

Tumor cell lines

The cell lines used in this study were the human non-small cell lung cancer cell lines (A549), ovarian cancer cell line (A2780), pancreatic cancer cell line (MIA-Paca-2), and stomach cancer cell line (SNU-638), and they were maintained using RPMI1640 cell growth medium (Gibco, Carlsbad, CA), supplemented with 5% fetal bovine serum (FBS) (Gibco), and grown at 37°C in a humidified atmosphere containing 5% CO_2 [28]. All the cancer cells used were adapted for 6 months at least to the RPMI1640 medium at Korea Research Institute of Chemical Technology, then used in the anti-proliferative assays. Cells were exposed to the isolated compounds at concentrations ranging from 0.1 to $30 \mu\text{g/ml}$.

Anti-proliferative assessment

All experiments were conducted by the NCI's protocol [28]. Experimental cultures were placed in 96-well microtiter plates (Corning) containing 0.15 ml of growth medium per well with a cell density of 5×10^3 (A549, A2780, and MIA-Paca-2) and 1×10^4 (SNU-638). The

culture was incubated at 37°C and humidified by 5% CO_2 for 1 day. Then, media were aspirated off and added the test material in triplicate which was dissolved in media at varying concentrations. In case of necessity, the test material was dissolved in small amount of dimethyl sulfoxide (DMSO), but the final concentration of DMSO in the medium did not exceed 0.5%. The culture was incubated for additional 3 days. After 3 days of continuous drug exposure, the medium was removed by flicking plates over a sink. The cells attached to the plastic substratum were fixed by gently layering with 0.1 ml of cold 10% trichloroacetic acid (TCA). Incubation at 4°C for 1 h was followed by wash with tap water five times to remove TCA solution. After being washed and dried at RT overnight, TCA fixed cells were stained with 0.1 ml of 0.4% sulforhodamine B (SRB) in 1% acetic acid per well for 30 min. At the end of the staining period, SRB supernatant was removed and the remaining cells were rinsed with 1% acetic acid five times. It was dried until no standing moisture was visible, and then the bound dye in cells was extracted with 0.1 ml of 10 mM unbuffered Tris base (pH 10.5) per well by stirring on a gyratory shaker for 5–10 min, followed by measured the optical density at 520 nm by MR700 microplate reader (Dynatech Laboratories). Antitumor activity of the test material at varying concentrations was estimated as the net growth % of cells compared with that of control (without test material, net growth = 100%). The dose–response curves of test material were constructed and the IC_{50} value was calculated as the concentration of the test material that caused 50% inhibition of cell growth against the cancer lines A549, A2780, MIA-PaCa-2, and SNU638. Etoposide, a standard drug was used as a positive control. IC_{50} values of etoposide were compared with those for crude extract, *n*-hexane fraction, and isolated compounds.

Results

Isolation of compounds

Flash column chromatography of the *n*-hexane fraction using *n*-hexane/EtOAc (7:3) as an eluent furnished two pure compounds: commafric A (**1**) the most abundant isolated molecule and the known compound α -amyirin (**2**), were obtained as white solids. The structures of the isolated compounds were elucidated employing ^{13}C and ^1H -NMR as well as 2D-NMR, IR, FT-ESI–MS mass fragmentation pattern, and comparing with literature data reported for structurally related compounds. The ^1H NMR and ^{13}C NMR data of compound **2** agreed with corresponding published data for α -amyirin (**2**) [29–31].

Characterization of compound **1**

Compound **1** was obtained as a white powder (mp $126\text{--}127^\circ\text{C}$), with $[\alpha]_D^{22}$: $+4^\circ$ (*c* 1.0, CHCl_3) and its

molecular formula was established on the basis of a high resolution positive-ion mode HR-ESI-MS² scanned from 170.00 to 600.00 *m/z*. The molecular formula was established as C₃₀H₄₈O₄ on the basis of the positive-ion mode HRESIMS data due to Na adduct formation (*m/z* 495.3442 [M+Na]⁺, calcd. 495.3445) and NMR data indicating seven degrees of unsaturation (Additional file 1: Fig. S1). The two peaks with less intensity at *m/z* 473.36 and *m/z* 455.3515 corresponds to protonation of the molecule [M+H]⁺ and protonation of a dehydrate molecule respectively (Additional file 1: Fig. S1).

The UV spectrum of **1** (EtOH) exhibited an absorption band at 209 nm indicating the absence of conjugated double bonds. The experimental IR-spectrum agrees with the simulated spectrum of commafric A (Fig. 2); the most prominent features comprise free (3607 cm⁻¹) and hydrogen-bonded (3400 cm⁻¹) OH stretching bands, split (2956/2872 cm⁻¹) CH stretching signal indicating the presence of both sp² and sp³ carbons, and the C=O stretching band (1695 cm⁻¹).

¹H NMR resonances (Table 1) of **1** included two near triplets at δ_H 5.30 and 5.04, and one doublet of a triplet at δ_H 5.16, suggesting the presence of three olefinic protons. Two geminally coupled protons appearing as doublets at δ_H 4.17 and 4.07 indicated the presence one oxy methylene moiety. A signal integrated as one proton at δ_H 4.02 suggested the presence of an oxy methine group. Two moderately deshielded methyl signals were observed (1.57 and 1.77 ppm), indicating that two methyls are attached to sp² hybridized carbons (see Additional file 1: Fig. S2). Additionally, the compound has four aliphatic methyl signals (0.75, 0.86, 0.91, and 1.18).

The ¹³C NMR (Table 1 and Additional file 1: Fig. S3) and multiplicity edited HSQC/DEPT confirmed the presence of thirty carbons, of which seven were quaternary,

ten methylene, seven methine, and six methyl groups. A set of 2D NMR experiments, HSQC, HMBC, H2BC, HSQC-TOCSY, DQF-COSY, and 1,1-ADEQUATE (Additional file 1: Fig. S4–S9), was used to establish the molecular framework of commafric A as a tricyclic triterpenoid with structural similarity to podioda-7,17,21-trienol [21]. All carbon–carbon connections were unambiguously confirmed by 1,1-ADEQUATE, except for the two quaternary to quaternary carbon bonds (C4 to C23 and C8 to C13), which did not correlate in this pulse sequence because of the absence of protons on both sides of the C–C bond (Fig. 3b). The C23 carboxyl group could be placed by HMBC correlations to H3, H5, and H24 from C23, while the C8 to C13 bond was confirmed by HMBC correlations between H26 and H12, and C8. The location of the hydroxymethylene group as well as the position of the 21, 22 double bond was confirmed by 2D HMBC (Fig. 3a), which showed three bond couplings between the olefinic proton H21 (δ_H 5.30) and the carbons at the C29 methyl group (δ_C 21.4) and the C30 hydroxymethylene carbon (δ_C 61.5). Furthermore, H2BC two-bond couplings appeared between C22 and Me29 and hydroxymethylene protons H30''' (Fig. 3a).

Determination of the relative configuration

Based on ³J_{CH} couplings measured by selective CLIP-HSQMBC [32], as well as NOESY/ROESY analysis, the C17/C18 configuration was determined as *E* (³J_{C28H17} = 8.0 Hz and ³J_{C19H17} = 6.0 Hz) and the C21/C22 configuration was determined as *Z* (³J_{C29H21} = 6.0 Hz and ³J_{C30H21} = 9.3 Hz, Additional file 1: Figs. S10–S12). These conclusions are based on the fact that the *trans*-³J_{CH} is expected to be stronger than the corresponding *cis*-³J_{CH}. This was also consistent with the direct observations of the presence of the *NOE*_{H21H29} and *ROE*_{H21H29} correlations, and the absence of the *NOE*_{H21H29} and *ROE*_{H21H29} correlations. The *Z*-configuration of the C21 to C22-double bond is also consistent with the ¹³C NMR chemical shifts of C21, C22, C29, and C30 in previously reported compounds with similar side chain configurations [33, 34].

The relative configuration of the tricyclic system was established by NOESY and ROESY correlations (Additional file 1: Fig. S12) supplemented with some ³J_{HH} and ³J_{CH} couplings. Most notably, an N/ROE correlation trace between H3–H5–H9–H11''–H12'' place these protons below the ring plane while the trace between H24–H25–H11'–H12'–H26 place these above the ring plane. The key correlations are displayed in Fig. 3c. The configuration at the C14 stereocenter could not be unambiguously determined from the N/ROE correlations without a full conformational analysis because of relatively free rotation about the C13–C14 bond.

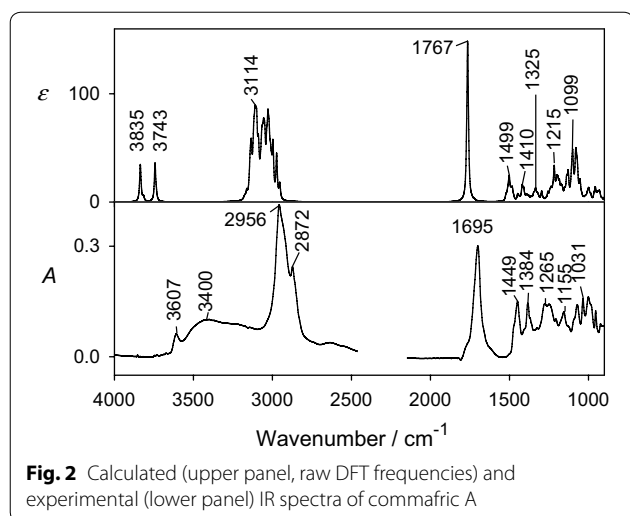


Fig. 2 Calculated (upper panel, raw DFT frequencies) and experimental (lower panel) IR spectra of commafric A

Table 1 NMR parameters of commafric A in CD₂Cl₂:¹H (600 MHz) and ¹³C (150 MHz) NMR, HMBC, H2BC, ADEQUATE-1,1, and ROESY

No.	δ _C	δ _H (multi, J in Hz)	HMBC (H → C) ^d	H2BC (H → [H]C) ^d	1,1-ADEQUATE ([H]C → C) ^d	Key ROESY
1	38.1	1.72 (dt, J = 13.3, 3.1)/1.32 (m ^c)	25	2 ^{''''}	2 ^{''''}	2 ^{''''} , 25, 2 ^{''''}
2	27.3	1.67 (m ^c)	3	1', 1'', 3	1', 1'', 3	1 ^{''''} , 25
3	76.2	4.02 (dd, J = 11.2, 4.7)	1'', 2'', 5, 24	2 ^{''''}	2 ^{''''}	2 ^{''''} , 5
4	52.9		2', 2'', 3, 5, 24		3, 5, 24	
5	46.6	1.88 (m ^c)	24, 25	6', 6''	6', 6''	3, 9
6	25.8	2.05 (m ^c)/1.80 (m ^c)		5, 7	5, 7	7, 24, 25
7	114.0	5.16 (dt, J = 5.1, 2.6)	6'	6', 6''	6', 6''	14
8	151.0		6 ^{''''} , 11 ^{''''} , 12 ^{''''} , 26		7, 9	
9	59.5	2.01 (m ^c)	1', 5, 11', 12 ^{''''} , 25	11', 11''	11', 11''	1'', 5, 11'', 12''
10	34.1		1 ^{''''} , 5, 25		1', 1'', 5, 9, 25	
11	23.1	1.25 (m ^c)/1.53 (m ^c)	12 ^{''''}	12''	9, 12', 12''	25, 26/9
12	33.0	1.25 (m ^c)/1.48 (m ^c)	11 ^{''''} , 14, 26 ^a	11', 11''	11', 11''	26/9, 15 ^{''''} , 27
13	48.3		12'', 14, 26, 27		12', 12'', 14, 26	
14	41.2	1.36 (m ^c)	9, 12'', 26, 27	15', 27	15', 27	6', 6'', 7
15	33.0	1.34 (m ^c)/1.00 (m ^c)	16'', 27 ^a	14, 16', 16''	14, 16', 16''	
16	26.6	2.02 (m ^c)/1.87 (m ^c)	15 ^{''''} , 17 ^b	15'', 17	15', 15'', 17	
17	125	5.04 (ddq, J = 7.5, 6.3, 1.3)	15 ^{''''} , 16 ^{''''} , 19 ^{''''} , 28	16', 16'', 28 [*]	16', 16''	
18	135		16 ^{''''} , 19 ^{''''} , 28		17, 19', 19'', 28	
19	40.0	1.96 (m ^c)/1.93 (m ^c)	20'', 28, 29	20', 20''	20', 20''	
20	26.7	2.14 (m ^c)/2.09 (m ^c)	21 ^b	19', 19'', 29 ^{**}	19', 19'', 21	
21	129.0	5.30 (t, J = 7.0)	19 ^{''''} , 20 ^{''''} , 29, 30 ^{''''}	19', 19'', 29 [*]	20', 20''	29
22	134.0		20 ^{''''} , 29, 30 ^{''''}		21, 29, 30', 30''	
23	181.0		3, 5, 24			
24	10.7	1.18 (s)	3, 5			6', 25
25	14.1	0.75 (s)	1'', 5			1', 2 ^{''''} , 6', 11', 24
26	26.8	0.91 (s)	12 ^{''''} ^{mb}			11', 12'
27	15.1	0.86 (d, J = 6.8)	14, 15 ^{''''}	14	14	12''
28	16.4	1.57 (s)	17, 19 ^{''''}			
29	21.4	1.77 (s)	21, 30 ^{''''}			21
30	61.5	4.07 (d, J = 11.7)/4.17 (d, J = 11.7)	21, 29			

^a Overlap between C12 and C15^b Overlap between C16, C20, and C26^c Overlapping multiplets in ¹H^d Correlations listed on each receiving carbon row from the denoted proton(s)

Determination of the C14 configuration Vibrational circular dichroism spectroscopy

In order to relate the measured VCD spectra to the structure, theoretical VCD spectra were simulated computationally. The theoretical modelling focused on the tricyclic system supposedly dominating in VCD spectrum, because a full conformer analysis (> 10⁶ possible conformers) was not possible with available computational means. A reduced ensemble of 27 conformers was generated by 120° rotations around the C13–C14, C4–C23, and C3–O3 bonds only, and relative conformer

energies were obtained for both the *R* and *S* C14 isomers. The molecular tail (C14–C30) was kept in the extended conformation and its contribution to VCD was not considered. The equilibrium geometries and spectral properties were calculated using the Gaussian software [24] and the B3LYP/6-311++G**/PCM (CHCl₃) level of theory, relative enthalpies were used for property averaging. The simulation reproduced some spectral features observed experimentally (Fig. 4), although the theoretical *R* and *S* VCD sign patterns of **1** are similar. The 1150–1000 cm⁻¹ spectral region is however predicted to be significantly

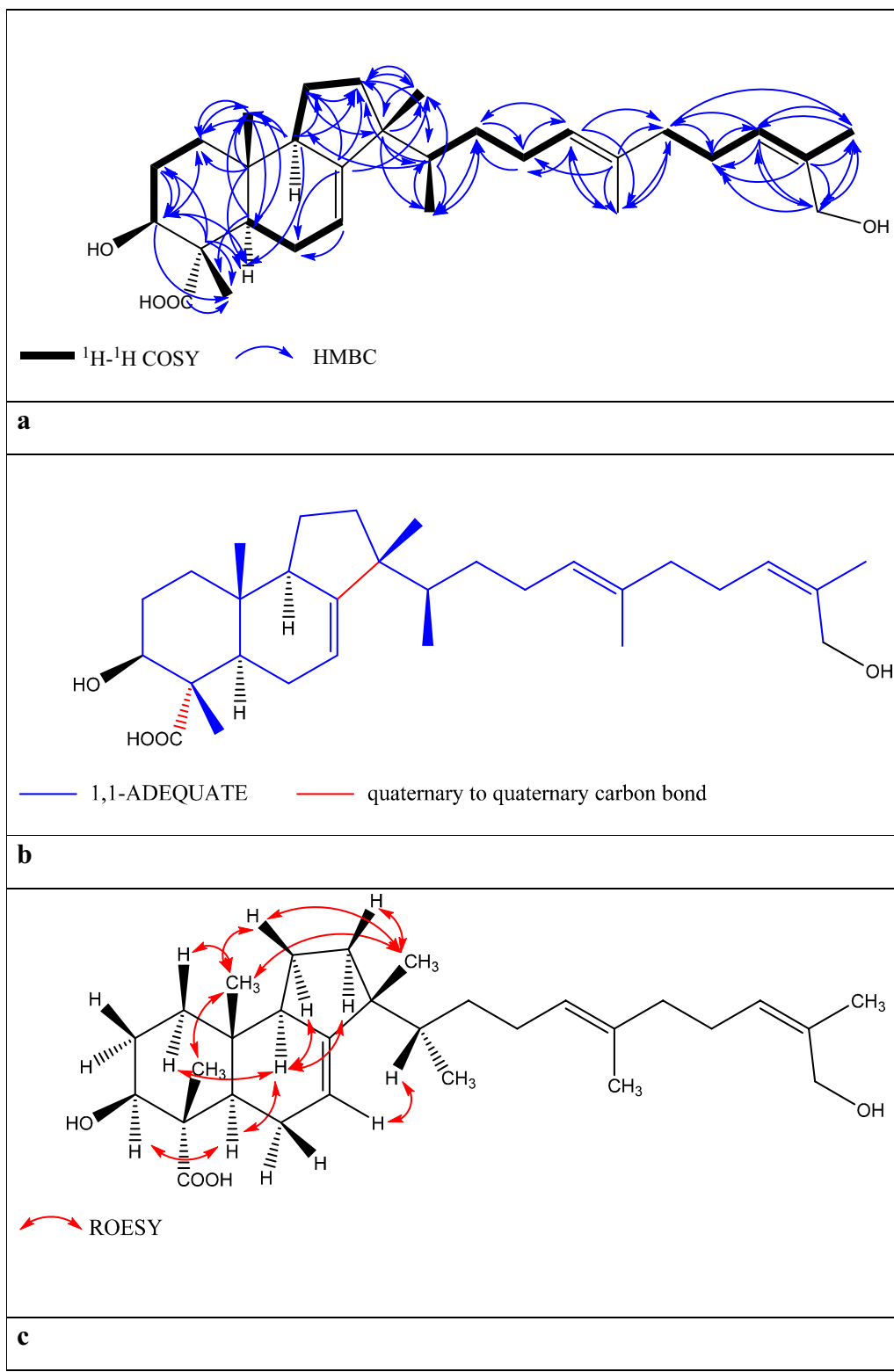


Fig. 3 2D NMR correlations through bonds, **a** COSY, HMBC and, **b** 1,1-ADEQUATE; and through space, **c** NOESY/ROESY of commafric A

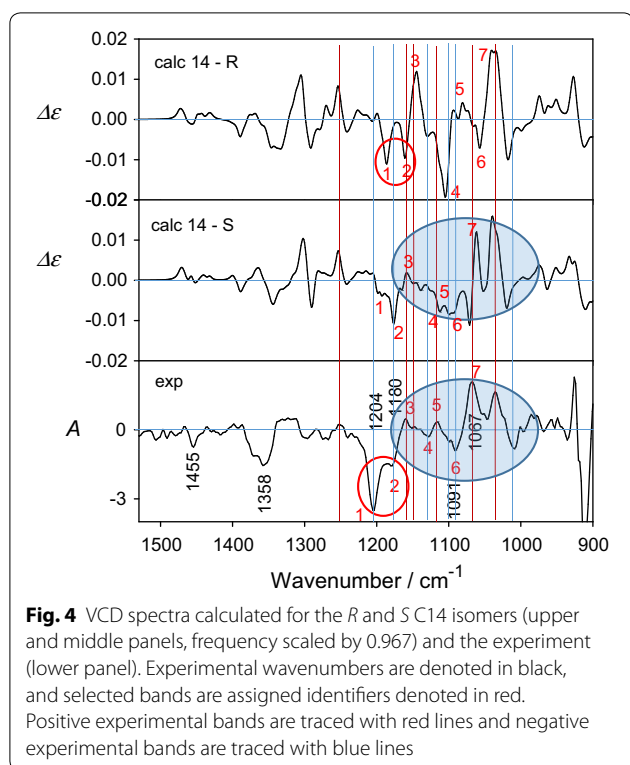


Fig. 4 VCD spectra calculated for the *R* and *S* C14 isomers (upper and middle panels, frequency scaled by 0.967) and the experiment (lower panel). Experimental wavenumbers are denoted in black, and selected bands are assigned identifiers denoted in red. Positive experimental bands are traced with red lines and negative experimental bands are traced with blue lines

Table 2 Calculated C13–C14 angular distribution (p , %), for the C14 enantiomers

	R-C14		S-C14	
	p	$\tau(\delta\epsilon)_a$	p	$\tau(\delta\epsilon)_a$
Gauche +	12	71.9	11.1	44.9
Gauche –	87.7	–58.9	11.7	–64.9
Anti	0.3	–164.6	77.2	170.6

^a \angle C26–C13–C14–C27, torsion angle between the two methyl groups as obtained for the optimized DFT geometries

different for the *R*- and *S* configurations, and comparison of the calculated and experimental VCD signs and relative intensities for this region strongly suggests the *S* configuration on C14.

Isotropic NMR parameters

For a more detailed NMR data analysis of distances and coupling constants localized near the C14, only the three Boltzmann averaged rotamers around the C13–C14 bond were used. The H14 proton is preferentially pointing towards the edge of the ring system (and H-7) in both the *R*- and the *S* C14 configurations (Table 2). This was problematic for using the otherwise very informative $^3J_{CH}$ couplings originating from the only proton (H14) directly attached to the rotating C13–C14 bond since

Table 3 Calculated and experimental $^3J_{CH}$ scalar couplings for the C14 enantiomers

	Population	$^3J_{C8H14}$	J_{C12H14}	J_{C26H14}	Configuration
Gauche +	12	0.68	2.12	4.56	R
Gauche –	87.7	0.98	4.6	2.11	
Anti	0.3	4.79	0.82	3.29	
Averaged		0.96	4.38	2.32	
Gauche +	11.1	5.2	3.16	0.87	S
Gauche –	11.7	1.44	1.64	4.41	
Anti	77.2	0.68	4.4	2.55	
Averaged		1.23	3.98	2.57	
Experimental		0.8	5.3	3.7	

^a \angle C26–C13–C14–C27, torsion angle between the two methyl groups as obtained for the optimized DFT geometries

the dihedral angles formed between the H14–C14 vector and the C13–C8, C12, C26 vectors will be very similar for *R*- and *S*. The predicted differences between the two configurations were smaller than 0.5 Hz. The experimental couplings (Table 3) are in agreement with the calculated rotamer populations of both configurations. These couplings were very challenging to measure accurately experimentally as the signal of H14 overlaps with that of H15s. That made it necessary to use heavily chemical shift filtered selective methods and there is unavoidable phase modulation from J-coupling. Coupling sums were utilized because of significant second order/phase contributions. For all these reasons, the experimental error is estimated to at least 1 Hz.

Furthermore, the possibility to determine the relative configuration from NOE buildup rates involving the C27 methyl group were investigated. The C27 methyl group is predicted to be predominantly *anti* to the C26 methyl in the *S*-configuration and *gauche* to the C26 methyl in the *R*-configuration. NOE buildups are intrinsically difficult to quantify for flexible molecules due to the fact that they depend on the distance as r^{-6} . A scarcely populated rotamer can contribute significantly to the observed NOE if the two protons are positioned very close to each other. The measured NOEs around and across the C13–C14 bond (Additional file 1: Fig. S13) are not conclusive alone as both theoretical configurations result in r^2 values in the order of 0.7. However, the most important NOE between H26 and H27 that is expected to be the most sensitive to the C14 configuration indicates the *S*-configuration. The weighted experimental NOE was determined to $\eta = 0.0054$ (corresponding to $r = 2.9$ Å), *i.e.*, closer to the value predicted for the *S*-model ($\eta = 0.0032$, $r = 3.2$ Å), than that predicted for the *R*-model ($\eta = 0.0144$, $r = 2.5$ Å).

Confirmation of the C14 configuration by anisotropic NMR parameters

Anisotropic NMR parameters have emerged as powerful tools in structural elucidation [35, 36]. Residual dipolar coupling (RDC) depend on the relative orientation of the ^{13}C - ^1H bond vectors, while residual chemical shift anisotropy (RCSA) depend on the relative orientations of the carbon chemical shielding tensors. When combined, they can provide the configuration of stereogenic centers that are difficult to establish by traditional methods. A method described by Liu et al. [35] utilizing poly(γ -benzyl-L-glutamate) (PBLG) to form a liquid crystal that induces anisotropy in chloroform- d_1 was employed in the present study. ^{13}C residual chemical shifts were referenced to TMS, and combined with RDC data from HSQC-IPAP spectra (Additional file 1: Figs. S14–S16, Tables S1 and S2). In the comparison of the experimental and theoretical anisotropic parameters for the commafric A the *S*-model provided lower quality factors ($Q=0.19$) than the *R*-model ($Q=0.33$, Fig. 5). Based on the anisotropic parameters, together with the VCD and NOE data, we conclude that commafric A's stereocenter C14 has the (*S*)-configuration.

Based on the above experimental evidence the structure of the novel compound commafric A was elucidated as (3*S*,4*S*,14*S*,7*E*,17*E*,21*Z*)-3,30-dihydroxydioda-7,17,21-trien-4-carboxylic acid.

In vitro anti-proliferative effect of the MeOH extract, *n*-hexane fraction, and isolated compounds

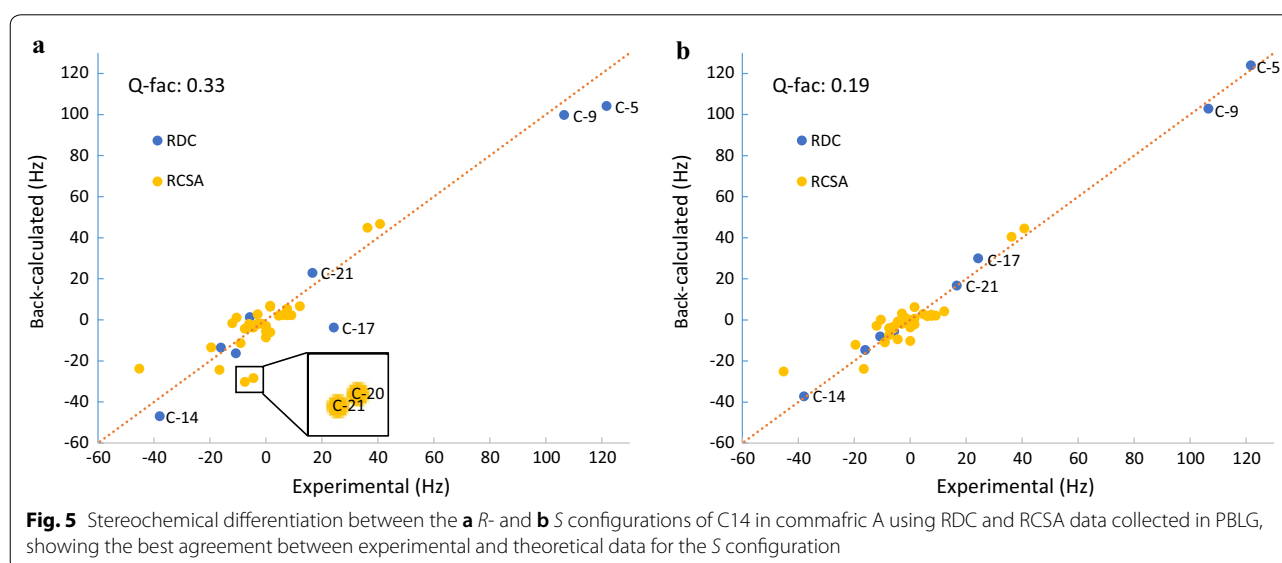
The anti-proliferative effects of the crude MeOH extract, *n*-hexane fraction, and isolated compounds commafric A

Table 4 IC_{50} values of MeOH extract, *n*-hexane fraction, and isolated compounds of resin of *Commiphora africana* against four cancer cell lines using SRB assay

Sample	Cell lines and IC_{50} ($\mu\text{g/ml}$)			
	A549	A2780	MIA-PaCa-2	SNU638
MeOH extract	3.55	9.98	19.20	10.09
<i>n</i> -Hexane fraction	9.64	9.62	17.21	10.30
α -Amyrin	9.28	21.96	16.14	28.22
Commafric A	4.52	10.17	10.04	9.73
Etoposide	0.2	0.34	0.42	0.14

IC_{50} (Inhibition of cell growth by 50%), data was generated by experiments performed in triplicates

and α -amyrin were tested for four cancer cell lines, A549 (non-small cell lung cancer), A2780 (ovarian cancer), MIA-PaCa-2 (pancreatic cancer), and SNU638 (stomach cancer). The crude methanol extract showed a strong anti-proliferative activity against A549 ($\text{IC}_{50}=3.55 \mu\text{g/ml}$) (Table 4, Additional file 1: Fig. S17). The crude extract exhibited weaker activity against A2780, SNU-638, and MIA-Paca-2 compared with A549 cell lines. Among the cell lines tested the methanol crude extract showed strong effect on A549 cell lines ($3.55 \mu\text{g/ml}$). The *n*-hexane fraction exhibited significant inhibition of cell proliferation on the all four cell lines with dose dependent relationship in vitro. However, it was less sensitive and had a weaker net growth effect on A549 cell lines compared with the crude methanol extract (Table 4, Additional file 1: Fig. S17).



Discussion

A number of bioactive compounds were previously reported from different *Commiphora* species. In this study, the *n*-hexane fraction of *C. africana* resin yielded a new compound commafric A. Cancer, cardiovascular diseases, chronic respiratory disorders and diabetes are the primary cause of deaths worldwide. The knowledge of herbal medications and anticancer activity tests assist in the development of important anticancer drugs [37].

In our study for in vitro anti-proliferative activity, we found that the crude extract and related *n*-hexane fraction is lower than 30 µg/ml, which is within the limit of criteria set by the American National Cancer Institute for further purification [38]. For compound **1**, a moderate anti-proliferative activity was observed for the A549 cancer cell lines, with IC₅₀ value of 4.52 µg/ml. This is comparable with the activity of the crude extract and more than twice better than for α-amyrin. On the other hand, compound **1** showed weak anti-proliferative effects > 9 µg/ml for the other cell lines. The compound exhibited about twice higher activity on MIA-PaCa-2 compared with the methanol extract. The presence of carboxylic acid or terminal hydroxyl group in the compound might be the reason for its bioactivity. α-Amyrin (**2**) having an ursane skeleton showed weaker activity on A549, A2780, and SNU638 cell lines compared with both compound **1** and the crude methanol extract. Compounds with similar skeleton to α-amyrin such as ursolic acid and its derivatives showed strong anti-proliferative activity against ovarian carcinoma, pancreatic carcinoma, prostate cancer, cervical carcinoma, hepatic cancer, breast cancer, colorectal cancer, leukemia, neuroblastoma, and colon adenocarcinoma [39]. The weak activity of α-amyrin might be due to lack of carboxylic acid group. According to the literature on α-amyrin pentacyclic triterpenes stimulate proliferation of human keratinocytes but do not protect them against UVB damage [40–42]. A review on antitumor effect of triterpene acid compounds revealed that triterpene acid type compounds have many effects including anti-inflammatory, regulating blood sugar level, antiviral, and antitumor activity. More important, triterpene acid type compounds have become one of the most popular topics recently because of its selective toxic effects on cancer cells and harmless to normal cells [43].

The tricyclic triterpene acid (3*S*,4*S*,14*S*,7*E*,17*E*,21*Z*)-3,30-dihydroxypodiocic-7,17,21-trien-4-carboxylic acid (commafric A) was isolated from the *n*-hexane fraction of the resin of *C. africana* and its structure was determined. It showed the variable IC₅₀ values against the four cancer cell lines studied. The anti-proliferative effect against non-small cell lung cancer (A549) cells with IC₅₀ values of 4.52 µg/ml was the highest among the

cancer cells tested. The anti-proliferative effect suggests that commafric A has a potential in further investigations as a drug against different cancer lines. Further work is required to evaluate the mechanism of action of the commafric A as an antitumor agent against non-small cell lung cancer and evaluate its anti-proliferative on a number of cancer cell lines. Further isolation of compounds from the resin and other parts of this plant will be pursued which might yield some novel bioactive compounds.

Supplementary information

Supplementary information accompanies this paper at <https://doi.org/10.1186/s13765-020-00499-w>.

Additional file 1. Additional figures and tables.

Abbreviations

HRESIMS: High resolution electrospray ionization mass spectroscopy; SRB: Sulphorhodamine B; VCD: Vibrational Circular Dichroism; RDC: Residual dipolar coupling; RCSA: Residual chemical shift anisotropy; PBLG: Poly(γ-benzyl-L-glutamate).

Acknowledgements

We thank Prof. Ermias Dagne for initiating a research project work on the chemical composition of *Commiphora* resins especially those of Ethiopian origin in his research laboratory and his assistance in this study.

Authors' contributions

WD conducted the experimental studies such as extraction, isolation, characterization of compounds. WD also contributed in drafting the manuscript. PB and EB were involved in VCD analysis. JI and FG performed NMR analysis. JSMS participated in the interpretation of the NMR data and substantially revised the manuscript draft. AJA supervised the project. SU and SL conducted the bioassay and HRMS analysis. YJ and ZS contributed the crucial help in supervision of the bioassay tests. AD conceptualized, designed and directed the study. All authors read and approved the final manuscript.

Funding

Financial support for this work such as research materials required for extraction, isolation of compounds and cytotoxicity tests was provided by National Research Foundation of Korea (No. 2016K1A3A1A09939937), RDA Troms: TFK2014-207, Norway provided support in materials required for NMR studies. Funding from Digital Life Norway/Research Council of Norway, project ID: 269425, is gratefully acknowledged. Adama Science and Technology University supported for some research materials required for extraction, isolation of compounds and salary of WD and AD. The Czech Grant Agency (18-05770S) provided salary for PB and EB, Ministry of Education (LTC17012 and CZ.02.1.0/0.0/0.0/16_019/0000729) provided computational resources. The funders of Grants play no role in the design of the study and collection, analysis, and interpretation of data and in writing the manuscript. All the responsibilities starting from the design of the study up to the write up of the manuscript were undertaken by the authors.

Availability of data and materials

The datasets used and analysed during the current study are available from the corresponding author on reasonable request.

Ethics approval and consent to participate

Not applicable because we did not work with animals or humans.

Consent to publish

Not applicable.

Competing interests

The authors declare that they have no competing interests.

Author details

¹ Department of Applied Chemistry, Adama Science and Technology University, Adama, Ethiopia. ² Department of Chemistry, UiT the Arctic University of Tromsø, 9037 Tromsø, Norway. ³ Institute of Organic Chemistry and Biochemistry, Academy of Sciences, Flemingovo Náměstí 2, Dejvice, 16610 Prague 6, Czech Republic. ⁴ Department of Analytical Chemistry, University of Chemistry and Technology, Technická 5, 16628 Prague, Czech Republic. ⁵ Bio & Drug Discovery Division, Korea Research Institute of Chemical Technology, Daejeon, Republic of Korea. ⁶ Institute of Pharmaceutical Science, Adama Science and Technology University, Adama, Ethiopia.

Received: 3 January 2020 Accepted: 28 February 2020

Published online: 17 March 2020

References

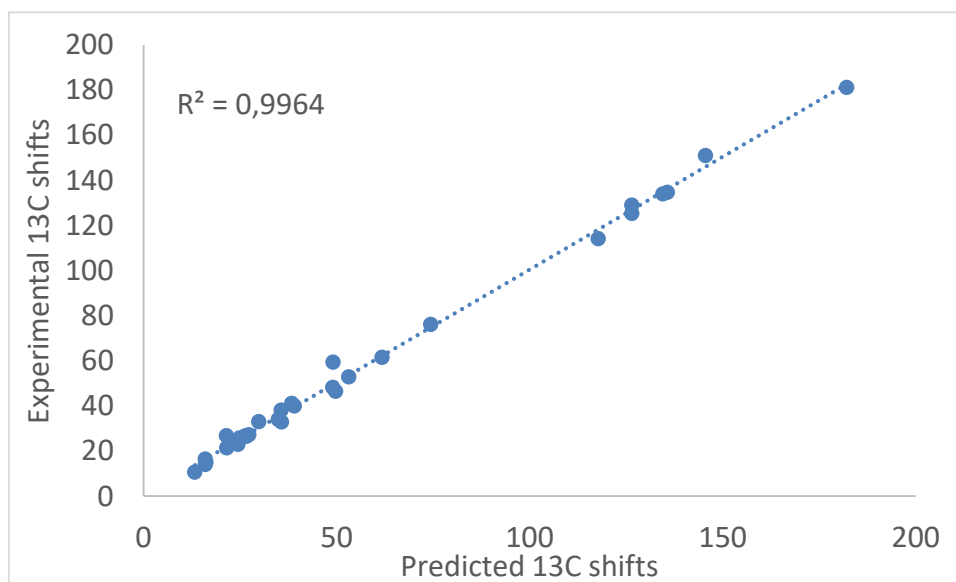
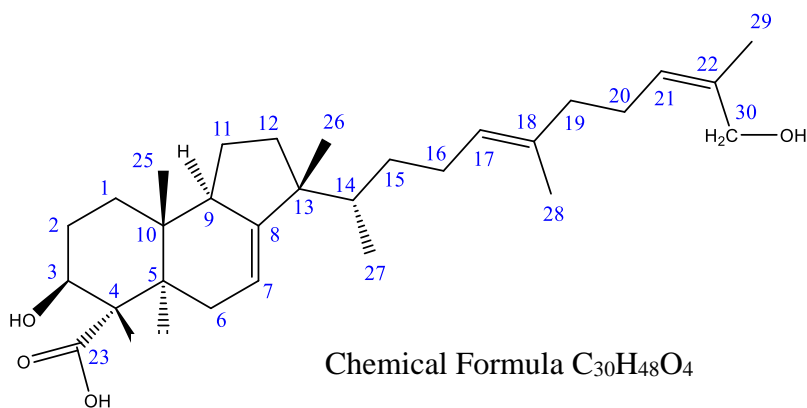
- Aziz MM, Raza MA, Saleem H, Wajid M, Bashir K, Ikram M (2014) Medicinal values of herbs and plants, importance of phytochemical evaluation and ethnopharmacological screening: an illustrated review essay. *J Pharm Cosmet Sci* 2(1):6–10
- Burkill HM (1994) The useful plants of west tropical Africa. Volume 2: Families E-I: Royal Botanic Gardens
- Adebayo H, Aliyu R, Gatsing D, Garba H (2006) The effects of ethanolic leaf extract of *Commiphora africana* (Bursaceae) on lipid profile in rats. *Int J Pharmacol* 2(6):618–622
- Akor J, Anjorin T (2009) Phytochemical and antimicrobial studies of *Commiphora africana* root extracts. *Int J Agric Biol* 11(6):795–797
- Abbiw D (1990) Useful plants of Ghana, Intermediate Tech. Publication London, Royal Botanic Gardens, Kew, p 207
- Worku A, Lemenih M, Fetene M, Teketay D (2011) Socio-economic importance of gum and resin resources in the dry woodlands of Borana, southern Ethiopia. *Forests Trees Livelihoods*. 20(2–3):137–155
- Ahmed IM, Gadir SA, Elgilany EE, Abdallah TM (2016) *Commiphora africana* resin phytochemical analysis and some biological aspects. *Europ J Med Plant* 13(3):1–11
- Mullauer FB, Kessler JH (2019) Medema JP (2009) Betulin is a potent anti-tumor agent that is enhanced by cholesterol. *PLoS ONE* 4(4):e1. <https://doi.org/10.1371/journal.pone.0005361>
- Aiken C, Chen CH (2005) Betulinic acid derivatives as HIV-1 antivirals. *Trends Mol Med* 11(1):31–36
- Brieskorn CH, Noble P (1983) Two furanosesquiterpenes from the essential oil of myrrh. *Phytochemistry* 22(1):187–189
- Dekebo A, Dagne E, Sterner O (2002) Furanosesquiterpenes from *Commiphora sphaerocarpa* and related adulterants of true myrrh. *Fitoterapia* 73(1):48–55
- Dolara P, Luceri C, Ghelardini C, Monserrat C, Aiolfi S, Luceri F, Lodovici M, Menichetti S, Romanelli MN (1996) Analgesic effects of myrrh. *Nature* 379(6560):29
- Dekebo A, Dagne E, Hansen LK, Gautun OR, Aasen AJ (2000) Crystal structures of two furanosesquiterpenes from *Commiphora sphaerocarpa*. *Tetrahedron Lett* 41(50):9875–9878
- Başer K, Demirci B, Dekebo A, Dagne E (2003) Essential oils of some *Boswellia* spp, myrrh and opopanax. *Flavour Fragrance J* 18(2):153–156
- Messina F, Gliarelli G, Palmier A, Marcotullio C (2017) Furanodienone: an emerging bioactive furanosesquiterpenoid. *Curr Org Chem* 21(4):305–310
- Nguyen TT, Truong BN, Mai HDT, Litaudon M, Do Thi T, Chau VM, Pham VC (2017) Cytotoxic dammarane-type triterpenoids from the leaves of *Viburnum sambucinum*. *Bioorganic Med Chem Lett* 27(8):1665–1669
- Dekebo A, Dagne E, Curry P, Gautun OR, Aasen AJ (2002) Dammarane triterpenes from the resins of *Commiphora confusa*. *Bull Chem Soc Ethiopia* 16(1):81–86
- Yan H-J, Wang J-S, Kong L-Y (2014) Cytotoxic dammarane-type triterpenoids from the stem bark of *Dysoxylum binectiferum*. *J Nat Prod* 77(2):234–242
- Dekebo A, Lang M, Polborn K, Dagne E, Steglich W (2002) Four lignans from *Commiphora erlangeriana*. *J Nat Prod* 65(9):1252–1257
- Habtemariam S (2003) Cytotoxic and cytostatic activity of erlangerins from *Commiphora erlangeriana*. *Toxicol* 41(6):723–727
- Lodeiro S, Xiong Q, Wilson WK, Kolesnikova MD, Onak CS, Matsuda SP (2007) An oxidosqualene cyclase makes numerous products by diverse mechanisms: a challenge to prevailing concepts of triterpene biosynthesis. *J Am Chem Soc* 129(36):11213–11222
- Arai Y, Hirohara M, Ageta H (1989) Fern constituents: three new skeletal triterpenoid hydrocarbons isolated from *Polypodiodes niponica*. *Tetrahedron Lett* 30(51):7209–7212
- Frisch M, Trucks G, Schlegel H, Scuseria G, Robb M, Cheeseman J, Scalmani G, Barone V, Petersson G, Nakatsuji H (2016) Gaussian 16, Revision A. 03, Gaussian, Inc., Wallingford CT
- Becke AD (1993) Density functional thermochemistry III The role of exact exchange. *J Chem Phys* 98(7):5648–5652
- Cossi M, Rega N, Scalmani G, Barone V (2003) Energies, structures, and electronic properties of molecules in solution with the C-PCM solvation model. *J Comput Chem* 24(6):669–681
- Stephens P (1987) Gauge dependence of vibrational magnetic dipole transition moments and rotational strengths. *J Phys Chem* 91(7):1712–1715
- Stephens P, Ashvar C, Devlin F, Cheeseman J, Frischo M (1996) Ab initio calculation of atomic axial tensors and vibrational rotational strengths using density functional theory. *Mol Phys* 89(2):579–594
- Skehan P, Storeng R, Scudiero D, Monks A, McMahon J, Vistica D, Warren JT, Bokesch H, Kenney S, Boyd MR (1990) New colorimetric cytotoxicity assay for anticancer-drug screening. *J Nat Cancer Inst* 82(13):1107–1112
- Otuki MF, Ferreira J, Lima FV, Meyre-Silva C, An Malheiros, Muller LA, Cani GS, Santos AR, Yunes RA, Calixto JB (2005) Antinociceptive properties of mixture of α -amyrin and β -amyrin triterpenes: evidence for participation of protein kinase C and protein kinase A pathways. *J Pharmacol Exp Ther* 313(1):310–318
- Aragao GF, Carneiro LM, Júnior AP, Bandeira PN, Lemos TL, Viana GS (2007) Antiplatelet activity of α - and β -amyrin, Isomeric mixture from *Protium heptaphyllum*. *Pharm Biol* 45(5):343–349
- Vázquez LH, Palazon J, Navarro-Ocaña A (2012) The pentacyclic triterpenes & #x03B1; β -amyryns: A review of sources and biological activities. In: Vázquez LH (ed) *Phytochemicals—A global perspective of their role in nutrition and health*. IntechOpen, New York, pp 487–502
- Sauri J, Parella T, Espinosa JF (2013) CLIP-HSQMBC: easy measurement of small proton–carbon coupling constants in organic molecules. *Organic Biomol Chem* 11(27):4473–4478
- Stuppner H, Moller E (1993) Cucurbitacins with unusual side chains from *Picrohiza kurroa*. *Phytochemistry* 33(5):1139–1145
- Tai T, Shingu T, Kikuchi T, Tezuka Y, Akahori A (1995) Triterpenes from the surface layer of *Poria cocos*. *Phytochemistry* 39(5):1165–1169
- Liu Y, Cohen RD, Gustafson KR, Martin GE, Williamson RT (2018) Enhanced measurement of residual chemical shift anisotropy for small molecule structure elucidation. *Chem Commun* 54(34):4254–4257
- Liu Y, Navarro-Vázquez A, Gil RR, Griesinger C, Martin GE, Williamson RT (2019) Application of anisotropic NMR parameters to the confirmation of molecular structure. *Nat Protoc* 14(1):217
- Saleem H, Zengin G, Ahmad I, Lee JTB, Htar TT, Mahomoodally FM, Naidu R, Ahemad N (2019) Multidirectional insights into the biochemical and toxicological properties of *Bougainvillea glabra* (Choisy.) aerial parts: a functional approach for bioactive compounds. *J Pharmaceut Biomed* 170:132–138
- Radovanovic A (2015) Evaluation of potential cytotoxic effects of herbal extracts. *Serbian J Exp Clin Res* 16(4):333–342
- Chudzik M, Korzonek-Szlacheta I, Król W (2015) Triterpenes as potentially cytotoxic compounds. *Molecules* 20(1):1610–1625
- Chaturvedula VP, Schilling JK, Miller JS, Andriantsiferana R, Rasamison VE, Kingston DG (2004) New cytotoxic terpenoids from the wood of *vepris p unctata* from the Madagascar Rainforest. *J Nat prod* 67(5):895–898
- Biskup E, Gołębiowski M, Gniadecki R, Stepnowski P, Lojkowska E (2012) Triterpenoid α -amyrin stimulates proliferation of human keratinocytes but does not protect them against UVB damage. *Acta Biochim Pol* 59(2):255–260
- Sun H, Fang W-S, Wang W-Z, Hu C (2006) Structure-activity relationships of oleanane- and ursane-type triterpenoids. *Bot Stud* 47(4):339–368
- Zhang W, Men X, Lei P (2014) Review on anti-tumor effect of triterpene acid compounds. *J Cancer Res Ther* 10(5):14

Publisher's Note

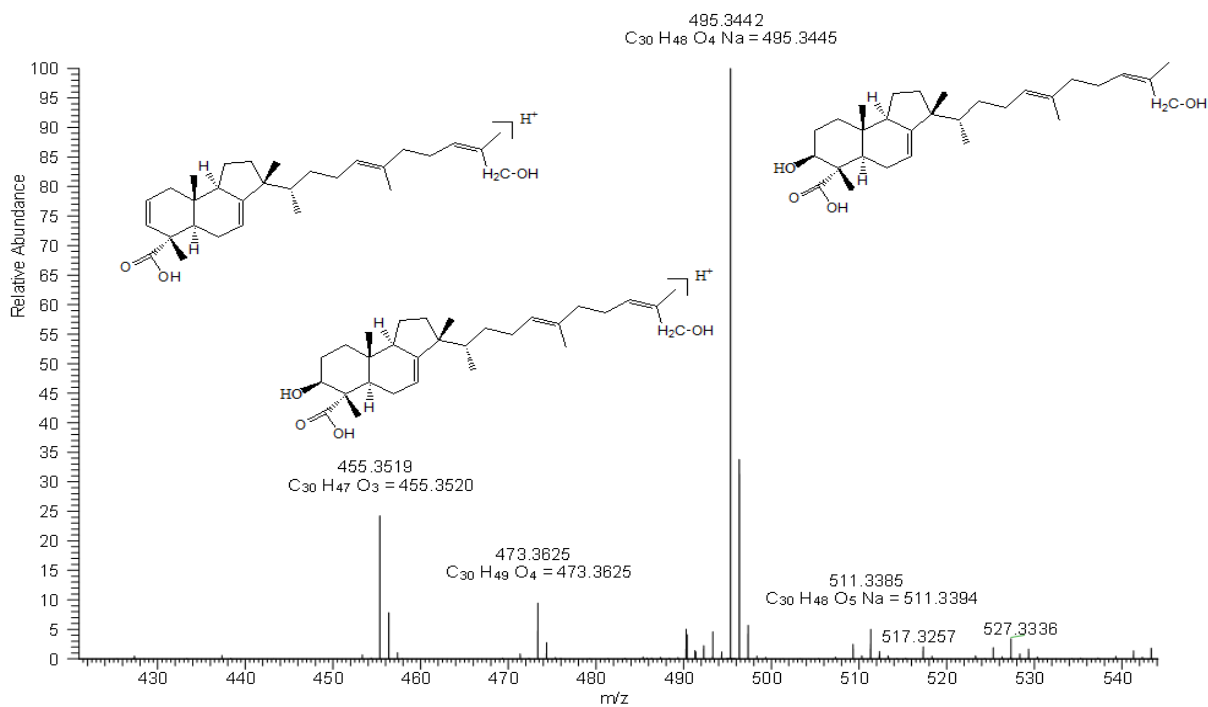
Springer Nature remains neutral with regard to jurisdictional claims in published maps and institutional affiliations.

Supporting Information

Antiproliferative activity of a novel tricyclic triterpenoid acid from *Commiphora africana* resin against four human cancer cell lines



a)



b)

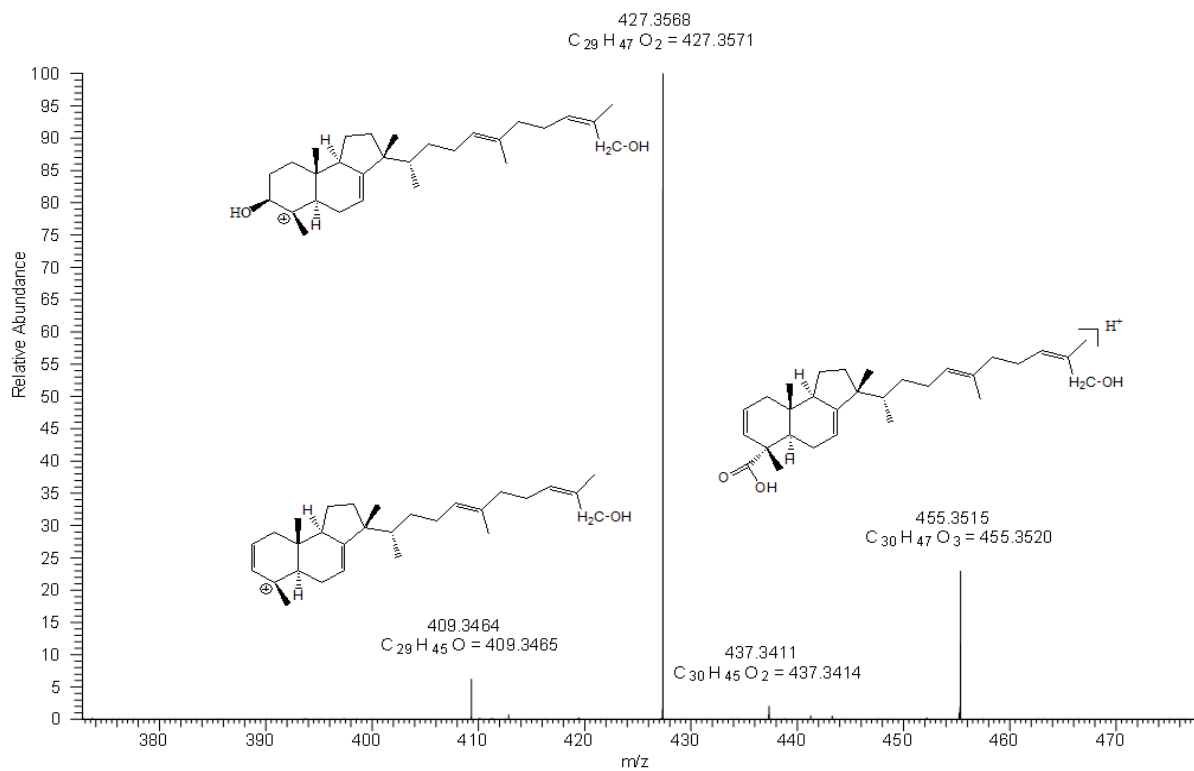


Fig. S1. Precursor ions and calculated fragment ions elemental composition of commafric A (**1**)

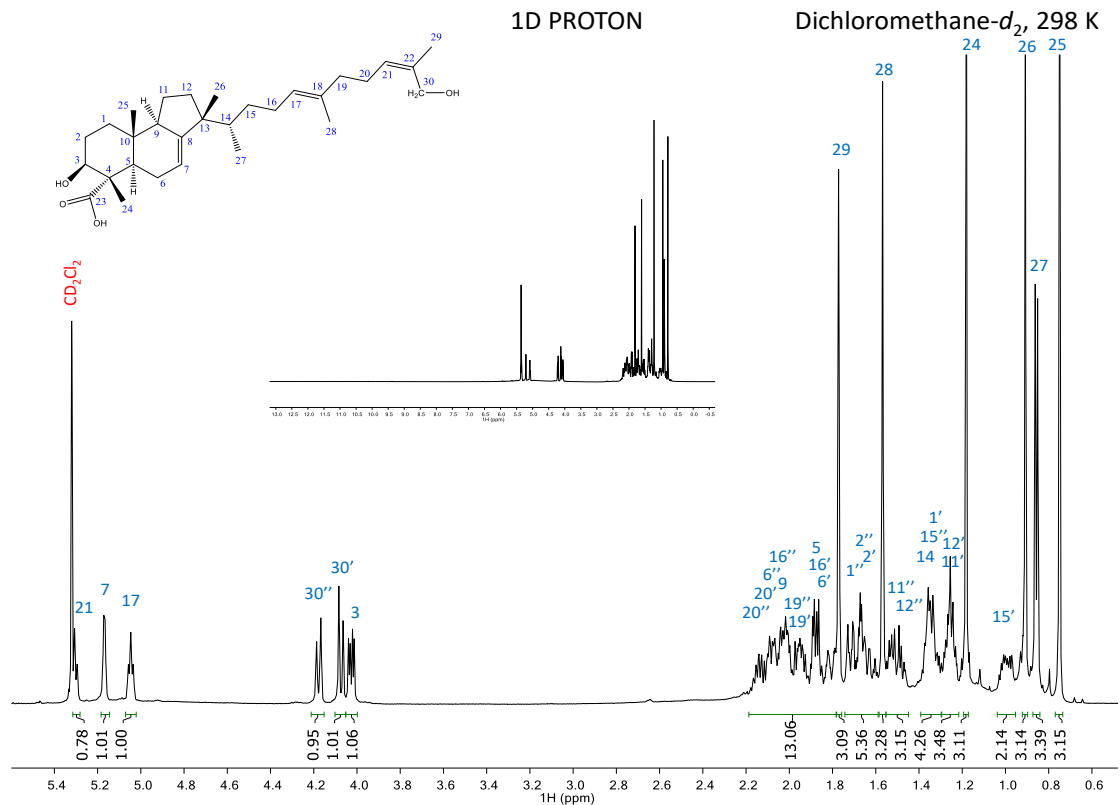


Fig. S2. 1D proton NMR spectrum of commafric A (**1**)

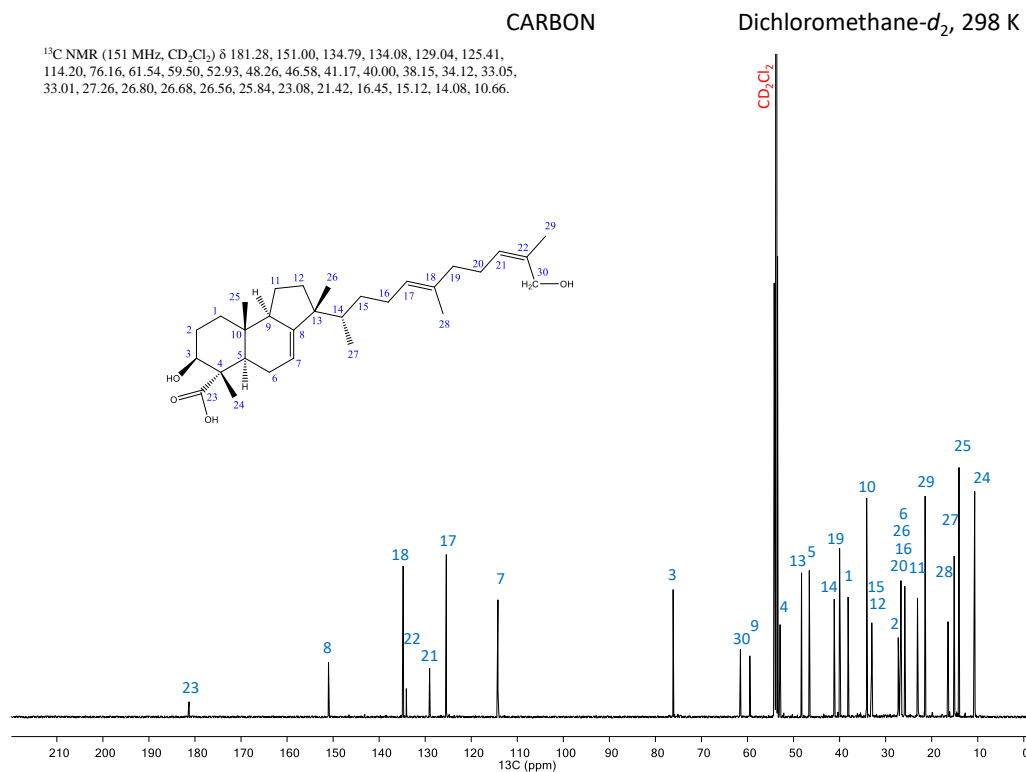


Fig. S3. 1D carbon spectrum of **1**

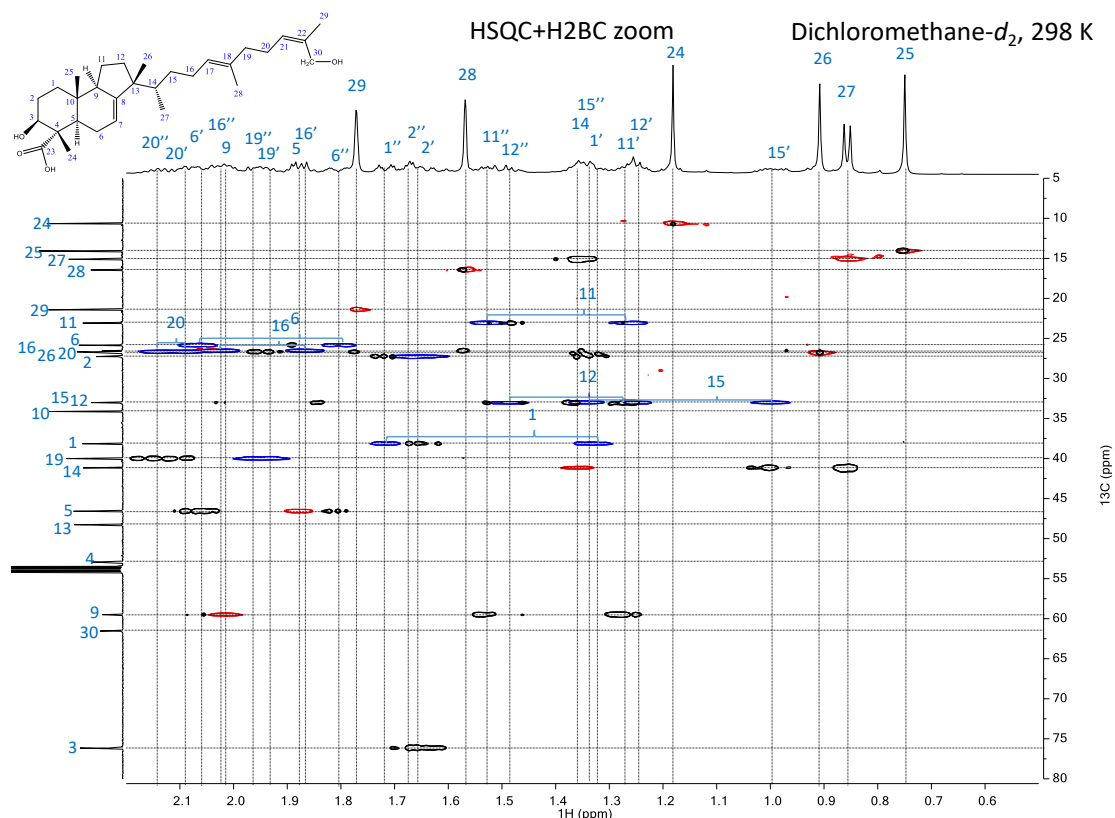


Fig. S6. Expansion of the aliphatic region of superimposed HSQC+H2BC of **1**

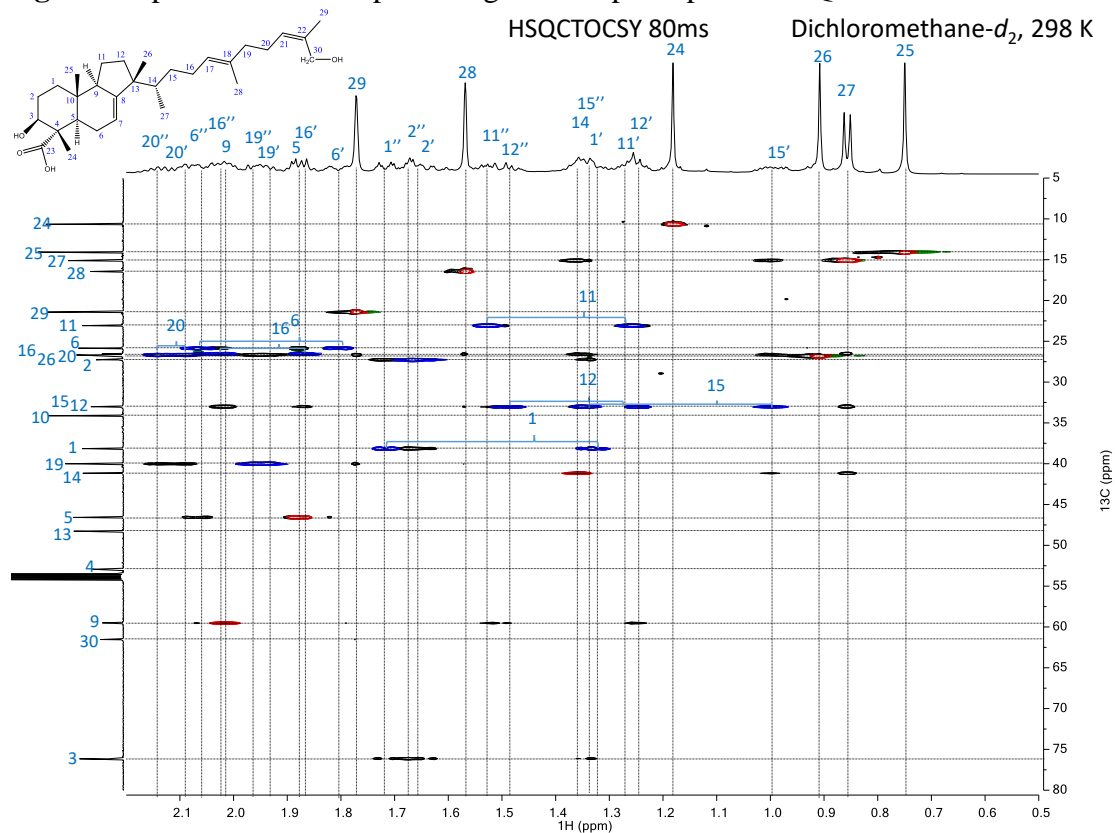


Fig. S7. Expansion of the aliphatic region of superimposed HSQC+HSQC-TOCSY of **1**

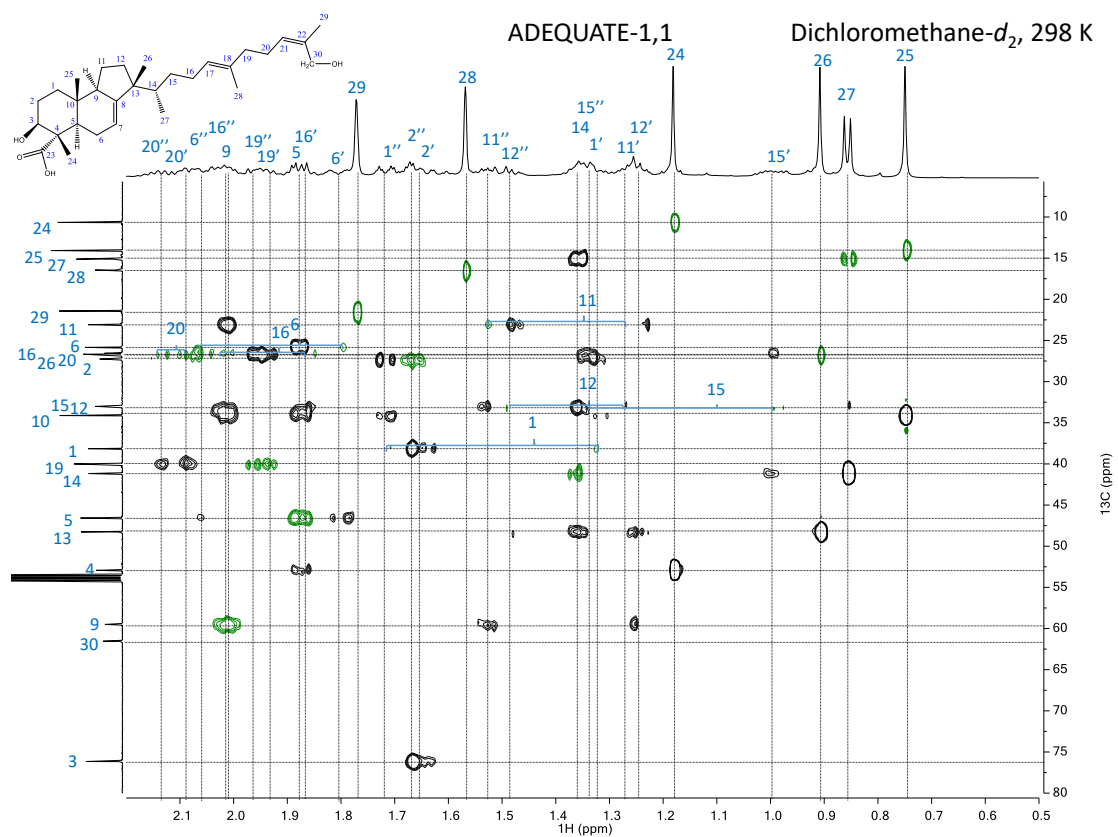


Fig. S8. 1,1-ADEQUATE of **1**

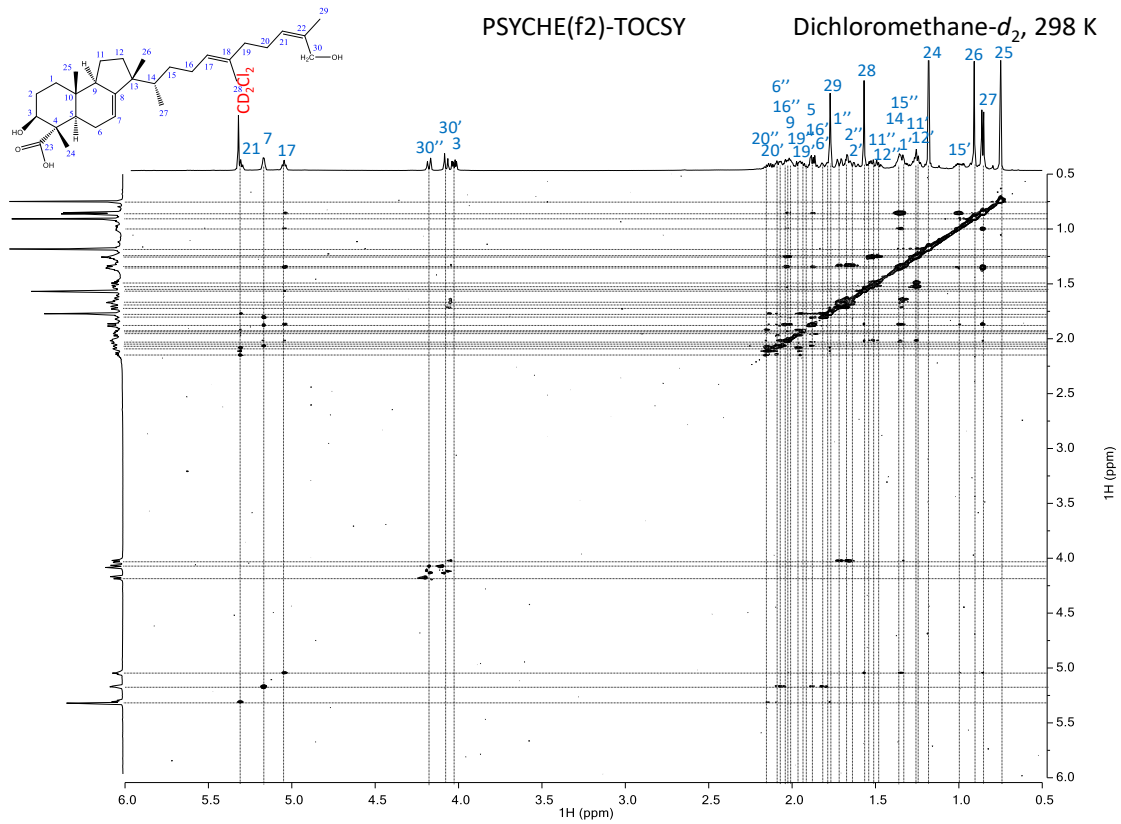


Fig. S9. PSYCHE-TOCSY of **1**

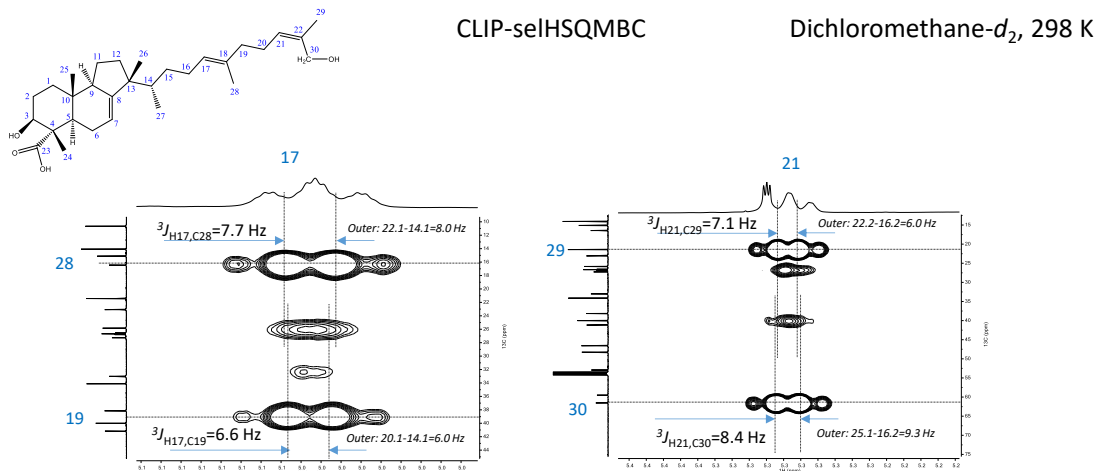


Fig. S10. CLIP-seIHSMBC of H17 (left panel) and H21 (right panel) of **1**

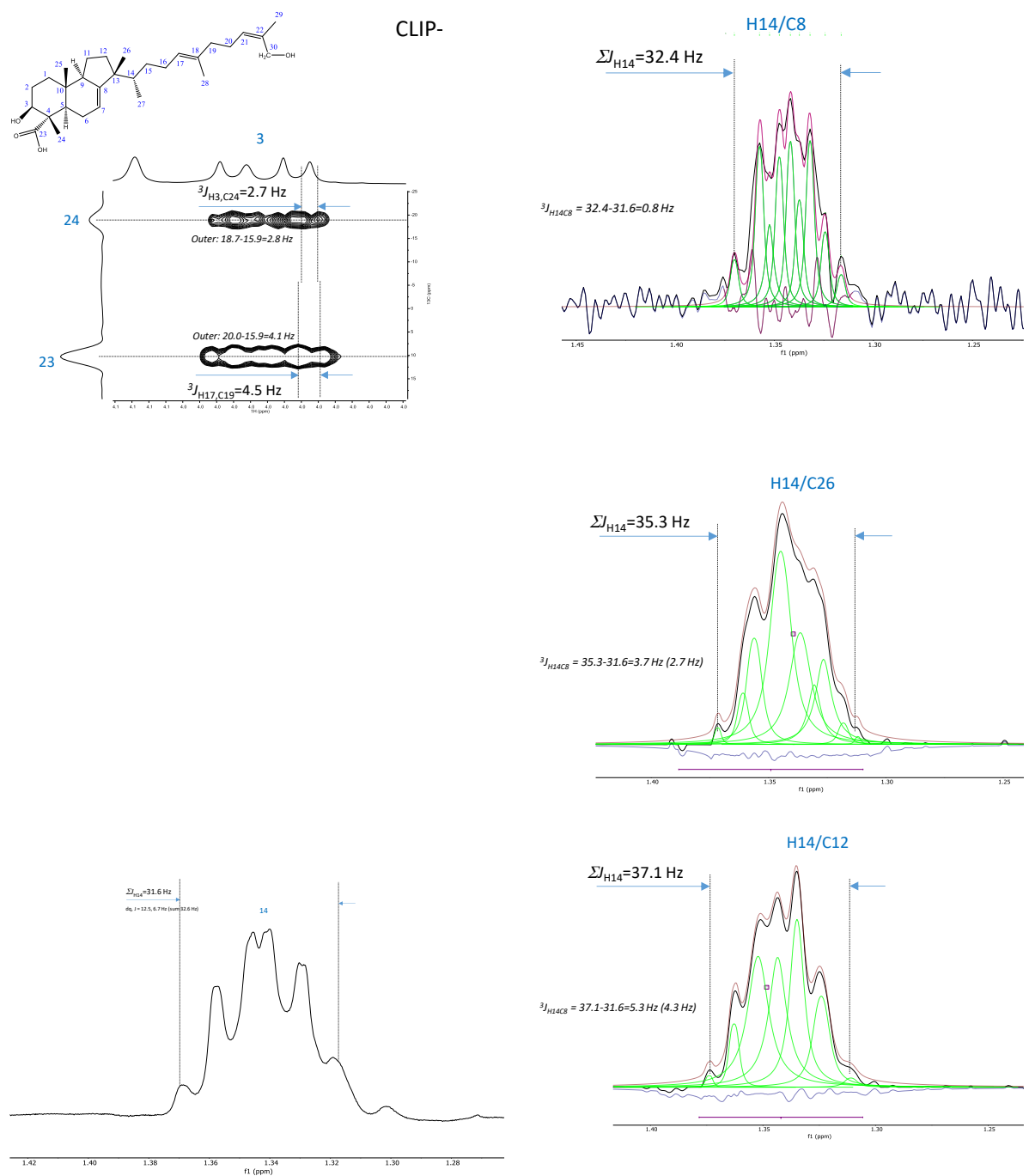


Fig. S11. CLIP-seHSQMBC of H3 (upper left panel), CLIP-seHSQMBC projections of H14 (right panels), and CSSF-1D of H-14 (lower left panel) of **1**

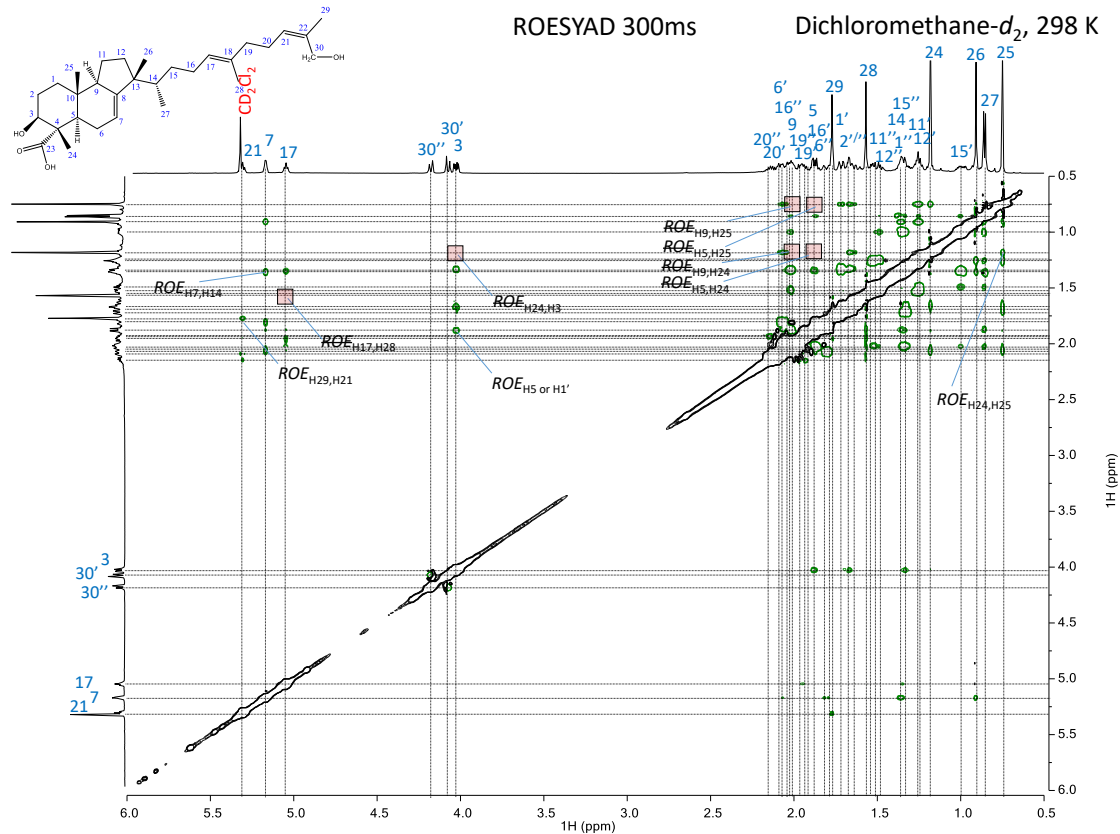


Fig. S12. 300ms ROESY of **1**

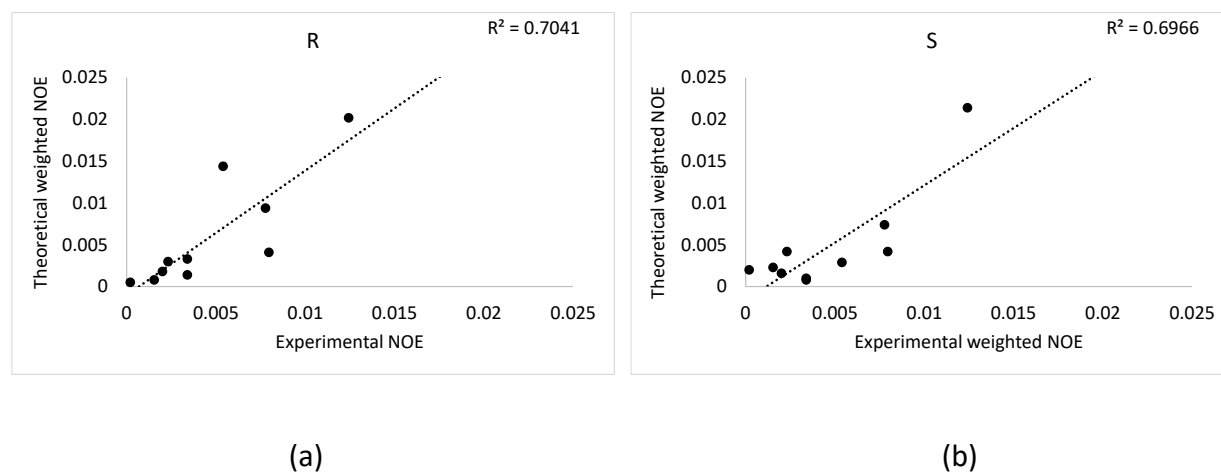


Fig. S13. Selected experimental vs theoretical Boltzmann weighted NOEs calculated from the rotamer ensembles for the (a) R- and (b) S configurations of C14 of **1**

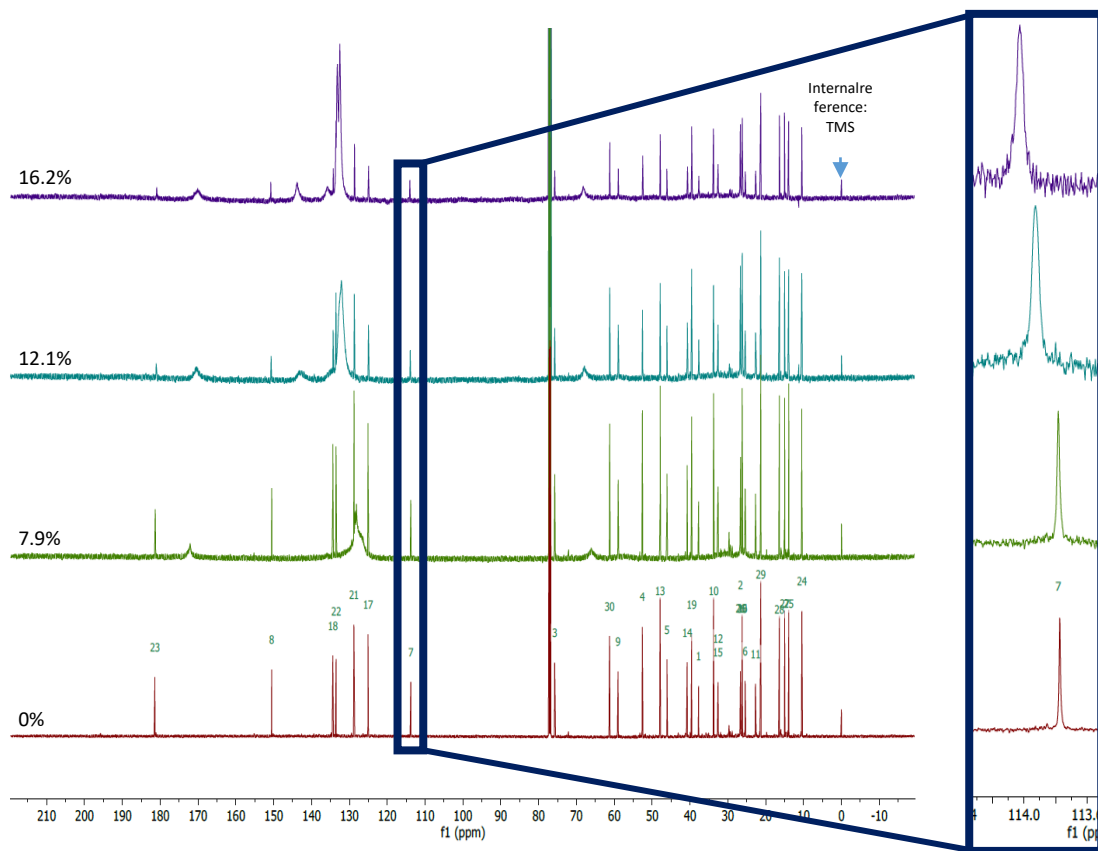


Fig. S14. ^{13}C spectra for commafric A in CDCl_3 with 0.03% (v/v) TMS at different PBLG concentrations. Zoomed-in outclip of C7, showing the change in ppm values, as well as decrease of signal-to-noise ratio.

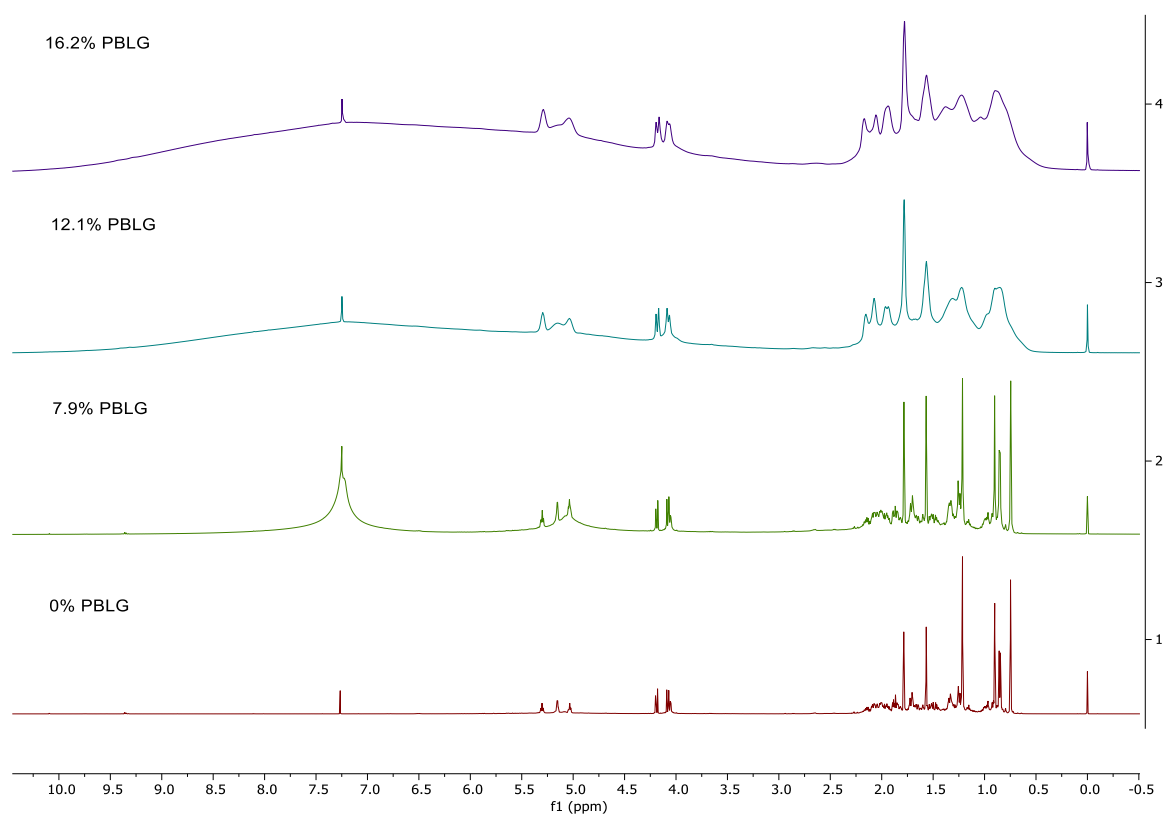


Fig. S15: ¹H spectra of commafric A in CDCl₃ with 1% (v/v) TMS at different PBLG concentrations.

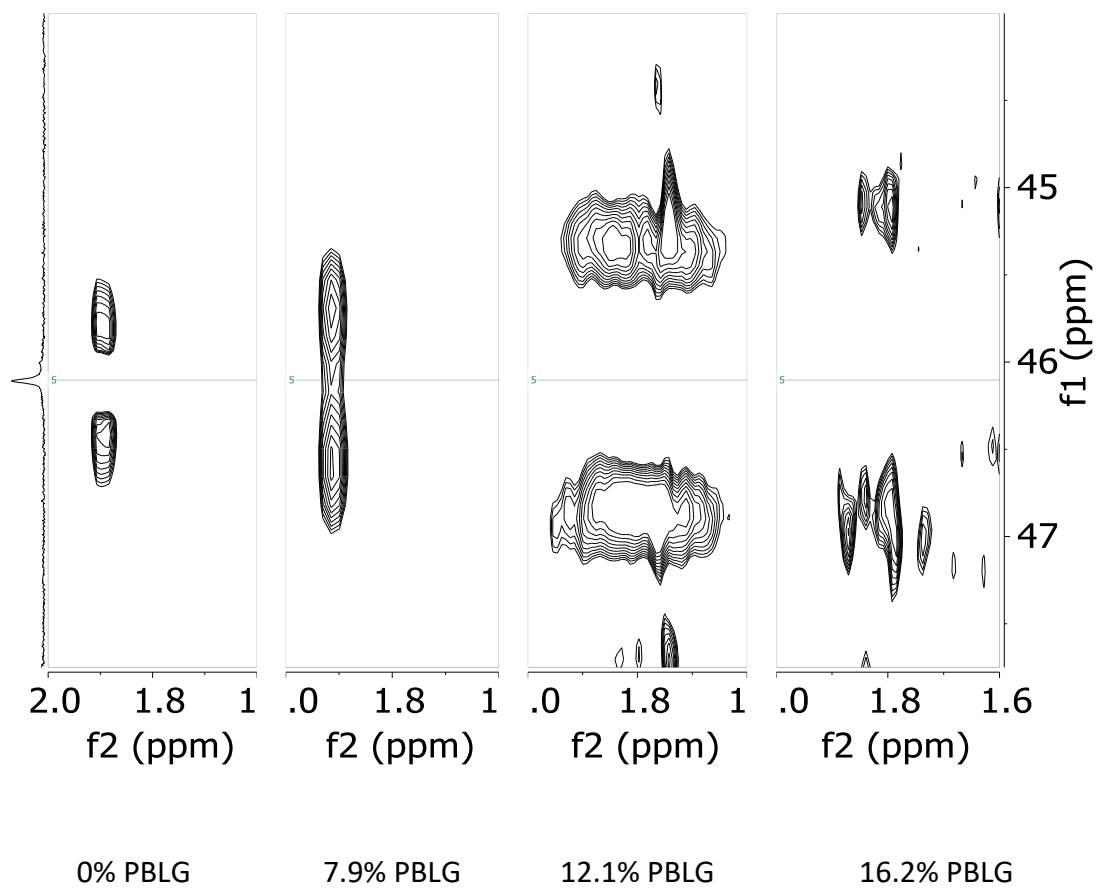


Fig. S16. Outclips of the HSQC-IPAP spectra of C5 of commafric A at different PBLG concentrations, showcasing how the RDC increases the ^1H splitting in the f1 dimension.

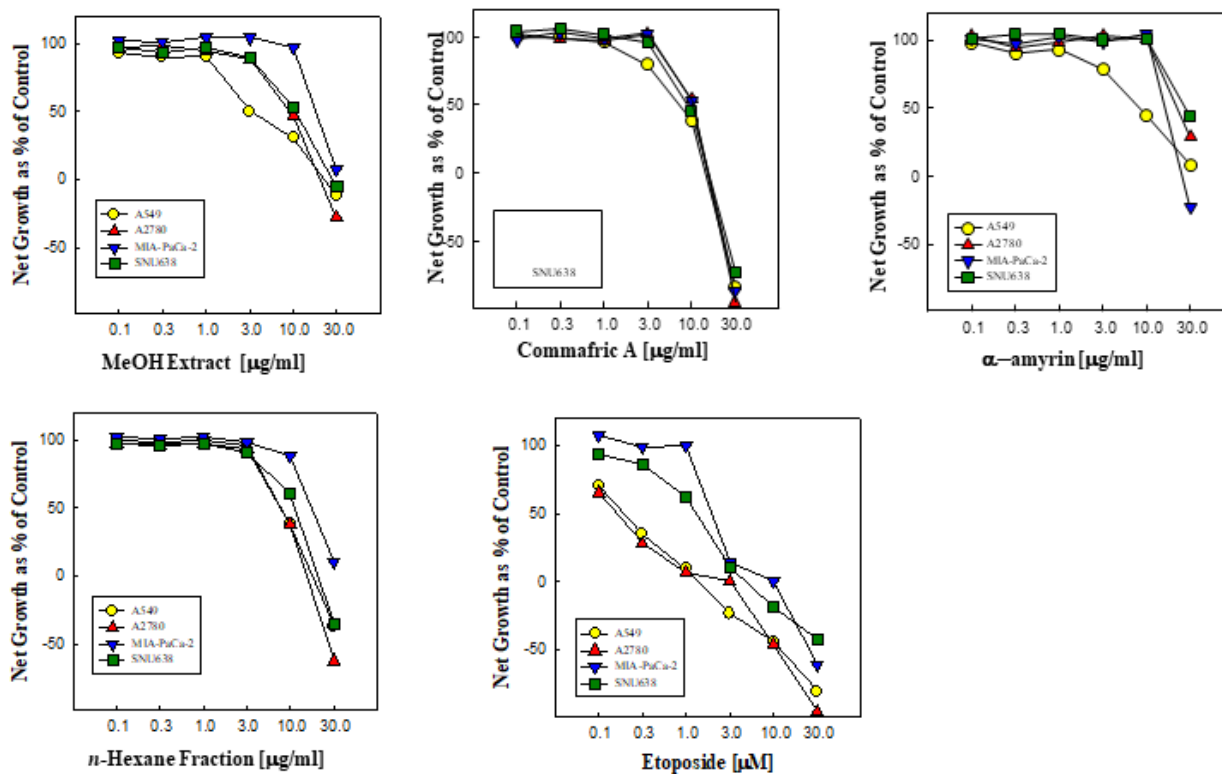


Fig. S17. Dose response curve of MeOH extract, *n*-hexane fraction, commafric A, and α -amyryn isolated from *C. africana n*-hexane fraction against A549, A2780, MIA-PaCa-2 and SNU-638. Etoposide used as a positive control using the SRB assay

Table S-1. Experimental ^{13}C data of commafric A, with the corresponding RCSA values. The RCSA values are calculated from equation 1.

Carbon atom	^{13}C shifts (ppm)				RCSA
	[PBLG] (w/v)				
	0	7.9	12.1	16.2	
1	37.75	37.74	37.7	37.67	-0.06
2	26.69	26.68	26.69	26.71	0.04
3	75.76	75.74	75.74	75.73	0.01
4	52.59	52.57	52.54	52.51	-0.04
5	46.09	46.09	46.11	46.12	0.03
6	25.45	25.44	25.42	25.41	-0.02

7	113.77	113.78	113.98	114.03	0.24
8	150.53	150.51	150.66	150.76	0.27
9	59.02	58.98	58.96	58.94	0.00
10	33.79	33.77	33.8	33.81	0.06
11	22.72	22.71	22.68	22.65	-0.05
12	32.61	32.6	32.59	32.59	0.00
13	47.91	47.9	47.88	47.87	-0.02
14	40.77	40.75	40.69	40.65	-0.08
15	32.67	32.7	32.67	32.66	-0.07
16	26.15	26.16	26.14	26.13	-0.04
17	125.08	125.07	124.98	124.93	-0.13
18	134.38	134.37	134.3	134.25	-0.11
19	39.58	39.57	39.57	39.57	0.01
20	26.24	26.23	26.21	26.19	-0.03
21	128.81	128.76	128.7	128.66	-0.05
22	133.52	133.54	133.53	133.53	-0.03
23	181.39	181.29	181.06	180.89	-0.30
24	10.46	10.46	10.47	10.47	0.01
25	13.92	13.91	13.94	13.95	0.05
26	26.67	26.65	26.69	26.71	0.08
27	15	14.99	15.02	15.03	0.05
28	16.39	16.38	16.38	16.37	0.00
29	21.31	21.31	21.30	21.30	-0.01
30	61.26	61.23	61.2	61.18	-0.02

Table S-2: Experimental ^1H - ^{13}C splitting data of commafric A, with the corresponding RDC values. The RDC values are found as the difference in the splitting at two different [PBLG], and then dividing by the amount of hydrogen atoms connected to that carbon atom. With the obtainable data, the RDCs were collected as the difference between 12.1% and 0% PBLG.

HSQC-IPAP (Hz) (f1 splitting)					RDC
Carbon atom	[PBLG] (w/v)				
	0	7.9	12.1	16.2	
5	133.94	138.47	255.58	-	121.11
6	260.37	261.51	-	-	-
7	146.11	156.66	-	-	-146.11
9	127.66	127.49	234.20	-	106.54
11	266.61	265.40	255.00	-	-5.81
12	258.28	257.64	311.75 ^a	-	26.74
14	135.01	132.91	97.04	-	-37.97
17	153.91	162.31	178.13	185.34	24.22
21	150.87	145.67	167.48	171.24	16.61
25	371.64	369.02	-	-	-
26	375.88	376.08	327.56	-	-16.11
27	381.60	375.68	349.19	326.76 ^a	-10.80

^a Uncertain

Paper II



Article

Editor's Choice

Goldilocks Dilemma: LPS Works Both as the Initial Target and a Barrier for the Antimicrobial Action of Cationic AMPs on *E. coli*

Martin Jakubec, Fredrik G. Rylandsholm, Philip Rainsford, Mitchell Silk, Maxim Bril'kov, Tone Kristoffersen, Eric Juskewitz, Johanna U. Ericson and John Sigurd M. Svendsen

Special Issue

Mechanisms and Kinetics of Interactions of Biomolecules at Interfaces

Edited by

Dr. Monika Wasilewska, Dr. Aneta Michna, Dr. Maria Morga and Dr. Andrey G. Cherstvy



Article

Goldilocks Dilemma: LPS Works Both as the Initial Target and a Barrier for the Antimicrobial Action of Cationic AMPs on *E. coli*

Martin Jakubec^{1,*}, Fredrik G. Rylandsholm¹, Philip Rainsford¹, Mitchell Silk¹, Maxim Bril'kov², Tone Kristoffersen¹, Eric Juskewitz³, Johanna U. Ericson³ and John Sigurd M. Svendsen¹

¹ Department of Chemistry, Faculty of Science and Technology, UiT the Arctic University of Norway, 9019 Tromsø, Norway; fredrik.g.rylandsholm@uit.no (F.G.R.); philip.rainsford@uit.no (P.R.); tone.kristoffersen@uit.no (T.K.); john-sigurd.svendsen@uit.no (J.S.M.S.)

² Department of Pharmacy, Faculty of Health Sciences, UiT the Arctic University of Norway, 9019 Tromsø, Norway; maxim.bril'kov@uit.no

³ Department of Medical Biology, Faculty of Health Sciences, UiT the Arctic University of Norway, 9019 Tromsø, Norway; johanna.e.sollid@uit.no (J.U.E.)

* Correspondence: martin.jakubec@uit.no

Abstract: Antimicrobial peptides (AMPs) are generally membrane-active compounds that physically disrupt bacterial membranes. Despite extensive research, the precise mode of action of AMPs is still a topic of great debate. This work demonstrates that the initial interaction between the Gram-negative *E. coli* and AMPs is driven by lipopolysaccharides (LPS) that act as kinetic barriers for the binding of AMPs to the bacterial membrane. A combination of SPR and NMR experiments provide evidence suggesting that cationic AMPs first bind to the negatively charged LPS before reaching a binding place in the lipid bilayer. In the event that the initial LPS-binding is too strong (corresponding to a low dissociation rate), the cationic AMPs cannot effectively get from the LPS to the membrane, and their antimicrobial potency will thus be diminished. On the other hand, the AMPs must also be able to effectively interact with the membrane to exert its activity. The ability of the studied cyclic hexapeptides to bind LPS and to translocate into a lipid membrane is related to the nature of the cationic charge (arginine vs. lysine) and to the distribution of hydrophobicity along the molecule (alternating vs. clumped tryptophan).

Keywords: AMP; SPR; NMR; liposomes; LPS; lipid binding



Citation: Jakubec, M.; Rylandsholm, F.G.; Rainsford, P.; Silk, M.; Bril'kov, M.; Kristoffersen, T.; Juskewitz, E.; Ericson, J.U.; Svendsen, J.S.M. Goldilocks Dilemma: LPS Works Both as the Initial Target and a Barrier for the Antimicrobial Action of Cationic AMPs on *E. coli*. *Biomolecules* **2023**, *13*, 1155. <https://doi.org/10.3390/biom13071155>

Academic Editors: Monika Wasilewska, Aneta Michna, Maria Morga and Andrey G. Cherstvy

Received: 22 June 2023
Revised: 18 July 2023
Accepted: 19 July 2023
Published: 20 July 2023



Copyright: © 2023 by the authors. Licensee MDPI, Basel, Switzerland. This article is an open access article distributed under the terms and conditions of the Creative Commons Attribution (CC BY) license (<https://creativecommons.org/licenses/by/4.0/>).

1. Introduction

The rapid spread of multidrug-resistant bacteria and the slow discovery of new classes of antibiotics is leading researchers to consider alternatives to classical antibiotics. Antimicrobial peptides (AMPs) represent one promising alternative [1,2]. AMPs are a ubiquitous part of the innate immune defense in all living organisms, from humans to bacteria themselves. They have been widely studied, and today, more than 3000 natural AMPs have been reported and characterized [3–5]. However, most natural AMPs are ill-suited as drug candidates due in part to either poor ADME-Tox properties (absorption, distribution, metabolism, and toxicity) or overly complex chemistry [6,7]. Consequently, de novo-designed antimicrobial peptides (AMP) are being developed with simplified sequences focusing on a small number of core residues [8]. These synthetic AMPs combine intelligent design, microbiology, chemistry, and a knowledge of human metabolism in a series of iterations to provide highly efficient compounds. However, despite decades of AMP study, there is a lack of in-depth knowledge of their modes of action, including potential targets for the AMPs in live bacteria. Case in point: while a number of proposed modes have been put forth, such as pore-formation, carpeting, and detergent-like, these models are often founded on observations in simplified model systems, at concentrations

that are poorly representative of biological conditions—at least with regards to antimicrobial assays [9,10].

Currently, the largest class of AMPs contains a significant fraction of cationic residues [11]. The net cationic charge of these peptides is believed to be essential to their mode of action and selectivity, with the cationic sites playing a crucial electrostatic role in the interaction between the AMPs and components of the bacterial membrane. Arginine and lysine are the most common acids in cationic AMPs, with very similar overall abundances. Still, lysine is more common in AMPs; meanwhile, arginine is more common in antiviral peptides [12,13]. Studies with synthetic cationic AMPs, either as derivatives of natural peptides or of de novo design, have unequivocally shown that arginine analogs display higher antimicrobial efficacy than corresponding lysine analogs [14–16]. While the effect of arginine on antimicrobial activity is well established, the underlying mechanism is not fully understood. For example, it has been observed that increased arginine content enhances peptide embedding in artificial POPC:POPG membranes [15], with the ability of arginine to stabilize its charge in the bilayer [17] or the ability of arginine to hydrogen bond with surrounding water when involved with cation- π interactions with tryptophan [17,18], being linked to arginine's ability to embed efficiently. However, no consensus hypothesis on this phenomenon exists.

Another essential component of AMP activity is the hydrophobic volume of the peptide. The ratio of charged amino acids and hydrophobic volume is reported to correspond with the activity of AMPs on phospholipid-based model membranes, an observation suggesting that the main mode of action for cationic AMPs is bilayer disruption [19]. The antimicrobial peptide database—ADP3 shows that 80% of all entries possessing reported antimicrobial activities contain at least one of the hydrophobic phenylalanine or tryptophan [20]. The hydrophobic bulk of these residues is believed to be important to the membrane disruption by positioning in the interfacial region of the bilayer [10]. In particular, the paddle-like tryptophan leverages its unique indole moiety, forming hydrogen bonds with the lipid-tail carbonyl group, and at the same time, its aromatic bulk is able to disturb the lipid packing. Indeed, it has been previously shown that tryptophan substitution with less hydrophobic amino acids can be used to fine-tune the natural lytic ability of rationally designed peptides [19].

While the importance of the interplay between hydrophobicity and charge for membrane interaction and disruption is well ingrained in the consciousness of AMP research, what is often not considered is that the charge and lipophilic nature of AMPs are important properties for binding to the lipopolysaccharides (LPS) of Gram-negative bacteria. LPS is a major component of the outer membrane of Gram-negative bacteria and acts as a barrier that AMPs need to cross in order to reach the bacterial membrane [21–23]. The sequence of initial LPS binding before membrane localization or intracellular binding cannot be avoided, and thus initial LPS interaction acts as a major bottleneck for most AMPs. In this work, we have observed that the initial binding to LPS needs to be fine-tuned for cationic AMPs to attain their antimicrobial activity. Just as in Southey's tale [24], Goldilocks needed to find her ideal conditions, so the initial interaction between AMPs and the LPS needs to be ideal. Too strong LPS binding may prevent AMPs from reaching the membrane target or cause aggregation of peptides in the cell wall [25]; LPS interaction that is too weak would reduce the amount of AMP available and prevent adequate permeation through the tight network of LPS to the bacterial membrane. In short, AMPs need to find their 'Goldilocks' zone of LPS affinity, where the interaction is not too tight, not too loose, but "just right".

Here we present evidence that the interaction between AMPs and Gram-negative bacteria is driven by an initial binding to the LPS. All compounds reaching the bilayer, or an intracellular target, must first cross the LPS. In addition, we introduce a toolbox of suitable experiments that can be used to quantify this kinetic process—a combination of surface plasma resonance (SPR) and NMR experiments with live bacteria: live-cell NMR. We have tested this toolbox in the study of the interactions of a series of cyclic cationic AMPs (cAMPs) and several *E. coli* strains, including LPS-deficient and colistin-resistant

strains. Using this toolbox, we can quantify the initial binding events towards several *E. coli* strains, and we are able to identify lysine as an LPS binder in the ‘Goldilocks’ zone of affinity.

2. Materials and Methods

All the common chemicals are of analytical purity and supplied by Merck KGaA, Darmstadt, Germany. All the lipid samples had been supplied by Avanti Lipids (Alabaster, AL, USA).

2.1. Peptide Synthesis

The peptides were prepared from 2-Chlorotrityl chloride resin and Fmoc-Trp(Boc)-OH as the first amino acid using a solid phase peptide synthesis strategy. The synthesis followed synthetic protocols previously reported [26]. The side-chain-protected linear peptide precursors were prepared by an automated peptide synthesizer (Biotage Initiator + Altra). Following resin cleavage, the peptides were head-to-tail cyclized in solution, side-chain deprotected, and the crude peptides were purified by preparative reverse-phase high-performance liquid chromatography. Chemical analysis of synthesized peptides is available in the Supplementary Materials.

2.2. MIC Testing

The bacterial strains tested were *E. coli* ATCC 25922, *E. coli* CCUG 70562, and *E. coli* NR-698. The MIC assays followed the CLSI guidelines [27]. Overnight cultures and MIC assays were performed in MHBII (212322, Becton, Dickson and Company, Sparks, MD, USA). In addition, *E. coli* NR-698 was tested after cultivation with 4 µg/mL of colistin to induce alternation in surface charge.

2.3. Liposomes Preparation

The large unilamellar liposomes of DMPC and DMPC:PG (95:5) were prepared for the SPR experiment using standard methods [28]. In brief, lipid mixtures were weighted from dry powder (Avanti, USA) and dissolved in 3:1 dichloromethane:methanol mixtures. The organic mixture was dried in a vacuum rotavapor to form a lipid film which was hydrated to 20 mM total concentration of lipids (for DMPC and DMPC:PG mixture) by adding 10 mM HEPES buffer pH 7.4 with 150 mM NaCl. For DMPC:LPS mixtures, dried LPS was dissolved in water and mixed with DMPC dissolved in dichloromethane. Isopropanol was added to the mixture until only one phase—dichloromethane:isopropanol:water was formed [29]. Dry film was prepared and then hydrated using the same method as above to a concentration of 18 mM of DMPC and 10% (*w/w*) LPS in HEPES buffer. Lipid liposomes were extruded 13 times through a 100 nm diameter pore using an Avanti Mini Extruder kit.

2.4. SPR

The SPR experiments were performed at room temperature using the L1 chip and T200 Biacore instrument (GE Healthcare, Chicago, IL, USA). The experimental setup is the same as in Jakubec et al. (2020) [30]. Briefly, lipid liposomes were immobilized on a cleaned surface of the chip using a flow rate of 2 µL/min for 2400 s. The immobilization efficiency was tested by injecting 0.2 mg/mL of bovine serum albumin (BSA, A7030, Sigma-Aldrich, Saint Louis, MO, USA) for 1 min at 30 µL/min. The change of RU less than 400 indicated sufficient coverage. Next, diluted peptides were injected over immobilized liposomes using a flow rate of 15 µL/min for 200 s with a subsequent 400 s dissociation phase. The peptide concentration was from 4 to 128 µM, except for poorly binding peptides c(LWwNKR) and c(WKWKWK), which were set from 24 to 768 µM to reach vesicle saturation. Samples were injected from low to high concentrations due to the possibility of sample retention in the liposomes. Between individual injections, liposomes were regenerated by three subsequent 30 s injections of 10 mM NaOH at a 30 µL/min flow rate. The control flow cell was treated the same way as the sample cells, except sample injections were replaced by

HEPES buffer. The results were processed using in-laboratory written MATLAB scripts (MATLAB R2022a; scripts are available at [31]). K_D was obtained Using Equation (1) from a standard steady-state fit:

$$RU = \frac{RU_{MAX}}{1 + \frac{K_D}{[P]}} + \text{off}, \quad (1)$$

where RU is measured SPR response; RU_{MAX} is RU response during saturation; [P] is peptide concentration; and off is offset of response.

K_P was obtained from steady-state using a method developed by Figueira et al. (2017) [32] using Equation (2):

$$\frac{RU_S}{RU_L} = \frac{\gamma_L K_P \frac{M_S}{M_L} [S]_W}{1 + \delta \gamma_L K_P [S]_W}, \quad (2)$$

where RU_S is the relative response of the solute (peptides); RU_L is the total lipid deposition response; γ_L is the molar volume of the lipids (average for mixtures); M_S and M_L are the molecular mass of the solute and lipid, respectively; and $[S]_W$ is the concentration of solute in water. K_P is the partitioning constant, while σ is the lipid-to-solute ratio. The two latter are obtained from the fit.

The k_{off} rate was obtained from the first 200 s of dissociation using adapted formalism from Figueira et al. (2017) [32] using Equation (3). Contributions from two populations were identified, so the average k_{off} response was calculated by Equation (4).

$$S_L(t) = \alpha e^{-k_{off}, \alpha t} + \beta e^{-k_{off}, \beta t} + S_{L,r}, \quad (3)$$

$$k_{off} = \frac{\alpha k_{off}, \alpha + \beta k_{off}, \beta}{\alpha + \beta}, \quad (4)$$

where S_L is the linearised ratio of responses of the solute and lipid, which is plotted against the time of dissociation; α and β are individual populations; and $S_{L,r}$ is the retained solute fraction.

The association rate k_{on} was obtained from experimentally measured K_D and k_{off} by Equation (5):

$$K_D = \frac{k_{off}}{k_{on}}. \quad (5)$$

2.5. NMR Experiments

NMR spectra were acquired on a Bruker Avance III HD spectrometer operating at 600 MHz for ^1H , equipped with an inverse TCl cryo probe. All NMR spectra were acquired at 298 K using 5 mm tubes using standard pulse programs [31].

2.5.1. Live Cell NMR

E. coli strains ATCC 25922, CCUG 70662, and NR 698 were grown until $OD_{600} \approx 0.6$ – 0.8 in standard Lysogeny Broth at 37°C from overnight colonies on agar plates. This allowed bacterial cultures to reach an exponential state of growth. CCUG 70662 was cultivated with and without $4 \mu\text{g}/\text{mL}$ of colistin in both agar and broth to allow for modification of the lipid A part of LPS [33]. After that, cells were carefully centrifuged by $6000 \times g$ for 10 min, the supernatant was discarded, and the cell pellet was resuspended in 10 mM Tris buffer with 100 mM NaCl and pH 7.4. The process was repeated two more times to wash out broth components and leftover colistin. Cells were then resuspended in 1 mL of Tris buffer, and OD_{600} was checked by dilution of 100 μL of the sample. The number of cells was estimated from OD_{600} of the sample using the formulation presented by Beal et al. (2022) [34]. Furthermore, lipid concentration was estimated to be 50 mmol per bacterial cell [35]. The part of samples was diluted to $OD = 1$ in Tris buffer, and zeta potential was measured on Malvern Zetasizer Nano (Malvern Ins., Malvern, UK). The concentrated cell sample was then titrated (from 5 to 160 μL) into the 500 μL of peptide

(1 mg/mL) in Tris buffer with 5% D₂O and ¹H spectra was collected using double solvent suppression with excitation sculpting and presaturation (zqesgppepr) with extended delay d1 = 8 s to allow for complete relaxation of nuclei.

Spectra were processed automatically using TopSpin 4.0.8 (Bruker, Bremen, Germany) and by Matlab R2020b with Signal processing and Bioinformatics toolbox (Natick, MA, USA). The processing scripts are available at Github [31].

K_D was estimated from individual signal integral by using Equation (6) developed by Shortridge et al. (2008) [36] for invisible binding states:

$$B_{\text{expt}} = 1 - \frac{1}{1 + \frac{[\text{Lip}]_{\text{T}}}{[\text{AMP}]_{\text{T}} + K_{\text{D}}} \left(\frac{\gamma_{\text{B}}}{\gamma_{\text{F}}} - 1 \right)}, \quad (6)$$

where B_{expt} is measured integral decrease; [Lip]_T is total lipid concentration estimated from the amount of titrated cells; [AMP]_T is total peptide concentration; and γ_B and γ_F are the line widths of bound and free AMP, respectively. Due to the nature of interaction and the invisibility of the bound state line, the width ratio was estimated from the fit, and it was used for all proton signals. This value was different for each combination of AMP and bacterial sample, and it is noted in the Supplementary Materials.

2.5.2. Assignment

NOESY, TOCSY, DQF-COSY, ¹⁵N-HSQC, HSQC, HMBC, and H2BC NMR spectra were recorded with standard settings. NOESY and TOCSY spectra were recorded with mixing times of 100–400 ms and 80 ms, respectively. Spectra were processed with TopSpin 3.6.0, and assignments were done manually. The full assignment is reported in the Supplementary Materials.

3. Results and Discussion

3.1. Cyclic Peptides with Balanced Lipophilic Bulk and Cationic Charge

In the present work, we have selected to limit the conformational freedom the peptides may adopt with head-to-tail cyclization. The peptides designed for this study were cyclohexapeptides with an equal number of cationic residues (Arg or Lys) and bulky lipophilic residues (Trp), thus fulfilling the pharmacophore for short synthetic cationic antimicrobial peptides against both Gram-positive and Gram-negative bacteria [26]. Two types of sequences were selected, either sequence where the cationic residues and tryptophan are alternating or a “clumped” sequence where the cationic residues are adjacent in the sequence and the tryptophan residues likewise. In addition, we have included a fifth peptide with a similar general structure—a cyclohexapeptide which proved to be both a very poor antimicrobial and lipid binder (Figure 1).

Cyclic hexapeptides tend to adopt conformations where two opposing β-turns link two short antiparallel β-strands. Using the Dunitz–Waser concept [27], there are two gross variants of the cyclic hexapeptide; one resembling the chair conformation of cyclohexane through the twisted βI turns, the other resembling the boat conformation of cyclohexane due to the presence of the flatter βII turns (Figure 1). An alternating sequence c(WR)3 or c(WK)3 would, due to the internal symmetry, give rise to only one structure within each gross conformation, whereas the clumped sequences, c(WWWRRR) and c(WWWKKK), would possibly form two different structures within each gross conformational category.

Moreover, the linear variants of selected peptides have already been shown to possess interesting antimicrobial potential. The linear peptide WWWRRR has been demonstrated to exhibit the best combination of length and activity [14]. Additionally, the peptide WRWRWR had demonstrated promising activity against methicillin-resistant *S. aureus* [37], while the peptide WKWKWK exhibited decreased activity when the sequence was shifted to KWKWKW [38]. Presented peptides thus correspond to new cyclic variants of linear antimicrobial peptide analogs.

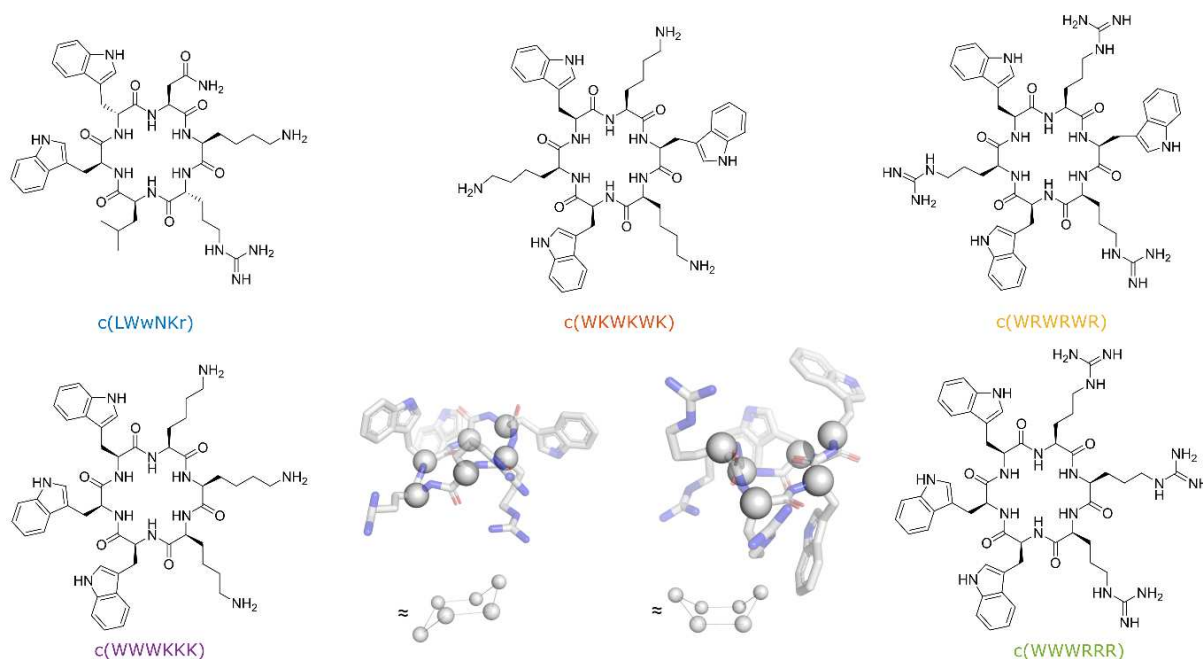


Figure 1. Structures of the synthesized peptides. Snapshots of c(WWWRRR) generated from CREST (provided by Prof. Kenneth Ruud) calculations showcasing the Dunitz–Waser concept [39]. Chair conformation (**left**) and boat conformation (**right**) with the alpha carbons outlined as spheres for a better overview.

3.2. Antimicrobial Activity of Peptides

The antimicrobial activity of the five cyclic cationic AMPs was determined against *S. aureus*, *P. aeruginosa*, and three strains of *E. coli*: ATCC 25922, LPS colistin-resistant strain CCUG 70662, and LPS deficient strain NR 698 (Table 1). CCUG 70662 was cultivated in two conditions, both in the absence (–) and in the presence (+) of colistin (4 µg/mL). Resistance development can be monitored by measuring changes in the ζ -potential, reflecting the overall charge of the bacteria. Indeed, cultivating CCUG 70662 in the presence of colistin caused a decrease in the ζ -potential [33]. This change is due to the addition of phosphoethanolamine to the lipid A moiety of LPS, reducing the overall negative charge of the LPS [33,40]. In the NR 698 strain, translocation of LPS from the periplasmic space to the outer leaflet is hindered. This increases the susceptibility of the bacteria to bile salts, chlorobiphenyl-vancomycin, vancomycin, bacitracin, novobiocin, rifampicin, and erythromycin, amongst others, suggesting that the poor LPS translocation results in a deficient outer membrane [41]. The most active AMPs were those with clumped residues, c(WWWRRR) and c(WWWKKK), followed by the peptides with alternating sequences, c(WRWRWR) and c(WKWKWK). Subsequently, the AMP c(LWwNKr) was included as a negative control as it showed no detectable antimicrobial activity on *E. coli* strains except the NR 698 strain and had only a weak affinity towards lipid membranes during the preliminary experiments.

One important observation is that the colistin-resistant strain CCUG 70662 is still susceptible to the tested hexapeptides even after cultivation with colistin which induced the modification of lipid A. Colistin has been shown to bind LPS and displace divalent cations from lipid A. This will increase the fluidity of LPS and cause major disruption of the outer membrane, and allows for the colistin to reach the periplasmic space [42,43]. The following bacterial toxicity is not fully explained, as outer membrane integrity is not crucial for bacteria survival. Currently, there are three major theories on colistin antimicrobial activity: direct disruption of the inner membrane, vesicle-vesicle contact pathways, or targeting of lipid A in the periplasmic space [42–44]. Regardless, these theories lead to the final disruption of inner membrane integrity and subsequent cell death. No change in

activity against CCUG 70662+ with modified lipid A suggests that the mode of action of the tested hexapeptides is not directly related to lipid A binding. Therefore, following these MIC results, we have utilized surface plasmon resonance experiments to directly measure the compounds' ability to translocate into lipid bilayers.

Table 1. MIC and ζ potentials for the tested peptides against *P. aeruginosa*, *S. aureus*, and the three *E. coli* strains: ATCC 25922, LPS deficient—NR 698, and colistin-resistant CCUG 70662, which was tested after cultivation with (+) and without (−) 4 $\mu\text{g}/\text{mL}$ of colistin, which caused a decrease of negative charge of the cell wall. MIC values for *P. aeruginosa*, *S. aureus*, and *E. coli* ATCC 25922 are reproduced from [45].

AMP	MIC ($\mu\text{g}/\text{mL}$)					
	<i>P. aeruginosa</i> ATCC 27853	<i>S. aureus</i> ATCC 9144	<i>E. coli</i> ATCC 25922	<i>E. coli</i> CCUG 70662−	<i>E. coli</i> CCUG 70662+	<i>E. coli</i> NR 698
Zeta potential	-	-	-21.3 ± 0.6 mV	-21.8 ± 0.8 mV	-14.3 ± 0.5 mV	-21.2 ± 0.6 mV
c(LWwNKr)	>250	>250	>250	>250	>250	32
c(WKWKWK)	>250	128	64	64	64	4
c(WRWRWR)	64	32	32	16	32	2
c(WWWKKK)	32	32	8	4	4	2
c(WWWRRR)	16	4	8	8	8	4

3.3. SPR and Choice of Lipid Models

SPR is emerging as the method of choice for measuring the partitioning of small compounds into lipid bilayers [32,45,46]. In SPR, liposomes are immobilized on the surface of the SPR chip, and AMPs are injected over the lipid layer at increasing concentrations. The measured change in the response of the plasmon wave allows for the determination of both the partitioning, K_P , which is defined as the concentration of peptide in the lipid bilayer over the concentration of peptide in water ($[\text{AMPs}]_{\text{in lipid}} / [\text{AMPs}]_{\text{in water}}$), and the dissociation rate k_{off} [32]. In addition, the dissociation constant (K_D —Supplementary Materials) can be estimated from the steady-state data using a generalized binding model. From the estimated K_D and the measured k_{off} values, the association rate k_{on} can be calculated (Equation (5)). For the lipid models, DMPC and DMPC:DMPG (95:5) liposomes, as well as DMPC liposomes containing 10% LPS (isolates from *E. coli* O111:B4), were used. The rationale behind the selection of models is their representation of key membranes. The DMPC liposomes possess a neutral membrane, akin to a eucaryotic membrane, and a useful probe of the lipophilic nature of the AMPs in the membrane interaction. The presence of 5% DMPG in the DMPC:DMPG liposomes provide a net anionic lipid surface, more similar to a procaryotic membrane. Finally, the LPS-containing liposomes are used to model the outer membrane of Gram-negative bacteria, with LPS being a unique and abundant component of the Gram-negative outer membrane.

3.4. Antimicrobial Activity Broadly Correlates with K_P for DMPC Liposomes

The measured K_P for the different peptide and lipid membrane combinations spans a wide range of values covering three orders of magnitude (Figure 2). c(WWWRRR) strongly partitions into the DMPC lipid bilayer, with the highest K_P of the series—6649, whereas the negative control peptide, c(LWwNKr), showed a very poor preference for DMPC with a K_P of 278. Introducing 5% of a negatively charged component (DMPG) to the liposomes doubled the K_P of all peptides except c(WKWKWK), where the increase was less substantial.

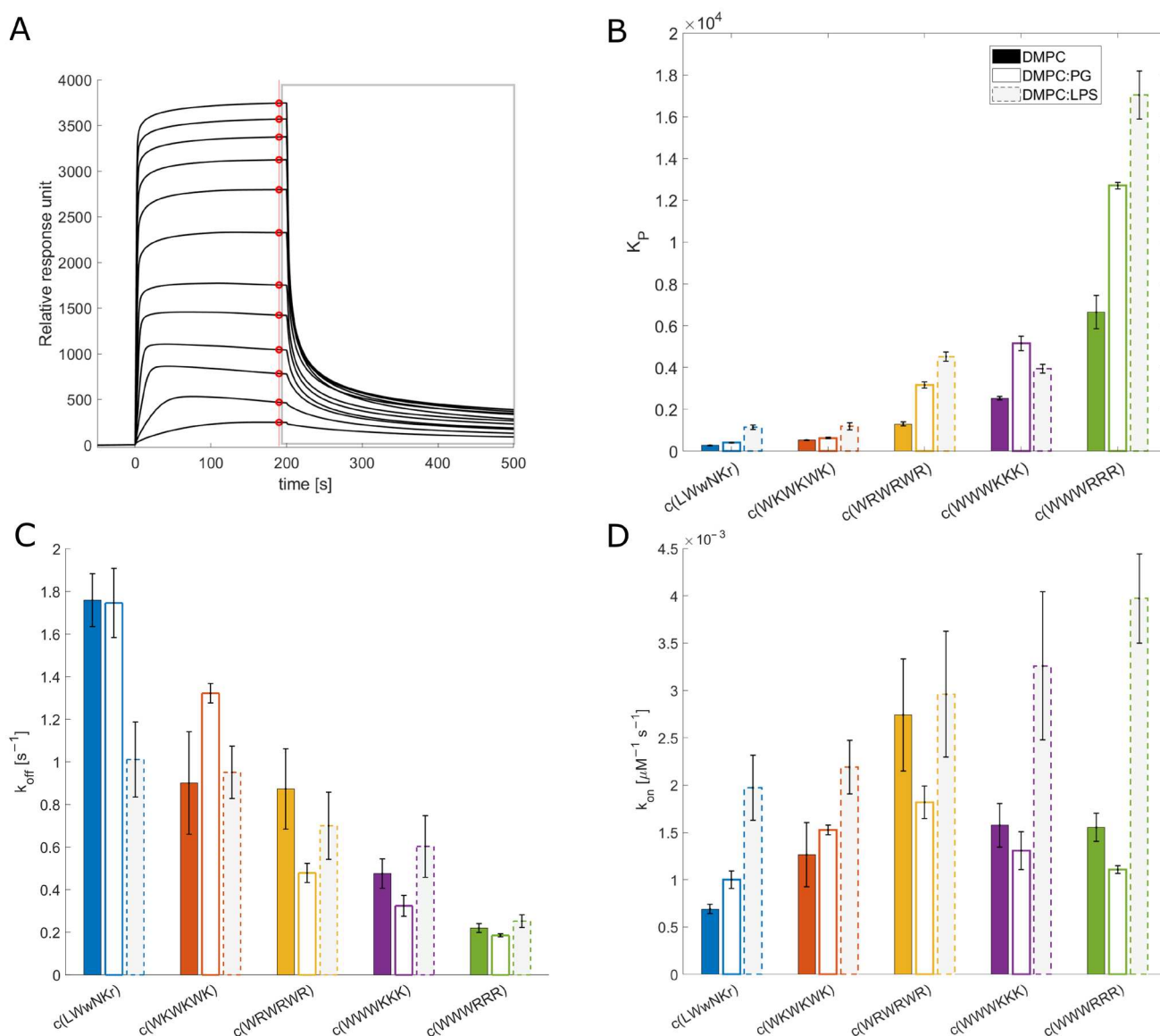


Figure 2. SPR results (A): Example SPR traces from c(WWWRRR) interaction (from 4 to 128 μM) with DMPC:PG liposomes. Red points indicate values used for steady-state fitting (to obtain K_D and K_P). The grey rectangle indicates the dissociation process which is used to obtain k_{off} , according to Figuera et al. (2017) [32]. (B): Partitioning constants K_P . Full, empty, and grey bars correspond to DMPC, DMPC:PG (95:5), and DMPC:LPS (90:10) liposomes, respectively. (C): Dissociation rate k_{off} . (D): Association rate k_{on} , which is obtained by calculation using measured K_D (Figure S1) and k_{on} . Values used in the plot are available in Table S1. Values for DMPC and DMPC:PG interaction are reproduced from [45].

The antimicrobial activity against Gram-positive *S. aureus* closely follows the K_P in DMPC liposomes. However, the trend for MIC against Gram-negative bacteria was less clear. The K_P is calculated from steady-state conditions, so the value corresponds to the sum of possible interaction states, including “coating” of the surface membrane, self-aggregation, and any penetration. This sum of values does not correspond closely with antibacterial activity against Gram-negative bacteria. This could be due to the hindrance of peptide translocation through LPS-loaded outer membranes of Gram-negatives [47]. Despite this, K_P can still be used for activity ranging against Gram-negatives, as the most active peptides have K_P values up to one order of magnitude higher than the inactive peptides.

3.5. The Initial Peptide:Membrane Association Is Affected by LPS

Both c(WWWRRR) and c(WWWKKK) display significantly different K_P and k_{off} values when measured against DMPC and DMPC:PG liposomes, a finding that was unexpected due to their similar MIC against *E. coli*. As such, further explorations of the model space were warranted to achieve a better model for the Gram-negative. To this end, 10% LPS was incorporated into the DMPC liposomes. LPS is a crucial component of the outer membrane of Gram-negative bacteria and is absent in Gram-positive bacteria. The ketodeoxyoctanic acid component in LPS confers an anionic charge to the DMPC:LPS construct [48]. We have previously observed that the binding efficacy of the peptides was significantly enhanced by the introduction of negatively charged head groups, pointing to the importance of negative charge in the membrane for binding the cationic peptides. When 10% LPS was introduced to the DMPC membranes, enhanced binding of the AMPs to the DMPC:LPS construct was observed—similar to the introduction of DMPG to the DMPC membranes.

All active peptides demonstrated an increase in K_P to the DMPC:LPS membranes compared to DMPC. A greater increase in binding to the LPS membrane relative to the negatively charged DMPC:PG membranes was also generally observed. However, two noteworthy exceptions can be identified. Firstly, c(LWwNKr) sees a four-fold increase in K_P compared to the DMPC and DMPC:PG constructs, suggesting a strong preference for the LPS. Secondly, although c(WWWKKK) sees an enhanced K_P when LPS is present, this effect is less pronounced than in DMPG:DMPC membranes. This indicates that the anionic charge of the lipid head group is a greater driver of the interaction between the AMP and the lipid bilayer than LPS. The presence of LPS has no effect on k_{off} for any of the active peptides. Instead, LPS significantly increases their association rate k_{on} . This is coherent with the proposal that LPS is a driving force for the initial interactions of AMPs but that it is not the final destination; this remains the lipid bilayer. Hence, the introduction of LPS in the bilayer boosts k_{on} while k_{off} remains largely unchanged.

LPS forms a unique combination of two barriers: a hydrophilic barrier is provided by a densely packed oligosaccharide core, and a hydrophobic barrier is provided by the hydrocarbon chain region of lipid A buried in the phospholipid membrane [49]. During the initial interaction between AMPs and LPS, the oligosaccharides can hinder the cationic AMPs and slow their localization into the membrane. This has been shown previously with the linear peptide K_5L_7 , where its association with LPS prevents it from reaching its target, reducing its activity [21]. Meanwhile, its diastereomer 4D- K_5L_7 , which can penetrate LPS, has higher activity. This modification of peptide configuration changes its binding mode with LPS without affecting the lipophilicity of the peptide and renders one peptide active and the other inactive. The difference in K_P for the clumped c(WWWRRR) and c(WWWKKK) is not reflected in their antimicrobial activity and can be interpreted as a consequence of the same LPS-induced phenomenon. In the presence of LPS, a much stronger association of c(WWWRRR) than c(WWWKKK) to the DMPC:LPS liposomes can be observed. If the activity was to follow affinity directly, c(WWWRRR) would be expected to be the most active of the two; however, both peptides have similar MIC values across all strains. This suggests that the antimicrobial activity of c(WWWRRR) is hindered by LPS association; that is to say, it is bound too tightly and strays out of the Goldilocks zone of LPS binding. The loss of activity in the presence of LPS can also be observed on the less lipophilic peptides (with lower K_P) c(LWwNKr), c(WKWKWK), and c(WRWRWR) as the MIC of these peptides is improved against NR-698. This strain has deficient LPS transport to the outer membrane, and as a result, there is a lower abundance of LPS in the outer membrane, which is replaced by phospholipids [41].

The SPR results, taken as a whole, suggest that peptides with a good combination of hydrophobicity and hydrophilicity, translating into a beneficial combination of k_{on} and k_{off} rates, will pass the LPS and outer membrane unperturbed reaching their antimicrobial target—either the inner membrane or an intracellular binding partner. From the tested peptides, the best combination of these rates is observed for c(WWWKKK)—a high k_{on} towards LPS allows efficient entry, but a relatively high k_{off} allows for translocation towards

the inner bilayer and prevents peptide sequestration in the outer membrane. Indeed, of the tested AMPs, c(WWWKKK) seems to have k_{off} and k_{on} rates within the most efficient combined range, following the Goldilocks principle. However, lysine is known to be generally less destructive towards lipid bilayers [17].

3.6. NMR Line Shape Analysis Can Be Used to Probe Binding Strength of AMPs towards Lipid Liposomes

In addition to SPR, 1D ^1H line shape NMR analysis was performed by titration of lipid liposomes into a fixed concentration of peptide. The size of the vesicle/AMP complex will result in line broadening and signal loss of the monitored compound with an increasing concentration of liposomes. This loss of the signal can be quantified, and the dissociation constant, K_{D} , can be estimated [36,50]. This method has previously been used to monitor the kinetics of enzymes and various inhibitors [51], to monitor protein binding to different lipid models [30], or in the qualitative assessment of AMP binding towards bacterial cells [52]. However, it is important to note that signal attenuation and line broadening are caused by relaxation, sample inhomogeneity, as well as contributions from the chemical exchange in the NMR time scale, which can vary for different molecules, different interactions, and different concentration ranges. Nevertheless, SPR showed that all five tested peptides have relatively slow off-rates, $k_{\text{off}} < 10 \text{ s}^{-1}$ [53]. If we assume that the off-rates for free liposomes in solution are comparable to those of immobilized and partially fused liposomes to the SPR chips [32], then the contributions from on/off-exchange processes are not expected to significantly affect the effective relaxation, and the major source of attenuation is fast relaxation caused by the slow correlation time of the peptides in complex with the lipid bilayer or LPS (Figure 3).

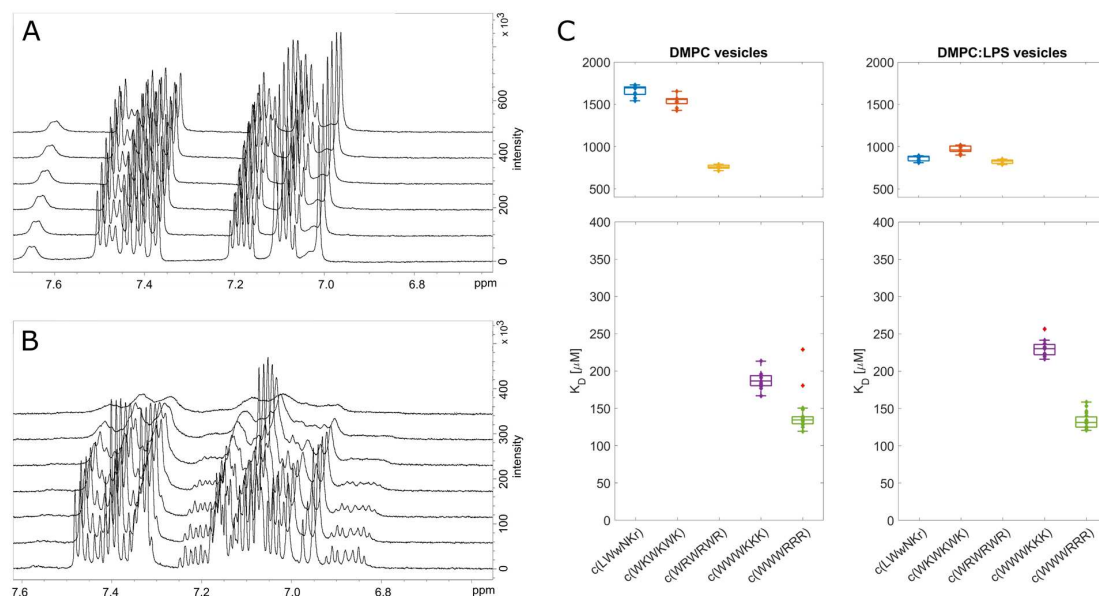


Figure 3. Line shape analysis of liposomes and AMP interaction. On the left are ^1H spectra of c(LWwNKr) (A) and c(WWWRRR) (B) after titration of DMPC liposomes (from 0 to 655 μM). The signal loss (attenuation) can then be used to quantify K_{D} (C). Stars in the box plots indicate outliers.

The results from the line shape analysis can be used to rate the peptides in the same order as SPR from highest to lowest affinity: $c(\text{WWWR}) > c(\text{WWWK}) \gg c(\text{WRWR}) > c(\text{WKWK}) > c(\text{LWwNKr})$. When LPS was present, the c(LWwNKr) and c(WKWKWK) peptides were most affected by the change, with a notable decrease in K_{D} . The most efficiently bound peptides, $c(\text{WWWR}) > c(\text{WWWK})$, were not affected by the LPS addition. The NMR line shape analysis data follows the same general qualitative trend of the SPR with minor quantitative differences, which could be caused by the different states of the lipid bilayer

between the NMR and SPR experiments. Nevertheless, line shape analysis offers a simple, alternative method to explore peptide binding towards model lipid membranes.

3.7. Live Cell NMR Highlights Strain Differences

While binding of the AMPs is a necessity to achieve bacterial killing, it may neither be sufficient to explain the differences between the activities of individual compounds nor the main factor for the mode of action. We aimed to expand the NMR toolbox to include live cells with the aim of connecting the observed lipid partitioning, MIC activities, and mode of action. To our knowledge, this is the first time the live cell NMR approach has been used to quantify peptide:bacterial cell binding.

For the live cell NMR, the same *E. coli* strains as for the MIC testing (see above) were used. In addition, the ATCC 25922 cell lysate was used to observe the effect the release of intracellular components has on peptide binding. To measure the initial AMP:bacterial cell binding, we titrated an increasing number of cells into a known and fixed concentration of AMP and monitored the signal attenuation of the peptide (Figure 4A,B). From this, we have extracted the K_D for each AMP towards the bacteria using the method developed by Shortridge et al. (2008) [36] (Figure 4C), which allows us to estimate the binding affinity based on signal broadening (see Section 2). There were major affinity differences for individual strains tested, as summarized in Figure 4D.

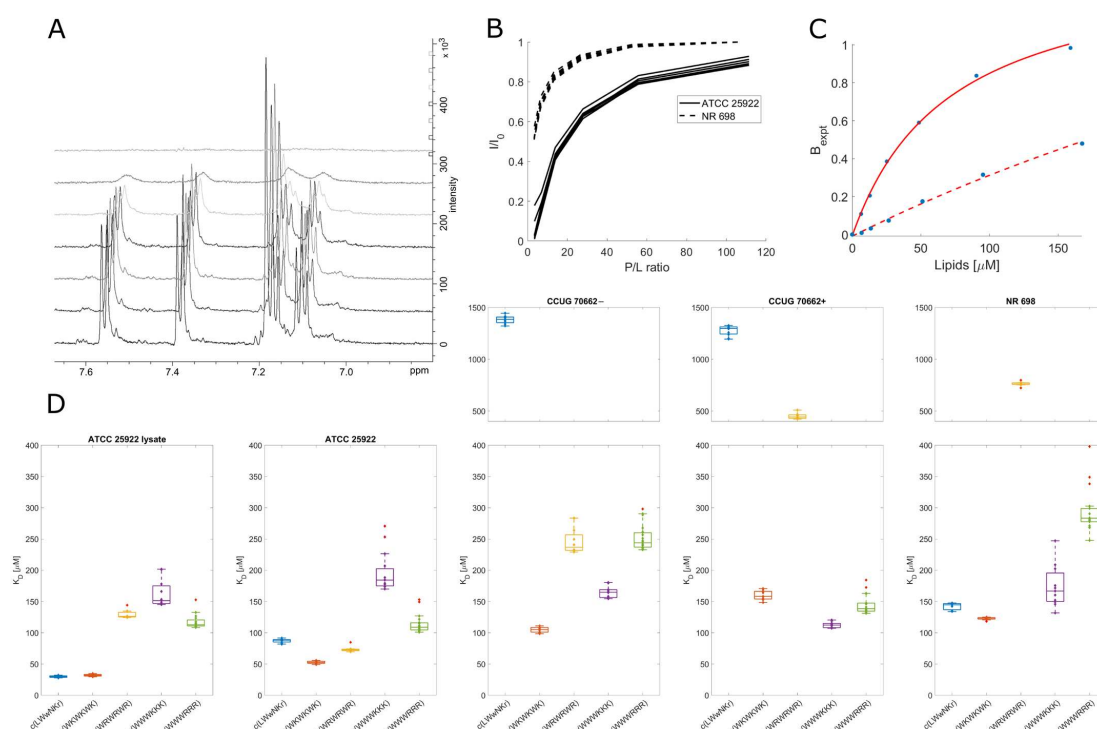


Figure 4. Peak broadening and signal loss during titration of *E. coli* live cells into AMPs. (A): ¹H NMR spectra of c(WRWRWR) during titration of *E. coli* ATCC 25922 (increasing cell concentration from bottom to top). (B): Changes in proton integrals for c(WRWRWR) during titration of *E. coli* ATCC 25922 and NR 698. During titration peptide:lipid ratio decreases with the addition of more cells. (C): Example of fit (according to Shortridge et al. (2008) [36]) of attenuation for tryptophan ¹H signal ζ3 of c(WRWRWR) in the presence of ATCC 25,992 (solid) or NR 698 (dashed). The assignment is included in Supplementary Materials. The concentration of lipids per bacterial cell is estimated to be 50 mmol [35]. (D): Overview of K_D obtained from live cell NMR. For the sonication method of ATCC 25922, see Supplementary Materials. CCUG 70662, a colistin-resistant strain, was grown without (–) and with (+) 4 μg/mL of colistin, which caused modification of lipid A and change of overall zeta potential (Table 1). NR 698 is strain deficient in LPS transport to the outer membrane, which causes membrane deficiency. Stars in the box plots indicate outliers.

3.8. Inactive Peptide c(LWwNKr) Binds Strongly to ATCC 25922 and NR 698

No direct correlation between the live cell affinity and MIC activity is seen in the data. Furthermore, there were significant differences between the different *E. coli* cell lines, highlighting AMP:strain specificity. Accordingly, a conservative interpretation of the differences in binding affinity between different strains is called for. However, interesting observations of the differences in AMP binding within each individual strain exist. For example, the SPR results showed that peptide c(LWwNKr) has poor partitioning and retention in a lipid bilayer, which is only slightly improved by the presence of LPS. Now, the markedly different affinity of c(LWwNKr) to different strains suggests that this peptide can interact with an unknown component (possibly membrane proteins) in the outer part of the bacterium, different than phospholipids and LPS, which is more abundant in ATCC 25922 and NR 698 and less present or mutated in CCUG 70662. In addition, the K_D is decreased for the lysate ATCC 25922 sample, suggesting non-specific binding with intracellular components (larger surface area) or increased availability of alternate binding sites. Still, binding of the c(LWwNKr) peptide provides no or very inefficient antimicrobial effect, as shown by its high MIC values.

3.9. Active Peptides Are Less Affected by Changes in Membrane Composition

There is no significant change in K_D for c(WWRRRR), c(WWWKKK), and c(WKWKWK) between the lysate and live cell ATCC 25922. This suggests that these peptides are able to interact with their target in intact cells and are not affected by the presence of free intracellular components. Meanwhile, with c(WRWRWR), there is a two-fold increase in K_D (a decrease in affinity after sonication). This may be caused by the partial disintegration of LPS molecules by sonication [54], and so eliminating the major binding site of c(WRWRWR).

The preference of c(WRWRWR) towards LPS can also be seen from a decreased affinity towards the activated CCUG 70662+, where lipid A is modified, compared to the native CCUG 70662-, highlighting the impact of the charged component of LPS on the binding of c(WRWRWR). The decrease in affinity may also be accompanied by a decrease in antimicrobial activity, with a single titer increase in MIC against CCUG 70662+ (Table 1). Taken together, this may indicate that c(WRWRWR) derives its activity by binding to the lipid A component of LPS. An increase in K_D is also observed in c(WKWKWK) when lipid A is modified, though this is less pronounced in comparison to c(WRWRWR). In opposition to this trend, both clumped peptides had decreased K_D when lipid A was modified. These results point to the main driving force of clumped peptides being hydrophobic interactions, while the alternating peptides are driven by charge. The SPR results support the observation that arginine is a more proficient LPS binder than lysine, suggesting that arginine-containing peptides should be most affected by the LPS modification. c(WWRRRR) is able to compensate for the reduced LPS affinity with increased hydrophobicity, which allows the peptide to efficiently partition into the lipid bilayer. However, this advantage is lost in the alternating peptide c(WRWRWR), and this is evidenced by the large increase in K_D towards the modified LPS strain.

Due to strain differences, it is not possible to compare ATCC 25922 and NR 698 directly. However, c(WRWRWR) demonstrated K_D differences between the two strains that were not evident for the other peptides. For ATCC 25922, the K_D of c(WRWRWR) is in a similar range to the other peptides (~50–200 μ M), and for NR 698, it moves beyond 500 μ M. This could be explained by the decrease of LPS in the outer membrane of NR 698. The notion that c(WRWRWR) binds lipid A may be further strengthened by the fact that there is reduced affinity towards the NR-698 strain, as the reduced transport of LPS to the outer membrane results in lower availability of lipid A [41].

3.10. Different Binding Modes of Hexapeptides towards ATCC 25922

The protons of most of the tested peptides experienced similar attenuation through the whole peptide; this led to uniform K_D values, as shown in Figure 5D. This is especially

true for peptides with alternating sequences where due to their molecule symmetry, we can only observe the average proton signal for dipeptides units (WR or WK). However, some combinations of the clumped peptides and strains showed outliers for specific protons. These outliers suggest that there is a shift in the average binding of the peptide, i.e., a preference for a particular orientation/conformation of the peptide or a change in the internal dynamics of the ring. A breakdown of these outliers for binding towards ATCC 25922 is in Figure 5. For c(WWWKKK), the highest K_D was observed for the protons on C β of the three tryptophan residues (Figure 5E). Meanwhile, the highest K_D for c(WWWRRR) was localized on C β of Arg2 and C γ of Arg3 (Figure 5F). This shows that, on average, there is a markedly different type of interaction between these two peptides and the bacteria. This deviation could be due to either structural differences or different interaction dynamics of the peptides—suggesting differences in binding modes.

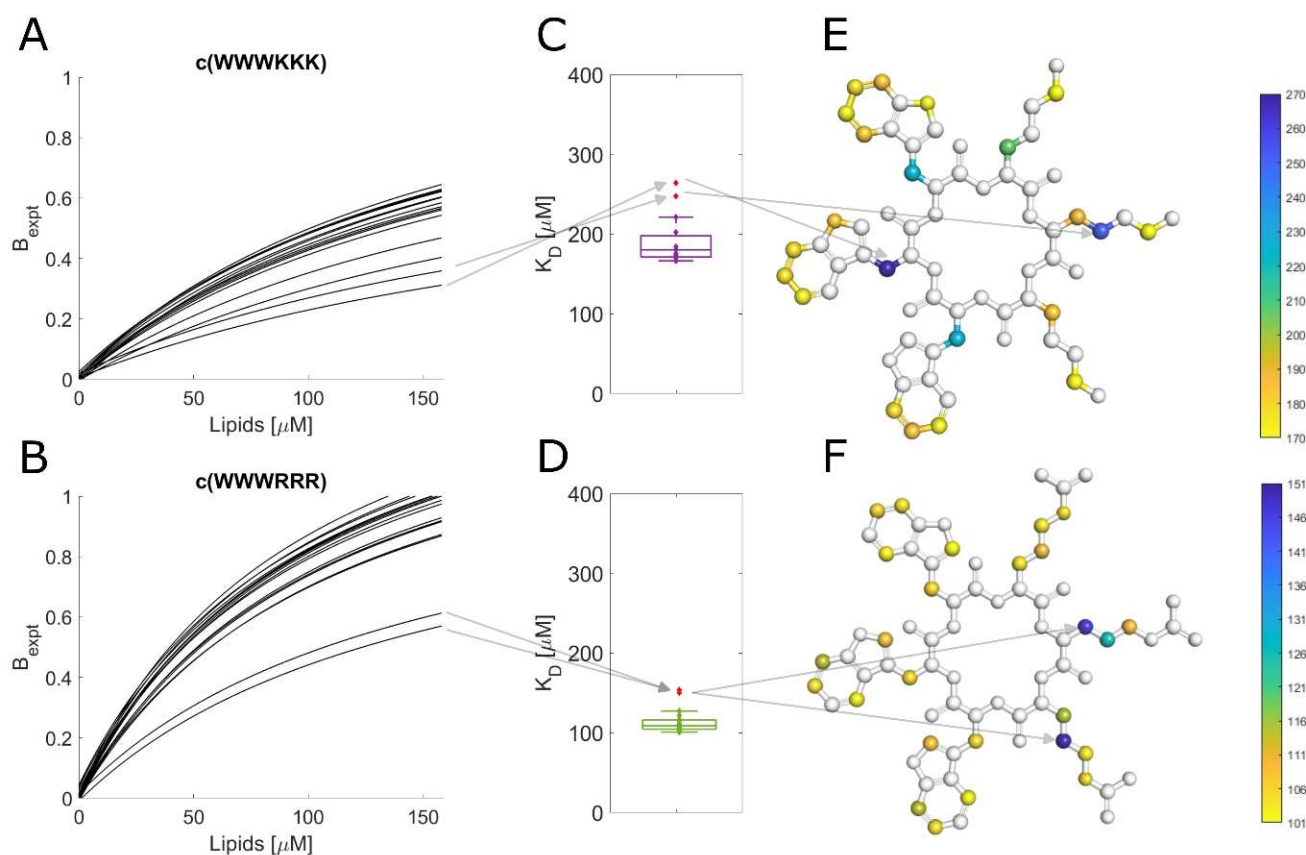


Figure 5. Comparison of c(WWWKKK) and c(WWWRRR) binding to ATCC 25922. (A,B): Fit of signal attenuation for all resolved proton traces according to Shortridge. (C,D): Box plot of K_D s obtained from the fit. Arrows highlight outliers from previous proton integrals. (E,F): Structures of peptides color-coded according to measured K_D . Arrows highlight the position of outliers: C β of Trp2 and C γ of Lys2 for c(WWWKKK) and C β of Arg2 and C γ of Arg3 for c(WWWRRR).

Arginine and lysine are both cationic residues with very similar properties. They are both basic amino acids with similar pK_A in an aqueous environment (~ 12.5 for Arg [55] and ~ 10.5 for Lys [56]), which enables them to be charged in most physiological circumstances. It has been shown that these amino acids can be, to some extent, exchangeable without affecting the peptide's secondary structure [15,57]. However, it has also been shown that Arg is more lipophilic as poly-Arg can cross cells more efficiently than oligomers of Lys [58]. In fact, the substitution of Arg for Lys has been shown to decrease the translocation efficiency of host defensive peptides [59,60]. Li et al. (2013) [17] showed that this enhanced lipophilicity could be explained by Arg's ability to maintain its diffused charge even in the

bilayer, unlike Lys, which seems to cross the bilayer deprotonated, or by the ability of Arg to form hydrogen bonds and cation- π interaction at the same time [18].

This difference in the nature of the arginine and lysine interactions with the lipid bilayer could explain some differences in signal attenuation observed in the live cell NMR. Where the poorer affinity of Lys will cause c(WWWKKK) to bind with preferable sidechains, meanwhile c(WWWRRR) will quickly orient itself in the bilayer, burying its hydrophobic groups with the Arg chains available for exchange closer to the lipid headgroups; this will lead to the higher disruption effect of arginine. Arg has a strong killing efficacy; however, it can be sequestered in the LPS layer [61]. Opposingly, Lys is able to reach the bilayer unhindered, though it is not as efficient in its disruption. The combination of these effects could lead to the similar antimicrobial activity of c(WWWKKK) and c(WWWRRR).

4. Conclusions

Using lipid model systems, we have observed a correlation between AMPs amino acid composition and its binding towards DMPC liposomes and its correlation of lipid affinity with antimicrobial activity. Arginine has shown to be a more efficient lipid binder than lysine (c(WWWRRR) > c(WWWKKK)), and the clumped hydrophobic bulk of peptides formed by tryptophan showed to be more efficient than alternating sequences (c(WWWRRR) > c(WRWRWR)). This trend was further enhanced when we introduced 5% of DMPG in liposomes, highlighting the increased selectivity of cationic peptides towards anionic membranes.

However, when moving from these simple models to more complex bacterial membranes, the complexity of interactions radically increases, and the simple correlation of binding = activity is lost. The presence of only one additional component, LPS, shows drastic changes in AMPs rating, partially explaining why peptides c(WWWRRR) and c(WWWKKK) have different lipid partitioning but the same MIC for Gram-negative bacteria; LPS efficiently binds to c(WWWRRR), lowering its potential.

Nevertheless, it is within live cells where the activity takes place, and these environments should be explored further. Live cell NMR (line shape analysis on live bacterial cells) could help bridge this gap and offer a simple tool to measure complex interaction processes. It has already helped to identify several potential binding partners, such as c(WRWRWR) and lipid A binding or c(LWwNKr) and protein interactions. Further investigations are required to fully understand the mode of action of these AMPs, but the identified targets provide a starting point.

Supplementary Materials: The following supporting information can be downloaded at: <https://www.mdpi.com/article/10.3390/biom13071155/s1>, Figure S1: K_D extracted from steady-state SPR analysis; Figure S2: The five peptides with numbered amino acids for structure elucidation; Figure S3: Labelled amino acids. Table S1: K_P and k_{off} values used in Figure 2; Table S2: γ_B/γ_F-1 ratios; Table S3: Full assignment of c(WWWKKK); Table S4: Full assignment of c(WKWKWK); Table S5: Full assignment of c(WRWRWR); Table S6: Full assignment of c(WWWRRR); Table S7: Full assignment of c(LWwNKr).

Author Contributions: M.J. conceived the research questions and designed the experiments. M.S., T.K. and J.S.M.S. established peptide synthesis. M.J. and M.B. collected and analyzed the SPR data. M.J., F.G.R. and P.R. collected and analyzed the NMR data. E.J. and J.U.E. obtained bacterial strains and collected MIC values. M.J., F.G.R. and P.R. prepared figures. J.U.E. and J.S.M.S. conceived, designed, and wrote the original grant proposal and obtained funding. All authors have read and agreed to the published version of the manuscript.

Funding: This project received funding from the DigiBiotics project (ID 269425) and by the NanoAMP project (ID 275186), both granted by the Research Council of Norway. The APC was covered by the open-access publishing fund, UiT.

Data Availability Statement: All processed data can be found in the paper and Supplementary Materials. The scripts utilized for data processing are available at [31]. Raw data can be obtained upon request.

Conflicts of Interest: The authors declare no conflict of interest.

References

1. Aslam, B.; Wang, W.; Arshad, M.I.; Khurshid, M.; Muzammil, S.; Rasool, M.H.; Nisar, M.A.; Alvi, R.F.; Aslam, M.A.; Qamar, M.U.; et al. Antibiotic Resistance: A Rundown of a Global Crisis. *Infect. Drug Resist.* **2018**, *11*, 1645–1658. [[CrossRef](#)] [[PubMed](#)]
2. Hancock, R.E.W.; Sahl, H.G. Antimicrobial and Host-Defense Peptides as New Anti-Infective Therapeutic Strategies. *Nat. Biotechnol.* **2006**, *24*, 1551–1557. [[CrossRef](#)] [[PubMed](#)]
3. Ageitos, J.M.; Sánchez-Pérez, A.; Calo-Mata, P.; Villa, T.G. Antimicrobial Peptides (AMPs): Ancient Compounds That Represent Novel Weapons in the Fight against Bacteria. *Biochem. Pharmacol.* **2017**, *133*, 117–138. [[CrossRef](#)]
4. Zasloff, M. Antimicrobial Peptides of Multicellular Organisms. *Nature* **2002**, *415*, 389–395. [[CrossRef](#)]
5. Chen, Y.; Mant, C.T.; Farmer, S.W.; Hancock, R.E.W.; Vasil, M.L.; Hodges, R.S. Rational Design of α -Helical Antimicrobial Peptides with Enhanced Activities and Specificity/Therapeutic Index. *J. Biol. Chem.* **2005**, *280*, 12316–12329. [[CrossRef](#)]
6. Dijksteel, G.S.; Ulrich, M.M.W.; Middelkoop, E.; Boekema, B.K.H.L. Review: Lessons Learned from Clinical Trials Using Antimicrobial Peptides (AMPs). *Front. Microbiol.* **2021**, *12*, 616979. [[CrossRef](#)] [[PubMed](#)]
7. Luo, X.; Chen, H.; Song, Y.; Qin, Z.; Xu, L.; He, N.; Tan, Y.; Dessie, W. Advancements, Challenges and Future Perspectives on Peptide-Based Drugs: Focus on Antimicrobial Peptides. *Eur. J. Pharm. Sci.* **2023**, *181*, 106363. [[CrossRef](#)]
8. Fjell, C.D.; Hiss, J.A.; Hancock, R.E.W.; Schneider, G. Designing Antimicrobial Peptides: Form Follows Function. *Nat. Rev. Drug Discov.* **2012**, *11*, 37–51. [[CrossRef](#)]
9. Zhang, Q.Y.; Yan, Z.B.; Meng, Y.M.; Hong, X.Y.; Shao, G.; Ma, J.J.; Cheng, X.R.; Liu, J.; Kang, J.; Fu, C.Y. Antimicrobial Peptides: Mechanism of Action, Activity and Clinical Potential. *Mil. Med. Res.* **2021**, *8*, 48. [[CrossRef](#)]
10. Wimley, W.C. Describing the Mechanism of Antimicrobial Peptide Action with the Interfacial Activity Model. *ACS Chem. Biol.* **2010**, *5*, 905–917. [[CrossRef](#)]
11. Pirtskhalava, M.; Amstrong, A.A.; Grigolava, M.; Chubinidze, M.; Alimbarashvili, E.; Vishnepolsky, B.; Gabrielian, A.; Rosenthal, A.; Hurt, D.E.; Tartakovsky, M. DBAASP v3: Database of Antimicrobial/Cytotoxic Activity and Structure of Peptides as a Resource for Development of New Therapeutics. *Nucleic Acids Res.* **2021**, *49*, D288–D297. [[CrossRef](#)] [[PubMed](#)]
12. Mishra, B.; Wang, G. The Importance of Amino Acid Composition in Natural Amps: An Evolutional, Structural, and Functional Perspective. *Front. Immunol.* **2012**, *3*, 31946. [[CrossRef](#)] [[PubMed](#)]
13. You, Y.H.; Liu, H.Y.; Zhu, Y.Z.; Zheng, H. Rational Design of Stapled Antimicrobial Peptides. *Amin. Acids* **2023**, *55*, 421–442. [[CrossRef](#)] [[PubMed](#)]
14. Clark, S.; Jowitt, T.A.; Harris, L.K.; Knight, C.G.; Dobson, C.B. The Lexicon of Antimicrobial Peptides: A Complete Set of Arginine and Tryptophan Sequences. *Commun. Biol.* **2021**, *4*, 605. [[CrossRef](#)]
15. Cutrona, K.J.; Kaufman, B.A.; Figueroa, D.M.; Elmore, D.E. Role of Arginine and Lysine in the Antimicrobial Mechanism of Histone-Derived Antimicrobial Peptides. *FEBS Lett.* **2015**, *589*, 3915–3920. [[CrossRef](#)]
16. Liu, Z.; Brady, A.; Young, A.; Rasimick, B.; Chen, K.; Zhou, C.; Kallenbach, N.R. Length Effects in Antimicrobial Peptides of the (RW)_n Series. *Antimicrob. Agents Chemother.* **2007**, *51*, 597–603. [[CrossRef](#)]
17. Li, L.; Vorobyov, I.; Allen, T.W. The Different Interactions of Lysine and Arginine Side Chains with Lipid Membranes. *J. Phys. Chem. B* **2013**, *117*, 11906–11920. [[CrossRef](#)]
18. Chan, D.I.; Prenner, E.J.; Vogel, H.J. Tryptophan- and Arginine-Rich Antimicrobial Peptides: Structures and Mechanisms of Action. *Biochim. Biophys. Acta Biomembr.* **2006**, *1758*, 1184–1202. [[CrossRef](#)]
19. Khemaissa, S.; Walrant, A.; Sagan, S. Tryptophan, More Than Just an Interfacial Amino Acid in the Membrane Activity of Cationic Cell-Penetrating and Antimicrobial Peptides. *Q. Rev. Biophys.* **2022**, *55*, e10. [[CrossRef](#)]
20. Wang, G.; Li, X.; Wang, Z. APD3: The Antimicrobial Peptide Database as a Tool for Research and Education. *Nucleic Acids Res.* **2016**, *44*, D1087. [[CrossRef](#)]
21. Papo, N.; Shai, Y. A Molecular Mechanism for Lipopolysaccharide Protection of Gram-Negative Bacteria from Antimicrobial Peptides. *J. Biol. Chem.* **2005**, *280*, 10378–10387. [[CrossRef](#)] [[PubMed](#)]
22. Papo, N.; Oren, Z.; Pag, U.; Sahl, H.G.; Shai, Y. The Consequence of Sequence Alteration of an Amphipathic α -Helical Antimicrobial Peptide and Its Diastereomers. *J. Biol. Chem.* **2002**, *277*, 33913–33921. [[CrossRef](#)] [[PubMed](#)]
23. Needham, B.D.; Trent, M.S. Fortifying the Barrier: The Impact of Lipid A Remodelling on Bacterial Pathogenesis. *Nat. Rev. Microbiol.* **2013**, *11*, 467–481. [[CrossRef](#)] [[PubMed](#)]
24. Southey, R. *The Story of the Three Bears*; W. NICOL: London, UK, 1839.
25. Joo, H.S.; Fu, C.I.; Otto, M. Bacterial Strategies of Resistance to Antimicrobial Peptides. *Philos. Trans. R. Soc. B Biol. Sci.* **2016**, *371*, 20150292. [[CrossRef](#)]
26. Eikås, K.D.R.; Krupová, M.; Kristoffersen, T.; Beerepoot, M.T.P.; Ruud, K. Can the Absolute Configuration of Cyclic Peptides Be Determined with Vibrational Circular Dichroism? *Phys. Chem. Chem. Phys.* **2023**, *25*, 14520–14529. [[CrossRef](#)]
27. Clinical and Laboratory Standards Institute. *Methods for Dilution Antimicrobial Susceptibility Tests for Bacteria That Grow Aerobically*; Clinical and Laboratory Standards Institute: Berwyn, PA, USA, 2006; ISBN 1562386263.
28. Torchilin, V.; Weissig, V. *Liposomes: A Practical Approach*; Oxford University Press: Oxford, UK, 2003; ISBN 0-19-963654-0.
29. Palusińska-Szys, M.; Zdybicka-Barabas, A.; Luchowski, R.; Reszeczyńska, E.; Śmiałek, J.; Mak, P.; Gruszecki, W.I.; Cytryńska, M. Choline Supplementation Sensitizes *Legionella Dumoffii* to Galleria Mellonella Apolipophorin III. *Int. J. Mol. Sci.* **2020**, *21*, 5818. [[CrossRef](#)]

30. Jakubec, M.; Bari as, E.; Furse, S.; Govasli, M.L.; George, V.; Turcu, D.; Iashchishyn, I.A.; Morozova-Roche, L.A.; Halskau,  . Cholesterol-containing Lipid Nanodiscs Promote an A-synuclein Binding Mode That Accelerates Oligomerization. *FEBS J.* **2020**, *288*, 1887–1905. [[CrossRef](#)]
31. Jakubec, M. GitHub—Martin Jakubec. Available online: <https://github.com/MarJakubec> (accessed on 21 June 2023).
32. Figueira, T.N.; Freire, J.M.; Cunha-Santos, C.; Heras, M.; Gonalves, J.; Moscona, A.; Porotto, M.; Salom e Veiga, A.; Castanho, M.A.R.B. Quantitative Analysis of Molecular Partition towards Lipid Membranes Using Surface Plasmon Resonance. *Sci. Rep.* **2017**, *7*, 45647. [[CrossRef](#)]
33. Li, B.; Yin, F.; Zhao, X.; Guo, Y.; Wang, W.; Wang, P.; Zhu, H.; Yin, Y.; Wang, X. Colistin Resistance Gene Mcr-1 Mediates Cell Permeability and Resistance to Hydrophobic Antibiotics. *Front. Microbiol.* **2020**, *10*, 3015. [[CrossRef](#)]
34. Beal, J.; Farny, N.G.; Haddock-Angelli, T.; Selvarajah, V.; Baldwin, G.S.; Buckley-Taylor, R.; Gershater, M.; Kiga, D.; Marken, J.; Sanchania, V.; et al. Robust Estimation of Bacterial Cell Count from Optical Density. *Commun. Biol.* **2020**, *3*, 512. [[CrossRef](#)]
35. Lee, S.; Bayley, H.; Lee, S.; Bayley, H. Reconstruction of the Gram-Negative Bacterial Outer-Membrane Bilayer. *Small* **2022**, *18*, 2200007. [[CrossRef](#)] [[PubMed](#)]
36. Shortridge, M.D.; Hage, D.S.; Harbison, G.S.; Powers, R. Estimating Protein-Ligand Binding Affinity Using High-Throughput Screening by NMR. *J. Comb. Chem.* **2008**, *10*, 948–958. [[CrossRef](#)] [[PubMed](#)]
37. Lau, Q.Y.; Ng, F.M.; Cheong, J.W.D.; Yap, Y.Y.A.; Tan, Y.Y.F.; Jureen, R.; Hill, J.; Chia, C.S.B. Discovery of an Ultra-Short Linear Antibacterial Tetrapeptide with Anti-MRSA Activity from a Structure-Activity Relationship Study. *Eur. J. Med. Chem.* **2015**, *105*, 138–144. [[CrossRef](#)] [[PubMed](#)]
38. Gopal, R.; Kim, Y.J.; Seo, C.H.; Hahm, K.S.; Park, Y. Reversed Sequence Enhances Antimicrobial Activity of a Synthetic Peptide. *J. Pept. Sci.* **2011**, *17*, 329–334. [[CrossRef](#)]
39. Jwad, R.; Weissberger, D.; Hunter, L. Strategies for Fine-Tuning the Conformations of Cyclic Peptides. *Chem. Rev.* **2020**, *120*, 9743–9789. [[CrossRef](#)]
40. Feng, S.; Liang, W.; Li, J.; Chen, Y.; Zhou, D.; Liang, L.; Lin, D.; Li, Y.; Zhao, H.; Du, H.; et al. MCR-1-Dependent Lipid Remodelling Compromises the Viability of Gram-Negative Bacteria. *Emerg. Microbes Infect.* **2022**, *11*, 1236–1249. [[CrossRef](#)] [[PubMed](#)]
41. Kr uger, M.; Richter, P.; Strauch, S.M.; Nasir, A.; Burkovski, A.; Antunes, C.A.; Meißgeier, T.; Schl ucker, E.; Schwab, S.; Lebert, M. What an Escherichia Coli Mutant Can Teach Us About the Antibacterial Effect of Chlorophyllin. *Microorganisms* **2019**, *7*, 59. [[CrossRef](#)]
42. Aghapour, Z.; Gholizadeh, P.; Ganbarov, K.; Bialvaei, A.Z.; Mahmood, S.S.; Tanomand, A.; Yousefi, M.; Asgharzadeh, M.; Yousefi, B.; Kafil, H.S. Molecular Mechanisms Related to Colistin Resistance in Enterobacteriaceae. *Infect. Drug Resist.* **2019**, *12*, 965–975. [[CrossRef](#)]
43. Rhouma, M.; Beaudry, F.; Th eriauult, W.; Letellier, A. Colistin in Pig Production: Chemistry, Mechanism of Antibacterial Action, Microbial Resistance Emergence, and One Health Perspectives. *Front. Microbiol.* **2016**, *7*, 1789. [[CrossRef](#)]
44. Elias, R.; Duarte, A.; Perdig o, J. A Molecular Perspective on Colistin and Klebsiella Pneumoniae: Mode of Action, Resistance Genetics, and Phenotypic Susceptibility. *Diagnostics* **2021**, *11*, 1165. [[CrossRef](#)]
45. Rainsford, P.; Rylandsholm, F.; Jakubec, M.; Juskewitz, E.; Silk, M.; Engh, R.A.; Isaksson, J. Label-Free Measurement of Antimicrobial Peptide Interactions with Lipid Vesicles and Nanodiscs Using Microscale Thermophoresis. *Sci. Rep.* **2023**, preprint. [[CrossRef](#)]
46. Juskewitz, E.; Mishchenko, E.; Dubey, V.K.; Jenssen, M.; Jakubec, M.; Rainsford, P.; Isaksson, J.; Andersen, J.H.; Ericson, J.U. Lulworthinone: In Vitro Mode of Action Investigation of an Antibacterial Dimeric Naphthopyrone Isolated from a Marine Fungus. *Mar. Drugs* **2022**, *20*, 277. [[CrossRef](#)] [[PubMed](#)]
47. Malanovic, N.; Lohner, K. Gram-Positive Bacterial Cell Envelopes: The Impact on the Activity of Antimicrobial Peptides. *Biochim. Biophys. Acta Biomembr.* **2016**, *1858*, 936–946. [[CrossRef](#)] [[PubMed](#)]
48. Rietschel, E.T.; Kirikae, T.; Schade, F.U.; Mamat, U.; Schmidt, G.; Loppnow, H.; Ulmer, A.J.; Z ahringer, U.; Seydel, U.; Padova, F.D.; et al. Bacterial Endotoxin: Molecular Relationships of Structure to Activity and Function. *FASEB J.* **1994**, *8*, 217–225. [[CrossRef](#)] [[PubMed](#)]
49. Snyder, S.; Kim, D.; McIntosh, T.J. Lipopolysaccharide Bilayer Structure: Effect of Chemotype, Core Mutations, Divalent Cations, and Temperature. *Biochemistry* **1999**, *38*, 10758–10767. [[CrossRef](#)]
50. Waudby, C.A.; Alfonso, I. An Introduction to One- and Two-Dimensional Lineshape Analysis of Chemically Exchanging Systems. *J. Magn. Reson. Open* **2023**, *16–17*, 100102. [[CrossRef](#)]
51. Luchinat, E.; Barbieri, L.; Cremonini, M.; Nocentini, A.; Supuran, C.T.; Banci, L. Drug Screening in Human Cells by NMR Spectroscopy Allows the Early Assessment of Drug Potency. *Angew. Chemie Int. Ed.* **2020**, *59*, 6535–6539. [[CrossRef](#)]
52. Pandit, G.; Biswas, K.; Ghosh, S.; Debnath, S.; Bidkar, A.P.; Satpati, P.; Bhunia, A.; Chatterjee, S. Rationally Designed Antimicrobial Peptides: Insight into the Mechanism of Eleven Residue Peptides against Microbial Infections. *Biochim. Biophys. Acta Biomembr.* **2020**, *1862*, 183177. [[CrossRef](#)]
53. Waudby, C.A.; Ramos, A.; Cabrita, L.D.; Christodoulou, J. Two-Dimensional NMR Lineshape Analysis. *Sci. Rep.* **2016**, *6*, 95–109. [[CrossRef](#)]
54. Komuro, T.; Murai, T.; Kawasaki, H. Effect of Sonication on the Dispersion State of Lipopolysaccharide and Its Pyrogenicity in Rabbits. *Chem. Pharm. Bull.* **1987**, *35*, 4946–4952. [[CrossRef](#)]
55. Angyal, S.J.; Warburton, W.K. The Basic Strengths of Methylated Guanidines. *J. Chem. Soc.* **1951**, 2492–2494. [[CrossRef](#)]
56. Harms, M.J.; Schlessman, J.L.; Chimenti, M.S.; Sue, G.R.; Damjanovi c, A.; Damjanovi c, D.; Garc a, B.; Garc a-Moreno, G. A Buried Lysine That Titrates with a Normal PKa: Role of Conformational Flexibility at the Protein–Water Interface as a Determinant of PKavalues. *Protein Sci.* **2008**, *17*, 833–845. [[CrossRef](#)] [[PubMed](#)]

57. Koo, Y.S.; Kim, J.M.; Park, I.Y.; Yu, B.J.; Jang, S.A.; Kim, K.S.; Park, C.B.; Cho, J.H.; Kim, S.C. Structure–Activity Relations of Parasin I, a Histone H2A-Derived Antimicrobial Peptide. *Peptides* **2008**, *29*, 1102–1108. [[CrossRef](#)]
58. Mitchell, D.J.; Steinman, L.; Kim, D.T.; Fathman, C.G.; Rothbard, J.B. Polyarginine Enters Cells More Efficiently than Other Polycationic Homopolymers. *J. Pept. Res.* **2000**, *56*, 318–325. [[CrossRef](#)]
59. Åmand, H.L.; Fant, K.; Nordén, B.; Esbjörner, E.K. Stimulated Endocytosis in Penetratin Uptake: Effect of Arginine and Lysine. *Biochem. Biophys. Res. Commun.* **2008**, *371*, 621–625. [[CrossRef](#)]
60. Zou, G.; De Leeuw, E.; Li, C.; Pazgier, M.; Li, C.; Zeng, P.; Lu, W.Y.; Lubkowski, J.; Lu, W. Toward Understanding the Cationicity of Defensins: Arg and Lys Versus Their Noncoded Analogs. *J. Biol. Chem.* **2007**, *282*, 19653–19665. [[CrossRef](#)]
61. Savini, F.; Loffredo, M.R.; Troiano, C.; Bobone, S.; Malanovic, N.; Eichmann, T.O.; Caprio, L.; Canale, V.C.; Park, Y.; Mangoni, M.L.; et al. Binding of an Antimicrobial Peptide to Bacterial Cells: Interaction with Different Species, Strains and Cellular Components. *Biochim. Biophys. Acta Biomembr.* **2020**, *1862*, 183291. [[CrossRef](#)]

Disclaimer/Publisher’s Note: The statements, opinions and data contained in all publications are solely those of the individual author(s) and contributor(s) and not of MDPI and/or the editor(s). MDPI and/or the editor(s) disclaim responsibility for any injury to people or property resulting from any ideas, methods, instructions or products referred to in the content.

Supplementary material for:

Goldilocks Dilemma: LPS Works Both as the Initial Target and a Barrier for the Antimicrobial Action of Cationic AMPs on *E. coli*

Martin Jakubec ^{1,*}, Fredrik G. Rylandsholm ¹, Philip Rainsford ¹, Mitchell Silk ¹, Maxim Bril'kov ², Tone Kristoffersen ¹, Eric Juskewitz ³, Johanna U. Ericson ³ and John Sigurd M. Svendsen ¹

¹ Department of Chemistry, Faculty of Science and Technology, UiT the Arctic University of Norway, 9019 Tromsø, Norway; fredrik.g.rylandsholm@uit.no (F.G.R.); philip.rainsford@uit.no (P.R.); tone.kristoffersen@uit.no (T.K.); john-sigurd.svendsen@uit.no (J.S.M.S.)

² Department of Pharmacy, Faculty of Health Sciences, UiT the Arctic University of Norway, 9019 Tromsø, Norway; maxim.brilkov@uit.no

³ Department of Medical Biology, Faculty of Health Sciences, UiT the Arctic University of Norway, 9019 Tromsø, Norway; johanna.e.sollid@uit.no (J.U.E.)

* Correspondence: martin.jakubec@uit.no

Peptide chemical analysis

The crude cyclic peptides were purified by preparative reverse phase-HPLC using gradients from 15 to 40 % buffer B (buffer A: water/0.1% TFA, buffer B: acetonitrile/0.1% TFA) over 50 minutes (11 ml/min flow rate). c(LWwNKr) was isolated as a white fluffy solid. **HRMS** (ESI): Calculated for: $C_{44}H_{62}N_{13}O_7^+$ [M+H]⁺ 884.4890; found; 884.4885. c(WWWRRR) was isolated as a white solid. **HRMS** (ESI): Calculated for: $C_{51}H_{68}N_{18}O_6^{2+}$ [M+H]²⁺ 514.2779; found; 514.2775. c(WRWRWR) was isolated as a white solid. **HRMS** (ESI): Calculated for: $C_{51}H_{68}N_{18}O_6^{2+}$ [M+H]²⁺ 514.2779; found; 514.2773. c(WWWKKK) was isolated as a white solid. **HRMS** (ESI): Calculated for: $C_{51}H_{68}N_{12}O_6^{2+}$ [M+H]²⁺ 472.2687; found; 472.2682. c(WKWKWK) was isolated as a white solid. **HRMS** (ESI): Calculated for: $C_{51}H_{68}N_{12}O_6^{2+}$ [M+H]²⁺ 472.2687; found; 472.2681.

Table S1: K_p and k_{off} from Figure 2.

AMP	K_p			k_{off} (s ⁻¹)		
	DMPC	DMPC:PG	DMPC:LPS	DMPC	DMPC:PG	DMPC:LPS
LWwNKr	278 ± 8	401 ± 19	1145 ± 99	1.76 ± 0.12	1.75 ± 0.16	1.01 ± 0.18
WKWKWK	531 ± 10	630 ± 33	1191 ± 166	0.90 ± 0.24	1.32 ± 0.05	0.95 ± 0.12
WRWRWR	1299 ± 94	3160 ± 15	4520 ± 215	0.87 ± 0.19	0.48 ± 0.05	0.70 ± 0.16
WWWKKK	2534 ± 80	5156 ± 34	3943 ± 218	0.48 ± 0.07	0.32 ± 0.05	0.60 ± 0.15
WWWRRR	6649 ± 80	12705 ± 16	17040 ± 1150	0.22 ± 0.02	0.19 ± 0.01	0.25 ± 0.03

Table S2: γ_B/γ_F -1 ratios.

AMP	γ_B/γ_F -1						
	DMPC	DMPC:LPS	<i>E. coli</i> ATCC 25922 lysate	<i>E. coli</i> ATCC 25922	<i>E. coli</i> CCUG 70662-	<i>E. coli</i> CCUG 70662+	<i>E. coli</i> NR 698
LWwNKr	7.830	2.620	0.035	0.106	5.202	4.990	0.186
WKWKWK	7.127	3.915	0.044	0.083	0.170	0.295	0.180
WRWRWR	2.900	3.475	0.275	0.143	0.549	1.062	3.059
WWWKKK	0.297	0.402	0.225	0.289	0.317	0.197	0.370
WWWRRR	0.247	0.199	0.216	0.239	0.473	0.238	0.819

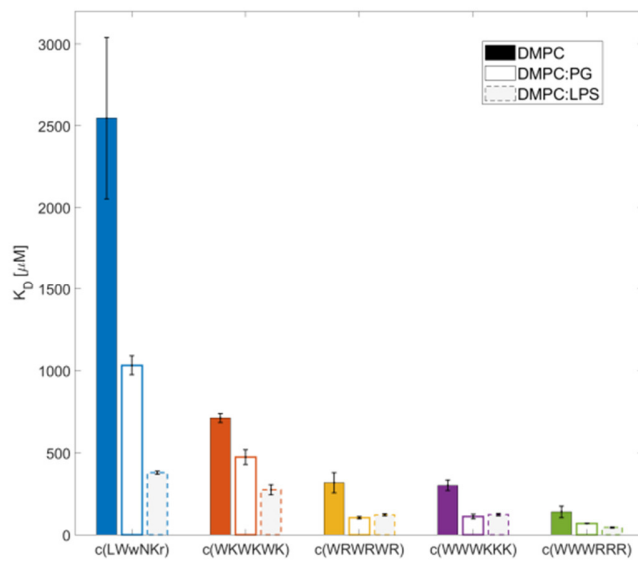


Figure S1: K_D extracted from steady state SPR analysis

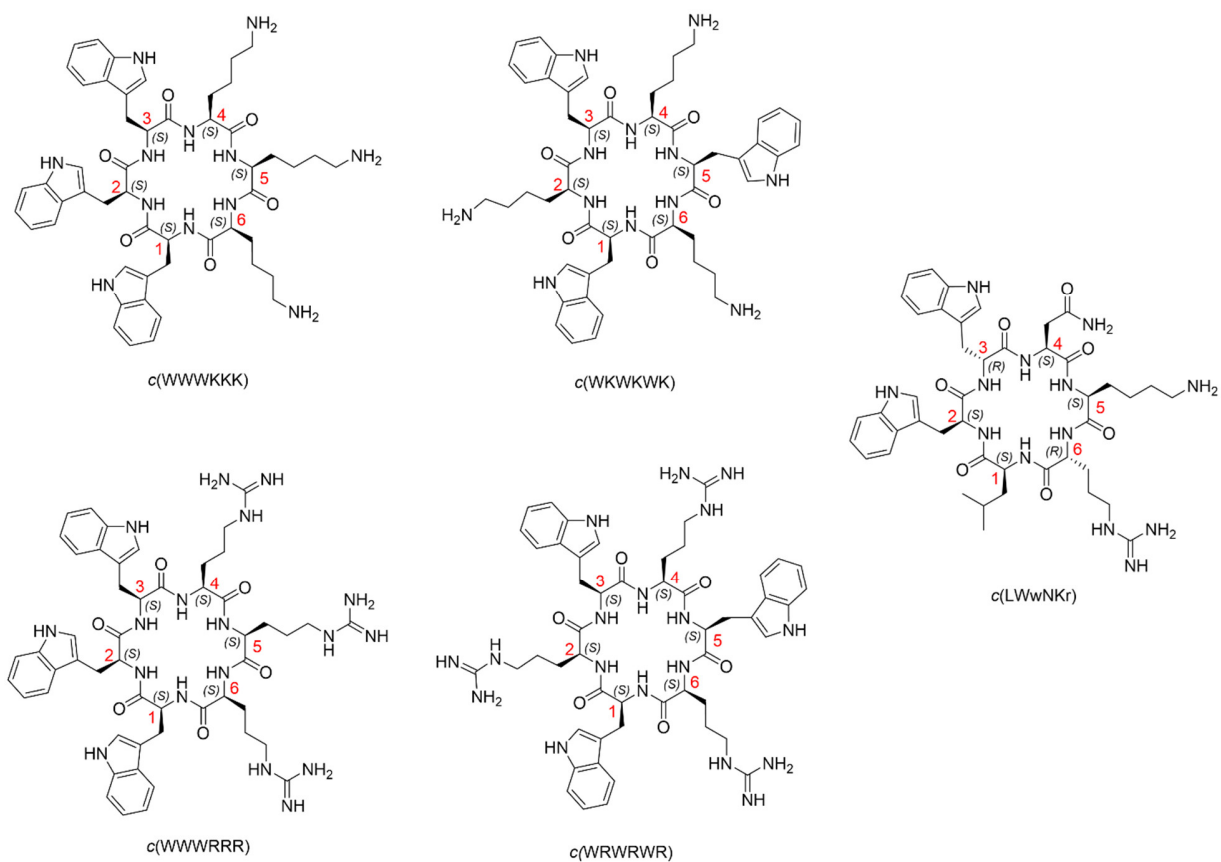


Figure S2: The five peptides with numbered amino acids for structure elucidation.

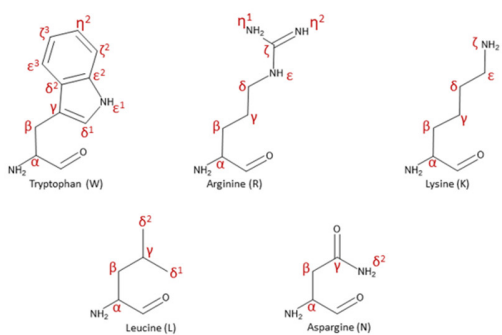


Figure S3: Labelled amino acids.

Table S3: Full assignment of c(WWWKKK) according to Figure S2

c(WWWKKK)														
Residue #	Amino acid	Chemical shift (δ)												
		NH α	CO	α	β	ϵ 1	δ 1	γ	δ 2	ϵ 3	ζ 3	η 2	ζ 2	ϵ 2
1	W - Tryptophan	7.85	-	4.48	2.99/2.86	10.10	7.06	-	-	7.46	7.09	7.17	7.41	-
	$^{13}\text{C}/^{15}\text{N}$	118.01	173.41	54.70	26.00	129.28	124.45	108.96	127.01	118.48	119.41	122.04	111.98	136.34
2	W - Tryptophan	NH α	CO	α	β	ϵ 1	δ 1	γ	δ 2	ϵ 3	ζ 3	η 2	ζ 2	ϵ 2
	$^{13}\text{C}/^{15}\text{N}$	7.33	-	4.51	3.11/2.87	10.05	6.95	-	-	7.30	7.05	7.15	7.39	-
3	W - Tryptophan	NH α	CO	α	β	ϵ 1	δ 1	γ	δ 2	ϵ 3	ζ 3	η 2	ζ 2	ϵ 2
	$^{13}\text{C}/^{15}\text{N}$	119.00	172.67	54.55	26.36	130.00	124.76	108.30	127.06	118.30	119.59	122.16	112.04	136.20
4	K - Lysine	NH α	CO	α	β	γ	δ	ϵ	ζ					
	$^{13}\text{C}/^{15}\text{N}$	7.84	-	3.75	1.49/1.67	0.66	1.30/1.58	2.26	7.41	-	-	-	-	-
5	K - Lysine	NH α	CO	α	β	γ	δ	ϵ	ζ					
	$^{13}\text{C}/^{15}\text{N}$	120.75	173.08	54.90	30.07	21.86	26.19	39.24	96.51	-	-	-	-	-
6	K - Lysine	NH α	CO	α	β	γ	δ	ϵ	ζ					
	$^{13}\text{C}/^{15}\text{N}$	7.77	-	3.88	1.22	0.85/0.74	1.33	2.61	7.37	-	-	-	-	-
		119.35	173.76	54.55	29.43	21.86	X	39.24	96.52	-	-	-	-	-

Table S4: Full assignment of c(WKWKWK) according to Figure S2.

c(WKWKWK)														
Residue #	Amino acid	Chemical shift (δ)												
		NH α	CO	α	β	ϵ 1	δ 1	γ	δ 2	ϵ 3	ζ 3	η 2	ζ 2	ϵ 2
1	W - Tryptophan	7.99	-	4.54	3.09	10.17	7.16	-	-	-	-	7.17	7.37	-
	^1H	119.292	173.01	54.66	25.99	129.67	124.35	108.77	127.06	118.37	119.46	122.03	112.04	136.21
2	K - Lysine	7.62	-	3.89	1.42	0.67	1.28	2.55	7.35	-	-	-	-	-
	$^{13}\text{C}/^{15}\text{N}$	120.24	172.91	54.55	29.59	21.59	26.21	39.25	134.12/95.83	-	-	-	-	-

Table S5: Full assignment of c(WRWRWR) according to Figure S2.

c(WRWRWR)														
Residue #	Amino acid	Chemical shift (δ)												
		NH α	CO	α	β	ϵ 1	δ 1	γ	δ 2	ϵ 3	ζ 3	η 2	ζ 2	ϵ 2
1	W - Tryptophan	8.07	-	4.54	3.13	10.13	7.16	-	-	7.53	7.10	7.16	7.37	-
	^1H	119.43	172.84	54.84	26.04	129.65	124.44	108.78	126.96	118.23	119.39	122.07	111.97	136.23
2	R - Arginine	7.65	-	3.90	1.41	0.82	2.71	6.77	-	X	X	-	-	-
	$^{13}\text{C}/^{15}\text{N}$	119.96	172.88	54.39	27.28	23.71	40.44	84.78	153.71	X	X	-	-	-

Table S6: Full assignment of c(WWWRRR) according to Figure S2.

c(WWWRRR)														
Residue #	Amino acid	Chemical shift (δ)												
		NH α	CO	α	β	ϵ 1	δ 1	γ	δ 2	ϵ 3	ζ 3	η 2	ζ 2	ϵ 2
1	W - Tryptophan	7.88	-	4.52	2.85/3.04	10.03	7.04	-	-	7.46	7.07	7.15	7.38	-
	$^{13}\text{C}/^{15}\text{N}$	118.00	173.20	54.68	26.04	129.05	124.44	109.20	126.79	118.31	119.29	122.02	111.89	136.27
2	W - Tryptophan	7.42	-	4.54	2.98/3.03	10.05	7.02	-	-	7.38	7.08	7.16	7.40	-
	$^{13}\text{C}/^{15}\text{N}$	119.05	172.55	54.36	26.68	130.00	124.76	108.40	127.37	118.30	119.44	122.03	112.02	136.22
3	W - Tryptophan	7.64	-	4.43	2.85/3.05	10.03	6.94	-	-	7.36	7.04	7.12	7.33	-
	$^{13}\text{C}/^{15}\text{N}$	121.23	173.10	55.49	26.04	129.50	124.27	108.40	126.82	118.17	119.34	122.03	111.87	136.23
4	R - Arginine	7.94	-	3.72	1.58/1.50	0.74/0.87	2.75/2.73	6.77	-	X	X	-	-	-
	$^{13}\text{C}/^{15}\text{N}$	120.23	172.89	54.85	26.37	24.11	40.38	85.03	156.63	X	X	-	-	-
5	R - Arginine	8.15	-	4.18	1.48/1.75	1.49	3.11	7.12	-	X	X	-	-	-
	$^{13}\text{C}/^{15}\text{N}$	119.02	172.78	53.24	27.98	24.43	40.54	84.97	156.89	X	X	-	-	-
6	R - Arginine	7.87	-	3.85	1.29/1.24	0.85/0.93	2.78/2.72	6.80	-	X	X	-	-	-
	$^{13}\text{C}/^{15}\text{N}$	119.50	173.54	54.83	27.01	23.76	40.21	84.97	156.57	X	X	-	-	-

Table S7: Full assignment of c(LWwNKr) according to Figure S2.

c(LWwNKr)													
Residue #	Amino acid	Chemical shift (δ)											
		NH α	CO	α	β	γ	δ						
1	L - Leucine												
	1H	8.597	-	4.01	1.32	1.43	0.80/0.72	-	-	-	-	-	-
	13C/15N	126.00	173.54	53.33	39.17	24.35	22.25/19.98	-	-	-	-	-	-
2	W - Tryptophan												
	1H	7.45	-	4.70	3.09/3.13	10.01	7.10	-	-	7.49	7.07	7.19	7.43
	13C/15N	117.50	172.00	53.34	28.21	129.07	124.68	108.88	127.14	118.34	119.17	121.87	113.01 136.17
3	w - (R)-Tryptophan												
	1H	8.35	-	3.90	2.82/2.91	10.00	7.00	-	-	7.36	7.08	7.16	7.40
	13C/15N	126.00	174.22	56.72	25.70	129.48	124.58	108.26	126.50	118.15	119.35	122.01	112.05 136.25
4	N - Asparagine												
	1H	7.68	-	4.28	1.70/2.36	-	6.39/7.03	-	-	-	-	-	-
	13C/15N	124.00	172.41	49.63	34.71	174.06	110.50	-	-	-	-	-	-
5	K - Lysine												
	1H	7.67	-	4.33	1.52/1.72	1.24/1.15	1.52	2.86	X	-	-	-	-
	13C/15N	119.00	172.23	52.56	31.03	21.62	26.24	39.49	X	-	-	-	-
6	r - (R)-Arginine												
	1H	8.11	-	4.21	1.60	1.36/1.49	3.08	7.11	-	X	X	-	-
	13C/15N	124.00	174.05	53.66	27.34	24.51	40.61	84.49	156.81	X	X	-	-

Paper III



OPEN

Label-free measurement of antimicrobial peptide interactions with lipid vesicles and nanodiscs using microscale thermophoresis

Philip Rainsford¹, Fredrik G. Rylandsholm¹, Martin Jakubec¹, Mitchell Silk¹, Eric Juskewitz², Johanna U. Ericson², John-Sigurd Svendsen¹, Richard A. Engh¹ & Johan Isaksson^{1,3}✉

One strategy to combat antimicrobial resistance is the discovery of new classes of antibiotics. Most antibiotics will at some point interact with the bacterial membrane to either interfere with its integrity or to cross it. Reliable and efficient tools for determining the dissociation constant for membrane binding (K_D) and the partitioning coefficient between the aqueous- and membrane phases (K_P) are therefore important tools for discovering and optimizing antimicrobial hits. Here we demonstrate that microscale thermophoresis (MST) can be used for label-free measurement of K_D by utilising the intrinsic fluorescence of tryptophan and thereby removing the need for chromophore labelling. As proof of principle, we have used the method to measure the binding of a set of small cyclic AMPs to large unilamellar vesicles (LUVs) and two types of lipid nanodiscs assembled by styrene maleic acid (SMA) and quaternary ammonium SMA (SMA-QA). The measured K_D values correlate well with the corresponding measurements using surface plasmon resonance (SPR), also broadly reflecting the tested AMPs' minimal inhibition concentration (MIC) towards *S. aureus* and *E. coli*. We conclude that MST is a promising method for fast and cost-efficient detection of peptide-lipid interactions or mapping of sample conditions in preparation for more advanced studies that rely on expensive sample preparation, labelling and/or instrument time.

Antimicrobial peptides (AMPs) have attracted increasing attention as a source of inspiration to combat the looming antimicrobial resistance crisis as the discovery of new antibiotics classes has ground to a halt¹. AMPs are a class of peptides that have antimicrobial activity, though they are also known to possess some anti-fungal and anti-cancer properties^{2,3}. They are typically short, cationic peptides of about 12–50 amino acids, with typically at least 4 residues required for activity⁴. Found in most living organisms, they are natural and indispensable components of innate immune defences^{5–8}. Currently, more than 20 000 peptide sequences with antimicrobial properties are published in dedicated depositories^{9–13}, providing a pool of potential therapeutic candidates. The antimicrobial mode of action of most AMPs seems to be to target the integrity and/or the electric potential of the membrane bilayer, or to have multiple targets and combinations of modes of action—something that makes resistance more difficult to develop and comes with a higher fitness cost to maintain. With some exceptions, this contrasts with traditional antibiotics, which usually have a well-defined target. A second advantage of AMPs is that there is no requirement to entirely cross the membrane, with membrane active peptides often exerting their activities by disrupting, permeabilising or lysing the bacterial membrane itself^{14,15}.

AMP affinity towards bacterial membranes is often described in two ways: As a binding event which can be described via the dissociation constant K_D ¹⁶; or as a biphasic system, where the AMP interaction with lipids is viewed as a partitioning between a lipid phase and an aqueous phase, characterized by the partitioning constant K_P ¹⁷. Both K_D and K_P are thus useful descriptors for screening compounds based on their interactions with the target bacterial membrane.

¹Department of Chemistry, Faculty of Science and Technology, UiT the Arctic University of Norway, 9019 Tromsø, Norway. ²Research Group for Host Microbe Interactions, Department of Medical Biology, Faculty of Health Sciences, UiT the Arctic University of Norway, 9019 Tromsø, Norway. ³Natural Products and Medicinal Chemistry, Department of Pharmacy, Faculty of Health Sciences, UiT the Arctic University of Norway, 9037 Tromsø, Norway. ✉email: johan.isaksson@uit.no

Current methods used to assess lipid affinity typically suffer from several disadvantages. They may not be applicable to stronger bindings (NMR)¹⁸, require labelling that impacts binding (fluorescence assays)¹⁹, be time-consuming (NMR and SPR)^{20,21}, demand large quantities of samples (NMR) or require fine-tuning for each individual compound (SPR and ITC)^{20,21}. Microscale thermophoresis (MST) is a method that does not possess these disadvantages²². It is a simple but powerful tool, that enables binding parameter determination by observation of the effects of binding on a fluorophore and on the relative thermophoretic properties of the complexes formed. Bindings are obtained by monitoring changes in the fluorescence intensity of a complex over time upon exposure to an IR laser. The laser heats a series of samples with differing ligand concentrations, causing a redistribution of molecules according to their relative Gibbs energies in solution at the different temperatures (thermophoresis). Changes in fluorescence due to ligand binding effects are monitored upon heating and re-cooling. The method is sensitive to changes in fold, shape, solvation shell, charge, or overall size of the ligand-bound complex. These changes can affect the local environment of a fluorophore by altering dynamic and static quenching, as well as the thermophoretic properties of the complex, and make MST sensitive to potentially minor changes in properties that arise from binding²³. MST is currently primarily used to assess biomolecular interactions, including the binding of ligands to various substrates²² and polymerisation²⁴. A previous related application of MST by Yu et al. assessed the binding of an AMP using FITC-labelling²⁵. MST can be performed using fluorophore labelling or label-free, taking advantage of intrinsically fluorescent amino acids like W, Y and F. The near ubiquity of W in many AMPs provides an opportunity to study AMP binding properties directly by utilising the intrinsic fluorescence of W. Additional important advantages of MST are low sample requirements, short measurement times and simple experimental setup^{20,21,26}.

Herein we demonstrate that MST is a viable method for the rapid label-free determination of AMP affinity towards lipid bilayers. We used label-free MST to study five cyclic antimicrobial hexapeptides (Fig. 1) and their bindings to three lipid systems, comparing the results to SPR data on binding to lipid vesicles.

AMPs 1–4 were selected based on a previously established pharmacophore of alternating versus clustered distribution of charged and hydrophobic moieties^{27–31}, where the clustering of W and charged residues is shown to be positively correlated with antimicrobial activity⁴. AMPs 1–4 were confirmed to have antimicrobial activity (Table 1) and are a combination of alternating and clustered W residues with either R or K residues. AMP 5 was included as a negative control, as it was inactive against the tested bacterial strains (Table 1) and it showed poor lipophilic preference.

The three different lipid systems that were selected for the study were large unilamellar vesicles (LUVs), styrene-maleic acid (SMA) nanodiscs³², and styrene-maleic acid functionalised with quaternary ammonium (SMA-QA) nanodiscs³³. The different systems were chosen to investigate both the suitability of different lipid models to the application of MST and lipid-AMP binding, and the impact the choice of model system can have on the binding. SMA nanodiscs and vesicles were chosen as they have been previously utilised in MST^{23,34}, and the effects of differences in surface curvature could be investigated. SMA-QA was selected as it possesses a cationic polymer belt, in contrast to SMA which has an anionic belt.

As the electrostatic attraction of cationic AMPs and anionic lipids is known to enhance their interactions, the association of the AMPs with both pure DMPC and a mixture of 95% DMPC and 5% PG were assessed in each of the three lipid systems. Finally, SPR was used as an orthogonal method to which the MST derived bindings could be compared.

Results and discussion

Surface plasmon resonance (SPR) characterization. The interactions between AMPs 1–5 and LUVs were first investigated by SPR as a benchmark for the MST measurements. The data was acquired using the same lipid compositions as used in the MST data acquisition. LUVs were immobilized on an L1 chip, and an increasing concentration of AMPs was injected over them. Figure 2 displays typical steady state fits of the SPR measurements, and the disassociation- and partitioning constants, K_D and K_p , extracted after 180 s are listed in Tables 3 and 4. The dissociation rate, k_{off} , was calculated from the dissociation step, using the methodology presented by Figueira et al.²¹, summarized in Table 2.

SPR showed values for K_D , K_p and k_{off} in the range of 50–800 μM , 1–150 10^{-3} and 0.2–1.0 s^{-1} respectively. 1 was the strongest binding compound, followed by 3, 2 and 4, with inactive AMP 5 being the weakest. This trend was also preserved when anionic lipids were present, but as expected, the overall affinities of all compounds was increased. The k_{off} values also followed this trend with the most active AMP, 1, having the slowest dissociation. The overall conclusion from SPR points towards increased affinities of the clustered peptides over alternating ones towards both zwitterionic and ionic lipid bilayers.

Vesicle MST response profiles. For K_D evaluation by MST, F_{Hot} was registered during the temperature related intensity change (TRIC) phase of the MST trace (see “Methods”). The advantage of evaluating K_D during the TRIC phase is that any potential effects of prolonged heating on the thermostability of the sample that may influence the binding can be avoided³⁶. The dose–response profile of MST response against lipid concentration for 1–5 largely follows a sigmoidal curve shape (Fig. 3A,B). In the cases of 5 and 4, the weaker binding resulted in truncation of the sigmoidal curve, with the asymptotic region at high lipid concentration not being fully sampled.

A blank series consisting of only lipids was collected for each lipid composition, and a weak MST response could be detected at the highest lipid concentrations despite the lack of a fluorophore. The blank response was stable up to concentrations around 1 mM. The two to three highest lipid concentrations measured did however build up a background response above the noise level of the baseline (Fig. 3C,D), most likely due to increasing turbidity. The added unspecific response to the last two data points thus imposes a limitation on how weak

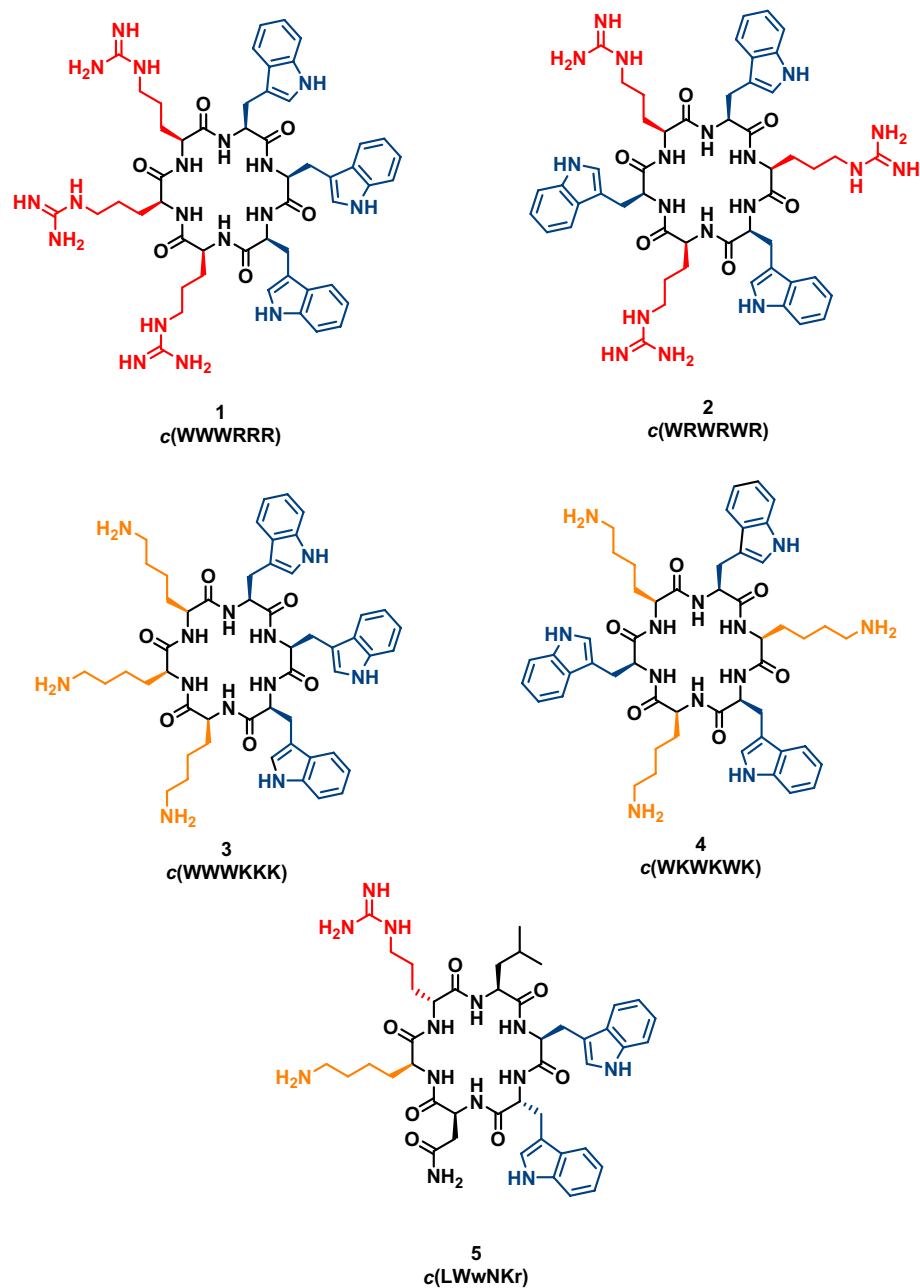


Figure 1. Structures of the five AMPs Coloured red/orange—R/K, blue—W. Uppercase letters indicate L-amino acids, lowercase letters indicate D-amino acids.

#	Sequence	<i>E. coli</i> MIC ($\mu\text{g/mL}$) (ATCC 25922)	<i>S. aureus</i> MIC ($\mu\text{g/mL}$) (ATCC 9144)	Net charge	Hydrophobic residues
1	WWWRRR	8	4	+3	3
2	WRWRWR	32	32	+3	3
3	WWWKKK	8	32	+3	3
4	WKWKWK	64	128	+3	3
5	LWwNKr	>256	>256	+2	2

Table 1. Summary of the cyclic hexapeptides and their minimal inhibition concentration (MIC).

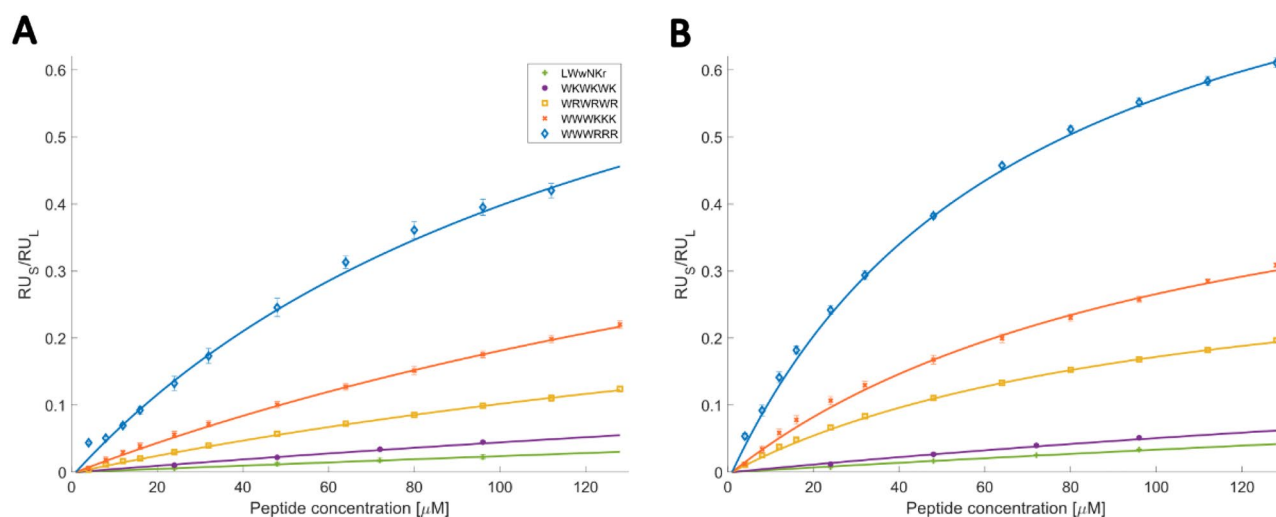


Figure 2. Ratio of RU_s (peptide signal) and RU_L (lipid bilayer) obtained from steady state using SPR for (A) 100% DMPC LUVs. (B) 95% DMPC 5% DMPG LUVs. Scatter plot present experimental values and full line represent fit obtained from Eq. (2). Full sensograms are available at the UiT open research data depository³⁵.

#	Peptide	k_{off}^{PC} (s ⁻¹)	$k_{off}^{PC/PG}$ (s ⁻¹)
1	WWWRRR	0.22 ± 0.02	0.19 ± 0.01
2	WRWRWR	0.87 ± 0.19	0.48 ± 0.05
3	WWWKKK	0.48 ± 0.07	0.32 ± 0.05
4	WKWKWK	0.90 ± 0.24	1.32 ± 0.05
5	LWwNKr	1.76 ± 0.12	1.75 ± 0.16

Table 2. Summary of k_{off} of AMPs 1–5 evaluated by SPR.

interactions can be reliably measured (mM lipid concentration range). The turbidity did however not notably impact the extraction of F_{norm} in the presence of AMPs (carrying the fluorophore), as the much stronger signal of the fluorophore did not display any signs of inheriting the turbidity contribution to F_{norm} from the blank profile (raw data shown in Fig. S1). This suggests that W fluorescence was the dominant contribution to the measured response when it was present. It is however not possible to rule out that the light scattering effect may dominate the response for very weak binders. Peptide 5, for example, shows a change in F_{norm} for the final two points together with DMPC liposomes, the same points that are significantly affected by light scattering effects in the blank measurement (Fig. 3A). The effect is however absent for the same peptide together with DMPC:PG liposomes even though the two blanks behave similarly, demonstrating that potential light scattering contributions are difficult to predict or compensate for.

That light scattering is present at higher lipid concentrations may raise concerns that the density of lipids could potentially hinder the thermophoresis of analytes in the sample, even for non-interacting species. However, as demonstrated by Yu et al.²⁵, the MST response of non-interacting moieties, demonstrated with FITC, is unaffected up to lipid concentrations of 2.5 mM. Further, sampling of the MST response in the TRIC phase of the MST trace means that thermophoretic effects are less dominant, minimising the risk of artefacts caused by the lipids³⁷.

Nanodisc MST response profiles. The MST data for two nanodisc types, SMA and SMA-QA, were evaluated using the same methodology as the vesicle data, with F_{Hot} taken during the TRIC, and F_{norm} plotted against $\log[\text{lipid}]$ and fit to Eq. (6). The binding profiles of AMPs binding to SMA and SMA-QA nanodiscs show significantly different behaviours (Fig. 4).

The SMA-QA nanodiscs produce a sigmoidal-like response curve (Fig. 4D,E), as was observed for the vesicles, though the curve is right-shifted to higher lipid concentrations, i.e., AMPs bind more weakly to the SMA-QA nanodiscs than to the corresponding vesicles. The consequence of the right-shift is that the binding curves of the weaker binders are not fully sampled, and in some cases only a minimum K_D can be determined. As with vesicles, at the highest lipid concentrations light scattering can become a factor in the measurement of F_{norm} . The result is that it becomes impractical to fully sample the binding curve by further increasing the lipid concentration, as an increased influence of light scattering effects would be expected.

By contrast, the SMA-nanodiscs response is left-shifted to lower lipid concentrations, corresponding to a stronger binding than to the corresponding vesicles (Fig. 4A,B). The curves also deviate from the sigmoidal F_{norm} profile with a secondary drop in F_{norm} after reaching the maximum, in the mM range. Such profiles have

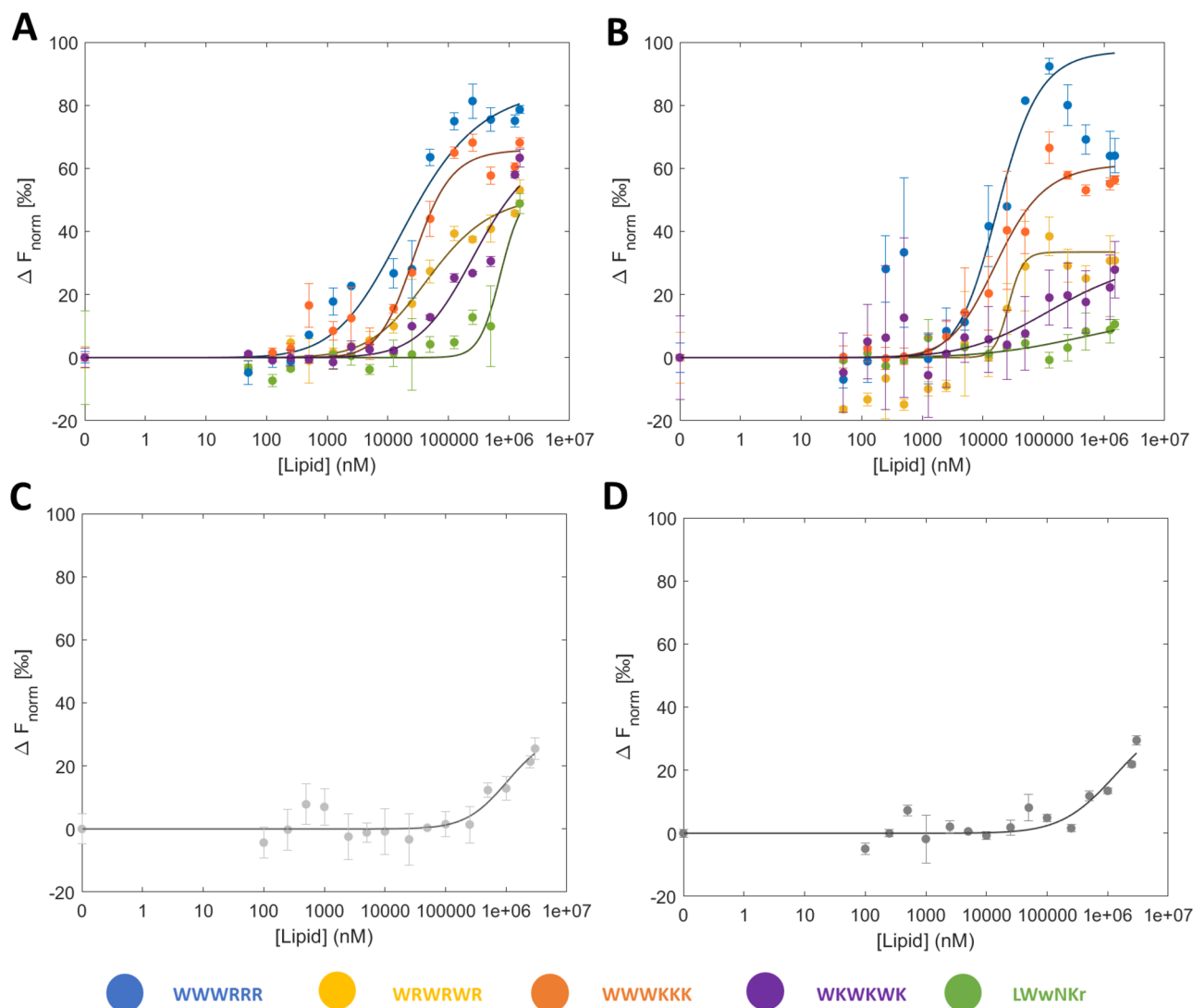


Figure 3. MST response against lipid concentration and average K_D fits of 1–5 in different lipid vesicles compositions. The upper panels show 100 nm vesicles. (A) 100% DMPC. (B) 95% DMPC 5% DMPG. The lower panels show the blank MST response. (C) 100% DMPC. (D) 95% DMPC/5% DMPG. Error bars represent the standard deviation of the triplicates.

previously been observed in the MST response of higher stoichiometric bindings where additional interacting ligands gave rise to a new species of the complex²². In the case of nanodisc-AMP interactions, the most plausible explanation is that direct interactions between 1–5 and the SMA polymer gives rise to the atypical binding profile. A direct interaction between the free SMA polymer and the AMPs can indeed be observed in the high nM–low μ M range in a control experiment without lipids present (Fig. 4C,G). The presence of strong interactions to the SMA polymer, and a multiple-phase response profile, indicates that the interaction with the polymer dominates the measurement to the extent that the AMP-lipid interaction cannot be directly measured in SMA nanodiscs (Table 3). The strength of the interaction with the SMA polymer, together with its role in stabilizing the nanodisc, led to the assumption that the system would be significantly perturbed. Therefore, no further attempts were made to deconvolute multiple interactions from these response curves.

The strong interaction to the SMA polymer can be attributed to the rich anionic maleic acid content (deprotonated at pH 7.4), resulting in favourable electrostatic interactions to the cationic AMPs. Consequently, no such binding is observed for the SMA-QA polymer, which is instead rich in cationic moieties, and thus has the attractive electrostatic interaction potential to cationic AMPs replaced by a repulsive potential, which is reflected in the response profiles being shifted towards weaker binding.

K_D comparison. Comparison of the MST and SPR derived K_D for LUVs shows that the absolute K_D obtained are systematically offset by an approximate factor 4 (Fig. 5C,D and Table 3), but the relative values within each dataset result in the same stratification of the peptides binding strength to LUVs as measured by MST and SPR. The inactive peptide 5 had a considerably higher K_D compared to 1–4, though the profile of 5 could not be fully sampled. Therefore, only the minimum K_D was determined, providing an explanation as to why MST did not

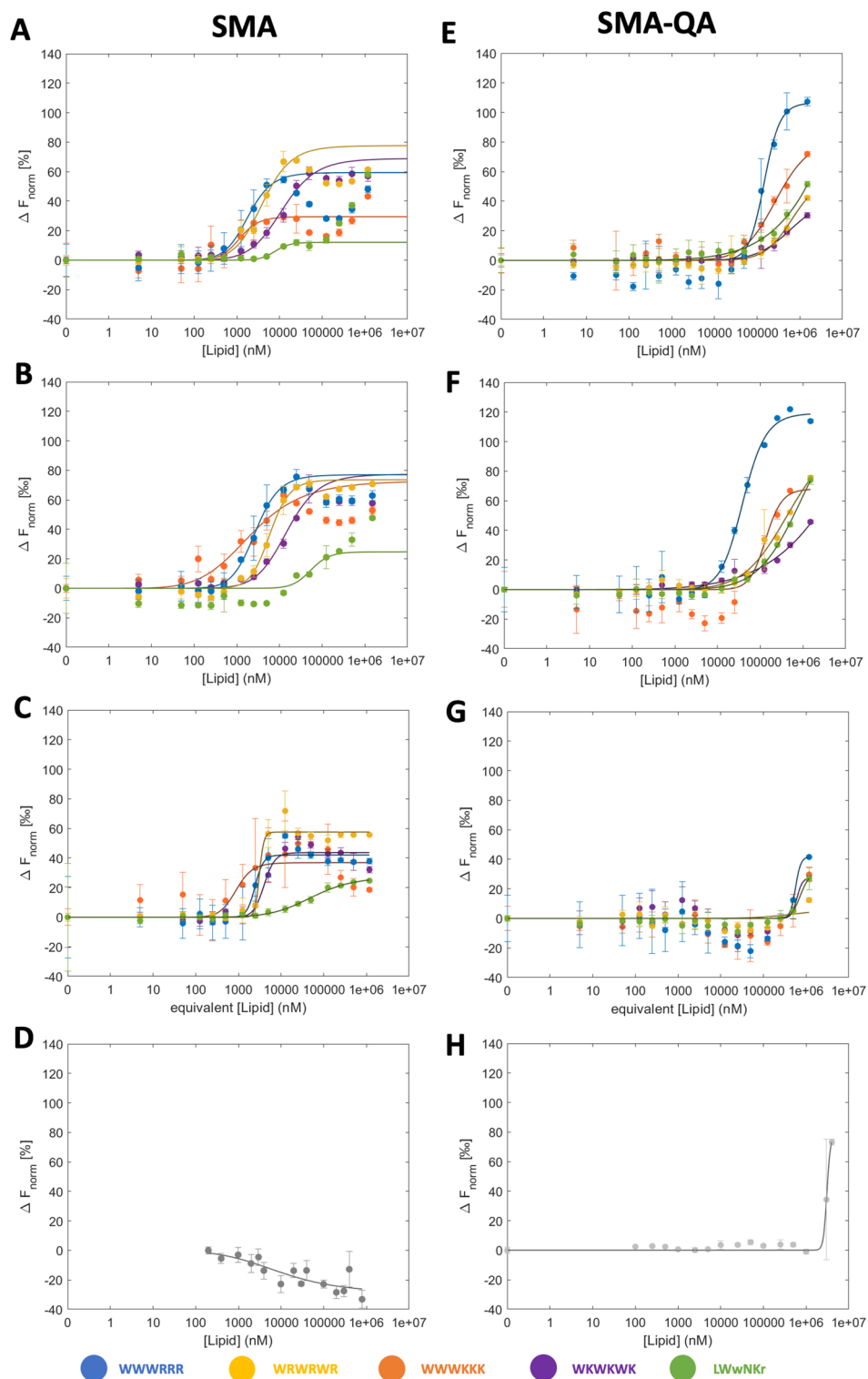


Figure 4. MST response against lipid concentration and K_D fits of 1–5 in different lipid nanodisc compositions. The left panels show SMA nanodiscs, and the right SMA-QA nanodiscs consisting of (A/E) 100% DMPC, (B/F) 95% DMPC/5% DMPG, (C/G) polymer (no lipids*), and (D/H) nanodisc only (no peptide). *Equivalent [lipid] is used to estimate the amount of SMA that would be present at that lipid concentration in the corresponding nanodiscs. Error bars represent the range in the triplicates.

Peptide	SPR (K_D μM)		Vesicle (K_D μM)		SMA-QA (K_D μM)		SMA (K_D μM)	
	DMPC	DMPC/PG	DMPC	DMPC/PG	DMPC	DMPC/PG	DMPC	DMPC/PG
LWwNKr	2548 \pm 493	1033 \pm 58	>670	>650	–	>1000	–	–
WKWKWK	712 \pm 27	474 \pm 45	282 \pm 58	112 \pm 29	>713	–	8.6 \pm 0.5	9.8 \pm 0.3
WRWRWR	318 \pm 62	105 \pm 7	73 \pm 53	24 \pm 7	>541	>615	2.7 \pm 0.5	5.6 \pm 1.1
WWWKKK	302 \pm 32	112 \pm 15	28 \pm 3	17 \pm 13	267 \pm 47	145 \pm 55	1.1 \pm 0.3	1.1 \pm 0.5
WWWRRR	142 \pm 35	70 \pm 1	21 \pm 3	10 \pm 5	142 \pm 17	40 \pm 5	1.2 \pm 0.5	2.2 \pm 0.4

Table 3. Summary of K_D determined using SPR and MST. Errors represent the standard deviation of the triplicates. Where K_D is preceded by '>', the value represents a minimum value due to insufficient curve sampling and no error is reported.

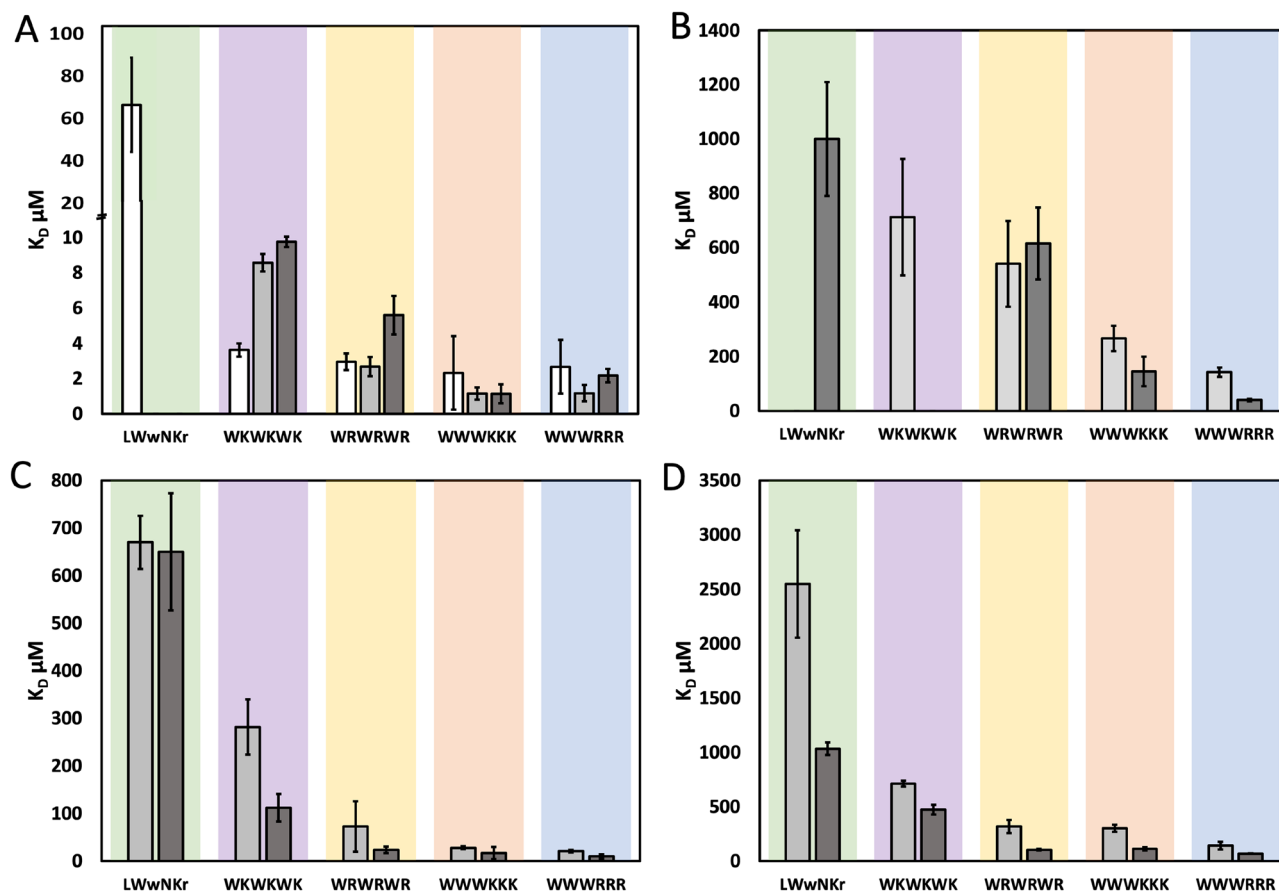


Figure 5. K_D s determined by MST and SPR to DMPC (light grey) and DMPC/PG (dark grey). (A) K_D determined using SMA nanodiscs (white: SMA polymer), (B) K_D determined using SMA-QA nanodiscs, (C) K_D determined using 100 nm vesicles, (D) K_D determined using SPR and Vesicles (extruded through 100 nm filter). Error bars represent the standard deviation of the triplicates.

identify the same strong dependence on the lipid composition as SPR for this peptide. Consistent with SPR, the clustered sequence peptides 1 and 3 had significantly stronger binding than 4. This is also consistent with the determined MICs, with 1 and 3 being the most active peptides. These observations are in line with previous reports that clustering of W residues is positively correlated with antimicrobial activity⁴.

The SMA-QA derived K_D compare favourably with the SPR results in the instances where the curve is adequately sampled (Fig. 5B, Table 3). However, as the K_D approach the mM region, the SMA-QA data set are not sampled sufficiently to produce reliable results. This is expressed most evidently as large errors, where, with no maximum reached in the sampled lipid concentrations, the fitted K_D is sensitive to outliers and small deviations in the slope of the curve. One example of insufficient sampling and the resulting error is shown by the poor reproduction of the PC/PG discrimination observed in SPR for 2. Importantly though, when the curve is adequately sampled, the K_D error is consistent with user reported MST errors²⁶.

This is however not the case for the more active AMPs where the binding strength is well inside the sampling range. SMA-QA nanodiscs are thus only viable for assessing AMP-lipid interactions stronger than the mM range by MST.

The SMA discs exhibit overestimated binding strengths, showing all peptides to have apparent K_D of 10 μM or lower (Table 3), and show poor discrimination between PC and PC/PG lipids (Fig. 5A). The lack of discrimination is attributed to the strong interaction with the anionic SMA polymer dominating the response and masking the expected binding enhancement from the addition of the anionic lipids.

In general, the presence of PG lipids leads to a decrease in K_D for all peptides by an approximate factor of 2 when the sigmoidal binding curve could be fully sampled. In previously published work, Christiaens et al.³⁸ found that individual peptides had a broad range of binding strengths, from a weak 350 μM towards PC vesicles, to stronger binding in the low μM –nM range to vesicles rich in anionic charges. Analysing MSP-nanodiscs by ITC and NMR, Zhang et al.³⁹ observed binding to anionic lipid nanodiscs in the range of 1–2 μM . The K_D s measured by MST are thus in line with results in the literature that shows that AMPs can bind in the low μM range to both vesicles and nanodiscs in the presence of anionic lipids, with an expected weakening of the interaction towards zwitterionic membranes. It is known that cationic AMPs have a selectivity towards bacterial membranes where anionic lipids and LPS are present on the outer membrane over cells with a more neutral surface. While the reduction in K_D upon introduction of anionic lipids observed for 1–5 is not as large as described in the above studies, the anionic component introduced in this work (5%) is low in comparison to the 20% used by Zhang et al. and Christiaens et al.

The calculated K_D in this work is fit using a two-state model⁴⁰. This is however not necessarily expected to be an accurate representation of lipid interactions, where the target has no defined binding site, and it is possible that self-aggregation on the lipid surface, saturation effects, cooperative- or competitive binding will occur that will influence the binding of further AMPs^{41,42}. For this reason, K_D is a useful illustrative and communicable descriptor of AMP-lipid binding, but care would be advised to not overinterpret the absolute value. The measured apparent K_D is best considered a composite value representing multiple processes of a complex interaction, that is system- and method dependent—as also highlighted in this work.

Fluorescence intensity and K_p . The partition coefficient (K_p) describes the preference of compounds for lipid or aqueous phases, with a high K_p indicating a greater preference for the lipid phase. K_D in contrast describes the bound state as a molecular complex rather than phase. Both K_D and K_p are useful descriptors of AMP-lipid interactions, and instruments that can determine both can offer users a great deal of flexibility in exploring biophysical interactions. To explore the possibility to determine the K_p of AMPs 1–5 using MST, the single wavelength fluorescence intensities measured by the MST instrument were used. This data is routinely acquired during the MST measurements during the initial phase of the MST trace for use as the F_{Cold} measurement and is reported as the ‘initial fluorescence’. Thus, no additional acquisition time is required. To the best of our knowledge, this is the first attempt to make use of this data to determine K_p using MST hardware. K_p was extracted by fitting the data to a hyperbolic partition curve described by Eq. (8), after removal of non-hyperbolic points⁴³.

Lipid-only blanks were collected to assess the effect the turbidity had on the measurements (Fig. 6). For the vesicles, this is a modest signal that increases linearly in the mM lipid concentration range. The increase is consistent with the observed MST response reported above (Fig. 3C,D), attributed to light scattering effects. Both types of SMA nanodiscs similarly follow a mostly linear trend but the signals are more intense (Fig. 6).

The background fluorescence for the vesicles is modest at the initial concentrations compared to the measured fluorescence intensities of the AMP and does not have the same profile as lipid concentration is increased (Fig. S2). A larger increase is observed for the highest lipid concentrations, showing the influence of the turbidity of the system (Fig. 6). The SMA-QA nanodiscs initial background fluorescence signal is significantly stronger,

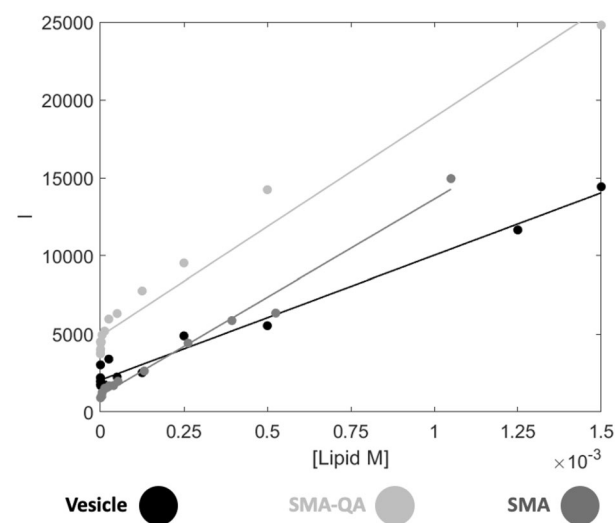


Figure 6. The measured fluorescent intensities of the blank lipid only samples of SMA and SMA-QA nanodiscs, and vesicles.

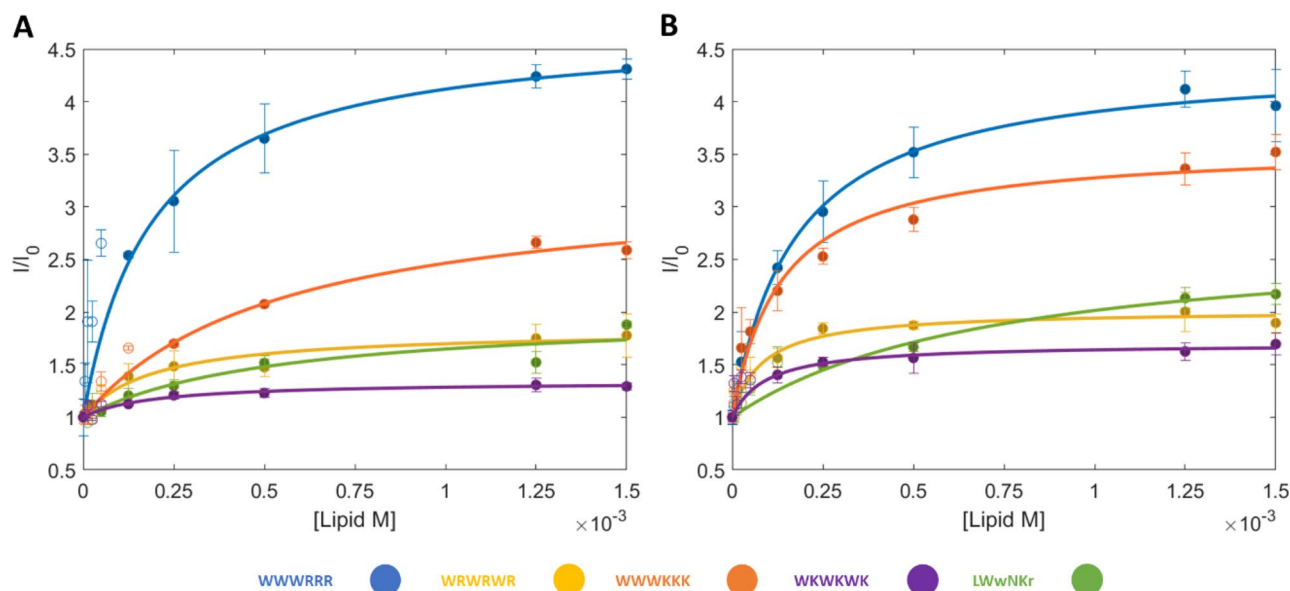


Figure 7. Initial fluorescence and K_p fits of 1–5 in different lipid compositions of LUVs. (A) 100% DMPC. (B) 95% DMPC with 5% DMPG. Lines and filled circles indicate the fit and the points used, unfilled circles are points not included. Error bars represent the standard deviation of the triplicates.

and a substantial level is maintained over the measured concentration range. As with the vesicles and SMA-nanodiscs, the intensity profile of the SMA-QA sample with AMP present does not match the profile when the AMP is present (Fig. S2). For this reason, it is not possible to subtract the blank baseline from the AMP signal. Hence, the final points carry increased uncertainty because of potential, but inconsistent, light scattering contributions (Fig. 7 and Fig. S3).

Many AMPs, especially when using vesicles, showed a spike in fluorescence at low lipid concentrations (at high peptide:lipid ratio). This phenomenon has previously been described by Melo and Castanho⁴⁴, where they attribute the deviation to the saturation of the bilayer with AMP that prevents the uptake of additional AMPs. It has also been attributed to changes in conformation and peptide-peptide interactions within the bilayer when it is saturated with AMPs⁴⁵. To extract K_p where deviations are observed, the deviant points are excluded from the fit. At lower lipid concentrations (high peptide:lipid ratio), a critical point is reached where the hyperbolic model is no longer followed and points beyond the critical point cannot be described by Eq. (8). It should be noted that the removal of points introduces uncertainty and increases the error of the extraction of K_p ; this is particularly problematic as the hyperbolic shape is best described by the initial points along the curve, but these are also the points that are the most affected by the high peptide:lipid ratios^{43,44}. For both SMA-QA and LUVs, many points deviated from the hyperbolic shape, and a large number of points needed to be removed, typically leaving the final 4–5 points for the final fit.

In brief, the SPR determined K_p follows the K_D trend that $1 > 3 > 2 > 4 > 5$ for both lipid compositions, with K_p determined in the range of $0.3\text{--}7 \times 10^3$ for DMPC and $0.4\text{--}13 \times 10^3$ for DMPC/PG. The MST derived K_p on the other hand are inconsistent with both the SPR results and the MST derived K_D , including the expected differences in partitioning to DMPC and DMPC/PG (Table 4 and Fig. 8). The difficulties in the MST K_p extraction compared to SPR likely lies in the intrinsic differences in the methods. Label-free MST relies on the intrinsic fluorescence of W and the instrument measures the intensity at a fixed wavelength. The fluorescent intensity of W is influenced by static and dynamic quenching and may experience blue-shifting, processes that differ significantly between different environments, modes of binding and tendency to self-aggregate⁴⁶. Significant blue-shifts of the W emission will displace the signal maximum to varying degrees away from the static detection frequency, resulting to a lower signal intensity being detected. Thus, there are additional factors that can negatively affect the detected signal in addition to the phase distribution.

Together, these results showed that the explored MST method was unreliable to extract K_p for our panel of AMPs, and that care should be taken in the interpretation of the obtained results. However, there are some correlations present that suggests that with some further work, particularly around alleviating some issues around the blue-shifting, that MST might become a viable tool to estimate K_p in the future. The spectral shift technology employed in newer Nanotemper devices may be ideal to further explore K_p extraction by MST⁴⁷.

Vesicle and nanodisc comparison. The SMA-QA- and vesicle derived K_D showed differences between the two lipid systems. The vesicles produced had a diameter of ~ 140 nm and should therefore consist of approximately 200,000 lipids (with a molecular weight of ~ 140 MDa). In comparison the 22 nm DMPG SMA-QA nanodiscs contain approximately 1300 lipids (lipid weight of ~ 760 kDa), but also a substantial fraction of polymer (Table 5). The AMPs used have molecular weights between 884 and 1027 Da, therefore when multiple AMPs are binding to a single disc, the relative change in weight, size, and shape of the nanodisc-complex will be dif-

Peptide	SPR $K_p \times 10^3$		Vesicle $K_p \times 10^3$		SMA $K_p \times 10^3$		SMA-QA $K_p \times 10^3$	
	DMPC	DMPC/PG	DMPC	DMPC/PG	DMPC	DMPC/PG	DMPC	DMPC/PG
LWwNKr	0.28 ± 0.01	0.40 ± 0.02	3.10 ± 2.17	1.47 ± 0.07	6.98 ± 1.24	4.75 ± 0.32	17.12 ± 12.90	3.35 ± 0.57
WKWKWK	0.53 ± 0.01	0.63 ± 0.03	8.56 ± 7.41	14.90 ± 4.84	0.70 ± 0.11	<i>1.14 ± 0.12</i>	6.15 ± 6.54	3.23 ± 1.87
WRWRWR	1.30 ± 0.09	3.16 ± 0.15	7.08 ± 2.32	16.97 ± 3.83	9.72 ± 2.69	3.57 ± 0.36	36.55 ± 11.82	12.62 ± 4.16
WWWKWK	2.53 ± 0.08	5.16 ± 0.34	2.55 ± 0.89	11.05 ± 4.49	2.34 ± 1.40	4.21 ± 0.43	9.16 ± 2.86	4.93 ± 0.81
WWWRRR	6.65 ± 0.80	12.71 ± 0.16	7.24 ± 1.73	7.73 ± 1.58	10.40 ± 1.52	10.27 ± 2.13	7.07 ± 1.78	7.63 ± 1.89

Table 4. Summary of K_p determined using SPR and MST $K_p \times 10^3$. Bold: good correlation with SPR. Italics: reasonable correlation. Errors correspond to the standard deviation of the triplicate fits.

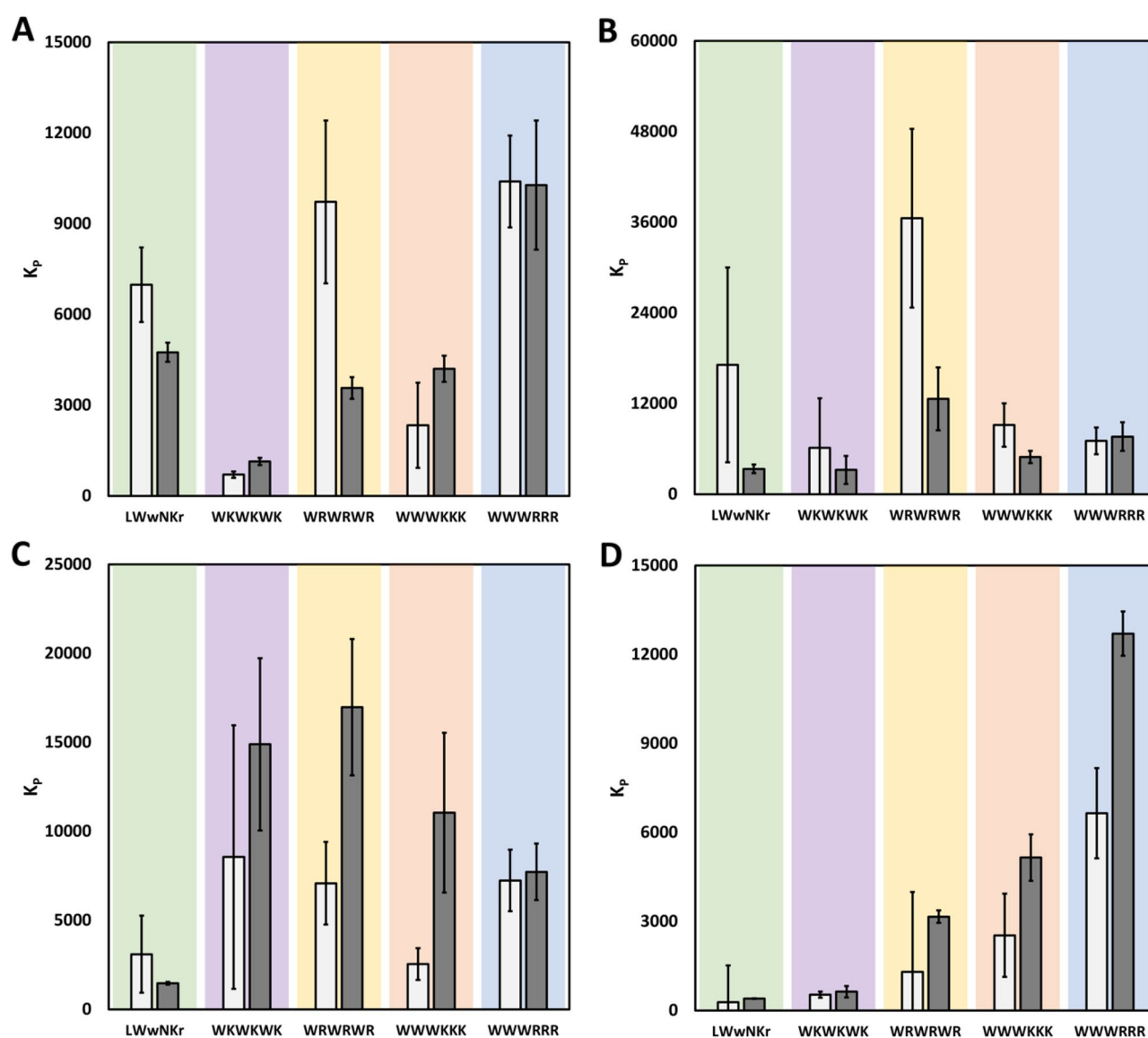


Figure 8. K_p s determined by MST with DMPC (light grey) and DMPC/PG (dark grey) compared to SPR. **A** K_p determined using MST and SMA-nanodiscs. **B** K_p determined using MST and SMA-QA-nanodiscs. **C** K_p determined using MST and 100 nm vesicles. **D** K_p determined using SPR and 100 nm vesicles. Error bars correspond to the range of values for the triplicate fits.

Model	Vesicle	SMA-QA nanodisc DMPC	SMA-QA nanodisc DMPC/PG
Radius (nm)	72	6	11
Surface area (nm ²)*	120,000	260	790
Total number of lipids**	200,000	430	1320
Approx. weight**	140 MDa	290 kDa***	890 kDa***

Table 5. Comparison of estimated vesicle and nanodisc sizes. *Surface area of both sides of the bilayer. **Assuming 100% DMPC composition with head area of 0.6 nm² per lipid. ***Weight excludes SMA-QA polymer due to the uncertainty of the amount of SMA-QA per disc.

ferent than with a vesicle-complex, such relative changes may impact the F_{norm} measurement as MST is sensitive to these properties of the complexes measured⁴⁸. Furthermore, the fractions of the lipids in the models that are accessible by the AMPs differ. In nanodiscs both sides of the bilayer are accessible, and potentially enable cooperative interactions from opposite sides of the discs. In contrast, for vesicles only the outer leaflet of the vesicle surface is initially accessible, with the inner leaflet only accessible to AMPs by first translocating across the bilayer. However, as MST is a steady state measurement, it is unclear if this affects the observed values.

Another difference between vesicles and nanodiscs, aside from the size, is the planarity of the lipid surfaces. Solubilised as LUVs, vesicles have a slightly convex surface curvature which introduces surface stress⁴⁹. Nanodiscs on the other hand have a planar surface⁵⁰—like the surface of the cell wall that is planar at a local level. In this context, nanodiscs may be a more representative model system. The difference in the curvature of the two systems may contribute to the difference in bindings observed towards the LUVs and SMA-QA nanodiscs. Peptides have demonstrated curvature-sensing properties, due to their preferential binding to packing defects that arise due to the curvature stress. Curvature-sensing is facilitated by hydrophobic motifs in peptides and can significantly improve the binding of peptides to more curved membranes^{51–53}. The importance of hydrophobic motifs to peptides is also characterised by the correlation of the clustering of W residues with antimicrobial activity⁴. Indeed, such effects can be observed in the difference of measured K_D s of 1–4 between the planar lipid conditions (SPR and SMA-QA) and curved lipid species (LUVs): the clustered-residue 1 and 3 having a tenfold improvement in binding to LUVs compared to the alternating-residue 2 and 4 which demonstrated only a fourfold improvement.

The difference in curvature between the two systems can affect the lipid phase in the bilayers of the nanodiscs and vesicles. The lipids solubilised as vesicles, have a uniform phase (at 25 °C this is near the T_m of DMPC and in the liquid-ordered phase)⁵⁴. In contrast, the lipids in SMA-nanodiscs are less tightly packed than those solubilised as vesicles and have a reduced melting point⁵⁵, and the same characteristics is expected of the SMA-QA nanodiscs. The central lipids of nanodiscs are in a more ordered phase⁵⁰, while the outermost lipids, closest to the SMA-belt, are perturbed by the styrene groups of SMA⁵⁵. AMPs are known to favour lipids that are in a more disordered phase and therefore one would expect heterogeneous interactions and distributions within the nanodiscs⁵⁶.

In addition to the lipids, the role and impact of the respective belt polymers net charge is interesting to consider with regards to the two nanodisc systems. Some peptides have been shown to de-mix lipids into anionic lipid rich domains⁵⁷. When such domains are formed, disorder at the domain boundaries can be exploited⁵⁸. Polymer charge is known to affect the reconstitution of proteins and lipid species into nanodiscs^{59,60}, and so it is therefore expected that it will influence the radial distribution of both the anionic DMPG and the studied cationic peptides. The negatively charged SMA will favourably interact with the cationic AMPs through electrostatic interactions, thereby also retaining the peptide in the proximity of the disordered lipid region. The unwanted effect of electrostatic interactions between SMA polymers and oppositely charged species has been previously reported by Ravula et al.⁵⁹, where protein–nanodisc aggregates were reported due to strong electrostatic and hydrophobic interactions with the polymer. In MST, this was observed as a strong binding of the AMPs to both the SMA nanodiscs and the polymer alone, but any formation of nanodisc-aggregates was not apparent. In contrast, the cationic SMA-QA can have a repulsive effect on the AMPs, potentially repelling the AMPs from parts of the most disordered region near the polymer, containing the most favourable interactions on the nanodisc (Fig. 9). Similarly, Ravula et al.⁵⁹ noted the beneficial effect of repulsive charges on the reconstitution of membrane proteins.

The cationic polymer charge could also, for example, have contributed to SMA-QA-DMPG forming larger and more heterogeneous nanodiscs compared to the SMA-QA-DMPC and SMA nanodiscs (Table 5). The polymer charge may also have affected the final lipid content of the nanodiscs. ³¹P NMR estimated that the DMPG content in the SMA and SMA-QA nanodiscs were 2.7 and 4.5% respectively, from the initial vesicle content of 5% (Figs. S4–S7), demonstrating a negative effect on the yield for matched lipid and SMA charges.

The difference in the size of the two nanodisc preparations may also influence the interactions, with the larger SMA-QA PG containing discs having more lipids in an ordered phase than the smaller SMA discs. The role of the net charge of the belt is however expected to be the main driving factor behind the 20–200 times stronger interaction between the SMA nanodiscs and cationic AMPs compared to vesicles and SMA-QA nanodiscs. Surprisingly, while the respective K_D of the AMPs towards the two systems showed much more enhanced binding to the anionic SMA nanodiscs, K_p appeared to be measurable and consistent with SPR. Further studies are required to establish if the MST measured K_p reflects the true partitioning to the lipids in the SMA nanodiscs in this case, or if the apparent correlation is a product of cancellation effects. Accordingly, the interaction between the AMPs and the SMA-QA is approximately 4–10 times weaker than for the vesicles, likely affected by the difference in curvature and an electrostatic repulsion between the mutually cationic AMPs and SMA-QA. This could reduce the area of accessible lipids to interact with, in particular the lipids near the polymer that are in a less ordered phase.

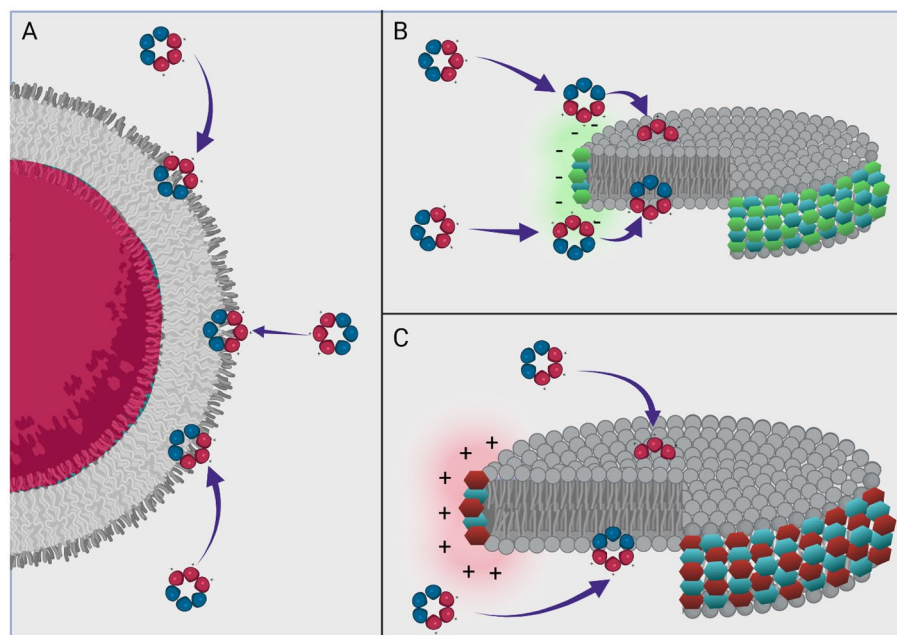


Figure 9. Visualisation of the difference in shape and characteristics of the lipid models and how this impacts the interactions of antimicrobial peptides.

The differences between the SPR and MST K_D could be explained by the experimental differences between the two methods. In MST, peptide response is monitored as a function of lipid concentration, whereas in SPR the added peptide mass to lipids immobilized on a chip is monitored as a function of peptide concentration. By keeping the AMP concentration fixed, any changes in activity due to concentration dependent processes, such as self-aggregation of AMPs, either pre- or post-binding, is not monitored. For the same reason, concentration dependent processes of the lipid system such as fusion, aggregation or turbidity are part of the response profile. Despite these differences, the vesicle MST and SPR produce binding data that are consistent relative to one another with regards to the ranking of the AMPs and the relative differences between the determined K_D values.

Conclusions

We have demonstrated that MST, leveraging the intrinsic fluorescence of W, can be used to extract K_D , and potentially K_p , of W-rich AMPs towards model lipid bilayers in a fast and label-free manner. The measured K_D of 1–5 correlate well with both of their respective bactericidal activities (represented by MIC values) and with the ranking of binding obtained using SPR. We have successfully shown that MST can be used with various lipid particles (LUVs and nanodiscs) demonstrating robustness for studying membrane activities. The SMA-nanodiscs negatively charged polymer belt is not a suitable nanodisc scaffold for interaction studies with cationic AMPs, while SMA-QA nanodiscs are able to accurately reproduce the SPR derived results of the strongly binding AMPs. The results therefore highlight the need for careful consideration with regards to the lipid system to be used and the interaction to be analysed. Both SMA- and SMA-QA based nanodiscs are suitable constructs for ligands that do not directly interact with the polymers.

The extraction of the binding parameters of weak binders can be challenging due to potential interference from light scattering effects at high lipid concentrations compared to state-of-the-art SPR. On the other hand, MST analysis has much faster acquisition time and small sample/lipid requirements. With the introduction of automated hardware⁶¹, MST provides a low-cost and accessible alternative with high throughput for studying ligand-lipid interactions that is complementary to assays that detect AMP membrane disruptive properties such as for example WIND-PVPA, vesicle leakage, or patch-clamp experiments^{62–64}.

MST would also be a highly suitable method to perform cost efficient scout experiments of sample conditions for lipid interactions, before initiating more advanced studies that rely on expensive sample preparation, labelling and/or instrument time.

Methods

Materials. Lipids were purchased from Avanti Polar Lipids via Sigma Aldrich (Merck KgaA, Darmstadt, Germany). MST consumables from Maricks AS (Oslo, Norway). SPR consumables were purchased from Cytiva Europe—Norge (Tyristrand, Norway). All other materials were purchased from Sigma Aldrich in analytical purity, unless otherwise stated. Peptides and SMA-QA were prepared in house.

The bacterial strains used were *E. coli* ATCC 25922 and *S. aureus* ATCC 9144. Overnight cultures and MIC assays were performed in cationic-adjusted BD BBL Mueller Hinton II Broth (MHB II, 212322, Becton, Dickson and Company, Sparks, MD, USA).

Peptide synthesis. *Linear peptide synthesis.* 2-chlorotrityl chloride resin (0.15 mmol, 1.0 meq, 150 mg) was swelled in DCM (5 mL) for 30 min. The resin was drained and treated with a solution of Fmoc-amino acid (0.3 mmol) and diisopropylethylamine (1.8 mmol, 313 mL) in DCM (5 mL). The resin mixture was left overnight under gentle agitation at room temperature. The resin mixture was drained, treated with MeOH (3 × 5 mL) to cap unreacted sites and dried with diethyl ether (3 × 5 mL). The linear peptides were prepared using an automated solid-phase peptide synthesizer (Biotage Initiator + Microwave System with Robot Sixty). The pre-loaded 2-chlorotrityl chloride resin was first swelled in DMF (20 min, 70 °C). Fmoc deprotections involved treatment of the resin with 20% piperidine/DMF (4.5 mL, 3 min) once at room temp. followed by a second treatment at 70 °C by microwave reactor. Amino acid couplings involved treatment of the resin with 4 eq. of Fmoc-amino acid (0.5 M in DMF), 4 eq. of HOBt (0.5 M in DMF), 4 eq. of HBTU (0.6 M in DMF) and 8 eq. of DIEA (2 M in NMP) for 5 min at 75 °C by microwave reactor for all Fmoc-amino acids except Fmoc-Arg(Pbf)-OH, which was coupled for 60 min at room temp. After each Fmoc deprotection and amino acid coupling, the resin was washed with DMF (4 × 4.5 mL × 45 s). After preparation of the resin-bound sidechain protected linear peptide, a final Fmoc deprotection and wash was performed and the resin dried (3 × 5 mL MeOH, 3 × 5 mL Et₂O). The resin-bound peptide was treated with 20% 1,1,1,3,3,3-Hexafluoro-2-propanol in DCM (2 × 5 mL × 15 min), followed by rinsing of the resin with DCM (5 mL). The filtrates were combined and concentrated under reduced pressure to yield the sidechain protected linear peptide.

Head-to-tail cyclisation and deprotection. The linear peptide (approx. 0.15 mmol) and diisopropylethylamine (0.9 mmol, 157 mL) were dissolved in DMF (10 mL) and added to a solution of PyBOP (0.45 mmol, 234 mg) in DMF (100 mL) under light stirring at room temperature. After 1–2 h (monitored for completion by mass spectrometry), the mixture was concentrated by reduced pressure and treated with a solution of TFA/triisopropylsilane/water (4 mL, 95%, 2.5%, 2.5%) then left to stand for 3 h. The mixture was concentrated under N₂ gas flow followed by precipitation with ice-cold diethyl ether (15 mL). The precipitate was collected by filtration, washed with diethyl ether (15 mL), dissolved in 50% acetonitrile/water, and lyophilized to yield the crude, cyclic, sidechain deprotected peptide.

Purification. Peptides were purified by preparative reverse-phase HPLC (Waters 600 instrument with Waters 2487 Dual Absorbance detector) with a SunFire Prep. C18 OBD column (10 mm, 19 × 150 mm) using linear gradients of 0.1% TFA/water (buffer A) and 0.1% TFA/acetonitrile (buffer B) with a flow rate of 10 mL/min unless otherwise stated.

Analysis. Crude and final cyclic peptide products were analysed by FT-MS (Thermo Scientific LTQ Orbitrap XL instrument) and by analytical reverse-phase HPLC (Waters 2795 Alliance HT system with Waters 2996 PDA Detector), using an Ascentis C18 column (3 mm, 3 × 100 mm) and solvents of 0.1% TFA/water (buffer A) and 0.1% TFA/acetonitrile (buffer B) with a linear gradient of 0–60% buffer B over 15 min and a flow rate of 0.5 mL/min.

Minimum inhibitory concentration (MIC) assay. The MICs for 1–5 were determined using the CLSI M07-A9 guidelines⁶⁵. Working solutions were prepared in double distilled water containing max. 1% DMSO. A concentration range between 256–0.25 µg/mL was tested for each peptide. The bacterial inoculum was 1 × 10⁶ cells/mL and incubated 1:1 with each test compound in a polypropylene 96-well round-bottom plate (655209, Greiner Bio-One, Kresmmuenster, Austria). Each MIC test was performed in three biological replicates, consisting of four technical replicates. Positive controls (without antibiotics) and negative controls (without bacteria) were included for each technical replicate. The reference antibiotic erythromycin was included to assure quality control. The plates were incubated for 24 h at 37 °C. The MIC value was defined as the lowest concentration of compound resulting in no visible bacterial growth.

Synthesis of SMA-QA. Following the procedure of Ravula et al.³³ (2-aminoethyl)trimethylammonium chloride hydrochloride (9.38 mmol, 1.3 g) was added to a solution of styrene maleic acid anhydride (SMA, 1 g) in anhydrous DMF (5 mL), followed by trimethylamine (56.7 mmol, 5 mL) upon which the mixture took a dark yellow colour. The reaction mixture was stirred at 70 °C for 2 h, then cooled to room temperature, and precipitated with diethyl ether. The precipitate was washed 3 times with diethyl ether and dried *in vacuo*. The dried intermediate was dissolved in acetic anhydride (317 mmol, 30 mL), to which sodium acetate (8.05 mmol, 660 mg) and triethyl amine (1.98 mmol, 200 mg) were added. The reaction mixture was stirred at 80 °C for 12 h, cooled down, and precipitated in ether. The precipitate was washed 3 times in ether and dried *in vacuo*. The product was then dissolved in water and passed through a Sephadex LH-20 column. The product was collected and then lyophilized to give a crystalline brown powder and confirmed by IR stretching frequency shift from 1774 to 1693 cm⁻¹ (Fig. S8).

Vesicle preparation. DMPC and DMPC:5% DMPG vesicles were prepared by solubilising a known weight of lipid in chloroform with a small amount of methanol to assist in the dissolution of the PG lipid head groups. The chloroform stock was dried *in vacuo* to produce a lipid film, which was further dried for additional 3 h. The lipid film was solubilised in 10 mM TRIS buffer (pH 7.4) containing 100 mM NaCl to yield a 20 mM milky lipid stock.

To produce the working vesicle stock, 1 mL of vesicle stock was extruded 20 times through a 0.1 µm filter using an Avanti Lipids mini-extruder. Vesicle size was confirmed using a Malvern Zetasizer Nano ZS (Malvern

Panalytical Ltd, Malvern, United Kingdom). 200 μL vesicle sample measured in 40 μL microcuvettes revealed vesicle diameters to be 144 ± 44 nm (DMPC) and 140 ± 48 nm (DMPC/PG).

Nanodiscs preparation. The DMPC, and DMPC with 5% DMPG 21 mM vesicle stocks were used for the nanodisc preparation. The stocks were combined with an 8% SMA stock solution to yield a final SMA concentration of 1% for SMA nanodiscs. The stocks were combined with a 100 mg/mL SMA-QA stock to yield a final lipid:SMA-QA w/w ratio of 1:1.5. The combined SMA/SMA-QA and lipid mixture were incubated at room temperature overnight and purified by SEC. Fractions containing SMA/SMA-QA discs were concentrated using centrifugation filters. Total lipid concentration was determined by ^{31}P NMR (Figs. S4–S7). Nanodisc size was confirmed using a Malvern Zetasizer Nano ZS (Malvern Panalytical Ltd, Malvern, United Kingdom). 200 μL nanodisc sample measured in 40 μL microcuvettes revealed nanodisc diameters to be 10.1 ± 3.0 nm (SMA DMPC), 9.2 ± 2.9 nm (SMA DMPC/PG), 12.8 ± 4.1 nm (SMA-QA DMPC), and 22.5 ± 11.8 nm (SMA-QA DMPC/PG) (Figs. S9–S11).

SPR experimental procedure. The SPR measurements were performed using a T200 Biacore instrument (GE Healthcare, Oslo, Norway) at room temperature. An L1 chip was covered with extruded DMPC liposomes (1 mM in 10 mM HEPES buffer pH 7.4 with 100 mM NaCl) using a flowrate of 2 $\mu\text{L}/\text{min}$ for 2400 s. Chip coverage was tested by injection of 0.1 mg/mL of bovine serum albumin for 1 min at 30 $\mu\text{L}/\text{min}$, with a change of < 400 RU indicating sufficient coverage.

An increasing concentration of tested peptides (peptides 1, 2, 3 and 4—from 4 to 128 μM ; peptide 5—from 24 to 768 μM) was injected over immobilized vesicles with a flowrate of 15 $\mu\text{L}/\text{min}$ for 200 s with a 400 s dissociation phase. The liposome surface was stabilized after each injection by three subsequent injections of 10 mM NaOH at 30 $\mu\text{L}/\text{min}$ for 30 s each. Between experiments, the chip surface was cleaned by 20 mM CHAPS, 40 mM octyl- β -D-glucopyranoside and 30% ethanol in turn, with each solution injected for 1 min at 30 $\mu\text{L}/\text{min}$. The control flow cell was treated identically, with the exception that only the HEPES buffer solution was injected. The results were processed using in-house MATLAB scripts (MATLAB R2020a; scripts are available at <https://github.com/MarJakubec>).

SPR data processing. K_D was obtained from a steady state analysis using the intensities at the 190 s dissociation time, using Eq. (1):²¹

$$R_{eq} = \frac{cR_{max}}{K_D + c} + R_{off} \quad (1)$$

where R_{eq} is the response at the steady state equilibrium, c is the peptide concentration, R_{max} is the maximum response and R_{off} the response offset.

K_p was obtained from same steady state affinity values using the method presented by Figuera et al., Eq. (2):²¹

$$\frac{RU_S}{RU_L} = \frac{\gamma_L K_p \frac{M_S}{M_L} [S]_W}{1 + \sigma \gamma_L K_p [S]_W} \quad (2)$$

where RU_S and RU_L are the relative responses of solute (peptides) and lipids respectively, γ_L is the molar volume of the lipids, M_S and M_L are the molecular mass of solute and lipid, respectively, and $[S]_W$ is the concentration of solute in water. K_p and σ are obtained from fitting (with σ being lipid to solute ratio).

For k_{off} evaluation we have used the formalism of Figuera et al.²¹ for linearization of the dissociation process, where we have identified the contribution from two different populations in the dissociation response. K_{off} values were then obtained by Eq. (3) and averaged by Eq. (4):

$$S_L(t) = \alpha e^{-k_{off,\alpha}t} + \beta e^{-k_{off,\beta}t} + S_{L,r} \quad (3)$$

$$k_{off} = \frac{\alpha k_{off,\alpha} + \beta k_{off,\beta}}{\alpha + \beta} \quad (4)$$

where S_L is the linearized ratio of solute and lipid, α and β are individual populations, and $S_{L,r}$ is the retained solute fraction.

MST experimental procedure. All MST measurements were conducted on a NanoTemper Monolith NT. Labelfree instrument, using Monolith NT. Labelfree standard treated zero background capillaries.

A dilution series of vesicles/nanodiscs was prepared from 3 mM to 100 nM lipid concentrations, comprising 15 discrete samples, and an additional zero lipid sample, for a total of 16 lipid concentrations. Final MST samples were prepared as a combination of 25 μL lipid solution and 25 μL 5 μM peptide solution (Table S1 in the Supporting Information).

MST measurements were conducted with excitation power set to 15%, with the MST power set to high. Laser time settings were: 3 s pre-laser, 30 s on time, and 3 s after heating. F_{Hot} was taken from the T-jump period after 1.5 s and F_{Cold} taken in the second prior to IR laser activation. For the evaluation of K_p , the initial fluorescence was taken as the value reported during the period before the application of the laser. The MST response and initial fluorescence were extracted directly as a text file for further processing in MATLAB.

MST data processing. The dissociation constant K_D describes the equilibrium between the concentration of bound and unbound ligand⁴⁰.

$$K_D = \frac{[AMP][Lipid]}{[AMPLipid]} \quad (5)$$

In a typical binding experiment that yields a sigmoidal curve, the Hill equation can be fitted to yield K_D .⁶⁶

$$y = y_0 + \frac{E_{Max}[Lipid]^n}{K_D^n + [Lipid]^n} \quad (6)$$

where y is the MST response, y_0 is the MST response of the AMP in an aqueous solution (i.e., in the absence of lipids), n is the Hill coefficient, and E_{Max} is the maximal effect of the tested substrate⁶⁶. The removal of outlying MST response points was necessary. Erroneous points were identified by poor MST trace shapes or higher than expected initial fluorescence that was absent in the other replicates or subsequent points, but otherwise no further treatment of data was necessary. In all instances the MST response was plotted against log lipid concentration in nM and fit to Eq. (6).

The partition coefficient K_p defines the preference of a solute for an aqueous or lipidic environment, with a larger K_p indicating a greater preference for the lipidic environment.

$$K_p = \frac{S[Lipid]}{S[Aqueous]} \quad (7)$$

The K_p of a molecule can be determined experimentally by observing changes in fluorescent intensity in the presence of an increasing concentration of lipid, and fitting to Eq. (8)⁴³.

$$\frac{I}{I_{aq}} = 1 + \frac{\left(K_p V_m [Lipid] \frac{I_L}{I_{aq}}\right)}{1 + \left(K_p V_m [Lipid]\right)} \quad (8)$$

In Eq. (8) the fluorescence intensity of the AMP (I) is normalised to the fluorescence intensity of the AMP in an aqueous environment (I_{aq}), V_m is the molar volume of the lipids and I_L is the fluorescence intensity of the AMP in the lipidic environment. For V_m , the average molar volume of the lipid composition is used. In the case of the DMPC only environments it is taken as the V_m of DMPC (1.023 nm³), and in the DMPC-DMPG mixture it is the weighted average relative to the composition used ($V_{m\text{DMPC}} = 0.997 \text{ nm}^3$)⁵⁴.

Data availability

The datasets generated and analysed during the current study are available in the UiT Open Research Data repository <https://doi.org/10.18710/XZB5KI>.

Received: 2 May 2023; Accepted: 31 July 2023

Published online: 03 August 2023

References

- Mahlapuu, M., Håkansson, J., Ringstad, L. & Björn, C. Antimicrobial peptides: An emerging category of therapeutic agents. *Front. Cell. Infect. Microbiol.* **6**, 194 (2016).
- Tornesello, A. L., Borrelli, A., Buonaguro, L., Buonaguro, F. M. & Tornesello, M. L. Antimicrobial peptides as anticancer agents: Functional properties and biological activities. *Molecules* **25**(12), 2850 (2020).
- DeLucca, A. J. *et al.* Fungicidal activity of cecropin A. *Antimicrob. Agents Chemother.* **41**(2), 481–483 (1997).
- Clark, S., Jowitt, T. A., Harris, L. K., Knight, C. G. & Dobson, C. B. The lexicon of antimicrobial peptides: A complete set of arginine and tryptophan sequences. *Commun. Biol.* **4**(1), 605 (2021).
- Le, C.-F., Fang, C.-M. & Sekaran, S. D. Intracellular targeting mechanisms by antimicrobial peptides. *Antimicrob. Agents Chemother.* **61**(4), e02340-16 (2017).
- Wang, G. Human antimicrobial peptides and proteins. *Pharmaceuticals (Basel)* **7**(5), 545–594 (2014).
- Huan, Y., Kong, Q., Mou, H. & Yi, H. Antimicrobial peptides: Classification, design, application and research progress in multiple fields. *Front. Microbiol.* **11**, 2559 (2020).
- Kumar, P., Kizhakkedathu, J. N. & Straus, S. K. Antimicrobial peptides: Diversity, mechanism of action and strategies to improve the activity and biocompatibility in vivo. *Biomolecules* **8**(1), 4 (2018).
- Shi, G. *et al.* DRAMP 3.0: An enhanced comprehensive data repository of antimicrobial peptides. *Nucleic Acids Res.* **50**(D1), D488–D496 (2021).
- Wang, G., Li, X. & Wang, Z. APD3: The antimicrobial peptide database as a tool for research and education. *Nucleic Acids Res.* **44**(D1), D1087–D1093 (2016).
- Waghu, F. H. & Idicula-Thomas, S. Collection of antimicrobial peptides database and its derivatives: Applications and beyond. *Protein Sci.* **29**(1), 36–42 (2020).
- Pirtskhalava, M. *et al.* DBAASP v3: Database of antimicrobial/cytotoxic activity and structure of peptides as a resource for development of new therapeutics. *Nucleic Acids Res.* **49**(D1), D288–D297 (2021).
- Piotto, S. P., Sessa, L., Concilio, S. & Iannelli, P. YADAMP: Yet another database of antimicrobial peptides. *Int. J. Antimicrob. Agents* **39**(4), 346–351 (2012).
- Scheinplüg, K. *et al.* Antimicrobial peptide cFWF kills by combining lipid phase separation with autolysis. *Sci. Rep.* **7**(1), 44332 (2017).
- Omaidien, S., Brul, S. & Zaat, S. A. J. Antimicrobial activity of cationic antimicrobial peptides against Gram-positives: Current progress made in understanding the mode of action and the response of bacteria. *Front. Cell Dev. Biol.* **4**, 111 (2016).

16. Rice, A. & Wereszczynski, J. Probing the disparate effects of arginine and lysine residues on antimicrobial peptide/bilayer association. *Biochim. Biophys. Acta Biomembr.* **1859**(10), 1941–1950 (2017).
17. Hollmann, A. *et al.* Role of amphipathicity and hydrophobicity in the balance between hemolysis and peptide–membrane interactions of three related antimicrobial peptides. *Colloids Surf. B* **141**, 528–536 (2016).
18. Huang, R. & Leung, I. K. H. Protein-small molecule interactions by WaterLOGSY, chapter 14. In *Methods in Enzymology* Vol. 615 (ed. Wand, A. J.) 477–500 (Academic Press, 2019).
19. Hedegaard, S. F. *et al.* Fluorophore labeling of a cell-penetrating peptide significantly alters the mode and degree of biomembrane interaction. *Sci. Rep.* **8**(1), 6327 (2018).
20. Williamson, M. P. Using chemical shift perturbation to characterise ligand binding. *Prog. Nucl. Magn. Reson. Spectrosc.* **73**, 1–16 (2013).
21. Figueira, T. N. *et al.* Quantitative analysis of molecular partition towards lipid membranes using surface plasmon resonance. *Sci. Rep.* **7**, 45647 (2017).
22. Jerabek-Willemsen, M. *et al.* MicroScale thermophoresis: Interaction analysis and beyond. *J. Mol. Struct.* **1077**, 101–113 (2014).
23. Jerabek-Willemsen, M., Wienken, C. J., Braun, D., Baaske, P. & Duhr, S. Molecular interaction studies using microscale thermophoresis. *Assay Drug Dev. Technol.* **9**(4), 342–353 (2011).
24. Topf, A., Franz, P. & Tsiavaliaris, G. MicroScale thermophoresis (MST) for studying actin polymerization kinetics. *Biotechniques* **63**(4), 187–190 (2017).
25. Yu, L., Fan, Q., Yue, X., Mao, Y. & Qu, L. Activity of a novel-designed antimicrobial peptide and its interaction with lipids. *J. Pept. Sci.* **21**(4), 274–282 (2015).
26. López-Méndez, B. *et al.* Reproducibility and accuracy of microscale thermophoresis in the NanoTemper Monolith: A multi-laboratory benchmark study. *Eur. Biophys. J.* **50**(3), 411–427 (2015).
27. Speck, S. *et al.* Cationic synthetic peptides: Assessment of their antimicrobial potency in liquid preserved boar semen. *PLoS One* **9**(8), e105949 (2014).
28. Lau, Q. Y. *et al.* Discovery of an ultra-short linear antibacterial tetrapeptide with anti-MRSA activity from a structure–activity relationship study. *Eur. J. Med. Chem.* **105**, 138–144 (2015).
29. Gopal, R., Kim, Y. J., Seo, C. H., Hahm, K.-S. & Park, Y. Reversed sequence enhances antimicrobial activity of a synthetic peptide. *J. Pept. Sci.* **17**(5), 329–334 (2011).
30. Gopal, R., Na, H., Seo, C. H. & Park, Y. Antifungal activity of (KW)_n or (RW)_n peptide against *Fusarium solani* and *Fusarium oxysporum*. *Int. J. Mol. Sci.* **13**(11), 15042–15053 (2012).
31. Finger, S., Kerth, A., Dathe, M. & Blume, A. The efficacy of trivalent cyclic hexapeptides to induce lipid clustering in PG/PE membranes correlates with their antimicrobial activity. *Biochim. Biophys. Acta (BBA) Biomembr.* **1848**(11, Part A), 2998–3006 (2015).
32. Dörr, J. M. *et al.* Detergent-free isolation, characterization, and functional reconstitution of a tetrameric K⁺ channel: The power of native nanodiscs. *Proc. Natl. Acad. Sci.* **111**(52), 18607 (2014).
33. Ravula, T., Hardin, N. Z., Ramadugu, S. K., Cox, S. J. & Ramamoorthy, A. Formation of pH-resistant monodispersed polymer-lipid nanodiscs. *Angew. Chem. Int. Ed. Engl.* **57**(5), 1342–1345 (2018).
34. Bernhard, M. & Laube, B. Thermophoretic analysis of ligand-specific conformational states of the inhibitory glycine receptor embedded in copolymer nanodiscs. *Sci. Rep.* **10**(1), 16569 (2020).
35. Rainsford, P. *et al.* Supplementary Data for: Label-free measurement of antimicrobial peptide interactions with lipid vesicles and nanodiscs using microscale thermophoresis. *ChemRxiv* (2023).
36. Scheuermann, T. H., Padrick, S. B., Gardner, K. H. & Brautigam, C. A. On the acquisition and analysis of microscale thermophoresis data. *Anal. Biochem.* **496**, 79–93 (2016).
37. López-Méndez, B., Uebel, S., Lundgren, L. P. & Sedivy, A. Microscale thermophoresis and additional effects measured in NanoTemper Monolith instruments. *Eur. Biophys. J.* **50**(3), 653–660 (2021).
38. Christiaens, B. *et al.* Tryptophan fluorescence study of the interaction of penetratin peptides with model membranes. *Eur. J. Biochem.* **269**(12), 2918–2926 (2002).
39. Zhang, A. H. *et al.* Elucidating the lipid binding properties of membrane-active peptides using cyclised nanodiscs. *Front. Chem.* **7**, 238–238 (2019).
40. Jarmoskaite, I., AlSadhan, I., Vaidyanathan, P. P. & Herschlag, D. How to measure and evaluate binding affinities. *Elife* **9**, e57264 (2020).
41. Lee, T.-H., Hall, N. K. & Aguilar, M.-I. Antimicrobial peptide structure and mechanism of action: A focus on the role of membrane structure. *Curr. Top. Med. Chem.* **16**(1), 25–39 (2016).
42. Bortolotti, A. *et al.* Mechanism of lipid bilayer perturbation by bactericidal membrane-active small molecules. *Biochim. Biophys. Acta (BBA) Biomembr.* **1865**(1), 184079 (2023).
43. Matos, P. M., Franquelim, H. G., Castanho, M. A. R. B. & Santos, N. C. Quantitative assessment of peptide–lipid interactions: Ubiquitous fluorescence methodologies. *Biochim. Biophys. Acta (BBA) Biomembr.* **1798**(11), 1999–2012 (2010).
44. Melo, M. N. & Castanho, M. A. R. B. Omiganan interaction with bacterial membranes and cell wall models. Assigning a biological role to saturation. *Biochim. Biophys. Acta (BBA) Biomembr.* **1768**(5), 1277–1290 (2007).
45. Stauffer, F. *et al.* Interaction between dengue virus fusion peptide and lipid bilayers depends on peptide clustering. *Mol. Membr. Biol.* **25**(2), 128–138 (2008).
46. Bocchinfuso, G., Bobone, S., Mazzuca, C., Palleschi, A. & Stella, L. Fluorescence spectroscopy and molecular dynamics simulations in studies on the mechanism of membrane destabilization by antimicrobial peptides. *Cell. Mol. Life Sci.* **68**(13), 2281–2301 (2011).
47. Langer, A. *et al.* A new spectral shift-based method to characterize molecular interactions. *Assay Drug Dev. Technol.* **20**(2), 83–94 (2022).
48. Duhr, S. & Braun, D. Why molecules move along a temperature gradient. *Proc. Natl. Acad. Sci.* **103**(52), 19678–19682 (2006).
49. Terakawa, M. S. *et al.* Impact of membrane curvature on amyloid aggregation. *Biochim. Biophys. Acta (BBA) Biomembr.* **1860**(9), 1741–1764 (2018).
50. Stepien, P. *et al.* Complexity of seemingly simple lipid nanodiscs. *Biochim. Biophys. Acta (BBA) Biomembr.* **1862**(11), 183420 (2020).
51. Bhatia, V. K. *et al.* Amphipathic motifs in BAR domains are essential for membrane curvature sensing. *EMBO J.* **28**(21), 3303–3314 (2009).
52. Kawano, K. *et al.* Structural factors governing binding of curvature-sensing peptides to bacterial extracellular vesicles covered with hydrophilic polysaccharide chains. *Biophys. Chem.* **299**, 107039 (2023).
53. Kawano, K., Ogushi, M., Masuda, T. & Futaki, S. Development of a membrane curvature-sensing peptide based on a structure–activity correlation study. *Chem. Pharm. Bull.* **67**(10), 1131–1138 (2019).
54. Marsh, D. *Handbook of Lipid Bilayers* 2nd edn. (CRC Press, 2013).
55. Grethen, A., Oluwale, A. O., Danielczak, B., Vargas, C. & Keller, S. Thermodynamics of nanodisc formation mediated by styrene/maleic acid (2:1) copolymer. *Sci. Rep.* **7**(1), 11517 (2017).
56. Su, J., Marrink, S. J. & Melo, M. N. Localization preference of antimicrobial peptides on liquid-disordered membrane domains. *Front. Cell Dev. Biol.* **8**, 350 (2020).
57. Epand, R. F., Maloy, W. L., Ramamoorthy, A. & Epand, R. M. Probing the “charge cluster mechanism” in amphipathic helical cationic antimicrobial peptides. *Biochemistry* **49**(19), 4076–4084 (2010).

58. Epand, R. M. & Epand, R. F. Lipid domains in bacterial membranes and the action of antimicrobial agents. *Biochim. Biophys. Acta (BBA) Biomembr.* **1788**(1), 289–294 (2009).
59. Ravula, T. *et al.* Effect of polymer charge on functional reconstitution of membrane proteins in polymer nanodiscs. *Chem. Commun. (Camb.)* **54**(69), 9615–9618 (2018).
60. Krishnarjuna, B., Ravula, T. & Ramamoorthy, A. Detergent-free isolation of CYP450-reductase's FMN-binding domain in *E. coli* lipid-nanodiscs using a charge-free polymer. *Chem. Commun. (Camb.)* **58**(31), 4913–4916 (2022).
61. Linke, P. *et al.* An automated microscale thermophoresis screening approach for fragment-based lead discovery. *J. Biomol. Screen.* **21**(4), 414–421 (2016).
62. Fiedler, S. & Heerklotz, H. Vesicle leakage reflects the target selectivity of antimicrobial lipopeptides from *Bacillus subtilis*. *Biophys. J.* **109**(10), 2079–2089 (2015).
63. Rispoli, G. Studying the mechanism of membrane permeabilization induced by antimicrobial peptides using patch-clamp techniques. In *Antimicrobial Peptides: Methods and Protocols* (ed. Hansen, P. R.) 255–269 (Springer, 2017).
64. Rainsford, P. *et al.* WIND-PVPA: Water/ion NMR detected PVPA to assess lipid barrier integrity in vitro through quantification of passive water- and ion transport. *Biochim. Biophys. Acta (BBA) Biomembr.* **1864**(7), 183911 (2022).
65. Clinical and Laboratory Standards Institute. *Methods for Dilution Antimicrobial Susceptibility Tests for Bacteria That Grow Aerobically*. Approved Standard. M07-A9, 9th ed. (2012).
66. Salahudeen, M. S. & Nishtala, P. S. An overview of pharmacodynamic modelling, ligand-binding approach and its application in clinical practice. *Saudi Pharm. J.* **25**(2), 165–175 (2017).

Acknowledgements

This project received funding from the DigiBiotics project (Research Council of Norway, project ID 269425), the AntiBioSpec project of UiT the Arctic University of Norway (Cristin ID 20161326) and the NanoAMP project (Research Council of Norway, project ID 275186).

Author contributions

Conceptualisation: P.R. Peptide synthesis and purification: M.S. MIC assay: E.J. Nanodisc and vesicle preparation, and MST: P.R. and F.G.R. Vesicle preparation and SPR: M.J. Data analysis: P.R., M.J. and J.I. Original draft: P.R. Visualisation: P.R. Writing and editing: P.R., M.J., F.G.R., M.S., J.I., R.E. Supervision: J.I., R.E., J.S.S. and J.E. All authors reviewed and approved final version.

Funding

Open access funding provided by UiT The Arctic University of Norway (incl University Hospital of North Norway).

Competing interests

The authors declare no competing interests.

Additional information

Supplementary Information The online version contains supplementary material available at <https://doi.org/10.1038/s41598-023-39785-0>.

Correspondence and requests for materials should be addressed to J.I.

Reprints and permissions information is available at www.nature.com/reprints.

Publisher's note Springer Nature remains neutral with regard to jurisdictional claims in published maps and institutional affiliations.



Open Access This article is licensed under a Creative Commons Attribution 4.0 International License, which permits use, sharing, adaptation, distribution and reproduction in any medium or format, as long as you give appropriate credit to the original author(s) and the source, provide a link to the Creative Commons licence, and indicate if changes were made. The images or other third party material in this article are included in the article's Creative Commons licence, unless indicated otherwise in a credit line to the material. If material is not included in the article's Creative Commons licence and your intended use is not permitted by statutory regulation or exceeds the permitted use, you will need to obtain permission directly from the copyright holder. To view a copy of this licence, visit <http://creativecommons.org/licenses/by/4.0/>.

© The Author(s) 2023

Supplemental materials: Label-free measurement of antimicrobial peptide interactions with lipid vesicles and nanodiscs using microscale thermophoresis

Philip Rainsford,^a Fredrik G. Rylandsholm,^a Martin Jakubec,^a Mitchell Silk,^a Eric Juskewitz,^b Johanna U. Ericson,^b John-Sigurd Svendsen,^a Richard A. Engh,^a Johan Isaksson^{*,a,c}

^a Department of Chemistry, Faculty of Science and Technology, UiT the Arctic University of Norway, 9019 Tromsø, Norway

^b Research Group for Host Microbe Interactions, Department of Medical Biology, Faculty of Health Sciences, UiT the Arctic University of Norway, 9019 Tromsø, Norway

^c Natural products and Medicinal Chemistry, Department of Pharmacy, Faculty of Health Sciences, UiT the Arctic University of Norway, 9037 Tromsø, Norway

*johan.isaksson@uit.no

Supp. 1

Cyclic Peptide Purification and characterisation:

1; *Cyclo(WWWRRR)*. *Linear precursor:* H₂N-Arg(Pbf)-Arg(Pbf)-Arg(Pbf)-Trp(Boc)-Trp(Boc)-Trp(Boc)-OH. *Cyclic:* *cyclo*(Trp-Trp-Trp-Arg-Arg-Arg). Purification gradient: 15-75% buffer B over 60 min, t_R = 18 min (33% buffer B). Yield: 46.7 mg (30.0% relative to linear precursor) as a white solid. ESI-FTMS [M + H]⁺ calculated: 1027.5419, found: 1027.5473, [M + 2H]²⁺ calculated: 514.2785, found: 514.2770, [M + 3H]³⁺ calculated: 343.1882, found: 343.1872.

2; *Cyclo(WRWRWR)*. *Linear precursor:* H₂N-Arg(Pbf)-Trp(Boc)-Arg(Pbf)-Trp(Boc)-Arg(Pbf)-Trp(Boc)-OH. *Cyclic:* *cyclo*(Trp-Arg-Trp-Arg-Trp-Arg). Purification gradient: 5-65% buffer B over 60 min, t_R = 25 min (30% buffer B). Yield: 26.9 mg (22.6% relative to linear precursor) as a white solid. ESI-FTMS [M + 2H]²⁺ calculated: 514.2785, found: 514.2779, [M + 3H]³⁺ calculated: 343.1882, found: 343.1883.

3; *Cyclo(WWWKKK)*. *Linear precursor:* H₂N-Lys(Boc)-Lys(Boc)-Lys(Boc)-Trp(Boc)-Trp(Boc)-Trp(Boc)-OH. *Cyclic:* *cyclo*(Trp-Trp-Trp-Lys-Lys-Lys). Purification gradient: 10-70% buffer B over 60 min, t_R = 22 min (32% buffer B). Yield: 49.5 mg (39.0% relative to linear precursor) as a white solid. ESI-FTMS [M + H]⁺ calculated: 943.5307, found: 943.5354, [M + Na]⁺ calculated: 965.5126, found: 965.5159, [M + 2H]²⁺ calculated: 472.2693, found: 472.2702.

4; *Cyclo(WKWKWK)*. *Linear precursor:* H₂N-Trp(Boc)-Lys(Boc)-Trp(Boc)-Lys(Boc)-Trp(Boc)-Lys(Boc)-OH. *Cyclic:* *cyclo*(Trp-Lys-Trp-Lys-Trp-Lys). Purification gradient: 5-65% buffer B over 60 min, t_R = 21 min (26% buffer B). Yield: 40.7 mg (41.8% relative to linear precursor) as a white solid. ESI-FTMS [M + H]⁺ calculated: 943.5307, found: 943.5308, calculated: 472.2693, found: 472.2689.

5; *Cyclo(LWwNKr)*. *Linear precursor:* H₂N-Trp(Boc)-D-Trp(Boc)-Asn(Trt)-Lys(Boc)-D-Arg(Pbf)-Leu-OH. *Cyclic:* *cyclo*(Leu-Trp-D-Trp-Asn-Lys-D-Arg). Purification gradient: 10-70% buffer B over 60 min, 6 mL/min, t_R = 23 min (33% buffer B). Yield: 35.1 mg (44.9% relative to linear

precursor) as a white solid. ESI-FTMS $[M + H]^+$ calculated: 884.4895, found: 884.4895, $[M + 2H]^{2+}$ calculated: 442.7487, found: 442.7483.

Table S1: Table of lipid and peptide concentrations for MST

MST Sample	Final lipid concentration (nM)	Final AMP concentration (nM)
1	1500000	2500
2	1250000	2500
3	500000	2500
4	250000	2500
5	125000	2500
6	50000	2500
7	25000	2500
8	12500	2500
9	5000	2500
10	2500	2500
11	1250	2500
12	500	2500
13	250	2500
14	125	2500
15	50	2500
16	0	2500

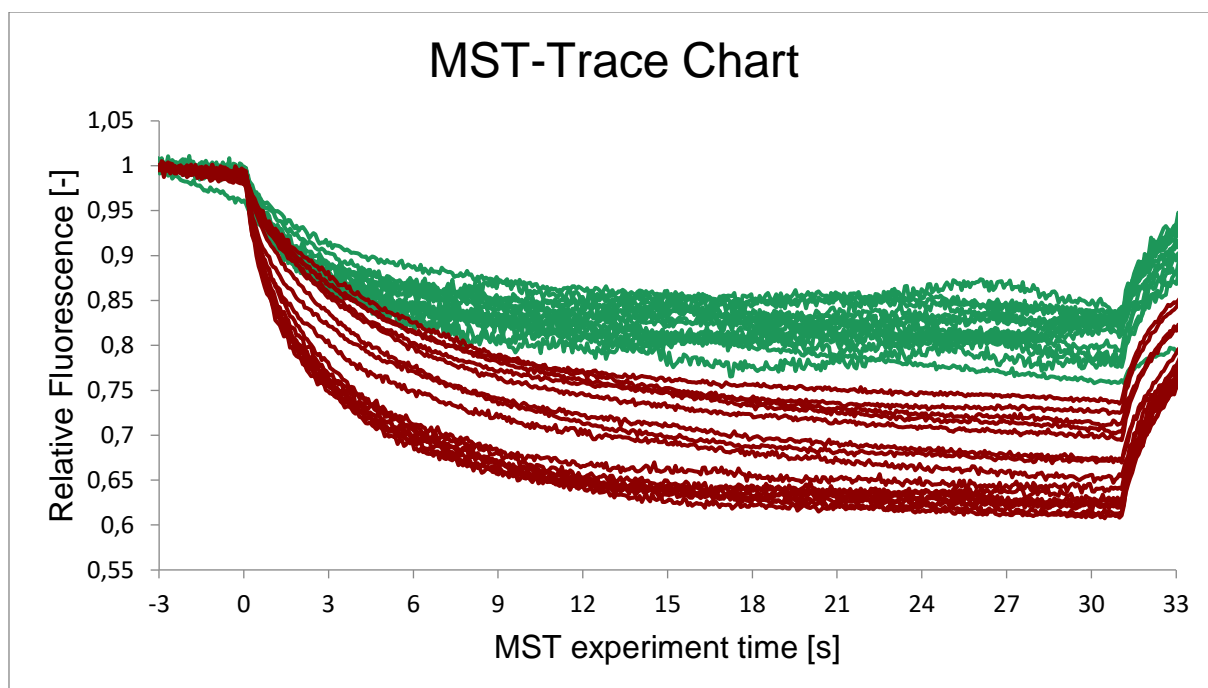


Figure S1: MST traces of increasing DMPC/PG vesicle concentration with **1** (red) and with no peptide (green), demonstrating the typical differences of the MST traces when peptide is present. Notably a more irregular trace can only be observed in the absence of the fluorophore carrying peptides, with a smaller thermophoretic change.

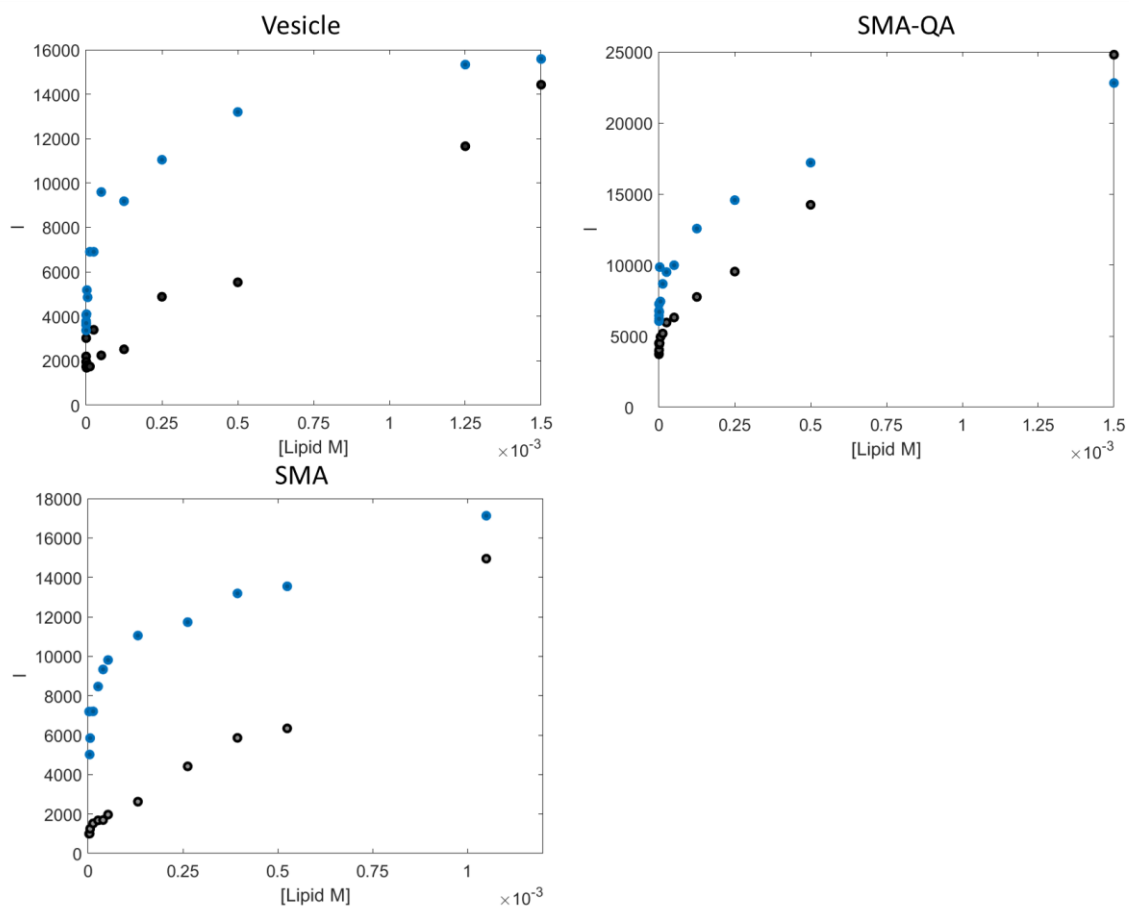


Figure S2: Fluorescent intensities of samples in the presence of 1 (blue) and without any peptide i.e. lipid only (gray). Both SMA and vesicle samples show markedly higher intensities when an AMP is present in the samples with a (generally) parabolic line shape. In SMA-QA the lipid only sample has a higher fluorescent intensity compared to SMA and vesicles, however the parabolic line shape is clearly differentiated when an AMP is present.

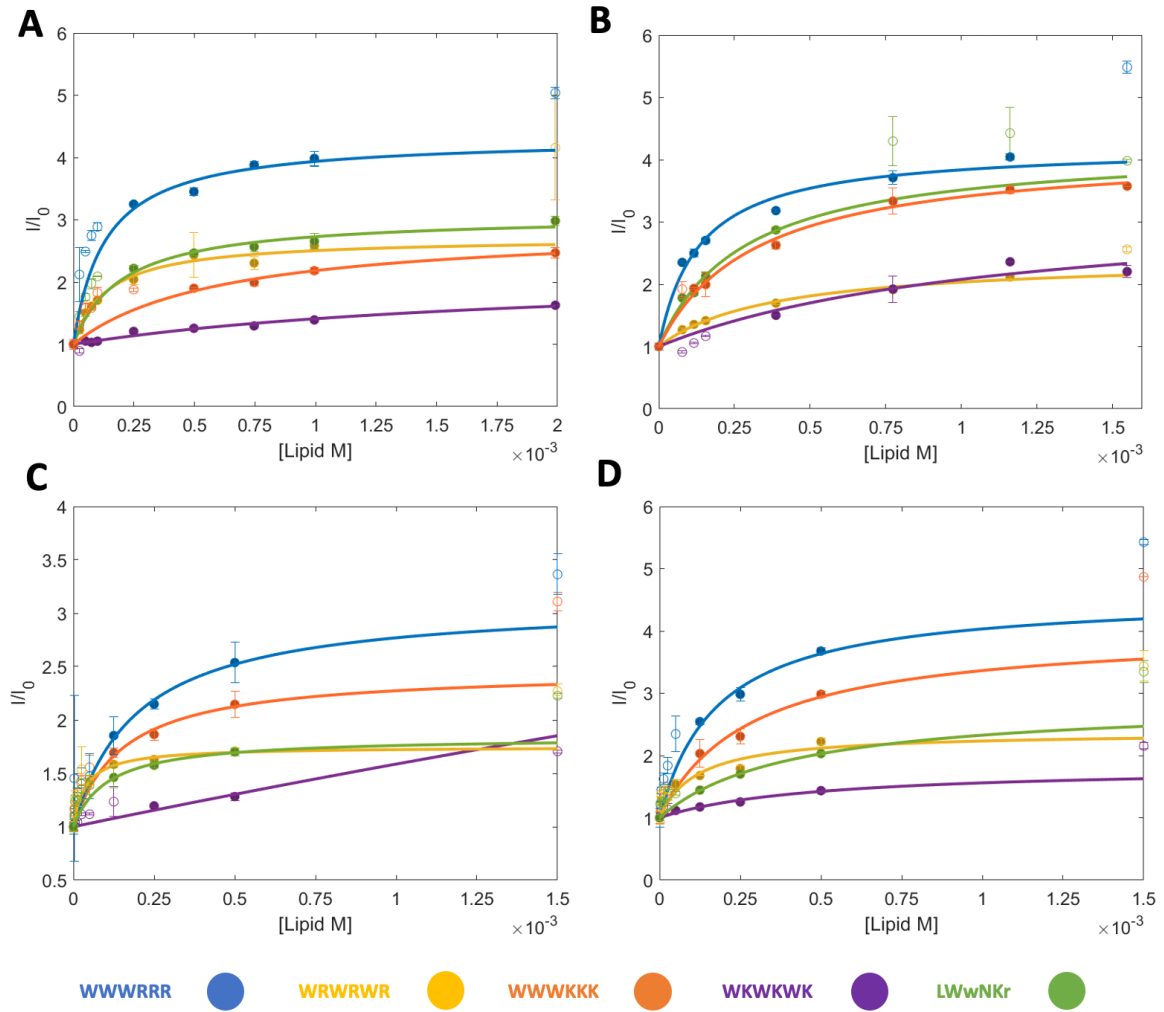


Figure S3: Initial fluorescence and K_p fits of 1-5 in different lipid compositions of nanodiscs. **A:** SMA 100% DMPC. **B:** SMA 95% DMPC with 5% DMPG. **C:** SMA-QA 100% DMPC. **D:** SMA-QA 95% DMPC with 5% DMPG. Lines and filled circles indicate the fit and the points used, unfilled circles are points not included. Error bars represent the range in the triplicates.

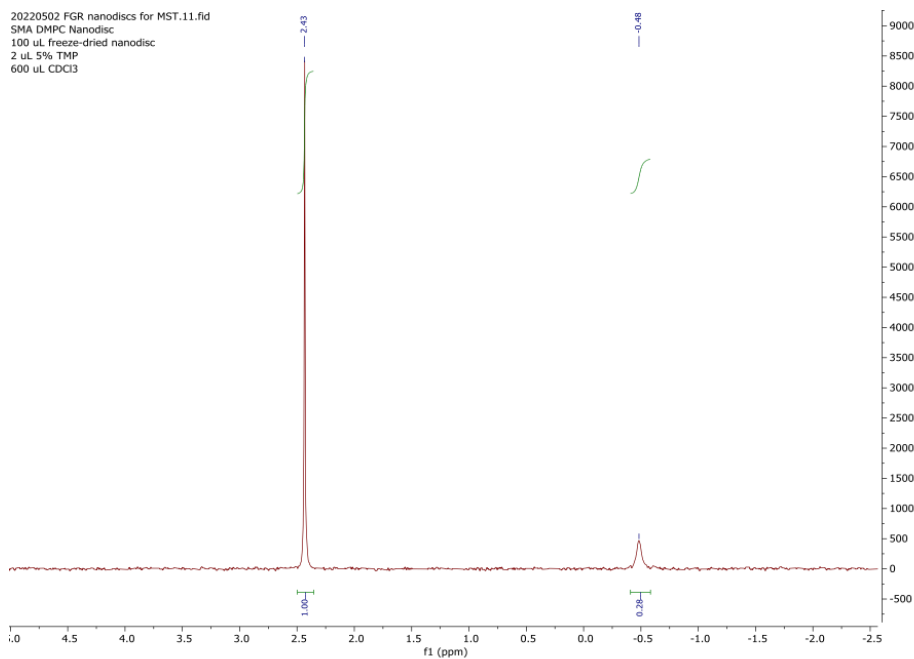


Figure S4: ³¹P NMR spectrum of freeze dried SMA DMPC nanodiscs dissolved in CDCl₃ with TMP internal standard. From the integrals and volumes, we calculate the DMPC concentration to be 2.39 mM.

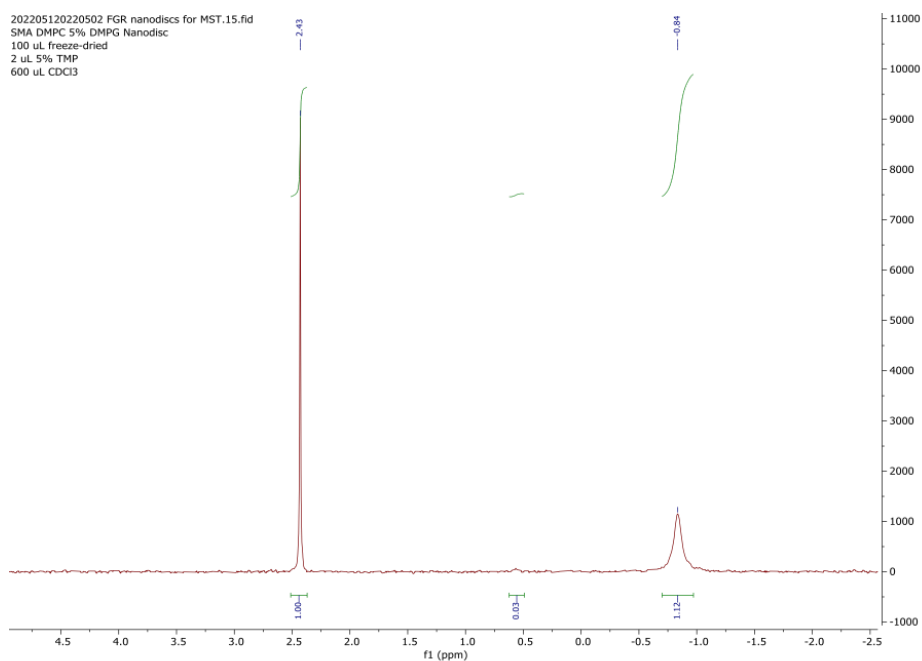


Figure S5: ³¹P NMR spectrum of freeze dried SMA DMPC 5% DMPG nanodiscs dissolved in CDCl₃ with TMP internal standard. From the integrals and volumes, we calculate the DMPC concentration to be 9.57 mM and the DMPG concentration to be 0.26 mM (2.72% DMPG).

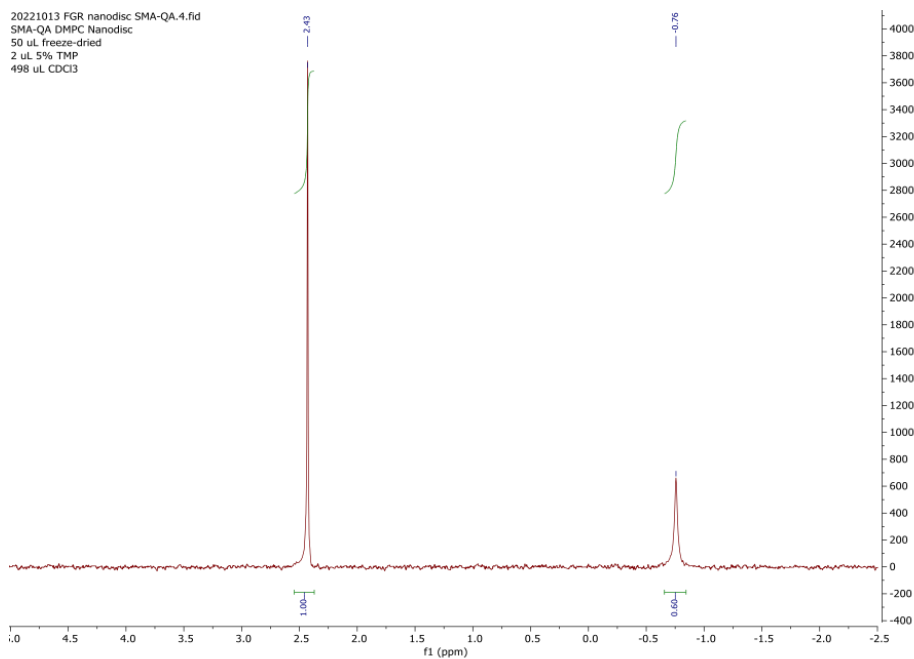


Figure S6: ³¹P NMR spectrum of freeze dried SMA-QA DMPC nanodiscs dissolved in CDCl₃ with TMP internal standard. From the integrals and volumes, we calculate the DMPC concentration to be 10.26 mM.

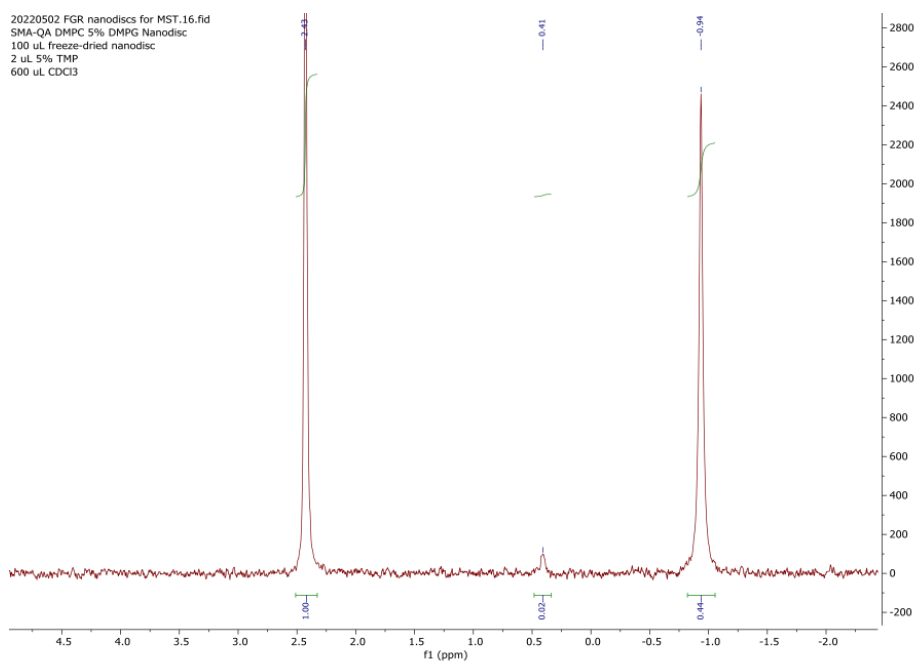


Figure S7: ³¹P NMR spectrum of freeze dried SMA-QA DMPC 5% DMPG nanodiscs dissolved in CDCl₃ with TMP internal standard. From the integrals and volumes, we calculate the DMPC concentration to be 5.13 mM and the DMPG concentration to be 0.23 mM (4.5% DMPG).

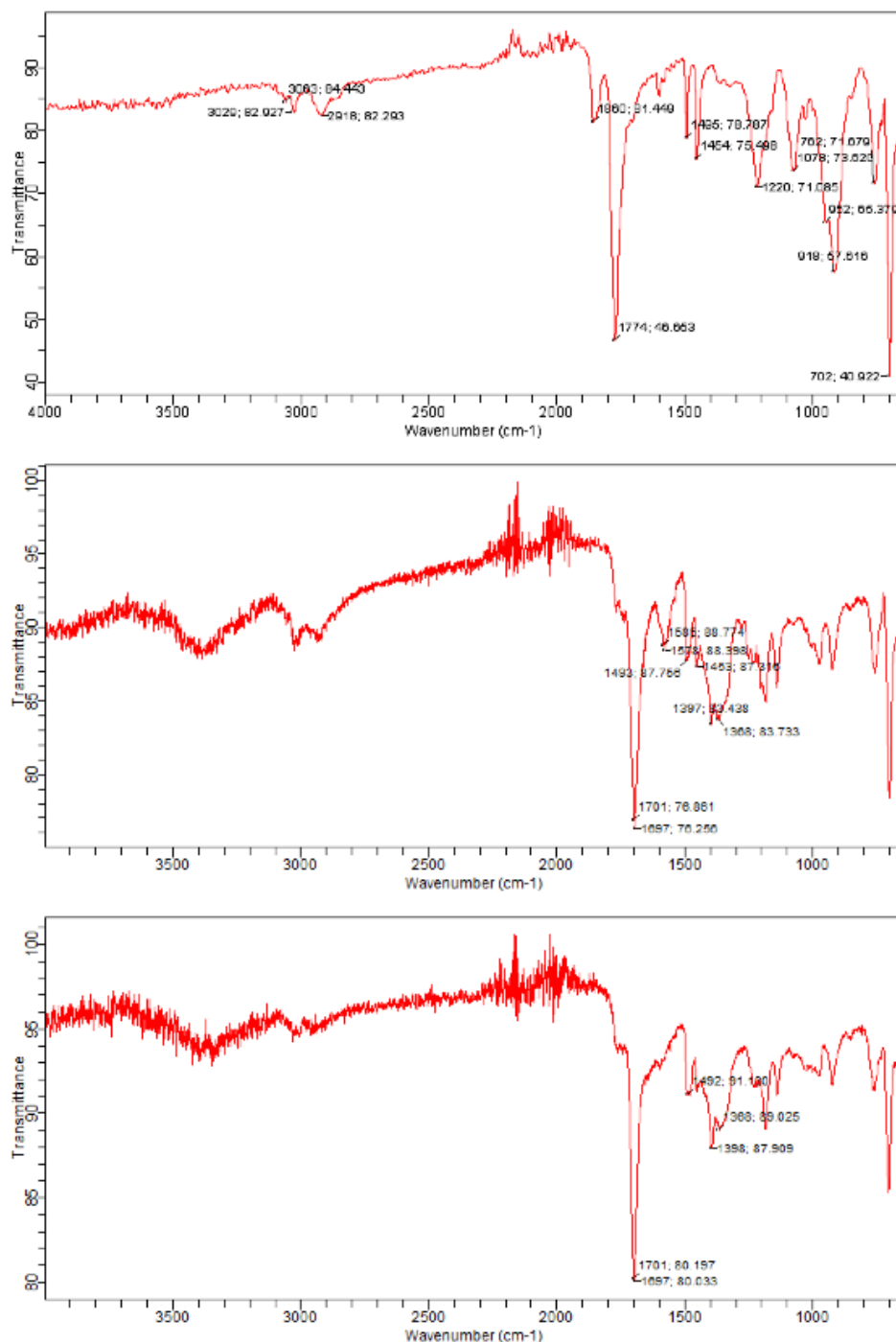


Figure S8: TOP: FT-IR spectrum of SMA anhydride, the starting material for the synthesis of SMA-QA. MIDDLE: FT-IR spectrum of SMA-QA, synthesized from SMA anhydride. BOTTOM: FT-IR spectrum of SMA-QA, bought from BioNordika AS, and produced by anatrice.

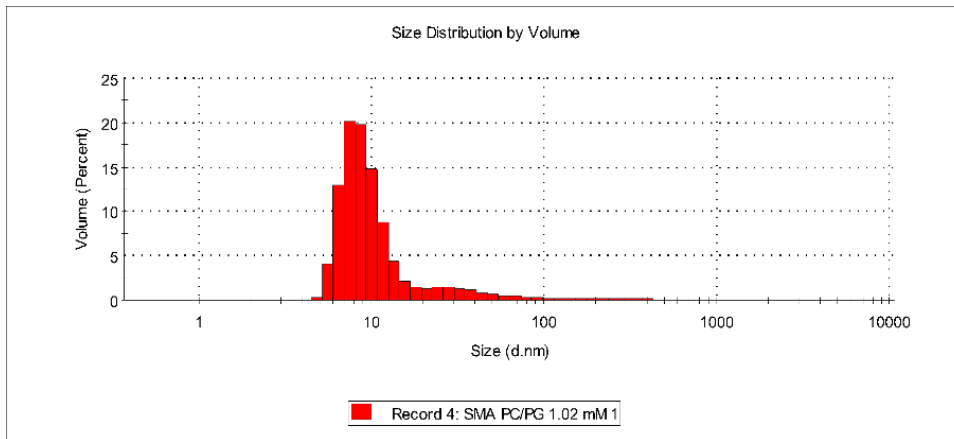


Figure S9: DLS Size distribution by volume of SMA DMPC/PG nanodiscs.

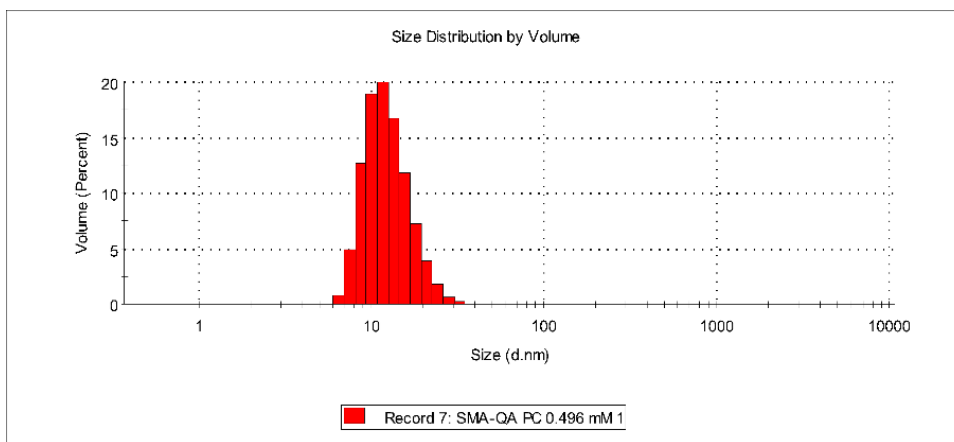


Figure S10: DLS Size distribution by volume of SMA-QA DMPC nanodiscs.

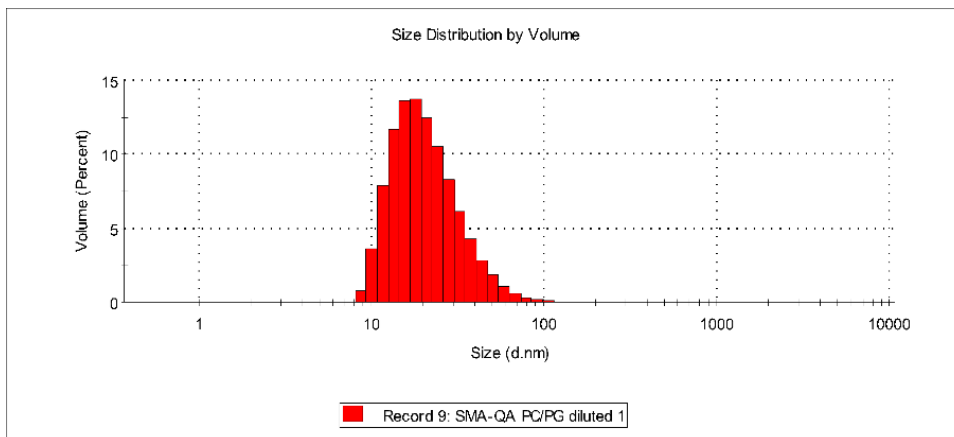


Figure S11: DLS Size distribution by volume of SMA-QA DMPC/PG nanodiscs.

Paper IV

The role of amphipathicity and *L*- to *D*-amino acid substitution in a small antimicrobial cyclic tetrapeptide scaffold containing a halogenated α,α -disubstituted $\beta^{2,2}$ -amino acid residue

Danijela Simonovic^a, Fredrik G. Rylandsholm^b, Martin Jakubec^b, Johan Mattias Isaksson^{a,b}, Hege Devold^c, Hymonti Dey^c, Trude Anderssen^a, Tor Haug^c, Morten B. Strøm^{a*}

^a Department of Pharmacy, Faculty of Health Sciences, UiT – The Arctic University of Norway, NO-9037 Tromsø, NORWAY.

^b Department of Chemistry, UiT – The Arctic University of Norway, NO-9037 Tromsø, NORWAY.

^c The Norwegian College of Fishery Science, Faculty of Biosciences, Fisheries and Economics, UiT – The Arctic University of Norway, NO-9037 Tromsø, NORWAY.

ARTICLE INFO

ABSTRACT

Keywords:

Antibacterial
Antimicrobial peptides
Beta-amino acids
Cyclic peptides
Peptidomimetics
SMAMPs – synthetic mimics of antimicrobial peptides

A small library of nine cyclic tetrapeptides having cationic (Lys or Arg) and lipophilic residues were synthesised and their antimicrobial activity and haemolytic toxicity were investigated. All cyclic tetrapeptides contained a fluorinated lipophilic $\beta^{2,2}$ -amino acid. Membrane-peptide interactions were studied by Surface Plasmon Resonance (SPR), whereas Nuclear Magnetic Resonance spectroscopy (NMR) was used for conformational studies.

By changing the order of the last two residues in the starting sequence c(Lys- $\beta^{2,2}$ -Leu-Lys), effects of amphipathicity on antimicrobial activity and haemolytic toxicity were investigated. Introducing a cationic *D*-Lys/*D*-Arg residue allowed for the study of stereochemical aspects related to positioning of the cationic side chains relative to the plane of the cyclic tetrapeptide scaffold. Effects of substitution of Leu with more bulky, lipophilic Phe were also studied.

Surprisingly, many of the modifications had minimal effect on antimicrobial activity while having a substantial impact on haemolytic toxicity. The overall most potent cyclic tetrapeptide **006** c(Arg- $\beta^{2,2}$ -Arg-Arg) had a minimum inhibitory concentration (MIC) of 1 – 4 $\mu\text{g}/\text{mL}$ against both Gram-positive and Gram-negative bacteria, and low haemolytic toxicity (EC_{50} 279 $\mu\text{g}/\text{mL}$). SPR studies supported the bioactivity studies and revealed important differences in the way the cyclic tetrapeptides interacted with membrane models. NMR did not indicate any significant changes in backbone conformation, suggesting that the observed differences in activity could be attributed to different side chain properties.

In conclusion, changes in amphipathicity and in stereochemistry of a single cationic residue in small cyclic tetrapeptide scaffold encompassing a lipophilic $\beta^{2,2}$ -amino acid, can be used as a powerful tool for reducing haemolytic toxicity while maintaining antimicrobial activity of membrane active cyclic tetrapeptides.

Keywords: Short antimicrobial peptides; AMPs; cyclic tetrapeptides; structure-activity relationship; $\beta^{2,2}$ -amino acid residue.

1. Introduction

Effective antimicrobial drugs are the very core of modern medicine, enabling successful prevention and treatment of infectious diseases. However, systemic misuse and overuse of antibiotics in human medicine, as well as in animal husbandry have led to widespread antibiotic-resistance, rendering many of these drugs ineffective.

Antimicrobial peptides (AMPs), also called host defense peptides (HDPs), are compounds that widely exist in nature. They are an important part of the innate immune system of different organisms, and as such protect the host from a wide range of pathogens, including bacteria, viruses, and fungi. (1) Due to their broad-spectrum antimicrobial activity and unique mechanisms of action (predominantly membrane disruption), they are hailed as a potential alternative to conventional antibiotics. Moreover, AMPs have been regarded as a viable therapeutic option against infections caused by multidrug-resistant bacteria. (2, 3) It is believed that resistance towards AMPs is less likely to develop compared to conventional antibiotics, as it would be highly costly for the bacterium to alter the components of its membrane, which AMPs usually target. (4) Despite their potential as drug candidates, their application has been hindered by several obstacles, one of them being low selectivity for bacterial cells over mammalian cells.

Head-to-tail cyclic tetrapeptides isolated from natural sources are attractive lead compounds due to their small size and a diverse biological activity. They are found to have, among others, anticancer- (e.g., inhibitors of histone deacetylase) and antibacterial properties. (5) One interesting example is a recently discovered AMP teixobactin, a macrocyclic natural product, which contains a cyclotetrapeptide structural motif. This antibiotic exhibits a potent activity against several Gram-positive pathogenic bacteria. (6)

2. Peptide design and synthesis

To study more closely factors influencing selectivity of small cyclic peptidomimetics, we synthesised a series of cyclic tetrapeptides, containing a halogenated α,α -disubstituted $\beta^{2,2}$ -amino acid with two 4-trifluoromethyl-benzyl substituents on the α -carbon. (**Figure 1**) In a previous work done by our group, this particular $\beta^{2,2}$ -amino acid was incorporated in a tetrapeptide scaffold c(Lys- $\beta^{2,2}$ -Xaa-Lys), where Xaa stands for one of the four residues: Lys, Gly, Ala, or Phe. (7) The resulting cyclic peptides had relatively high potency and they were active against multidrug-resistant bacterial strains. Therefore, we decided to use the same achiral lipophilic residue $\beta^{2,2}$ in a similar tetrapeptide scaffold c(Lys- $\beta^{2,2}$ -Leu-Lys) which enabled us to study effects of amphipathicity and *L*- to *D*-amino acid substitution on peptide antimicrobial and haemolytic properties.

Synthesis of the Fmoc- $\beta^{2,2}$ amino acid building block

The α,α -disubstituted $\beta^{2,2}$ -amino acid containing two 4-(trifluoromethyl)benzyl sidechains, termed $\beta^{2,2}$, was synthesised following the protocol described by Paulsen *et al.* (**Figure 1**) (8) In brief the initial dialkylation of methyl cyanoacetate with 1-(bromomethyl)-4-(trifluoromethyl)benzene using 1,8-diazabicyclo-[5.4.0]undec-7-ene (DBU) as a base was followed by nitrile reduction with H_2 (g)/Raney Nickel. The resulting $\beta^{2,2}$ -amino ester was hydrolysed with lithium hydroxide (LiOH) pre-dissolved in water. After pH adjustment to 8, the final step included the protection of the free amine by subsequent addition of *N*-(9-fluorenylmethoxy-carbonyloxy) succinimide (Fmoc-OSu). The reactions were followed by thin layer chromatography (TLC) using Silica gel 60 F₂₅₄ (Merck TLC plates) and visualised with either UV light (254 nm) or by immersion in potassium permanganate after light heating of the plates with a heating gun.

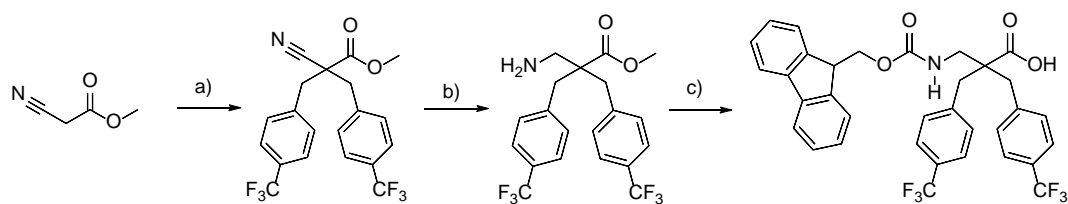


Figure 1. Synthesis of the $\beta^{2,2}$ -amino acid building block by (a) $CF_3C_6H_4CH_2Br$, DBU, CH_2Cl_2 , r.t.; (b) H_2 (g)/Raney-Nickel, EtOAc, $45\text{ }^\circ\text{C}$, 18 h; (c) i. LiOH, dioxane:water (4:1) reflux, 5 h, ii. aq. HCl to pH 8 then Fmoc-OSu, r.t. 18 h. (8)

Synthesis of cyclic tetrapeptides

A series of nine cyclic tetrapeptides was synthesised by Fmoc-solid phase peptide synthesis (Fmoc-SPPS) using a preloaded 2-Cl-trityl resin and microwave assisted peptide coupling. (**Figure 2**) Fully side chain protected peptides were cleaved from the resin with hexafluoroisopropanol (HFIP). Head-to-tail cyclisation was performed under *pseudo-high dilution* conditions as described by Malesevic *et al.* (9) This involved using a mechanical pump with two syringes, enabling slow addition (0.01 mL/min) of a pre-dissolved peptide, a coupling reagent PyBOP (benzotriazolyl-oxo-tris[pyrrolidino]-phosphonium hexafluorophosphate) and a base *N,N*-diisopropylethylamine (DIEA). Upon completion of the cyclisation reaction, the side chain protecting groups were cleaved using a trifluoroacetic acid (TFA) based cleavage cocktail, and the peptides were precipitated in diethyl ether before purification by reversed-phase high performance liquid chromatography (RP-HPLC). After lyophilisation the cyclic tetrapeptides were characterised by high-resolution mass spectrometry (HRMS) and nuclear magnetic resonance spectroscopy (NMR). Purity was determined to be $>95\%$ by reversed phase-ultra performance liquid chromatography (RP-UPLC). All peptides were tested for antimicrobial activity against the Gram-positive bacteria *Bacillus subtilis*, *Corynebacterium glutamicum*, *Staphylococcus aureus*, and *Staphylococcus epidermidis*, and the Gram-negative bacteria *Escherichia coli* and *Pseudomonas aeruginosa*. Haemolytic toxicity was determined against human red blood cells (RBCs) as a measure of toxicity.

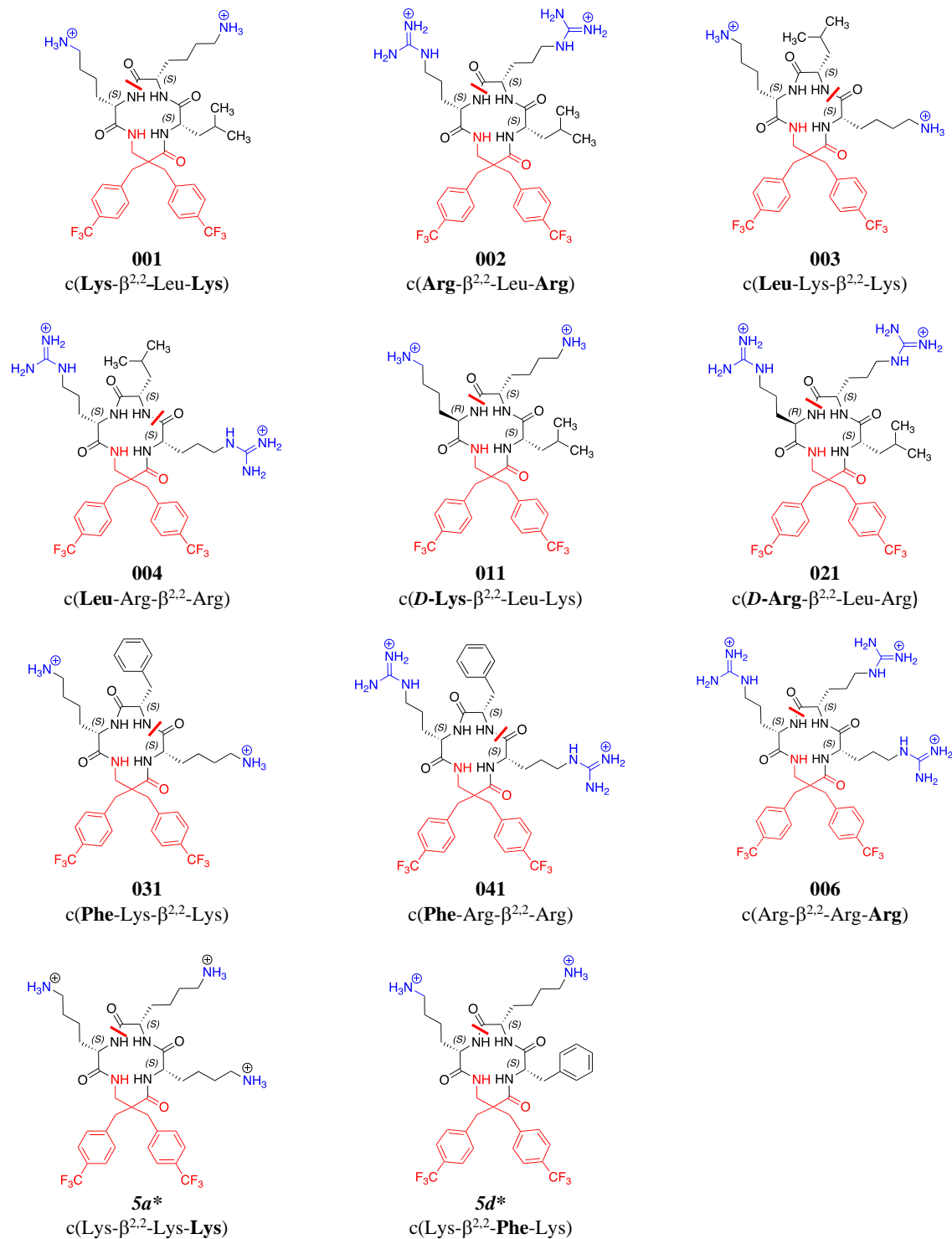


Figure 2. Structures of the cyclic tetrapeptides screened for antimicrobial activity and haemolytic toxicity. The red line in the structures shows the site of head-to-tail cyclisation. In the peptide sequences key modifications are shown in **bold**. * Compounds synthesised by Paulsen *et al.* (7)

3. Results and discussion

Antimicrobial activity and haemolytic toxicity

The sequence of the first peptide synthesised in this study **001** c(Lys- $\beta^{2,2}$ -Leu-Lys) was based on the previously reported highly potent cyclic tetrapeptide **5d** c(Lys- $\beta^{2,2}$ -Phe-Lys) (MIC 0.1 – 4 $\mu\text{g}/\text{mL}$). (**Figure 2**) (7) As we initially wanted to investigate how the reduction in the overall lipophilic bulkiness affects peptides and their haemolytic properties, we synthesised the first peptide in this series **001** by substituting a Phe-residue in the sequence of **5d** with Leu. Although the cyclic tetrapeptide **001** was somewhat less potent than its parent peptide **5d**, it had good antimicrobial activity against both Gram-positive bacteria (MIC 2 – 4 $\mu\text{g}/\text{mL}$) and Gram-negative bacteria (MIC 4 – 8 $\mu\text{g}/\text{mL}$). (**Table 1**) In addition, **001** was less haemolytic (EC_{50} 105 $\mu\text{g}/\text{mL}$) than the previously reported peptide **5d** (EC_{50} 88 $\mu\text{g}/\text{mL}$). Since there was no major change in bioactivity following the substitution of a Phe-residue in **5d** with Leu, the cyclic tetrapeptide **001** became a suitable model peptide for our further investigations.

To study the effect of different cationic groups, the Lys-residues in the sequence of **001** were replaced by Arg, resulting in **002** c(Arg- $\beta^{2,2}$ -Leu-Arg). The cyclic tetrapeptide **002** displayed similar antimicrobial activity to **001** against both Gram-positive (MIC 2 – 4 $\mu\text{g}/\text{mL}$) and Gram-negative (MIC 4 – 8 $\mu\text{g}/\text{mL}$) bacteria, but surprisingly **002** was considerably more haemolytic (EC_{50} 33 $\mu\text{g}/\text{mL}$). Thus, the cationic guanidine groups in **002** were clearly unfavourable with respect to RBC toxicity when compared to the primary amines of the Lys-residues in **001**.

In the next two cyclic tetrapeptides, **003** c(Leu-Lys- $\beta^{2,2}$ -Lys) and **004** c(Leu-Arg- $\beta^{2,2}$ -Arg), the amphipathicity was interrupted compared to the amphipathic peptides **001** and **002**. (**Figure 1**) Both cyclic tetrapeptides **003** and **004** had a sequence of alternating cationic and lipophilic residues, in which **003** contained two cationic Lys-residues, whereas **004** contained two cationic Arg-residues. Our results showed that antimicrobial activity against Gram-positive bacteria was slightly reduced for the Lys-containing non-amphipathic peptide **003** (MIC 2 – 8 $\mu\text{g}/\text{mL}$) but maintained for the Arg-containing non-amphipathic peptide **004** (MIC 2 – 4 $\mu\text{g}/\text{mL}$). A major reduction in antimicrobial activity was, however, observed for **003** against Gram-negative bacteria (MIC 32 – 64 $\mu\text{g}/\text{mL}$), and for **004** (MIC 8 – 32 $\mu\text{g}/\text{mL}$). This reduction was especially prominent against *P. aeruginosa*. Interestingly, haemolytic toxicity was considerably reduced for both peptides, with **003** being non-haemolytic (EC_{50} >492 $\mu\text{g}/\text{mL}$), whereas **004** exhibited low haemolytic toxicity (EC_{50} 215 $\mu\text{g}/\text{mL}$). Thus, interruption of amphipathicity had in general little effect on antimicrobial activity against Gram-positive bacteria, while activity against Gram-negative bacteria, as well as haemolytic toxicity, were considerably reduced.

To assess the cell selectivity of the peptides, a selectivity index was calculated as the ratio of the haemolytic toxicity (EC_{50}) to the geometric mean (GM_{Tot}) of the MIC values against all bacterial strains (i.e., $\text{SI} = \text{EC}_{50}/\text{GM}_{\text{Tot}}$). (**Table 1**) By interrupting amphipathicity, the selectivity for bacteria compared to mammalian RBCs increased, namely non-amphipathic cyclic tetrapeptides **003** and **004** displayed approx. SI: 50, whereas the SI for their amphipathic counterparts **001** (SI: 30) and **002** (SI: 9) were considerably lower.

To investigate the effects of changes in stereochemistry, a *D*-Lys analogue of **001** and a *D*-Arg analogue of **002** were synthesised. As shown in **Figure 2**, incorporation of a single *D*-residue resulted in **011** c(*D*-Lys- $\beta^{2,2}$ -Leu-Lys) and **021** c(*D*-Arg- $\beta^{2,2}$ -Leu-Arg) having the side chains of their two cationic residues pointing below and above the plane of the cyclic tetrapeptide scaffold. Although no major change in antimicrobial activity was observed compared to their corresponding all-*L* analogues, the striking difference was again observed regarding their toxicity towards human RBCs. Namely, both

D-Lys analogue **011** (EC₅₀ 426 µg/mL, SI: 75) and *D*-Arg analogue **021** (EC₅₀ 181 µg/mL, SI: 64) were considerably less haemolytic than their all-*L* analogues, and thus had high SI values.

To further study the effects of increasing overall bulkiness, we decided to use the two cyclic tetrapeptides **003** c(**Leu**-Lys-β^{2,2}-Lys) and **004** c(**Leu**-Arg-β^{2,2}-Arg) with interrupted amphipathicity as templates, since both peptides showed more favourable haemolytic properties than their amphipathic counterparts **001** and **002**. This was achieved by Leu to Phe substitution in the sequences of **003** and **004**, resulting in **031** c(**Phe**-Lys-β^{2,2}-Lys) and **041** c(**Phe**-Arg-β^{2,2}-Arg), respectively. It can be noted that **031** was also a non-amphipathic analogue of the previously reported cyclic tetrapeptide **5d** c(Lys-β^{2,2}-**Phe**-Lys). (**Figure 2**) (7)

For both the Phe-containing cyclic tetrapeptides **031** and **041**, this structural change resulted in a generally improved antimicrobial activity compared to their respective Leu-analogues, **003** and **004**. The non-amphipathic cyclic tetrapeptide **031** displayed MIC 1 – 8 µg/mL against Gram-positive bacteria, while **041** had MIC values in the range of 0.3 – 2 µg/mL. (**Table 1**) For these Phe-analogues, compared to **003** and **004**, improved antimicrobial activity was also obtained against Gram-negative bacteria, **031** (MIC 16 – 32 µg/mL) and **041** (MIC 4 – 16 µg/mL). Thus, for both peptides **031** and **041** substitution of Leu with Phe was shown to be beneficial regarding their antimicrobial potency.

As for haemolytic toxicity, the Lys containing cyclic tetrapeptide **031** remained non-haemolytic (EC₅₀ >509 µg/mL), which resulted in a very high SI: 90. However, for the Arg containing cyclic tetrapeptide **041** this modification had an unfavourable effect on its haemolytic properties, as it was nearly 2-fold more haemolytic **041** (EC₅₀ 116 µg/mL) than **004** (EC₅₀ 215 µg/mL). Still, **041** had an acceptable high SI: 56 due to its high antimicrobial activity against Gram-positive bacteria and *E. coli*.

When compared to its previously reported amphipathic analogue **5d**, the cyclic tetrapeptide **031** was less potent, especially against Gram-negative bacteria. These two analogues differed more with respect to haemolytic toxicity, namely the non-amphipathic cyclic tetrapeptide **031** was non-haemolytic (EC₅₀ >509 µg/mL), whereas **5d** was reported to be highly haemolytic (EC₅₀ 88 µg/mL). (7) Thus, interruption of amphipathicity may be a promising strategy for reducing haemolytic toxicity of such short cyclic peptides.

The overall most potent analogue prepared in this study was the cyclic tetrapeptide **006** c(Arg-β^{2,2}-Arg-**Arg**). It exhibited very high antimicrobial activity against both Gram-positive (MIC 1 – 2 µg/mL) and Gram-negative bacteria (MIC 2 – 4 µg/mL). In addition, this analogue, which had three Arg-residues and a net charge of +3, was shown to have very low haemolytic toxicity (EC₅₀ 279 µg/mL) and was thereby the most selective cyclic tetrapeptide prepared with SI: 176. Compared to the previously synthesised analogue **5a** c(Lys-β^{2,2}-Lys-**Lys**), with three Lys-residues, **006** was equally potent against Gram-positive bacteria while being more potent against Gram-negative bacteria. (7) Despite having the same net charge (+3) and lipophilic β^{2,2}-residue, there was a difference in RBC toxicity, with **006** being more haemolytic (EC₅₀ 279 µg/mL) than **5a** (EC₅₀ >500 µg/mL). These results confirmed the general pattern in which Lys-containing cyclic tetrapeptides were less haemolytic than their Arg-containing analogues.

In summary, the results of this study indicate that changes in stereochemistry of one cationic residue, as well as amphipathicity, in the above-described tetrapeptide scaffold, could serve as useful strategies in reducing haemolytic toxicity of resultant peptides. In addition, substitution of Leu with bulkier Phe-residue could improve antimicrobial activity, although its effect on haemolytic toxicity may vary.

Table 1. Antimicrobial activity (MIC in $\mu\text{g/mL}$), haemolytic toxicity against human RBCs (EC_{50} in $\mu\text{g/mL}$) and selectivity index (SI). The SI was calculated as the ratio between haemolytic toxicity (EC_{50}) and the geometric mean (GM_{Tot}) of the MIC values against all bacterial strains, i.e., $\text{SI} = \text{EC}_{50} / \text{GM}_{\text{Tot}}$. In the peptide sequences key modifications are shown in bold.

Entry	Sequence	Mw ²	Charge ³	Rt ⁴	Gram-positive bacteria ^{1,5}					Gram-negative bacteria			RBC [$\mu\text{g/mL}$]	GM _{Tot} G+, G-	SI RBC/GM _{Tot}
					Bs	Cg	Sa	Se	Ec	Pa	RBC				
001	c(Lys- $\beta^{2,2}$ -Leu-Lys)	756.8	+2	6.23	2	2	4	4	4	8	105	3.6	30		
002	c(Arg- $\beta^{2,2}$ -Leu-Arg)	812.9	+2	6.38	2	2	4	4	4	8	33	3.6	9		
003	c(Leu-Lys- $\beta^{2,2}$ -Lys)	756.8	+2	5.30	4	2	8	8	32	64	>492	10.1	49		
004	c(Leu-Arg- $\beta^{2,2}$ -Arg)	812.9	+2	5.46	2	2	4	2	8	32	215	4.5	48		
011	c(D-Lys- $\beta^{2,2}$ -Leu-Lys)	756.8	+2	6.07	4	2	8	8	8	8	426	5.7	75		
021	c(D-Arg- $\beta^{2,2}$ -Leu-Arg)	812.9	+2	6.18	1	4	2	2	4	8	181	2.8	64		
031	c(Phe-Lys- $\beta^{2,2}$ -Lys)	790.9	+2	5.33	2	1	8	4	16	32	>509	5.7	90		
041	c(Phe-Arg- $\beta^{2,2}$ -Arg)	846.9	+2	5.47	1	0.3	2	2	4	16	116	2.1	56		
006	c(Arg- $\beta^{2,2}$ -Arg-Arg)	855.9	+3	5.08	1	2	1	1	2	4	279	1.6	176		
5a*	c(Lys- $\beta^{2,2}$ -Lys-Lys)	771.8	+3	-	-	2	1	-	8	8	>500	-	-		
5d*	c(Lys- $\beta^{2,2}$ -Phe-Lys)	790.8	+2	-	-	0.1	2	-	4	2	88	-	-		
Polymyxin B ^{2*}		1301.6	+5		3.1	3.1	12.5	6.3	3.1	3.1	-	-	-		
Chlorhexidine ^{2*}		505.5	+2		1.6	0.8	1.6	1.6	1.6	6.3	-	-	-		

¹ Microbial strains; Bs – *Bacillus subtilis*, Cg – *Corynebacterium glutamicum*, Sa – *Staphylococcus aureus*, Se – *Staphylococcus epidermidis*, Ec – *Escherichia coli*, Pa – *Pseudomonas aeruginosa*. ² Average molecular mass without including a TFA salt for each cationic charge. ³ Net charge at physiological pH (7.4). ⁴ Lipophilicity measured as retention time (Rt; min) on a RP-UPLC C₁₈ column using a linear acetonitrile/water gradient. ‘-’; not tested/not calculated. * Original MIC and RBC values can be found in Paulsen *et al.*(7) ^{2*} Original MIC values for Polymyxin B and Chlorhexidine can be found in Dey *et al.* (10)

Retention time as with antimicrobial activity and haemolytic toxicity

Next, we wanted to ascertain if there was a correlation between retention time (Rt) values with both antimicrobial activity ($GM_{T_{50}}$) and haemolytic toxicity of the synthesised cyclic tetrapeptides. (**Figure 3**) As shown in **Figure 3**, the Arg cyclic tetrapeptides (orange line in **Figure 3**), which eluted later, were more potent and haemolytic than the cyclic Lys tetrapeptides (blue line in **Figure 3**).

Both Lys-containing peptide **001** and its Arg-analogue **002** had MIC values in the same range. However, the latter, **002** had a longer Rt and was thereby seemingly more lipophilic than **001**, what might explain the observed higher haemolytic toxicity of **002**.

The two non-amphipathic Lys analogues, Leu-containing **003** and Phe-containing **031** displayed close to identical retention times, but as mentioned previously, the analogue with a bulkier Phe-residue, **031** was in general more potent against tested bacterial strains. As both peptides were non-haemolytic, a correlation with their corresponding Rt values could not be determined.

Similarly, the non-amphipathic Arg-analogues, Leu-containing **004** and Phe-containing **041** had similar Rt, however, the latter **041** had slightly higher antimicrobial potency with increased haemolytic toxicity. Our data suggest that even minute difference in Rt values, and therefore in relative hydrophobicity (as observed for **003/031** and **004/041**), could serve as an indicator of significant changes in peptide antimicrobial and haemolytic properties.

The substitution of *L*-Lys in **001** with *D*-Lys, resulted in a diastereomer **011** with slightly lower potency and reduced haemolytic toxicity. Much greater reduction in haemolytic toxicity was observed for Arg-containing diastereomer **021**, which had very similar potency to its *L*-Arg analogue **002**. Both *D*-Lys and *D*-Arg containing tetrapeptides had slightly shorter retention times, which could be correlated with lower haemolytic toxicity and greater selectivity. Of note, **002** had the longest Rt of all synthesised tetrapeptides.

The most potent, hydrophilic tetrapeptide containing three Arg-residues, **006** had the shortest retention time of all synthesised analogues, indicating its more hydrophilic character. It had low haemolytic toxicity (EC_{50} 279 μ g/mL) and the highest selectivity of all synthesised peptides (SI: 176). Compared to its Lys-analogue **5a**, it was more haemolytic, but with improved activity against Gram-negative bacteria.

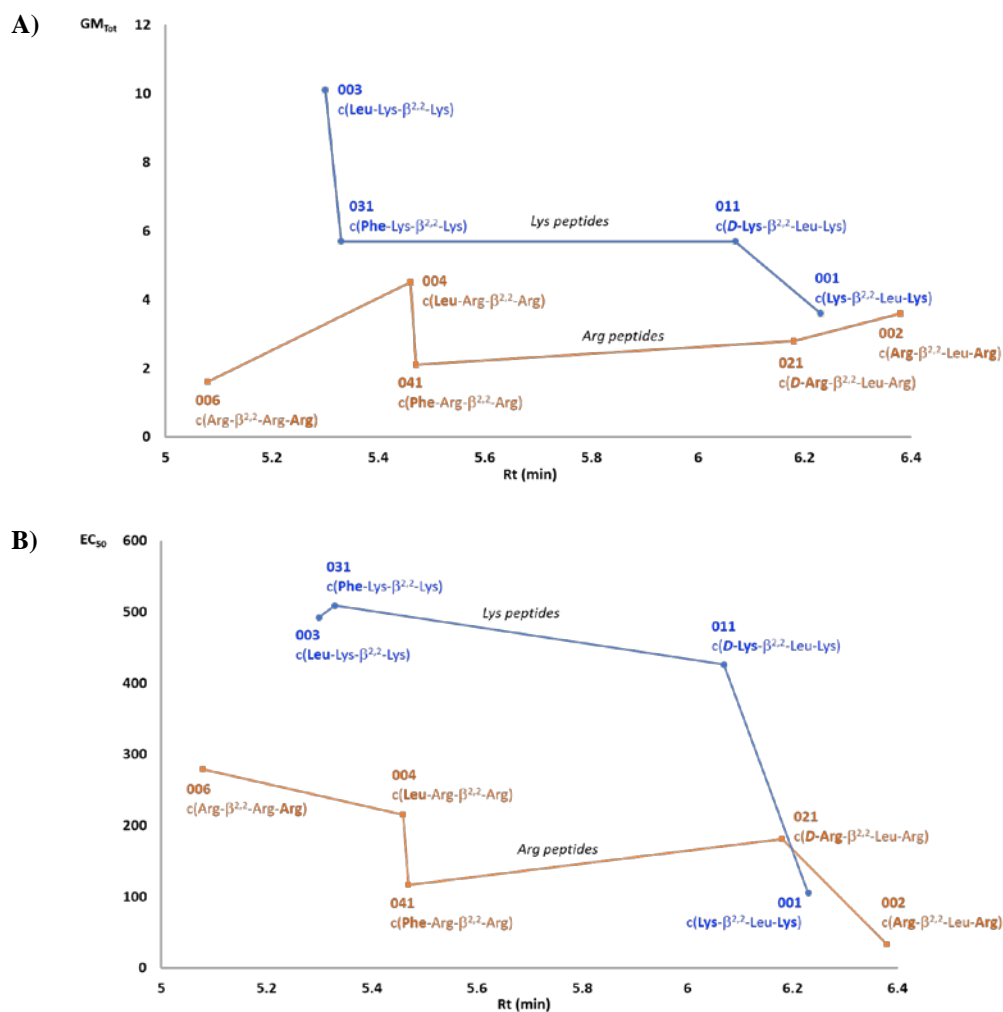


Figure 3. Comparison of retention time (Rt) with **A)** geometric mean (GM_{Tot}) of antimicrobial activity and **B)** haemolytic toxicity (EC₅₀) for Lys (blue) and Arg (orange) cyclic tetrapeptides.

Conformational analysis by NMR

In general, cyclic tetrapeptides with 12-membered backbone have a high ring strain, which makes them notoriously hard to synthesise. (11) However, introduction of a thirteenth atom into the ring structure by using a β^{2,2}-amino acid residue, alleviates some of the strain, making the synthesis of such small cycles easier, and the ring structure accordingly more flexible. It is also important to note that different cyclic tetrapeptides will also have very similar backbone conformations. In the present work five peptides **001** c(Lys-β^{2,2}-Leu-Lys), **002** c(Arg-β^{2,2}-Leu-Arg), **003** c(Leu-Lys-β^{2,2}-Lys), **011** c(D-Lys-β^{2,2}-Leu-Lys), and **021** c(D-Arg-β^{2,2}-Leu-Arg) were selected for conformational analysis by NMR to investigate the extent to which the observed effects of changes in sequence and stereochemistry were accompanied by induced changes in the backbone conformation. For simplicity of comparison in the conformational analysis, the amino acids in the cyclic tetrapeptides were numbered according to **Figure 4**, with the β^{2,2}-amino acid always being the fourth amino acid residue.

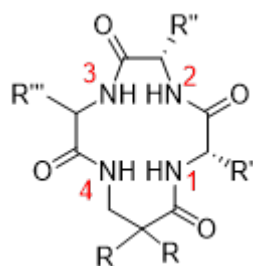


Figure 4. Amino acid sequence numbering for backbone analysis by NMR.

Secondary chemical shifts are a well-documented method for predicting secondary structure of peptides and proteins. (12-15) By comparing the experimental chemical shifts of the backbone to random coil chemical shifts from the literature, it is possible to estimate the α -helix-, β -sheet-, or random coil character of each residue. (14-16) Positive values indicate an α -helical character, negative numbers indicate β -sheet character, while values close to zero indicate random coil.

However, due to the tetrapeptides being cyclic and including a non-native amino acid residue, we had to make certain modifications to the procedure. The predicted random coil chemical shifts are estimated from random coil values of peptides with only native amino acids in linear peptides. (16) Therefore, we have treated the cyclic tetrapeptides as linear peptides for this analysis. Additionally, it is known that aromatic residues have a long-range effect on chemical shifts, especially on protons. (13) To mimic this effect from the $\beta^{2,2}$ -amino acid, we have flanked amino acids 1-3 with two phenylalanines on each side (Ac-F-F-X₁-X₂-X₃-F-F-H₂N). With these modifications, as well as the small sample size of the tetrapeptides, we note that the secondary structure cannot be accurately divided into α -, β -, or random coil character by this method. We can, however, use it to accurately compare the cyclic tetrapeptides, to investigate if there are any clear deviations in the backbone conformation.

Using the secondary chemical shift values as a probe for structural change, our results showed that changes in the sequence and/or stereochemistry of the cyclic tetrapeptides did not induce any consistent and significant changes to the backbone conformation. (**Figure 5**) No major backbone conformational shift was identified by secondary chemical shifts as a response to the different sequence and/or stereochemistry of the studied peptides – a result which is consistent with the expected rigidity of the tetrapeptide ring.

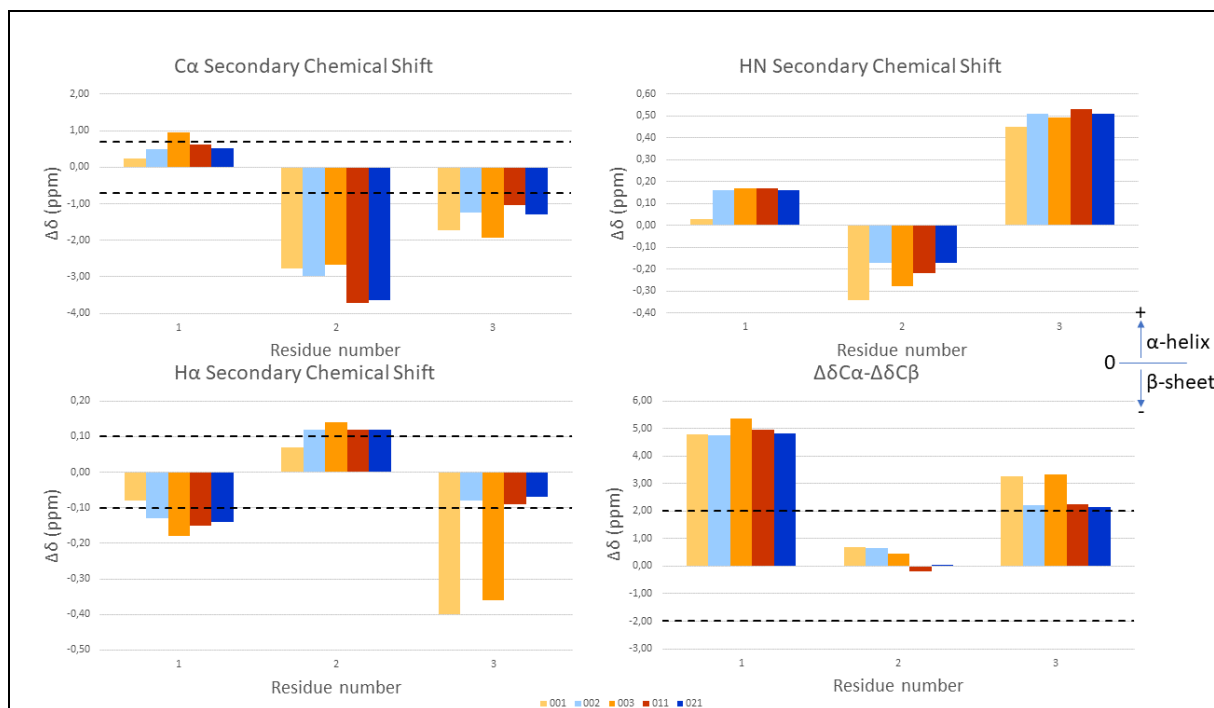


Figure 5. Comparison of the secondary chemical shift of the five peptides **001** c(Lys- $\beta^{2,2}$ -Leu-Lys), **002** c(Arg- $\beta^{2,2}$ -Leu-Arg), **003** c(Leu-Lys- $\beta^{2,2}$ -Lys), **011** c(D-Lys- $\beta^{2,2}$ -Leu-Lys), and **021** c(D-Arg- $\beta^{2,2}$ -Leu-Arg) by residue. The chemical shift analysis was performed by using random coil values by Kjaergaard *et al.* (16) with corresponding correction values. Dashed lines indicate cut-off values for the identification of secondary structure elements, as defined by Wishart *et al.* (17) The figure was based on the analysis of Farina *et al.* (12) The Arg containing peptides **002** and **021** are listed in hues of blue, while the Lys containing peptides **001**, **003**, and **011** are in hues of orange. A positive $\Delta\delta$ indicates α -helix, a negative value indicates β -sheet, while values close to zero indicate random coil.

Cross-relaxation rates and coupling constants were used as direct secondary probes for conformational change in order not to fully rely on chemical shifts models based on native proteins. The NOE build-ups were extracted from NOESY experiments for the Arg containing cyclic tetrapeptides (**002** and **021**). However, for the Lys containing cyclic tetrapeptides (**001**, **003**, and **011**), ROESY had to be used due to intermediate tumbling rates of these peptides. The spectra were analysed in TopSpin Dynamics Center. Experiments with increasing mixing times were recorded, and integrals from the linear phase were used (typically 200 ms for NOESY, and 100 ms for ROESY). All integrals were referenced to the ortho aromatic protons of the $\beta^{2,2}$ -amino acid residue, defined as a reference distance of 2.46 Å, and cross-checked against the ortho aromatic protons of the other benzene ring, as well as the stereotopic geminal α -protons of the same amino acid (defined as 1.75 Å). (18) As seen in **Figure 6**, the calculated NOE distances showed that the backbone conformation did not change significantly between the different peptides, neither as a response to the order of amino acids nor by the introduction of a D-amino acid residue into the sequence.

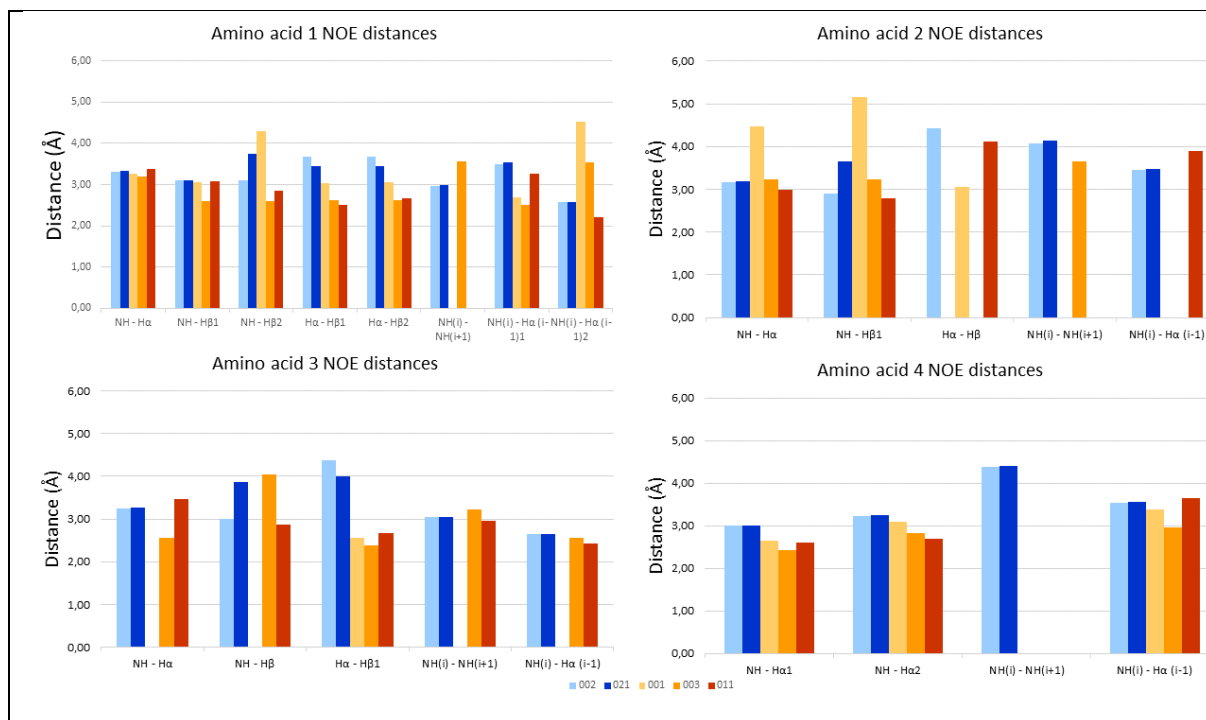


Figure 6. ^1H - ^1H distances of the backbone found by Nuclear Overhauser Effect (NOE) analysis. The Arg containing peptides **002** and **021** are listed in hues of blue, while the Lys containing peptides **001**, **003**, and **011** are in hues of orange.

The ^1H - ^1H J-coupling constants were analysed, both through 1D ^1H NMR coupling patterns and E.COSY. Water suppression and overlap made some couplings difficult to assess in 1D ^1H NMR, while the splitting pattern in E.COSY were unresolved for some of the signals. The coupling constants that could be extracted were mostly consistent between the five peptides, and in agreement with the secondary chemical shifts and cross-relaxation rates, showing no significant changes in backbone conformation between the peptides. (**Table 2**)

Table 2. ^1H - ^1H J-coupling constants, as measured by 1D ^1H NMR. The residues follow the same numbering system as with the rest of the conformation assignment. The linewidth of **002** was too broad to get any measurements, most likely due to aggregation.

1D ^1H coupling constants (Hz)											
	1			2			3			4	
	NH - H α	H α - H β 1	H α - H β 2	NH - H α	H α - H β 1	H α - H β 2	NH - H α	H α - H β 1	H α - H β 2	NH - H α 1	NH - H α 2
001	5.47	7.10	9.63	8.89	7.32	9.48	8.12	5.44	10.40	8.84	3.64
003	4.95	2.48	8.11	7.52	8.07	8.31	7.46	4.58	11.61	8.72	3.41
011	4.95	2.31	9.29	9.56	6.55	10.38	6.22	4.56	7.59	9.49	2.95
021	4.99	7.50	9.50	9.68	8.71	6.97	6.56	5.70	9.19	9.26	2.75

In conclusion, secondary chemical shifts, NOE distances, and J-coupling constants did not indicate any major changes in backbone conformation between the peptides. Thus, we can be confident that the side chains of the amino acids point in the expected directions when comparing peptide for peptide, as discussed in the SAR section above.

Interaction studies with SPR

Next, we tested the ability of the cyclic tetrapeptides to interact with lipid vesicles by surface plasmon resonance (SPR). For this, we used dimyristoylphosphatidylcholine (DMPC) vesicles without and with 10% (w/w) *E. coli* O111:B4 lipopolysaccharides (LPS). Pure DMPC vesicles represent a general zwitterionic bilayer of the human cell plasma membrane, while LPS-loaded vesicles mimic the outer membrane of Gram-negative bacteria. (19) By using a method developed by Figuera *et al.* and modified by Jakubec *et al.* we were able to measure the lipid partitioning (K_P) and dissociation rate (k_{off}) of individual cyclic tetrapeptides into the lipid bilayer. (20, 21) K_P is calculated as the ratio of the peptide concentration in lipid environment over peptide concentration in water ($K_P = [\text{peptide}_{lipid}] / [\text{peptide}_{H_2O}]$). Thus, higher K_P indicates a preference of the cyclic tetrapeptides for the lipid environment, whereas k_{off} represents the dissociation speed, where higher speed indicates a faster release from the lipid bilayer, that is, low retention.

The most lipophilic peptide and with highest preference for the DMPC lipid environment was the *D*-Arg cyclic tetrapeptide **021** c(*D*-Arg- $\beta^{2,2}$ -Leu-Arg), with more than four times higher K_P than the *L*-Arg variant **002** c(Arg- $\beta^{2,2}$ -Leu-Arg). (Figure 7a [full bars]) This radical change in lipophilicity could not be explained by changes in the backbone structure, as shown by NMR. However, it is possible that a simple change in stereochemistry by *L*- to *D*-amino acid substitution allowed for a more favourable orientation of these cationic side chains. Similar improvement, albeit with smaller changes, was also observed for the Lys variants, **011** c(*D*-Lys- $\beta^{2,2}$ -Leu-Lys) and **001** c(Lys- $\beta^{2,2}$ -Leu-Lys), suggesting similar changes in charge distribution caused by cationic side chain orientation.

An interesting observation was the overall decrease in K_P of most cyclic tetrapeptides in the presence of LPS. (Figure 7a [empty bars]) LPS contains the fatty acid component lipid A, which has a negatively charged phospholipid headgroup and long oligosaccharide chains. (22) One of the roles of LPS in bacteria is the sequestration of potentially harmful compounds before they can reach the inner cytoplasmic membrane. (23) Thus, lower K_P for LPS-loaded vesicles can be viewed as a positive feature, indicating more efficient translocation of the cyclic tetrapeptides through the outer membrane. This could be recognised from the partitioning of the cyclic tetrapeptides **002** c(Arg- $\beta^{2,2}$ -Leu-Arg) and **003** c(Leu-Lys- $\beta^{2,2}$ -Lys). Both cyclic tetrapeptides had very similar K_P for DMPC vesicles. However, when LPS was present, the K_P of **003** was only slightly changed, whereas the K_P of **002** was reduced by more than a half. These observations suggested that the cyclic tetrapeptide **003** may be sequestered in the outer membrane and thus unable to reach its target, what in turn could explain the loss of activity against Gram-negative bacteria. In comparison, the more potent cyclic tetrapeptide **002** seemed able to cross the LPS bilayer unaffected. (Figure 7a [empty bars])

Contrary to K_P , the dissociation rate k_{off} was not affected by the presence of LPS as we measured bulk changes of dissociation. (Figure 7b) The fact that there was no change in k_{off} for DMPC:LPS mixtures, indicated that dissociation from LPS was much faster than from DMPC. Thus, it is the lipid environment, not the LPS, which commands k_{off} and it is responsible for major retention of the cyclic tetrapeptides in the vesicles. This retention of peptides in the bilayer can be a major source of disruption, directly reflected in the haemolytic toxicity of peptides. The cyclic tetrapeptide with the slowest dissociation rate, **002** was also the most haemolytic with EC_{50} 33 $\mu\text{g/mL}$, while the cyclic tetrapeptides with high k_{off} rate, i.e., low retention, **003**, **011** and **031** had lowest haemolytic toxicity.

In addition, SPR showed that peptides **002** and **041** had a significant deviation from the binding model for both types of vesicles. (Figure 8) This deviation suggested a cooperative mode of binding and possible interaction between monomers of the cyclic tetrapeptides themselves, such as formation of micelles or aggregation. (24) Similar deviation, although on a much smaller scale, was observed for peptides **001**, **004** and **021**. However, these changes were too small to be conclusive. Nevertheless, all

five cyclic tetrapeptides in these deviation models had very good antimicrobial activity, but some were also haemolytic. This, again points to a bigger bilayer disruption when this cooperation is present.

According to SPR results, the ideal antimicrobial cyclic tetrapeptide should have a good combination of high partitioning into the lipid bilayer with high enough k_{off} rate, which is still damaging to bacteria, but that does not negatively affect human RBCs.

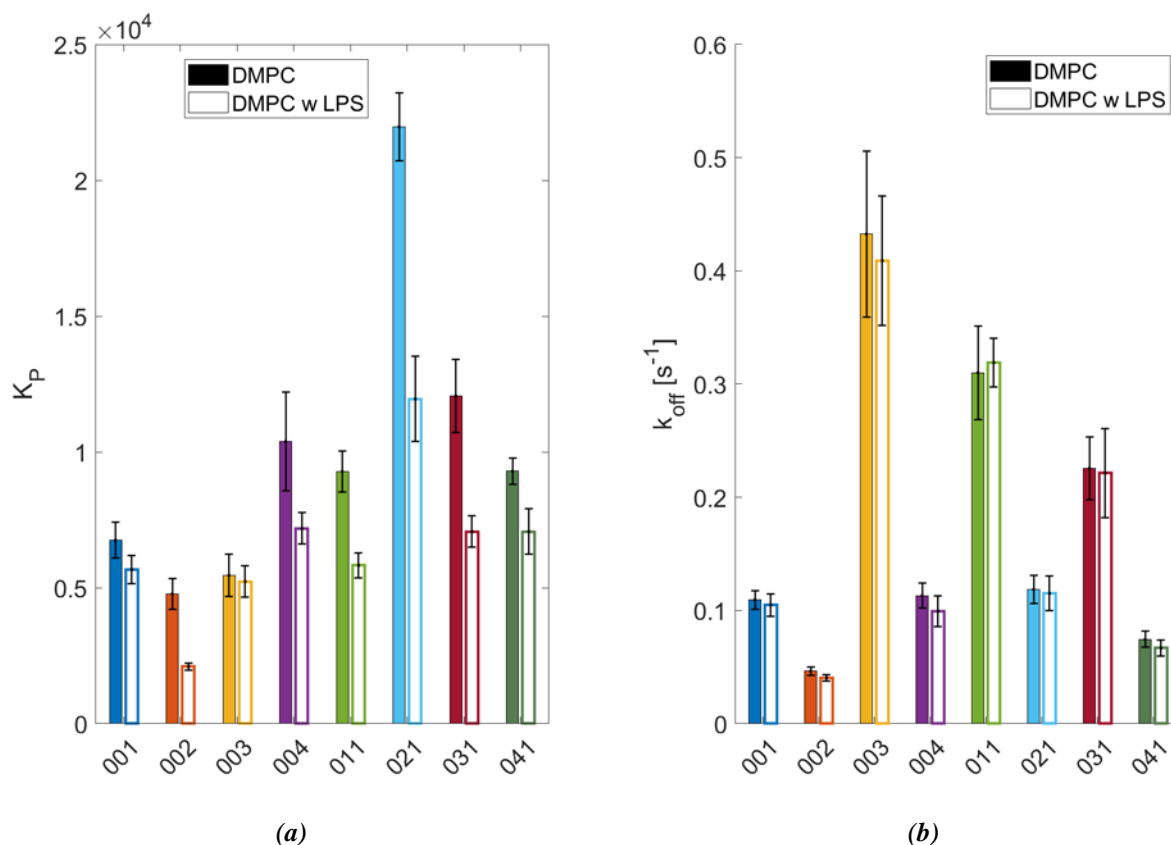


Figure 7. Results from SPR analysis of the cyclic tetrapeptides. Partitioning constant K_p (a) and dissociation rate k_{off} (b) of the cyclic tetrapeptides towards DMPC vesicles without and with 10% (w/w) LPS marked by full and empty bars, respectively.

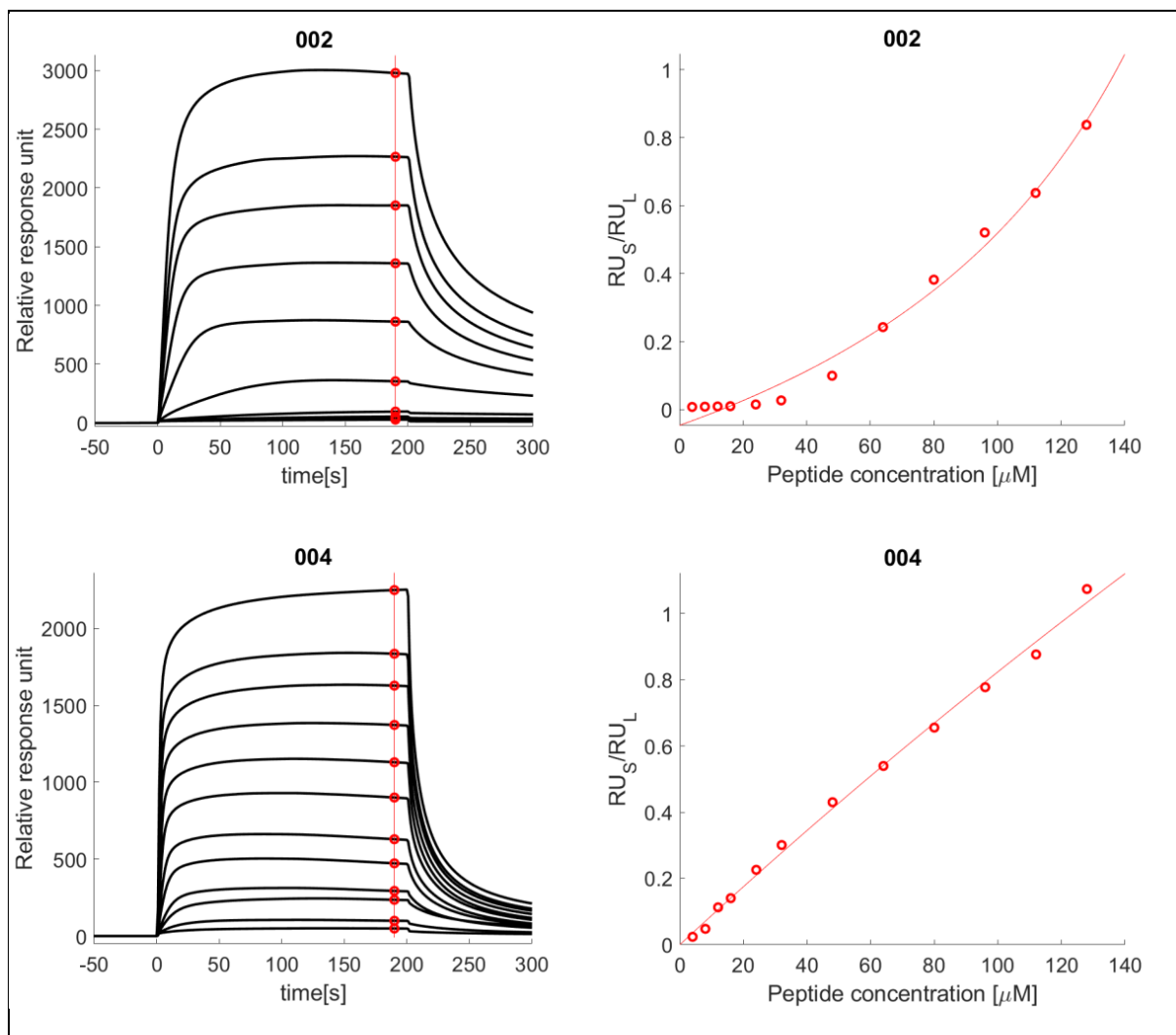


Figure 8. Example of cooperative (**002**) and noncooperative (**004**) binding towards DMPC vesicles. SPR traces of cyclic tetrapeptides are shown on the left (concentration from 4 to 128 μM) and K_P fitting on the right side.

4. Methods and materials

Chemicals

All reagents and solvents were purchased from commercial sources and used as supplied.

General protocol for linear peptide synthesis

The stepwise assembly of the linear peptides was performed using microwave assisted Fmoc solid phase peptide synthesis method at 0.22 mmol scale on preloaded 2-chlorotritylchloride resin (0.75 mmol/g for the resin with preloaded Lys, 0.54 mmol/g for the resin with preloaded Arg). The Fmoc group was removed with 20% piperidine in DMF. Peptide couplings were performed using the appropriate amino acid (3 equiv.), HCTU (3 equiv.) and DIPEA (6 equiv.). Prior to synthesis, all amino acids were dissolved in DMF (0.5M), whereas DIPEA was dissolved in NMP (2M). Microwave heating (75°C, 15 min) was applied during coupling of all amino acids, except for arginine, where coupling was done at room temperature for 60 min to avoid side reactions.

Cyclisation method

Upon completion of the synthesis, cleavage of the linear protected tetrapeptides from the 2-Chlorotrityl chloride resin was performed with the mixture of hexafluoropropanol-dichloromethane (HFIP:DCM, 3:7, v/v, 15 mL) for 45 min under slow stirring conditions, followed by two more cleavage rounds, each lasting 10 min. The collected peptide solution was evaporated under reduced pressure. Head-to-tail cyclisation was performed using modified procedure previously described by Malesevic *et al.* (9) To maintain microdilution conditions during cyclisation two 10 mL syringes were used. First syringe contained linear protected tetrapeptide (100 µmol) pre-dissolved in *N,N*-dimethylformamide (DMF, 10 mL). The second syringe was filled with a solution containing PyBOP (300 µmol), pre-dissolved in DMF (10 mL). Both syringes were fixed to the dual-syringe programmable pump and the flow rate was set to 0.01 mL/min. This enabled simultaneous, dropwise addition of both solutions into the flask which initially contained *N,N*-diisopropylethylamine (DIEA) (600 µmol), PyBOP (10 µmol) and DMF (10 mL). The reaction proceeded under constant stirring. Dimerisation was not observed using HRMS, although such observation was made in previous cyclisation attempts with much greater volumes of DMF. (7) After the cyclisation step, the reaction mixture was diluted with water (approx. 20 mL) prior to extraction with ethylacetate (2 x 10 mL). The organic phase was washed with 5% LiCl solution (3 x 20 mL) and brine (1 x 10 mL), before drying over Na₂SO₄. The organic phase was filtered and concentrated under vacuum. Upon addition of the cleavage cocktail containing TFA:TIS:H₂O (95:2.5:2.5, 5 mL) to the cyclic protected peptide, reaction mixture was left to stir for 3 hours prior to evaporation under reduced pressure. The crude peptide was washed with diethyl ether (3 x 20 mL) and again dried under vacuum prior to purification by RP-HPLC.

Peptide Purification by Preparative Reversed-Phase High-Performance Liquid Chromatography (RP-HPLC)

Purification of crude peptides was performed by RP-HPLC using a preparative SunFire C₁₈ OBD, 5 µm, 19 × 250 mm column (Waters, Milford, MA, USA) at room temperature. The HPLC system (Waters) was equipped with a 2998 photodiode array (PDA) detector, a 2702 autosampler and an automated fraction collector. The peptides were purified using a linear gradient of eluent A (water with 0.1% TFA) and eluent B (acetonitrile with 0.1% TFA), ranging from 20–60% B, over 25 min. The flow rate was set at 10 mL/min. Purified fractions were collected and freeze-dried prior to further characterisation.

Purity Determination by Ultra-Performance Liquid Chromatography (UPLC)

The purity of the synthesised peptides was determined by an analytical UPLC-PDA H-class system (Waters, Milford, MA, USA). The analysis was performed on an Acquity UPLC BEH 1.7 μ m, 2.1 \times 100 mm C18 column, with a linear gradient of eluent A (water with 0.1% TFA) and eluent B (acetonitrile with 0.1% TFA), from 0.5–95.0% B over 10 min. The flow rate and the temperature of the column were set at 0.5 mL/min and 60 °C, respectively. A 2996 PDA detector was used to record the UV absorbance of the purified peptides at the wavelength range of 210–400 nm.

Peptide Characterisation by High-Resolution Mass Spectrometry (HRMS)

The characterisation of the purified peptides was performed by HRMS, using an Orbitrap Id-X Tribrid mass analyser equipped with an electrospray ionisation (ESI) source (Thermo Fischer Scientific, Waltham, MA, USA), with a Vanquish UHPLC system (Waters), coupled to an Acquity Premier BEH C₁₈, 1.7 μ m, 2.1 \times 100 mm column (Waters). Mass spectral acquisition was performed in positive ion mode. All samples were dissolved in 1 mL of Milli-Q water prior to analysis. The UHPLC was operated in a linear gradient with mobile phases A (water with 0.1% formic acid) and B (acetonitrile with 0.1% formic acid) from 0.5% – 95.0% B over 10 min, with a flow rate of 0.5 mL/min. The injection volume was 2 μ L, and the column temperature was set to 60 °C.

Peptide Characterisation by Nuclear Magnetic Resonance spectroscopy (NMR)

The purified peptides were characterised by NMR using a Bruker Avance III HD spectrometer equipped with an inverse TCI probe cryogenically enhanced for ¹H, ¹³C and ²H operating at 600 MHz for proton. Experiments for assignment and verification were acquired in DMSO-d₆, while experiments for conformation analysis were acquired in H₂O:D₂O 95:5 and D₂O. All experiments were acquired at 298 K, using standard pulse sequences from TopSpin 3.7.pl2, including 1H, 13C, HSQC, HMBC, H2BC, DQF-COSY, ROESY, NOESY, E.COSY and selective IPAP HSQMBC-TOCSY. Versions with presat or excitation sculpting, gradient selection and adiabatic pulses were used when applicable.

(3S,6S,9S)-3,6-Bis(4-aminobutyl)-9-isobutyl-12,12-bis(4-(trifluoromethyl)benzyl)-1,4,7,10-tetraazacyclotridecane-2,5,8,11-tetraone x TFA (001)

¹H NMR (600 MHz, DMSO-d₆) δ 8.39 (d, J = 8.3 Hz, 1H), 7.90 (d, J = 6.4 Hz, 1H), 7.69 (d, J = 8.2 Hz, 2H), 7.58 (d, J = 8.1 Hz, 4H), 7.54 (d, J = 8.7 Hz, 1H), 7.27 (d, J = 8.0 Hz, 2H), 6.46 (dd, J = 8.4, 3.2 Hz, 1H), 4.26 – 4.10 (m, 2H), 4.00 – 3.80 (m, 1H), 3.37 (dd, J = 13.4, 8.4 Hz, 1H), 3.15 (s, 1H), 3.09 (d, J = 14.2 Hz, 1H), 2.95 (d, J = 13.6 Hz, 2H), 2.81 – 2.71 (m, 4H), 2.66 (d, J = 13.8 Hz, 1H), 1.98 (tdt, J = 18.0, 9.1, 7.9, 4.7 Hz, 1H), 1.68 (tdt, J = 19.4, 9.7, 5.1 Hz, 1H), 1.61 (q, J = 7.7 Hz, 1H), 1.58 – 1.47 (m, 4H), 1.39 (ddd, J = 14.0, 8.8, 5.5 Hz, 1H), 1.35 – 1.18 (m, 3H), 0.91 (d, J = 6.6 Hz, 3H), 0.88 (d, J = 6.6 Hz, 3H).

¹³C NMR (151 MHz, DMSO-d₆) δ 173.77, 172.37, 171.49, 170.48, 141.88, 141.58, 131.43, 130.92, 127.25 (q, J = 31.4 Hz), 127.17 (d, J = 31.4 Hz), 124.87 (q, J = 3.5 Hz), 124.73 (q, J = 3.4 Hz), 124.41 (q, J = 271.8 Hz), 124.36 (q, J = 271.8 Hz), 116.06, 54.55, 53.80, 52.73, 51.24, 42.84, 35.62, 30.46, 28.94, 26.52, 26.44, 24.33, 22.87, 22.66, 22.32, 21.43.

HRMS-ESI: C₃₇H₅₁F₆N₆O₄⁺ [M + H]⁺ calcd: 757,3871, found: 757,3872, UPLC purity 98%.

1,1'-(((3S,6S,9S)-9-Isobutyl-2,5,8,11-tetraoxo-12,12-bis(4-(trifluoromethyl)benzyl)-1,4,7,10-tetraazacyclotridecane-3,6-diyl)bis(propane-3,1-diyl)diguanidine x TFA (002)

¹H NMR (600 MHz, DMSO-d₆) δ 8.53 (d, J = 8.1 Hz, 1H), 7.99 (d, J = 6.3 Hz, 1H), 7.69 (d, J = 7.9 Hz, 3H), 7.64 (t, J = 5.4 Hz, 1H), 7.61 (d, J = 8.1 Hz, 2H), 7.57 (d, J = 8.2 Hz, 2H), 7.33 (s, 2H), 7.26 (d, J = 8.0 Hz, 2H), 6.92 (s, 4H), 6.48 (dd, J = 8.8, 3.0 Hz, 1H), 4.20 (q, J = 8.2 Hz, 1H), 4.16 (dt, J = 10.4, 5.9 Hz, 1H), 3.90 (ddd, J = 10.0, 7.9, 4.5 Hz, 1H), 3.40 (dd, J = 13.4, 8.6 Hz, 1H), 3.19 (d, J = 14.2 Hz,

1H), 3.16 – 3.04 (m, 5H), 2.99 (d, J = 13.7 Hz, 1H), 2.93 (dd, J = 13.3, 3.0 Hz, 1H), 2.62 (d, J = 13.7 Hz, 1H), 2.06 – 1.94 (m, 0H), 1.70 (dtd, J = 19.2, 9.7, 4.8 Hz, 2H), 1.64 – 1.57 (m, 2H), 1.56 – 1.33 (m, 2H), 0.91 (d, J = 6.6 Hz, 2H), 0.89 (d, J = 6.5 Hz, 2H).

¹³C NMR (151 MHz, DMSO-d₆) δ 173.91, 172.61, 171.49, 170.24, 156.73, 141.92, 141.62, 131.52, 130.92, 127.25 (q, J = 31.9 Hz), 127.16 (q, J = 31.4 Hz), 124.83 (q, J = 3.5 Hz), 124.71 (q, J = 3.4 Hz), 124.44 (q, J = 271.7 Hz), 124.37 (q, J = 271.8 Hz), 54.62, 53.63, 52.89, 51.33, 40.32, 40.15, 40.06, 38.79, 38.31, 28.17, 26.45, 25.57, 25.11, 24.35, 22.84, 21.43.

HRMS-ESI: C₃₇H₅₁F₆N₁₀O₄⁺ [M + H]⁺ calcd: 813,3994, found: 813,3994, UPLC purity 100%.

(3S,6S,9S)-3,9-Bis(4-aminobutyl)-6-isobutyl-12,12-bis(4-(trifluoromethyl)benzyl)-1,4,7,10-tetraazacyclotridecane-2,5,8,11-tetraone x TFA (003)

¹H NMR (600 MHz, DMSO-d₆) δ 8.48 (d, J = 8.4 Hz, 1H), 8.13 (d, J = 5.9 Hz, 1H), 7.77 (t, J = 5.8 Hz, 3H), 7.70 (d, J = 8.2 Hz, 5H), 7.59 (d, J = 8.0 Hz, 2H), 7.56 (d, J = 8.1 Hz, 2H), 7.25 (d, J = 8.0 Hz, 2H), 6.44 (dd, J = 8.5, 3.1 Hz, 1H), 4.32 (td, J = 8.7, 6.3 Hz, 1H), 4.08 (dt, J = 9.1, 6.2 Hz, 1H), 3.92 (ddd, J = 10.3, 8.4, 4.3 Hz, 1H), 3.32 (dd, J = 13.3, 8.5 Hz, 1H), 3.20 – 3.12 (m, 2H), 2.96 – 2.92 (m, 1H), 2.90 (d, J = 14.1 Hz, 1H), 2.64 (d, J = 13.8 Hz, 1H), 1.96 (dtt, J = 13.6, 9.2, 3.7 Hz, 1H), 1.75 (dtd, J = 14.5, 9.4, 5.5 Hz, 1H), 1.67 (ddq, J = 19.3, 9.3, 5.5 Hz, 2H), 1.41 – 1.33 (m, 0H), 1.33 – 1.21 (m, 3H), 0.90 (d, J = 5.8 Hz, 2H), 0.87 (d, J = 5.8 Hz, 3H).

¹³C NMR (151 MHz, DMSO-d₆) δ 173.96, 171.72, 171.65, 170.58, 141.84, 141.53, 131.51, 130.88, 127.27 (q, J = 31.7 Hz), 127.12 (q, J = 31.7 Hz), 124.89 (q, J = 3.8 Hz), 124.77 (q, J = 3.9 Hz), 124.40 (q, J = 272.2 Hz), 124.35 (q, J = 272.2 Hz), 56.44, 52.62, 52.56, 51.26, 42.71, 40.15, 40.06, 38.91, 38.71, 38.62, 35.34, 29.04, 28.92, 26.56, 26.50, 24.62, 22.77, 22.64, 22.45, 22.09.

HRMS-ESI: C₃₇H₅₁F₆N₆O₄⁺ [M + H]⁺ calcd: 757,3871, found: 757,3872, UPLC purity 97%.

1,1'-(((2S,5S,8S)-5-Isobutyl-3,6,9,13-tetraoxo-12,12-bis(4-(trifluoromethyl)benzyl)-1,4,7,10-tetraazacyclotridecane-2,8-diyl)bis(propane-3,1-diyl)diguandine x TFA (004)

¹H NMR (600 MHz, DMSO-d₆) δ 8.62 (d, J = 8.1 Hz, 1H), 8.31 (d, J = 5.4 Hz, 1H), 7.77 (t, J = 5.5 Hz, 1H), 7.71 (d, J = 8.1 Hz, 2H), 7.65 (d, J = 7.5 Hz, 2H), 7.63 (s, 1H), 7.57 (d, J = 8.1 Hz, 2H), 7.45 (d, J = 9.1 Hz, 1H), 7.23 (d, J = 8.0 Hz, 2H), 6.46 (dd, J = 8.9, 2.9 Hz, 1H), 4.34 (q, J = 8.5 Hz, 1H), 4.06 (td, J = 7.8, 5.3 Hz, 1H), 3.86 (ddd, J = 10.9, 8.1, 4.3 Hz, 1H), 3.24 (d, J = 13.9 Hz, 1H), 3.22 – 3.06 (m, 4H), 3.00 (d, J = 13.7 Hz, 1H), 2.92 – 2.86 (m, 1H), 1.99 (tq, J = 10.5, 5.0 Hz, 1H), 1.84 – 1.68 (m, 3H), 1.67 – 1.57 (m, 1H), 1.56 – 1.35 (m, 4H), 0.91 (d, J = 6.0 Hz, 2H), 0.88 (d, J = 5.9 Hz, 3H).

¹³C NMR (151 MHz, DMSO-d₆) δ 174.27, 171.70, 171.65, 170.19, 156.85, 156.69, 141.84, 141.58, 131.71, 130.86, 127.28 (q, J = 31.8 Hz), 127.13 (q, J = 31.9 Hz), 124.84 (q, J = 3.9 Hz), 124.72 (q, J = 4.0 Hz), 124.46 (q, J = 271.8 Hz), 124.37 (q, J = 271.9 Hz), 56.50, 52.90, 52.21, 51.47, 41.71, 40.32, 40.28, 39.17, 36.22, 26.56, 26.25, 25.64, 25.37, 24.57, 22.44, 22.14.

HRMS-ESI: C₃₇H₅₁F₆N₁₀O₄⁺ [M + H]⁺ calcd: 813,3994, found: 813,3994, UPLC purity 98%.

(3R,6S,9S)-3,6-Bis(4-aminobutyl)-9-isobutyl-12,12-bis(4-(trifluoromethyl)benzyl)-1,4,7,10-tetraazacyclotridecane-2,5,8,11-tetraone x TFA (011)

¹H NMR (600 MHz, DMSO-d₆) δ 8.66 (d, J = 6.8 Hz, 1H), 7.95 (d, J = 6.3 Hz, 1H), 7.69 (d, J = 8.3 Hz, 2H), 7.65 (d, J = 8.6 Hz, 2H), 7.64 (b, 6H), 7.57 (d, J = 8.1 Hz, 2H), 7.34 (d, J = 9.1 Hz, 1H), 7.25 (d, J = 8.0 Hz, 2H), 6.55 (dd, J = 7.7, 4.0 Hz, 1H), 4.25 (q, J = 7.9 Hz, 1H), 4.07 (dt, J = 9.6, 6.2 Hz, 1H), 4.01 (ddd, J = 9.5, 6.7, 5.1 Hz, 1H), 3.32 (dd, J = 13.6, 7.7 Hz, 1H), 3.12 (d, J = 13.6 Hz, 1H), 3.10 (d, J = 13.6 Hz, 1H), 2.99 (d, J = 13.4 Hz, 1H), 2.98 (d, J = 13.6 Hz, 1H), 2.81 – 2.69 (m, 4H), 1.69 (td, J = 10.6, 5.4 Hz, 1H), 1.65 – 1.61 (m, 1H), 1.61 – 1.43 (m, 7H), 1.38 (m, 3H), 1.29-1.20 (m, 1H), 1.20 – 1.12 (m, 1H), 0.92 (d, J = 6.4 Hz, 3H), 0.88 (d, J = 6.5 Hz, 3H).

¹³C NMR (151 MHz, DMSO-d₆) δ 173.49, 172.53, 171.82, 171.05, 141.85, 141.35, 131.87, 130.94, 127.32 (q, J=32.2 Hz), 127.12 (q, J=32.2 Hz), 124.75 (q, J=3.9 Hz), 124.67 (q, J=3.9 Hz), 124.45 (q, J=272.3 Hz), 124.35 (q, J=272.3 Hz), 55.14, 54.55, 51.98, 51.60, 40.06, 39.18, 38.70, 38.60 (2C), 38.01, 30.72, 29.74, 26.87, 26.57, 24.25, 22.69, 22.64, 22.14, 21.62.

HRMS-ESI: C₃₇H₅₁F₆N₆O₄⁺ [M + H]⁺ calcd: 757,3871, found: 757,3874, UPLC purity 100%.

1,1'-(((3*R*,6*S*,9*S*)-9-Isobutyl-2,5,8,11-tetraoxo-12,12-bis(4-(trifluoromethyl)benzyl)-1,4,7,10-tetraazacyclotridecane-3,6-diyl)bis(propane-3,1-diyl)diguanidine x TFA (021)

¹H NMR (600 MHz, DMSO-d₆) δ 8.67 (d, J = 6.8 Hz, 1H), 7.98 (d, J = 6.2 Hz, 1H), 7.69 (d, J = 8.3 Hz, 2H), 7.65 (d, J = 8.2 Hz, 2H), 7.57 (d, J = 8.2 Hz, 2H), 7.54 (s, 1H), 7.41 (d, J = 9.1 Hz, 1H), 7.25 (d, J = 8.0 Hz, 2H), 6.60 (dd, J = 7.6, 4.1 Hz, 1H), 4.27 (td, J = 8.7, 6.6 Hz, 1H), 4.06 (ddt, J = 18.1, 8.9, 6.4 Hz, 2H), 3.32 (dd, J = 13.6, 7.7 Hz, 1H), 3.16 – 3.04 (m, 6H), 2.99 (td, J = 12.2, 7.1 Hz, 2H), 2.53 (d, J = 13.0 Hz, 1H), 1.73 (td, J = 7.5, 4.5 Hz, 1H), 1.66 – 1.46 (m, 7H), 1.39 (dt, J = 13.5, 7.0 Hz, 2H), 1.37 – 1.28 (m, 1H), 0.92 (d, J = 6.5 Hz, 3H), 0.88 (d, J = 6.4 Hz, 3H).

¹³C NMR (151 MHz, DMSO-d₆) δ 173.52, 172.81, 171.66, 170.94, 156.65, 156.60, 141.85, 141.36, 131.86, 130.94, 127.29 (q, J = 31.8 Hz), 127.16 (q, J = 31.8 Hz), 124.46 (q, J = 271.9 Hz), 124.76 (q, J = 3.3 Hz), 124.67 (q, J = 2.5 Hz), 55.08, 54.35, 51.90, 51.59, 40.37, 40.29, 40.23, 39.16, 38.64, 38.04, 28.29, 27.47, 25.44, 25.04, 24.25, 22.63, 21.67.

HRMS-ESI: C₃₇H₅₁F₆N₁₀O₄⁺ [M + H]⁺ calcd: 813,3994, found: 813,3995, UPLC purity 99%.

(3*S*,6*S*,9*S*)-3,9-Bis(4-aminobutyl)-6-benzyl-12,12-bis(4-(trifluoromethyl)benzyl)-1,4,7,10-tetraazacyclotridecane-2,5,8,11-tetraone x TFA (031)

¹H NMR (600 MHz, DMSO-d₆) δ 8.22 (d, J = 5.3 Hz, 1H), 7.71 (d, J = 8.2 Hz, 2H), 7.65 (d, J = 8.1 Hz, 2H), 7.56 (t, J = 6.7 Hz, 2H), 7.28 (t, J = 7.4 Hz, 2H), 7.23 (d, J = 8.0 Hz, 2H), 7.21 (t, J = 7.8 Hz, 1H), 7.19 (d, J = 8.5 Hz, 2H), 6.46 (d, J = 8.3 Hz, 1H), 4.52 (q, J = 8.6 Hz, 1H), 3.93 (q, J = 7.4 Hz, 1H), 3.70 (dt, J = 11.3, 4.7 Hz, 1H), 3.36 (dd, J = 13.3, 8.8 Hz, 1H), 3.21 (d, J = 13.9 Hz, 1H), 3.17 (d, J = 13.7 Hz, 1H), 3.01 – 2.92 (m, 2H), 2.89 (d, J = 12.8 Hz, 1H), 2.84 (dd, J = 13.6, 8.6 Hz, 1H), 2.77 – 2.66 (m, 4H), 1.96 – 1.87 (m, 1H), 1.75 – 1.64 (m, 2H), 1.64 – 1.53 (m, 1H), 1.55 – 1.39 (m, 4H), 1.29 – 1.22 (m, 1H), 1.14 – 0.99 (m, 3H).

¹³C NMR (151 MHz, DMSO-d₆) δ 174.04, 171.25, 170.84, 170.24, 141.81, 141.53, 137.12, 131.76, 130.86, 129.09, 128.14, 127.26 (q, J = 31.9 Hz), 127.07 (q, J = 31.8 Hz), 124.82 (q, J = 3.3 Hz), 124.70 (q, J = 3.3 Hz), 124.46 (q, J = 271.8 Hz), 124.37 (q, J = 271.8 Hz), 56.77, 54.60, 53.34, 51.43, 41.56, 38.69, 38.62, 37.27, 36.35, 29.05, 28.24, 26.64, 26.62, 22.57, 22.48.

HRMS-ESI: C₄₀H₄₉F₆N₆O₄⁺ [M + H]⁺ calcd: 791,3714, found: 791,3717, UPLC purity 100%.

1,1'-(((2*S*,5*S*,8*S*)-5-Benzyl-3,6,9,13-tetraoxo-12,12-bis(4-(trifluoromethyl)benzyl)-1,4,7,10-tetraazacyclotridecane-2,8-diyl)bis(propane-3,1-diyl)diguanidine x TFA (041)

¹H NMR (600 MHz, DMSO-d₆) δ 8.67 (d, J = 7.5 Hz, 1H), 8.38 (d, J = 4.9 Hz, 1H), 7.73 (s, 4H), 7.55 (d, J = 8.2 Hz, 2H), 7.53 (d, J = 5.5 Hz, 1H), 7.43 (d, J = 9.4 Hz, 1H), 7.42 – 7.39 (m, 1H), 7.27 (dd, J = 8.5, 6.6 Hz, 2H), 7.21 (d, J = 8.1 Hz, 2H), 7.19 (t, J = 8.0 Hz, 1H), 7.18 (d, J = 8.2 Hz, 2H), 6.50 (dd, J = 9.3, 2.7 Hz, 1H), 4.52 (dt, J = 9.7, 8.1 Hz, 1H), 3.94 (td, J = 8.0, 4.8 Hz, 1H), 3.60 (td, J = 8.6, 4.1 Hz, 1H), 3.29 (d, J = 13.8 Hz, 1H), 3.17 (d, J = 13.6 Hz, 1H), 3.14 – 3.07 (m, 3H), 3.02 (tt, J = 13.7, 6.5 Hz, 2H), 2.93 (dd, J = 13.5, 8.2 Hz, 1H), 2.86 – 2.78 (m, 2H), 2.38 (d, J = 13.4 Hz, 1H), 1.95 (td, J = 14.3, 4.2 Hz, 1H), 1.83 – 1.63 (m, 3H), 1.52 (tt, J = 13.4, 7.4 Hz, 1H), 1.37 (ddd, J = 20.7, 13.1, 7.2 Hz, 1H), 1.19 (tt, J = 12.5, 6.3 Hz, 1H), 1.10 (ddt, J = 18.6, 12.5, 6.5 Hz, 1H).

¹³C NMR (151 MHz, DMSO-d₆) δ 174.38, 171.39, 170.81, 169.82, 156.70, 156.57, 141.82, 141.58, 136.99, 131.95, 130.83, 129.09, 128.17, 127.27 (q, J = 31.5 Hz), 127.07 (q, J = 31.4 Hz), 124.78 (q, J =

3.5 Hz), 124.66 (d, J = 2.8 Hz), 124.49 (q, J = 272.0 Hz), 124.35 (q, J = 271.8 Hz), 56.75, 54.33, 53.66, 51.61, 40.61, 40.47, 40.34, 37.48, 37.19, 26.41, 25.49, 25.37, 25.11.

HRMS-ESI: C₄₀H₄₉F₆N₁₀O₄⁺ [M + H]⁺ calcd: 847,3837, found: 847,3836, UPLC purity 99%.

1-(3-((2*S*,5*S*,8*S*)-2,8-Bis(3-guanidinopropyl)-3,6,9,13-tetraoxo-12,12-bis(4-(trifluoromethyl)benzyl)-1,4,7,10-tetraazacyclotridecan-5-yl)propyl)guanidine x TFA (006)

¹H NMR (600 MHz, DMSO-d₆) δ 8.62 (d, J = 8.0 Hz, 1H), 8.33 (d, J = 5.6 Hz, 1H), 7.83 (t, J = 5.5 Hz, 1H), 7.74 (t, J = 5.7 Hz, 1H), 7.70 (d, J = 8.2 Hz, 2H), 7.67 (t, J = 5.8 Hz, 1H), 7.64 (d, J = 8.1 Hz, 2H), 7.56 (d, J = 8.0 Hz, 2H), 7.52 (d, J = 8.7 Hz, 1H), 7.22 (d, J = 8.0 Hz, 2H), 6.51 (dd, J = 8.9, 3.1 Hz, 1H), 4.22 (q, J = 8.2 Hz, 1H), 4.09 (dt, J = 9.1, 6.1 Hz, 1H), 3.86 (ddd, J = 10.3, 7.9, 4.5 Hz, 1H), 3.42 (dd, J = 13.4, 8.9 Hz, 1H), 3.25 (d, J = 13.9 Hz, 1H), 3.15 (q, J = 7.1 Hz, 1H), 3.14 – 3.07 (m, 4H), 3.02 (d, J = 13.8 Hz, 1H), 2.91 – 2.85 (m, 1H), 2.06 – 1.97 (m, 1H), 1.85 – 1.78 (m, 1H), 1.77 – 1.66 (m, 2H), 1.68 – 1.58 (m, 2H), 1.59 – 1.51 (m, 1H), 1.51 – 1.34 (m, 3H).

¹³C NMR (151 MHz, DMSO-d₆) δ 174.30, 172.15, 171.38, 170.13, 156.89, 156.79, 156.75, 141.86, 141.59, 131.63, 130.86, 127.26 (q, J = 31.9 Hz), 127.12 (q, J = 31.7 Hz), 124.82 (q, J = 3.7 Hz), 124.70 (q, J = 3.9 Hz), 124.44 (q, J = 271.9 Hz), 124.36 (q, J = 271.8 Hz), 56.25, 53.58, 53.03, 51.41, 41.82, 40.32, 40.26, 40.16, 36.24, 28.38, 26.42, 26.27, 25.61, 25.33, 25.10.

HRMS-ESI: C₃₇H₅₂F₆N₁₃O₄⁺ [M + H]⁺ calcd: 856,4164, found: 856,4163, UPLC purity 97%.

Bacterial Strains and Antibacterial Activity Testing

Antimicrobial activity testing was performed using the following test strains: The Gram-positive bacteria *B. subtilis* 168 (ATCC 23857), *C. glutamicum* (ATCC 13032), *S. aureus* (ATCC 9144) and *S. epidermidis* RP62A (ATCC 35984) and the Gram-negative bacteria *E. coli* (ATCC 25922) and *P. aeruginosa* (ATCC 27853). The antibacterial activity was assessed using a microdilution assay according to a modified CLSI-based method. (25) Briefly, bacterial cultures were grown overnight in Mueller–Hinton (MH) broth medium (Difco Laboratories, Detroit, MI, USA) and adjusted to 2.5–3 × 10⁴ CFU/mL in MH medium. The peptides were diluted in ultrapure water to a concentration of 250 µg/mL. The suspension of actively growing bacteria (50 µL) was distributed in 96-well microplates (Nunc, Roskilde, Denmark) preloaded with 50 µL of two-fold dilutions of peptide solution. The microplates were incubated in an EnVision 2103 microplate reader (PerkinElmer, Llantrisant, UK) at 35 °C, with OD595 recorded every hour for 24 h. The minimum inhibitory concentration (MIC) was defined as the lowest concentration of peptides resulting in no bacterial growth, compared to the bacterial growth control, consisting of bacterial suspension and water. Polymyxin B sulfate (Sigma-Aldrich, St. Louis, MO, USA) and chlorhexidine acetate (Fresenius Kabi, Halden, Norway) served as positive (growth inhibition) controls, whereas media plus water served as a negative control. All peptides and controls were tested in triplicates.

Haemolytic Toxicity Assay

The synthesised tetrapeptides were screened for haemolytic toxicity against human red blood cells (RBC) in concentrations ranging from 500 to 3.9 µM, according to a previously described protocol. (10) In brief, haemolysis was determined using a heparinized (10 IU/mL) fraction of freshly drawn human blood. Another fraction of blood, which was collected in test tubes with ethylenediaminetetraacetic acid (EDTA, Vacutest, KIMA, Arzergrande, Italy), was used for determination of the haematocrit (hct). Plasma was removed from heparinized blood by washing three times with prewarmed phosphate-buffered saline (PBS) before being adjusted to a final hct of 4%. Tested peptides, which were dissolved in dimethyl sulfoxide (DMSO), were subsequently diluted with PBS to a final DMSO content of ≤1%.

A 1% solution of Triton X-100 (Sigma-Aldrich, St. Louis, MO, USA) served as a positive control for 100% haemolysis, whereas 1% DMSO in PBS buffer served as a negative control. Duplicates of test solutions and erythrocytes (1% hct final concentration) were prepared in a 96-well polypropylene V-bottom plate (Nunc, Fischer scientific, Oslo, Norway). They were incubated under agitation at 37 °C and 800 rpm for 1 h. After centrifugation (5 min, 3000 × g), 100 µL from each well was transferred to a flat-bottomed 96-well plate. Absorbance was measured at 545 nm with a microplate reader (SpectraMax 190, Molecular Devices, San Jose, CA, USA). After subtracting PBS background, the percentage of haemolysis was determined as the ratio of the absorbance in the peptide-treated and surfactant-treated samples. Three independent experiments were performed. EC₅₀ values, which represent the concentration of the peptide giving 50% haemolysis, are presented as averages.

Surface Plasmon Resonance

The SPR experiments were performed using the L1 chip and T200 Biacore instrument (GEHealthcare, Chicago, IL, USA). The experiment setup, including flow rates, chip modification, immobilisation of vesicles and liposome recovery can be found at Jakubec *et al.* (21) Briefly, DMPC vesicles were prepared by the standard method from dry lipid film. (26) DMPC vesicles with 10% (w/w) LPS (from *Escherichia coli* O111:B4, Merk, Germany) were prepared by the same method with modification according to Palusińska-Szyszlak *et al.* (27) Vesicles were then extruded through 100 nm pore, using Avanti Lipids mini-extruder. An L1 chip was covered with extruded vesicles using flowrate of 2 µl/min for 2400 seconds. Coverage was tested by injection of 0.1 mg/ml bovine serine albumin for 1 minute at a flowrate of 30 µl/min; a change < 400 RU indicated sufficient coverage. Increasing concentration of peptides (from 4 to 128 µM) were injected onto the chip for 200 s association and 400 s dissociation using flowrate of 15 µl/min.

The results were processed using MATLAB R2022a (scripts available at <https://github.com/MarJakubec>) using the method presented by Figueira *et al.* and modified by Juskewitz *et al.* (20, 28) Briefly, K_P was calculated from steady state affinity using Eq (1):

$$\frac{RU_S}{RU_L} = \frac{\gamma_L K_P \frac{M_S}{M_L} [S]_W}{1 + \sigma \gamma_L K_P [S]_W} \quad (\text{Eq 1})$$

where RU_S and RU_L are the relative responses of solute (peptides) and lipids respectively, γ_L is the molar volume of the lipids (average for mixture of DMPC and LPS), M_S and M_L are the molecular mass of solute and lipid, respectively, and [S]_W is the concentration of solute in water. K_P and σ are obtained from fitting (with σ being lipid to solute ratio).

For k_{off} we have first linearised dissociation process using Eq (2) and then calculated average k_{off} values by Eq (3):

$$S_L(t) = \alpha e^{-k_{off,\alpha} t} + \beta e^{-k_{off,\beta} t} + S_{L,r} \quad (\text{Eq 2})$$

$$k_{off} = \frac{\alpha k_{off,\alpha} + \beta k_{off,\beta}}{\alpha + \beta} \quad (\text{Eq 3})$$

where S_L is the linearised ratio of solute and lipid, α and β are individual populations, and S_{L,r} is the retained solute fraction.

Acknowledgments

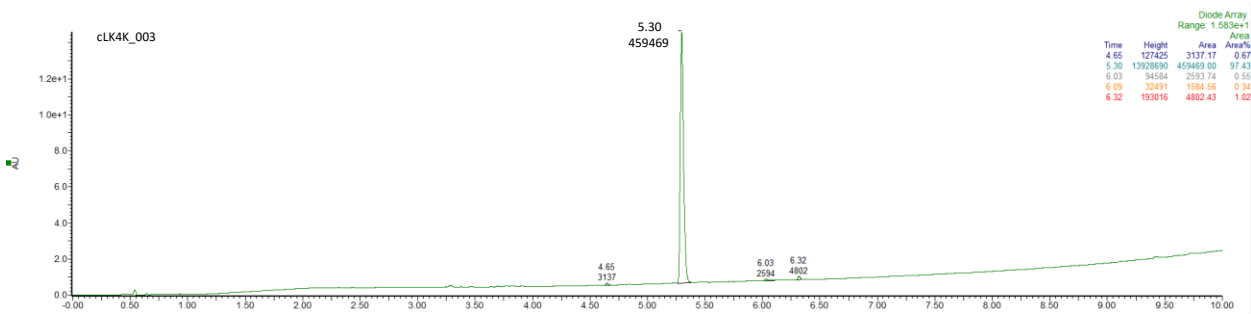
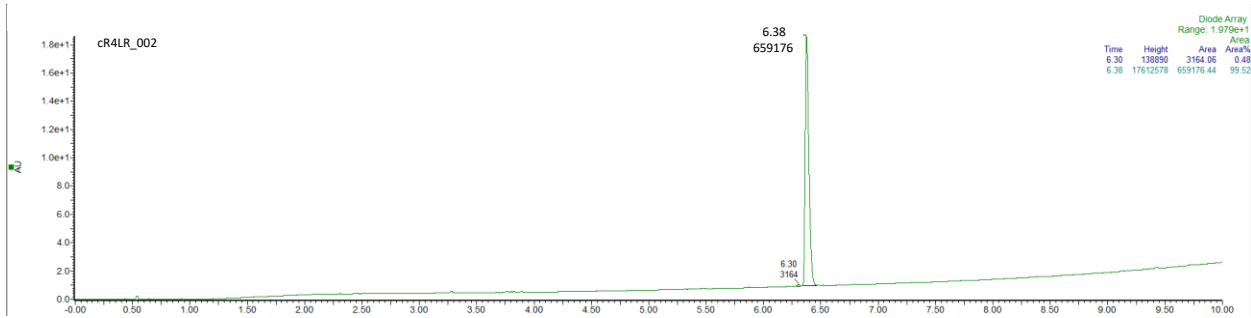
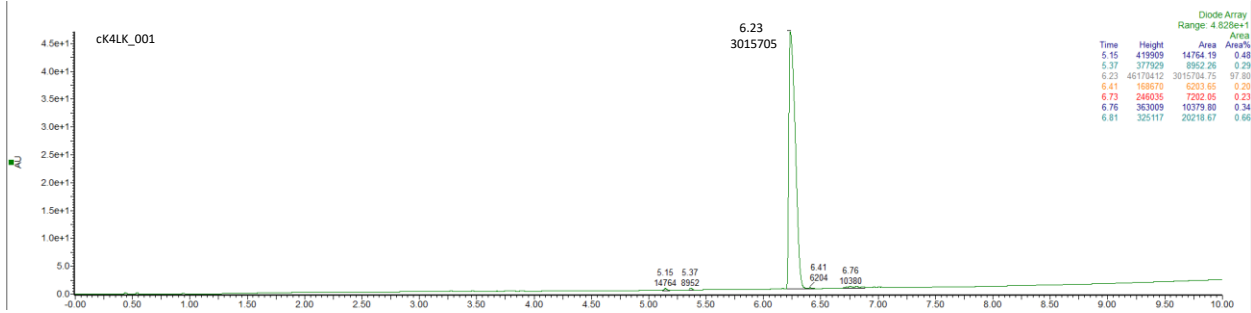
This work was funded by a grant (no. 217/6770) from UiT The Arctic University of Norway.

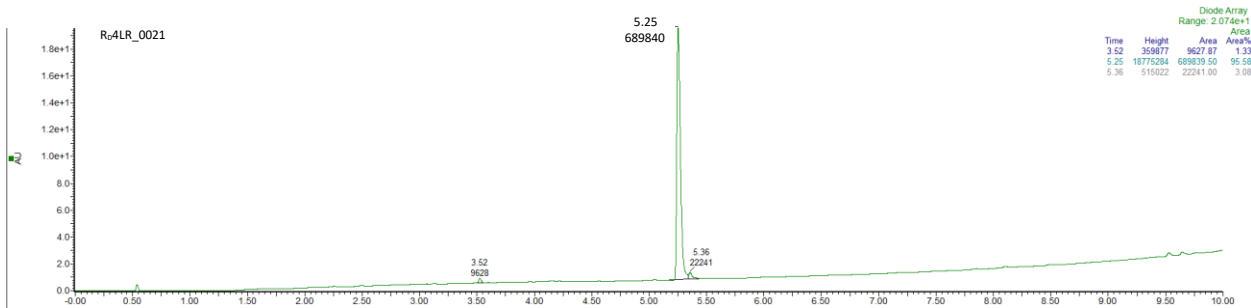
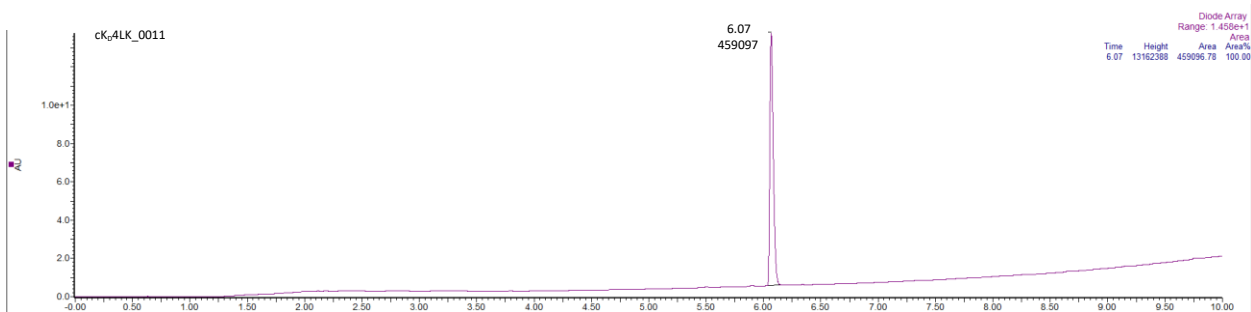
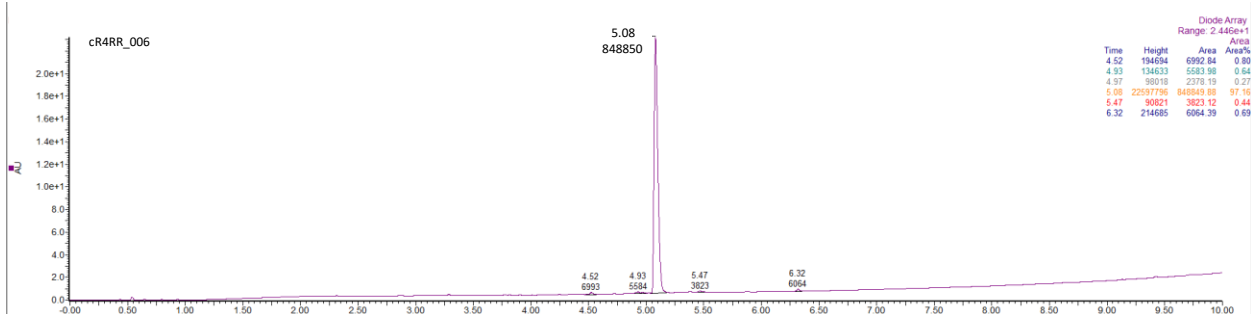
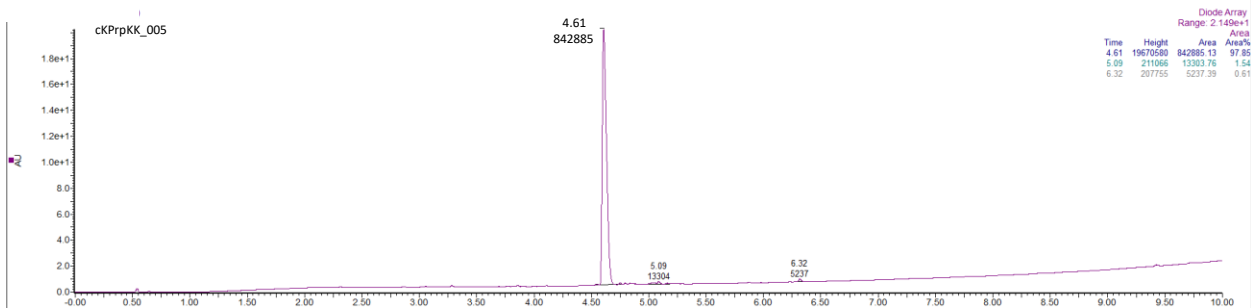
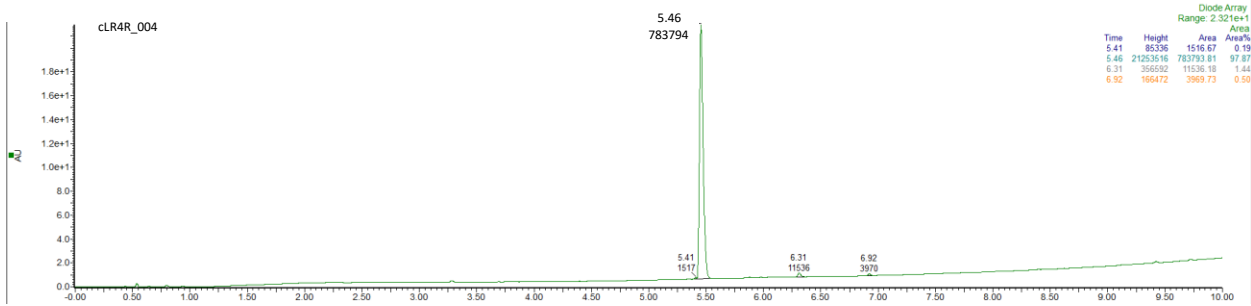
References

1. Erdem Büyükkiraz M, Kesmen Z. Antimicrobial peptides (AMPs): A promising class of antimicrobial compounds. *J Appl Microbiol.* 2022;132(3):1573-96.
2. Rončević T, Puizina J, Tossi A. Antimicrobial Peptides as Anti-Infective Agents in Pre-Post-Antibiotic Era? *Int J Mol Sci.* 2019;20(22).
3. Amis AS, Henriques ST, Lawrence N. Antimicrobial peptides provide wider coverage for targeting drug-resistant bacterial pathogens. *Pept Sci.* 2022;114(2):e24246.
4. Moretta A, Scieuzo C, Petrone AM, Salvia R, Manniello MD, Franco A, et al. Antimicrobial Peptides: A New Hope in Biomedical and Pharmaceutical Fields. *Front Cell Infect Microbiol.* 2021;11.
5. Chakraborty S, Tai DF, Lin YC, Chiou TW. Antitumor and antimicrobial activity of some cyclic tetrapeptides and tripeptides derived from marine bacteria. *Mar Drugs.* 2015;13(5):3029-45.
6. Gunjal VB, Thakare R, Chopra S, Reddy DS. Teixobactin: A Paving Stone toward a New Class of Antibiotics? *J Med Chem.* 2020;63(21):12171-95.
7. Paulsen MH, Karlsen EA, Ausbacher D, Anderssen T, Bayer A, Ochtrup P, et al. An amphipathic cyclic tetrapeptide scaffold containing halogenated $\beta(2,2)$ -amino acids with activity against multidrug-resistant bacteria. *J Pept Sci.* 2018;24(10):e3117.
8. Paulsen MH, Engqvist M, Ausbacher D, Strøm MB, Bayer A. Efficient and scalable synthesis of α,α -disubstituted β -amino amides. *Org Biomol Chem.* 2016;14(31):7570-8.
9. Malešević M, Strijowski U, Bächle D, Sewald N. An improved method for the solution cyclization of peptides under pseudo-high dilution conditions. *J Biotechnol.* 2004;112(1):73-7.
10. Dey H, Simonovic D, Norberg-Schulz Hagen I, Vasskog T, Fredheim EGA, Blencke HM, et al. Synthesis and Antimicrobial Activity of Short Analogues of the Marine Antimicrobial Peptide Turgencin A: Effects of SAR Optimizations, Cys-Cys Cyclization and Lipopeptide Modifications. *Int J Mol Sci.* 2022;23(22).
11. Sarojini V, Cameron AJ, Varnava KG, Denny WA, Sanjayan G. Cyclic Tetrapeptides from Nature and Design: A Review of Synthetic Methodologies, Structure, and Function. *Chem Rev.* 2019;119(17):10318-59.
12. Farina B, Del Gatto A, Comegna D, Di Gaetano S, Capasso D, Isernia C, et al. Conformational studies of RGDechi peptide by natural-abundance NMR spectroscopy. *J Pept Sci.* 2019;25(5):e3166.
13. Schwarzinger S, Kroon GJ, Foss TR, Chung J, Wright PE, Dyson HJ. Sequence-dependent correction of random coil NMR chemical shifts. *J Am Chem Soc.* 2001;123(13):2970-8.
14. De Simone A, Cavalli A, Hsu S-TD, Vranken W, Vendruscolo M. Accurate Random Coil Chemical Shifts from an Analysis of Loop Regions in Native States of Proteins. *J Am Chem Soc.* 2009;131(45):16332-3.
15. Tamiola K, Acar B, Mulder FAA. Sequence-Specific Random Coil Chemical Shifts of Intrinsically Disordered Proteins. *J Am Chem Soc.* 2010;132(51):18000-3.
16. Kjaergaard M, Brander S, Poulsen FM. Random coil chemical shift for intrinsically disordered proteins: effects of temperature and pH. *J Biomol NMR.* 2011;49(2):139-49.
17. Wishart DS, Sykes BD, Richards FM. The chemical shift index: a fast and simple method for the assignment of protein secondary structure through NMR spectroscopy. *Biochemistry.* 1992;31(6):1647-51.
18. Claridge TD. High-resolution NMR techniques in organic chemistry: Elsevier; 2016.
19. Snyder DS, McIntosh TJ. The Lipopolysaccharide Barrier: Correlation of Antibiotic Susceptibility with Antibiotic Permeability and Fluorescent Probe Binding Kinetics. *Biochemistry.* 2000;39(38):11777-87.
20. Figueira TN, Freire JM, Cunha-Santos C, Heras M, Gonçalves J, Moscona A, et al. Quantitative analysis of molecular partition towards lipid membranes using surface plasmon resonance. *Sci Rep.* 2017;7(1):45647.
21. Jakubec M, Bariás E, Furse S, Govasli ML, George V, Turcu D, et al. Cholesterol-containing lipid nanodiscs promote an α -synuclein binding mode that accelerates oligomerization. *FEBS J.* 2021;288(6):1887-905.
22. Snyder S, Kim D, McIntosh TJ. Lipopolysaccharide Bilayer Structure: Effect of Chemotype, Core Mutations, Divalent Cations, and Temperature. *Biochemistry.* 1999;38(33):10758-67.
23. Savini F, Loffredo MR, Troiano C, Bobone S, Malanovic N, Eichmann TO, et al. Binding of an antimicrobial peptide to bacterial cells: Interaction with different species, strains and cellular components. *Biochim Biophys Acta Biomembr.* 2020;1862(8):183291.
24. Papo N, Shai Y. A Molecular Mechanism for Lipopolysaccharide Protection of Gram-negative Bacteria from Antimicrobial Peptides*. *J Biol Chem.* 2005;280(11):10378-87.
25. Igumnova EM, Mishchenko E, Haug T, Blencke H-M, Sollid JUE, Fredheim EGA, et al. Synthesis and antimicrobial activity of small cationic amphipathic aminobenzamide marine natural product mimics and evaluation of relevance against clinical isolates including ESBL-CARBA producing multi-resistant bacteria. *Bioorg Med Chem.* 2016;24(22):5884-94.
26. Lasch J, Weissig V, Brandl M. General methods: Preparation of liposomes. In: Torchilin V, Weissig V, editors. *Liposomes : a practical approach.* 2nd ed. Oxford: Oxford University Press; 2003. p. 3-27.

27. Palusińska-Szys M, Zdybicka-Barabas A, Luchowski R, Reszczyńska E, Śmiałek J, Mak P, et al. Choline Supplementation Sensitizes *Legionella dumoffii* to *Galleria mellonella* Apolipophorin III. *Int J Mol Sci.* 2020;21(16).
28. Juskevitz E, Mishchenko E, Dubey VK, Jenssen M, Jakubec M, Rainsford P, et al. Lulworthinone: In Vitro Mode of Action Investigation of an Antibacterial Dimeric Naphthopyrone Isolated from a Marine Fungus. *Mar Drugs.* 2022;20(5):277.

Tetrapeptides	Sequence	Charge	Comment	Purity (%)	Retention time (min)
001	cK4LK	+2	L-lysine	97.8	6.23
002	cR4LR	+2		99.52	6.38
003	cLK4K	+2		97.43	5.30
004	cLR4R	+2		97.87	5.46
005	cKPrpKK	+3		97.85	4.61
006	cR4RR	+3		97.16	5.08
0011	cK _D 4LK	+2	D-lysine	100	6.07
0021	R _D 4LR	+2	D-Arg,linear	95.58	5.25
0021	R _D 4LR	+2	D-Arg, cyclic	99.33	6.18
0031	cFK4K	+2		100	5.33
0041	FR4R	+2	linear	99.21	4.99
0041	cFR4R	+2	cyclic	98.56	5.47





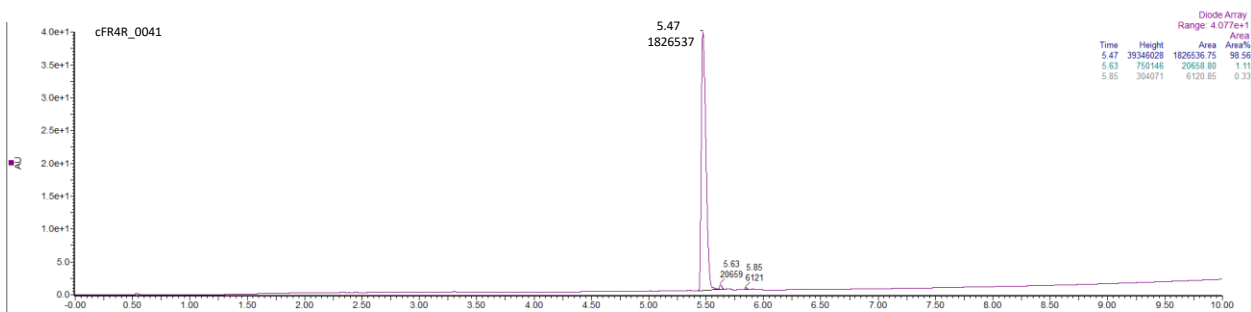
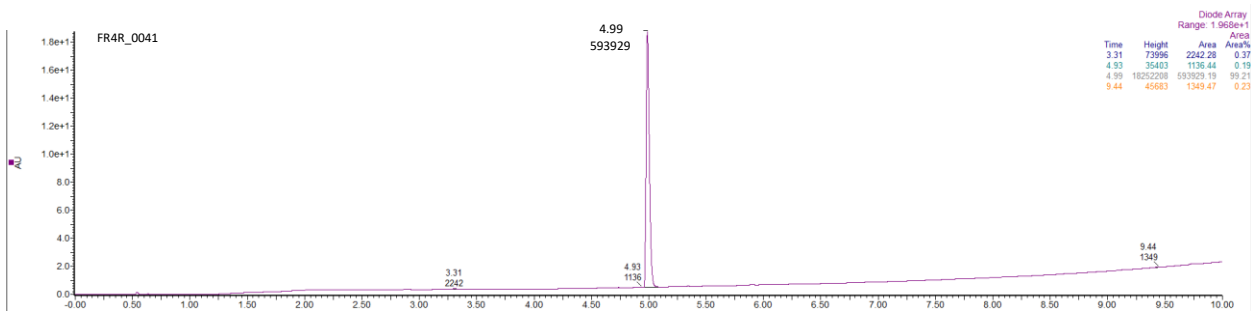
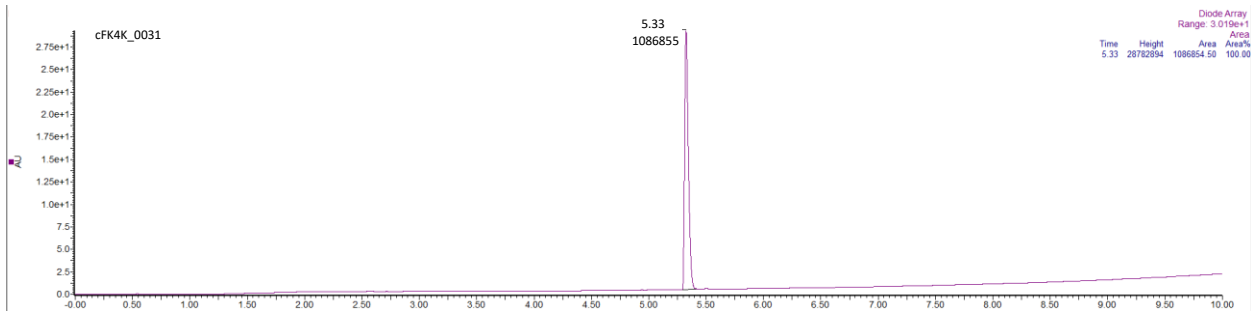
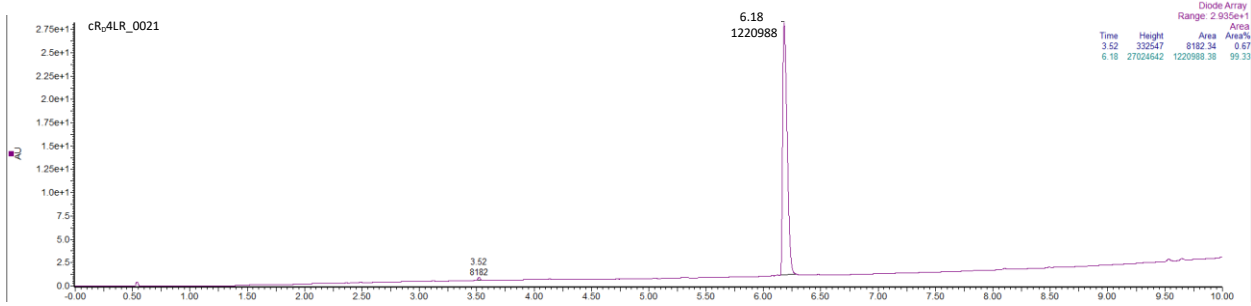


Table S1. Calculated and observed m/z values for the synthesized tetrapeptides

Tetrapeptide	Molecular mass	Monoisotopic	[M+H] ⁺		[M+2H] ²⁺		[M+3H] ³⁺		[M+4H] ⁴⁺	
			calculated	observed	calculated	observed	calculated	observed	calculated	observed
cK4LK_001	756.8354	756.3798	757.387076	757.38721	379.197176	379.19749	253.133876	-	190.102226	-
cR4LR_002	812.8634	812.3921	813.399376	813.39941	407.203326	407.2036	271.804643	-	204.105301	-
cLK4K_003	756.8354	756.3798	757.387076	757.38716	379.197176	379.19743	253.133876	-	190.102226	-
cLR4R_004	812.8634	812.3921	813.399376	813.39938	407.203326	407.20364	271.804643	-	204.105301	-
cK6KK_005	691.962	691.4785	692.485776	692.48589	346.746526	346.74682	231.500109	-	173.876901	-
cR4RR_006	855.8924	855.4091	856.416376	856.41631	428.711826	428.71219	286.143643	286.1438	214.859551	-
cK _D 4LK_0011	756.8354	756.3798	757.387076	757.38742	379.197176	379.19766	253.133876	-	190.102226	-
R _D 4LR_0021 linear	830.8784	830.4026	831.409876	831.4097	416.208576	416.2091	277.808143	-	208.607926	-
cR _D 4LR_0021 cyclic	812.8634	812.3921	813.399376	813.3995	407.203326	407.2039	271.804643	-	204.105301	-
cFK4K_0031	790.8524	790.3641	791.371376	791.37167	396.189326	396.18968	264.461976	-	198.598301	-
FR4R_0041 linear	864.8954	864.387	865.394276	865.39398	433.200776	433.20119	289.136276	-	217.104026	-
cFR4R_0041 cyclic	846.8804	846.3764	847.383676	847.38359	424.195476	424.19595	283.132743	-	212.601376	-
cFK4K_0031 diaster	790.8524	790.3641	791.371376	791.37139	396.189326	396.18981	264.461976	-	198.598301	-

Tetrapeptide	Sequence	Charge x TFA	Charge	Molecular mass	TFA salt	Comment	Purity (%)	Retention time (min)	EC uM	EC ug/ml
1	cK4LK	228.0464	+2	756.8354	984.8818	L-Lysine	97.8	6.23	107.4	105.776305
2	cR4LR	228.0464	+2	812.8634	1040.9098		99.52	6.38	31.5	32.7886587
3	cLK4K	228.0464	+2	756.8354	984.8818		97.43	5.3	500	492.4409
4	cLR4R	228.0464	+2	812.8634	1040.9098		97.87	5.46	206.6	215.051965
5	cKPrpKK	342.0696	+3	691.962	1034.0316		97.85	4.61	500	517.0158
6	cR4RR	342.0696	+3	855.8924	1197.962		97.16	5.08	233	279.125146
11	cK _D 4LK	228.0464	+2	756.8354	984.8818	D-Lysine	100	6.07	433	426.453819
21	R _D 4LR	342.0696	+3	830.8784	1172.948	Linear	95.58	5.25	500	586.474
21	cR _D 4LR	228.0464	+2	812.8634	1040.9098	Cyclic	99.33	6.18	174	181.118305
31	cFK4K	228.0464	+2	790.8524	1018.8988		100	5.33	500	509.4494
41	FR4R	342.0696	+3	864.8954	1206.965	Linear	99.21	4.99	354	427.26561
41	cFR4R	228.0464	+2	846.8804	1074.9268	Cyclic	98.56	5.47	108	116.092094

Peptide	Sequence	RBC [μM]	Gram-positive bacteria [$\mu\text{g/mL}$]				Gram-negative bacteria [$\mu\text{g/mL}$]	
			Bs	Cg	Sa	Se	Ec	Pa
1	cK4LK_001	107.4	2.03	2.03	4.06	4.06	4.06	8.12
2	cR4LR_002	31.5	1.92	1.92	3.84	3.84	3.84	7.69
3	cLK4K_003	500	4.06	2.03	8.12	8.12	32.49	64.98
4	cLR4R_004	206.6	1.92	1.92	3.84	1.92	7.69	30.74
5	cKPrpKK_005	500	1.93	1.93	15.47	3.87	30.95	30.95
6	cR4RR_006	233	0.83	1.67	0.83	0.83	1.67	3.34
11	cK _D 4LK_0011	433	3.90	1.95	7.80	7.80	7.80	7.80
21	R _D 4LR_0021	500	1.71	6.82	13.64	6.82	13.64	13.64
21	cR _D 4LR_0021	174	0.96	3.84	1.92	1.92	3.84	7.69
31	cFK4K_0031	500	1.95	0.98	7.80	3.90	15.60	31.25
41	FR4R_0041	354	3.9	0.98	15.6	7.8	15.6	15.6
41	cFR4R_0041	108	0.98	0.24	1.95	1.95	3.90	15.60

^1H NMR (600 MHz, DMSO) δ 8.39 (d, J = 8.3 Hz, 1H), 7.90 (d, J = 6.4 Hz, 1H), 7.69 (d, J = 8.2 Hz, 2H), 7.58 (d, J = 8.1 Hz, 4H), 7.54 (d, J = 8.7 Hz, 1H), 7.27 (d, J = 8.0 Hz, 2H), 6.46 (dd, J = 8.4, 3.2 Hz, 1H), 4.26 – 4.10 (m, 2H), 4.00 – 3.80 (m, 1H), 3.37 (dd, J = 13.4, 8.4 Hz, 1H), 3.15 (s, 1H), 3.09 (d, J = 14.2 Hz, 1H), 2.95 (d, J = 13.6 Hz, 2H), 2.81 – 2.71 (m, 4H), 2.66 (d, J = 13.8 Hz, 1H), 1.98 (dtd, J = 18.0, 9.1, 7.9, 4.7 Hz, 1H), 1.68 (tdt, J = 19.4, 9.7, 5.1 Hz, 1H), 1.61 (q, J = 7.7 Hz, 1H), 1.58 – 1.47 (m, 4H), 1.39 (ddd, J = 14.0, 8.8, 5.5 Hz, 1H), 1.35 – 1.18 (m, 3H), 0.91 (d, J = 6.6 Hz, 3H), 0.88 (d, J = 6.6 Hz, 3H).

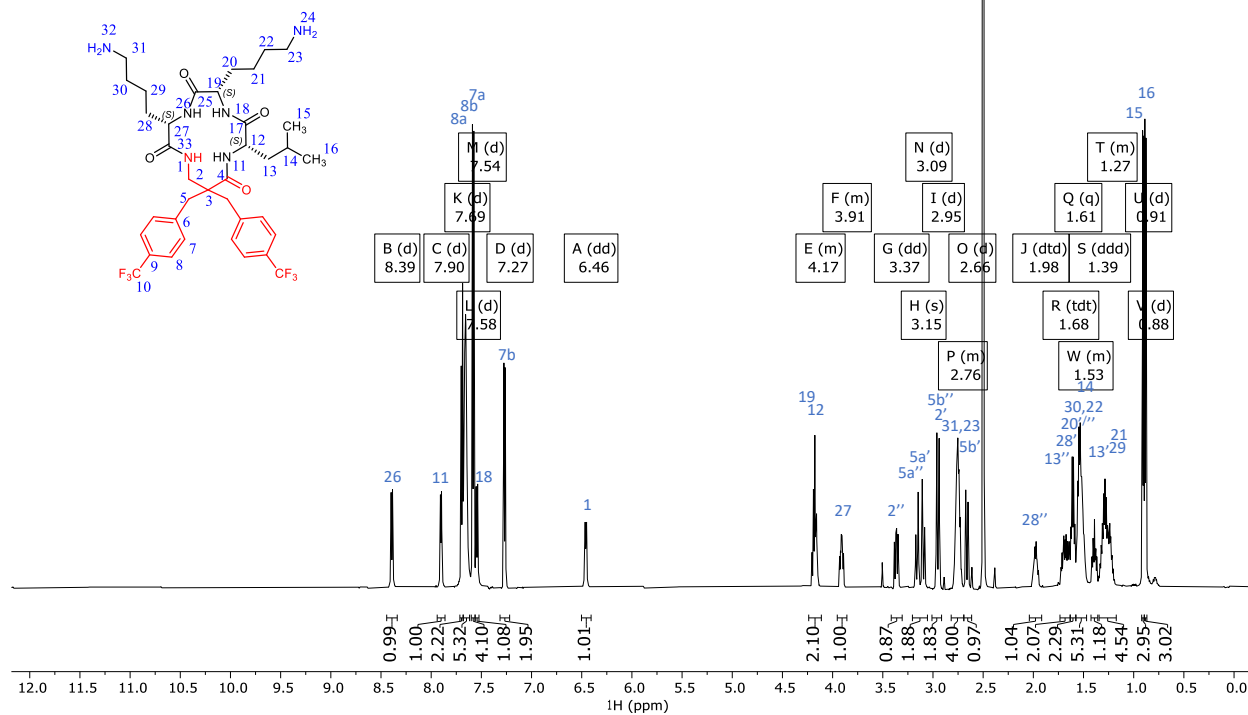


Figure Sx. ^1H NMR spectrum of **001**

^{13}C NMR (151 MHz, DMSO) δ 173.77, 172.37, 171.49, 170.48, 141.88, 141.58, 131.43, 130.92, 127.25 (q, $J = 31.4$ Hz), 127.17 (d, $J = 31.4$ Hz), 124.87 (q, $J = 3.5$ Hz), 124.73 (q, $J = 3.4$ Hz), 124.41 (q, $J = 271.8$ Hz), 124.36 (q, $J = 271.8$ Hz), 116.06, 54.55, 53.80, 52.73, 51.24, 42.84, 35.62, 30.46, 28.94, 26.52, 26.44, 24.33, 22.87, 22.66, 22.32, 21.43.

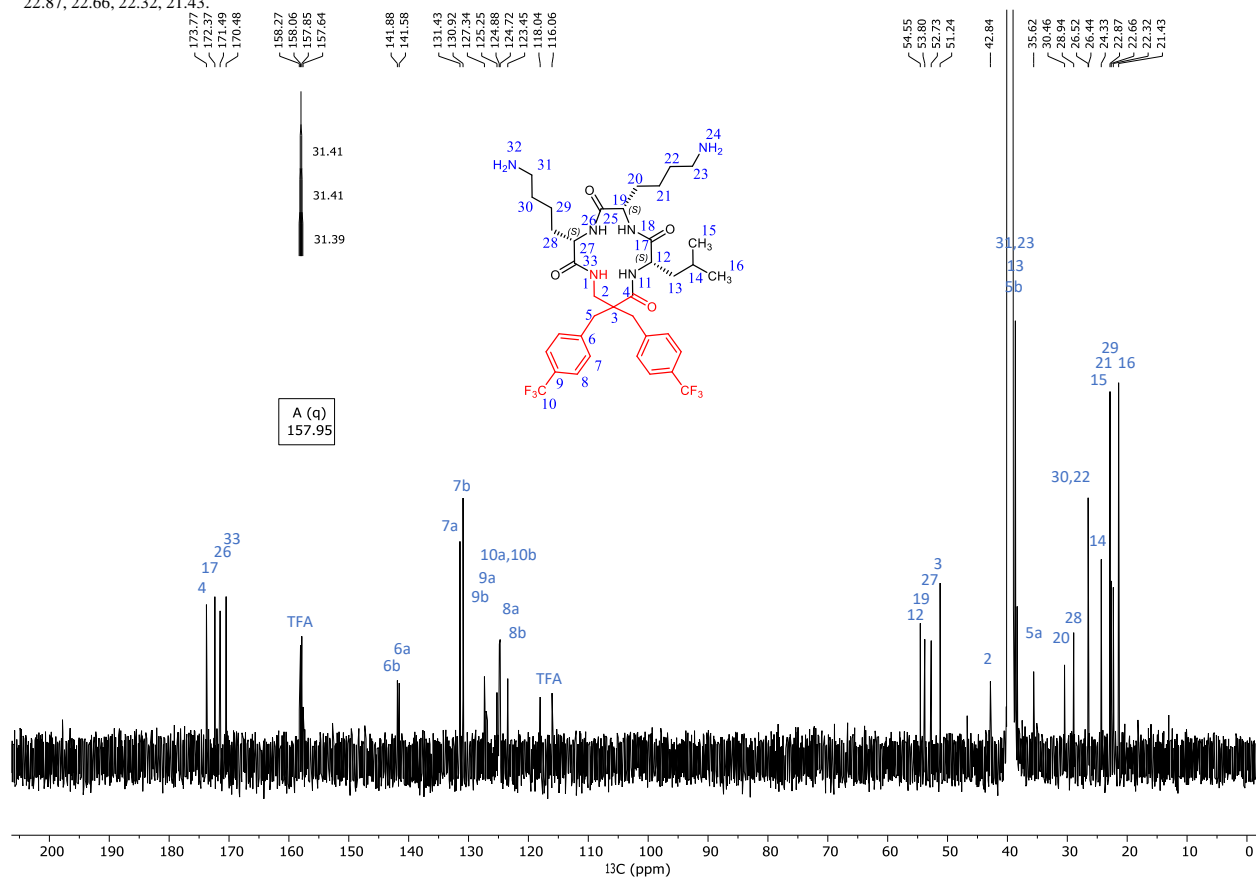


Figure Sx. ^{13}C NMR spectrum of **001**

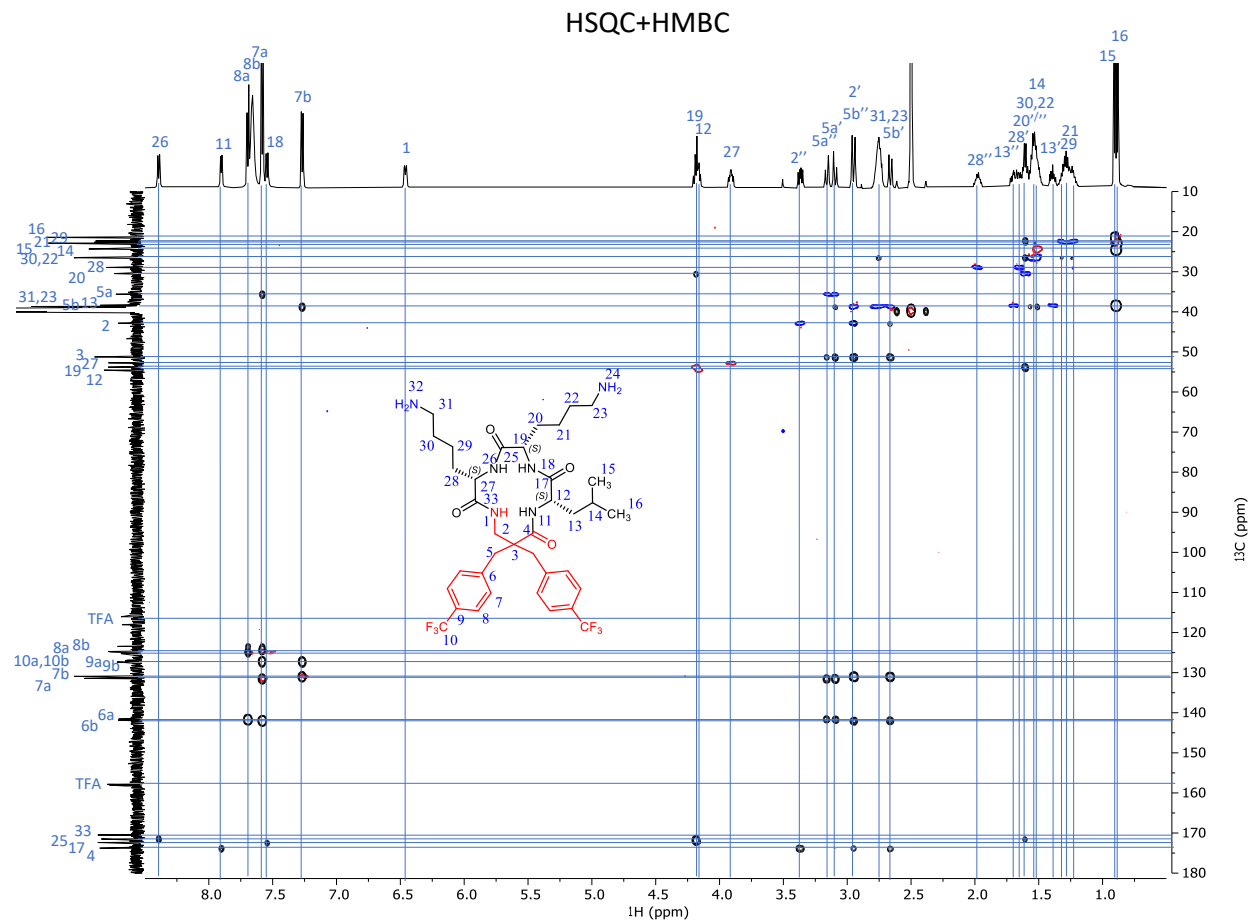


Figure Sx. Superimposed HSQC (red CH, CH₃, blue CH₂) and HMBC (black) spectra of **001**

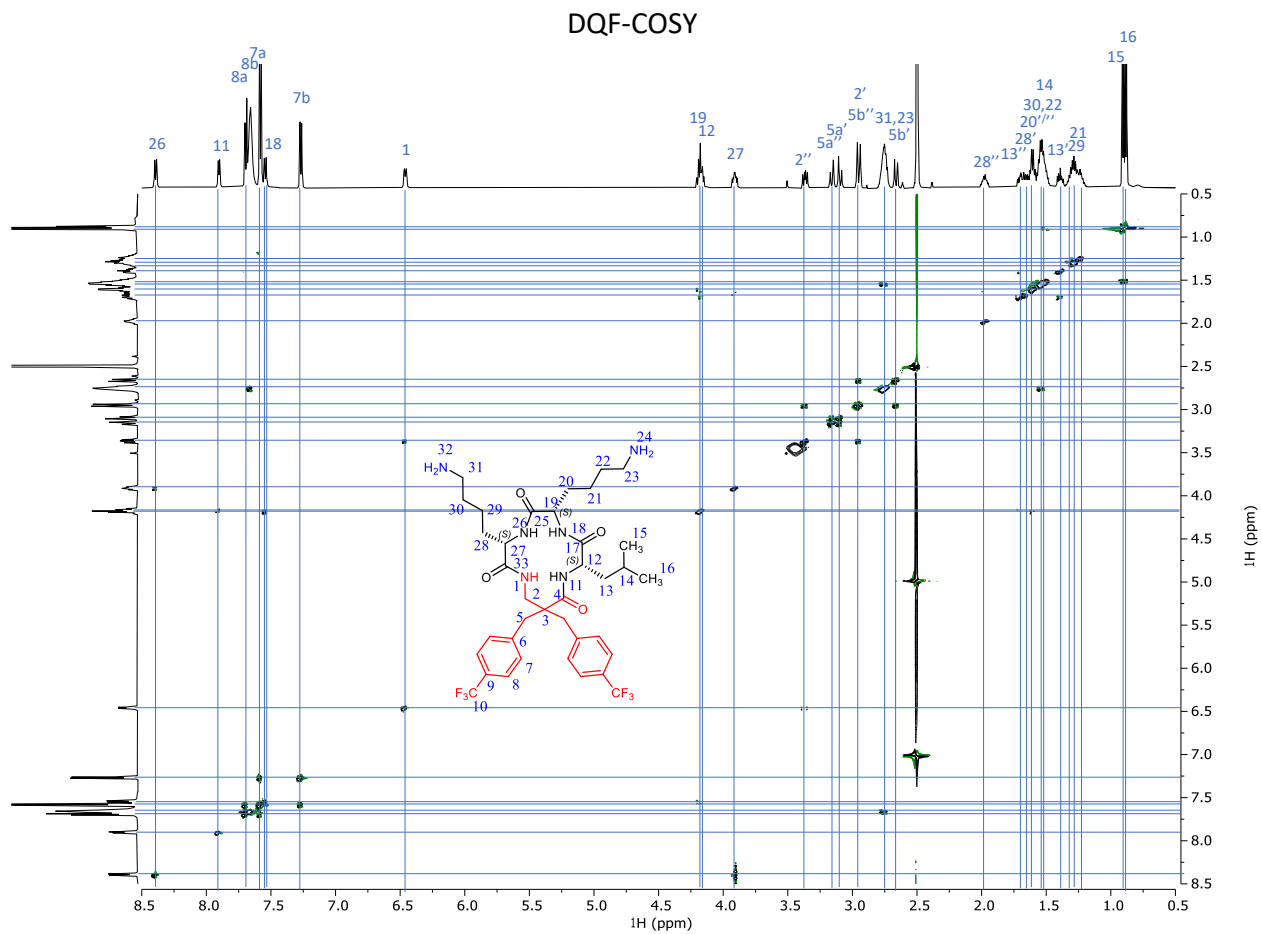


Figure Sx. DQF-COSY spectrum of **001**

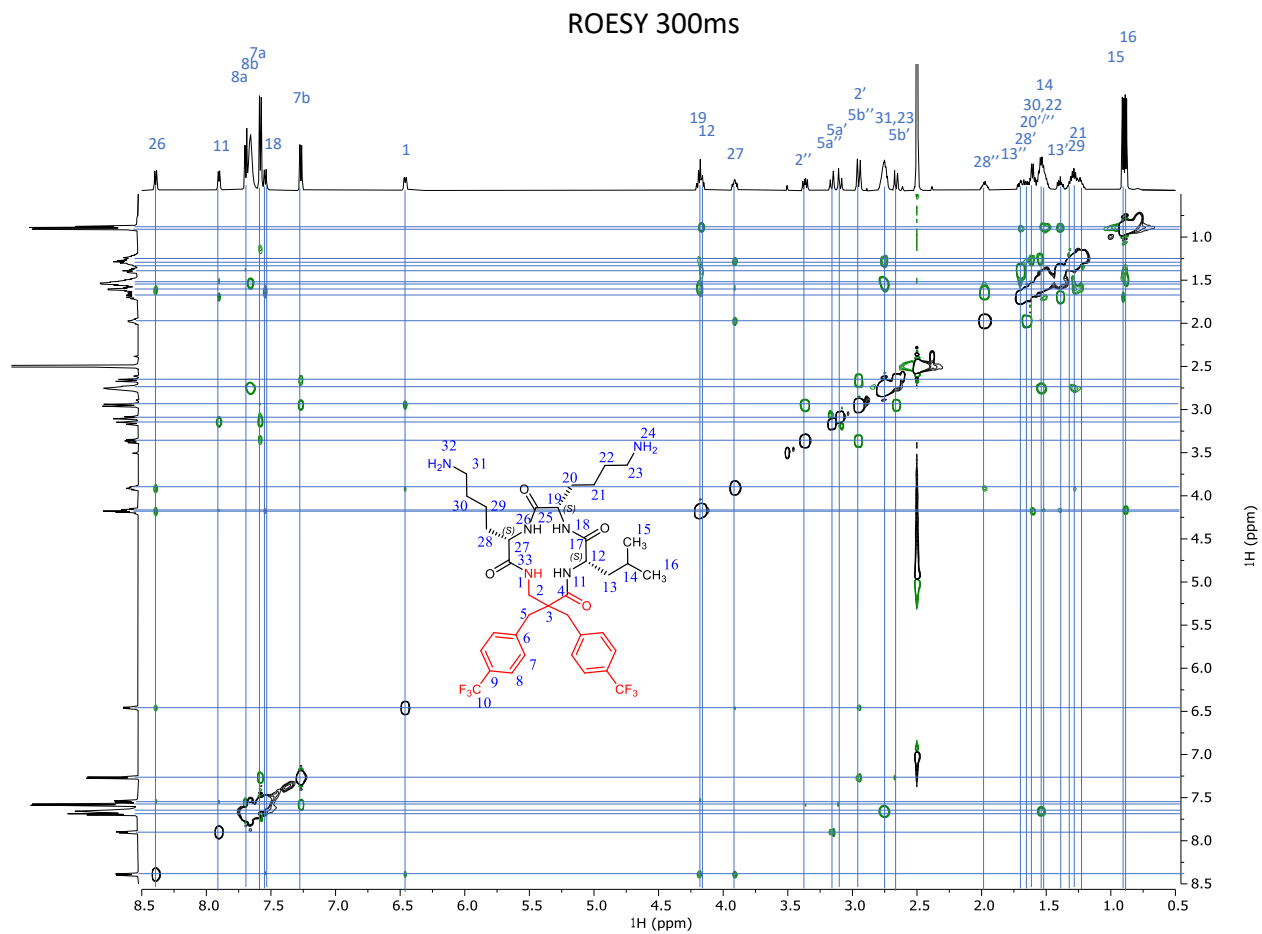


Figure Sx. ROESY (300ms spinlock duration) spectrum of **001**

¹H NMR (600 MHz, DMSO) δ 8.66 (d, *J* = 6.8 Hz, 1H), 7.95 (d, *J* = 6.3 Hz, 1H), 7.69 (d, *J* = 8.3 Hz, 2H), 7.65 (d, *J* = 8.6 Hz, 2H), 7.64 (b, 6H), 7.57 (d, *J* = 8.1 Hz, 2H), 7.34 (d, *J* = 9.1 Hz, 1H), 7.25 (d, *J* = 8.0 Hz, 2H), 6.55 (dd, *J* = 7.7, 4.0 Hz, 1H), 4.25 (q, *J* = 7.9 Hz, 1H), 4.07 (dt, *J* = 9.6, 6.2 Hz, 1H), 4.01 (ddd, *J* = 9.5, 6.7, 5.1 Hz, 1H), 3.32 (dd, *J* = 13.6, 7.7 Hz, 1H), 3.12 (d, *J* = 13.6 Hz, 1H), 3.10 (d, *J* = 13.6 Hz, 1H), 2.99 (d, *J* = 13.4 Hz, 1H), 2.98 (d, *J* = 13.6 Hz, 1H), 2.81 – 2.69 (m, 4H), 1.69 (td, *J* = 10.6, 5.4 Hz, 1H), 1.65 – 1.61 (m, 1H), 1.61 – 1.43 (m, 7H), 1.38 (m, 3H), 1.29–1.20 (m, 1H), 1.20 – 1.12 (m, 1H), 0.92 (d, *J* = 6.4 Hz, 3H), 0.88 (d, *J* = 6.5 Hz, 3H).

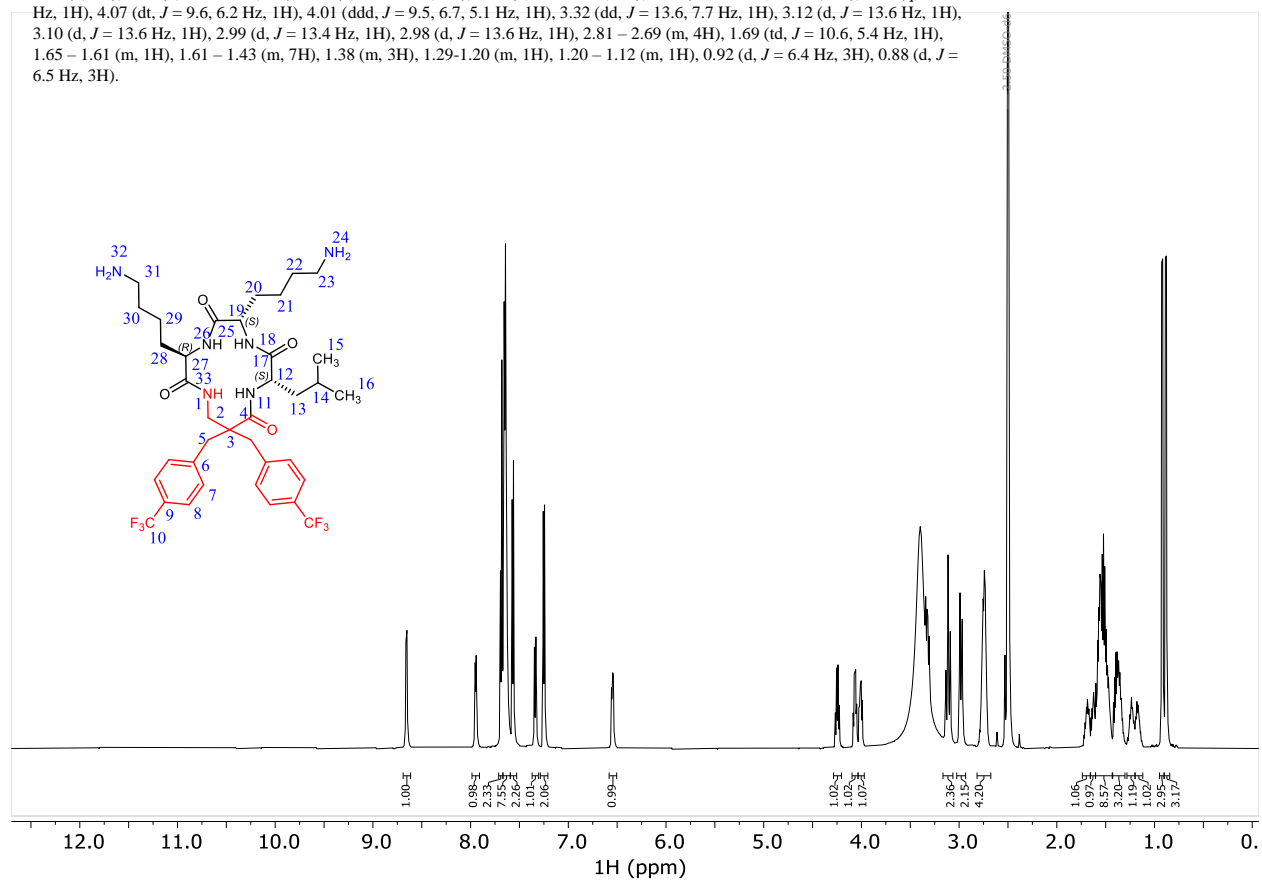


Figure Sx. ¹H NMR spectrum of **0011**

^{13}C NMR (151 MHz, DMSO) δ 173.49, 172.53, 171.82, 171.05, 141.85, 141.35, 131.87, 130.94, 127.32 (q, $J=32.2$ Hz), 127.12 (q, $J=32.2$ Hz), 124.75 (q, $J=3.9$ Hz), 124.67 (q, $J=3.9$ Hz), 124.45 (q, $J=272.3$ Hz), 124.35 (q, $J=272.3$ Hz), 55.14, 54.55, 51.98, 51.60, 40.06, 39.18, 38.70, 38.60 (2C), 38.01, 30.72, 29.74, 26.87, 26.57, 24.25, 22.69, 22.64, 22.14, 21.62.

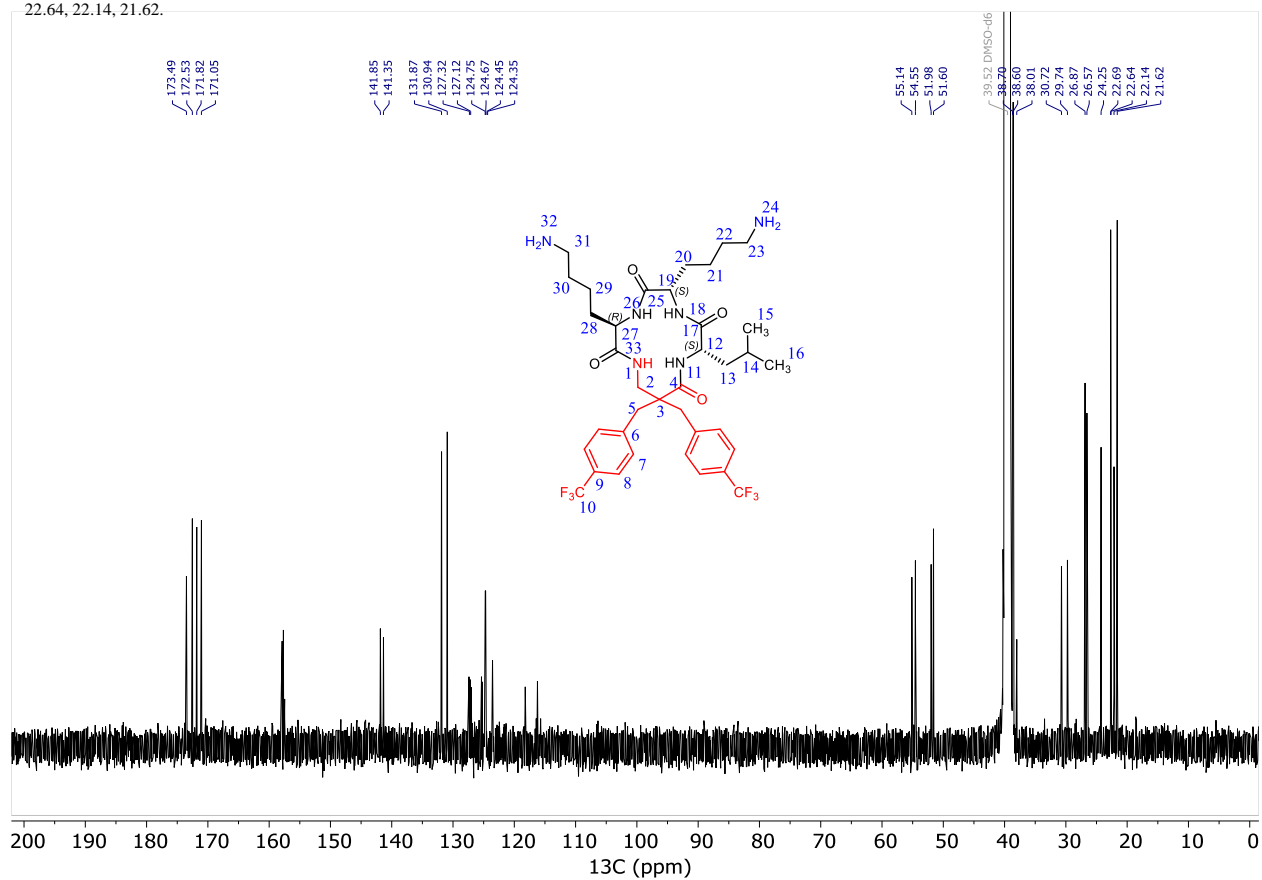


Figure Sx. ^{13}C NMR spectrum of **0011**

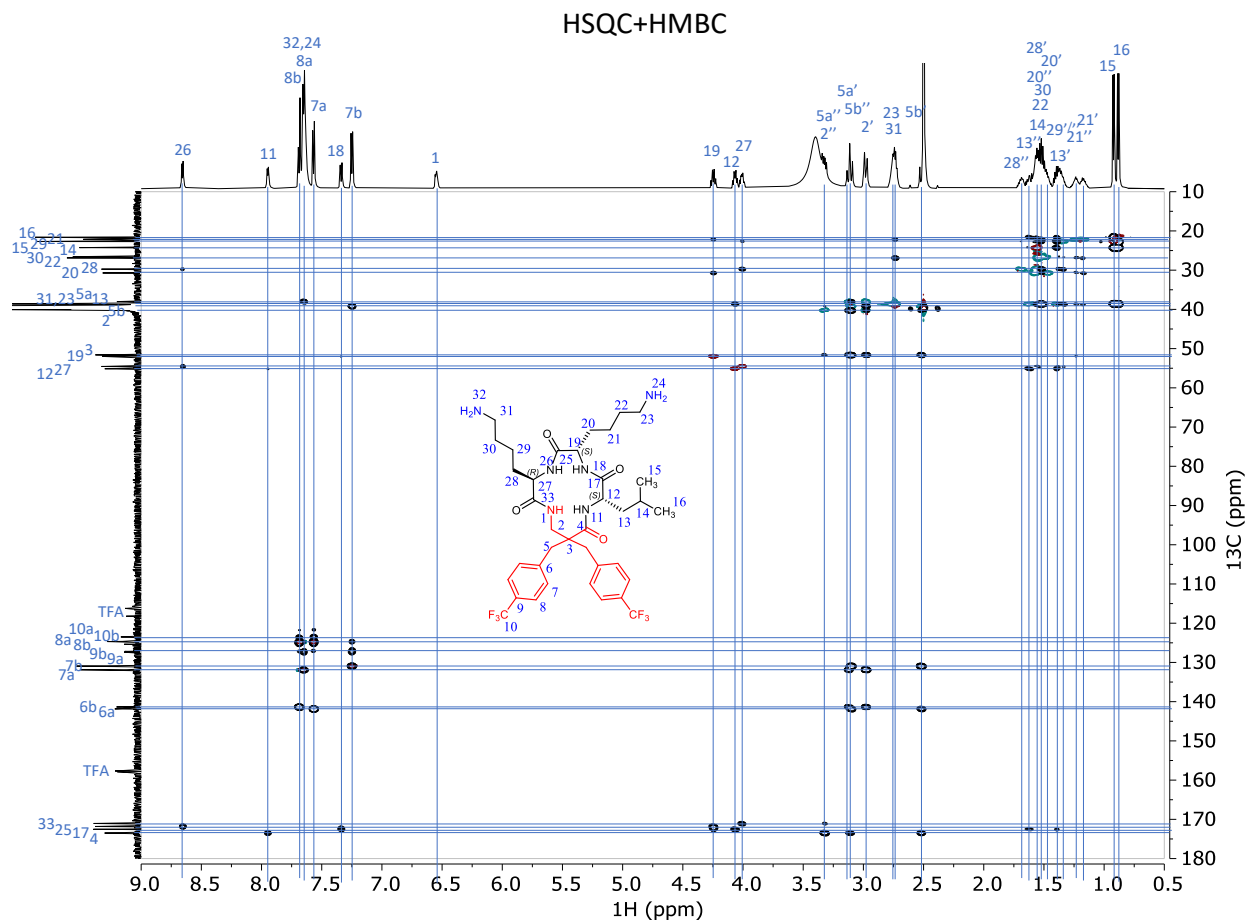


Figure Sx. Superimposed HSQC (red CH, CH₃, blue CH₂) and HMBC (black) spectra of **0011**

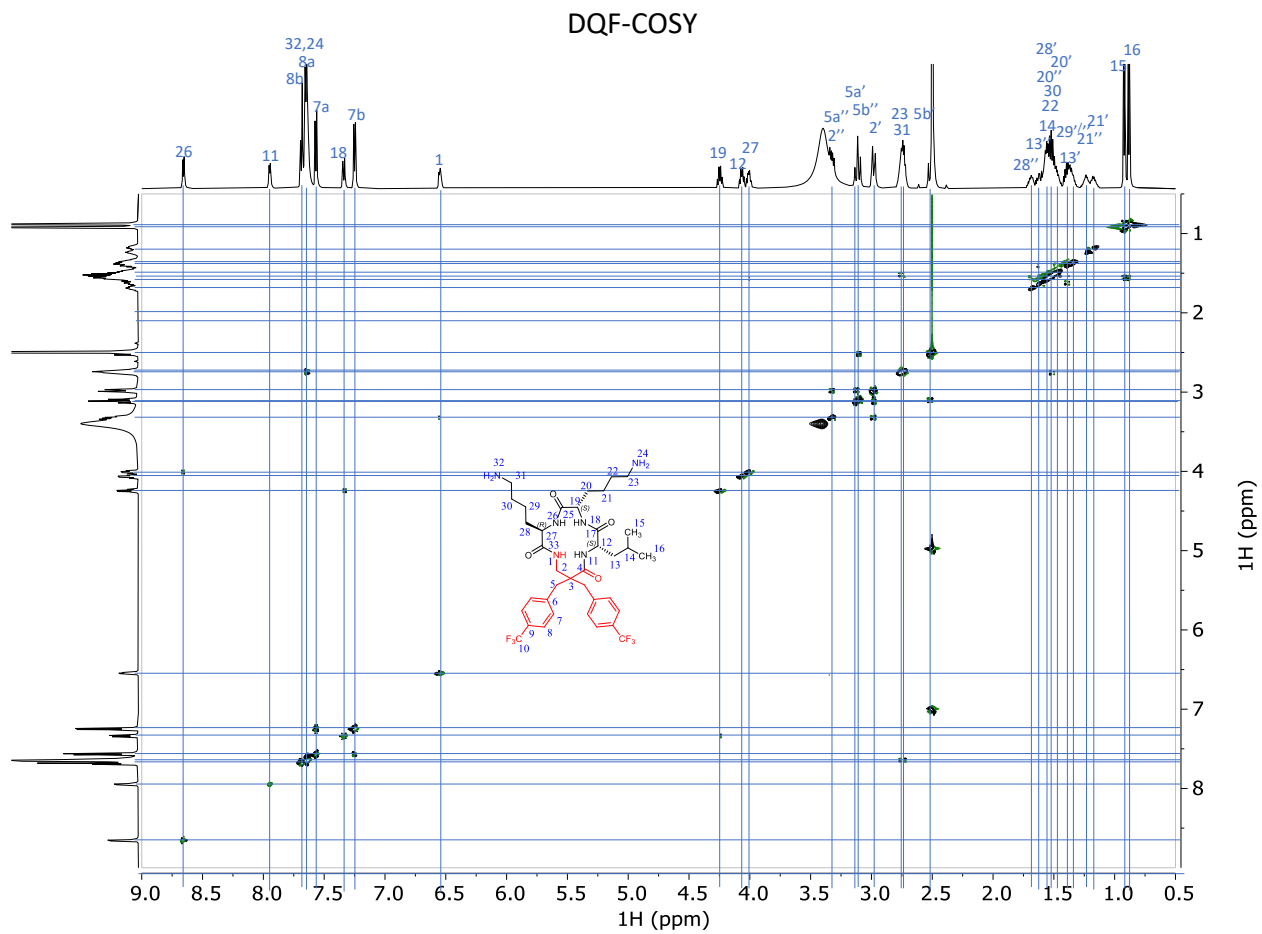


Figure Sx. DQF-COSY spectrum of **0011**

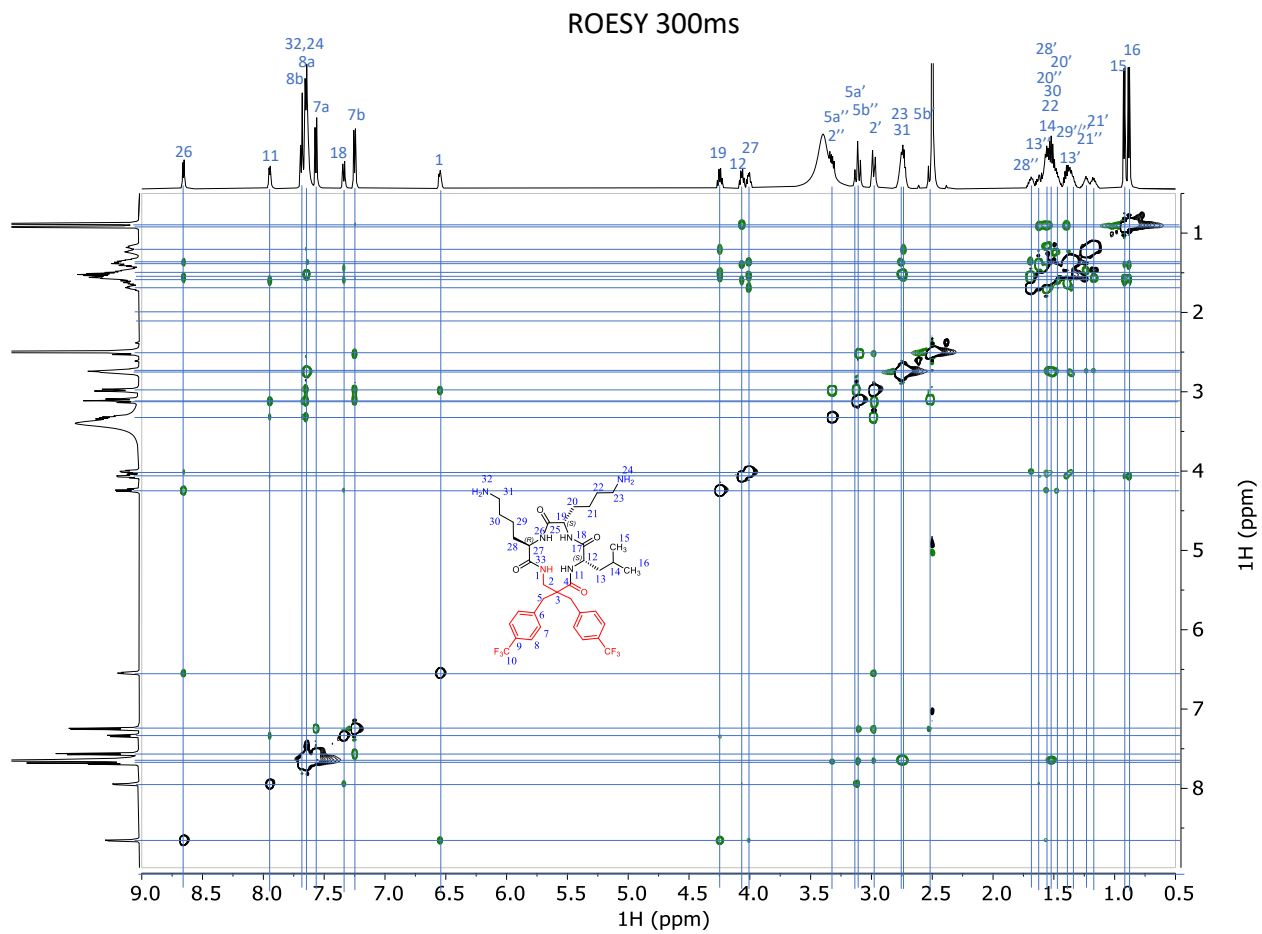


Figure Sx. ROESY (300ms spinlock duration) spectrum of **0011**

¹H NMR (600 MHz, DMSO) δ 8.48 (d, *J* = 8.4 Hz, 1H), 8.13 (d, *J* = 5.9 Hz, 1H), 7.77 (t, *J* = 5.8 Hz, 3H), 7.70 (d, *J* = 8.2 Hz, 5H), 7.59 (d, *J* = 8.0 Hz, 2H), 7.56 (d, *J* = 8.1 Hz, 2H), 7.25 (d, *J* = 8.0 Hz, 2H), 6.44 (dd, *J* = 8.5, 3.1 Hz, 1H), 4.32 (td, *J* = 8.7, 6.3 Hz, 1H), 4.08 (dt, *J* = 9.1, 6.2 Hz, 1H), 3.92 (ddd, *J* = 10.3, 8.4, 4.3 Hz, 1H), 3.32 (dd, *J* = 13.3, 8.5 Hz, 1H), 3.20 – 3.12 (m, 2H), 2.96 – 2.92 (m, 1H), 2.90 (d, *J* = 14.1 Hz, 1H), 2.64 (d, *J* = 13.8 Hz, 1H), 1.96 (dt, *J* = 13.6, 9.2, 3.7 Hz, 1H), 1.75 (dtd, *J* = 14.5, 9.4, 5.5 Hz, 1H), 1.67 (ddq, *J* = 19.3, 9.3, 5.5 Hz, 2H), 1.41 – 1.33 (m, 0H), 1.33 – 1.21 (m, 3H), 0.90 (d, *J* = 5.8 Hz, 2H), 0.87 (d, *J* = 5.8 Hz, 3H).

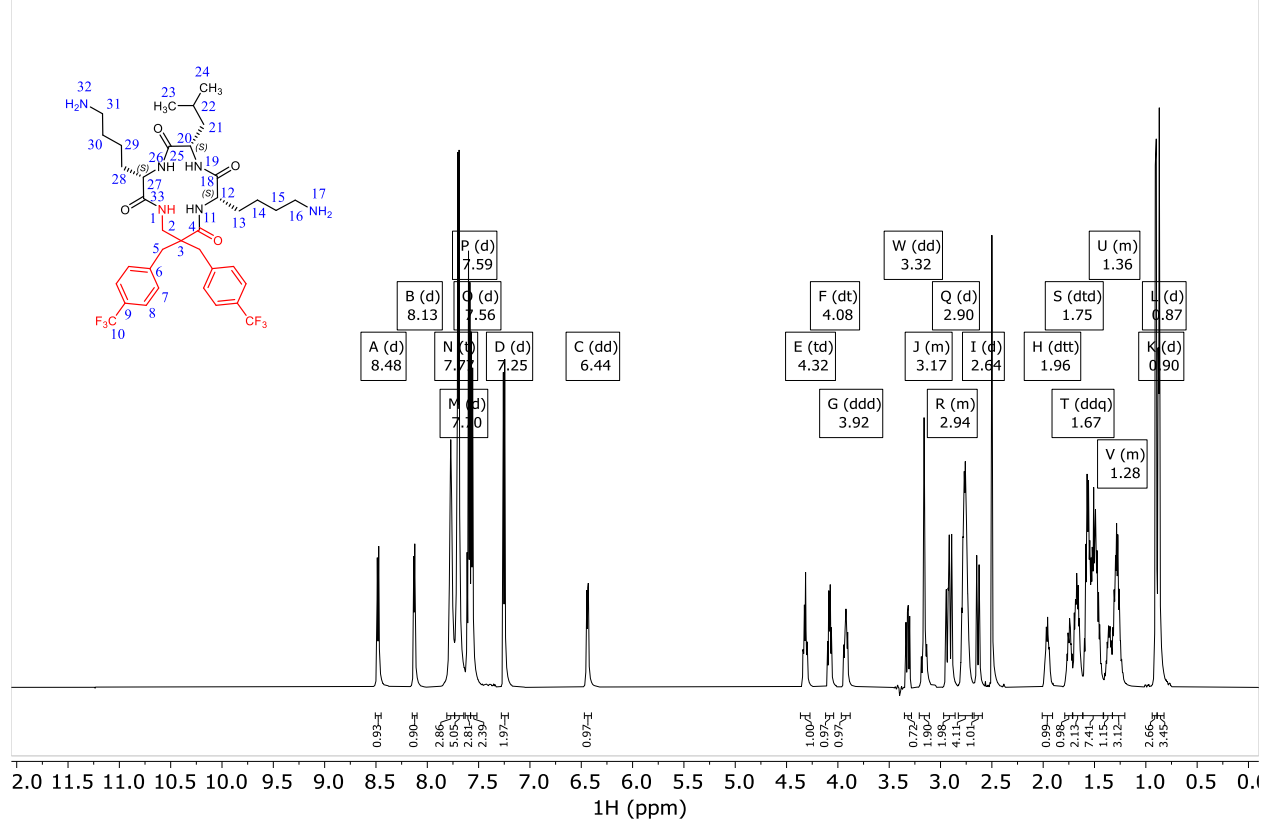


Figure Sx. ¹H NMR spectrum of **003**

^{13}C NMR (151 MHz, DMSO) δ 173.96, 171.72, 171.65, 170.58, 141.84, 141.53, 131.51, 130.88, 127.27 (q, $J = 31.7$ Hz), 127.12 (q, $J = 31.7$ Hz), 124.89 (q, $J = 3.8$ Hz), 124.77 (q, $J = 3.9$ Hz), 124.40 (q, $J = 272.2$ Hz), 124.35 (q, $J = 272.2$ Hz), 56.44, 52.62, 52.56, 51.26, 42.71, 40.15, 40.06, 38.91, 38.71, 38.62, 35.34, 29.04, 28.92, 26.56, 26.50, 24.62, 22.77, 22.64, 22.45, 22.09.

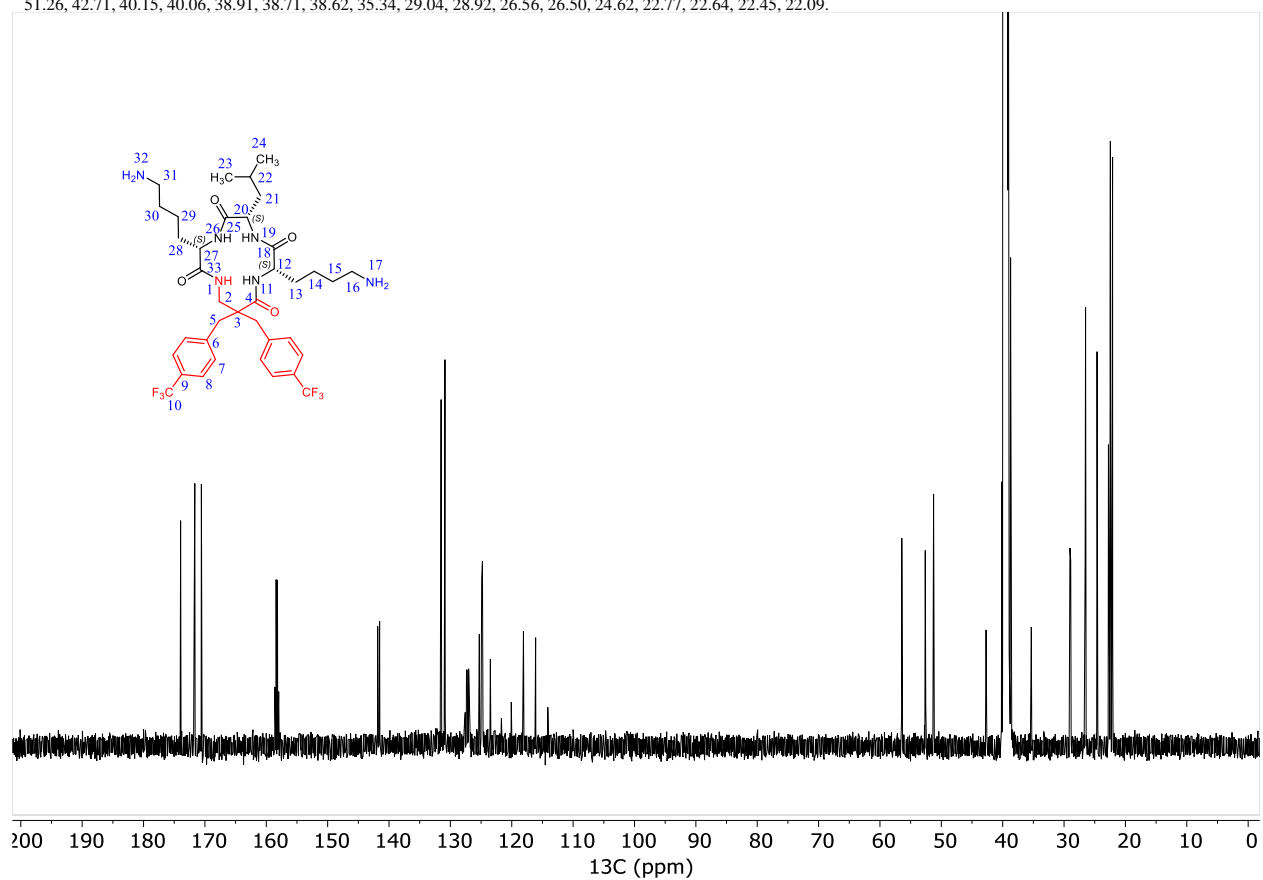


Figure Sx. ^{13}C NMR spectrum of **003**

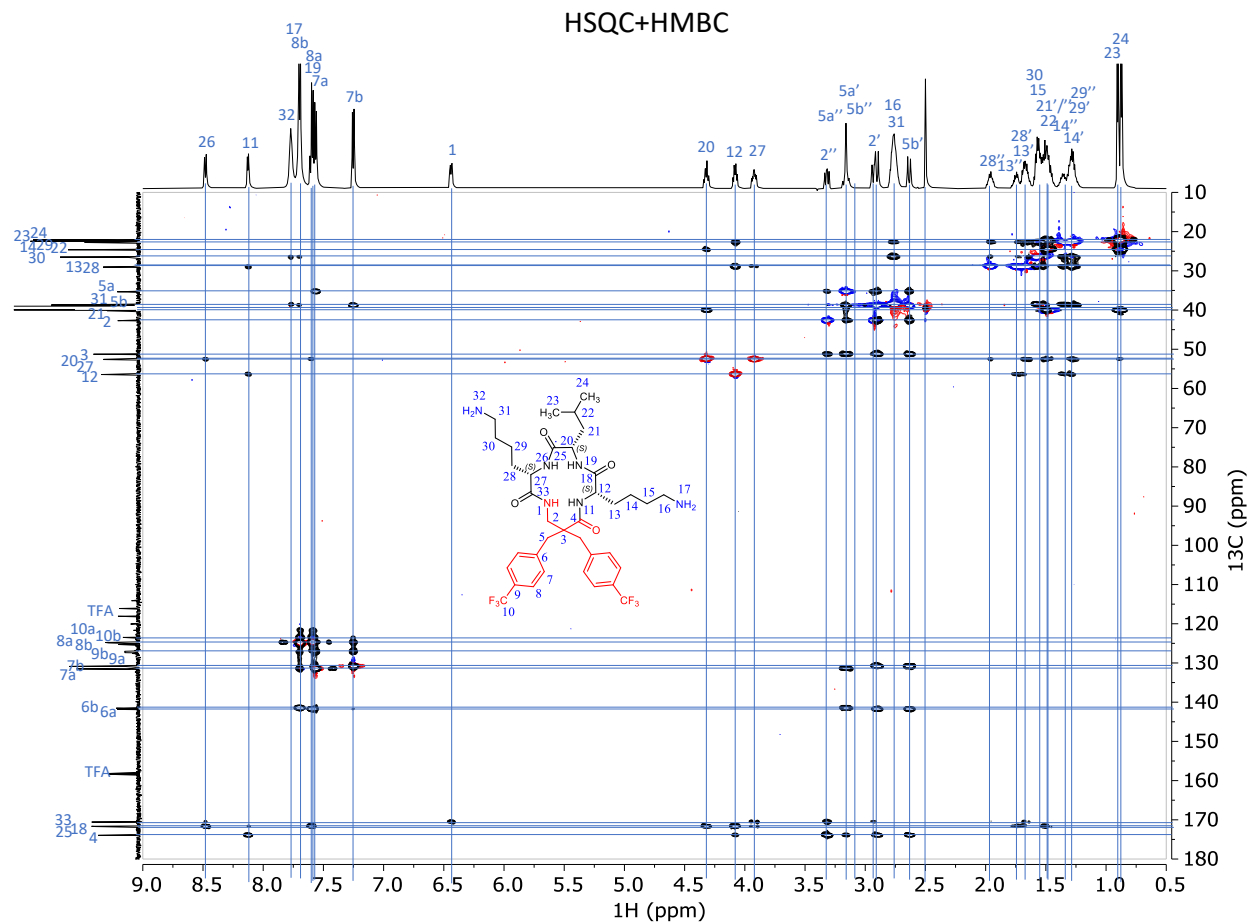


Figure Sx. Superimposed HSQC (red CH, CH₃, blue CH₂) and HMBC (black) spectra of **003**

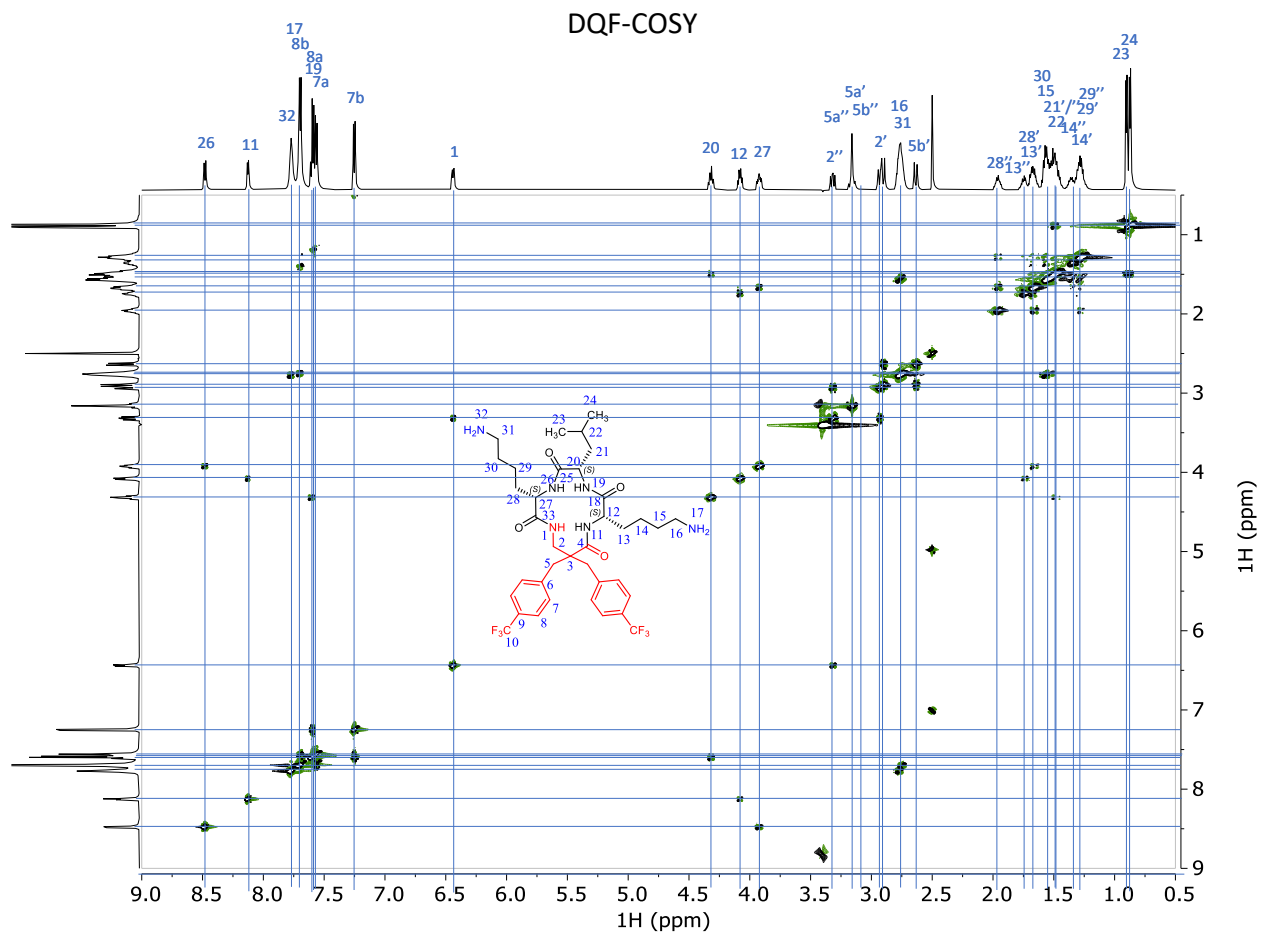


Figure Sx. DQF-COSY spectrum of **003**

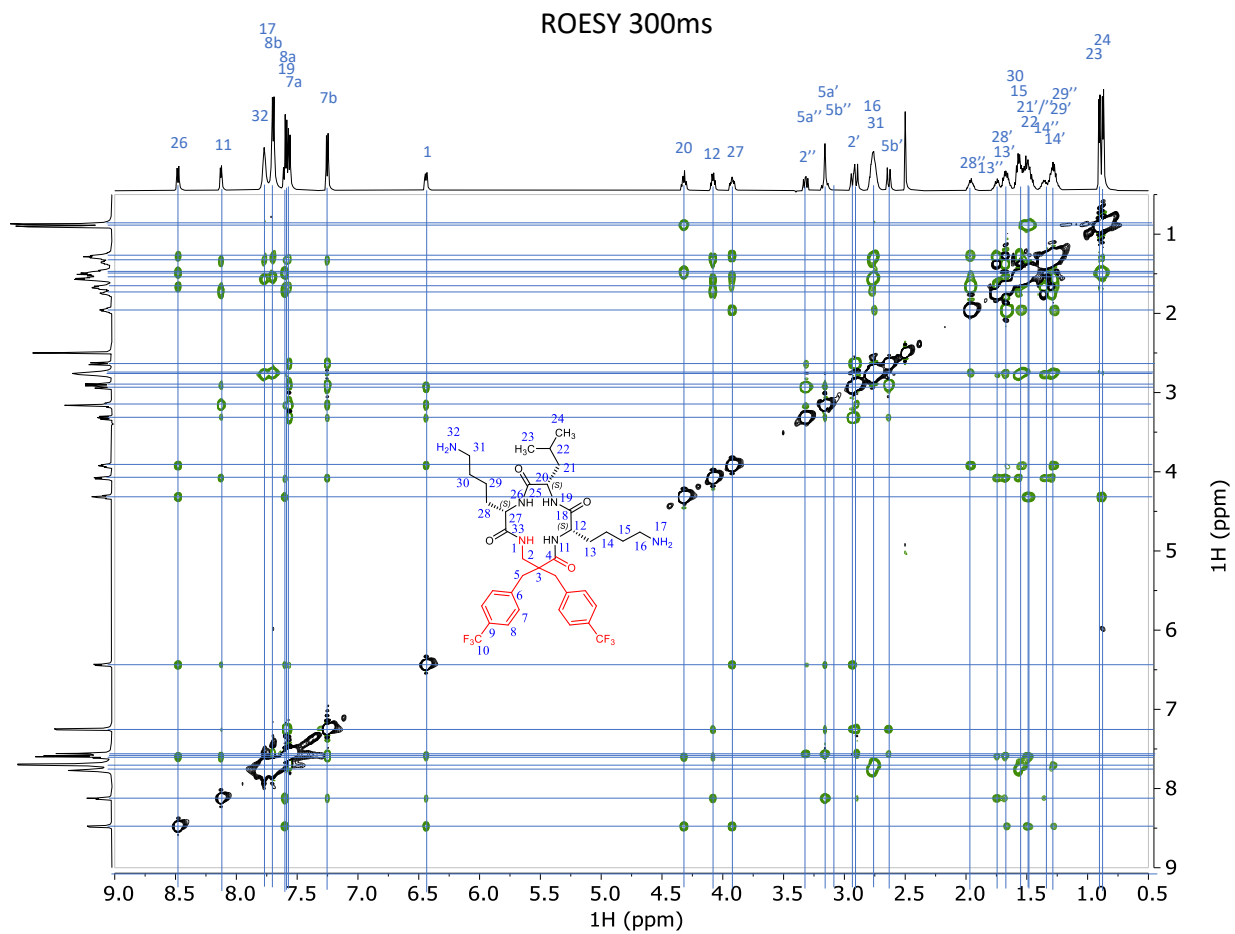


Figure Sx. ROESY (300ms spinlock duration) spectrum of **003**

¹H NMR (600 MHz, DMSO) δ 8.53 (d, *J* = 8.1 Hz, 1H), 7.99 (d, *J* = 6.3 Hz, 1H), 7.69 (d, *J* = 7.9 Hz, 3H), 7.64 (t, *J* = 5.4 Hz, 1H), 7.61 (d, *J* = 8.1 Hz, 2H), 7.57 (d, *J* = 8.2 Hz, 2H), 7.33 (s, 2H), 7.26 (d, *J* = 8.0 Hz, 2H), 6.92 (s, 4H), 6.48 (dd, *J* = 8.8, 3.0 Hz, 1H), 4.20 (q, *J* = 8.2 Hz, 1H), 4.16 (dt, *J* = 10.4, 5.9 Hz, 1H), 3.90 (ddd, *J* = 10.0, 7.9, 4.5 Hz, 1H), 3.40 (dd, *J* = 13.4, 8.6 Hz, 1H), 3.19 (d, *J* = 14.2 Hz, 1H), 3.16 – 3.04 (m, 5H), 2.99 (d, *J* = 13.7 Hz, 1H), 2.93 (dd, *J* = 13.3, 3.0 Hz, 1H), 2.62 (d, *J* = 13.7 Hz, 1H), 2.06 – 1.94 (m, 0H), 1.70 (dtd, *J* = 19.2, 9.7, 4.8 Hz, 2H), 1.64 – 1.57 (m, 2H), 1.56 – 1.33 (m, 2H), 0.91 (d, *J* = 6.6 Hz, 2H), 0.89 (d, *J* = 6.5 Hz, 2H).

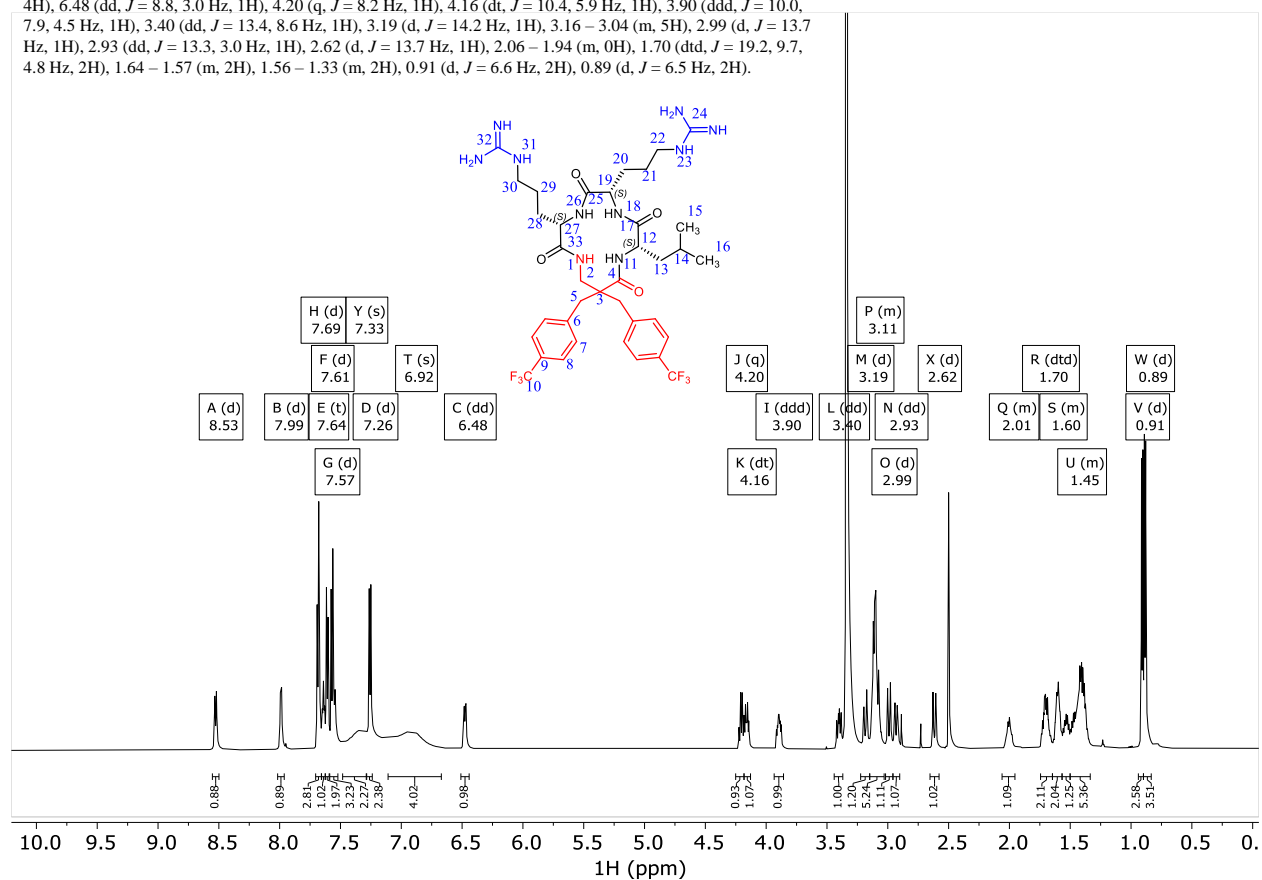


Figure Sx. ¹H NMR spectrum of **002**

^{13}C NMR (151 MHz, DMSO) δ 173.91, 172.61, 171.49, 170.24, 156.73, 141.92, 141.62, 131.52, 130.92, 127.25 (q, J = 31.9 Hz), 127.16 (q, J = 31.4 Hz), 124.83 (q, J = 3.5 Hz), 124.71 (q, J = 3.4 Hz), 124.44 (q, J = 271.7 Hz), 124.37 (q, J = 271.8 Hz), 54.62, 53.63, 52.89, 51.33, 40.32, 40.15, 40.06, 38.79, 38.31, 28.17, 26.45, 25.57, 25.11, 24.35, 22.84, 21.43.

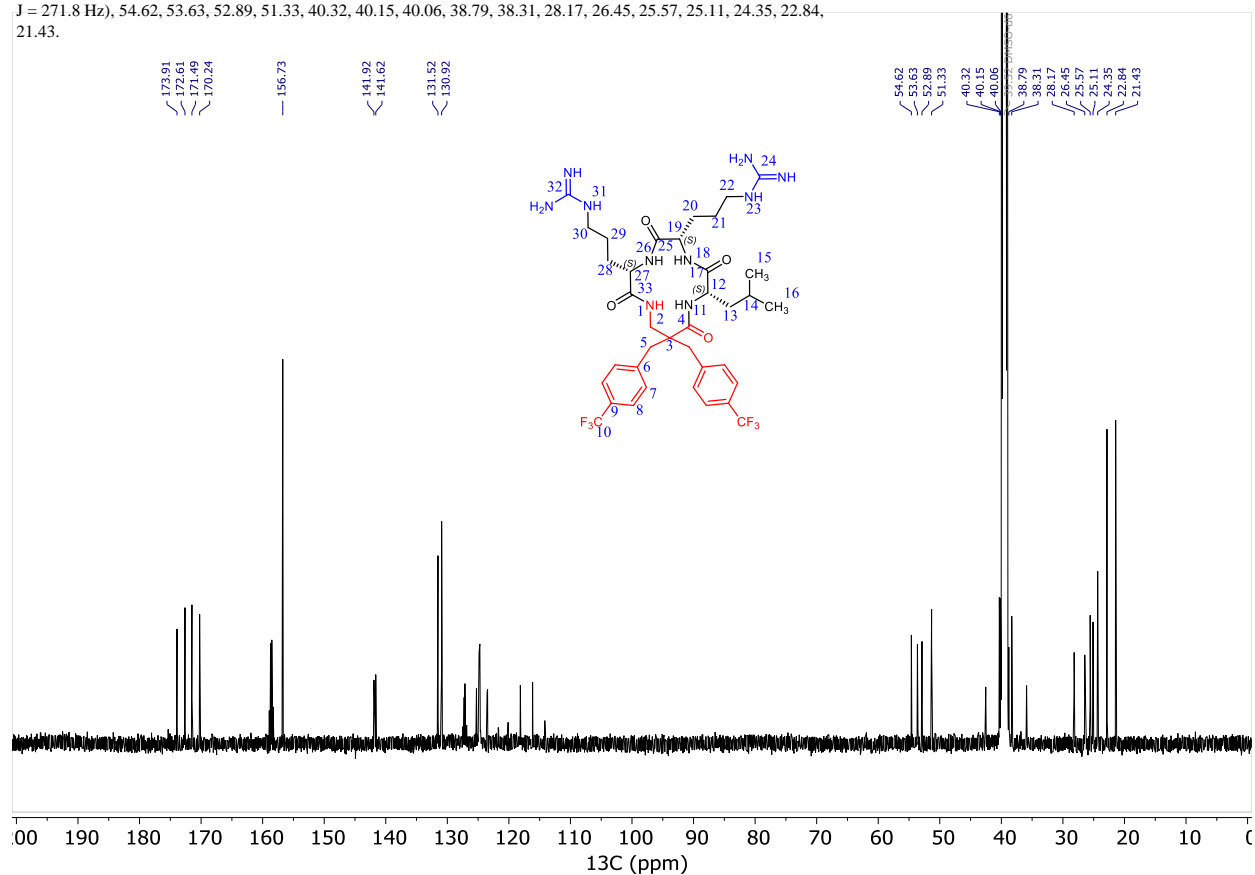


Figure Sx. ^{13}C NMR spectrum of **002**

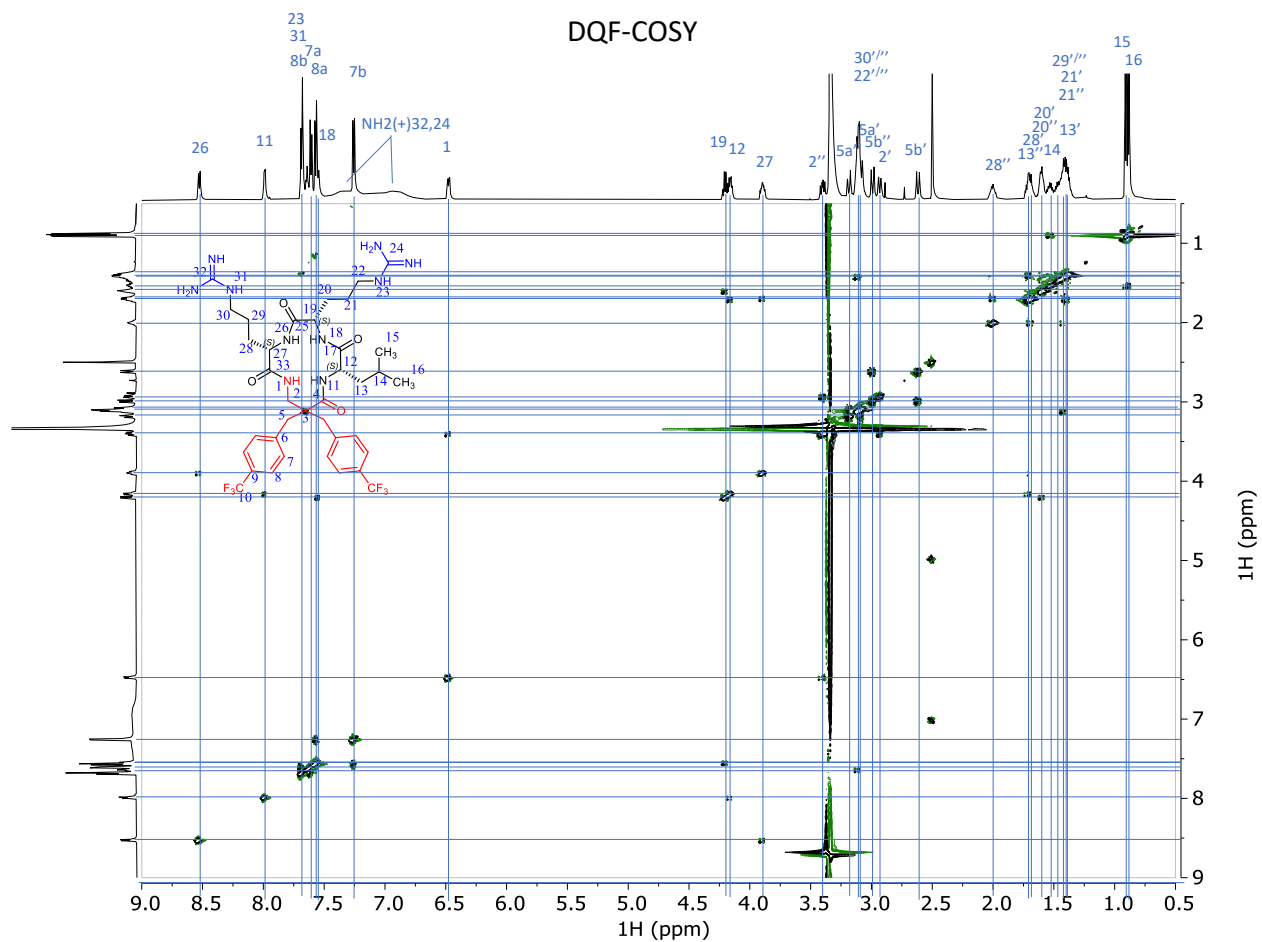


Figure Sx. DQF-COSY spectrum of **002**

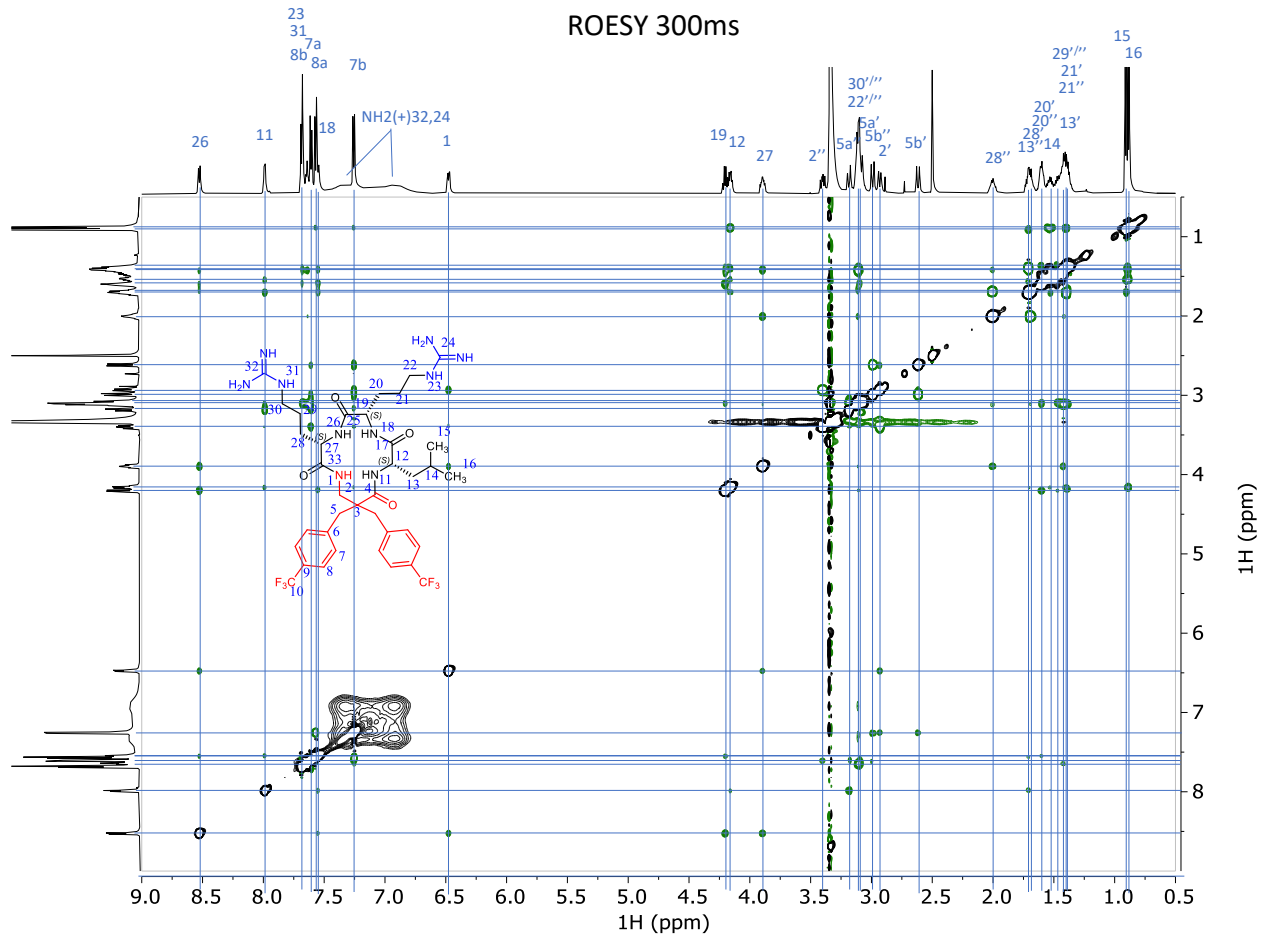


Figure Sx. ROESY (300ms spinlock duration) spectrum of **002**

Paper V

Conformational Studies of Cyclic Hexapeptides with Vibrational Circular Dichroism and Nuclear Magnetic Resonance

Karolina Di Remigio Eikås,^{1,2} Fredrik Garnås Rylandsholm,² Tone Kristoffersen,² Martin Jakubec,² Mitchell Ramesh Silk,² John Sigurd Mjøen Svendsen,^{2,3} Johan Mattias Isaksson,^{2,4} Kenneth Ruud,^{1,2,5} and Monika Krupová^{1,2}

1 Hylleraas Centre for Quantum Molecular Sciences, Department of Chemistry, UiT The Arctic University of Norway, N-9037 Tromsø, Norway

2 Department of Chemistry, Faculty of Science and Technology, UiT The Arctic University of Norway, N-9037 Tromsø, Norway

3 Amicoat AS, Sykehusvegen 23, 9019 Tromsø, Norway

4 Department of Pharmacy, Faculty of Health Sciences, UiT The Arctic University of Norway, N-9037 Tromsø, Norway

5 Norwegian Defense Research Establishment, P.O.Box 25, 2027 Kjeller, Norway

E-mail: monika.krupova@uit.no

Abstract

Due to growing antibiotic resistance, new types of antimicrobials such as antimicrobial peptides (AMPs) are widely studied. Since their antimicrobial activity is often dependent on their structure and conformation, methods capable of providing such information quickly and easily are in high demand.

In this work, we use vibrational circular dichroism (VCD) spectroscopy and molecular modelling to study the structure and conformation of four cyclohexapeptides with antimicrobial activity. Since cyclohexapeptides generally possess significant conformational flexibility, an extensive conformational search must precede the *ab initio* calculation of VCD spectra. A typical workflow for this task is to do a statistical averaging of spectra for a large number of structures produced by molecular dynamics (MD) simulations. However, this approach is very computationally demanding, since it requires geometry optimization and VCD property calculation for a significant number of structures. Therefore, less expensive computational approaches based on Boltzmann averaging of conformers are also commonly used.

We here compare a classical MD conformational sampling approach with CREST based computational protocol based on meta-dynamics simulations and Boltzmann averaging for calculation of VCD spectra of model cyclohexapeptides in two solvents (water and DMSO). While calculations based on an MD conformational ensemble provide very good agreement with experimental spectra for both solvents, the CREST based calculations in most cases fail to reproduce the experimental spectral patterns. This is due to a strong preference of the CREST approach for conformations with internal side chain – backbone hydrogen bonding, which is caused by a combination of several factors, such as use of an implicit solvent model during the simulation, the length and nature of amino acid side chains, and/or use of dispersion-corrected energies. The quality of conformational sampling by CREST and MD-based approach is further validated using experimental and theoretical NMR spectra.

Introduction

Growing antibiotic resistance is becoming one of the world's most urgent public health problems, with wide implications also for food security and technology development.¹⁻³ Bacterial infections are becoming increasingly difficult to treat as available antibiotics become less effective. Therefore, efforts to develop new classes of antimicrobials with reduced risk of triggering antibiotic resistance, such as antimicrobial peptides, are accelerating.⁴⁻⁶

Antimicrobial peptides (AMPs) are short and mostly positively charged peptides that can be found in a variety of organisms with direct and indirect (immunomodulatory) antimicrobial activity.^{7, 8} The mode of action can vary in different AMPs but often involves peptide-membrane interactions, including association and membrane disruption.^{9, 10} Although AMPs have diverse amino acid sequences, they often include hydrophobic and positively charged amino acids in their structure. The positively charged amino acids such as lysine (Lys, K) and arginine (Arg, R) are responsible for initial electrostatic interactions with the negatively charged bacterial membrane, while hydrophobic amino acids such as tryptophan (Trp, W) enable the peptide to interact with the hydrophobic parts of the phospholipid bilayer.¹¹⁻¹³

In addition to the amino acid composition, the antimicrobial activity of AMPs also depends on their structure and conformation.^{14, 15} Therefore, rapid and reliable experimental methods able to assess the dominating and/or antimicrobially active conformations of AMPs in various environments are much needed. The most common experimental techniques to study the conformation of peptides include X-ray crystallography^{16, 17} and nuclear magnetic resonance (NMR) spectroscopy.^{18, 19} Even though these techniques provide atomic-resolution structures, they have several drawbacks. For example, X-ray crystallography requires extensive experimental work in preparation of the diffracting crystal, which may in some cases even fail. In addition, the crystal structure of a molecule may deviate from its structure in the solution.^{20, 21} More advanced NMR spectroscopy techniques have in many cases been successful in structural studies of small molecules in solution,²² however, preparation of isotopically labeled samples may be complicated and expensive for bigger molecules.²³ Therefore, other techniques such as vibrational circular dichroism (VCD) that can quickly and easily provide insight into the general structure of peptides are becoming more and more important.²⁴⁻²⁹ In VCD, the differential absorption of left- and right-handed circularly

polarized light in the infrared spectral range is measured, providing additional and often complementary information to that obtained in regular infrared absorption spectroscopy.

In the last decades, VCD has been used not only for absolute configuration determination of chiral molecules, but also for structural studies of biopolymers such as nucleic acids, proteins and peptides.³⁰⁻³⁴ In the case of proteins and peptides, VCD has proven to be highly sensitive to backbone conformation and has enabled identification of the major structural motifs present in the biopolymers (α -helix, β -sheet, random coil, etc.).^{35,36} In peptides, also turns are common structural motifs. But, in contrast to rather rigid structural motifs such as α -helices and β -sheets, empirical comparisons of experimental VCD spectra with standardized spectral patterns for individual structural motifs cannot always reliably estimate the dominating turn. Thus, a theoretical interpretation of the spectra is needed to extract such information.^{37,38} The theoretical modeling of the spectra is straightforward and well-established for small rigid molecules; however, the situation gets more complicated with increasing size and flexibility of the molecules.

Besides VCD, the structural information on conformation of peptides can be extracted from nuclear magnetic resonance (NMR) spectroscopy.^{39,40} NMR spectroscopy is a robust and versatile tool in analytical chemistry that can be used to monitor changes in single atoms within a target molecule. By observing different magnetic properties, we can observe how molecules behave in different environments.

Using J_{HH} coupling constants to estimate dihedral angles through the Karplus equation is a well-established technique in NMR spectroscopy. Moreover, anisotropic NMR has emerged as a powerful technique for structural studies of small molecules.⁴¹⁻⁴³ Residual dipolar couplings (RDC) depend on the relative orientation of the ^1H - ^{13}C bond vectors, and Residual chemical shift anisotropy (RCSA) depend on the relative orientation of the carbon chemical shielding tensors relative to the magnetic field. Together, they provide information on the relative orientation of different parts of the molecule and configuration of stereogenic centers. Combined with chemical shifts, anisotropic NMR conducts a rich informational content on peptide structure.

In this work we use VCD spectroscopy combined with theoretical interpretation of the experimental data to investigate the structure of four cyclohexapeptides with potential antimicrobial activity (data not published yet). All the investigated peptides contain Trp as a hydrophobic amino acid, and either Lys or Arg as a positively charged amino acid. The

hydrophobic and charged amino acids either appear in alternating (cyclo(WXWXWX); X = K or R) or clustered (cyclo(WWWXXX); X = K or R) sequences. The structural information obtained using VCD methodology is further validated by both experimental and theoretical NMR spectroscopy data.

Even though cyclization of small peptides generally results in lower flexibility, cyclohexapeptides still possess significant conformational flexibility. Therefore, *ab initio* calculation of the IR, VCD and NMR spectra needs to be preceded by an extensive conformational search. In previous works, we developed a computational protocol to identify the most relevant conformations of cyclic peptides using CREST (Conformer-Rotamer Ensemble Sampling Tool).^{44, 45} Compared to the cyclic peptides this protocol was validated for, the peptides investigated in this work have longer and charged side chains that can participate in intramolecular interactions. To ensure that the structures predicted by a CREST protocol are valid also for such peptides, we have compared the VCD and NMR spectra of the structures determined as relevant by the CREST protocol with a more traditional approach where the sampling of the conformational space is performed with classical molecular dynamics (MD) simulations.

There are two significant differences between the two approaches. First difference lies in how these computational methods model the solvent. While CREST uses an implicit solvent model during the simulation, explicit water molecules are present in the MD simulation allowing specific solvent-solute interactions to be explicitly accounted for, which may be important for obtaining the correct conformational ensemble, in particular for systems and solvents with strong intermolecular interactions. Second difference is related to how the relevant conformers in each approach are determined. In CREST, energies and Boltzmann averages are used to identify important conformers and to calculate the final vibrational spectra, while MD provides a statistical averaging of conformations observed during the simulation run. In this work we investigate which of these approaches leads to the best agreement with experimental spectra, and thus is best suited to aid in the structural analysis of cyclohexapeptides.

Methods

Synthesis of Cyclohexapeptides

The cyclic peptides **1** – **4** (Figure 1) were synthesized using solid-phase peptide synthesis methodology⁴⁶ and fluorenylmethoxycarbonyl (Fmoc) chemistry procedures⁴⁷ as described previously. Briefly, the first amino acid was coupled to 2-Chlorotrityl chloride resin and the linear peptide precursors were prepared by an automated peptide synthesizer. The linear peptides were cleaved from the resin under mild acidic conditions and head-to-tail cyclized in solution. Next, the sidechains were deprotected and the crude cyclic peptides were purified by preparative reverse-phase HPLC. A detailed description of the synthetic procedure and characterization of the products can be found in the *Supporting Information*.

Vibrational Spectroscopy of Cyclohexapeptides

IR and VCD Spectra Acquisition. IR absorption and VCD spectra were measured with an Invenio R FTIR spectrometer with PMA50 module for polarization measurements (Bruker) at 8 cm⁻¹ resolution and PEM set to 1600 cm⁻¹ using a demountable BaF₂ cell and a 50 μm Mylar spacer. For spectra in water, D₂O was used as a solvent in order to avoid a strong deformation vibration band of H₂O overlapping with the amide I band of peptides. The peptides were mixed with D₂O and lyophilized overnight, and then dissolved in D₂O at a concentration of 20 mg/mL. For DMSO, non-deuterated peptides were dissolved in DMSO-d₆ at concentration 25 mg/mL. These solutions were used for IR and VCD spectra measurements.

Usually, 50 μL of peptide solution was deposited on the bottom cell window and covered with the top window. Five blocks of 22500 scans (15 hours of total accumulation time) were collected and averaged. Spectra of D₂O / DMSO-d₆ measured at the same conditions were subtracted from the sample spectra. The values of *g*-factor were calculated as $\Delta A/A$, where ΔA is the amplitude of a VCD couplet and *A* is the absorption intensity of the corresponding IR band.

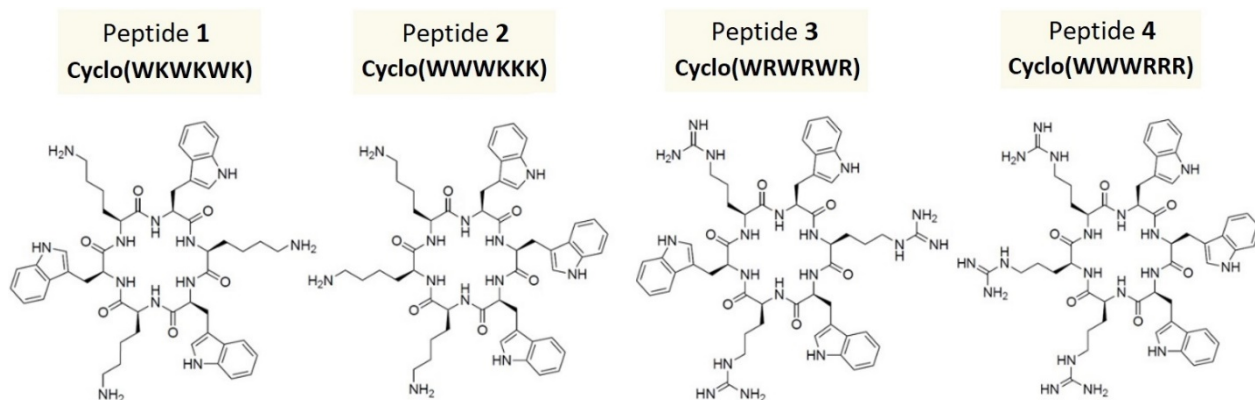


Figure 1. Investigated cyclohexapeptides **1 – 4**.

Calculation of VCD Spectra with CREST Conformational Sampling. The general workflow for conformational sampling described in our previous work⁴⁸ is based on meta-dynamics simulations as implemented in CREST 2.10. The conformer ensemble generated by CREST was then re-ranked by a DFT single-point energy calculation (B3LYP/6-31+G*⁴⁹/CPCM^{50, 51}) using Gaussian 16 (Rev. B.01)⁵². Conformers with energy within the 2.5 kcal/mol from the lowest-lying conformer after the DFT single-point energy calculations were geometry optimized, and the resulting structures were used to calculate IR and VCD intensities. If less than 20 conformers lied within 2.5 kcal/mol after the single-point energy calculation, we included the lowest-energy conformations above 2.5 kcal/mol up to a total number of 20 conformers to ensure that the conformational space was sufficiently sampled.⁴⁵

These structures were then geometry optimized and VCD properties were calculated at the DFT level (B3LYP/6-31+G*/CPCM) using Gaussian 16 (Rev. B.01). After geometry optimization, some of the conformers ended up in the same minimum. To remove these duplicates, we compared the energies and rotational constants for the individual conformers, and only unique conformers were included in the final spectra. Final IR and VCD spectra were generated as Boltzmann averages based on free energies for the unique conformers using a Lorentzian bandshape with a full width at half maximum (FWHM) of 10 cm⁻¹ with the CDSpecTech software.⁵³ The number of structures considered at each stage of the CREST calculation are summarized in Table 1.

Table 1. Number of conformers generated by CREST at each stage of IR and VCD spectra calculation.

	Solvent	Conformers found by CREST	Geom Opt Conformers	Unique conformer	Contributed to spectra >1 %
Peptide 1	water	326	20	19	5
	DMSO	297	34	25	3
Peptide 2	water	268	20	19	5
	DMSO	297	20	15	11
Peptide 3	water	368	20	20	5
	DMSO	230	20	20	7
Peptide 4	water	142	20	20	4
	DMSO	143	20	18	12

Calculation of VCD Spectra with MD Conformational Sampling. The initial structure of the investigated cyclic peptides was prepared using the Maestro molecular modelling package.⁵⁴ The cyclic peptides were constructed by linking the N- and C-terminal residues of the linear peptides followed by an energy minimization. MD simulations were performed with some modifications according to the protocol of McHugh *et al.*⁵⁵ using GROMACS 2020⁵⁶⁻⁵⁹ in water and in DMSO. For water, the RSFF1 force field⁶⁰ and TIP4P-Ew waters were used for the MD simulation. In the case of DMSO, we used the OPLS-AA/L force field⁶¹ and a box of pre-equilibrated DMSO molecules. Some modifications to the GROMACS library files as described by Jiang and Geng⁶² were applied to generate input files suitable for cyclic peptides.

The peptides were placed in a cubic box containing pre-equilibrated solvent molecules (~2000 and ~500 molecules for the H₂O and DMSO simulations, respectively). The dimensions of the box were such that the minimum distance between solute molecule and the edges of the box was 1.0 nm. The solvated system was energy minimized with the steepest descent algorithm. The equilibration was performed in two stages with a step size of 2 fs. The first stage of equilibration consisted of a 50 ps *NVT* simulation at 300 K followed by a 50 ps *NPT* simulation at 300 K and a

pressure of 1 bar. During the first step of equilibration, a position restraint with a force constant of $1000 \text{ kJ mol}^{-1} \text{ nm}^{-2}$ on the heavy atoms in the peptide was used. The second stage of equilibration was done without the position restraint on the peptide and consisted of a 100 ps *NVT* simulation at 300 K followed by a 100 ps *NPT* simulation at 300 K and 1 bar.

The production run was performed within the *NVP* ensemble at 300 K and 1 bar with a leapfrog algorithm⁶³ for 1 μs with a step size of 2 fs. The temperature was controlled using the V-rescale thermostat method⁶⁴ with a coupling time constant of 0.1 ps. The solute and solvent molecules were coupled to separate thermostats. The pressure was maintained by the Parrinello-Rahman barostat method with a coupling time constant of 2.0 ps and a compressibility of $4.5 \times 10^{-5} \text{ bar}^{-1}$.

To constrain bonds involving hydrogens to their equilibrium value, the LINCS algorithm⁶⁵ was used. Non-bonding interactions were treated with a cut-off radius of 1.0 nm. Electrostatic interactions beyond this threshold were treated with the Particle Mesh Ewald method⁶⁶ with a Fourier spacing of 0.12 nm and an interpolation order of 4. To account for the truncation of the Lennard-Jones interactions, long-range analytic dispersion corrections to both energy and pressure were applied. The simulation trajectories were sampled every 10 ps. For each molecule, 200 snapshots were extracted from the trajectory, stripped of solvent, and the resulting structures were used for DFT calculation of IR and VCD spectra.

The geometry optimizations and VCD property calculations for conformers generated by the MD simulations were performed at the DFT level (B3LYP/6-31+G*/CPCM) using Gaussian 16 (Rev. B.01). The final spectra were generated using the CDSpecTech software⁵³ as a simple average of spectra of all 200 snapshot geometries. A Lorentzian bandshape with a FWHM of 10 cm^{-1} was applied.

Clustering of the MD Conformers for Investigation of Their Backbone Structure. The geometry optimized structures from the MD simulations were clustered by the Conformer Cluster Panel script in Maestro.⁵⁴ The clustering was done based on the atomic root-mean-square deviation (RMSD) of the backbone, including hydrogens on both the α -carbons and amide groups. Based on the statistics from a test run, the Kelley index⁶⁷ was used to choose the optimal number of clusters. The clustering was then done with the number of clusters resulting in the lowest Kelley Penalty using the Average linkage method implemented in Maestro.⁵⁴ From each of the largest clusters,

accounting for up to 90 % of the spectra, one structure was extracted and characterized in terms of dihedral angles, internal hydrogen bonding and turns.

Nuclear Magnetic Resonance Spectroscopy of Cyclohexapeptides

NMR Spectra Acquisition. NMR spectra were acquired on a Bruker Avance III HD spectrometer operating at 600 MHz for ^1H , equipped with an inverse TCI cryoprobe. NMR spectra for all studied cyclic peptides were acquired at 298 K in 5mm tubes (in 3mm Shigemi tube for c(WWWRRR) peptide) using standard pulse programs in water and d-DMSO.

ROESY, TOCSY, DQF-COSY, ^{15}N -HSQC, HSQC, and HMBC NMR spectra were recorded with gradient selection and adiabatic pulses when applicable. ROESY and TOCSY spectra were recorded with mixing times of 25–200 ms and 80 ms, respectively. Spectra were processed with TopSpin 3.6.0, and assignments were done manually. The full assignment in H_2O was previously published,⁶⁸ while the assignment in d-DMSO is reported in the *Supporting Information* (Tables S1-S4).

The experimental J -coupling constants were found by using the deconvolution tool in MestreNova on 1D ^1H spectra. For a few less resolved signals, the coupling constants were found by a lineshape fitting from a high resolution and zero filled ^{15}N -HSQC F2 slice.

Sample Preparation and Data Acquisition of Anisotropic NMR. Polyacrylamide (PAA) gels were cast at room temperature in the form of rods with a 40mm length and 5.4mm diameter, approximately 1.3 mm more than the inner diameter of the standard 5mm NMR tube, in a NewEra Gel Chamber under a blanket of Argon gas.^{69, 70} The gel was cast using a solution of 223 μL acrylamide (acrylamide/bisacrylamide 19:1), 105 μL freshly prepared 1% ammonium persulphate solution, 10.5 μL of N,N,N',N' -Tetramethylethylenediamine (TEMED), and 712 μL of H_2O , for a total volume of 1050 μL . After gelation and washing with water 3 times, the gel was dried overnight at room temperature. The dried gel was inserted into a 5mm NMR tube with a 2.5mM solution of cyclic hexapeptide in 500 μL of $\text{H}_2\text{O}/\text{D}_2\text{O}$ (90/10 %) with 0.5 % TMS- d_4 as internal standard. The gel was fully stretched after two weeks, then HSQC-CLIP and 1D ^{13}C NMR spectra were collected, together with HMBC, HSQC, and DQF-COSY for chemical shift referencing. The RDCs were extracted as a difference in splitting of the signal in HSQC-CLIP in ppm between the samples with- and without PAA gel. RCSAs were extracted as a shift of the ^{13}C signal in Hz between the

samples with- and without PAA gel. The experimental RDC and RCSA values were compared to the ones calculated for conformers using MSpin, and Quality factors (Q-factors) were collected.

Calculation of NMR Chemical Shifts. Chemical shifts were calculated for the geometry optimized conformational ensembles used in the VCD spectra calculations. The NMR chemical shifts calculations for cyclohexapeptides were carried out at the DFT level (mPW1PW91⁷¹/6-311++G**/CPCM) using Gaussian 16 (Rev. B.01). Chemical shifts for TMS and TMSP-d4 in DMSO and water, respectively, were calculated at the same level of theory and used as a reference for ¹H and ¹³C chemical shifts calculations in their respective solvents. The final chemical shift spectra were generated either as Boltzmann averages based on free energies for the unique conformers (CREST-based conformers) or as a simple average of all conformations (MD-based ensemble). The comparison between experimental and calculated chemical shifts was performed using an in-house MatLab script.

Calculation of *J*-coupling Constants. *J*-coupling values for the calculated conformations were evaluated by MSpin using the built-in Pardi (1990) module for ³*J* H(N)-C_α-H coupling constants. The coupling constants were calculated for all six amino acids of the four cyclic hexapeptides. For CREST, all conformers evaluated. Due to time constraints, only some structures were used for evaluation of *J*-coupling constants in MD-based ensemble (every 10th conformer starting with nr. 1 and up to nr. 200; a total of 21 conformers). To justify this step, we compared the *J*-coupling constants of the reduced ensemble (21 conformers) with the unreduced one (200 conformers) for the c(WWWKKK) cyclopeptide and found no significant changes of the values (Table S6 in *Supporting Information*). The final *J*-coupling values were generated either as Boltzmann averages based on free energies for the unique conformers (CREST-based conformers) or as a simple average of all conformations (MD-based ensemble).

Results and Discussion

We first focus on the experimental IR absorption and VCD spectra of peptides **1** – **4** in D₂O. We then evaluate the performance of the CREST-based computational protocol for these systems, followed by a comparison of the CREST and MD conformational sampling methodology for peptide **1**. Finally, we compare the two computational approaches for the calculation of vibrational

spectra of peptide **1** in DMSO. The analysis is complemented by experimental and theoretical isotropic and anisotropic NMR parameters.

Experimental IR and VCD Spectra of Cyclohexapeptides in D₂O. Infrared absorption and VCD spectra of peptides are rich in structural information, since VCD spectral signatures can often be directly linked to the backbone conformation. Vibrational absorption spectra of proteins and peptides comprise mainly of two regions: the amide I region (1600 – 1700 cm⁻¹, mainly carbonyl stretching vibration) and the amide II region (~1550 cm⁻¹ in H₂O and ~1450 cm⁻¹ in D₂O, combination of N-H bending and C-N stretching vibrations). In Figure 2, we present experimental IR and VCD spectra of peptides **1** – **4** in D₂O. Heavy water was used as a solvent due to the strong absorption of H₂O in the carbonyl stretching region. This deuteration primarily affects the absorption energies in the amide II region, resulting in a significant shift to lower frequencies.

The infrared spectra of all investigated peptides in D₂O are dominated by a strong absorption band in the amide I region at 1672 cm⁻¹ with a single shoulder at 1630 cm⁻¹ for peptide **1** and **2**, and multiple other bands merged to a complex and wide feature with a maximum at 1610 cm⁻¹ for peptide **3** and **4**. The more complex nature of the amide I region for peptides **3** and **4** originates in vibrations connected to the guanidino groups in the Arg side chains (see Figure S1 and Table S6 in *Supporting Information*). The amide II region is similar for all investigated peptides and is comprised of a complex band with a maximum at 1456 cm⁻¹.

Interestingly, all investigated peptides measured in D₂O provide similar features in their VCD spectra, primarily in the amide I region. These are characterized by a strong (+/-) couplet with a positive wing at 1652 cm⁻¹ and a negative wing at 1627 cm⁻¹. The shape of the couplet is only slightly altered for individual peptides. Due to this remarkable similarity of the VCD spectra in the amide I region, we assume that the overall backbone conformation of the investigated cyclic peptides is similar and is only slightly altered by the amino acid side chains. More differences can be observed in the amide II region. For peptides **1** and **2** containing lysine, a negative band at 1423 cm⁻¹ can be observed. Other features in the amide II region have too low intensity to be interpreted. For peptides **3** and **4** containing arginine, the amide II region is unusually intense and provides several spectral features. In the VCD spectra of peptide **3**, a ‘W-shape’ feature can be recognized with local minima at 1423 and 1387 cm⁻¹. The most prominent feature in the amide II region of the

VCD spectrum of peptide **4** is a couplet with a positive wing at 1435 cm⁻¹ and a negative wing at 1418 cm⁻¹, which is only slightly less intense than the amide I couplet. The *g*-factors calculated as a ratio between the absorption intensity and the amplitude of the corresponding VCD couplet for all investigated cyclohexapeptides are $\sim 5 \times 10^{-5}$ (see Table S7 in *Supporting Information*), which is a typical value for peptides.

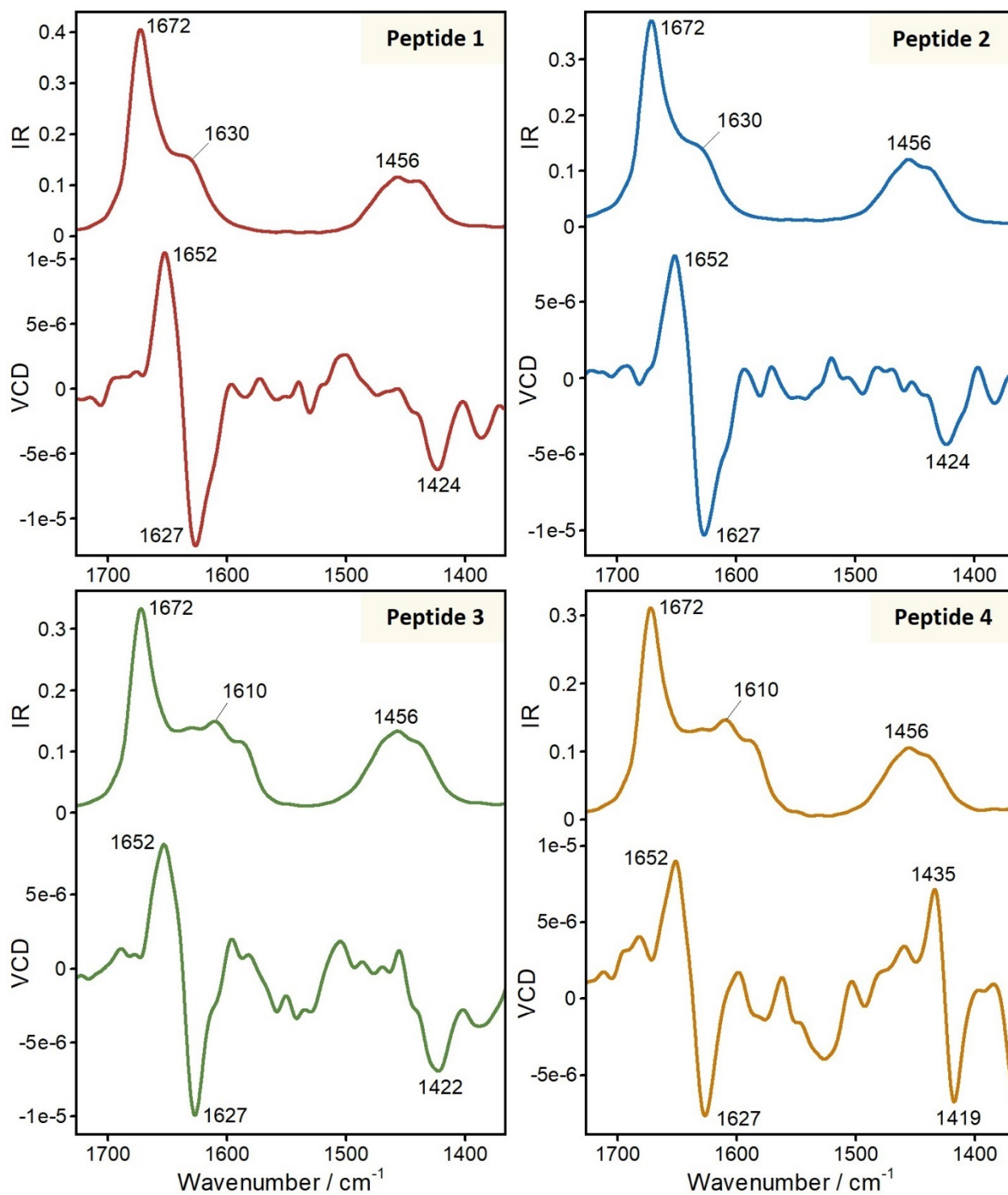


Figure 2. Experimental IR absorption and VCD spectra of investigated cyclohexapeptides **1 – 4** at 20 mg/mL in D₂O.

Calculation of Vibrational Spectra of Cyclohexapeptides Based on CREST Conformers in D₂O. To understand the structural information in the experimental spectra, we performed CREST conformational sampling and DFT spectra calculation for peptides **1** – **4** in D₂O. The results are summarized in Figure 3.

The spectra consist of the amide I region (1580 – 1720 cm⁻¹), which was in all cases simulated at significantly higher frequencies compared to experiment (shifts of 30 – 50 cm⁻¹), and the amide II region around 1450 cm⁻¹. The shift of the amide I region in the calculated spectra arises mainly from the neglect of specific solvent-solute interactions during the DFT spectra calculation using an implicit solvent model.⁴⁸ The overall agreement of the main VCD spectral signatures in the amide I region between the calculated and experimental spectra is poor. For peptide **1**, an experimental (+/-) VCD couplet centered at 1638 cm⁻¹ shows a (+/-/+) signature in the calculation based on CREST conformers. For peptides **2** and **3**, more complex VCD signatures in the amide I region are not in agreement with experimental couplets. The best agreement between calculation and experiment in the amide I region was observed for peptide **4**. In this case, CREST correctly predicted a (+/-) couplet centered at 1678 cm⁻¹. The agreement of CREST signatures with experiment is much better in the amide II region. For peptides **1** – **3**, CREST was able to predict the overall spectral shapes, although the fine spectral features cannot be compared due to high signal-to-noise ratio of the experimental VCD spectra in this region. Interestingly, the CREST-based spectra for peptide **4** which showed the best agreement with experiment in the amide I region failed to correctly predict the spectral signatures in amide II region. The experimental VCD spectra of peptide **4** in the amide II region show a relatively strong (+/-) couplet centered at 1427 cm⁻¹ that is not reproduced in the calculated spectra.

The backbone structures of the dominating conformers for peptides **1** – **4** predicted by CREST are illustrated in Figure S2 in the *Supporting Information*.

To investigate whether the poor agreement between the experimental and calculated VCD spectra lies in insufficient or erroneous conformational sampling, in the next section we compare the CREST conformational search with the statistical averaging of the MD conformational ensemble for peptide **1**.

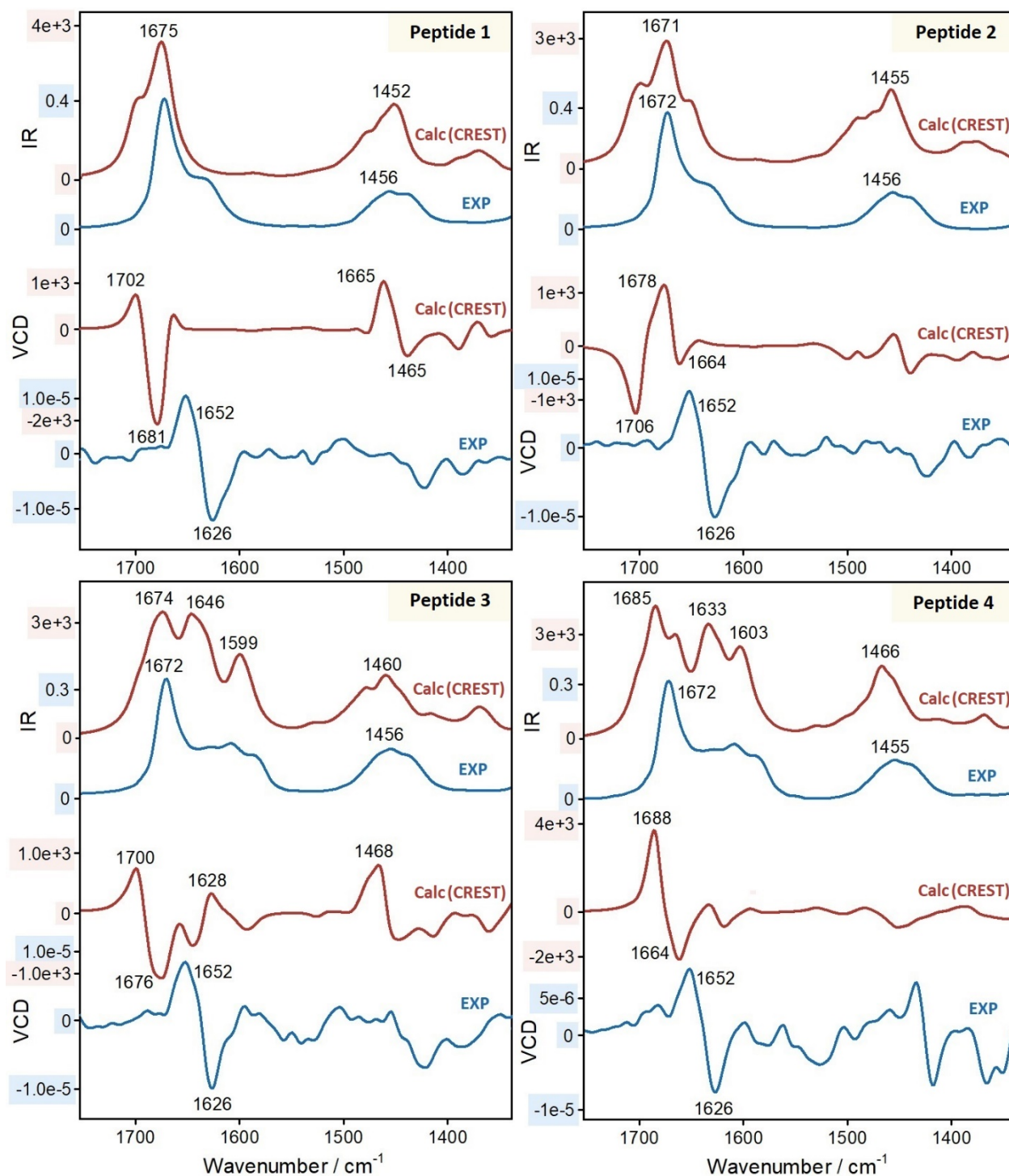


Figure 3. Experimental (D_2O , 20 mg/mL) and calculated (conformational sampling performed by CREST, spectra calculated at B3LYP/6-31+G*/CPCM level) IR and VCD spectra for cyclohexapeptides 1 – 4.

Vibrational Spectra of Peptide 1 in D₂O based on MD and CREST Conformers. To link the experimental spectral shapes to the backbone conformation of cyclohexapeptides, we compare the experimental and calculated IR absorption and VCD spectra for peptide 1 in D₂O in Figure 4. The conformational sampling preceding the DFT calculation of the spectra was performed either by MD simulations (middle spectrum, red line) or CREST sampling (top spectrum, blue line). In the following text, we use the term ‘MD based’ when referring to the spectra calculated based on the MD conformational ensemble, and ‘CREST based’ for spectra calculated based on the CREST conformers.

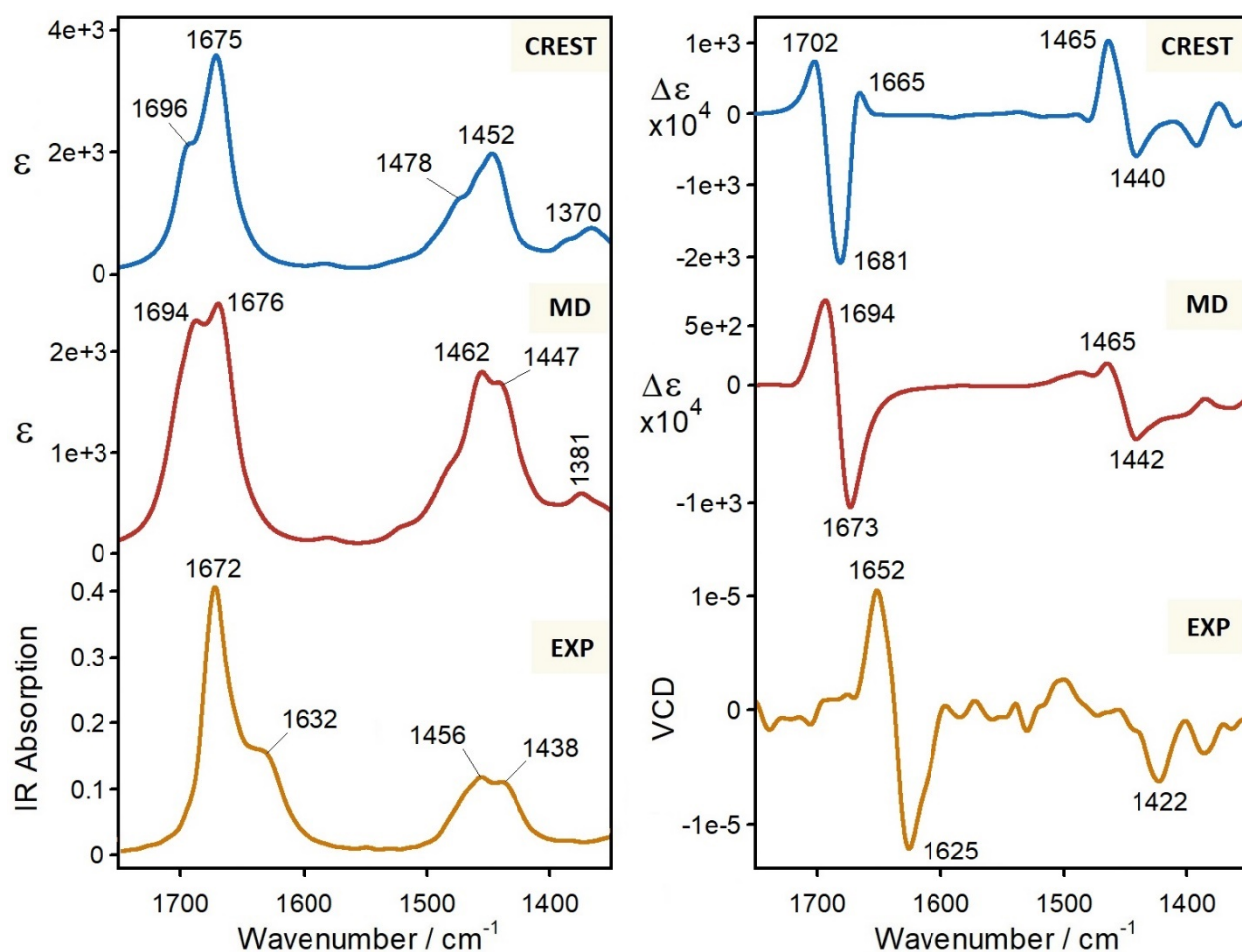


Figure 4. Comparison of experimental (orange; 20 mg/mL) and calculated IR absorption (left panel) and VCD (right panel) spectra of peptide 1 in D₂O. The conformational search for the peptide preceding DFT calculation was performed by two methods: CREST (blue) and MD (red).

Both MD and CREST based calculations correctly predicted the split of the amide I band in the IR spectrum into two components, although with opposite relative intensities. In this sense, the MD based calculation performed a bit better, predicting the relative intensities of the two peaks to be similar. In VCD, an experimental (+/-) couplet in the amide I region centered at 1638 cm^{-1} is very well reproduced in the MD based spectrum, although with a significant shift of $\sim 45\text{ cm}^{-1}$ to higher frequencies due to the implicit solvent used in the DFT calculation. In the amide II region, the MD calculation provides a composite spectral pattern in VCD with a local maximum at 1465 cm^{-1} and a local minimum at 1442 cm^{-1} , which is not consistent with the experimental 'W'-like pattern. The convergence of the spectra based on the number of averaged MD structures is shown in Figure S3 (*Supporting Information*).

Analysis of the Calculated Conformations of Peptide 1 in D₂O. It is evident that using MD and CREST conformers results in different spectral patterns. To better understand the origin of these differences, we investigated the backbone structure of the conformational ensembles produced by the two approaches.

The backbone structure of the investigated peptides is determined primarily by hydrogen bonding between the carbonyl oxygens and amide hydrogens within the backbone. Various backbone conformations can be classified as different turns, characterized by several parameters. The first parameter is the number of peptide bonds between a hydrogen acceptor (C=O) and a hydrogen donor (N-H). According to this, turns in peptides can be divided into different classes: π -turn (5 peptide bonds), α -turn (4 bonds), β -turn (3 bonds), γ -turn (2 bonds) and δ -turn (1 bond). Of these, β -turns are the most usual form followed by γ -turns, while δ -turn is the least common type due to high steric hindrance. These classes of turns are further divided into different subtypes depending on the dihedral angles the backbone assumes. The more common β -turns are classified by ϕ_{i+1} , ψ_{i+1} , ϕ_{i+2} and ψ_{i+2} dihedral angles, while the slightly less common γ -turns are classified based on the dihedral angles ϕ_{i+1} and ψ_{i+1} (Figure 5).

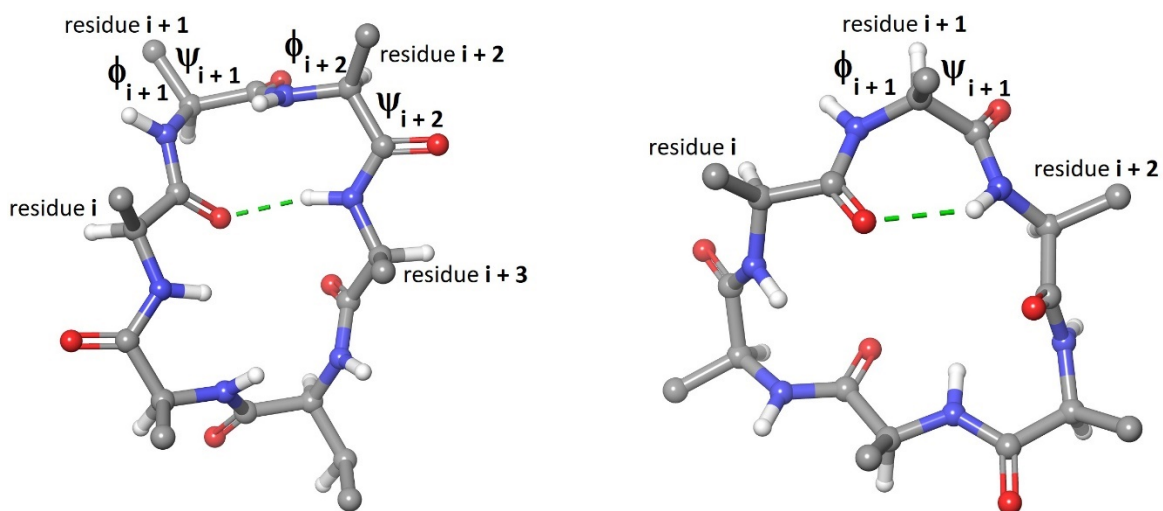


Figure 5. Example of peptide **1** backbone structure with a β - (left) and γ -turn (right). Peptide turns are further classified based on dihedral angles (ϕ_{i+1} , ψ_{i+1} , ϕ_{i+2} and ψ_{i+2} for β -turns, and ϕ_{i+1} and ψ_{i+1} for γ -turns).

The cyclohexapeptides discussed in this work contain mostly β - and γ -turns in their backbone structure. There are two types of γ -turns: a classical γ -turn (γ^{cl}) with dihedral angles approximately $\phi_{i+1} \sim 75^\circ$ and $\psi_{i+1} \sim -65^\circ$ and an inverse γ -turn (γ^{inv}) with dihedral angles $\phi_{i+1} \sim -75^\circ$ and $\psi_{i+1} \sim 65^\circ$. β -turns are in general more flexible and can assume at least 8 different conformations. Of these, five types of β -turns were identified in the investigated cyclohexapeptides and the values of the dihedral angles corresponding to these types of β -turns are summarized in Table 2.

Table 2. Ideal values for 4 types of β -turns identified in the investigated cyclohexapeptides.⁷²

	ϕ_{i+1}	ψ_{i+1}	ϕ_{i+2}	ψ_{i+2}
β_I	-60°	-30°	-90°	0°
$\beta_{I'}$	60°	30°	90°	0°
β_{II}	-60°	120°	80°	0°
$\beta_{II'}$	60°	-120°	-80°	0°
β_{IV}	does not fit any other β -turn criteria			

Based on a backbone similarity analysis, extracted and geometry optimized structures of peptide **1** from the MD simulation in water were divided into 19 clusters. The 9 largest clusters account for up to 90% of the spectra, and their backbone conformations are classified by their turns in Table 3. In water, β_{II} - and $\beta_{II'}$ -turns are the most prevalent in the MD structures. Both types of γ -turns are also present, but only in combination with β -turns. In the CREST ensemble, the two most populated conformers have a combination of β_{IV} - and γ^{inv} -turns in their structure. The remaining three conformers with lower Boltzmann weights have surprisingly symmetrical structures (see Figure S4 in *Supporting Information*) containing three γ^{cl} - and three γ^{inv} -turns.

Table 3. Structural analysis of conformational ensembles predicted by MD and CREST simulations of peptide **1** in water. For MD, individual clusters were obtained by backbone comparison in Maestro. Only the largest clusters that in sum contribute to 90% of the final spectra are included in the table. For CREST, all conformers that contribute more than 1% to the final spectra are included.

Molecular Dynamics				CREST		
	Turn(s)	Weight	# of conf		Turn(s)	Weight
Cluster 1	$\beta_{II'}$ and β_I	23.5 %	47	Conformer 1	β_{IV} and γ^{inv}	82.0 %
Cluster 2	β_{II}	23.0 %	46	Conformer 2	β_{IV} and γ^{inv}	7.5 %
Cluster 3	β_{II} and $\beta_{II'}$	10.5 %	21	Conformer 3	3 γ^{cl} , 3 γ^{inv}	5.2 %
Cluster 4	β_{II} and γ^{cl}	10.5 %	21	Conformer 4	3 γ^{cl} , 3 γ^{inv}	1.9 %
Cluster 5	β_{II} , γ^{inv} , γ^{cl}	8.0 %	16	Conformer 5	3 γ^{cl} , 3 γ^{inv}	1.8 %
Cluster 6	$\beta_{II'}$	7.0 %	14			
Cluster 7	$\beta_{II'}$ and γ^{inv}	5.5 %	11			
Cluster 8	β_I and $\beta_{II'}$	3.0 %	6			
Cluster 9	$\beta_{II'}$ and γ^{cl}	3.0 %	6			

To better understand the origin of the differences in backbone structure, we compare the structure of a representative MD conformer from the largest cluster and a CREST conformer with the largest Boltzmann weight (Figure 6, **(a)** and **(c)** for MD, and **(b)** and **(d)** for CREST). A representative MD conformer has fully extended Lys side chains, allowing for hydrogen bonding with water molecules. Although the general backbone conformation differs between the MD clusters, most of the conformers (~90 %) have fully extended Lys side chains interacting with solvent molecules. In contrast to the MD structures, the dominating CREST conformer contains two Lys side chain amino groups hydrogen bonded to the peptide backbone carbonyl oxygens.

One reason for the significant difference in conformations simulated by MD and CREST may originate in the way a solvent is included. Explicit water molecules are present during the MD simulation, while implicit solvation by a continuum model is used for CREST. The use of implicit solvation during the CREST simulation results in a strong preference for conformations with hydrogen bonding between the Lys amino group hydrogens and the backbone carbonyl oxygens. This internal hydrogen bonding has a considerable influence on the backbone conformation, resulting in an altered conformational ensemble that subsequently leads to the false signatures in the CREST based VCD spectra. Another reason for the unrealistic conformational ensemble may be the use of dispersion-corrected energies when choosing relevant conformers during the CREST simulation. As shown in other works, including dispersion corrections often results in a preference for structures with more internal interactions. Therefore, although CREST may find conformers more similar to the ones predicted by MD simulations, only the ones with more internal interactions are determined relevant due to the selection based on dispersion-corrected energies.

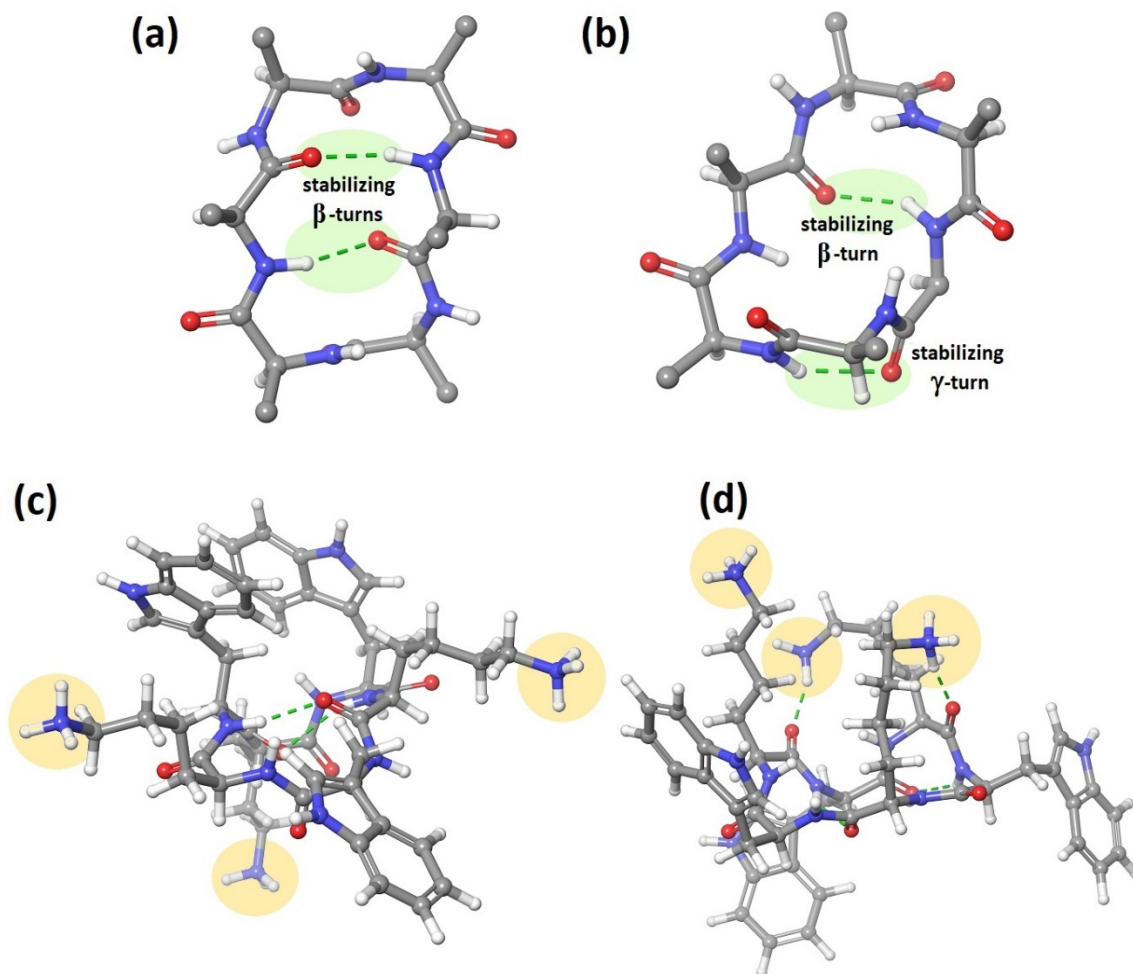


Figure 6. The dominating structures from MD (a and c) and CREST (b and d) conformational ensemble for peptide **1** in water. Hydrogen bonding is depicted by a green line. The top row shows only the backbone and hydrogen bonding within the backbone, while the bottom row shows the whole peptide including the side chains. For MD, a representative structure from the largest cluster is shown, while for CREST the conformer with the largest Boltzmann weight is shown.

Vibrational Spectra of Peptide 1 in DMSO based on MD and CREST Conformers. In our previous work, we successfully applied a protocol for CREST / DFT calculation of vibrational properties to cyclic peptides in various organic solvents. Therefore, in order to see if CREST based calculations of VCD spectra for peptides **1** – **4** work better in organic solvents than in water, we present the experimental and CREST / MD based IR absorption and VCD spectra for peptide **1** in DMSO in Figure 7. Moreover, since VCD signatures are linked to the backbone conformation,

which is strongly influenced by intra- and inter-molecular interactions, this allows us to investigate the solvent influence on peptide structure.

The experimental IR spectrum in the amide I region is dominated by a strong and relatively sharp absorption maximum at 1690 cm^{-1} accompanied by a prominent shoulder at 1653 cm^{-1} . The amide II region is broad with a maximum at 1530 cm^{-1} . In VCD, a strong (+/-) couplet in the amide I region centered at 1663 cm^{-1} can be observed. This couplet is asymmetric with a stronger positive wing at 1678 cm^{-1} and a less intense sharper negative wing at 1651 cm^{-1} . In the amide II region, a broad negative peak is located at 1506 cm^{-1} . The g -factor is 6×10^{-5} .

Since peptide **1** was not deuterated in DMSO, a direct spectral comparison with D_2O is not possible. However, some conclusions can still be made. Firstly, a carbonyl stretching band in DMSO is shifted to higher frequencies than in D_2O (maxima at 1672 cm^{-1} in D_2O vs. 1690 cm^{-1} in DMSO). This is due to strong non-covalent interactions between the carbonyl oxygen and water molecules, that decrease the strength of the $\text{C}=\text{O}$ bond and subsequently cause the shift of its stretching vibration to lower frequencies. Such interactions are not present for DMSO. Another consequence of this is a slightly broader bandwidth for D_2O .

Moreover, even though we cannot directly use spectral shapes for structural comparison, a difference in backbone structure in two solvents can be expected. DMSO is a strong hydrogen bond acceptor interacting strongly with amide and amine hydrogens of the peptide backbone and polar side chains and unlike water, it lacks hydrogens which can participate as donors in hydrogen bonding with carbonyls on the peptide backbone. Therefore, these varied peptide-solvent interactions in different solvents can lead to significant alterations of the peptide backbone conformation, leading to differences in the spectra.

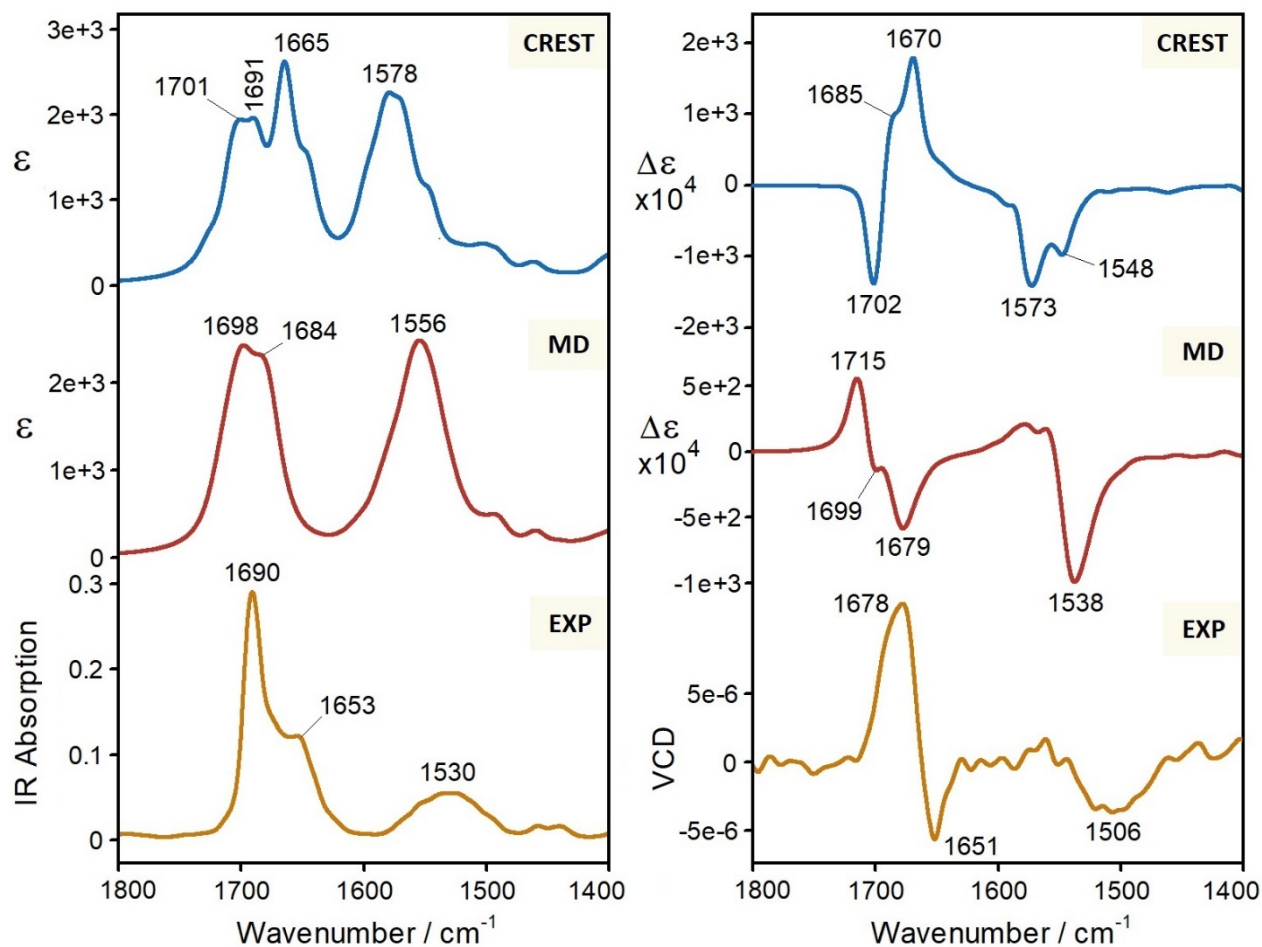


Figure 7. Comparison of experimental (orange, concentration 25 mg/mL) and calculated IR absorption (left panel) and VCD (right panel) spectra of peptide **1** in DMSO. The conformational search for cyclohexapeptide preceding the DFT calculation was performed by two methods: CREST (blue), and molecular dynamics sampling (red).

The calculated IR spectrum based on MD conformers bears some resemblance to the experiment. In the calculated spectrum, the amide I region consists of a superposition of two bands with maxima at 1698 and 1684 cm^{-1} . The separation of these two bands is smaller than in experiment (14 cm^{-1} vs. 37 cm^{-1} , respectively), and their relative intensities do not match the experiment well. In the amide II region, the calculation predicts a broad band at 1556 cm^{-1} , which is reproduced in the experiment at 1530 cm^{-1} . In VCD, the main sign of the couplet in amide I region is reproduced correctly, even though its shape is not entirely consistent with the experiment. Moreover, it is predicted at higher frequencies than in the experiment (1700 cm^{-1} vs. 1663 cm^{-1} , respectively). In

the amide II region, the calculation predicts a strong negative band located at 1538 cm^{-1} , which is in good agreement with the experiment, even though it is slightly shifted to higher frequencies. As for water, a convergence of the spectra based on the number of averaged MD structures is discussed in Figure S5 (*Supporting Information*).

For peptide **1** in DMSO, the CREST based spectra performed very poorly in predicting the correct shapes and signs of the experimental IR absorption and VCD spectra. In IR, the bandshape clearly consists of several peaks, of which the one located at 1665 cm^{-1} has the highest intensity, which is not in agreement with the experimental spectral shapes. The amide II region is correctly predicted with a broad single band, even though it is significantly shifted to higher frequencies when compared to experiment (1578 cm^{-1} vs. 1530 cm^{-1} , respectively). In the amide I region, the CREST based VCD spectra provided a strong $(-/+)$ couplet centered at 1690 cm^{-1} having opposite signs compared to experiment. In the amide II region, two negative peaks are observed at 1573 and 1548 cm^{-1} . Even though the sign of the bands in the amide II region is predicted correctly, there is a splitting of the amide II band in the CREST based spectrum that is not observed in the experimental spectrum.

Analysis of the Calculated Conformations of Peptide 1 in DMSO. As for water, we analyze the conformational ensemble from the CREST and MD simulations in terms of their backbone conformations. The MD structures were clustered based on their backbone structure and in DMSO this resulted in 27 clusters, where the 15 largest of them account for up to 90% of the spectra (Table 4). Most of the geometries have one or two internal hydrogen bonds in the backbone and adopt conformations with β - or γ -turns. The dominating β -turn is β_{I} followed by β_{II} . Classical and inverted γ -turns are almost equally represented. One structural cluster with low weight (2 %) adopted a backbone conformation with a combination of β_{I} - and π -turns.

The three CREST conformers identified as relevant have more or less identical backbone structures with three hydrogen bonds resulting in three turns: one β_{I} -, one β_{II} - and a classical γ -turn. Interestingly, all relevant conformers from CREST contain a β_{II} -turn, which is observed only in one of the structures analyzed from the MD ensemble. As for water, both CREST and MD in DMSO produce conformational ensembles with quite different backbone structures and this directly translates to differences in their spectra.

Table 4. Structural analysis of conformational ensembles predicted by MD and CREST simulations of peptide **1** in DMSO. For MD, individual clusters were obtained by backbone comparison in Maestro. Only the largest clusters that in sum contribute to 90% of the final spectra are included in the table. For CREST, all conformers that contribute more than 1% to the final spectra are included.

Molecular Dynamics				CREST		
	Turn(s)	Weight	# of conf		Turn(s)	Weight
Cluster 1	β_{II} and γ^{cl}	13.0 %	26	Conformer 1	β_{II} , β_I and γ^{cl}	97.0 %
Cluster 2	β_I	11.0 %	22	Conformer 2	β_{II} , β_I and γ^{cl}	2.0 %
Cluster 3	β_I	11.0 %	22	Conformer 3	β_{II} , β_I and γ^{cl}	1.0 %
Cluster 4	β_I	8.5 %	17			
Cluster 5	γ^{cl} and γ^{cl}	8.0 %	16			
Cluster 6	γ^{cl}	8.0 %	16			
Cluster 7	γ^{cl} and γ^{inv}	6.0 %	12			
Cluster 8	β_I	5.5 %	11			
Cluster 9	β_I and β_{II}	5.0 %	10			
Cluster 10	β_{II}	3.0 %	6			
Cluster 11	γ^{cl} and γ^{inv}	3.0 %	6			
Cluster 12	γ^{cl} and γ^{inv}	3.0 %	6			
Cluster 13	β_I and γ^{cl}	2.0 %	4			
Cluster 14	β_I and π	2.0 %	4			
Cluster 15	γ^{inv}	2.0 %	4			

We showed that hydrogen bonding of the side chains to the backbone significantly affects CREST based conformers in water. Therefore, we compare the side chain conformation of peptide **1** in

DMSO based on MD and CREST conformers in Figure 8. A representative MD conformer from the largest cluster (Figure 8; **(a)** only backbone, **(c)** backbone and amino acid side chains) and a CREST conformer with the largest Boltzmann weight (Figure 8; **(b)** only backbone, **(d)** backbone and amino acid side chains) are shown. As for water, the Lys side chains for most of the MD conformers in DMSO (~99 %) are fully extended and do not interact with the backbone. This is not the case for the CREST conformers, where all three of the Lys side chains are hydrogen bonded to carbonyl oxygens in the backbone. As for water, this hydrogen bonding seriously affects the backbone conformation, resulting in erroneous VCD signatures.

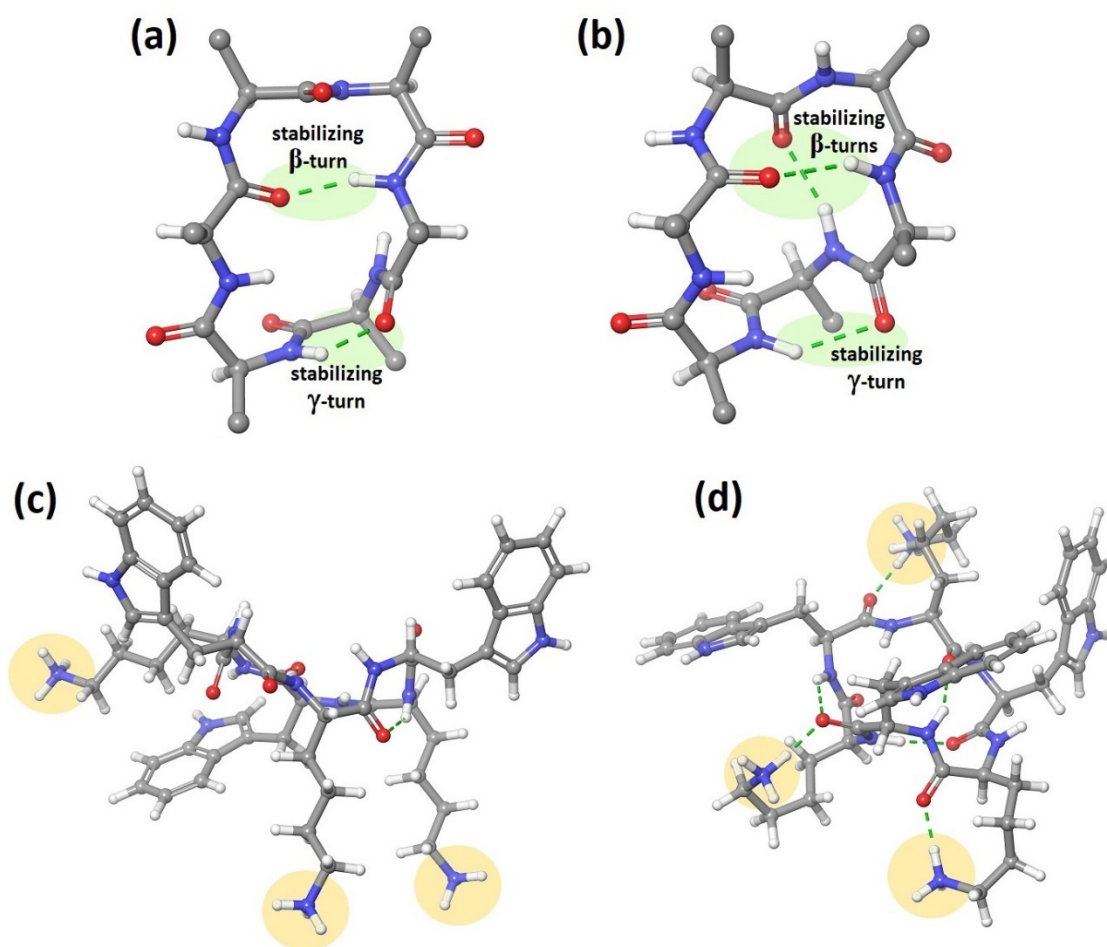


Figure 8. The dominating structures from MD (left) and CREST (right) ensemble of peptide **1** in DMSO. Hydrogen bonding is depicted by a green line. The top row shows only the backbone and hydrogen bonding within the backbone, while the bottom row shows the whole peptide including

the side chains. For MD, a representative structure from the largest cluster is shown, while for CREST the conformer with the largest Boltzmann weight is shown.

Analysis of the Calculated Conformations of Peptide 1 with respect to NMR parameters.

NMR spectroscopy is a well-established method in conformation and configuration analysis. In order to provide more experimental input, both isotropic (^{13}C chemical shifts and $^3J_{\text{HNHA}}$) and anisotropic (RDCs and RCSAs) NMR parameters were acquired for peptides 1-4 (Tables S8 – S16 and Figures S6 – S10 in *Supporting Information*).

For peptide 1, the experimental and simulated chemical shifts have a significantly better fit to the MD-based conformational ensemble than the CREST-based ensemble, in both water and DMSO (Table 5), as can be seen by the significantly lower mean absolute errors (MAEs). This is also consistent with the $^3J_{\text{HNHA}}$ couplings, which shows the MAE of 0.5 Hz for CREST conformers and 0.3 Hz for MD-based conformations, respectively, in water. In DMSO, the corresponding MAEs are 1.6 and 0.6 Hz in favor of the MD-based ensemble (all couplings are presented in Table S9).

Table 5. Mean absolute error for chemical shift comparison of c(WKWKWK). All values are given in ppm.

Solvent	Spectrum	Full Peptide		Backbone Only	
		CREST	MD	CREST	MD
Water	^1H	2.468	0.862	2.539	0.530
	^{13}C	14.875	8.108	15.812	7.758
DMSO	^1H	0.756	0.536	0.605	0.478
	^{13}C	7.026	6.291	7.972	6.293

The anisotropic parameters, RDCs and RCSAs, did not distinguish between the two ensembles (Table S8). This can likely be attributed to the fact that nearly all of the measurable RDCs originated from the side chains, while the backbone conformation was the basis for the clustering.

It is also possible that the single alignment tensor model used to fit the data is not optimal for this class of molecules, which are relatively flat and in two out of four cases also symmetric.

Summary and concluding remarks

In this work, we used VCD and NMR spectroscopy to study the conformation of four cyclohexapeptides with antimicrobial activity in two different solvents: D₂O and DMSO. We found that all the investigated peptides in D₂O show similar VCD signatures in the amide I region, suggesting that their backbone conformation is similar and only influenced to a very minor extent by the nature of the amino acid side chains or their sequence.

To understand the structural information contained in the spectra, we used theoretical modelling. Since cyclohexapeptides are flexible molecules and a proper sampling of conformational space is needed before the calculation of spectral properties, the simulation of the spectra consisted of two steps: (i) a conformational search performed either by meta-dynamics as implemented in CREST, or by a statistical conformational sampling using molecular dynamics simulations; and (ii) subsequent DFT calculation of spectral properties.

The conformational ensemble provided by MD proved to better reproduce VCD spectral signatures for a model cyclohexapeptide both in D₂O and DMSO. The calculation of spectral properties based on the CREST conformational ensemble was not in agreement with experimental data, and in some cases even provided opposite spectral signatures. A structural analysis of the conformational ensembles generated by both methods showed that CREST favors conformations with hydrogen bonding between the amine hydrogens on the Lys side chains and carbonyls of the backbone. Such internal hydrogen bonding was only rarely present amongst the MD structures. Similar trends were observed for NMR spectra; theoretical calculations using the MD conformational ensemble provided better agreement with the experimental results both in chemical shifts and in anisotropic NMR values.

This erroneous internal hydrogen bonding in the CREST conformers can originate from: (i) the inclusion of solvent effects during the meta-dynamics simulation by an implicit solvent model; (ii) dispersion correction of energies favoring the internal molecular interactions; and (iii) the length and polarity of amino acid side chains. The third point is especially important for our investigated

cyclohexapeptides since these contain Lys and Arg side chains which are charged (and therefore strongly interacting) and long / flexible enough to sterically interact with the backbone.

Very recently, Grimme *et al.* added the possibility of including explicit solvent molecules in the CREST simulation.⁷³ To what extent this would improve the predicted structures of these cyclic peptides needs to be explored in future works to improve the agreement between the calculated and experimental VCD and NMR spectra.

Acknowledgement

This work has received support from the Research Council of Norway through a Centre of Excellence Grant (Grant 262695) and a research project grant (Grant 269425). The calculations were performed on resources provided by Sigma2 – the National Infrastructure for High Performance Computing and Data Storage in Norway (Grant NN4654K).

Supporting Information

- Protocol for Synthesis of Cyclohexapeptides **1 – 4**
- Full Assignment of NMR Chemical Shifts for Investigated Cyclohexapeptides in DMSO
- Interpretation of Low-Frequency IR Bands in the Amide I Region of Peptides **3** and **4**
- Values of *g*-factors for VCD spectra of peptides **1 – 4** in D₂O
- Backbone structures for dominating conformers of peptides **1 – 4** calculated by CREST
- Convergence of the MD based IR and VCD spectra of peptide **1** in D₂O
- The low-energy conformer of peptide **1** in D₂O
- Convergence of the MD based IR and VCD spectra of peptide **1** in DMSO
- Isotropic and Anisotropic NMR Parameters for peptides **1 – 4**

References

- (1) Alanis, A. J. Resistance to antibiotics: Are we in the post-antibiotic era? *Arch Med Res* **2005**, *36* (6), 697-705. DOI: 10.1016/j.arcmed.2005.06.009.
- (2) Frieri, M.; Kumar, K.; Boutin, A. Antibiotic resistance. *J. Infect Public Health* **2017**, *10* (4), 369-378. DOI: 10.1016/j.jiph.2016.08.007.
- (3) Gandra, S.; Barter, D. M.; Laxminarayan, R. Economic Burden of Antibiotic Resistance: How Much Do We Really Know? *Clin. Microbiol. Infect.* **2014**, *20* (10), 973-980.
- (4) Chellat, M. F.; Raguz, L.; Riedl, R. Targeting Antibiotic Resistance. *Angew Chem Int Edit* **2016**, *55* (23), 6600-6626. DOI: 10.1002/anie.201506818.
- (5) Selvaraj, A.; Valliammai, A.; Muthuramalingam, P.; Sethupathy, S.; Subramenium, G. A.; Ramesh, M.; Pandian, S. K. Proteomic and Systematic Functional Profiling Unveils Citral Targeting Antibiotic Resistance, Antioxidant Defense, and Biofilm-Associated Two-Component Systems of *Acinetobacter baumannii* To Encumber Biofilm and Virulence Traits. *Msystems* **2020**, *5* (6). DOI: ARTN e00986-20
10.1128/mSystems.00986-20.
- (6) Mor, A. Peptide-based antibiotics: A potential answer to raging antimicrobial resistance. *Drug Develop Res* **2000**, *50* (3-4), 440-447. DOI: Doi 10.1002/1098-2299(200007/08)50:3/4<440::Aid-Ddr27>3.3.Co;2-W.
- (7) Lavery, G.; Gorman, S. P.; Gilmore, B. F. The Potential of Antimicrobial Peptides as Biocides. *Int J Mol Sci* **2011**, *12* (10), 6566-6596. DOI: 10.3390/ijms12106566.
- (8) Di Somma, A.; Moretta, A.; Cane, C.; Cirillo, A.; Duilio, A. Antimicrobial and Antibiofilm Peptides. *Biomolecules* **2020**, *10* (4). DOI: ARTN 652
10.3390/biom10040652.
- (9) Shai, Y. Mode of action of membrane active antimicrobial peptides. *Biopolymers* **2002**, *66* (4), 236-248. DOI: 10.1002/bip.10260.
- (10) Kumar, P.; Kizhakkedathu, J. N.; Straus, S. K. Antimicrobial Peptides: Diversity, Mechanism of Action and Strategies to Improve the Activity and Biocompatibility In Vivo. *Biomolecules* **2018**, *8* (1). DOI: ARTN 4
10.3390/biom8010004.
- (11) Malmsten, M. Interactions of Antimicrobial Peptides with Bacterial Membranes and Membrane Components. *Curr Top Med Chem* **2016**, *16* (1), 16-24. DOI: 10.2174/1568026615666150703121518.
- (12) Marcos, J. F.; Gandia, M. Antimicrobial peptides: to membranes and beyond. *Expert Opin Drug Dis* **2009**, *4* (6), 659-671. DOI: 10.1517/17460440902992888.
- (13) Ciunac, D.; Gong, H. N.; Hu, X. Z.; Lu, J. R. Membrane targeting cationic antimicrobial peptides. *J Colloid Interf Sci* **2019**, *537*, 163-185. DOI: 10.1016/j.jcis.2018.10.103.
- (14) Hwang, P. M.; Vogel, H. J. Structure-function relationships of antimicrobial peptides. *Biochem Cell Biol* **1998**, *76* (2-3), 235-246. DOI: DOI 10.1139/bcb-76-2-3-235.
- (15) Szej, E.; O'Connor, S.; Byrne, A.; Devocelle, M.; Gallagher, W.; O'Connor, K. Enhancement of the anticancer activity of a cationic antimicrobial peptide: an investigation of mechanism and structure-function relationship. *J Pept Sci* **2012**, *18*, S62-S63.
- (16) Fujii, K.; Young, M. T.; Harris, K. D. M. Exploiting powder X-ray diffraction for direct structure determination in structural biology: The P2X4 receptor trafficking motif YEQGL. *J Struct Biol* **2011**, *174* (3), 461-467. DOI: 10.1016/j.jsb.2011.03.001.
- (17) Spencer, R. K.; Nowick, J. S. A Newcomers Guide to Peptide Crystallography. *Isr J Chem* **2015**, *55* (6-7), 698-710. DOI: 10.1002/ijch.201400179.
- (18) Strandberg, E.; Ulrich, A. S. NMR methods for studying membrane-active antimicrobial peptides. *Concept Magn Reson A* **2004**, *23A* (2), 89-120. DOI: 10.1002/cmr.a.20024.

- (19) Wang, G. S. Structural biology of antimicrobial peptides by NMR spectroscopy. *Curr Org Chem* **2006**, *10* (5), 569-581. DOI: Doi 10.2174/138527206776055259.
- (20) Pusey, M. L.; Liu, Z. J.; Tempel, W.; Praissman, J.; Lin, D. W.; Wang, B. C.; Gavira, J. A.; Ng, J. D. Life in the fast lane for protein crystallization and X-ray crystallography. *Prog. Biophys. Mol. Biol.* **2005**, *88* (3), 359-386. DOI: 10.1016/j.pbiomolbio.2004.07.011.
- (21) Shi, Y. G. A Glimpse of Structural Biology through X-Ray Crystallography. *Cell* **2014**, *159* (5), 995-1014. DOI: 10.1016/j.cell.2014.10.051.
- (22) Tormena, C. F. Conformational analysis of small molecules: NMR and quantum mechanics calculations. *Prog Nucl Mag Res Sp* **2016**, *96*, 73-88. DOI: 10.1016/j.pnmrs.2016.04.001.
- (23) Frueh, D. P. Practical aspects of NMR signal assignment in larger and challenging proteins. *Prog Nucl Mag Res Sp* **2014**, *78*, 47-75. DOI: 10.1016/j.pnmrs.2013.12.001.
- (24) Borics, A.; Murphy, R. F.; Lovas, S. Fourier transform vibrational circular dichroism as a decisive tool for conformational studies of peptides containing tyrosyl residues. *Biopolymers* **2003**, *72* (1), 21-24. DOI: 10.1002/bip.10247.
- (25) Keiderling, T. A.; Silva, R. A. G. D.; Yoder, G.; Dukor, R. K. Vibrational circular dichroism spectroscopy of selected oligopeptide conformations. *Bioorgan Med Chem* **1999**, *7* (1), 133-141. DOI: Doi 10.1016/S0968-0896(98)00217-X.
- (26) Miyazawa, M.; Inouye, K.; Hayakawa, T.; Kyogoku, Y.; Sugeta, H. Vibrational circular dichroism of proline-containing oligopeptides. *Appl Spectrosc* **1996**, *50* (5), 644-648. DOI: Doi 10.1366/0003702963905817.
- (27) Petrovic, A. G.; Polavarapu, P. L.; Mahalakshmi, R.; Balaram, P. Characterization of Folded Conformations in a Tetrapeptide Containing Two Tryptophan Residues by Vibrational Circular Dichroism. *Chirality* **2009**, *21* (1e), E76-E85. DOI: 10.1002/chir.20779.
- (28) Wang, F.; Polavarapu, P. L. Conformational analysis of melittin in solution phase: Vibrational circular dichroism study. *Biopolymers* **2003**, *70* (4), 614-619. DOI: 10.1002/bip.10504.
- (29) Zhao, C. X.; Polavarapu, P. L.; Das, C.; Balaram, P. Vibrational circular dichroism of beta-hairpin peptides. *J. Am. Chem. Soc.* **2000**, *122* (34), 8228-8231. DOI: DOI 10.1021/ja000451j.
- (30) Krupova, M.; Kessler, J.; Bour, P. Recent Trends in Chiroptical Spectroscopy: Theory and Applications of Vibrational Circular Dichroism and Raman Optical Activity. *Chempluschem* **2020**, *85* (3), 561-575. DOI: 10.1002/cplu.202000014.
- (31) Polavarapu, P. L.; Zhao, C. X. Vibrational circular dichroism: a new spectroscopic tool for biomolecular structural determination. *Fresen J Anal Chem* **2000**, *366* (6-7), 727-734. DOI: DOI 10.1007/s002160051566.
- (32) Polyanichko, A.; Wieser, H. Fourier transform infrared/vibrational circular dichroism spectroscopy as an informative tool for the investigation of large supramolecular complexes of biological macromolecules. *Biopolymers* **2005**, *78* (6), 329-339. DOI: 10.1002/bip.20299.
- (33) Polyanichko, A. M.; Andrushchenko, V.; Bour, P.; Wieser, H. Vibrational Circular Dichroism Studies of Biological Macromolecules and Their Complexes. In *Circular Dichroism: Theory and Spectroscopy*, Rodgers, D. S. Ed.; Nova Science Publishers, Inc., 2012; pp 67-126.
- (34) Kurouski, D. Advances of Vibrational Circular Dichroism (VCD) in bioanalytical chemistry. A review. *Anal Chim Acta* **2017**, *990*, 54-66. DOI: 10.1016/j.aca.2017.08.014.
- (35) Keiderling, T. A. Protein and peptide secondary structure and conformational determination with vibrational circular dichroism. *Curr Opin Chem Biol* **2002**, *6* (5), 682-688. DOI: Doi 10.1016/S1367-5931(02)00369-1.
- (36) Pancoska, P.; Yasui, S. C.; Keiderling, T. A. Statistical-Analyses of the Vibrational Circular-Dichroism of Selected Proteins and Relationship to Secondary Structures. *Biochemistry-Us* **1991**, *30* (20), 5089-5103. DOI: DOI 10.1021/bi00234a036.

- (37) Kim, J.; Kapitan, J.; Lakhani, A.; Bour, P.; Keiderling, T. A. Tight beta-turns in peptides. DFT-based study of infrared absorption and vibrational circular dichroism for various conformers including solvent effects. *Theor Chem Acc* **2008**, *119* (1-3), 81-97. DOI: 10.1007/s00214-006-0183-4.
- (38) Kessler, J.; Andrushchenko, V.; Kapitan, J.; Bour, P. Insight into vibrational circular dichroism of proteins by density functional modeling. *Phys. Chem. Chem. Phys.* **2018**, *20* (7), 4926-4935. DOI: 10.1039/c7cp08016f.
- (39) Wu, A. N.; Cremer, D.; Auer, A. A.; Gauss, J. Extension of the Karplus relationship for NMR spin-spin coupling constants to nonplanar ring systems: Pseudorotation of cyclopentane. *J Phys Chem A* **2002**, *106* (4), 657-667. DOI: 10.1021/jp013160l.
- (40) Karplus, S.; Karplus, M. Nuclear Magnetic Resonance Determination of the Angle Psi in Peptides. *Proc. Natl. Acad. Sci. USA* **1972**, *69* (11), 3204-3206.
- (41) Dinku, W.; Isaksson, J.; Rylandsholm, F. G.; Bour, P.; Brichtová, E.; Choi, S. U.; Lee, S. H.; Jung, Y. S.; No, Z. S.; Svendsen, J. S. M.; et al. Anti-proliferative activity of a novel tricyclic triterpenoid acid from resin against four human cancer cell lines. *Appl Biol Chem* **2020**, *63* (1). DOI: ARTN 16 10.1186/s13765-020-00499-w.
- (42) Liu, Y. Z.; Cohen, R. D.; Gustafson, K. R.; Martin, G. E.; Williamson, R. T. Enhanced measurement of residual chemical shift anisotropy for small molecule structure elucidation. *Chemical Communications* **2018**, *54* (34), 4254-4257. DOI: 10.1039/c8cc00552d.
- (43) Liu, Y. Z.; Navarro-Vázquez, A.; Gil, R. R.; Griesinger, C.; Martin, G. E.; Williamson, R. T. Application of anisotropic NMR parameters to the confirmation of molecular structure. *Nat Protoc* **2019**, *14* (1), 217-+. DOI: 10.1038/s41596-018-0091-9.
- (44) Pracht, P.; Bohle, F.; Grimme, S. Automated exploration of the low-energy chemical space with fast quantum chemical methods. *Phys. Chem. Chem. Phys.* **2020**, *22* (14), 7169-7192. DOI: 10.1039/c9cp06869d.
- (45) Eikås, K. D. R.; Krupova, M.; Kristoffersen, T.; Beerepoot, M. T. P.; Ruud, K. Can the absolute configuration of cyclic peptides be determined with vibrational circular dichroism? *SUBMITTED* **2022**.
- (46) Merrifield, R. B. Solid Phase Synthesis. I. The Synthesis of a Tetrapeptide. *J. Am. Chem. Soc.* **1963**, *85*, 2149-2154.
- (47) Chan, W.; White, P. *Fmoc Solid Phase Peptide Synthesis: A Practical Approach*; Oxford University Press, 1999.
- (48) Eikås, K. D.; Beerepoot, M. T. P.; Ruud, K. A Computational Protocol for Vibrational Circular Dichroism Spectra of Cyclic Oligopeptides. *J. Phys. Chem. A* **2022**, *126* (32), 5458-5471. DOI: 10.1021/acs.jpca.2c02953.
- (49) McLean, A. D.; Chandler, G. S. Contracted Gaussian-Basis Sets for Molecular Calculations .1. 2nd Row Atoms, Z=11-18. *J. Chem. Phys.* **1980**, *72* (10), 5639-5648. DOI: Doi 10.1063/1.438980.
- (50) Barone, V.; Cossi, M. Quantum calculation of molecular energies and energy gradients in solution by a conductor solvent model. *J. Phys. Chem. A* **1998**, *102* (11), 1995-2001. DOI: DOI 10.1021/jp9716997.
- (51) Cossi, M.; Rega, N.; Scalmani, G.; Barone, V. Energies, structures, and electronic properties of molecules in solution with the C-PCM solvation model. *J. Comput. Chem.* **2003**, *24* (6), 669-681. DOI: DOI 10.1002/jcc.10189.
- (52) *Gaussian 16, Revision B.01*; Gaussian, Inc.: Wallingfor CT, 2016. (accessed).
- (53) *CDSpecTech: Computer Programs for Calculating Similarity Measures of Comparison Between Experimental and Calculated Dissymmetry Factors and Circular Intensity Differentials*; 2015. (accessed).
- (54) *Schrödinger Release 2022-3: Maestro*; Schrödinger, LLC: New York, NY, 2021. (accessed).
- (55) McHugh, S. M.; Rogers, J. R.; Yu, H. T.; Lin, Y. S. Insights into How Cyclic Peptides Switch Conformations. *J. Chem. Theory Comput.* **2016**, *12* (5), 2480-2488. DOI: 10.1021/acs.jctc.6b00193.

- (56) Abraham, M. J.; Murtola, T.; Schulz, R.; Pall, S.; Smith, J. C.; Hess, B.; Lindahl, E. GROMACS: High Performance Molecular Simulations Through Multi-level Parallelism from Laptops to Supercomputers. *SoftwareX* **2015**, *1*, 19-25.
- (57) Hess, B.; Kutzner, C.; van der Spoel, D.; Lindahl, E. GROMACS 4: Algorithms for highly efficient, load-balanced, and scalable molecular simulation. *J. Chem. Theory Comput.* **2008**, *4* (3), 435-447. DOI: 10.1021/ct700301q.
- (58) Pall, S.; Abraham, M. J.; Kutzner, C.; Hess, B.; Lindahl, E. Tackling Exascale Software Challenges in Molecular Dynamics Simulations with GROMACS. *Lect Notes Comput Sc* **2015**, *8759*, 3-27. DOI: 10.1007/978-3-319-15976-8_1.
- (59) Pronk, S.; Pall, S.; Schulz, R.; Larsson, P.; Bjelkmar, P.; Apostolov, R.; Shirts, M. R.; Smith, J. C.; Kasson, P. M.; van der Spoel, D.; et al. GROMACS 4.5: a high-throughput and highly parallel open source molecular simulation toolkit. *Bioinformatics* **2013**, *29* (7), 845-854. DOI: 10.1093/bioinformatics/btt055.
- (60) Jiang, F.; Zhou, C. Y.; Wu, Y. D. Residue-Specific Force Field Based on the Protein Coil Library. RSFF1: Modification of OPLS-AA/L. *J. Phys. Chem. B* **2014**, *118* (25), 6983-6998. DOI: 10.1021/jp5017449.
- (61) Kaminski, G. A.; Friesner, R. A.; Tirado-Rives, J.; Jorgensen, W. L. Evaluation and reparametrization of the OPLS-AA force field for proteins via comparison with accurate quantum chemical calculations on peptides. *J. Phys. Chem. B* **2001**, *105* (28), 6474-6487. DOI: 10.1021/jp003919d.
- (62) Jiang, F.; Geng, H. Computational Methods for Studying Conformational Behaviors of Cyclic Peptides. In *Cyclic peptide Design. Methods in Molecular Biology*, Goetz, G. Ed.; Humana, 2001.
- (63) Hockney, R. W.; Goel, S. P.; Eastwood, J. W. Quiet High-Resolution Computer Models of a Plasma. *J. Comput. Phys.* **1974**, *14* (2), 148-158. DOI: Doi 10.1016/0021-9991(74)90010-2.
- (64) Bussi, G.; Donadio, D.; Parrinello, M. Canonical sampling through velocity rescaling. *J. Chem. Phys.* **2007**, *126* (1). DOI: Artn 014101
10.1063/1.2408420.
- (65) Hess, B.; Bekker, H.; Berendsen, H. J. C.; Fraaije, J. G. E. M. LINCS: A linear constraint solver for molecular simulations. *J. Comput. Chem.* **1997**, *18* (12), 1463-1472. DOI: Doi 10.1002/(Sici)1096-987x(199709)18:12<1463::Aid-Jcc4>3.0.Co;2-H.
- (66) Essmann, U.; Perera, L.; Berkowitz, M. L.; Darden, T.; Lee, H.; Pedersen, L. G. A Smooth Particle Mesh Ewald Method. *J. Chem. Phys.* **1995**, *103* (19), 8577-8593. DOI: Doi 10.1063/1.470117.
- (67) Kelley, L. A.; Gardner, S. P.; Sutcliffe, M. J. An automated approach for clustering an ensemble of NMR-derived protein structures into conformationally related subfamilies. *Protein Eng.* **1996**, *9* (11), 1063-1065. DOI: DOI 10.1093/protein/9.11.1063.
- (68) Jakubec, M.; Rylandsholm, F. G.; Rainsford, P.; Silk, M.; Bril'kov, M.; Kristoffersen, T.; Juskewitz, E.; Ericson, J. U.; Svendsen, J. S. M. Goldilocks Dilemma: LPS Works Both as the Initial Target and a Barrier for the Antimicrobial Action of Cationic AMPs on *E. coli*. *Biomolecules* **2023**, *13* (7). DOI: 10.3390/biom13071155.
- (69) Tycko, R.; Blanco, F. J.; Ishii, Y. Alignment of Biopolymers in Strained Gels: A New Way To Create Detectable Dipole–Dipole Couplings in High-Resolution Biomolecular NMR. *Journal of the American Chemical Society* **2000**, *122* (38), 9340-9341. DOI: 10.1021/ja002133q.
- (70) NewEra. *Some Reflections on Gel NMR Sample Preparation*. <https://newera-spectro.com/some-reflection-on-gel-nmr-sample-preparation> (accessed 2023 03.08).
- (71) Adamo, C.; Barone, V. Exchange functionals with improved long-range behavior and adiabatic connection methods without adjustable parameters: The

PW and

PW1PW models. *J. Chem. Phys.* **1998**, *108* (2), 664-675. DOI: Doi 10.1063/1.475428.

(72) Rose, G. D.; Gierasch, L. M.; Smith, J. A. Turns in Peptides and Proteins. *Adv. Protein Chem.* **1985**, *37*, 1-109. DOI: Doi 10.1016/S0065-3233(08)60063-7.

(73) Spicher, S.; Plett, C.; Pracht, P.; Hansen, A.; Grimme, S. Automated Molecular Cluster Growing for Explicit Solvation by Efficient Force Field and Tight Binding Methods. *J. Chem. Theory Comput.* **2022**, *18* (5), 3174-3189. DOI: 10.1021/acs.jctc.2c00239.

Conformational Studies of Cyclic Hexapeptides with Vibrational Circular Dichroism and Nuclear Magnetic Resonance

Karolina Di Remigio Eikås, Fredrik Garnås Rylandsholm, Tone Kristoffersen, Martin Jakubec, Mitchell Ramesh Silk, John Sigurd Mjøen Svendsen, Johan Mattias Isaksson, Kenneth Ruud and
Monika Krupová

CONTENTS:

Protocol for Synthesis of Investigated Cyclohexapeptides

Full Assignment of NMR Chemical Shifts for Investigated Cyclohexapeptides in DMSO (Tables S1 – S4):

Table S1. Full assignment of c(WWWKKK) in DMSO.

Table S2. Full assignment of c(WKWKWK) in DMSO.

Table S3. Full assignment of c(WWWRRR) in DMSO.

Table S4. Full assignment of c (WRWRWR) in DMSO.

Table S5. Comparison of $^3J_{\text{HNHA}}$ coupling constants for peptide **1** in water extracted by averaging of 21 or 200 structures from MD-based conformational ensemble and the experimental values.

Interpretation of Low-Frequency IR Bands in the Amide I Region of Peptides 3 and 4 (Figure S1 and Table S6):

Figure S1. Illustration of C-N stretching vibrational modes in the Arg side chain resulting in the IR bands at 1610 cm^{-1} for peptide **4**.

Table S6. Calculated frequencies for the C-N stretches on the three Arg side chains of peptide **3** and **4** and their corresponding bands in experimental IR spectra.

Table S7. *g*-factors for experimental IR and VCD spectra of peptides **1** – **4** measured in D₂O.

Figure S2. Backbone structures for dominating conformers of peptides **1** – **4** calculated by CREST.

Figure S3. Convergence of the IR and VCD spectra based on the number of averaged MD structures for peptide **1** in D₂O

Figure S4. Structure of one of the CREST conformers for peptide **1** in water.

Figure S5. Convergence of the IR and VCD spectra based on the number of averaged MD structures for peptide **1** in DMSO.

Isotropic and Anisotropic NMR Parameters for peptides 1 – 4 (Tables S8 – SX):

Table S8. Summary of all the comparisons between experimental chemical shifts and chemical shifts calculated for the structures extracted from the MD-based conformational ensemble.

Table S9. Summary of all the comparisons between experimental chemical shifts and chemical shifts calculated for the structures extracted from the CREST-based conformational ensemble.

Table S10. Mean average error comparison of experimental and calculated chemical shifts for all investigated cyclohexapeptides.

Figure S6. Comparison of experimental chemical shifts (ppm) and calculated chemical shifts for MD-based conformational ensemble in water.

Figure S7. Comparison of experimental chemical shifts (ppm) and calculated chemical shifts for MD-based conformational ensemble in DMSO.

Figure S8. Comparison of experimental chemical shifts (ppm) and calculated chemical shifts for CREST-based conformational ensemble in water.

Figure S9. Comparison of experimental chemical shifts (ppm) and calculated chemical shifts for CREST-based conformational ensemble in DMSO.

Table S11. Mean absolute error for the comparison of experimental and calculated chemical shifts of c(WKWKWK).

Table S12. Q-factors obtained by comparing the experimental and calculated RDCs and RCSAs of the investigated cyclohexapeptides in water.

Figure S10. Overview of the theoretical ${}^3J_{HNHA}$ coupling constants from all 200 structures in the MD conformational ensemble separated to individual amino acids.

Table S13. Mean absolute errors from comparing the calculated and experimental ${}^3J_{HNHA}$ coupling constants for the investigated cyclic hexapeptides in water and DMSO.

Table S14. ${}^3J_{HNHA}$ coupling constants for investigated cyclic hexapeptides in water and DMSO.

Table S15. Theoretical ${}^3J_{HNHA}$ coupling constants for investigated cyclic hexapeptides in water, extracted by Pardi (1990) built-in module in MSpin.

Table S16. Theoretical ${}^3J_{HNHA}$ coupling constants for investigated cyclic hexapeptides in DMSO, extracted by Pardi (1990) built-in module in MSpin.

Protocol for Synthesis of Investigated Cyclohexapeptides

Peptide synthesis:

Resin loading: 2-chlorotrityl chloride resin (0.15 mmol, 1.0 meq, 150 mg) was swelled in DCM (5 mL) for 30 min. The resin was drained and treated with a solution of Fmoc-AA-OH (0.3 mmol, 2 eq.) and diisopropylethylamine (1.8 mmol, 12 eq.) in DCM (5 mL). The resin mixture was left overnight under gentle agitation at room temperature. The resin mixture was drained, treated with MeOH (3 x 5 mL) to cap unreacted sites and dried with diethyl ether (3 x 5 mL).

Linear peptide synthesis: The linear peptides were prepared using an automated solid-phase peptide synthesizer (Biotage Initiator+ Alstra). The pre-loaded 2-chlorotrityl chloride resin was first swelled in DMF (20 min, 70°C). Fmoc deprotections involved treatment of the resin with 20% piperidine/DMF (4.5 mL, 3 min) once at room temp. followed by a second treatment at 70°C by microwave reactor. Amino acid couplings were performed by treating the resin with 4 eq. of Fmoc-AA-OH (0.5 M in DMF), 4 eq. of HOBt (0.5 M in DMF), 4 eq. of HBTU (0.6 M in DMF) and 8 eq. of DIEA (2M in NMP) for 5 min at 75°C by microwave reactor for Fmoc-Trp(Boc)-OH and Fmoc-Lys(Boc)-OH, or 60 min at room temp. for Fmoc-Arg(Pbf)-OH. After each Fmoc deprotection and AA coupling, the resin was washed with DMF (4 x 4.5 mL x 45 sec).

Resin cleavage: The resin-bound side-chain protected linear peptide was treated with 20% 1,1,1,3,3,3-Hexafluoro-2-propanol in DCM (2 x 5 mL x 15 min), followed by rinsing of the resin with DCM (5 mL). The filtrates were combined and concentrated under reduced pressure to yield the sidechain protected linear peptide.

Head-to-tail cyclisation and deprotection: A solution of the linear peptide (approx. 0.15 mmol) and diisopropylethylamine (0.9 mmol, 157 mL) in DMF (10 mL) was added to a solution of PyBOP (0.45 mmol, 234 mg) in DMF (100 mL) under light stir at room temp. for 1-2 hr. The mixture was concentrated by reduced pressure and treated with 95:2.5:2.5 TFA/triisopropylsilane/water (4 mL) then left to stand for 3 hr. The mixture was concentrated under N₂ gas flow followed by precipitation with ice-cold diethyl ether (15 mL). The precipitate was collected by filtration, washed with diethyl ether (15 mL), dissolved in 50% acetonitrile/water, and lyophilized to yield the crude, cyclic, sidechain deprotected peptide.

Purification: Peptides were purified by preparative reverse-phase HPLC (Waters 600 instrument with Waters 2487 Dual Absorbance detector) with a SunFire Prep. C18 OBD column (10 mm, 19 x 150 mm) using linear gradients of 0.1% TFA/water (buffer A) and 0.1% TFA/acetonitrile (buffer B) with a flow rate of 10 mL/min.

Analysis: Crude and final cyclic peptide products were analyzed by FT-MS (Thermo Scientific LTQ Orbitrap XL instrument) and by analytical reverse-phase HPLC (Waters 2795 Alliance HT system with Waters 2996 PDA Detector), using an Ascentis C18 column (3 mm, 3 x 100 mm) and solvents of 0.1% TFA/water (buffer A) and 0.1% TFA/acetonitrile (buffer B) with a linear gradient of 0-60% buffer B over 15 min and a flow rate of 0.5 mL/min.

NMR (Nuclear Magnetic Resonance) spectrometry: 1D ^1H NMR spectra of final cyclic peptide products were recorded at 1.6-2.0 mM in DMSO- d_6 using a Bruker Avance III 400 MHz spectrometer with cryoprobe, at 298K. NMR spectra were processed using TopSpin 4.0.9 (Bruker BioSpin GmbH).

Peptides:

1: Cyclo(WKWKWK). Purification gradient: 5-65% buffer B over 60 min, RT = 21 min (26% buffer B). Yield: 40.7 mg (41.8 %) as a white solid. ^1H NMR (400 MHz, DMSO- d_6) δ 10.82 (s, 1H), 8.13 (d, J = 6.0 Hz, 1H), 7.99 (d, J = 5.4 Hz, 1H), 7.64 (s, 3H), 7.57 (d, J = 7.8 Hz, 1H), 7.35 (d, J = 8.1 Hz, 1H), 7.16 (s, 1H), 7.08 (t, J = 7.4 Hz, 1H), 7.00 (t, J = 7.4 Hz, 1H), 4.37 (q, J = 6.7 Hz, 1H), 3.88 (q, J = 6.3 Hz, 1H), 3.27-3.12 (m, 5H), 2.55 (m, 3H), 1.57 (m, 3H), 1.36 (m, 3H), 0.96 (m, 3H). ESI-FTMS $[\text{M} + \text{H}]^+$ calculated: 943.5307, found: 943.5370, $[\text{M} + \text{Na}]^+$ calculated: 965.5126, found: 965.5176, $[\text{M} + 2\text{H}]^{2+}$ calculated: 472.2693, found: 472.2713.

2: Cyclo(WWWKKK). Purification gradient: 10-70% buffer B over 60 min, RT = 22 min (32% buffer B). Yield: 49.5 mg (39.0 %) as a white solid. ^1H NMR (400 MHz, DMSO- d_6) δ 10.83 (d, J = 1.8 Hz, 1H), 10.80 (d, J = 2.0 Hz, 1H), 10.80 (d, J = 1.9 Hz, 1H), 8.20 (d, J = 5.5 Hz, 2H), 8.06 (d, J = 7.0 Hz, 1H), 8.02 (d, J = 6.9 Hz, 1H), 7.99 (d, J = 8.1 Hz, 1H), 7.93 (d, J = 7.1 Hz, 1H), 7.72-7.64 (m, J = 6.5 Hz, 9H), 7.56 (d, J = 7.6 Hz, 1H), 7.56 (d, J = 7.4 Hz, 1H), 7.50 (d, J = 8.0 Hz, 1H), 7.35-7.33 (m, 3H), 7.10-7.01 (m, 6H), 7.0-6.95 (m, 3H), 4.30 (q, J = 6.9 Hz, 2H), 4.22 (q, J = 7.2 Hz, 1H), 4.11 (q, J = 7.0 Hz, 1H), 3.93 (q, J = 6.8 Hz, 1H), 3.86 (q, J = 7.1 Hz, 1H), 3.26 (m, 2H), 3.12-2.99 (m, 6H), 2.75 (q, J = 6.7 Hz, 2H), 2.61-2.56 (m, 2H), 1.78-1.69 (m, 4H), 1.57-1.28 (m,

12H), 1.16-1.08 (m, 3H), 0.97 (m, 1H). ESI-FTMS $[M + H]^+$ calculated: 943.5307, found: 943.5354, $[M + Na]^+$ calculated: 965.5126, found: 965.5159, $[M + 2H]^{2+}$ calculated: 472.2693, found: 472.2702.

3: Cyclo(WRWRWR). Purification gradient: 5-65% buffer B over 60 min, RT = 25 min (30% buffer B). Yield: 26.9 mg (22.6 %) as a white solid. 1H NMR (400 MHz, DMSO-d₆) δ 10.78 (d, J = 1.7 Hz, 1H), 8.13 (d, J = 7.6 Hz, 1H), 8.10 (d, J = 7.1 Hz, 1H), 7.56 (d, J = 7.8 Hz, 1H), 7.45 (t, J = 5.5 Hz, 1H), 7.35 (d, J = 8.0 Hz, 1H), 7.16 (d, J = 2.1 Hz, 1H), 7.08 (t, J = 7.5 Hz, 1H), 7.00 (t, J = 7.5 Hz, 1H), 4.36 (q, J = 7.3 Hz, 1H), 3.94 (q, J = 7.0 Hz, 1H), 3.33-3.14 (m, 3H), 2.97 (q, J = 6.4 Hz, 2H), 1.68 (m, 1H), 1.56 (m, 1H), 1.26 (m, 2H). ESI-FTMS $[M + 2H]^{2+}$ calculated: 514.2785, found: 514.2779, $[M + 3H]^{3+}$ calculated: 343.1882, found: 343.1883.

4: Cyclo(WWWRRR). Purification gradient: 15-75% buffer B over 60 min, RT = 18 min (33% buffer B). Yield: 46.7 mg (30.0 %) as a white solid. 1H NMR (400 MHz, DMSO-d₆) δ 10.80 (d, J = 1.9 Hz, 1H), 10.78 (d, J = 1.6 Hz, 1H), 10.74 (d, J = 1.6 Hz, 1H), 8.31 (d, J = 6.5 Hz, 1H), 8.21 (d, J = 6.5 Hz, 1H), 8.15 (d, J = 6.6 Hz, 1H), 8.07 (d, J = 6.9 Hz, 1H), 8.02 (d, J = 7.6 Hz, 1H), 7.94 (d, J = 6.8 Hz, 1H), 7.61 (t, J = 5.4 Hz, 1H), 7.56 (d, J = 7.9 Hz, 1H), 7.53-7.47 (m, 4H), 7.36-7.33 (m, 4H), 7.09-7.05 (m, 6H), 7.02-7.01 (m, 2H), 6.99-6.94 (m, 6H), 4.31-4.24 (m, 3H), 4.08 (q, J = 7.4 Hz, 1H), 4.01-3.91 (m, 2H), 3.30-3.25 (m, 2H), 3.12-3.10 (m, 9H), 2.99 (q, J = 6.6 Hz, 4H), 1.85 (m, 2H), 1.71 (m, 3H), 1.54 (m, 3H), 1.39 (m, 3H), 1.24 (m, 1H). ESI-FTMS $[M + H]^+$ calculated: 1027.5419, found: 1027.5473, $[M + 2H]^{2+}$ calculated: 514.2785, found: 514.2770, $[M + 3H]^{3+}$ calculated: 343.1882, found: 343.1872.

Full Assignment of NMR Chemical Shifts for Investigated Cyclohexapeptides in DMSO

Table S1. Full assignment of $c(\text{WWWKKK})$ in DMSO.

Residue #	Amino Acid	Chemical Shift (δ)													
		NH α	CO	α	β	ϵ_1	δ_1	γ	δ_2	ϵ_3	ζ_3	η_2	ζ_2	ϵ_2	
1	W – Tryptophan	8.07		4.23	3.11/3.27	10.84	7.10			7.57	6.99	7.09	7.35		
	^1H $^{13}\text{C} / ^{15}\text{N}$	116.17	171.17	55.38	26.78	131.28	123.95	110.71	127.63	118.34	118.79	121.45	111.88	136.55	
2	W – Tryptophan	7.94		4.31	3.03/3.11	10.80	7.06			7.51	6.98	7.08	7.34		
	^1H $^{13}\text{C} / ^{15}\text{N}$	116.96	171.36	55.17	27.41	131.12	124.10	110.92	127.68	118.69	118.79	121.45	111.88	136.63	
3	W – Tryptophan	8.20		4.31	3.11/3.28	10.81	7.06			7.51	6.98	7.08	7.34		
	^1H $^{13}\text{C} / ^{15}\text{N}$	118.75	171.36	55.86	27.00	131.12	123.81	110.60	127.66	118.69	118.79	121.45	111.88	136.59	
4	K - Lysine	8.21		3.94	1.74/1.79	1.15	1.47	2.68	7.66						
	^1H $^{13}\text{C} / ^{15}\text{N}$	116.67		54.38	30.23	22.99	22.98	39.16	133.24						
5	K - Lysine	8.00		4.12	1.72/1.78	1.32/1.38	1.55	2.76	7.67						
	^1H $^{13}\text{C} / ^{15}\text{N}$	115.23	171.82	55.45	30.87	22.75	22.71	39.27	133.24						
6	K - Lysine	8.03		3.87	1.55	0.98/1.12	1.39	2.59	7.67						
	^1H $^{13}\text{C} / ^{15}\text{N}$	116.56	171.55	54.54	30.58	22.62	22.74	39.08	133.24						

Table S2. Full assignment of c(WKWKWK) in DMSO.

c(WKWKWK)														
Residue #	Amino Acid	Chemical Shift (δ)												
		NH α	CO	α	β	ϵ 1	δ 1	γ	δ 2	ϵ 3	ζ 3	η 2	ζ 2	ϵ 2
1	W – Tryptophan	NH α	CO	α	β	ϵ 1	δ 1	γ	δ 2	ϵ 3	ζ 3	η 2	ζ 2	ϵ 2
	¹ H ¹³ C / ¹⁵ N	8.15 117.10		4.37 55.20	3.16/3.25 27.11	10.85 131.24	7.17 123.92			7.58 118.84	7.00 118.84	7.08 121.48	7.35 111.83	
2	K - Lysine	NH α	CO	α	β	γ	δ	ϵ	ζ					
	¹ H ¹³ C / ¹⁵ N	8.03 116.70		3.89 54.41	1.60 30.56	1.00 22.69	1.38 27.12	2.58 39.13						
3	W – Tryptophan	NH α	CO	α	β	ϵ 1	δ 1	γ	δ 2	ϵ 3	ζ 3	η 2	ζ 2	ϵ 2
	¹ H ¹³ C / ¹⁵ N	8.15 117.10		4.37 55.20	3.16/3.25 27.11	10.85 131.24	7.17 123.92			7.58 118.84	7.00 118.84	7.08 121.48	7.35 111.83	
4	K - Lysine	NH α	CO	α	β	γ	δ	ϵ	ζ					
	¹ H ¹³ C / ¹⁵ N	8.03 116.70		3.89 54.41	1.60 30.56	1.00 22.69	1.38 27.12	2.58 39.13						
5	W – Tryptophan	NH α	CO	α	β	ϵ 1	δ 1	γ	δ 2	ϵ 3	ζ 3	η 2	ζ 2	ϵ 2
	¹ H ¹³ C / ¹⁵ N	8.15 117.10		4.37 55.20	3.16/3.25 27.11	10.85 131.24	7.17 123.92			7.58 118.84	7.00 118.84	7.08 121.48	7.35 111.83	
6	K - Lysine	NH α	CO	α	β	γ	δ	ϵ	ζ					
	¹ H ¹³ C / ¹⁵ N	8.03 116.70		3.89 54.41	1.60 30.56	1.00 22.69	1.38 27.12	2.58 39.13						

Table S3. Full assignment of c(WWRRRR) in DMSO.

Residue #	Amino Acid	c(WWRRRR)													
		NH α	CO	α	β	ϵ 1	δ 1	γ	δ 2	ϵ 3	ζ 3	η 2	ζ 2	ϵ 2	
1	W – Tryptophan														
	^1H	8.04		4.27	2.99/3.08	10.76	7.04			7.52	6.97	7.07	7.34		
2	W – Tryptophan														
	$^{13}\text{C} / ^{15}\text{N}$	116.61	171.27	55.27	27.16	130.99	123.81	110.76	127.40	118.65	118.81	121.47	112.14	136.64	
3	W – Tryptophan														
	^1H	7.96		4.30	3.00/3.09	10.79	6.99			7.52	6.97	7.07	7.34		
4	W – Tryptophan														
	$^{13}\text{C} / ^{15}\text{N}$	117.24	171.53	55.19	27.42	131.20	123.90	110.66	127.56	118.65	118.81	121.47	112.14	136.64	
5	R - Arginine														
	^1H	8.32		3.99	1.71/1.86	1.41	3.07	7.61							
6	R - Arginine														
	$^{13}\text{C} / ^{15}\text{N}$	116.86	171.73	55.67	27.01	131.23	123.96	110.69	127.46	118.69	118.81	121.47	111.88	136.56	
7	R - Arginine														
	^1H	8.18		4.08	1.71/1.85	1.53	3.11	7.68							
8	R - Arginine														
	$^{13}\text{C} / ^{15}\text{N}$	116.05	171.66	53.74	28.31	25.54	40.86	84.92							
9	R - Arginine														
	^1H	8.11		3.95	1.58/1.68	1.25/1.36	3.00	7.56							
10	R - Arginine														
	$^{13}\text{C} / ^{15}\text{N}$	116.54	171.26	54.22	28.12	25.37	40.70	84.89							

Table S4. Full assignment of c(WRWRWR) in DMSO.

c(WWRRRR)														
Residue #	Amino Acid	Chemical Shift (δ)												
		NH α	CO	α	β	ϵ 1	δ 1	γ	δ 2	ϵ 3	ζ 3	η 2	ζ 2	ϵ 2
1	W – Tryptophan													
	^1H	8.15		4.36	3.18/3.27	10.78	7.16			7.57	7.00	7.08	7.35	
2	R - Arginine													
	$^{13}\text{C}/^{15}\text{N}$	116.85	171.46	55.26	27.11	131.07	123.91	110.68	127.60	118.75	118.86	121.53	111.89	136.68
3	W – Tryptophan													
	^1H	8.11		3.94	1.57/1.70	1.26/1.29	2.98	7.45						
4	R - Arginine													
	$^{13}\text{C}/^{15}\text{N}$	116.92	171.54	54.04	28.27	25.36	40.79	84.97	157.22					
5	W – Tryptophan													
	^1H	8.15		4.36	3.18/3.27	10.78	7.16			7.57	7.00	7.08	7.35	
6	R - Arginine													
	$^{13}\text{C}/^{15}\text{N}$	116.85	171.46	55.26	27.11	131.07	123.91	110.68	127.60	118.75	118.86	121.53	111.89	136.68

Table S5. Comparison of $^3J_{\text{HNHA}}$ coupling constants for peptide **1** in water extracted by averaging of 21 (left column) or 200 (middle column) structures from MD-based conformational ensemble and the experimental values (right column).

21 structures	200 structures	Experimental
6.44	6.46	7.00
3.82	4.02	6.90
6.71	6.65	6.20
8.79	8.72	5.70
6.61	6.67	7.50
8.74	8.99	6.20

Interpretation of Low-Frequency IR Bands in the Amide I Region of Peptides **3** and **4**

The experimental IR absorption spectra of arginine-containing peptides **3** and **4** have a complex broad band with a maximum at 1610 cm^{-1} in the amide I region that is not present in the spectra of peptides **1** and **2** containing Lys. As shown by a DFT (Density Functional Theory) calculation of the dominating CREST conformer in D_2O , this band originates in the stretching vibrations of the C-N bonds of the guanidino group on the Arg side chains (Figure S1). The frequencies of these modes are summarized in Table S1. Each of the three Arg side chains contributes with two modes: one slightly higher in frequency resulting in the bands at 1646 cm^{-1} and 1633 cm^{-1} for peptide **3** and **4**, respectively, and one slightly lower in frequency resulting in the bands at 1599 cm^{-1} and 1603 cm^{-1} for peptide **3** and **4**, respectively.

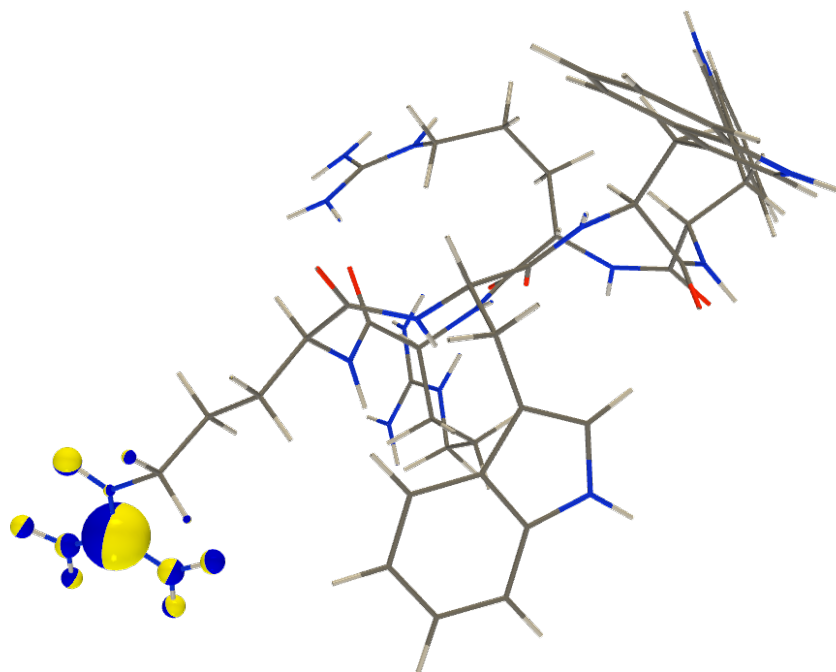


Figure S1. Illustration of C-N stretching vibrational modes in the Arg side chain resulting in the IR bands at 1610 cm^{-1} for peptide **4**. Similar C-H stretches are observed for all Arg side chains in peptide **4** and for peptide **3**.

Table S6. Calculated frequencies for the C-N stretches on the three Arg side chains of peptide **3** and **4** and their corresponding bands in experimental IR spectra.

	Peptide 3		Peptide 4	
	Resulting IR band	Individual mode	Resulting IR band	Individual mode
Arg 1	1646 cm^{-1}	1648 cm^{-1}	1633 cm^{-1}	1637 cm^{-1}
Arg 2		1639 cm^{-1}		1632 cm^{-1}
Arg 3		1631 cm^{-1}		1622 cm^{-1}

Arg 1	1599 cm^{-1}	1598 cm^{-1}	1603 cm^{-1}	1596 cm^{-1}
Arg 2		1591 cm^{-1}		1606 cm^{-1}
Arg 3		1602 cm^{-1}		1601 cm^{-1}

Table S7. *g*-factors for experimental IR and VCD spectra of peptides **1** – **4** measured in D₂O. The values of *g*-factor were calculated as $\Delta A/A$, where ΔA is the amplitude of a VCD couplet and *A* is the absorption intensity of the corresponding IR band.

	Peptide 1	Peptide 2	Peptide 3	Peptide 4
<i>g</i> -factor	5.54×10^{-5}	4.96×10^{-5}	5.52×10^{-5}	5.42×10^{-5}

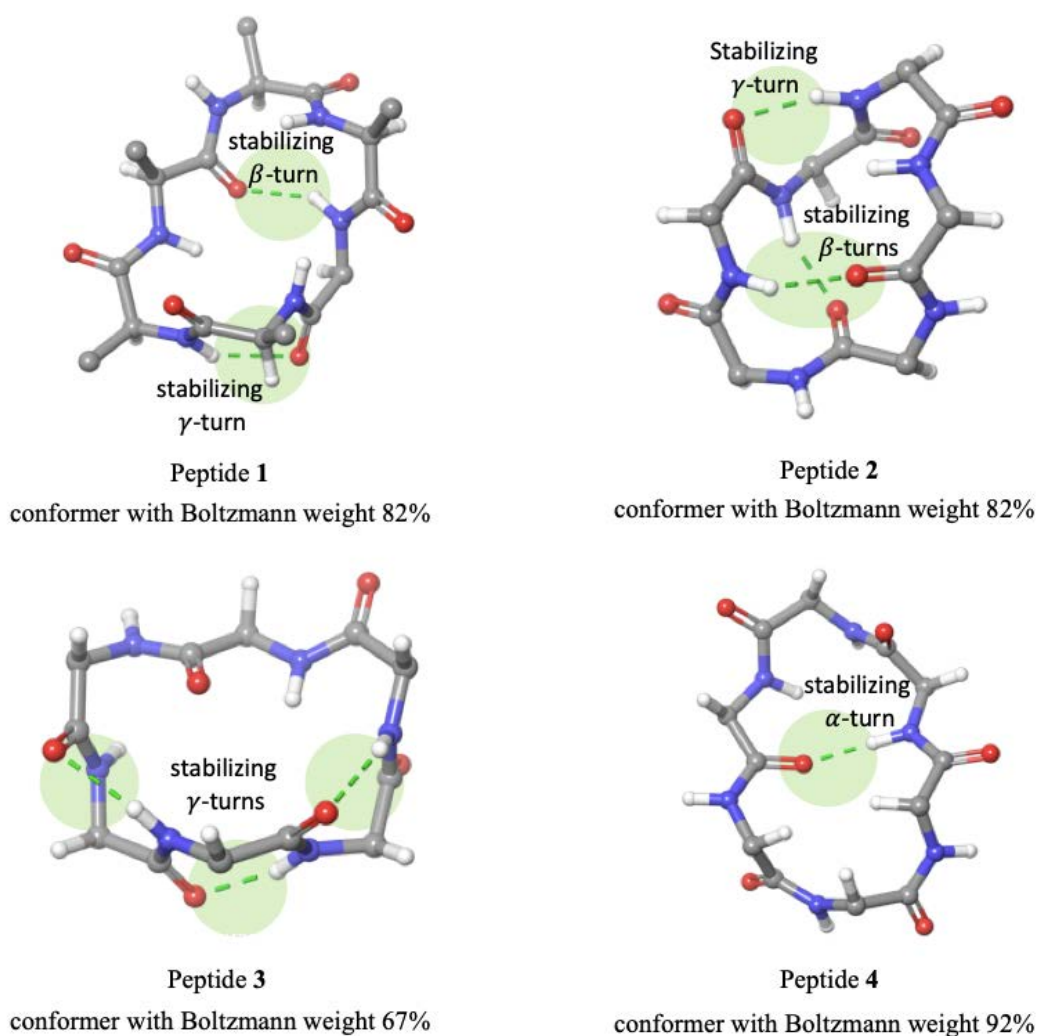


Figure S2. Backbone structures for dominating conformers of peptides **1** – **4** calculated by CREST. The dominating conformer of peptide **1** adopts a β - and a γ -turn, while the dominating conformer

of peptide **2** adopts two β -turns and one γ -turn. For peptide **3**, the dominating conformer adopts three γ -turns while for peptide **4** the dominating conformer adopts an α -turn.

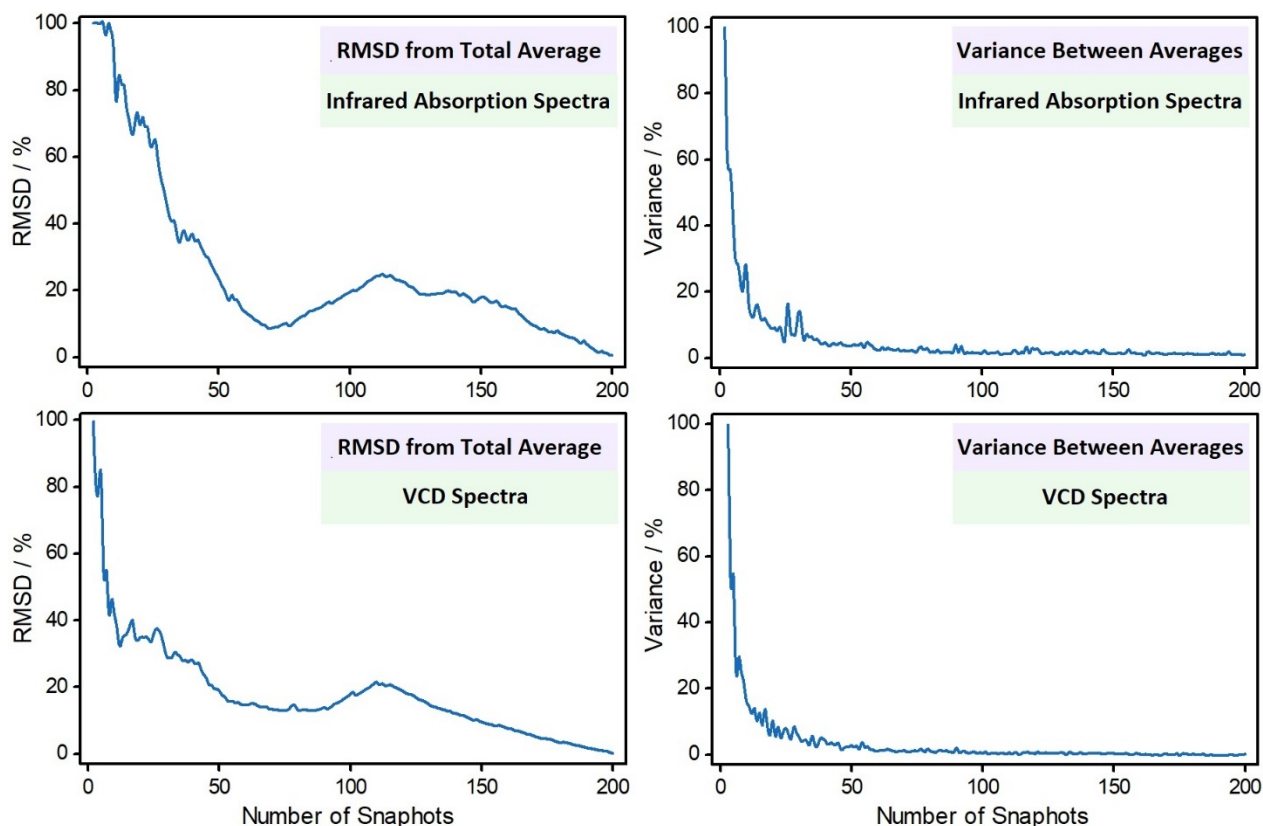


Figure S3. Convergence of the calculated IR absorption and VCD spectra on the number of averaged MD snapshots for peptide **1** in D_2O . Two ways of analysis are used: **left:** root-mean-square deviation (RMSD) of consecutive averages from a total average; **right:** variances C_n calculated as: $C_n = \frac{\int |f_n - f_{n-1}| d\omega}{\int |f_n| d\omega}$, where the cumulative spectra are $f_n = \frac{1}{n} \sum_{i=1}^n S_i(\omega)$; $S_i(\omega)$ is VCD intensity of the i^{th} spectrum at wavenumber ω .

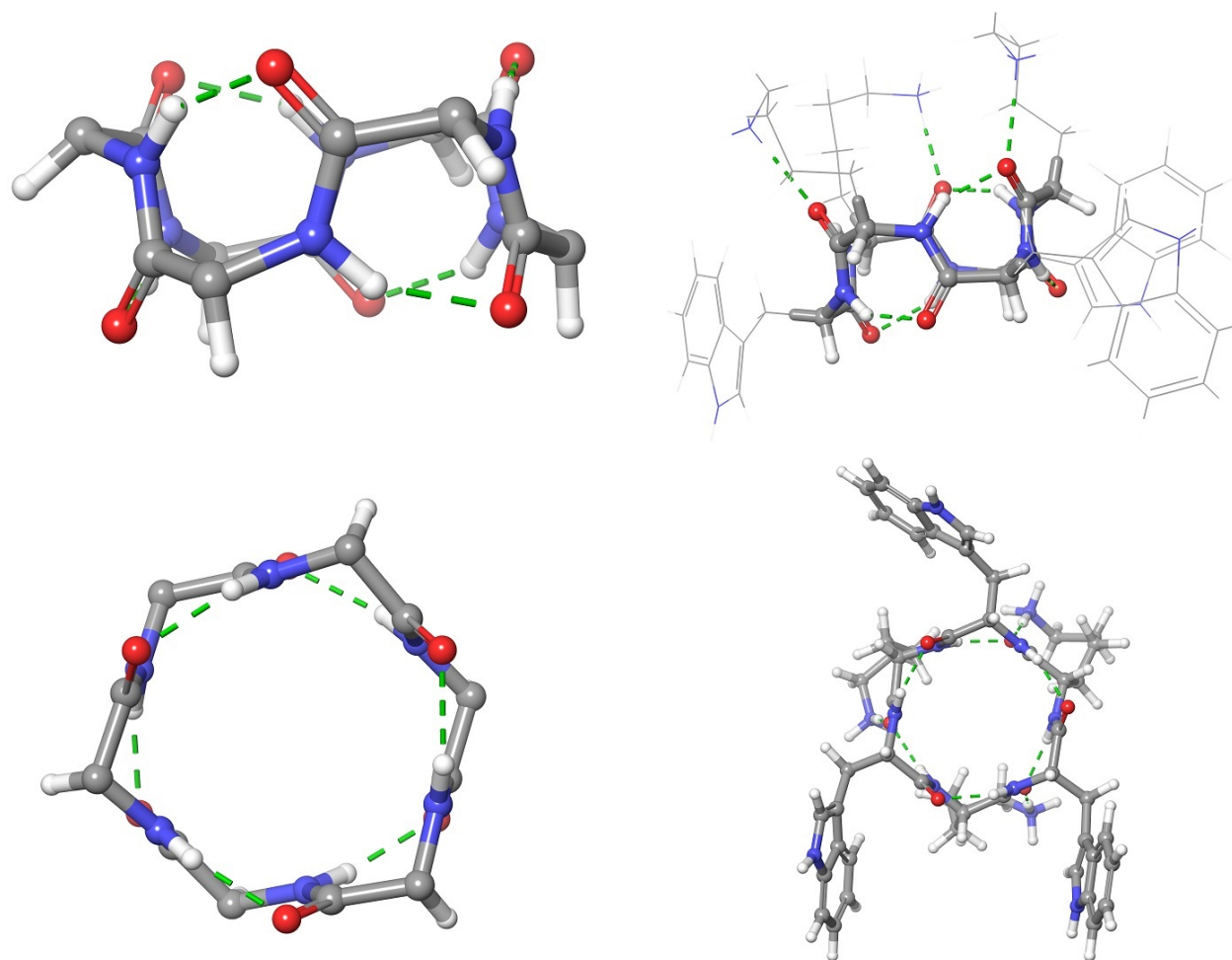


Figure S4. Structure of one of the CREST conformers for peptide **1** in water. It contains 6 turns in its backbone (3 γ^{cl} and 3 γ^{inv}), which makes it surprisingly symmetric. This particular conformer has a lower Boltzmann weight in the final spectra (5.2 %).

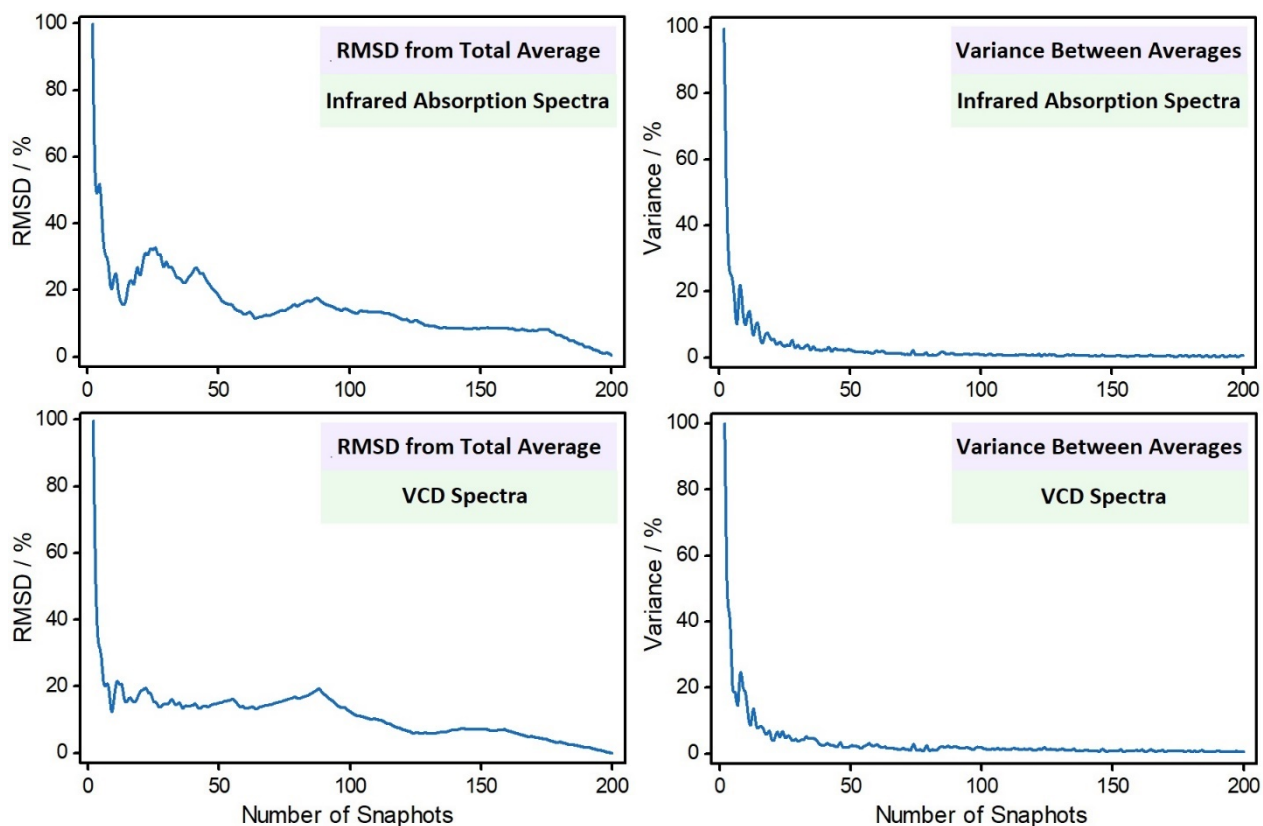


Figure S5. Convergence of the calculated IR absorption and VCD spectra on the number of averaged MD snapshots for peptide **1** in DMSO. Two ways of analysis are used: **left:** root-mean-square deviation (RMSD) of consecutive averages from a total average; **right:** variances C_n calculated as: $C_n = \frac{\int |f_n - f_{n-1}| d\omega}{\int |f_n| d\omega}$, where the cumulative spectra are $f_n = \frac{1}{n} \sum_{i=1}^n S_i(\omega)$; $S_i(\omega)$ is VCD intensity of the i^{th} spectrum at wavenumber ω .

Isotropic and Anisotropic NMR Parameters for peptides 1 – 4

Table S8. Summary of all the comparisons between experimental chemical shifts and chemical shifts calculated for the structures extracted from the MD-based conformational ensemble.

MD-based Structures														
			Full Peptide					Backbone Only						
Peptide	Solvent	Spectrum	r-square	slope	offset	MAE	r-square	slope	offset	MAE	r-square	slope	offset	MAE
c(WWWKKK)	water	¹ H	0.826	0.748	0.989	0.891	0.842	0.723	1.091	0.686	0.842	0.723	1.091	0.686
c(WWWKKK)	water	¹³ C	0.998	1.004	7.876	8.217	0.999	1.005	7.389	7.788	0.999	1.005	7.389	7.788
c(WKWKWK)	water	¹ H	0.834	0.769	0.855	0.862	0.930	0.760	0.921	0.530	0.930	0.760	0.921	0.530
c(WKWKWK)	water	¹³ C	0.999	1.014	6.797	8.108	0.999	1.017	6.283	7.758	0.999	1.017	6.283	7.758
c(WWWRRR)	water	¹ H	0.919	0.811	0.926	0.657	0.921	0.735	1.020	0.562	0.921	0.735	1.020	0.562
c(WWWRRR)	water	¹³ C	0.999	1.012	6.499	7.658	0.999	1.015	6.155	7.457	0.999	1.015	6.155	7.457
c(WRWRWR)	water	¹ H	0.899	0.847	0.770	0.718	0.900	0.755	0.926	0.621	0.900	0.755	0.926	0.621
c(WRWRWR)	water	¹³ C	0.999	1.015	6.580	8.106	0.999	1.015	6.361	7.603	0.999	1.015	6.361	7.603
c(WWWKKK)	DMSO	¹ H	0.813	0.711	1.016	0.898	0.855	0.736	0.917	0.646	0.855	0.736	0.917	0.646
c(WWWKKK)	DMSO	¹³ C	0.997	1.025	3.381	5.825	0.998	1.037	2.036	5.365	0.998	1.037	2.036	5.365
c(WKWKWK)	DMSO	¹ H	0.928	0.844	0.723	0.536	0.939	0.741	0.962	0.478	0.939	0.741	0.962	0.478
c(WKWKWK)	DMSO	¹³ C	0.999	1.022	4.229	6.291	1.000	1.030	3.702	6.293	1.000	1.030	3.702	6.293
c(WWWRRR)	DMSO	¹ H	0.919	0.811	0.926	0.657	0.921	0.735	1.020	0.562	0.921	0.735	1.020	0.562
c(WWWRRR)	DMSO	¹³ C	0.999	1.012	6.499	7.658	0.999	1.015	6.155	7.457	0.999	1.015	6.155	7.457
c(WRWRWR)	DMSO	¹ H	0.895	0.816	0.629	0.587	0.939	0.724	0.865	0.483	0.939	0.724	0.865	0.483
c(WRWRWR)	DMSO	¹³ C	0.999	1.020	3.783	5.801	0.999	1.031	3.380	6.042	0.999	1.031	3.380	6.042

Table S9. Summary of all the comparisons between experimental chemical shifts and chemical shifts calculated for the structures extracted from the CREST-based conformational ensemble.

CREST-based Structures														
				Full Peptide					Backbone Only					
Peptide	Solvent	Spectrum	r-square	slope	offset	MAE	r-square	slope	offset	MAE	r-square	slope	offset	MAE
c(WWWKKK)	water	¹ H	0.834	0.737	1.194	0.830	0.903	0.831	0.813	0.586	0.903	0.831	0.813	0.586
c(WWWKKK)	water	¹³ C	0.989	0.989	9.920	8.939	0.998	1.034	5.438	8.326	0.998	1.034	5.438	8.326
c(WKWKKW)	water	¹ H	0.838	0.738	3.602	2.468	0.958	0.904	2.938	2.539	0.958	0.904	2.938	2.539
c(WKWKKW)	water	¹³ C	0.997	0.964	18.215	14.875	0.996	0.976	17.887	15.812	0.996	0.976	17.887	15.812
c(WWWRRR)	water	¹ H	0.895	0.879	0.611	0.662	0.845	0.775	0.726	0.635	0.845	0.775	0.726	0.635
c(WWWRRR)	water	¹³ C	0.999	1.017	6.246	7.911	0.999	1.013	6.577	7.692	0.999	1.013	6.577	7.692
c(WRWRWR)	water	¹ H	0.908	0.849	0.997	0.729	0.920	0.803	0.872	0.564	0.920	0.803	0.872	0.564
c(WRWRWR)	water	¹³ C	0.998	1.032	4.723	7.911	0.997	1.037	4.879	8.054	0.997	1.037	4.879	8.054
c(WWWKKK)	DMSO	¹ H	0.888	0.774	0.918	0.688	0.926	0.809	0.761	0.419	0.926	0.809	0.761	0.419
c(WWWKKK)	DMSO	¹³ C	0.995	1.017	5.149	6.691	0.998	1.054	2.054	6.403	0.998	1.054	2.054	6.403
c(WKWKKW)	DMSO	¹ H	0.922	0.847	1.023	0.756	0.907	0.779	1.094	0.605	0.907	0.779	1.094	0.605
c(WKWKKW)	DMSO	¹³ C	0.998	1.034	3.852	7.026	0.998	1.039	4.544	7.972	0.998	1.039	4.544	7.972
c(WWWRRR)	DMSO	¹ H	0.858	0.868	0.468	0.673	0.814	0.757	0.660	0.681	0.814	0.757	0.660	0.681
c(WWWRRR)	DMSO	¹³ C	0.999	1.030	4.864	7.736	0.999	1.029	5.327	7.817	0.999	1.029	5.327	7.817
c(WRWRWR)	DMSO	¹ H	0.884	0.839	0.902	0.794	0.845	0.794	0.973	0.745	0.845	0.794	0.973	0.745
c(WRWRWR)	DMSO	¹³ C	0.998	1.029	3.586	6.442	0.999	1.049	2.479	6.641	0.999	1.049	2.479	6.641

Table S10. Mean average error comparison of experimental and calculated chemical shifts for all investigated cyclohexapeptides.

A		Mean Absolute Error of ¹H Spectra in Water		
		Full Peptide		Backbone Only
Peptide	CREST	MD	CREST	MD
c(WWWKKK)	0.830	0.891	0.586	0.686
c(WKWKK)	2.468	0.862	2.539	0.530
c(WWWRRR)	0.662	0.657	0.635	0.562
c(WRWRWR)	0.729	0.718	0.564	0.621

B		Mean Absolute Error of ¹H Spectra in DMSO		
		Full Peptide		Backbone Only
Peptide	CREST	MD	CREST	MD
c(WWWKKK)	0.688	0.898	0.419	0.646
c(WKWKK)	0.756	0.536	0.605	0.478
c(WWWRRR)	0.673	0.657	0.681	0.562
c(WRWRWR)	0.794	0.587	0.745	0.483

C		Mean Absolute Error of ¹³C Spectra in Water		
		Full Peptide		Backbone Only
Peptide	CREST	MD	CREST	MD
c(WWWKKK)	8.939	8.217	8.326	7.788
c(WKWKK)	14.875	8.108	15.812	7.758
c(WWWRRR)	7.911	7.658	7.692	7.457
c(WRWRWR)	7.911	8.106	8.054	7.603

D		Mean Absolute Error of ¹³C Spectra in DMSO		
		Full Peptide		Backbone Only
Peptide	CREST	MD	CREST	MD
c(WWWKKK)	6.691	5.825	6.403	5.365
c(WKWKK)	7.026	6.291	7.972	6.293
c(WWWRRR)	7.736	7.658	7.817	7.457
c(WRWRWR)	6.442	5.801	6.641	6.042

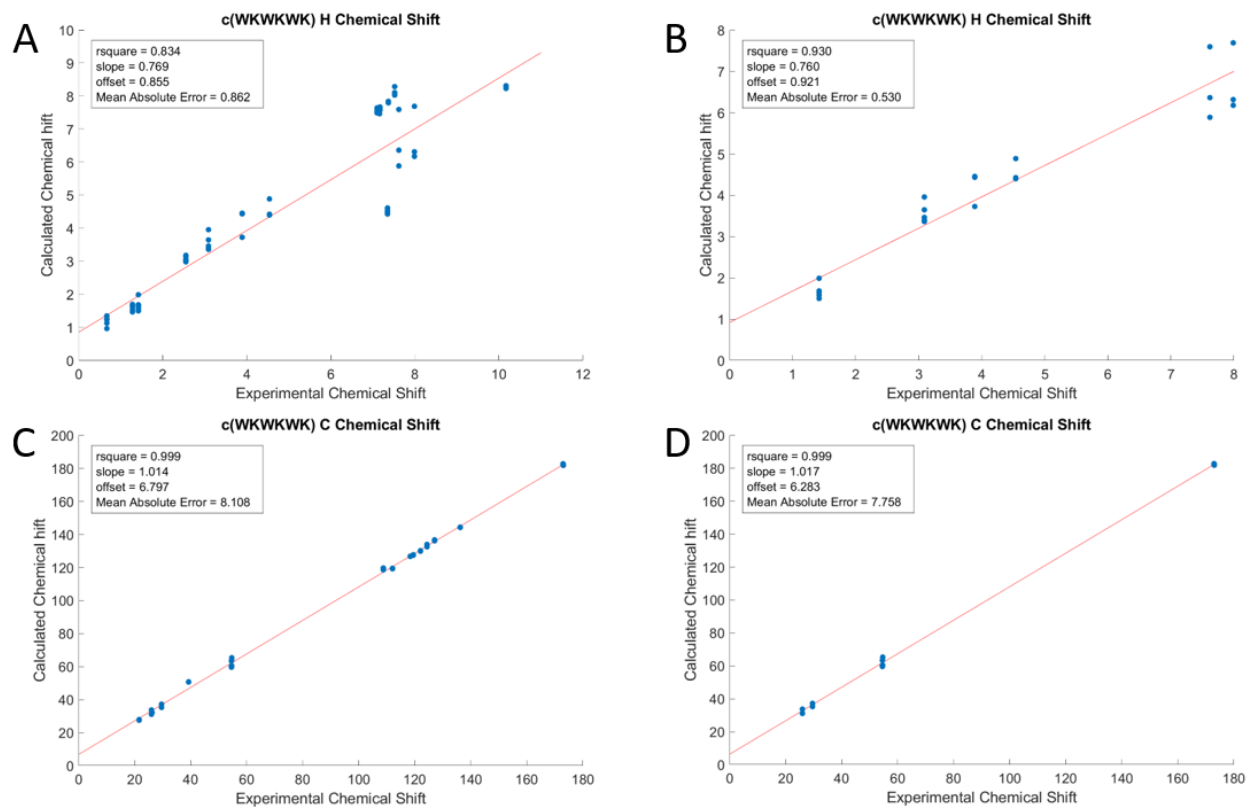


Figure S6. Comparison of experimental chemical shifts (ppm) and calculated chemical shifts for MD-based conformational ensemble in water. We compare either the chemical shifts for full peptide (A and C panel) or only for the backbone (B and D panel). ^1H (A and B panel) and ^{13}C (C and D panel) are shown.

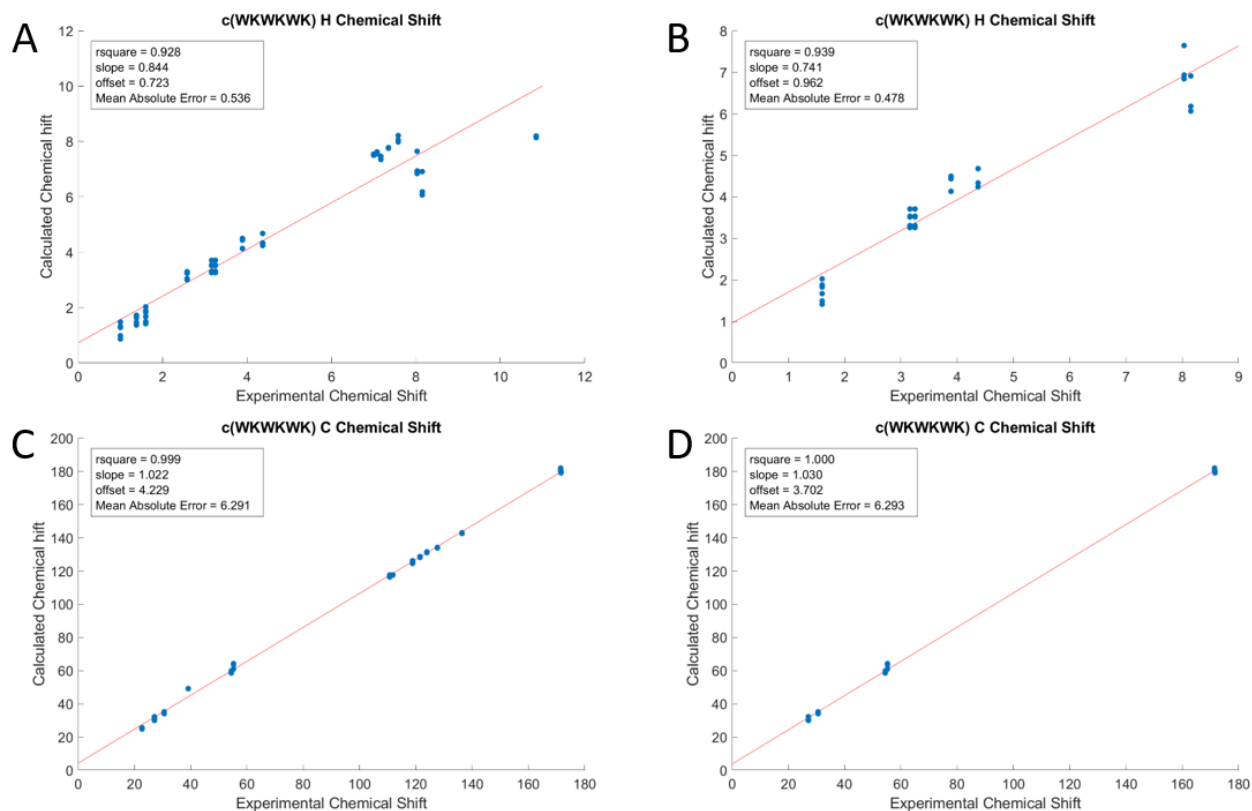


Figure S7. Comparison of experimental chemical shifts (ppm) and calculated chemical shifts for MD-based conformational ensemble in DMSO. We compare either the chemical shifts for full peptide (A and C panel) or only for the backbone (B and D panel). ^1H (A and B panel) and ^{13}C (C and D panel) are shown.

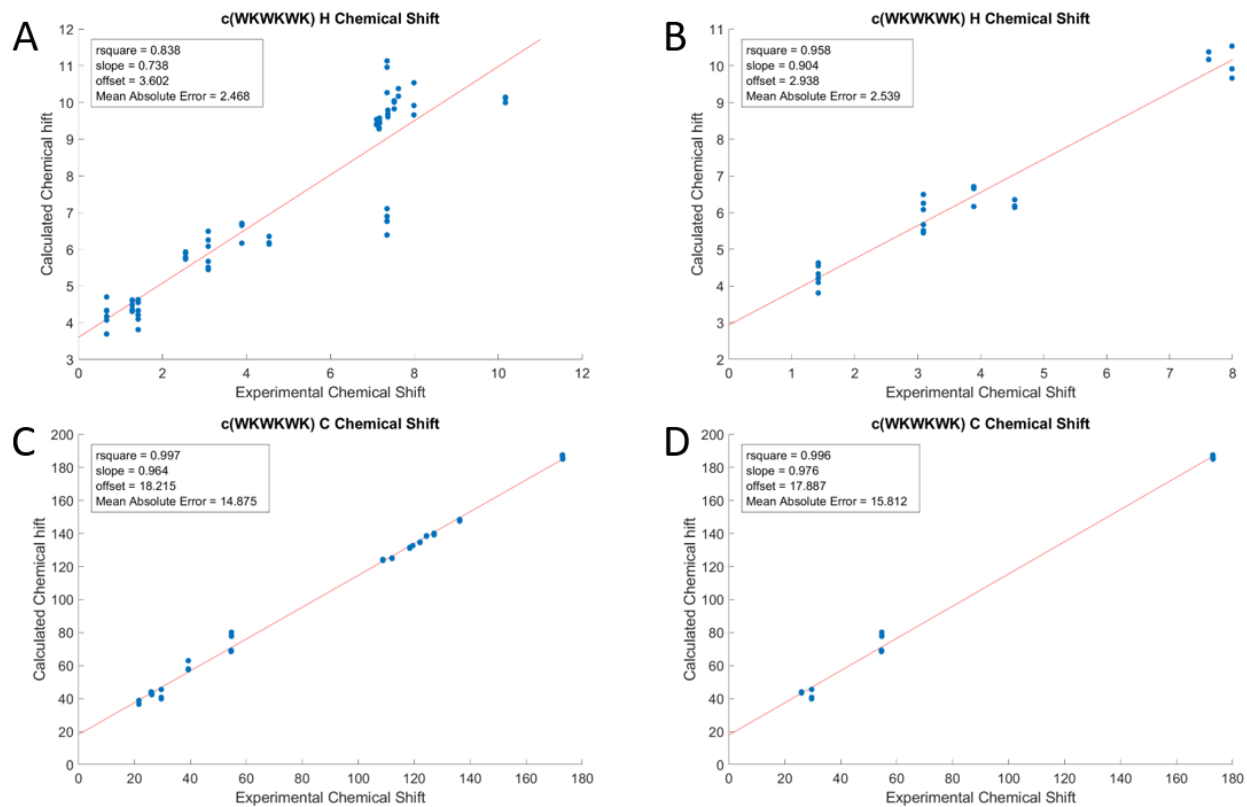


Figure S8. Comparison of experimental chemical shifts (ppm) and calculated chemical shifts for CREST-based conformational ensemble in water. We compare either the chemical shifts for full peptide (A and C panel) or only for the backbone (B and D panel). ^1H (A and B panel) and ^{13}C (C and D panel) are shown.

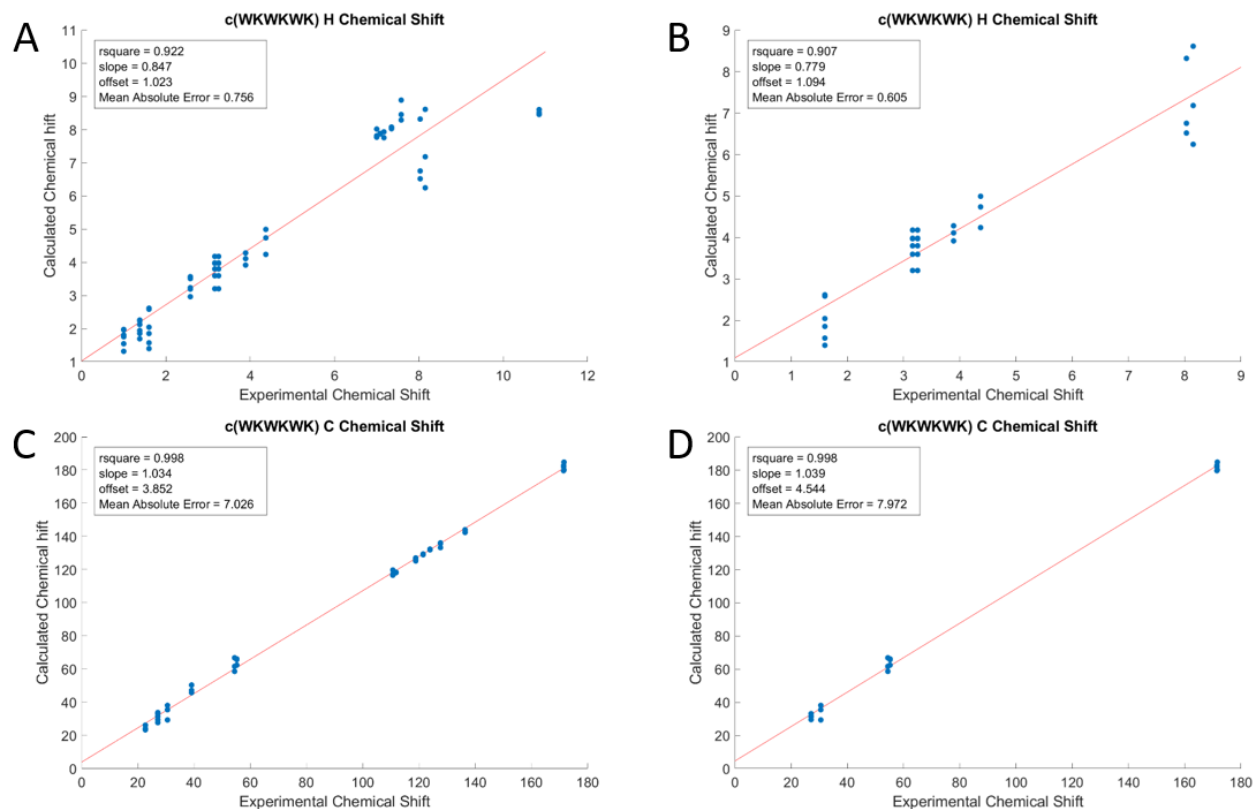


Figure S9. Comparison of experimental chemical shifts (ppm) and calculated chemical shifts for CREST-based conformational ensemble in DMSO. We compare either the chemical shifts for full peptide (A and C panel) or only for the backbone (B and D panel). ^1H (A and B panel) and ^{13}C (C and D panel) are shown.

Table S11. Mean absolute error for the comparison of experimental and calculated chemical shifts of c(WKWKWK).

Mean Absolute Error for Comparison of Experimental and Calculated Chemical Shifts of c(WKWKWK)					
Solvent	Spectrum	Full Peptide		Backbone Only	
		CREST	MD	CREST	MD
water	^1H	2.468	0.862	2.539	0.530
	^{13}C	14.875	8.108	15.812	7.758
DMSO	^1H	0.756	0.536	0.605	0.478
	^{13}C	7.026	6.291	7.972	6.293

Table S12. Q-factors obtained by comparing the experimental and calculated RDCs and RCSAs of the investigated cyclohexapeptides in water.

Q-factors from RDCs and RCSAs in Water		
Peptide	MD	CREST
c(WWWKKK)	0.971	0.965
c(WKWKWK)	0.990	0.996
c(WWWRRR)	0.991	0.992
c(WRWRWR)	0.964	0.985

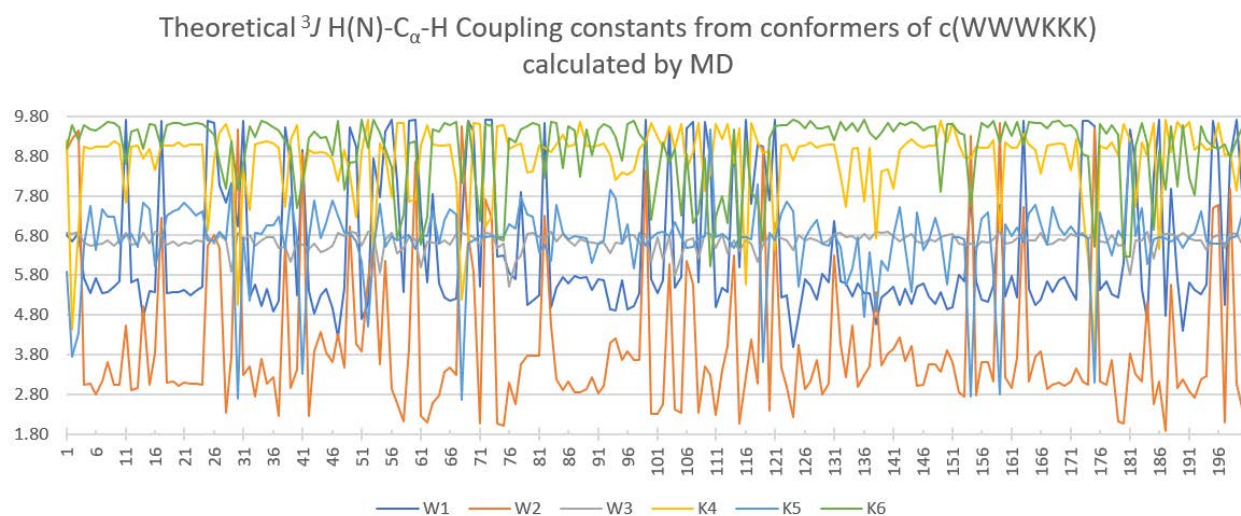


Figure S10. Overview of the theoretical $^3J_{HNHA}$ coupling constants from all 200 structures in the MD conformational ensemble separated to individual amino acids.

Table S13. Mean absolute errors from comparing the calculated and experimental $^3J_{HNHA}$ coupling constants for the investigated cyclic hexapeptides in water and DMSO.

Peptide	Water		DMSO	
	CREST	MD	CREST	MD
c(WWWKKK)	1.33	1.78	0.92	1.55
c(WKWKWK)	1.65	1.27	1.54	0.56
c(WWWRRR)	2.05	1.25	1.60	0.69
c(WRWRWR)	1.44	2.01	1.20	0.73

Table S14. $^3J_{HNHA}$ coupling constants for investigated cyclic hexapeptides in water and DMSO.

Residue #	Water				DMSO			
	Peptide 1	Peptide 2	Peptide 3	Peptide 4	Peptide 1	Peptide 2	Peptide 3	Peptide 4
1	7.0 ¹	7.1	7.9 ¹	6.2	6.5	7.1	8.3	7.6
2	6.9 ¹	6.2 ²	5.4 ²	5.8	7.1	6.9	7.4	6.7
3	6.2 ²	7.1	5.1 ²	6.2	8.2 ¹	7.1	7.1	7.6
4	5.7 ¹	6.2 ²	6.2	5.8	6.8 ¹	6.9	7.2	6.7
5	7.5	7.1	7.6	6.2	7.6	7.1	7.9	7.6
6	6.2	6.2 ²	6.2 ¹	5.8	5.9	6.9	7.3	6.7

1 lineshape fitted from a high resolution and zero filled ^{15}N -HSQC F2 slice

2 lineshape fitted from an unresolved doublet

Table S15. Theoretical $^3J_{HNHA}$ coupling constants for investigated cyclic hexapeptides in water, extracted by Pardi (1990) built-in module in MSpin.

Residue #	c(WWWKKK)		c(WKWKWK)		c(WWWRRR)		c(WRWRWR)	
	CREST	MD	CREST	MD	CREST	MD	CREST	MD
1	7.77	6.44	5.54	8.19	7.80	7.11	6.81	8.42
2	5.72	3.82	9.41	5.33	8.60	6.09	7.03	7.89
3	4.55	6.71	6.38	7.23	8.24	6.78	3.49	9.33
4	8.96	8.79	8.59	8.50	7.80	7.25	8.50	7.30

5	6.57	6.61	6.77	6.33	6.57	5.69	6.81	6.70
6	6.38	8.74	4.53	8.65	9.45	7.59	6.59	8.43

Table S16. Theoretical $^3J_{HNHA}$ coupling constants for investigated cyclic hexapeptides in DMSO, extracted by Pardi (1990) built-in module in MSpin.

Residue #	c(WWWKKK)		c(WKWKWK)		c(WWWRRR)		c(WRWRWR)	
	CREST	MD	CREST	MD	CREST	MD	CREST	MD
1	6.76	6.63	5.56	6.90	2.96	8.14	6.71	7.27
2	6.88	6.10	4.99	6.88	9.23	6.25	5.44	6.48
3	9.50	6.64	8.76	7.21	7.49	6.71	8.40	7.03
4	8.52	7.88	5.91	7.12	6.81	6.86	6.34	8.85
5	6.44	4.81	4.88	5.69	8.59	9.21	6.14	6.50
6	5.06	8.63	7.83	8.28	6.31	6.50	9.14	6.66

Paper VI

Structural analysis of four cyclic antimicrobial hexapeptides in aqueous solution and in micelles, towards membrane-mimicking nanodiscs

Fredrik Garnås Rylandsholm,¹ Philip Rainsford,^{1,3} Monika Krupova,^{1,4} Tone Kristoffersen,¹ Tonje Haugen,^{1,4} Bjørn Olav Brandsdal,^{1,4} John Sigurd Svendsen,¹ Johan Isaksson^{1,2*}

¹ *Department of Chemistry, Faculty of Science and Technology, UiT The Arctic University of Norway, N-9037 Tromsø, Norway*

² *Department of Pharmacy, Faculty of Health Sciences, UiT The Arctic University of Norway, N-9037 Tromsø, Norway*

³ *Department of Biomedical Sciences, Faculty of Health and Medical Sciences, University of Copenhagen, Panum Building 18.5, Blegdamsvej 3B, 2200, Copenhagen, Denmark*

⁴ *Hylleraas Centre for Quantum Molecular Sciences, Department of Chemistry, UiT The Arctic University of Norway, N-9037 Tromsø, Norway*

Abstract

Cationic, antimicrobial peptides (AMPs) are abundantly present in nature as host-defensive peptides, forming the backbone of the natural defence of many organisms. Their primary interaction with bacterial membranes is thought to be a binding to the outer layer, followed by a disruption of the lipid membrane. Investigating the mode-of-action of AMPs is an ever-growing field, where a plethora of different biophysical experiments are used to investigate this. Here, we explore the experimental limitation in NMR spectroscopy as we migrate towards increasingly realistic but larger membrane model systems with the aim to scout which data we could realistically extract from AMPs interacting with self-aligning nanodiscs.

A set of cyclic hexapeptides were used as model compounds, in water, DMSO, and SDS micelles. The quality of isotropic and anisotropic NMR parameters decreased as the result of faster relaxation due to size and dynamics, as well as the need for water suppression and buffer salts. Chemical shifts, scalar couplings, NOE derived distances, and simulated annealing suggested that the backbone conformation of both peptides remained mostly rigid, forming two

β -turns, while the sidechains remain flexible in all environments. The difference between Lys or Arg did not change the backbone conformation, even though the two peptides have different MIC concentrations, indicating that amino acid composition is more important than conformation for antimicrobial activity. Theoretical structures in an explicit lipid bilayer were simulated showing similar structures.

Pilot experiments on SMA-QA nanodiscs indicated that they are viable as membrane model for investigating the interaction between AMPs and lipid membranes. It was shown that signal can be obtained from bound peptide, but further investigations with isotopically labelled peptides are needed to extract relevant structural data under conditions where the nanodisc is not over-saturated by peptides.

Introduction

Antimicrobial peptides are a part of our innate and non-adoptive immune system, and serve as the first line of defence versus a variety of organisms.¹ In this class, cationic antimicrobial peptides are over-represented and have been found to possess a broad spectrum of activity against bacteria, fungi, protozoa, enveloped viruses, malignant cells and parasites.^{2, 3} Antimicrobial peptides make up a group of diverse molecules ranging from approximately 10 to 100 amino acids, having a net positive charge, often along with an amphipathic structure.⁴ Despite their similar overall physical properties little sequence homology is observed.⁵

In the light of the emerging antimicrobial resistance crisis, where our existing arsenal of antibiotics is becoming less and less efficient, the importance of potential new classes of antibiotics cannot be emphasised enough. An interesting feature of this class of peptides is that they physically destabilise cellular membranes with a preference for prokaryotic organisms, through a general mechanism (like for example Daptomycin,⁶ Nisin,⁷⁻¹² and Colistin¹³⁻¹⁵) instead of a well-defined bacterial target like most antibiotics on the market today (for example beta-lactams,¹⁶⁻²⁰ tetracyclines,¹⁸ quinolones, and amphenicols²¹). Cationic, antimicrobial peptides (AMPs) have proven more resilient to bacterial resistance development,³ and although this view has been challenged,²² even if resistance development against AMPs merely comes at a higher fitness cost, they are still an attractive class of compounds for further optimisation into antibiotic leads.

Most of the AMPs reported in the literature are proposed to act directly on the bacterial outer membrane and through the formation of pores, toroidal pores or collapsing carpets, either by reducing the membrane integrity to the point that extensive leakage leads to cell death, or by depolarising the electric gradient necessary to power essential bacterial intracellular processes.^{12, 23-27}

There are several examples in the literature where AMPs change conformation and/or physicochemical properties when they come into contact with amphipathic environments like the bacterial cell surface, sometimes mimicked by micelles or liposomes in structural studies.²⁸⁻

33

Nuclear magnetic resonance (NMR) spectroscopy is an information-rich and versatile tool that is routinely used to extract structural information from molecules. Chemical shifts hold information about the local chemical environment.³⁴ $^3J_{\text{HH}}$ -coupling constants are used to investigate the dihedral angle between two protons, and yields much information about the backbone of peptides.^{35, 36} Secondary chemical shifts are a good probe for the overall structure of a peptide, being used to describe the secondary structure by comparison between experimentally obtained chemical shifts and random coil reference shifts.³⁷⁻⁴⁵ Nuclear Overhauser effect (NOE) derived distances show correlations through space, allowing for analysis of the 3D structure of molecules.⁴⁶

A technique that has gained more traction in the last few decades is anisotropy, where induced order is forced upon the sample, usually through a liquid crystal (LC) or a strain-induced alignment in a gel (SAG), allow for measurement of a global alignment tensor through residual dipolar coupling (RDC), residual chemical shift anisotropy (RCSA), and residual quadrupolar coupling (RQC).⁴⁷⁻⁶⁰ Using anisotropic parameters can be used to distinguish enantiomers or diastereomers.^{51, 58, 61-63} The anisotropic NMR parameters are dependent on an assembly of theoretical structures to distinguish between.⁶⁰

Theoretical conformations are generally generated in two different ways.⁶⁴⁻⁶⁷ The first involves an extensive conformational search by *ab initio* computations. The resulting conformers are then geometry optimised, and corresponding structural information that can be used to compare to experimental data is calculated from the finalised structures. The second method involves using experimentally obtained data, such as NOE derived distances or *J*-coupling constants, as constraints in the calculations. Both methods have advantages and disadvantages but are usually

done with different intentions in mind: Simulating data that experimental data can be compared to in case of uncertainty, or creating conformers from the experimental data to get an idea of how the molecule behaves in different environments, or when binding to a ligand.

In this work we aimed to explore which NMR parameters we could extract and how sensitive they are to the conformation in aqueous solution and in multiple model systems mimicking the bacterial surface. We have employed a test set of cyclic AMPs provided by an associated project⁶⁸⁻⁷⁰ to probe their conformation in water, DMSO, SDS, and nanodiscs.

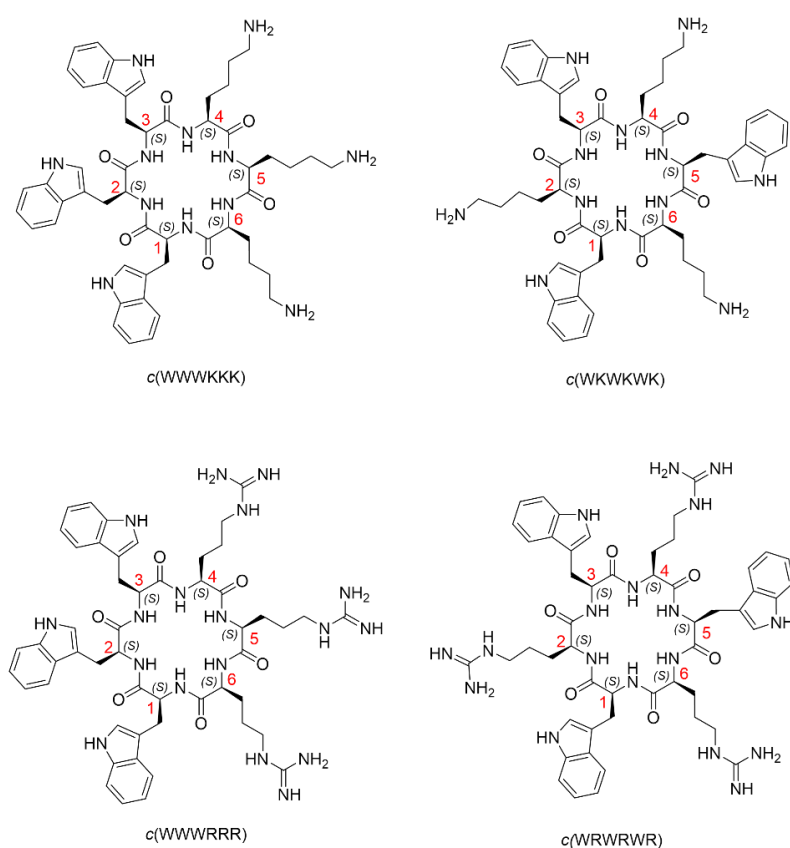


Figure 1. The chemical structures of peptides 1-4.

Results

Conformational analysis in aqueous solution

The baseline conformations of peptides 1-4 in aqueous solvent as well as dmsol has been briefly described in a previous work from our lab.⁷⁰ The main characteristics of the peptides were that

they displayed relatively small conformational backbone variations as a function of their amino acids sequence. The measured NMR parameters, reproduced in Tables S1-S12 in the Supporting materials.

The chemical shifts in aqueous buffer were compared to the chemical shifts in SDS micelles. Changes in the order of half a ppm were observed for multiple residues, and the general trend was that lysine containing peptides became more deshielded, while arginine containing peptides became more shielded in SDS compared to aqueous buffer (Table 1). Backbone amide changes like these are commonly dominated by the relation to the backbone carbonyl, which can be both shielding and deshielding, plus any changes in contributions from hydrogen bonds, where hydrogen bonds have a deshielding effect.

Table 1. Chemical shifts of the amides of peptides 1-4 in water, DMSO and in SDS micelles.

	c(WWWKKK)						c(WWWRRR)					
	Water		DMSO		SDS		Water		DMSO		SDS	
	¹ H (PPM)	¹⁵ N (PPM)	¹ H	¹⁵ N	¹ H	¹⁵ N	¹ H	¹⁵ N	¹ H	¹⁵ N	¹ H	¹⁵ N
1	7.85	118.0	8.07	116.2	8.12	119.1	7.88	118.0	8.04	116.6	8.03	118.8
2	7.33	119.0	7.94	117.0	7.91	116.7	7.42	119.0	7.96	117.2	7.40	127.06
3	7.55	121.2	8.20	118.8	7.91	116.7	7.64	121.2	8.22	118.0	7.17	-
4	7.84	120.8	8.21	116.7	7.81	120.2	7.94	120.2	8.32	116.90	7.71	120.81
5	8.03	119.5	8.00	115.2	7.92	116.7	8.15	119.0	8.18	116.0	7.93	116.93
6	7.77	119.4	8.03	116.6	7.22	117.7	7.87	119.5	8.11	116.5	7.29	117.44
	c(WKWKWK)						c(WRWRWR)					
	Water		DMSO		SDS		Water		DMSO		SDS	
	¹ H (PPM)	¹⁵ N (PPM)	¹ H	¹⁵ N	¹ H	¹⁵ N	¹ H	¹⁵ N	¹ H	¹⁵ N	¹ H	¹⁵ N
1	7.99	119.3	8.15	117.1	-	-	8.07	119.4	8.15	116.8	7.31	-
2	7.62	120.2	8.03	116.7	-	-	7.65	120.0	8.11	116.9	7.19	-

To visualise the significance of the amplitude of the chemical shift changes, TALOS+(N) was used to predict the phi/psi angles as well as the secondary structures implied by the changes in observed chemical shifts (Figure 1). It should be noted that TALOS is parametrised on large

well folded proteins and may have poor accuracy when applied to small cyclic peptides. Especially if the cyclisation pushes the peptide into normally less populated states. Nevertheless, it gives an indication as to what amplitude of chemical shift changes are associated with changes in secondary structure and the phi/psi dihedral angles. TALOS+(N) predicts significant changes in secondary structure between water and SDS for the arginine containing peptides (Figure 2). These predictions were however in poor agreement with the three state phi/psi distribution predictions in TALOS+(N) using the same input data (Figure S 7 and Figure S 8), which warranted a more detailed investigation into their conformations in different environments by other NMR observables.

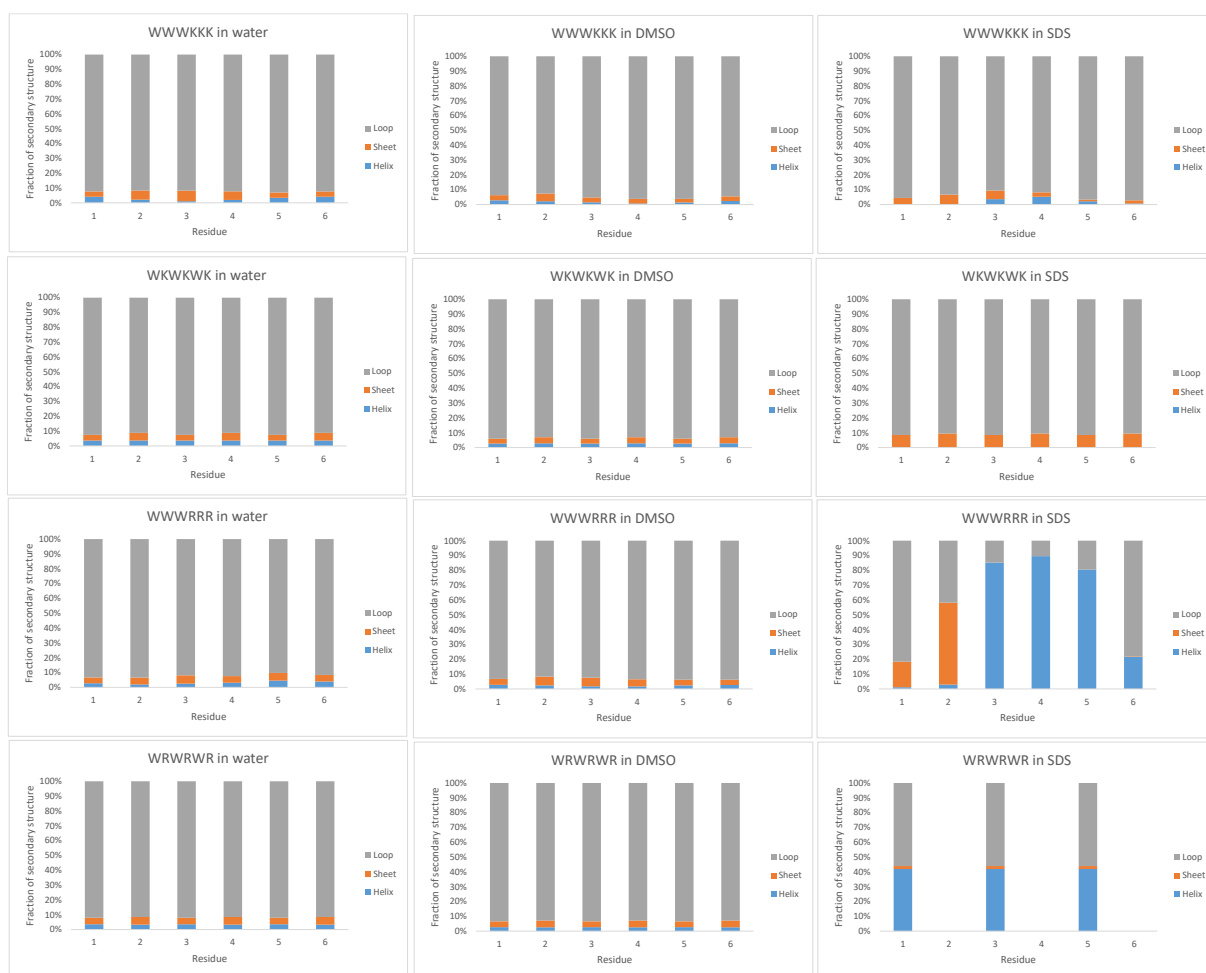


Figure 2. Neural network secondary structure prediction in TALOS+(N) as fractions of alpha helix (blue), beta sheets (orange), and loop (grey) secondary structure types, proposing a higher degree of folded helix-like conformations in SDS compared to water for the arginine containing peptides.

The $^3J_{\text{HNHA}}$ scalar couplings provide information about the phi dihedral angle. In peptides and proteins, the most commonly populated angles are approximately -60 degrees for alpha helices and 310-helices corresponding to a J -coupling of ~4 Hz, and approximately -120-(-140) degrees for beta sheets corresponding to ~9 Hz.⁷¹ The measured couplings, presented in Table 2, did not suggest as much alpha helix (folded) character as the chemical shifts alone did in water for the three-state distribution model in TALOS+(N) (Figure 3). The peptides instead predominantly displayed couplings somewhere in between the average values of the common defined secondary structures, which would fit better with the direct secondary structure prediction in TALOS+(N) (Figure 2). The Ramachandran plot of the phi/psi low energy space does show that there is overlap between the alpha helix- and the beta sheet regions with regards to phi angle alone, allowing the full range from -140 to -60, so there is no contradiction between the measured intermediate size of the couplings and either alpha helices or beta sheets, including the more unusual left-handed helices. It is also plausible that the small cyclic peptides maintain some flexibility in the cyclised form and display a time averaged coupling. There was a weak trend that peptides containing arginine displayed a slightly stronger preference for folded conformations (alpha helix like) than the lysine containing peptides did, as reflected by their average couplings being lower, and thus closer to 4 than to 9. The trend was also that several residues of the arginine containing peptides experienced 1-2 Hz changes in coupling constants when going from water to DMSO. This could indicate that a larger fraction of the time is spent in more extended beta sheet like conformations with phi angles in the -120 degrees range. The resolution was insufficient in SDS to allow of any line shape simulations to reliably extract the J_{HNHA} coupling constants without making excessive assumptions about the line width of the exchangeable amide protons.

Table 2. $^3J_{\text{HNHA}}$ coupling constants for peptides 1-4 in water and DMSO.

Resid	Water				DMSO			
	c(WWWKKK)	c(WKWKWK)	c(WWWRRR)	c(WRWRWR)	c(WWWKKK)	c(WKWKWK)	c(WWWRRR)	c(WRWRWR)
1	7.0 [#]	7.1	7.9 [#]	6.2	6.5	7.1	8.3	7.6
2	6.9 [#]	6.2 [*]	5.4 [*]	5.8	7.1	6.9	7.4	6.7
3	6.2 [*]	7.1	5.1 [*]	6.2	8.2 [#]	7.1	7.1	7.6
4	5.7 [#]	6.2 [*]	6.2	5.8	6.8 [#]	6.9	7.2	6.7
5	7.5	7.1	7.6	6.2	7.6	7.1	7.9	7.6
6	6.2	6.2 [*]	6.2 [#]	5.8	5.9	6.9	7.3	6.7

[#] lineshape fitted from a high resolution and zero filled ^{15}N -HSQC F2 slice

^{*} lineshape fitted from an unresolved doublet

NOE build-up between two protons is inversely proportional to the distance between them to the power of six (r^{-6}). For backbone structure, the most informative distances are those between HN-HN(n-1) which are ~ 2.8 Å in a helix and ~ 4.3 Å in a sheet, and HN-HA(n-1), which are ~ 3.5 Å in a helix and ~ 2.2 Å in a sheet. We would thus expect very strong NOE correlations between HN and HA(n-1) in beta sheet like structures and between HN and HN(n-1) in alpha helix like structures. The measured NOE buildups, translated into distances using the two-proton approximation with aromatic tryptophan crosspeaks as reference, are reported in Table 3. The NOE distances indicated no major changes in conformation between water and DMSO for either peptide. If anything, a somewhat strengthened extended conformation in DMSO. However, in SDS there is a significant increase in HN-HA(n-1) distances for the arginine containing peptides, suggesting a change in secondary structure towards a more folded form than in water, which is again in agreement with the direct secondary structure prediction from TALOS+(N) (Figure 2). Note that distances for residues 3 and 4 for this peptide are ambiguous due to spectral overlap.

Table 3. $H_N-H\alpha(n-1)$ distances of peptides 1 and 4 in different environments from NOE buildup experiments, given in Å. *overlapping peaks.

c(WWWKKK)						
	W1	W2	W3	K4	K5	K6
Water	2.83	3.01	3.28	2.45	3.03	2.83
DMSO	2.52	2.61	2.17*	2.17*	2.85	2.32
SDS	2.58	-	3.11	4.65	3.15	3.25
c(WWWRRR)						
	W1	W2	W3	R4	R5	R6
Water	2.85	2.95	3.39	3.01	3.48	3.28
DMSO	3.09	2.83	2.93	3.27	3.30	3.13
SDS	3.50	4.17	-	4.08	4.00	4.50

Conformational analysis by structure calculations

Structure calculations were performed using X-PLOR, introducing different NMR-derived constraints in the different environments; water, DMSO and SDS. Initially, the structures were based entirely on NOE constraints. Subsequently, scalar coupling constraints were introduced, and finally test calculations adding TALOS derived phi/psi dihedral constraints were performed to evaluate their accuracy. The generated structures are presented in Figure 3, with the averaged structures found in the Supporting Information (Figure S 9).

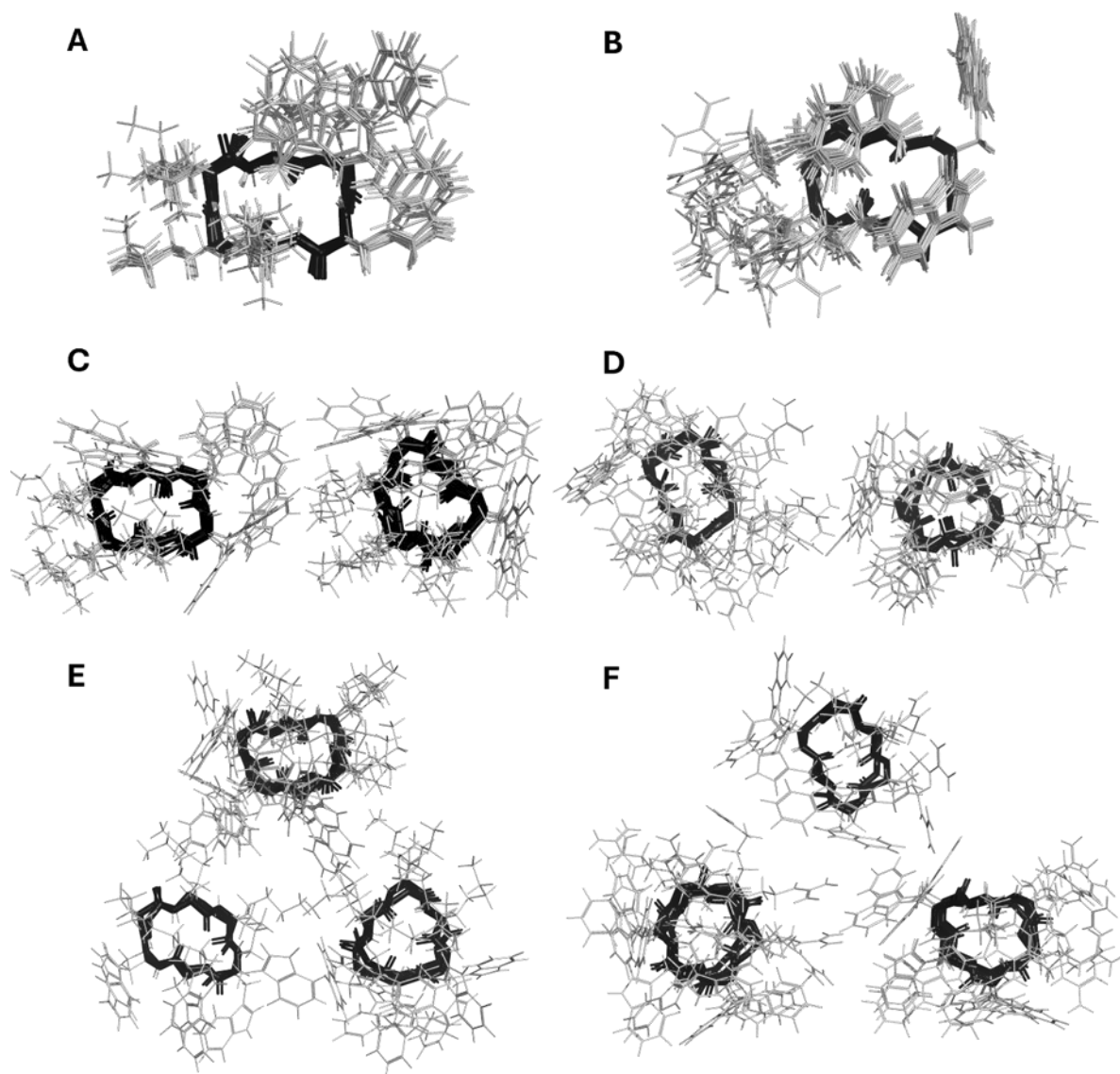


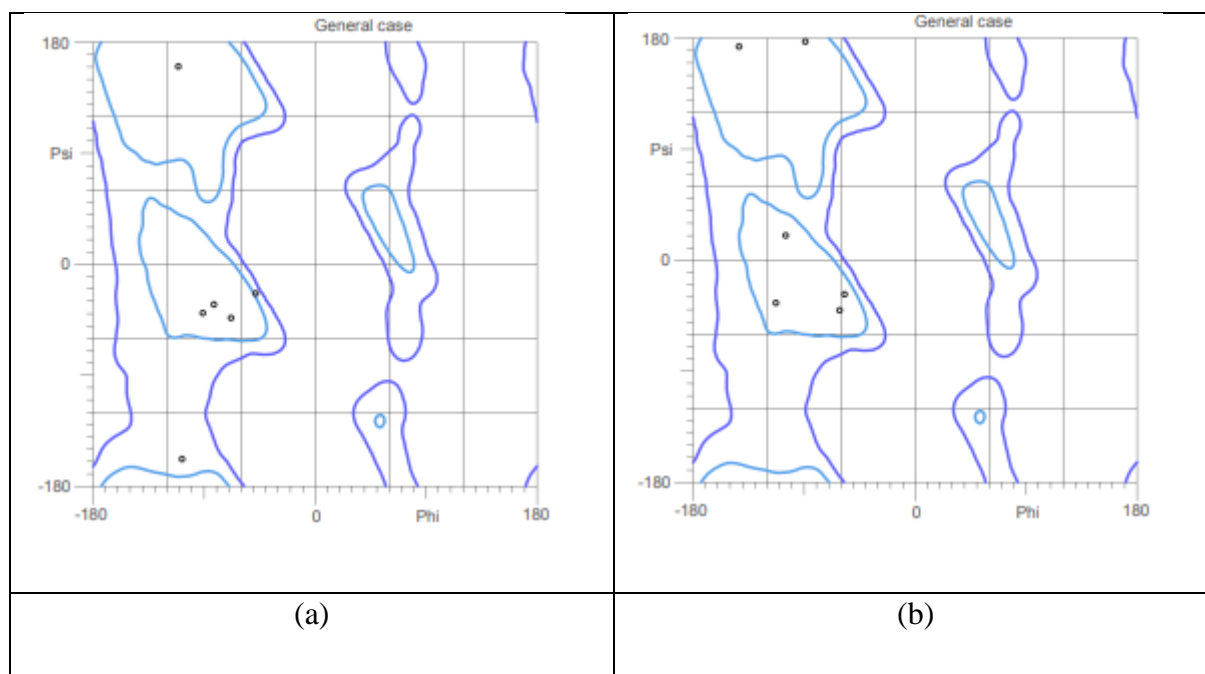
Figure 3. Superimposed representations of the ten lowest energy conformations based on NOE constraints of (A) *c*(WWWKKK) in water; (C) *c*(WWWKKK) in DMSO; (E) *c*(WWWKKK) in SDS ; (B) *c*(WWWRRR) in water; (D) *c*(WWWRRR) in DMSO; *c*(WWWRRR) in SDS.

Both peptides primarily adopt conformations consisting of two β -turns with the $i+1$ and $i+2$ residues being the same amino acid. *I.e.*, the turns occur between two Trps and two Lys/Arg. This is consistent with structures of similar cyclic hexapeptides reported in the literature.^{28, 72} In DMSO and SDS additional conformations are more prevalent. While the coupling constants and NOEs suggests that changes in populations may very well occur when moving from water to SDS, we are at the same time getting significantly fewer experimental constraints in the latter, and therefore the additional conformations can also be the effect of less constrained simulations.

In either case, the constraints could be satisfied by multiple conformations. In some cases, the additional conformations are still two β -turns with the turns occurring between Trp and Lys/Arg residues resulting in the clustered residues running parallel to one another

Table 4. Pairwise root mean square deviation (RMSD) calculated for the top-10 structures in different solvents to demonstrate the variance in the structure generation. NOE structures are those presented in Figure 3. NOE – NOE constraints only. NOE + CC – NOEs and coupling constants as constraints. NOE + CC + Diheds – NOEs, coupling constants and TALOS predicted dihedral angles as constraints.

	Water RMSD (Å)			DMSO RMSD (Å)			SDS RMSD (Å)
	NOE	NOE + CC	NOE + CC + Diheds	NOE	NOE + CC	NOE + CC + Diheds	NOE
WWWKKK	0.18 +/- 0.06	0.17 +/- 0.06	0.05 +/- 0.02	0.98 +/- 0.29	0.75 +/- 0.33	1.49 +/- 0.61	1.31 +/- 0.41
WWWRRR	0.11 +/- 0.00	0.03 +/- 0.00	0.02 +/- 0.00	0.38 +/- 0.00	0.58 +/- 0.00	0.65 +/- 0.00	0.18 +/- 0.00



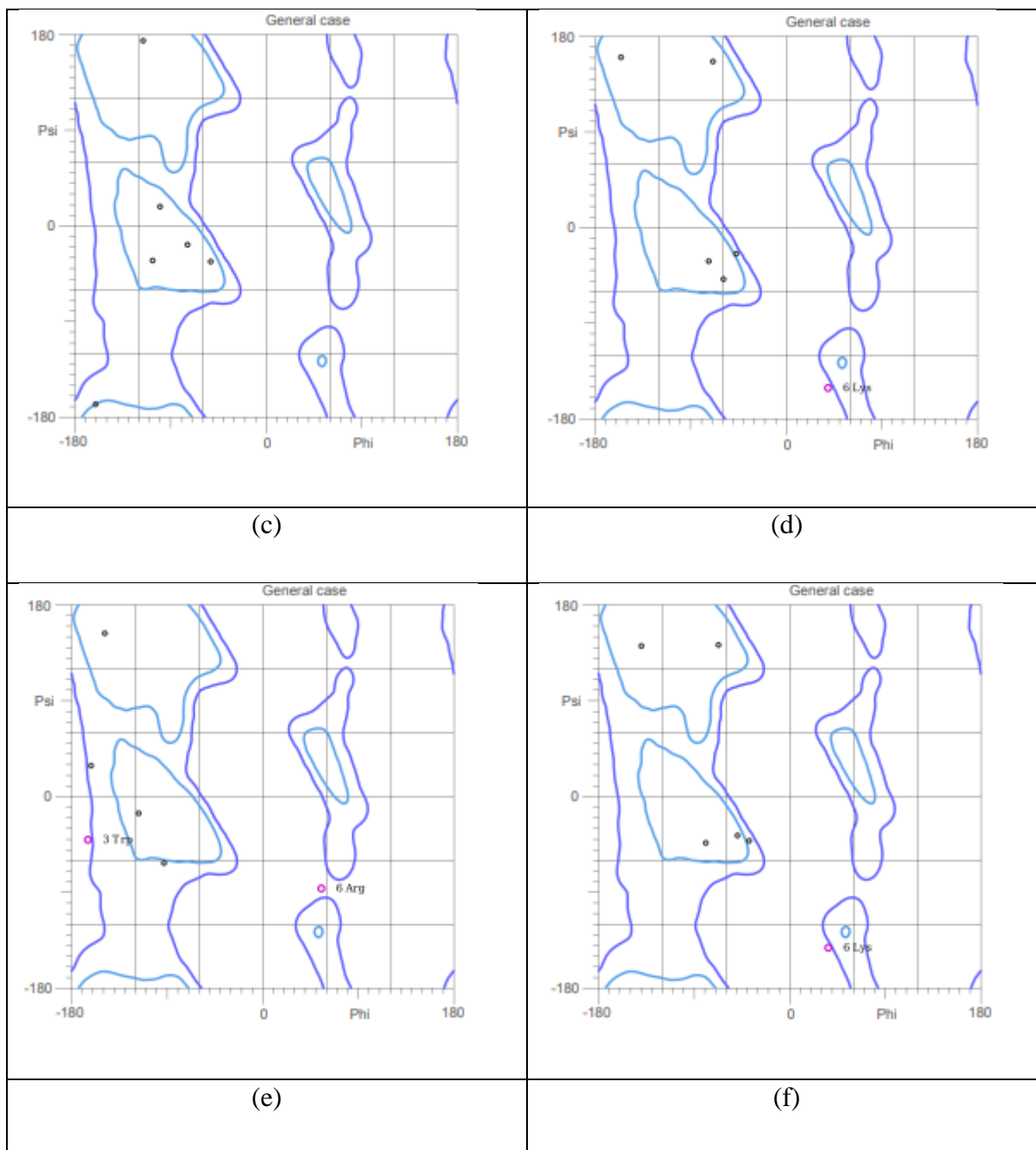


Figure 4. Ramachandran plots of (a) *cWWWRRR* in water, (b) *cWWWKKK* in water, (c) *cWWWRRR* in DMSO, (d) *cWWWKKK* in DMSO, (e) *cWWWRRR* in SDS and (f) *cWWWKKK* in SDS.

The introduction of the experimentally derived coupling constants as structural constraints alongside the NOEs during structure generation introduces a modest increase in the potential energy of the structures. However, when the TALOS predicted bond angles are subsequently added as a constraint, the potential energies are significantly higher. This effect is much more exaggerated in the DMSO-based structures, which is to be expected since the predictions are based on NMR data of proteins in aqueous conditions. It was therefore concluded that the three-

state predictions of phi/psi angles in TALOS+(N) were not consistent with the other experimental observations and did not contribute positively to structure calculations.

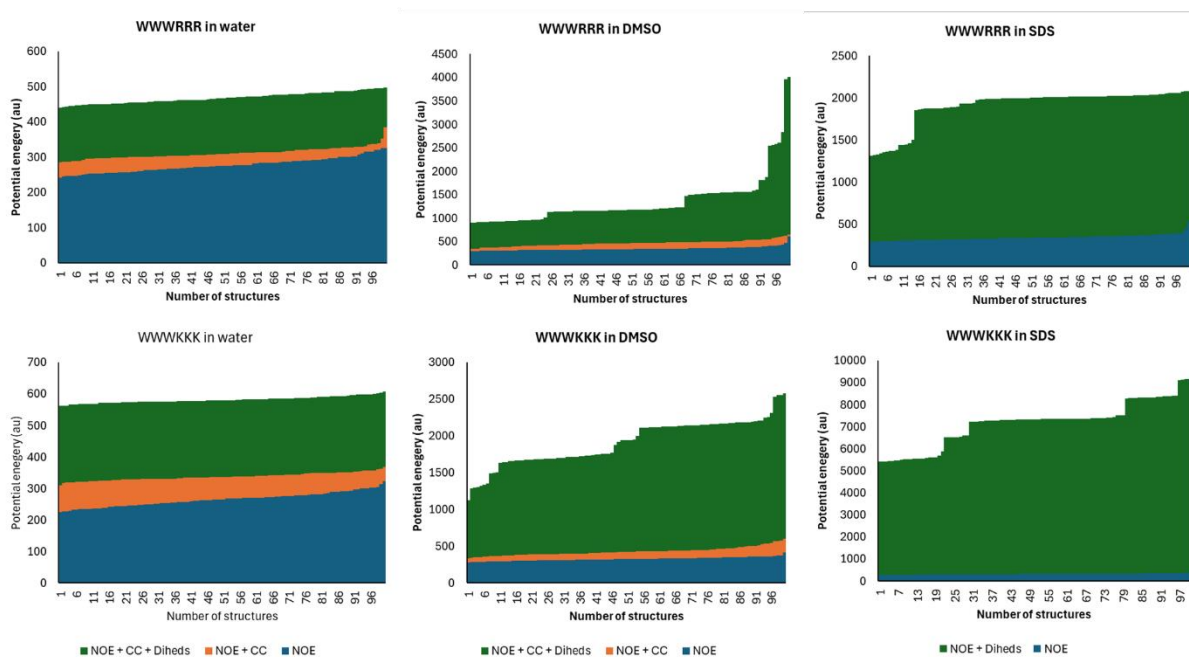
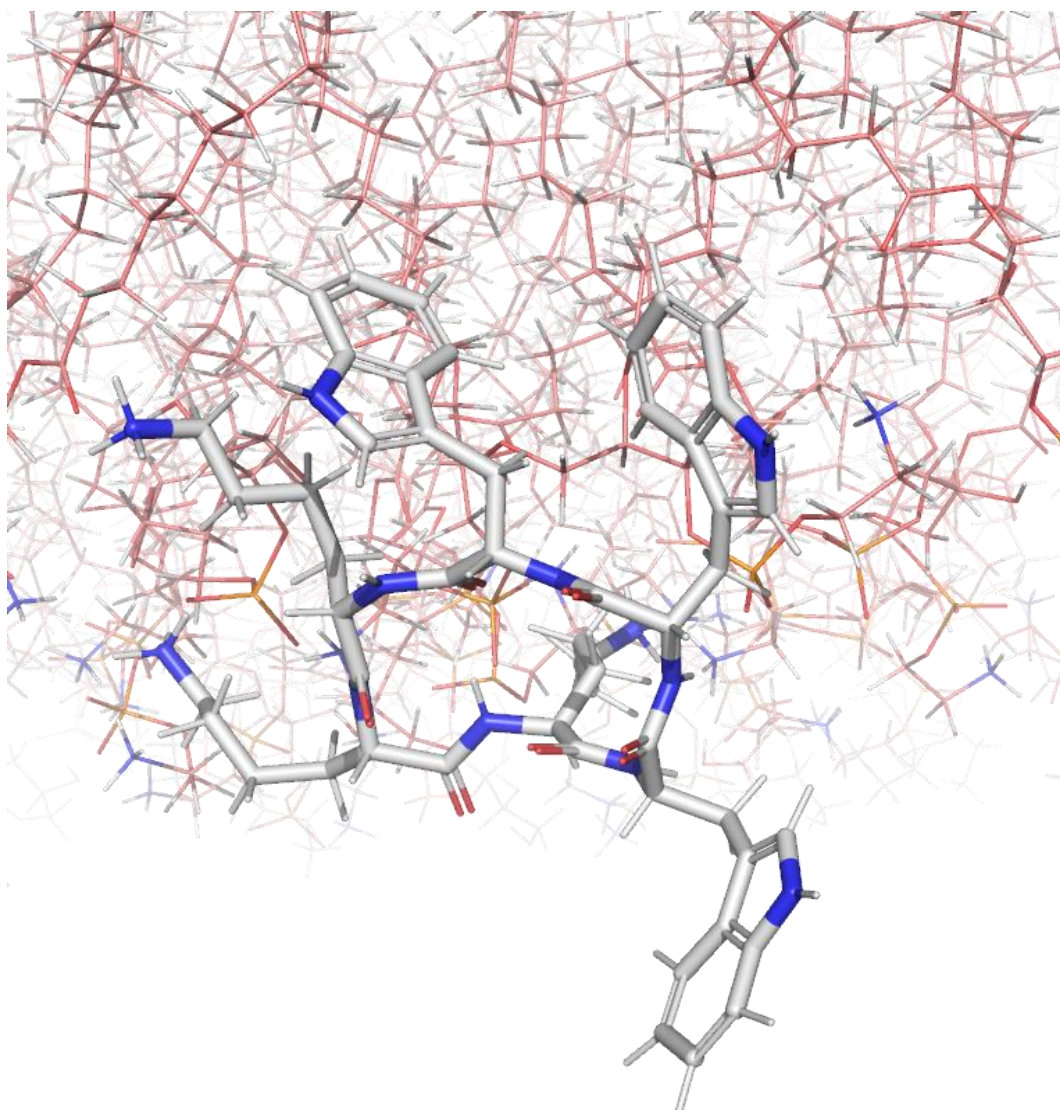


Figure 5. Potential energies of the 100 generated structures by the simulated annealing protocol in descending order using different constraints. NOE – NOE constraints only. NOE + CC – NOEs and coupling constants as constraints. NOE + CC + Diheds – NOEs, coupling constants and TALOS predicted dihedral angles as constraints.

Molecular dynamics (MD) simulations in POPE/POPG membranes

Theoretical MD trajectories of c(WWWRRR) and c(WWWKKK) were simulated in POPE/POPG membranes dissolved in a periodic box with explicit water, sodium and chloride ions to provide some insight into which conformations would be expected as we move towards increasingly realistic membrane models. The simulations revealed that the cyclic hexapeptides existed in an equilibrium between bound and free form, within the 260 ns simulation time of the trajectory, but the bound forms did not reveal any new conformational preferences. Representative structures of the two peptides inside the lipid bilayer are shown in Figure 6. Both peptides adopt a conformation with two beta turns, where the turn is between W1 and W2 for c(WWWKKK) and between W3 and R4 for c(WWWRRR). The general structure agreed with the NMR-constrained structures in water, DMSO and SDS, that all produced double beta turn structures with the turns in different positions. It was therefore concluded that the surrounding media does not significantly affect the energy minimized conformations of these

cyclic hexapeptides but is more likely to affect solubility derived properties like self-aggregation and the populations and/or dynamics between the low energy conformations. The conformations remained stable throughout the simulation, no transitions between conformations with the turns in different positions were observed. It is therefore possible that beta turns in different positions give rise to the two conformations in slow exchange observed in NMR for c(WWWRRR) (see Figure 6).



(a)

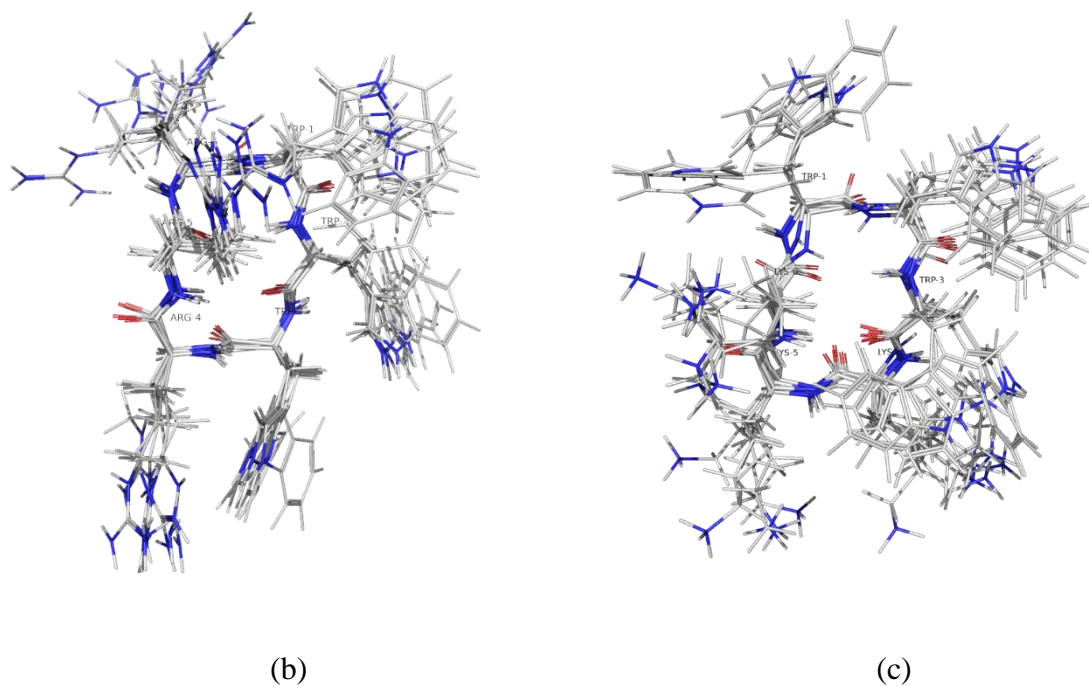
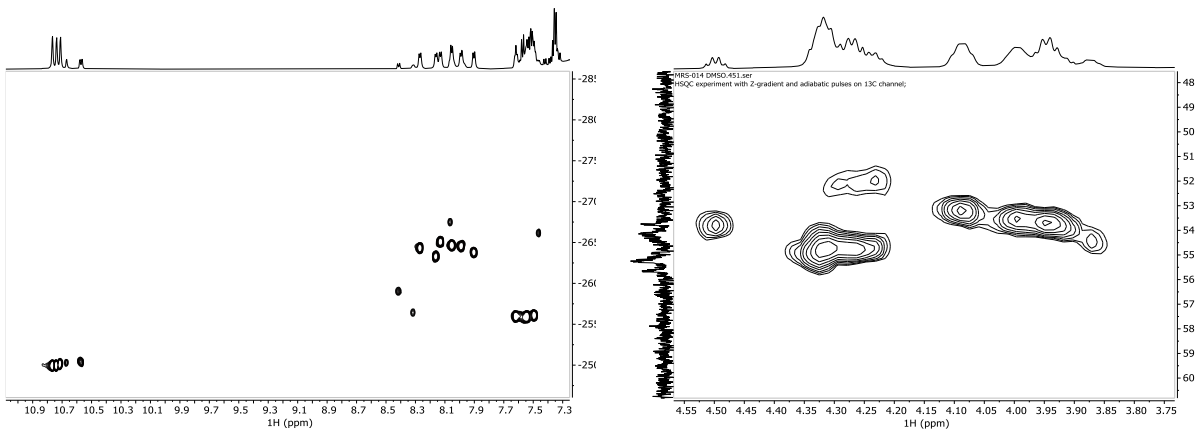


Figure 6. (a) A representative snapshot of the interaction between *c*(WWWKKK) and the POPE/POPG bilayer followed by periodically sampled snapshots of the second half of the MD trajectories of (b) *c*(WWWRRR) and (c) *c*(WWWKKK).

Slow conformational exchange of *c*(WWWRRR)

The spectra of peptide *c*(WWWRRR) displayed one extra set of resonances for several protons and carbons of the peptide with weaker intensity (see Figure 7). Potential epimerisation during the peptide synthesis was ruled out because there were no additional peaks in analytical HPLC, and there was only one extra set, not multiple as you would expect from a random process affecting 6 amino acids. Mass Spectrometry further excluded chemical modification of the peptide. Also, self-aggregation was considered highly unlikely due to it being present in all studied solvents. The extra peaks intensities are approximately in a 1:2 ratio to the main peaks.

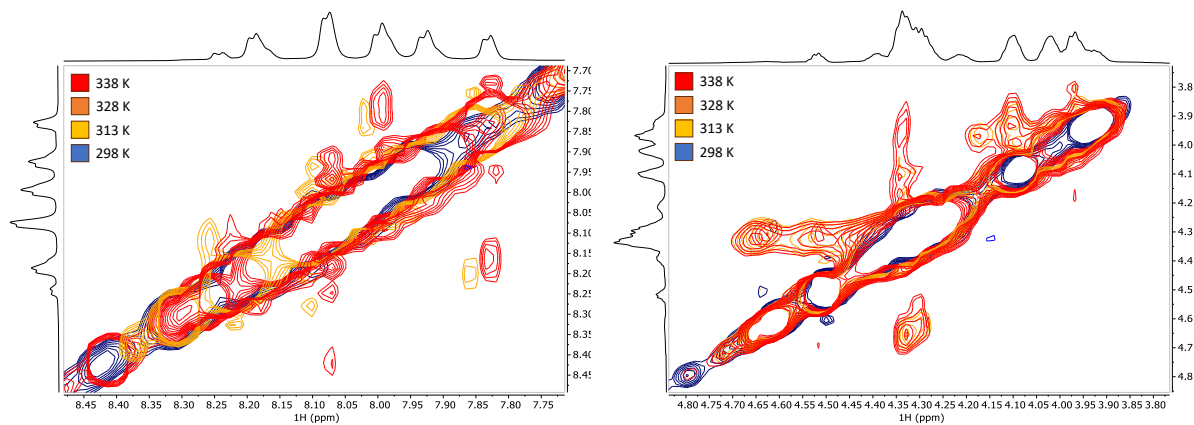


(a)

(b)

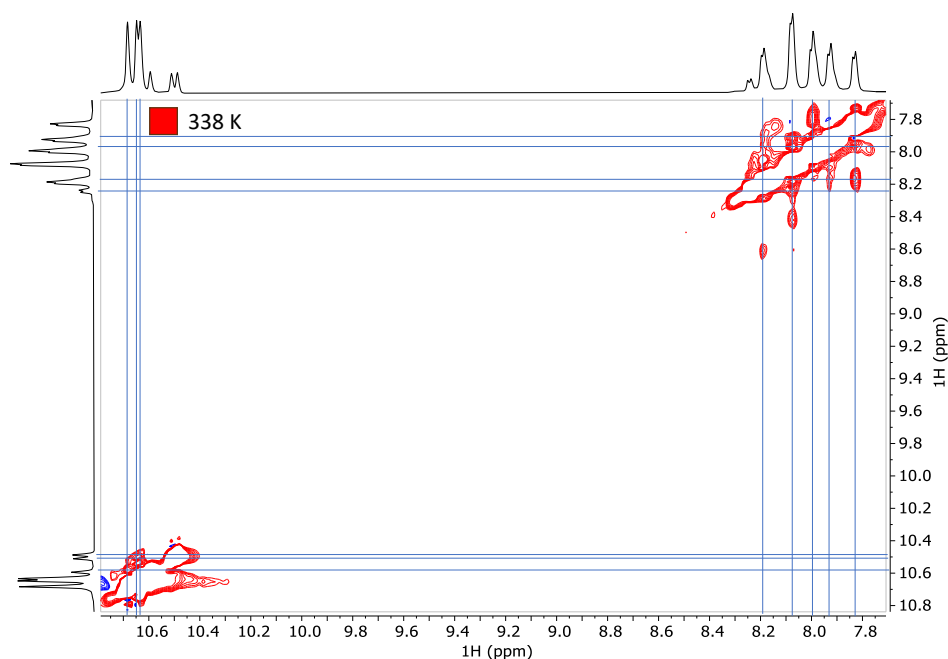
Figure 7. The ^{15}N -HSQC (a) and the HSQC (b) spectra of the alpha region of c(WWRRR) in DMSO displaying an extra set of resonances for the backbone NH and CA.

When the temperature was increased from 25°C up to 65°C, several in-phase peaks with the same sign and the diagonal started to appear in ROESY spectra, indicating the presence of very slow exchange between two conformers separated by a high energy barrier (Figure 8).



(a)

(b)



(c)

Figure 8. Expansions of ROESY spectra of *c*(WWRRR) in DMSO with 300 ms mixing time at increasing temperatures, showing the HN region (a) and HA region (b), corresponding to the HSQCs in Figure 4. There are multiple crosspeaks in phase with the diagonal that build up with increasing temperature, showing that the peptide is in slow conformational exchange (c) The highest temperature is highlighted to show that crosspeaks connect the major (vertical lines) and minor (horizontal lines) conformations. The projections are given for the ROESY at 338 K, represented in red.

The exchange is present in all studied solvents, in roughly the same populations. The temperature dependent buildup was only studied in DMSO, but there was no apparent lowering in energy barrier between the conformations in the different solvents as neither sample displayed any easily detectable exchange at room temperature between the subspecies. In SDS, especially the Tryptophan sidechains produce very broad peaks, as well as displaying multiple sets of chemical shifts.

SMA-QA nanodiscs

The polymer based SMA-QA nanodiscs have recently attracted attention for displaying self-aligning properties in strong magnetic fields under certain conditions.⁷³⁻⁷⁶ The SMA-QA based nanodiscs were therefore suggested as a more realistic membrane model systems to extract conformational information from, compared to micelles. While traditional micelle model

systems provide excellent spectral quality, there is always the troubling fact that tensides are themselves very different entities compared to phospholipids, and they also behave very differently from phospholipids, self-assembling into small lipid droplets with a high curvature while the phospholipids prefer to form flatter bilayered structures.⁷⁷⁻⁸⁰ In addition, there is also the uncertainty whether these droplets maintain any of that droplet structure after interacting with moderately sized AMPs, or if they partially or completely disassemble in contact with the AMP and rather solvate the AMP with dispersed lipids interacting in favourable positions across the AMP. It would therefore be highly attractive to access any structural information from any phospholipid-based model system that is stabilised by a scaffold to give resilience against complete disruption by small membrane active compounds.

There are examples in the literature of membrane protein structures being studied in lipid nanodiscs aligned using virus filaments.⁸¹ In the case of the AMPs studied herein however, there are direct interactions between virus filaments and the AMPs, making this approach difficult. The boundary conditions for using SMA-QA nanodiscs in combination with our set of AMPs was therefore explored to probe if conformational studies using isotope labelled peptides could be economically- and practically feasible. In addition to the challenges with concentration, solubility and nanodisc production, the system we were exploring was not a well-defined solubilised protein produced and isolated in 1 to 1 ratio with the nanodisc, but rather an unspecific interaction being gradually added to an already assembled disc.

The original paper describing the assembly and purification of the SMA-QA nanodiscs describe one of the strengths of the nanodiscs to be their very exact size-tuneability.⁷⁴ By mixing SMA-QA:lipid at ratios of 1.5:1, 1:1, or 0.25:1 nanodiscs can be assembled with a diameter of 10, 20, or 30 nm, respectively. The size control was first reproduced by mixing the same ratios of SMA-QA polymer and DMPC or DMPC with 5% DMPG. The nanodiscs separated in size exclusion chromatography (SEC) as a distribution of sizes around the target size. Nanodiscs of ~30 nm had a retention time of approximately 50 minutes, ~20 nm and ~10 nm discs had retention times of approximately 70 minutes, and SMA-QA of approximately 115 minutes. The nanodiscs and polymer were detected by UV absorbance at wavelengths 254 and 280 nm, and the polymer was detected by a distinct dip in conductivity (See Figure S 4-Figure S 6 in supporting information). When assembling the nanodiscs, several batches were made in parallel. Large unilamellar vesicles were prepared as 1 mL 20 mM samples in Eppendorf tubes, and they were incubated with SMA-QA from a stock solution. Normally, 2-4 samples were prepared simultaneously, and purified the next day. It was noticed that even when the parallel batches

were prepared identically, there were small changes in the retention times and line widths of the elution spectra, and dynamic light scattering spectra showed that the purified discs could range widely in structure, for example from 15 to 30 nm from the intended 20 nm. Therefore, it was concluded that the SMA-QA:lipid ratios to yield specific sizes are guidelines and that every batch needs to be thoroughly characterised.

Ravula *et al.* showed how the alignment of SMA-QA nanodiscs are dependent on lipid concentration.⁷⁶ Therefore, the sample collection area was set to approximately 60% of the centre part of the SEC peak, attempting to exclude the tails where the size deviation is the largest. The collected sample was then concentrated to about half the starting volume and the lipid concentration was determined by ³¹P NMR. The amount of lipids per disc was estimated from the diameter found by DLS at 30°C, the reference area of the DMPC lipid head group,⁸²⁻⁸⁴ and the width of the SMA polymer.⁸⁵ To the best of our knowledge, the width of the SMA-QA polymer has not been reported, hence the width of the SMA polymer was used in the calculations.

SMA-QA nanodiscs have been reported to self-align at higher temperatures,⁷⁶ and it could be confirmed that a deuterium splitting was indeed observable above 305 K, reaching a maximum around 310 K (Figure 9). This conveniently coincides with the body temperature, which could be useful for the studies of interactions relevant for an *in vivo* environment. The size of the splitting is also dependent on the size of the nanodisc.

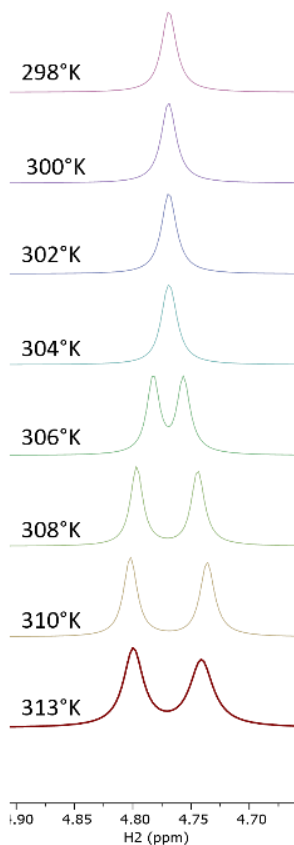


Figure 9. Increase of deuterium signal splitting in a 5 mm NMR tube with increased temperature. The concentration is 6.88 mM lipid in 30.57±12.72 nm SMA-QA DMPC nanodiscs.

The SMA-QA self-alignment also has a concentration and size dependence, and the deuterium doublet quickly collapses when dropping below 115 mM lipid concentration for the shown ~20 nm diameter nanodisc preparation (Figure 10). It was therefore important to ensure that any titration assay did not cause effective dilution of the nanodisc concentration, which can be achieved by adding nanodiscs to the peptide stock, or to assemble the SMA-QA nanodiscs with the AMPs together with the lipids already at the initial nanodisc assembly. Neither of these methods would be unproblematic for membrane active compounds like AMPs but would appear necessary to study interactions with SMA-QA nanodiscs.

It was also observed that the diameter of the sample tube affected the degree of alignment (Figure 10). The splitting collapses at higher concentrations in a 3 mm NMR tube compared to a 5 mm NMR tube, suggesting that the phase of the nanodisc alignment is directly affected by the physical boundaries imposed by the glass walls.

A titration was performed, gradually adding AMPs to a solution of SMA-QA nanodiscs, recording the ^1H NMR spectra (Figure 11). Below a 100:1 ratio of AMP per disc, there is virtually no detectable signal arising from the peptides. We interpret this as that the lipid system is being saturated between 100 and 500 AMP:disc ratio (between 20 and 4 lipids per peptide molecule), and at that point the relatively sharp signals from the unbound peptides are detected. It was also concluded that we have an unknown rate of exchange between the bound and the free forms in this system, leading to some but not extensive line broadening of the detectable signals at the extremely high peptide:lipid ratios. The efficiency of signal attenuation all the way up to peptide:lipid ratios in the 100-500 range does however suggest either a very significant k_{ex} rate for efficient time sharing of the high correlation time of the nanodisc complex, or an extremely high binding capacity of the nanodisc constructs themselves, likely through self-aggregation mechanisms on the lipid surface. In addition, the chemical shift and the line width of the bound state is unknown, further complicating any estimates. We do not expect direct interactions between the cationic peptides and the cationic polymer to contribute to the apparent K_D of the complex.

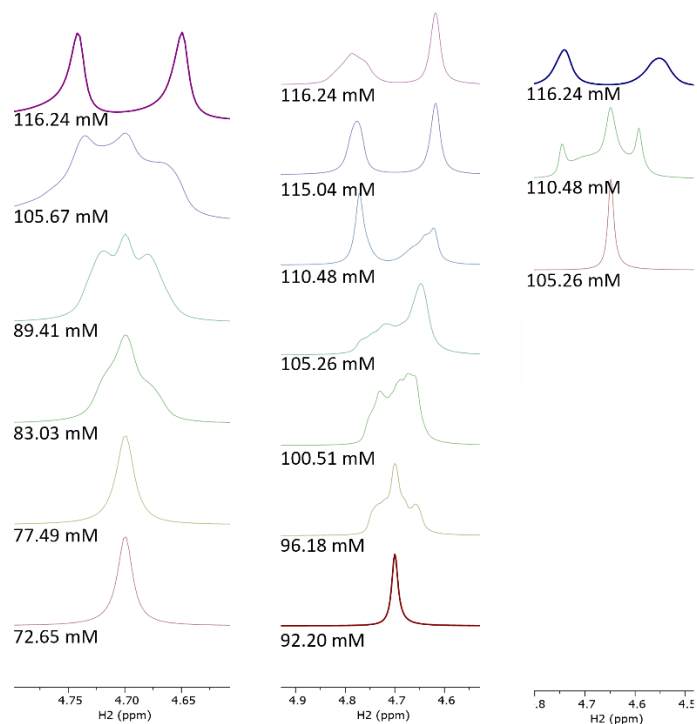


Figure 10. Loss of deuterium signal splitting by dilution in different conditions. (left) Dilution in a 5 mm NMR tube; (middle) dilution in a 3 mm NMR tube; (right) dilution by adding the cyclic tetrapeptide *c*(WKWKWK) in a 3 mm NMR tube. All NMR spectra were collected at 313 K, the concentrations are lipid concentration, and the size of the SMA-QA DMPC nanodiscs are 20.79 ± 11.14 nm. The dilution in both 3 mm tubes were done by the same volumes, to compare the loss of signal splitting with and without peptide. The dilutions were done with a 90/10 H₂O/D₂O mixture.

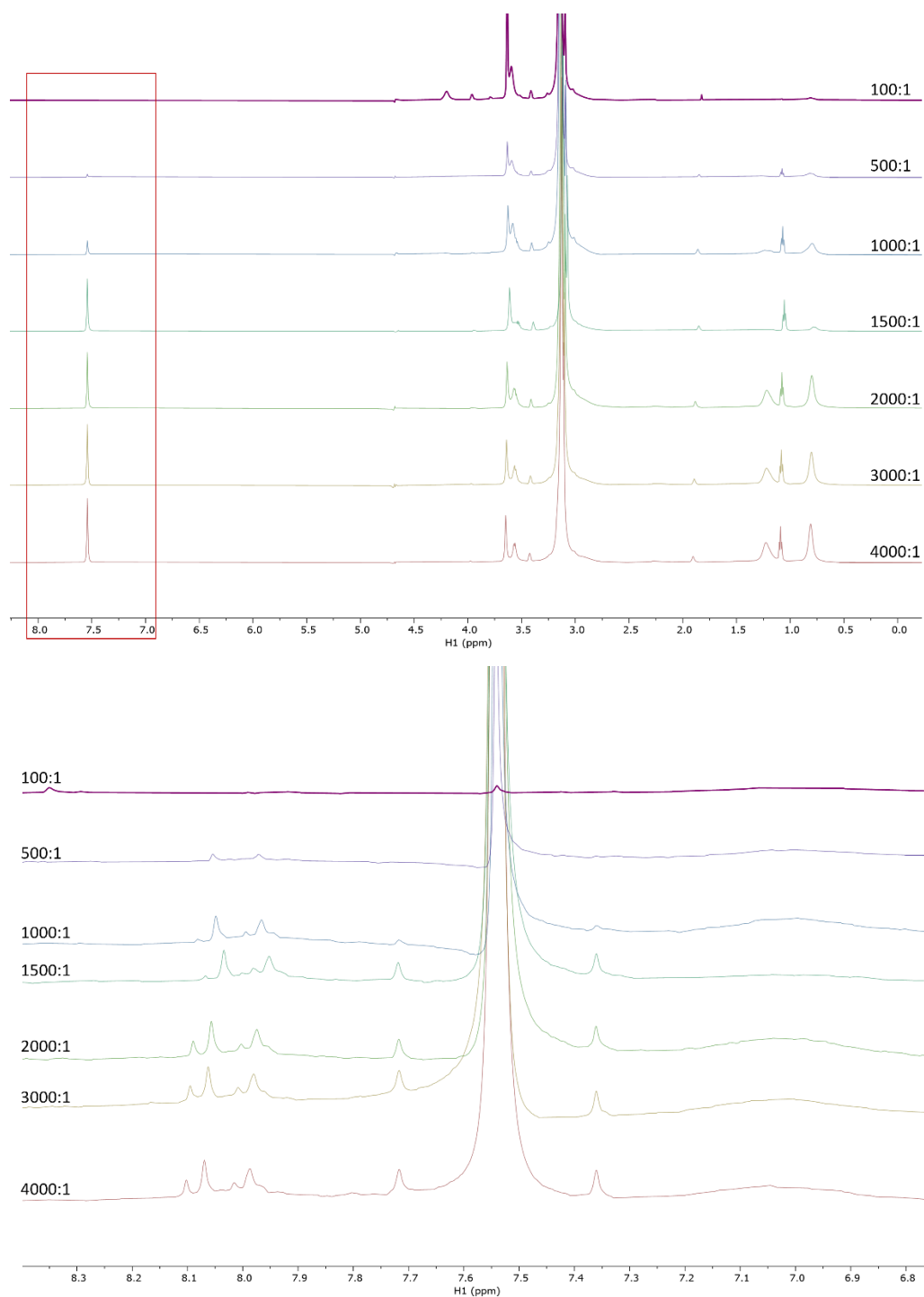


Figure 11. $1\text{D } ^1\text{H}$ spectra of 30.57 ± 12.72 nm SMA-QA DMPC nanodisc with increasing amounts of cyclic hexapeptide *c*(WWWKKK). Ratios given are peptides per disc, and the disc is estimated to contain ~ 2000 lipid molecules. Top spectrum is the full spectrum (no peaks outside borders), while bottom spectrum is the range highlighted in red.

Conclusion

The cyclic AMPs studied in this work did not exhibit any significant conformational changes in different environments, ranging from water to micelles and phospholipid bilayers. From a method development perspective, the amount of high qualitative structural data that can be extracted rapidly diminish as the lipid model system gets more realistic and inevitably larger and more heterogenic. From phospholipid-based model systems like nanodiscs or liposomes we only expect to be able to extract chemical shifts, RDCs and RCSAs, where the latter requires partial alignment. This is complicated by the fact that AMPs are membrane active and are notorious for interfering with both phages and lipid systems in general. Initial results from SMA-QA nanodiscs in the presence of the studied AMPs however indicated that the integrity of the discs was not compromised by the AMP activity. That said, we did observe a decrease in alignment in the presence of AMPs, which will have to be considered.

The pilot experiments to explore the viability of using self-aligning SMA-QA nanodiscs as a model system suggests that there is a potentially viable concentration interval above the detection limit of ^{15}N -TROSY for ^{15}N labelled peptides, but at a healthily low peptide:lipid ratio. Because the model peptides provided for this work turned out to be conformationally featureless, investing in isotope labelling could not be justified and was thus deemed outside the scope of this work. At this point we conclude that the pilot study finds it viable to use self-aligning SMA-QA nanodiscs for conformational studies of small AMPs, but also that there are several difficulties associated with unordered interactions, exchange processes and saturation. The discs themselves need to be more thoroughly studied to map their behaviour and capacity under different conditions.

Experimental Section

NMR spectroscopy.

The synthesis of the peptides has been described previously.⁶⁸ c(WWWKKK), c(WKWKWK), c(WWWRRR), and c(WRWRWR) were dissolved in D₂O/H₂O 90:10 or pure d-DMSO (130 μL in 3 mm NMR tube, 600 μL in 5 mm NMR tube, or 120 μL in Shigemi tube; final sample concentration 2.5 mM). To obtain sample of SDS-micelle bound peptide (25 mM SDSd-25) a stock solution of SDS was added.²⁸

NMR spectra were acquired on a Bruker Avance III HD spectrometer operating at 600 MHz for ¹H, equipped with an inverse TCI cryo probe. All NMR spectra were acquired at 298 K using 5 mm tubes, except c(WWWRRR) in d-DMSO, which was acquired using a 3 mm Shigemi tube because of the limited amount of material. NOESY/ROESY, TOCSY, DQF-COSY, ¹⁵N-HSQC, HSQC, HMBC, and H2BC NMR spectra were recorded with standard settings. NOESY and TOCSY spectra were recorded in water with mixing times of 100–400 ms and 80 ms, respectively. ROESY spectra were recorded in d-DMSO and SDSd-25 in water with mixing times of 25–200 ms.

Spectra were processed with TopSpin 3.6.0, and assignments were done manually.

NOE Buildup

The NOESY/ROESY spectra were imported into the Dynamics Center 2.8.3 NOE buildup toolbox under Method Center. Peaks were manually picked for their integrals and the buildup curves was reported in .pdf while the integrals were exported in .xlsx. The most isolated cross peak for the ortho aromatic protons on the Tryptophan furthest away from the diagonal was chosen as the internal reference at 2.46 Å distance.³⁴ All the cross peaks were registered, and the distances were given at the mixing time that had overall least outliers while being in the linear buildup phase, according to the .pdf file. Normally, 50 or 75 ms.

Structure calculation

Structure generation was performed with a standard simulated annealing (SA) protocol using X-PLOR 3.1 (NIH). An initial 25 structures were generated from which an average structure of the 10 lowest energy structures was produced as a starting point for a final SA round of 100 structures from which the top 10 lowest energy structures were selected. In all cases NOE derived distance constraints were used. The production protocol was repeated additionally with the inclusion of the experimentally derived coupling constants, as well as with the coupling constants and TALOS predicted dihedral angles.

Table 5. Summary of constraints used for structure generation.

	WWWKKK			WWWRRR		
	Water	DMSO	SDS	Water	DMSO	SDS
Intra-residue NOEs	34	10	31	25	25	17
Inter-residue NOEs	17	8	13	6	17	17
Of which are backbone	3	6	1	2	4	6
Ambiguous NOEs	31	60	32	36	63	25
Unassigned	17	47	51	25	24	6

The distances extracted from the NOE buildup were used as starting point for constructing the distance constraints for SA, with larger distances having more relaxed constraints using the first significant figure of the distance as a prompt, and up to the Van der Waals distance allowable. Constraints were optimised to relax any distance violations that arose during SA. This was done using the previously described SA protocol but with 10 structures and 25 structures generated in the initial and final SA steps.

Molecular dynamics calculations

The structures, c(WWWRRR) and c(WWWKKK), were constructed in Maestro (Schrödinger Release 2021–4: Maestro, Schrödinger, LLC, New York, NY, 2021), before TIP3P model water was added, and the topology and parameters was generated using CHARMM-GUI⁸⁶⁻⁸⁸ solvation builder. The NAMD⁸⁹ software was used for simulations, with the systems being equilibrated in a periodic boundary box under NPT conditions up to 310K before the they were simulated for 100 ns under NVT conditions in 310K in water with 2fs simulation step. The geometry of the water was constrained used the SHAKE method and for pressure e control the Langevin piston method at 1atm with an oscillation period of 50fs and dampening scale of 25fs. Langevin dynamics was also used to control temperature at 310K with a dampening coefficient at 1ps^{-1} , for long range electrostatic effects PME was used. New conformations were then found by calculating the RMSD value for each frame saved from the simulations and keeping the ones that had a difference higher than 2\AA^2 . Calculating relative energies based on each conformation resulted then in the final conformation which were used in the simulation with the membrane models, one for each of the cyclic peptides.

Two membrane models were investigated, the first consisting of a DMPG/DMPC lipid combination and the second model consisting of POPG/POPE lipids. The first model consists of 336 lipids, 319 DMPC lipids and 17 DMPG lipids, and the second consists of 170 lipids, 128 POPE lipids and 42 POPG lipids and they were both pre-equilibrated systems, the first by Sarre,⁹⁰ and the second by Hong.⁹¹ Both membrane systems had NaCl ions added to both neutralize the membrane as well as ending up with a concentration of 0.15M in the solution itself before TIP3P water was added as additional solution around the system using VMD.⁹²

As both the membranes and the cyclic peptides were already equilibrated, the equilibration was mainly focused on the water. This was done using NVT conditions with the peptide and membrane constrained before a general system equilibration in NPT conditions was conducted. The production simulations were in NPT conditions for 260ns with 2fs simulation step as well as the SHAKE method for the water and the previously explained method for temperature and pressure control.

Synthesis of SMA-QA

Following the procedure of Ravula *et al.*,^{68, 74} (2-aminoethyl)trimethylammonium chloride hydrochloride (9.38 mmol, 1.3 g) was added to a solution of styrene maleic acid anhydride (SMA, 1g) in anhydrous DMF (5 mL), followed by trimethylamine (56.7 mmol, 5 mL) upon which the mixture took a dark yellow colour. The reaction mixture was stirred at 70°C for 2 hours, then cooled to room temperature, and precipitated with diethyl ether. The precipitate was washed 3 times with diethyl ether and dried *in vacuo*. The dried intermediate was dissolved in acetic anhydride (317 mmol, 30 mL), to which sodium acetate (8.05 mmol, 660 mg) and triethyl amine (1.98 mmol, 200 mg) were added. The reaction mixture was stirred at 80°C for 12 hours, cooled down, and precipitated in ether. The precipitate was washed 3 times in ether and dried *in vacuo*. The product was then dissolved in water and passed through a Sephadex LH-20 column. The product was collected and then lyophilised to give a crystalline brown powder and confirmed by IR stretching frequency shift from 1774 cm⁻¹ to 1693 cm⁻¹.

Self-aligning nanodisc preparation

To a pear flask was added lipid (100 mg DMPC / 5.1 mg DMPG + 94.9 mg DMPC). Chloroform was added until all was dissolved. The solution was slowly evaporated on a rotavap at an angle for 1 hour to make a thin film. The film was then lyophilised overnight to get rid of trace amounts of chloroform. The film was diluted to a 20 mM solution by adding distilled water (7.15 mL). The solution was agitated with a pasteur pipette to make sure everything was dissolved and homogenous, then transferred to seven 1 mL eppendorf tubes. The tubes were freeze thawed three times by alternating between liquid nitrogen and hot water. The tubes were then stored in a freezer (-20°C) until needed.

SMA-QA nanodiscs were prepared by adding a 100mg/mL SMA-QA stock to a final concentration depending on size goal (lipid:SMA-QA ratio of 1:1.5 for 10 nm discs; 1:1 for 20 nm discs; 1:0.25 for 30 nm discs). The combined SMA-QA and lipid mixture was incubated over night at room temperature and purified by SEC (Superdex 200 Increase 200/16 GL column operated on an AKTA purifier (GE Healthcare, Freiburg, Germany)). Fractions containing nanodiscs were combined and upconcentrated using centrifugation filters. Total lipid concentration was determined by ³¹P NMR with 2 µL 5% Trimethyl Phosphate as internal reference. Nanodisc size was confirmed using a Malvern Zetasizer Nano ZS (Malvern Panalytical Ltd, Malvern, United Kingdom). The lipid/disc concentration was calculated according to equation (1).

$$\frac{\text{lipid}}{\text{disc}} = \frac{\pi(r_{\text{Disc}} - r_{\text{SMA}})^2}{A_{\text{LHG}}} \quad (1)$$

where r_{Disc} is half the measured diameter of the nanodisc at 30°C, r_{SMA} is the width of the SMA polymer, and A_{LHG} is the reference value of the DMPC lipid head group at 30°C.

Author contributions: Conceptualisation: J.I. and F.G.R. Nanodisc preparation and NMR: F.G.R. Structure calculations: P.R. Data analysis: F.G.R., P.R., and J.I. Original draft: F.G.R. and J.I. Writing and editing: F.G.R., P.R., and J.I. Supervision: J.I.

Acknowledgements

Funding from the DigiBiotics project (Research Council of Norway, project ID 269425), the AntiBioSpec project of UiT the Arctic University of Norway (Cristin ID 20161326) and the NanoAMP project (Research Council of Norway, project ID 275186) is greatly appreciated.

References

- (1) Hancock, R. E.; Lehrer, R. Cationic peptides: a new source of antibiotics. *Trends Biotechnol* **1998**, *16* (2), 82-88. DOI: S0167-7799(97)01156-6 [pii].
- (2) Hancock, R. E. W.; Chapple, D. S. Peptide antibiotics. *Antimicrob Agents Ch* **1999**, *43* (6), 1317-1323.
- (3) Zasloff, M. Antimicrobial peptides of multicellular organisms. *Nature* **2002**, *415* (6870), 389-395.
- (4) Jenssen, H.; Hamill, P.; Hancock, R. E. W. Peptide antimicrobial agents. *Clin Microbiol Rev* **2006**, *19* (3), 491-+.
- (5) Hancock, R. E. W. Peptide antibiotics. *Lancet* **1997**, *349* (9049), 418-422.
- (6) Robbel, L.; Marahiel, M. A. Daptomycin, a bacterial lipopeptide synthesized by a nonribosomal machinery. *J. Biol. Chem.* **2010**, *285* (36), 27501-27508. DOI: 10.1074/jbc.R110.128181 From NLM Medline.
- (7) Breukink, E.; de Kruijff, B. Lipid II as a target for antibiotics. *Nat Rev Drug Discov* **2006**, *5* (4), 321-332. DOI: 10.1038/nrd2004 From NLM Medline.
- (8) Kupferwasser, L. I.; Skurray, R. A.; Brown, M. H.; Firth, N.; Yeaman, M. R.; Bayer, A. S. Plasmid-mediated resistance to thrombin-induced platelet microbicidal protein in staphylococci: role of the *qacA* locus. *Antimicrob. Agents Chemother.* **1999**, *43* (10), 2395-2399. DOI: 10.1128/AAC.43.10.2395 From NLM Medline.
- (9) Li, Q.; Cebrian, R.; Montalban-Lopez, M.; Ren, H.; Wu, W.; Kuipers, O. P. Outer-membrane-acting peptides and lipid II-targeting antibiotics cooperatively kill Gram-negative pathogens. *Commun Biol* **2021**, *4* (1), 31. DOI: 10.1038/s42003-020-01511-1 From NLM Medline.
- (10) Reddy, K. V.; Yedery, R. D.; Aranha, C. Antimicrobial peptides: premises and promises. *Int J Antimicrob Agents* **2004**, *24* (6), 536-547. DOI: 10.1016/j.ijantimicag.2004.09.005 From NLM Medline.
- (11) Tanphaichitr, N.; Srakaew, N.; Alonzi, R.; Kiattiburut, W.; Kongmanas, K.; Zhi, R.; Li, W.; Baker, M.; Wang, G.; Hickling, D. Potential Use of Antimicrobial Peptides as Vaginal Spermicides/Microbicides. *Pharmaceuticals (Basel)* **2016**, *9* (1). DOI: 10.3390/ph9010013 From NLM PubMed-not-MEDLINE.
- (12) Wang, X.; van Beekveld, R. A. M.; Xu, Y.; Parmar, A.; Das, S.; Singh, I.; Breukink, E. Analyzing mechanisms of action of antimicrobial peptides on bacterial membranes requires multiple complimentary assays and different bacterial strains. *Biochim Biophys Acta Biomembr* **2023**, *1865* (6), 184160. DOI: 10.1016/j.bbamem.2023.184160 From NLM Medline.
- (13) Feng, S.; Liang, W.; Li, J.; Chen, Y.; Zhou, D.; Liang, L.; Lin, D.; Li, Y.; Zhao, H.; Du, H.; et al. MCR-1-dependent lipid remodelling compromises the viability of Gram-negative bacteria. *Emerg Microbes Infect* **2022**, *11* (1), 1236-1249. DOI: 10.1080/22221751.2022.2065934 From NLM Medline.
- (14) Li, B.; Yin, F.; Zhao, X.; Guo, Y.; Wang, W.; Wang, P.; Zhu, H.; Yin, Y.; Wang, X. Colistin Resistance Gene *mcr-1* Mediates Cell Permeability and Resistance to Hydrophobic Antibiotics. *Front Microbiol* **2019**, *10*, 3015. DOI: 10.3389/fmicb.2019.03015 From NLM PubMed-not-MEDLINE.
- (15) Skov, R. L.; Monnet, D. L. Plasmid-mediated colistin resistance (*mcr-1* gene): three months later, the story unfolds. *Euro Surveill* **2016**, *21* (9), 30155. DOI: 10.2807/1560-7917.ES.2016.21.9.30155.
- (16) Birnbaum, J.; Kahan, F. M.; Kropp, H.; MacDonald, J. S. Carbapenems, a new class of beta-lactam antibiotics. Discovery and development of imipenem/cilastatin. *Am J Med* **1985**, *78* (6A), 3-21. DOI: 10.1016/0002-9343(85)90097-x From NLM Medline.
- (17) Clarke, A. M.; Zemcov, S. J. Antibacterial activity of the cephamycin cefotetan: an in-vitro comparison with other beta-lactam antibiotics. *J. Antimicrob. Chemother.* **1983**, *11* Suppl, 67-72. DOI: 10.1093/jac/11.suppl_a.67 From NLM Medline.
- (18) D'Costa, V. M.; King, C. E.; Kalan, L.; Morar, M.; Sung, W. W.; Schwarz, C.; Froese, D.; Zazula, G.; Calmels, F.; Debruyne, R.; et al. Antibiotic resistance is ancient. *Nature* **2011**, *477* (7365), 457-461. DOI: 10.1038/nature10388 From NLM Medline.
- (19) Hall, B. G.; Barlow, M. Evolution of the serine beta-lactamases: past, present and future. *Drug Resist Updat* **2004**, *7* (2), 111-123. DOI: 10.1016/j.drup.2004.02.003 From NLM Medline.
- (20) Schneider, T.; Sahl, H. G. An oldie but a goodie - cell wall biosynthesis as antibiotic target pathway. *Int J Med Microbiol* **2010**, *300* (2-3), 161-169. DOI: 10.1016/j.ijmm.2009.10.005 From NLM Medline.
- (21) Allen, M. M.; Yuen, C.; Medeiros, L.; Zizlsperger, N.; Farooq, M.; Kolodny, N. H. Effects of light and chloramphenicol stress on incorporation of nitrogen into cyanophycin in *Synechocystis* sp. strain PCC 6308. *Biochim. Biophys. Acta* **2005**, *1725* (2), 241-246. DOI: 10.1016/j.bbagen.2005.04.011 From NLM Medline.
- (22) Perron, G. G.; Zasloff, M.; Bell, G. Experimental evolution of resistance to an antimicrobial peptide. *Proc Biol Sci* **2006**, *273* (1583), 251-256, Research Support, Non-U.S. Gov't. DOI: 10.1098/rspb.2005.3301.
- (23) Wimley, W. C.; Hristova, K. Antimicrobial peptides: successes, challenges and unanswered questions. *J. Membr. Biol.* **2011**, *239* (1-2), 27-34. DOI: 10.1007/s00232-011-9343-0 From NLM Medline.
- (24) Jean-Francois, F.; Elezgaray, J.; Berson, P.; Vacher, P.; Dufourc, E. J. Pore formation induced by an antimicrobial peptide: electrostatic effects. *Biophys. J.* **2008**, *95* (12), 5748-5756. DOI: 10.1529/biophysj.108.136655 From NLM Medline.

- (25) Gazit, E.; Boman, A.; Boman, H. G.; Shai, Y. Interaction of the mammalian antibacterial peptide cecropin P1 with phospholipid vesicles. *Biochemistry* **1995**, *34* (36), 11479-11488. DOI: 10.1021/bi00036a021 From NLM Medline.
- (26) Schmidt, N. W.; Wong, G. C. Antimicrobial peptides and induced membrane curvature: geometry, coordination chemistry, and molecular engineering. *Curr. Opin. Solid State Mater. Sci.* **2013**, *17* (4), 151-163. DOI: 10.1016/j.cossms.2013.09.004 From NLM PubMed-not-MEDLINE.
- (27) Bechinger, B.; Lohner, K. Detergent-like actions of linear amphipathic cationic antimicrobial peptides. *Biochim. Biophys. Acta* **2006**, *1758* (9), 1529-1539. DOI: 10.1016/j.bbamem.2006.07.001 From NLM Medline.
- (28) Appelt, C.; Wessolowski, A.; Soderhall, J. A.; Dathe, M.; Schmieder, P. Structure of the antimicrobial, cationic hexapeptide cyclo(RRWRF) and its analogues in solution and bound to detergent micelles. *ChemBioChem* **2005**, *6* (9), 1654-1662. DOI: 10.1002/cbic.200500095 From NLM Medline.
- (29) Roy, A.; Sarangi, N. K.; Ghosh, S.; Prabhakaran, A.; Keyes, T. E. Leaflet by Leaflet Synergistic Effects of Antimicrobial Peptides on Bacterial and Mammalian Membrane Models. *J Phys Chem Lett* **2023**, *14* (16), 3920-3928. DOI: 10.1021/acs.jpcllett.3c00119 From NLM Medline.
- (30) Avci, F. G.; Akbulut, B. S.; Ozkirimli, E. Membrane Active Peptides and Their Biophysical Characterization. *Biomolecules* **2018**, *8* (3). DOI: 10.3390/biom8030077 From NLM Medline.
- (31) Hadjicharalambous, A.; Bournakas, N.; Newman, H.; Skynner, M. J.; Beswick, P. Antimicrobial and Cell-Penetrating Peptides: Understanding Penetration for the Design of Novel Conjugate Antibiotics. *Antibiotics (Basel)* **2022**, *11* (11). DOI: 10.3390/antibiotics11111636 From NLM PubMed-not-MEDLINE.
- (32) Wojciechowska, M.; Miszkiewicz, J.; Trylska, J. Conformational Changes of Anoplin, W-MreB(1-9), and (KFF)(3)K Peptides near the Membranes. *Int J Mol Sci* **2020**, *21* (24). DOI: 10.3390/ijms21249672 From NLM Medline.
- (33) Eiriksdottir, E.; Konate, K.; Langel, U.; Divita, G.; Deshayes, S. Secondary structure of cell-penetrating peptides controls membrane interaction and insertion. *Biochim. Biophys. Acta* **2010**, *1798* (6), 1119-1128. DOI: 10.1016/j.bbamem.2010.03.005 From NLM Medline.
- (34) Claridge, T. D. W. *High-Resolution NMR Techniques*; Elsevier, 2016.
- (35) Ramsey, N. F. Electron Coupled Interactions between Nuclear Spins in Molecules. *Physical Review* **1953**, *91* (2), 303-307. DOI: 10.1103/PhysRev.91.303.
- (36) Ramsey, N. F.; Purcell, E. M. Interactions between Nuclear Spins in Molecules. *Physical Review* **1952**, *85* (1), 143-144. DOI: 10.1103/PhysRev.85.143.
- (37) Farina, B.; Del Gatto, A.; Comegna, D.; Di Gaetano, S.; Capasso, D.; Isernia, C.; Saviano, M.; Fattorusso, R.; Zaccaro, L.; Russo, L. Conformational studies of RGDechi peptide by natural-abundance NMR spectroscopy. *J. Pept. Sci.* **2019**, *25* (5), e3166. DOI: 10.1002/psc.3166 From NLM Medline.
- (38) Wishart, D. S.; Case, D. A. Use of chemical shifts in macromolecular structure determination. *Methods Enzymol.* **2001**, *338*, 3-34. DOI: 10.1016/s0076-6879(02)38214-4 From NLM Medline.
- (39) Wishart, D. S.; Nip, A. M. Protein chemical shift analysis: a practical guide. *Biochem. Cell Biol.* **1998**, *76* (2-3), 153-163. DOI: 10.1139/bcb-76-2-3-153 From NLM Medline.
- (40) Wishart, D. S.; Sykes, B. D. Chemical shifts as a tool for structure determination. *Methods Enzymol.* **1994**, *239*, 363-392. DOI: 10.1016/s0076-6879(94)39014-2 From NLM Medline.
- (41) Wishart, D. S.; Sykes, B. D.; Richards, F. M. The chemical shift index: a fast and simple method for the assignment of protein secondary structure through NMR spectroscopy. *Biochemistry* **1992**, *31* (6), 1647-1651. DOI: 10.1021/bi00121a010 From NLM Medline.
- (42) Schwarzingler, S.; Kroon, G. J.; Foss, T. R.; Chung, J.; Wright, P. E.; Dyson, H. J. Sequence-dependent correction of random coil NMR chemical shifts. *J. Am. Chem. Soc.* **2001**, *123* (13), 2970-2978. DOI: 10.1021/ja003760i From NLM Medline.
- (43) Ting, D.; Wang, G.; Shapovalov, M.; Mitra, R.; Jordan, M. I.; Dunbrack, R. L., Jr. Neighbor-dependent Ramachandran probability distributions of amino acids developed from a hierarchical Dirichlet process model. *PLoS Comput Biol* **2010**, *6* (4), e1000763. DOI: 10.1371/journal.pcbi.1000763 From NLM Medline.
- (44) Tamiola, K.; Acar, B.; Mulder, F. A. Sequence-specific random coil chemical shifts of intrinsically disordered proteins. *J. Am. Chem. Soc.* **2010**, *132* (51), 18000-18003. DOI: 10.1021/ja105656t From NLM Medline.
- (45) Tamiola, K.; Mulder, F. A. Using NMR chemical shifts to calculate the propensity for structural order and disorder in proteins. *Biochem. Soc. Trans.* **2012**, *40* (5), 1014-1020. DOI: 10.1042/BST20120171 From NLM Medline.
- (46) Dinku, W.; Isaksson, J.; Rylandsholm, F. G.; Bour, P.; Brichtová, E.; Choi, S. U.; Lee, S. H.; Jung, Y. S.; No, Z. S.; Svendsen, J. S. M.; et al. Anti-proliferative activity of a novel tricyclic triterpenoid acid from resin against four human cancer cell lines. *Applied Biological Chemistry* **2020**, *63* (1). DOI: 10.1186/s13765-020-00499-w.
- (47) Sarfati, M.; Courtieu, J.; Lesot, P. First successful enantiomeric discrimination of chiral alkanes using NMR spectroscopy. *Chem. Commun.* **2000**, (13), 1113-1114. DOI: 10.1039/b002806l.

- (48) Thiele, C. M. Simultaneous assignment of all diastereotopic protons in strychnine using RDCs: PELG as alignment medium for organic molecules. *J. Org. Chem.* **2004**, *69* (22), 7403-7413. DOI: 10.1021/jo049867w From NLM Medline.
- (49) Thiele, C. M.; Berger, S. Probing the diastereotopicity of methylene protons in strychnine using residual dipolar couplings. *Org. Lett.* **2003**, *5* (5), 705-708. DOI: 10.1021/ol0275163 From NLM PubMed-not-MEDLINE.
- (50) Meyer, N. C.; Krupp, A.; Schmidts, V.; Thiele, C. M.; Reggelin, M. Polyacetylenes as enantiodifferentiating alignment media. *Angew. Chem. Int. Ed. Engl.* **2012**, *51* (33), 8334-8338. DOI: 10.1002/anie.201201891 From NLM Medline.
- (51) Marx, A.; Schmidts, V.; Thiele, C. M. How different are diastereomorphous orientations of enantiomers in the liquid crystalline phases of PBLG and PBDG: a case study. *Magn. Reson. Chem.* **2009**, *47* (9), 734-740. DOI: 10.1002/mrc.2454 From NLM Medline.
- (52) Montag, T.; Thiele, C. M. Cross-linked helically chiral poly-(gamma-benzyl-L-glutamate) as enantiodiscriminating alignment medium. *Chemistry* **2013**, *19* (7), 2271-2274. DOI: 10.1002/chem.201202554 From NLM Medline.
- (53) Krupp, A.; Reggelin, M. Phenylalanine-based polyarylacetylenes as enantiomer-differentiating alignment media. *Magn. Reson. Chem.* **2012**, *50 Suppl 1*, S45-52. DOI: 10.1002/mrc.3894 From NLM Medline.
- (54) Luy, B.; Kobzar, K.; Kessler, H. An easy and scalable method for the partial alignment of organic molecules for measuring residual dipolar couplings. *Angew. Chem. Int. Ed. Engl.* **2004**, *43* (9), 1092-1094. DOI: 10.1002/anie.200352860 From NLM PubMed-not-MEDLINE.
- (55) Gayathri, C.; Tsarevsky, N. V.; Gil, R. R. Residual dipolar couplings (RDCs) analysis of small molecules made easy: fast and tuneable alignment by reversible compression/relaxation of reusable PMMA Gels. *Chemistry* **2010**, *16* (12), 3622-3626. DOI: 10.1002/chem.200903378 From NLM PubMed-not-MEDLINE.
- (56) Luy, B.; Kobzar, K.; Knor, S.; Furrer, J.; Heckmann, D.; Kessler, H. Orientational properties of stretched polystyrene gels in organic solvents and the suppression of their residual ¹H NMR signals. *J. Am. Chem. Soc.* **2005**, *127* (17), 6459-6465. DOI: 10.1021/ja043344o From NLM PubMed-not-MEDLINE.
- (57) Freudenberger, J. C.; Spittler, P.; Bauer, R.; Kessler, H.; Luy, B. Stretched poly(dimethylsiloxane) gels as NMR alignment media for apolar and weakly polar organic solvents: an ideal tool for measuring RDCs at low molecular concentrations. *J. Am. Chem. Soc.* **2004**, *126* (45), 14690-14691. DOI: 10.1021/ja046155e From NLM Medline.
- (58) Kobzar, K.; Kessler, H.; Luy, B. Stretched gelatin gels as chiral alignment media for the discrimination of enantiomers by NMR spectroscopy. *Angew. Chem. Int. Ed. Engl.* **2005**, *44* (20), 3145-3147. DOI: 10.1002/anie.200462736 From NLM PubMed-not-MEDLINE.
- (59) Marx, A.; Thiele, C. Orientational properties of poly-gamma-benzyl-L-glutamate: influence of molecular weight and solvent on order parameters of the solute. *Chemistry* **2009**, *15* (1), 254-260. DOI: 10.1002/chem.200801147 From NLM PubMed-not-MEDLINE.
- (60) Liu, Y.; Navarro-Vazquez, A.; Gil, R. R.; Griesinger, C.; Martin, G. E.; Williamson, R. T. Application of anisotropic NMR parameters to the confirmation of molecular structure. *Nat Protoc* **2019**, *14* (1), 217-247. DOI: 10.1038/s41596-018-0091-9.
- (61) Schmidt, M.; Sun, H.; Leonov, A.; Griesinger, C.; Reinscheid, U. M. Chiral discrimination of amines by anisotropic NMR parameters using chiral polyacrylamide-based gels. *Magn. Reson. Chem.* **2012**, *50 Suppl 1*, S38-44. DOI: 10.1002/mrc.3886 From NLM Medline.
- (62) Kummerlöwe, G.; Kiran, M. U.; Luy, B. Covalently cross-linked gelatin allows chiral distinction at elevated temperatures and in DMSO. *Chemistry* **2009**, *15* (45), 12192-12195. DOI: 10.1002/chem.200902193 From NLM Medline.
- (63) Buchler, S. S.; Kummerlöwe, G.; Luy, B. Naturally occurring biodegradable polymers as the basis of chiral gels for the distinction of enantiomers by partially oriented NMR spectroscopy. *Int J Artif Organs* **2011**, *34* (2), 134-138. DOI: 10.5301/ijao.2011.6419 From NLM Medline.
- (64) Pracht, P.; Bohle, F.; Grimme, S. Automated exploration of the low-energy chemical space with fast quantum chemical methods. *Phys. Chem. Chem. Phys.* **2020**, *22* (14), 7169-7192. DOI: 10.1039/c9cp06869d From NLM PubMed-not-MEDLINE.
- (65) Barone, V.; Cossi, M. Quantum Calculation of Molecular Energies and Energy Gradients in Solution by a Conductor Solvent Model. *The Journal of Physical Chemistry A* **1998**, *102* (11), 1995-2001. DOI: 10.1021/jp9716997.
- (66) Cossi, M.; Rega, N.; Scalmani, G.; Barone, V. Energies, structures, and electronic properties of molecules in solution with the C-PCM solvation model. *J. Comput. Chem.* **2003**, *24* (6), 669-681. DOI: 10.1002/jcc.10189 From NLM PubMed-not-MEDLINE.
- (67) Jiang, F.; Geng, H. Computational Methods for Studying Conformational Behaviors of Cyclic Peptides. *Methods Mol Biol* **2019**, *2001*, 61-71. DOI: 10.1007/978-1-4939-9504-2_4 From NLM Medline.

- (68) Rainsford, P.; Rylandsholm, F. G.; Jakubec, M.; Silk, M.; Juskewitz, E.; Ericson, J. U.; Svendsen, J. S.; Engh, R. A.; Isaksson, J. Label-free measurement of antimicrobial peptide interactions with lipid vesicles and nanodiscs using microscale thermophoresis. *Sci Rep* **2023**, *13* (1), 12619. DOI: 10.1038/s41598-023-39785-0 From NLM Medline.
- (69) Jakubec, M.; Rylandsholm, F. G.; Rainsford, P.; Silk, M.; Bril'kov, M.; Kristoffersen, T.; Juskewitz, E.; Ericson, J. U.; Svendsen, J. S. M. Goldilocks Dilemma: LPS Works Both as the Initial Target and a Barrier for the Antimicrobial Action of Cationic AMPs on *E. coli*. *Biomolecules* **2023**, *13* (7). DOI: 10.3390/biom13071155.
- (70) Eikås, K. D. R.; Rylandsholm, F. G.; Kristoffersen, T.; Jakubec, M.; Silk, M. R.; Svendsen, J. S. M.; Isaksson, J.; Ruud, K.; Krupová, M. Conformational Studies of Cyclic Hexapeptides with Vibrational Circular Dichroism and Nuclear Magnetic Resonance. .
- (71) Wüthrich, K. *NMR of Proteins and Nucleic Acids*; Wiley, 1986.
- (72) Appelt, C.; Wessolowski, A.; Dathe, M.; Schmieder, P. Structures of cyclic, antimicrobial peptides in a membrane-mimicking environment define requirements for activity. *J. Pept. Sci.* **2008**, *14* (4), 524-527. DOI: 10.1002/psc.924 From NLM Medline.
- (73) Ravula, T.; Ramadugu, S. K.; Di Mauro, G.; Ramamoorthy, A. Bioinspired, Size-Tunable Self-Assembly of Polymer-Lipid Bilayer Nanodiscs. *Angew. Chem. Int. Ed. Engl.* **2017**, *56* (38), 11466-11470. DOI: 10.1002/anie.201705569.
- (74) Ravula, T.; Hardin, N. Z.; Ramadugu, S. K.; Cox, S. J.; Ramamoorthy, A. Formation of pH-Resistant Monodispersed Polymer-Lipid Nanodiscs. *Angew. Chem. Int. Ed. Engl.* **2018**, *57* (5), 1342-1345. DOI: 10.1002/anie.201712017.
- (75) Ravula, T.; Hardin, N. Z.; Ramamoorthy, A. Polymer nanodiscs: Advantages and limitations. *Chem. Phys. Lipids* **2019**, *219*, 45-49. DOI: 10.1016/j.chemphyslip.2019.01.010.
- (76) Ravula, T.; Ramamoorthy, A. Magnetic Alignment of Polymer Macro-Nanodiscs Enables Residual-Dipolar-Coupling-Based High-Resolution Structural Studies by NMR Spectroscopy. *Angew. Chem. Int. Ed. Engl.* **2019**, *58* (42), 14925-14928. DOI: 10.1002/anie.201907655.
- (77) Stangl, M.; Veerappan, A.; Kroeger, A.; Vogel, P.; Schneider, D. Detergent properties influence the stability of the glycoporphin A transmembrane helix dimer in lysophosphatidylcholine micelles. *Biophys. J.* **2012**, *103* (12), 2455-2464. DOI: 10.1016/j.bpj.2012.11.004 From NLM Medline.
- (78) Gu, H.; Kato, T.; Kumeta, H.; Kumaki, Y.; Tsukamoto, T.; Kikukawa, T.; Demura, M.; Ishida, H.; Vogel, H. J.; Aizawa, T. Three-Dimensional Structure of the Antimicrobial Peptide Cecropin P1 in Dodecylphosphocholine Micelles and the Role of the C-Terminal Residues. *ACS Omega* **2022**, *7* (36), 31924-31934. DOI: 10.1021/acsomega.2c02778 From NLM PubMed-not-MEDLINE.
- (79) Terakawa, M. S.; Lin, Y.; Kinoshita, M.; Kanemura, S.; Itoh, D.; Sugiki, T.; Okumura, M.; Ramamoorthy, A.; Lee, Y. H. Impact of membrane curvature on amyloid aggregation. *Biochim Biophys Acta Biomembr* **2018**, *1860* (9), 1741-1764. DOI: 10.1016/j.bbamem.2018.04.012 From NLM PubMed-not-MEDLINE.
- (80) Stepien, P.; Augustyn, B.; Poojari, C.; Galan, W.; Polit, A.; Vattulainen, I.; Wisniewska-Becker, A.; Rog, T. Complexity of seemingly simple lipid nanodiscs. *Biochim Biophys Acta Biomembr* **2020**, *1862* (11), 183420. DOI: 10.1016/j.bbamem.2020.183420 From NLM Medline.
- (81) Bibow, S.; Carneiro, M. G.; Sabo, T. M.; Schwiegk, C.; Becker, S.; Riek, R.; Lee, D. Measuring membrane protein bond orientations in nanodiscs via residual dipolar couplings. *Protein Sci.* **2014**, *23* (7), 851-856. DOI: 10.1002/pro.2482 From NLM Medline.
- (82) Kučerka, N.; Liu, Y.; Chu, N.; Petrache, H. I.; Tristram-Nagle, S.; Nagle, J. F. Structure of Fully Hydrated Fluid Phase DMPC and DLPC Lipid Bilayers Using X-Ray Scattering from Oriented Multilamellar Arrays and from Unilamellar Vesicles. *Biophys. J.* **2005**, *88* (4), 2626-2637. DOI: 10.1529/biophysj.104.056606.
- (83) Hu, M.; de Jong, D. H.; Marrink, S. J.; Deserno, M. Gaussian curvature elasticity determined from global shape transformations and local stress distributions: a comparative study using the MARTINI model. *Faraday Discuss.* **2013**, *161*, 365-382; discussion 419-359. DOI: 10.1039/c2fd20087b From NLM Medline.
- (84) Marsh, D. *Handbook of Lipid Bilayers*; CRC Press, 2013.
- (85) Dorr, J. M.; Scheidelaar, S.; Koorengevel, M. C.; Dominguez, J. J.; Schafer, M.; van Walree, C. A.; Killian, J. A. The styrene-maleic acid copolymer: a versatile tool in membrane research. *Eur Biophys J* **2016**, *45* (1), 3-21. DOI: 10.1007/s00249-015-1093-y From NLM Medline.
- (86) Huang, J.; MacKerell, A. D., Jr. CHARMM36 all-atom additive protein force field: validation based on comparison to NMR data. *J. Comput. Chem.* **2013**, *34* (25), 2135-2145. DOI: 10.1002/jcc.23354 From NLM Medline.
- (87) Jo, S.; Kim, T.; Iyer, V. G.; Im, W. CHARMM-GUI: a web-based graphical user interface for CHARMM. *J. Comput. Chem.* **2008**, *29* (11), 1859-1865. DOI: 10.1002/jcc.20945 From NLM Medline.
- (88) Lee, J.; Cheng, X.; Swails, J. M.; Yeom, M. S.; Eastman, P. K.; Lemkul, J. A.; Wei, S.; Buckner, J.; Jeong, J. C.; Qi, Y.; et al. CHARMM-GUI Input Generator for NAMD, GROMACS, AMBER, OpenMM, and

- CHARMM/OpenMM Simulations Using the CHARMM36 Additive Force Field. *J Chem Theory Comput* **2016**, *12* (1), 405-413. DOI: 10.1021/acs.jctc.5b00935 From NLM Medline.
- (89) Phillips, J. C.; Hardy, D. J.; Maia, J. D. C.; Stone, J. E.; Ribeiro, J. V.; Bernardi, R. C.; Buch, R.; Fiorin, G.; Henin, J.; Jiang, W.; et al. Scalable molecular dynamics on CPU and GPU architectures with NAMD. *J. Chem. Phys.* **2020**, *153* (4), 044130. DOI: 10.1063/5.0014475 From NLM PubMed-not-MEDLINE.
- (90) Rainsford, P.; Sarre, B. R.; Falavigna, M.; Brandsdal, B. O.; Flaten, G. E.; Jakubec, M.; Isaksson, J. WIND-PVPA: Water/Ion NMR Detected PVPA to assess lipid barrier integrity in vitro through quantification of passive water- and ion transport. *Biochim Biophys Acta Biomembr* **2022**, *1864* (7), 183911. DOI: 10.1016/j.bbamem.2022.183911 From NLM Medline.
- (91) Hong, C.; Tieleman, D. P.; Wang, Y. Microsecond molecular dynamics simulations of lipid mixing. *Langmuir* **2014**, *30* (40), 11993-12001. DOI: 10.1021/la502363b From NLM Medline.
- (92) Humphrey, W.; Dalke, A.; Schulten, K. VMD: visual molecular dynamics. *J Mol Graph* **1996**, *14* (1), 33-38, 27-38. DOI: 10.1016/0263-7855(96)00018-5 From NLM Medline.

Supporting information

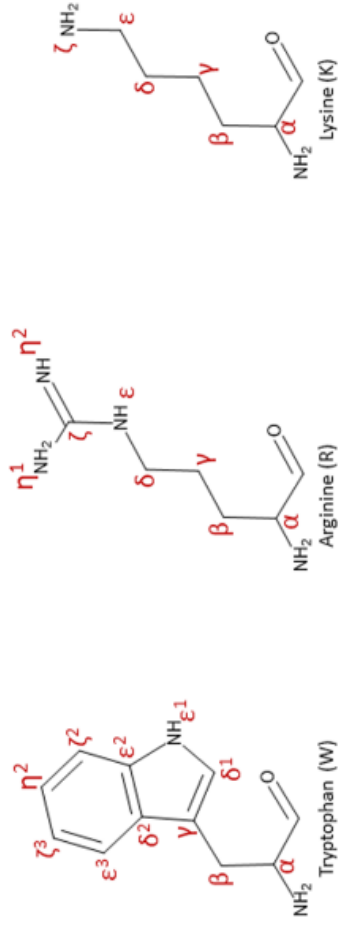


Figure S 1. Numbering of atoms on amino acids sidechains with Greek letters.

The chemical shifts of the four cyclic hexapeptides in water are already published,⁶⁹ but they are added in the Supporting information for convenience.

Table S1. Full assignment of c(WWWKKK) in water.

c(WWWKKK)														
Residue #	Amino acid	Chemical shift (δ)												
		NH α	CO	α	β	ϵ 1	δ 1	γ	δ 2	ϵ 3	ζ 3	η 2	ζ 2	ϵ 2
1	W - Tryptophan													
	^1H	7.85		4.48	2.99/2.86	10.10	7.06			7.46	7.09	7.17	7.41	
	$^{13}\text{C}/^{15}\text{N}$	118.01	173.41	54.70	26.00	129.28	124.45	108.96	127.01	118.48	119.41	122.04	111.98	136.34
2	W - Tryptophan													
	^1H	7.33		4.51	3.11/2.87	10.05	6.95			7.30	7.05	7.15	7.39	
	$^{13}\text{C}/^{15}\text{N}$	119.00	172.67	54.55	26.36	130.00	124.76	108.30	127.06	118.30	119.59	122.16	112.04	136.20
3	W - Tryptophan													
	^1H	7.55		4.45	3.06/2.76	10.07	6.92			7.30	7.02	7.11	7.33	
	$^{13}\text{C}/^{15}\text{N}$	121.25	172.67	55.19	26.06	129.56	124.19	108.54	126.86	118.30	119.44	122.05	111.94	136.24
4	K - Lysine													
	^1H	7.84		3.75	1.49/1.67	0.66	1.30/1.58	2.26	7.41					
	$^{13}\text{C}/^{15}\text{N}$	120.75	173.08	54.90	30.07	21.86	26.19	39.24	96.51					
5	K - Lysine													
	^1H	8.03		4.10	1.51	1.68/1.50	1.32/1.24	2.88	7.46					
	$^{13}\text{C}/^{15}\text{N}$	119.47	173.29	53.60	28.83	30.06	22.34	39.43	96.73					
6	K - Lysine													
	^1H	7.77		3.88	1.22	0.85/0.74	1.33	2.61	7.37					
	$^{13}\text{C}/^{15}\text{N}$	119.35	173.76	54.55	29.43	21.86	39.24	96.52						

Table S2. Full assignment of c(WKWKWK) in water.

c(WKWKWK)														
Residue #	Amino acid	Chemical shift (δ)												
		NH α	CO	α	β	ϵ 1	δ 1	γ	δ 2	ϵ 3	ζ 3	η 2	ζ 2	ϵ 2
1	W - Tryptophan	7.99		4.54	3.09	10.17	7.16							
	^1H								7.52	7.10	7.17	7.37		
	$^{13}\text{C}/^{15}\text{N}$	119.292	173.01	54.66	25.99	129.67	124.35	108.77	127.06	118.37	119.46	122.03	112.04	136.21
2	K - Lysine	NH α	CO	α	β	γ	δ	ϵ	ζ					
	^1H	7.62		3.89	1.42	0.67	1.28	2.55	7.35					
	$^{13}\text{C}/^{15}\text{N}$	120.24	172.91	54.55	29.59	21.59	26.21	39.25	134.12/95.83					

Table S3. Full assignment of c(WRWRWR) in water.

c(WRWRWR)														
Residue #	Amino acid	Chemical shift (δ)												
		NH α	CO	α	β	ϵ 1	δ 1	γ	δ 2	ϵ 3	ζ 3	η 2	ζ 2	ϵ 2
1	W - Tryptophan	8.07		4.54	3.13	10.13	7.16							
	^1H								7.53	7.10	7.16	7.37		
	$^{13}\text{C}/^{15}\text{N}$	119.43	172.84	54.84	26.04	129.65	124.44	108.78	126.96	118.23	119.39	122.07	111.97	136.23
2	R - Arginine	NH α	CO	α	β	γ	δ	ϵ	ζ	η 1	η 2			
	^1H	7.65		3.90	1.41	0.82	2.71	6.77						
	$^{13}\text{C}/^{15}\text{N}$	119.96	172.88	54.39	27.28	23.71	40.44	84.78	153.71					

Table S4. Full assignment of c(WWRRRR) in water.

c(WWWRRR)

Residue #	Amino acid	Chemical shift (δ)													
		NH α	CO	α	β	ϵ 1	δ 1	γ	δ 2	ϵ 3	ζ 3	η 2	ζ 2	ϵ 2	
1	W - Tryptophan														
	^1H	7.88		4.52	2.85/3.04	10.03	7.04			7.46	7.07	7.15	7.38		
	$^{13}\text{C}/^{15}\text{N}$	118.00	173.20	54.68	26.04	129.05	124.44	109.20	126.79	118.31	119.29	122.02	111.89	136.27	
2	W - Tryptophan														
	^1H	7.42		4.54	2.98/3.03	10.05	7.02			7.38	7.08	7.16	7.40		
	$^{13}\text{C}/^{15}\text{N}$	119.05	172.55	54.36	26.68	130.00	124.76	108.40	127.37	118.30	119.44	122.03	112.02	136.22	
3	W - Tryptophan														
	^1H	7.64		4.43	2.85/3.05	10.03	6.94			7.36	7.04	7.12	7.33		
	$^{13}\text{C}/^{15}\text{N}$	121.23	173.10	55.49	26.04	129.50	124.27	108.40	126.82	118.17	119.34	122.03	111.87	136.23	
4	R - Arginine														
	^1H	7.94		3.72	1.58/1.50	0.74/0.87	2.75/2.73	6.77							
	$^{13}\text{C}/^{15}\text{N}$	120.23	172.89	54.85	26.37	24.11	40.38	85.03	156.63						
5	R - Arginine														
	^1H	8.15		4.18	1.48/1.75	1.49	3.11	7.12							
	$^{13}\text{C}/^{15}\text{N}$	119.02	172.78	53.24	27.98	24.43	40.54	84.97	156.89						
6	R - Arginine														
	^1H	7.87		3.85	1.29/1.24	0.85/0.93	2.78/2.72	6.80							
	$^{13}\text{C}/^{15}\text{N}$	119.50	173.54	54.83	27.01	23.76	40.21	84.97	156.57						

Table S5. Full assignment of c(WWWKKK) in DMSO.

c(WWWKKK)												
Residue #	Amino acid	Chemical shift (δ)										
		NH α	CO	α	β	ϵ_1	δ_1	γ	δ_2	ϵ_2	ζ	η
1	W - Tryptophan	8.07		4.23	3.11/3.27	10.84	7.10		7.57	6.99	7.09	7.35
	¹³ C/ ¹⁵ N	116.17	171.17	55.38	26.78	131.28	123.95	110.71	127.63	118.34	118.79	121.45
2	W - Tryptophan											
	¹³ C/ ¹⁵ N	7.94		4.31	3.03/3.11	10.80	7.06		7.51	6.98	7.08	7.34
3	W - Tryptophan	116.96	171.36	55.17	27.41	131.12	124.10	110.92	127.68	118.69	118.79	121.45
	¹³ C/ ¹⁵ N	8.20		4.31	3.11/3.28	10.81	7.06		7.51	6.98	7.08	7.34
4	K - Lysine	118.75	171.36	55.86	27.00	131.12	123.81	110.60	127.66	118.69	118.79	121.45
	¹³ C/ ¹⁵ N											
5	K - Lysine	8.21		3.94	1.74/1.79	1.15	1.47	2.68	7.66			
	¹³ C/ ¹⁵ N	116.67		54.38	30.23	22.99	22.98	39.16	133.24			
6	K - Lysine	8.00		4.12	1.72/1.78	1.32/1.38	1.55	2.76	7.67			
	¹³ C/ ¹⁵ N	115.23	171.82	53.45	30.87	22.75	22.71	39.27	133.24			
6	K - Lysine	8.03		3.87	1.55	0.98/1.12	1.39	2.59	7.67			
	¹³ C/ ¹⁵ N	116.56	171.55	54.54	30.58	22.62	22.74	39.08	133.24			

Table S6. Full assignment of c(WKWKWK) in DMSO.

c(WKWKWK)														
Residue #	Amino acid	Chemical shift (δ)												
		NH α	CO	α	β	ϵ 1	δ 1	γ	δ 2	ϵ 3	ζ 3	η 2	ζ 2	ϵ 2
1	W - Tryptophan	8.15		4.37	3.16/3.25	10.85	7.17			7.58	7.00	7.08	7.35	
	¹³ C/ ¹⁵ N	117.10	171.58	55.20	27.11	131.24	123.92	110.70	127.65	118.84	118.84	121.48	111.83	136.40
2	K -Lysine	8.03		3.89	1.60	1.00	1.38	2.58						
	¹³ C/ ¹⁵ N	116.70	171.44	54.41	30.56	22.69	27.12	39.13						
3	W - Tryptophan	8.15		4.37	3.16/3.25	10.85	7.17			7.58	7.00	7.08	7.35	
	¹³ C/ ¹⁵ N	117.10	171.58	55.20	27.11	131.24	123.92	110.70	127.65	118.84	118.84	121.48	111.83	136.40
4	K -Lysine	8.03		3.89	1.60	1.00	1.38	2.58						
	¹³ C/ ¹⁵ N	116.70	171.44	54.41	30.56	22.69	27.12	39.13						
5	W - Tryptophan	8.15		4.37	3.16/3.25	10.85	7.17			7.58	7.00	7.08	7.35	
	¹³ C/ ¹⁵ N	117.10	171.58	55.20	27.11	131.24	123.92	110.70	127.65	118.84	118.84	121.48	111.83	136.40
6	K -Lysine	8.03		3.89	1.60	1.00	1.38	2.58						
	¹³ C/ ¹⁵ N	116.70	171.44	54.41	30.56	22.69	27.12	39.13						

Table S7. Full assignment of c(WRWRWR) in DMSO.

c(WRWRWR)														
Residue #	Amino acid	Chemical shift (δ)												
		NH α	CO	α	β	ϵ_1	δ_1	γ	δ_2	ϵ_3	ζ_3	η_2	ζ_2	ϵ_2
1	W - Tryptophan	8.15		4.36	3.18/3.27	10.78	7.16			7.57	7.00	7.08	7.35	
	¹³ C/ ¹⁵ N	116.85	171.46	55.26	27.11	131.07	123.91	110.68	127.60	118.75	118.86	121.53	111.89	136.68
2	R - Arginine						δ	ϵ	ζ	η_1	η_2			
	¹³ C/ ¹⁵ N	8.11		3.94	1.57/1.70	1.26/1.29	2.98	7.45						
3	W - Tryptophan	116.92	171.54	54.04	28.27	25.36	40.79	84.97	157.22					
	¹³ C/ ¹⁵ N	8.15		4.36	3.18/3.27	10.78	7.16			7.57	7.00	7.08	7.35	
4	R - Arginine						δ	ϵ	ζ	η_1	η_2			
	¹³ C/ ¹⁵ N	116.85	171.46	55.26	27.11	131.07	123.91	110.68	127.60	118.75	118.86	121.53	111.89	
5	W - Tryptophan	8.11		3.94	1.57/1.70	1.26/1.29	2.98	7.45						
	¹³ C/ ¹⁵ N	116.92	171.54	54.04	28.27	25.36	40.79	84.97	157.22					
6	R - Arginine						δ	ϵ	ζ	η_1	η_2			
	¹³ C/ ¹⁵ N	8.11		3.94	1.57/1.70	1.26/1.29	2.98	7.45						

Table S8. Full assignment of c(WWRRRR) in DMSO.

c(WWRRRR)															
Residue #	Amino acid	Chemical shift (δ)													
		NH α	CO	α	β	ϵ 1	δ 1	γ	δ 2	ϵ 3	ζ 3	η 2	ζ 2	ϵ 2	
1	W - Tryptophan	8.04		4.27	2.99/3.08	10.76	7.04			7.52	6.97	7.07	7.34		
	¹³ C/ ¹⁵ N	116.61	171.27	55.27	27.16	130.99	123.81	110.76	127.40	118.65	118.81	121.47	112.14	136.64	
2	W - Tryptophan		NH α	CO	α	β	ϵ 1	δ 1	γ	δ 2	ϵ 3	ζ 3	η 2	ζ 2	ϵ 2
	¹ H	7.96		4.30	3.00/3.09	10.79	6.99			7.52	6.97	7.07	7.34		
3	W - Tryptophan		NH α	CO	α	β	ϵ 1	δ 1	γ	δ 2	ϵ 3	ζ 3	η 2	ζ 2	ϵ 2
	¹³ C/ ¹⁵ N	117.24	171.53	55.19	27.42	131.20	123.90	110.66	127.56	118.65	118.81	121.47	112.14	136.64	
4	W - Tryptophan		NH α	CO	α	β	ϵ 1	δ 1	γ	δ 2	ϵ 3	ζ 3	η 2	ζ 2	ϵ 2
	¹ H	8.22		4.32	3.12/3.27	10.82	7.11			7.58	7.00	7.08	7.36		
5	R - Arginine		NH α	CO	α	β	γ	δ	ϵ	ζ	η 1	η 2			
	¹ H	8.32		3.99	1.71/1.86	1.41	3.07	7.61							
6	R - Arginine		NH α	CO	α	β	γ	δ	ϵ	ζ	η 1	η 2			
	¹³ C/ ¹⁵ N	116.86	171.75	54.07	27.99	25.62	40.86	85.03							
7	R - Arginine		NH α	CO	α	β	γ	δ	ϵ	ζ	η 1	η 2			
	¹ H	8.18		4.08	1.71/1.85	1.53	3.11	7.68							
8	R - Arginine		NH α	CO	α	β	γ	δ	ϵ	ζ	η 1	η 2			
	¹³ C/ ¹⁵ N	116.05	171.66	53.74	28.31	25.54	40.86	84.92							
9	R - Arginine		NH α	CO	α	β	γ	δ	ϵ	ζ	η 1	η 2			
	¹ H	8.11		3.95	1.58/1.68	1.25/1.36	3.00	7.56							
10	R - Arginine		NH α	CO	α	β	γ	δ	ϵ	ζ	η 1	η 2			
	¹³ C/ ¹⁵ N	116.54	171.26	54.22	28.12	25.37	40.70	84.89							

Table S9. Full assignment of c(WWWKKK) in SDS-d25 micelles.

c(WWWKKK)													
Residue #	Amino acid	Chemical shift (δ)											
		NH α	CO	α	β	ϵ 1	δ 1	γ	δ 2				
1	W - Tryptophan	8.12		4.27	3.17/2.81	9.84	7.12			7.41	6.95	7.00	7.34
	$^{13}\text{C}/^{15}\text{N}$	119.05		55.24		128.72	123.39	108.80	127.60	117.91	118.89	118.92	111.65
2	W - Tryptophan												
	$^{13}\text{C}/^{15}\text{N}$	7.91		4.42	2.48/2.78	9.84	7.36			7.19	6.49	6.91	7.21
3	W - Tryptophan	116.67		54.80		128.78	111.73	111.46	127.41	117.96	123.19	121.54	111.42
	$^{13}\text{C}/^{15}\text{N}$	116.67		54.80		128.78	111.73	111.46	127.41	117.96	123.19	121.54	111.42
4	K - Lysine	7.91		4.71	3.18/3.44	9.84	7.28			7.34	7.00	7.06	7.37
	$^{13}\text{C}/^{15}\text{N}$	120.20		56.03	29.52	22.21	123.90	109.75	128.2	111.65	118.92	121.49	111.75
5	K - Lysine	7.92		4.12	1.70	1.27/1.37	1.62	2.91	7.37				
	$^{13}\text{C}/^{15}\text{N}$	116.67		54.23	30.49	22.56	26.13	39.47	160.04				
6	K - Lysine	7.22		3.92	1.10/1.20	0.51/0.70	1.04/1.22	2.45/2.58	7.23				
	$^{13}\text{C}/^{15}\text{N}$	117.70		53.59	31.49	21.56	25.88	39.30	160.00				

Table S10. Full assignment of c(WKWKWK) in SDS-d25 micelles.

c(WKWKWK)													
Residue #	Amino acid	Chemical shift (δ)											
		NH α	CO	α	β	ϵ_1	ϵ_2	ϵ_3	ζ_1	ζ_2	ζ_3	ζ_4	
1	W - Tryptophan			4.48	3.24/3.41	9.93	7.30		7.64	7.02	6.99	7.36	
	^1H												
	$^{13}\text{C}/^{15}\text{N}$	55.96	48.99	129.57	123.77	109.08	128.02	117.67	119.03	121.55	111.88	136.17	
2	K - Lysine	NH α	CO	α	β	γ	δ	ϵ	ζ				
	^1H			3.88	1.08	0.38/0.47	1.06/1.15	2.58	7.26				
	$^{13}\text{C}/^{15}\text{N}$	54.55	30.22	21.28	26.08	39.28	96.16						

Table S11. Full assignment of c(WRWRWR) in SDS-d25 micelles.

c(WRWRWR)													
Residue #	Amino acid	Chemical shift (δ)											
		NH α	CO	α	β	ϵ_1	ϵ_2	ϵ_3	ζ_1	ζ_2	ζ_3	ζ_4	
1	W - Tryptophan			4.50	3.32/3.41	9.89	7.31		7.68	7.03	6.98	7.36	
	^1H												
	$^{13}\text{C}/^{15}\text{N}$	7.31		129.50	123.96	109.28	128.19	117.80	119.04	121.25	111.71	136.11	
2	R - Arginine	NH α	CO	α	β	γ	δ	ϵ	ζ	η_1	η_2		
	^1H			3.92	1.15	0.48	2.44	6.53					
	$^{13}\text{C}/^{15}\text{N}$	7.19		54.37	27.92	23.30	2.56	83.97					

Table S12. Full assignment of c(WWRRR) in SDS-d25 micelles.

c(WWWRRR)

Residue #	Amino acid	Chemical shift (δ)													
		NH α	CO	α	β	ϵ 1	δ 1	γ	δ 2	ϵ 3	ζ 3	η 2	ζ 2	ϵ 2	
1	W - Tryptophan														
	¹ H	8.03		4.26	2.77/3.00	9.73	7.08			7.40	6.95	6.99	7.32		
	¹³ C/ ¹⁵ N	118.8		40.71		128.67	123.64	109.05	118.10	121.45	121.46	118.16	136.16		
2	W - Tryptophan														
	¹ H	7.40		4.44	2.62/2.74	9.70	7.18		7.30						
	¹³ C/ ¹⁵ N	127.06				128.90	123.88						136.04		
3	W - Tryptophan														
	¹ H	7.17		4.66	3.24	9.67	7.17		7.40	6.95	6.99	7.32			
	¹³ C/ ¹⁵ N					128.79	123.84	109.50	118.10	121.45	121.46	118.16	135.96		
4	R - Arginine														
	¹ H	7.71		3.91	1.66/1.53	1.13/1.20	2.90	6.87							
	¹³ C/ ¹⁵ N	120.81			27.52	24.45	40.62	84.19							
5	R - Arginine														
	¹ H	7.93		4.10	1.72/1.84	1.51	3.14	7.07							
	¹³ C/ ¹⁵ N	116.93				25.07	40.70	83.91							
6	R - Arginine														
	¹ H	7.29		3.94	1.15	0.78/0.95	2.61/2	6.64							
	¹³ C/ ¹⁵ N	117.44			24.32	23.95	40.28	84.02							

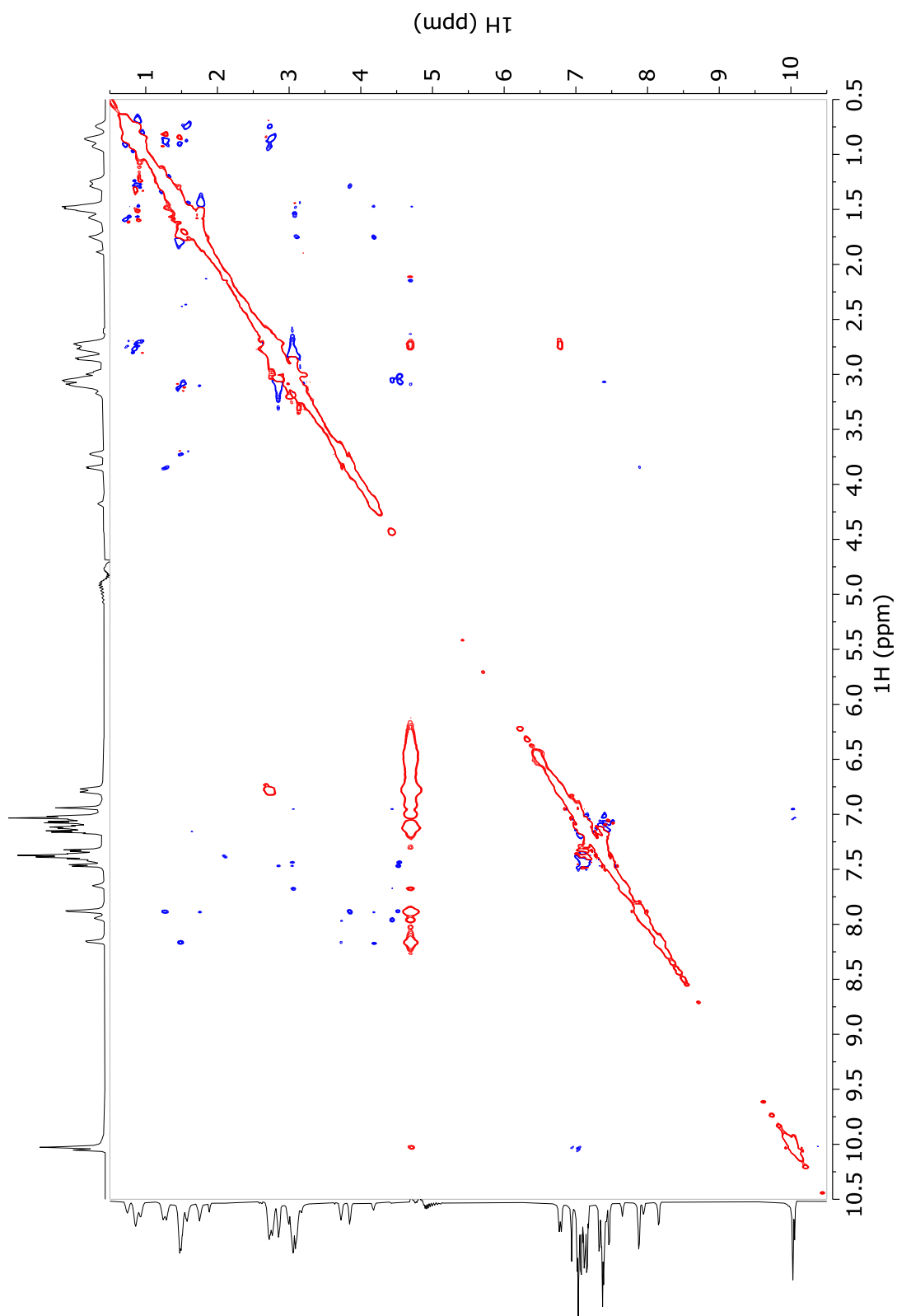


Figure S2. ROESY spectrum of c(WWWRRR) in water at 75 ms mixing time.

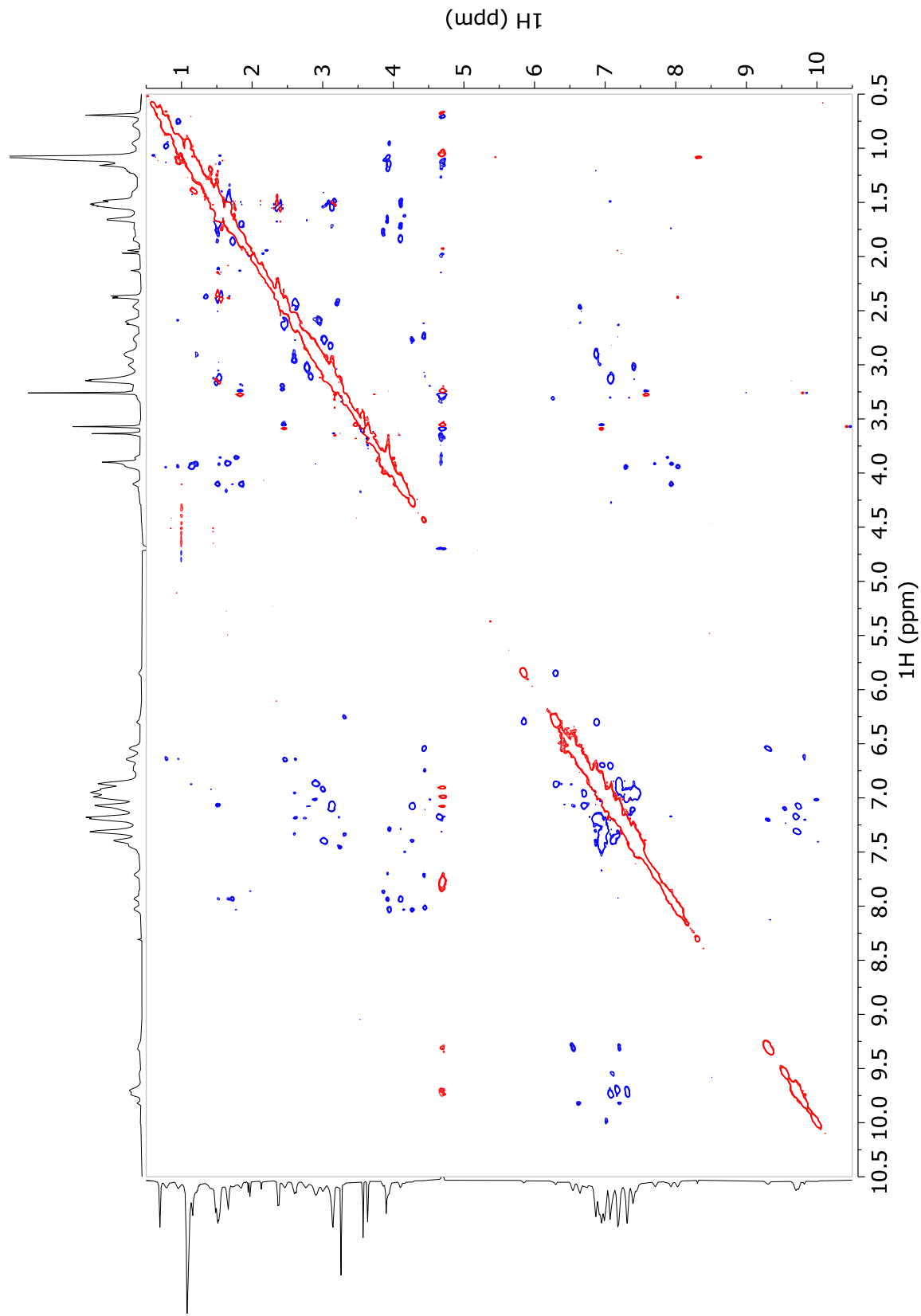
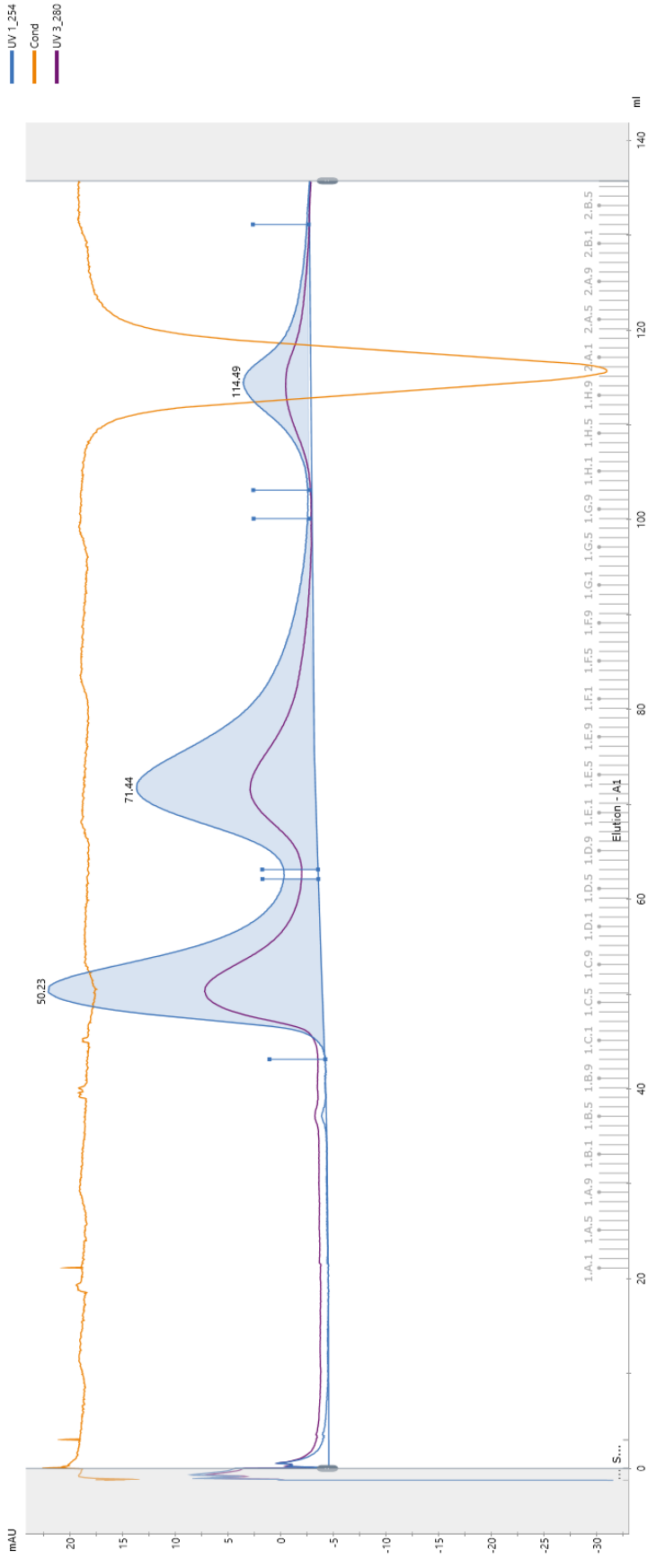


Figure S3. ROESY spectrum of c(WWWRRR) in SDS-d₂₅ at 75 ms mixing time.

2023.05.16 SMA-QA PC large nanodiscs 2 SEC 16 60 200 loop loading 2nd run Not last 001 001

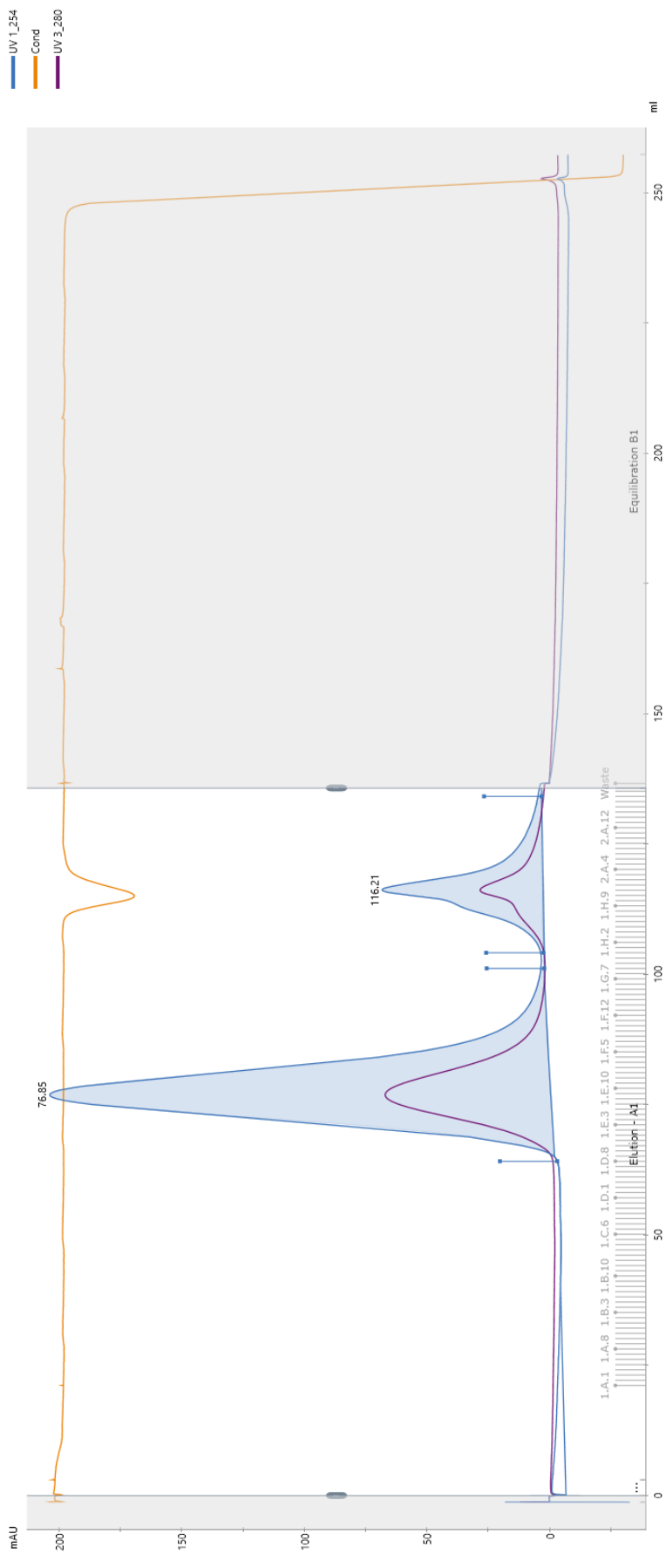


Peak Table - UV_1_254

Peak	Retention min	Area mAU	Area %	Ext coeff. mg/ml * cm ²	Fraction(s)	Volume ml	Conductivity mS/cm
Peak A	50.225	210.7	42.57		1.B.11 - 1.D.5	19.002	11.45
Peak B	71.438	224.3	45.42		1.D.7 - 1.G.7	37.001	11.46
Peak C	114.488	58.83	11.91		1.G.11 - 2.B.2	28.000	11.19

Figure S 4. SEC chromatography output for SMA-QA DMPC nanodiscs at approximately 30 nm diameter.

2023.03.17 SMA-QA PC nanodiscs SEC 16 60 200 loop loading 2nd run 001 001

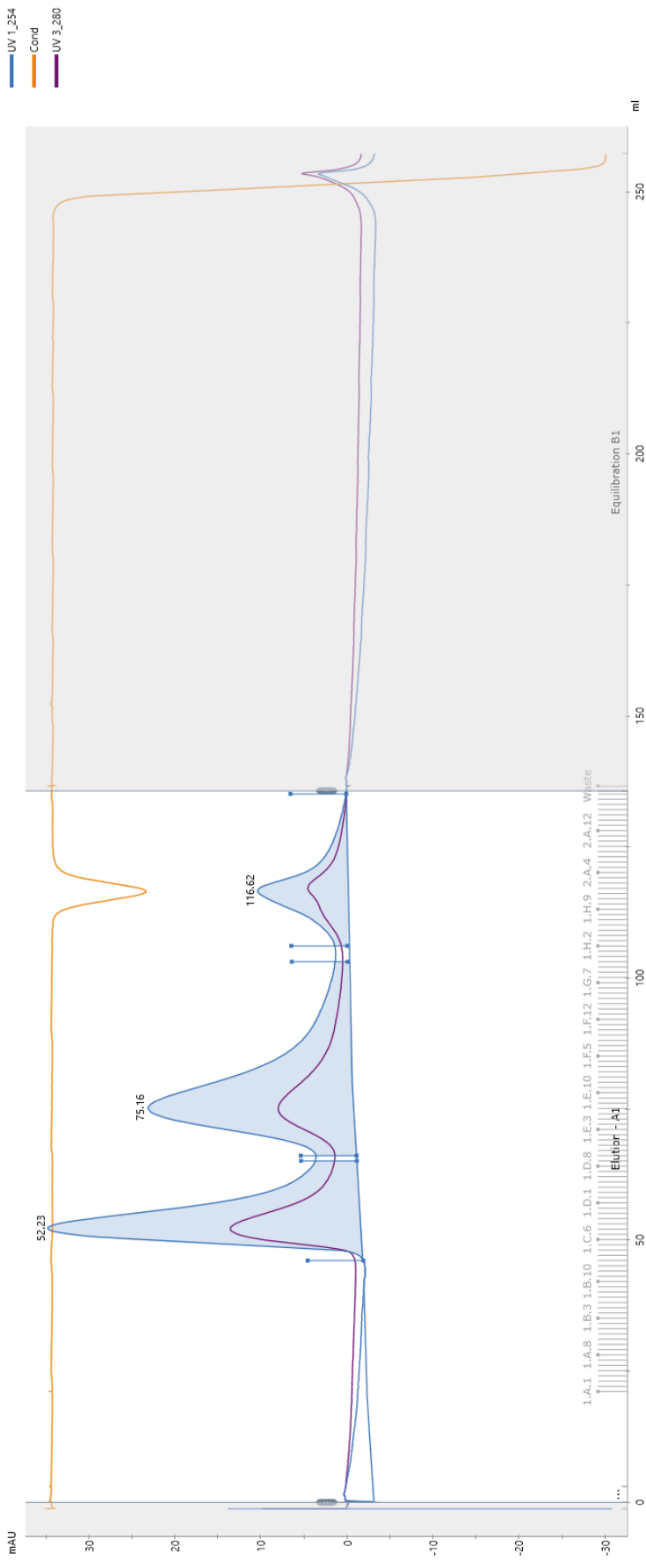


Peak Table - UV 1_254

Peak	Retention ml	Area mV.mAU	Area %	Ext coeff. mg ml ⁻¹ cm ⁻¹	Fraction(s)	Volume ml	Conductivity mS/cm
Peak A	76.847	2419	81.87		1.D.8 - 1.G.8	37.001	11.44
Peak B	116.210	535.5	18.13		1.G.12 - 2.B.5	30.000	11.22

Figure S 5. SEC chromatography output for SMA-QA DMPC nanodiscs at approximately 10 nm diameter.

2022.10.07 SMA-QA PCPG nanodisc SEC 16 60 200 loop loading 2nd run 001 001



Peak Table - UV_1_254

Peak	Retention ml	Area mAU	Area %	Ext coeff. mg ml ⁻¹ cm ⁻¹	Fraction(s)	Volume ml	Conductivity mS/cm
Peak A	52.234	305.6	40.24		1.C.2 - 1.D.8	19.001	11.62
Peak B	75.162	350.7	46.19		1.D.10 - 1.G.10	36.997	11.63
Peak C	116.617	103.1	13.57		1.H.2 - 2.B.6	29.004	11.33

Figure S 6. SEC chromatography output for SMA-QA DMPC/5% DMPG nanodiscs at approximately 10 nm diameter.

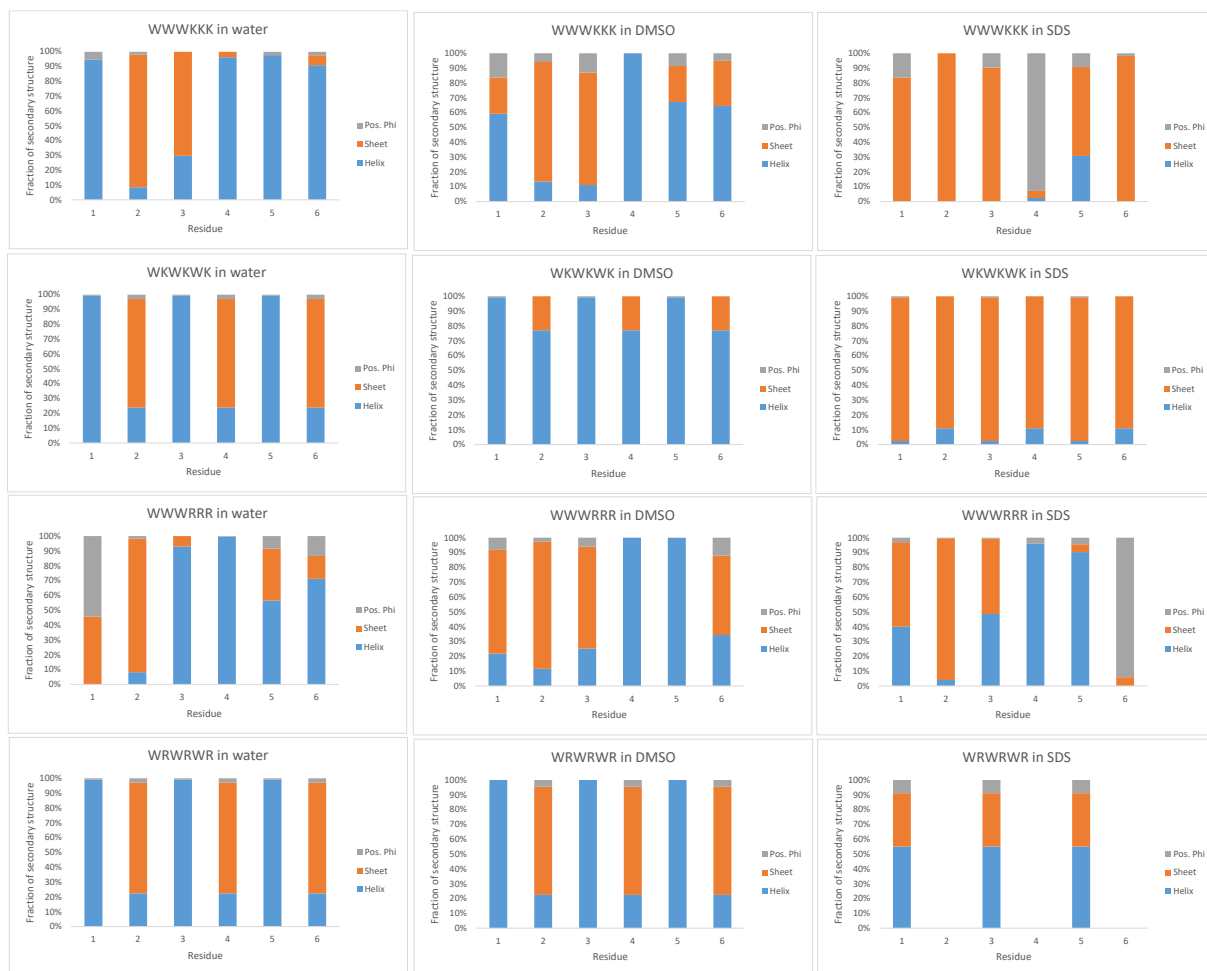


Figure S 7. 3-state phi/psi distribution prediction of the secondary structure as alpha helix, beta sheet and positive phi type of conformations in TALOS+(N). This model suggests significant changes for the lysine containing peptides in SDS compared to water, with DMSO in between, which was not the case for the direct secondary structure prediction in Figure 2.

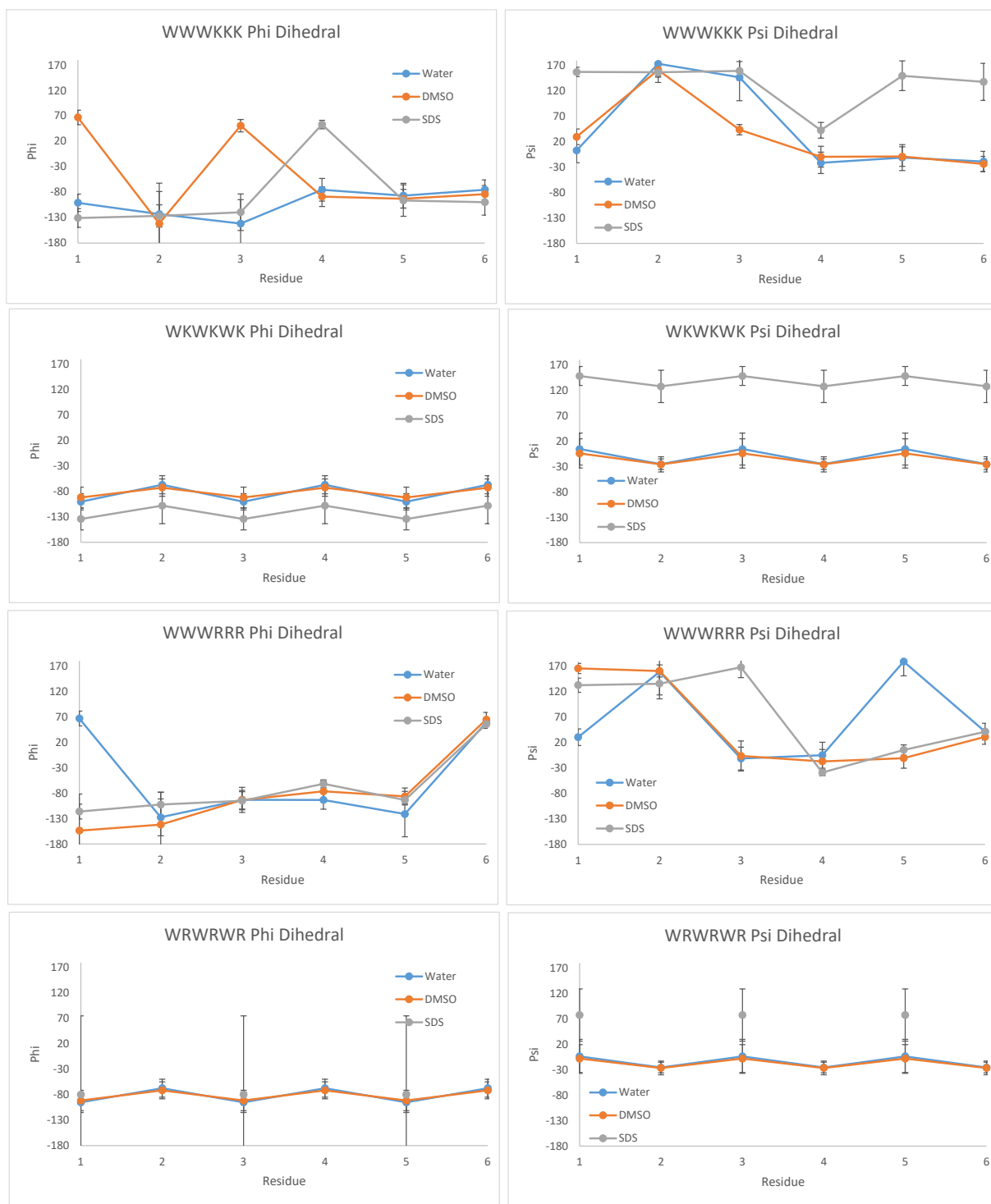


Figure S 8. Protein Backbone Torsion Angle Prediction in TALOS+(N), suggesting phi- and psi dihedral angles.

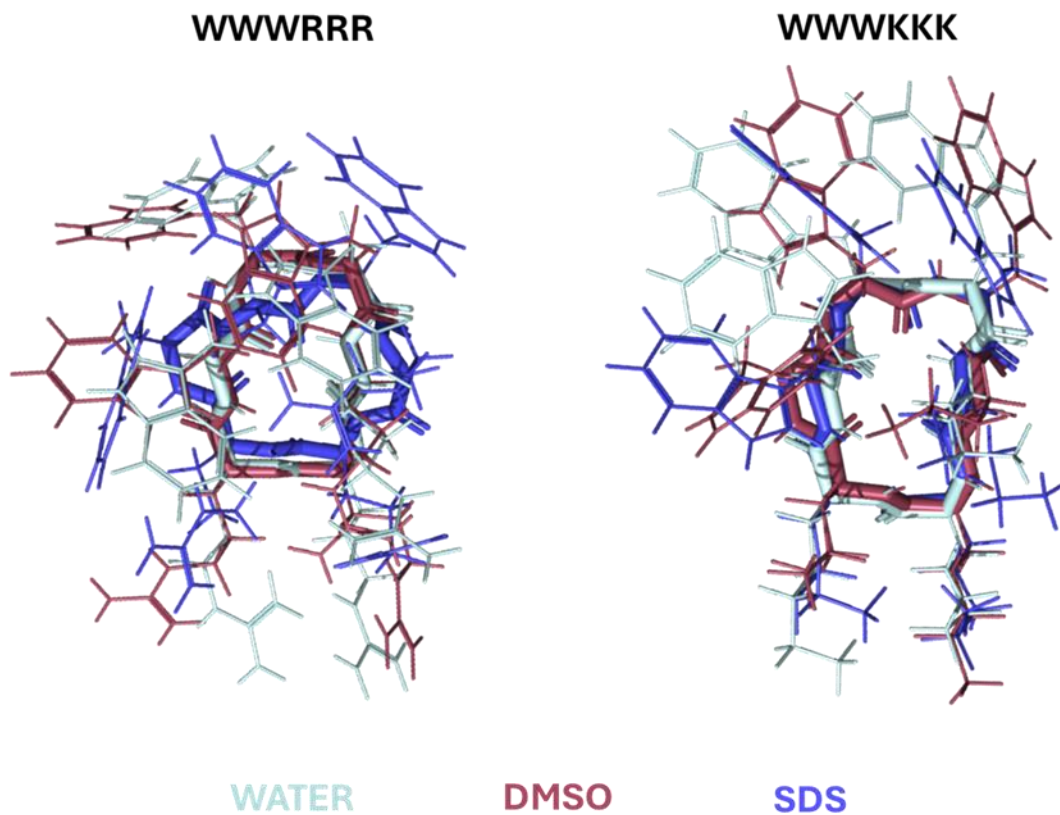


Figure S 9. Superimposed representations of average from the ten lowest energy conformations based on NOE constraints of c(WWWKKK) and c(WWWRRR) in water, DMSO, and SDS micelles.

